Alkane Separation

DOI: 10.1002/anie.201205040

Computer-Assisted Screening of Ordered Crystalline Nanoporous Adsorbents for Separation of Alkane Isomers**

David Dubbeldam, Rajamani Krishna, Sofía Calero, and Ahmet Özgür Yazaydın*

The separation of linear, mono-branched, and di-branched isomers of alkanes is of significant importance in the petrochemical industry. For example, the di-branched alkanes in the 5–7 carbon number range are preferred components of high-octane gasoline. Their selective removal from the other isomers produced in an alkane isomerization reactor can be achieved using ordered crystalline nanoporous materials, such as zeolites, metal–organic frameworks (MOFs), covalent organic frameworks (COFs), and zeolitic imidazolate frameworks (ZIFs), by exploiting subtle differences in molecular configurations. Literally, several thousands of such materials have been synthesized, making the choice of adsorbent a daunting task. Our approach is to carry out molecular simulations on a pre-screened list of more than 100 nanoporous structures. Our screening methodology demonstrates that ZIF-77, whose synthesis was reported in 2008,[1] has significantly higher selectivities, by about two orders of magnitude, over other materials that are currently used and for which patents have been issued.

In the petroleum industry, catalytic isomerization is used to convert linear alkanes into their branched isomers.[2] Isomerization processes generate a mixture of isomers that usually require separation and recycling of the non-isomerized components. For example, the effluent of a paraffin isomerization reactor may contain normal alkanes, mono-methyl alkanes and di-methyl alkanes. Traditionally, only the normal alkanes would be separated from the mixture by adsorption (e.g. using the LTA (Linde Type A) type sieve which only adsorbs linear alkanes) and recycled to the isomerization reactor, and any mono-methyl alkanes would be collected with the di-methyl alkanes as product. However, it is the di-methyl alkanes that are the most desired because they have the highest octane numbers. Therefore, a more efficient approach would be to adsorptively separate only the di-methyl alkanes as product and recycle the normal and the mono-methyl alkanes to the isomerization reactor,[3,4] schematically depicted in Figure 1. Ordered crystalline porous materials, such as zeolites, offer the potential for selective adsorption exploiting differences in molecular configurations. Zeolites are readily available, very stable, and cheap. The zeolite should have the right combination of high adsorption selectivity, combined with adequate capacity for use in traditionally used fixed-bed devices. CFI zeolite[5] and ATS zeolite[6] have been suggested for use in this separation in two patents. The undisclosed material in the patents[7,8] is most likely to be MFI-type zeolite.[9] It is of vital importance to improve the energy efficiency of this process to generate more and cleaner gasoline from every barrel of oil.

There has been a recent upsurge in next-generation nanoporous crystalline materials, such as MOFs,[10–15] COFs,[16,17] and ZIFs.[18] There are almost unlimited structural possibilities because of the wide variety of combinations of metal atoms, organic linker molecules, and the building blocks used in self-assembly during synthesis. Each year the synthesis of several hundred new structures is reported and this has created the need to screen these efficiently. There is also a need to understand structure–property relations, such as the mechanisms of alkane separation as a function of shape and size of the pore system. Molecular simulations have sufficiently advanced in both speed and accuracy to allow rapid evaluation of (hypothetical) structures for storage and/or separation devices.[19,20] The first step in our screening procedure is to pre-select, for further examination, only those nanoporous structures that have pore sizes that are large enough to accommodate alkanes molecules with seven or less carbon atoms. After this pre-screening, we performed a complete molecular simulation study on selected structures. The simulation model describes the system in full atomistic detail and is explained in detail in the Supporting Information (Section 1 on modeling and validation of the simulations). The force field we have used produces results in very good agreement with available experimental data and has good predictive capability (see Section 1 Supporting Information). The over one hundred structures we selected from zeolites, MOFs, COFs, and ZIFs provide a broad sample of available nanoporous materials. For each structure we have computed the nC6-2MP-3MP-22DMB-23DMB (nC6 = *n*-hexane, 2MP = 2-methylpentane, 3MP = 3-methylpentane, 22DMB = 2,2-dimetylbutane, 23DMB = 2,3-dimethylbutane) and nC7-2MH-3MH-22DMP-23DMP (nC7 = *n*-heptane, 2MH = 2-methylhexane, 3MH = 3-metylhexane, 22DMP = 2,2-dimethylpentane, 23DMP = 2,3-dimethylpentane) single compo-

[*] Dr. D. Dubbeldam, Prof. Dr. R. Krishna
Van't Hoff Institute for Molecular Sciences, University of Amsterdam
Science Park 904, 1098 XH Amsterdam (The Netherlands)
E-mail: D.Dubbeldam@uva.nl
Homepage: http://molsim.chem.uva.nl
Prof. Dr. S. Calero
Departamento de Sistemas Físicos, Químicos y Naturales, Universidad Pablo de Olavide, Sevilla (Spain)
Dr. A. Ö. Yazaydın
Department of Chemical Engineering, University of Surrey (UK)

[**] This work is supported by the Netherlands Research Council for Chemical Sciences (NWO/CW) through a VIDI grant (D.D.) and by the European Research Council through an ERC Starting Grant (S.C.). A.O.Y. acknowledges a Marie Curie International Reintegration Grant from the European Commission.

Supporting information for this article is available on the WWW under http://dx.doi.org/10.1002/anie.201205040.

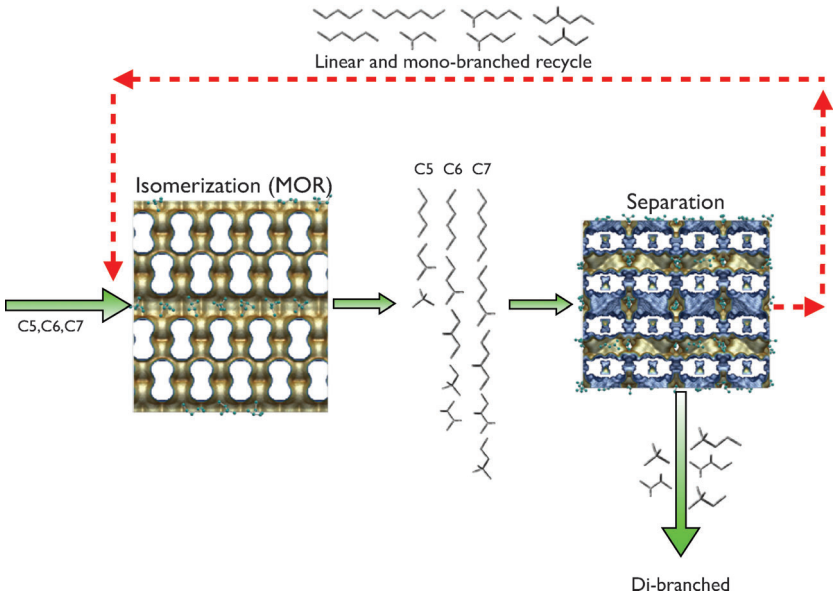

Figure 1. The separation process. The feed consists of mostly linear alkanes. In the first zone (left) linear alkanes are isomerized to branched alkanes, usually using MOR-zeolite which is first converted into the acid form and then acid-leached to increase the silica/alumina ratio. The second zone (right) separates linear and mono-branched (which are recycled back) from the desired di-branched alkanes. Our study focuses on optimizing this separation process.

nent and equimolar mixture isotherms at a typical reactor temperature of 433 K and a wide pressure range. Moreover, we computed surface areas, pore volume, and pore size distributions to relate the results to the pore size and shape. We will denote the order linear ≫ mono-branched ≫ di-branched as "normal hierarchy", and the order di-branched ≫ mono-branched ≫ linear as "reverse hierarchy". For structures that showed significant selectivity, the breakthrough (step-and pulse-style) curves of the nanoporous separation devices were computed.

In the Supporting Information we have compiled the simulation data for each structure (zeolites, MOFs, COFs, and ZIFs in Sections 3, 4, 5, and 6, respectively). Nomenclature and definitions are listed in the Supporting Information. Of all the structures examined, only a handful show an ordered adsorption hierarchy (this "shortlist" is studied in high detail in Section 2 of the Supporting Information). Figure 2 shows the mixture isotherms of highlighted structures: MFI, UiO-66, CoBDP, and ZIF-77. Previous computational studies found high selectivities occurring in MFI zeolite,[9,21,22] and the CoBDP metal–organic framework.[23] Recently, it has been reported (experimentally) that UiO-66 shows reverse shape selectivity: 22DMB = 23DMB > 3MP ≫ nC6.[24] Our simulated mixture isotherms (Figure 2c) as well as the simulated breakthrough for UiO-66 (Supporting information, Figure S6) agree well with this experimental finding. Herein we newly report the use of ZIF-77 for alkane separation, and Figure 2d shows the superior behavior of the ZIF-77 mixture isotherms. In contrast to MFI-zeolite, which has its highest efficiency at pressures that are unlikely to be obtainable in industrial applications, the ZIF-77 can operate efficiently at all pressures.

Figure 3a shows the selectivity of the most promising structures. The simulations appear to provide support of the information in the patent literature about the effectiveness of CFI and MFI zeolites for separation of hexane isomers. However, our simulations show that selectivity improvements by one to two orders of magnitude are possible by use of ZIF-77. Besides selectivity, it is also the capacity of the material that determines the efficiency of a separation device. In pressure swing adsorbers, higher adsorption capacities are desirable because they result in lower frequencies in the regeneration cycles.[25] Figure 3b compares the adsorption selectivity and capacity for various structures. ZIF-77 has not only a much higher adsorption selectivity, but at the same time has a comparable capacity to CFI- and MFI-zeolite. COF-102 and COF-103 have a very high capacity but low adsorption selectivity. The CoBDP and UiO-66 structures are in between; they have moderate selectivities combined with intermediate capacities. To demonstrate the separation potential of ZIF-77 we performed pulse chromatographic simulations. Figure 4 shows ZIF-77 is able to fractionate the components individually on the basis of the degree of branching. None of the other examined structure is able to do this; evidence provided in Supporting Information Figure S17, S24, S31, S38, S45, and S52. Note each component in the mixture seems to behave independently of the type of mixture it is in, as is evidenced by the fact that the breakthrough of the component pulses occurs at the same time, irrespective of whether it is present in a 5-component or 13-component mixture.

To provide insights into the reasons for the differences in selectivities of various structures we performed a systematic study of graphite slits and square channels of varying widths, and carbon nanotubes of different diameters. Graphite slits have been artificially kept at a fixed distance. The channels have been created by intersecting sheets orthogonally with other sheets. From the enthalpy of adsorption at large spacings and low loadings (i.e. this corresponds to the adsorption of a single molecule on a surface), plotted in Figure 5a relative to nC6, we find that natural order of adsorption on a flat surface is the normal hierarchy (see also Sections 8, 9, and 10, Supporting Information). The enthalpies for mono-branched molecules are higher than nC6 and the enthalpies of di-branches are even higher in energy. The normal hierarchy is therefore the order that would be expected and any modifications to the normal order are due to the specific confinement that favors specific molecules. This occurs at confinements around 6–7 Å, where the di-branched molecules fit most snugly because they interact strongly with multiple walls. The spacings of 5 Å and smaller deserve special attention. In this region, there is very strong confinement and size exclusion. In Figure 5b we show that the

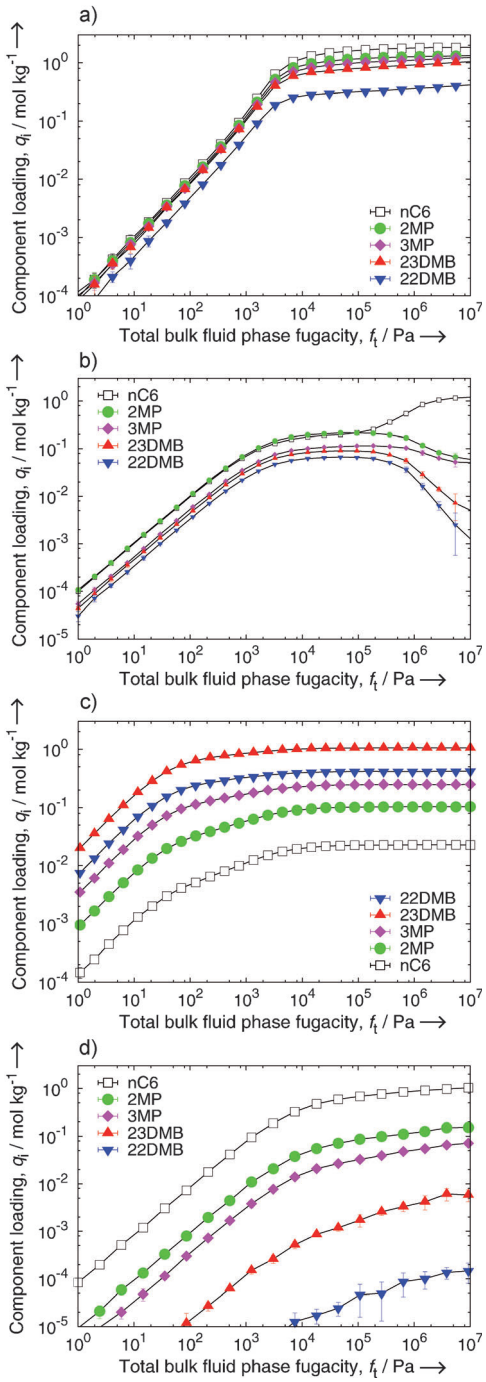

Figure 2. Equimolar mixture isotherms of C6 isomers in a) CoBDP, b) MFI, c) UiO-66, and d) ZIF-77 at 433 K.

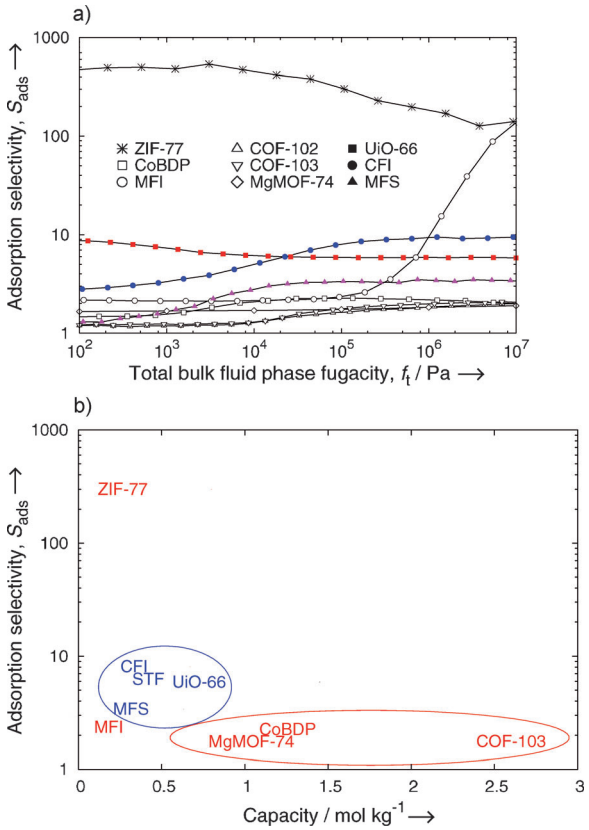

Figure 3. Summary of the screening results: the adsorption selectivity S_{ads}, a) as a function of the total bulk fluid phase fugacity at 433 K, and b) versus capacity for promising structures at 100 kPa. Typical operational reactor pressures are above atmospheric (above 10^5 Pa fugacity). Consider the separation of 5-component hexane isomer mixtures of nC6 (=component 1), 2MP (=component 2), 3MP (=component 3), 23DMB (=component 4), and 22DMB (=component 5) with partial fugacities, f_i, and corresponding loadings, q_i (where i=component number). For materials showing the normal hierarchy (star and open symbols in (a), red in (b)), S_{ads} is defined as $S_{ads}=[(q_1+q_2+q_3)/(q_4+q_5)]/[(f_1+f_2+f_3)/(f_4+f_5)]$, and the capacity as the averaged loadings of linear and mono-branched isomers. For materials with a reverse adsorption hierarchy (closed symbols in (a), blue in (b)), we defined $S_{ads}=[(q_4+q_5)/(q_1+q_2+q_3)]/[(f_4+f_5)/(f_1+f_2+f_3)]$, and capacity as the averaged loadings of the di-branched isomers.

reverse hierarchies we found are all in the 6–7 Å range. Below that range it is possible to have high selectivity (as observed for ZIF-77) owing to strong confinement and size-exclusion, and above the 6–7 Å region we also find the normal hierarchy with lower selectivities. Note that Figure 3b and 5b are qualitatively similar, and spacing and capacity go hand-in-hand. The selectivity is inversely related to spacing.

We have now the necessary information to rationalize the adsorption behavior of hexane isomers as a function of structure. Two hierarchies are possible: the normal hierarchy and the reverse hierarchy. The reverse hierarchy, as observed for UiO-66 and CFI, can only be found in strong-confinement structures and will therefore correspond to structures with relatively small pore volumes. An important disadvantage of the reverse hierarchy is that the hierarchy of the diffusion coefficient is the opposite to the hierarchy of adsorption strengths. The reverse hierarchy structure does show higher selectivities though, but much lower than ZIF-77 and MFI (at very high pressures). In contrast, for the normal adsorption hierarchy the normal hierarchy of diffusivities would enhanced the separation further (e.g. for MFI and ZIF-77). The ZIF-77 has a 2D channel system with larger main channels and smaller side channels. The larger main channels size-exclude the di-branched molecules, while the smaller channels size-exclude the mono- and di-branched. Also of

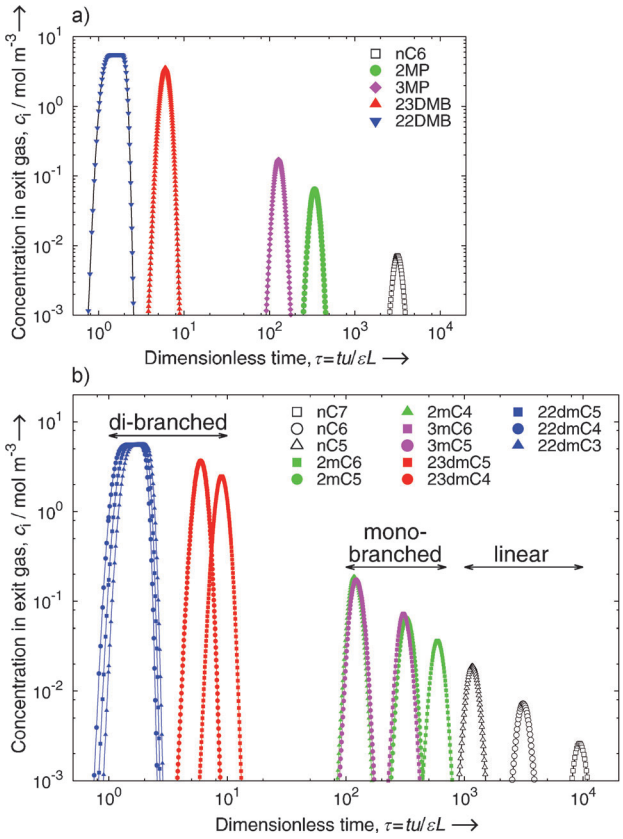

Figure 4. Simulated pulse-style breakthrough curves of a) C6 isomers, b) C5/C6/C7 isomers in ZIF-77 at partial fugacities of the bulk fluid phase of 20 kPa and 433 K. The pulse-style breakthrough clearly shows that ZIF-77 is able to fractionate the individual components of a C6 mixture, and when it is fed an alkane mixture differing in chain length it is still able to fractionate the mixture into linear, mono-branched, and di-branched components. Video animations of the breakthrough behavior as a function of time of ZIF-77 and other selected structures are provided as Supporting Information.

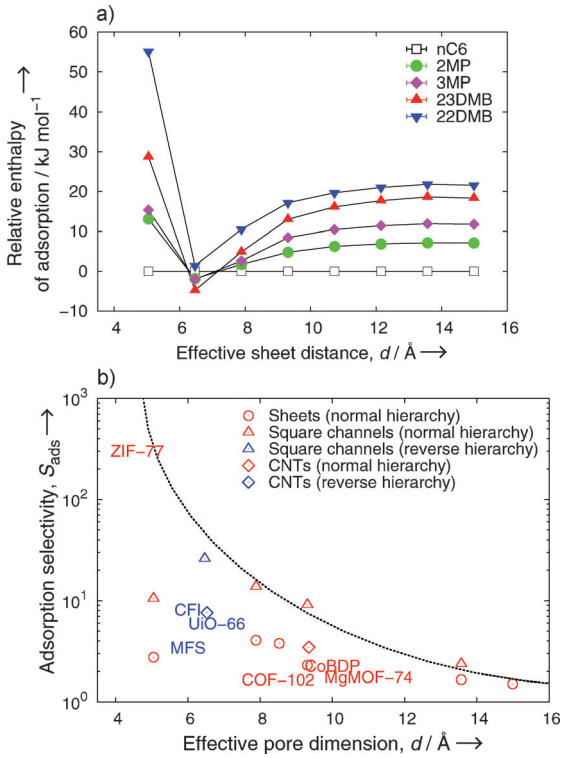

Figure 5. Hexane isomer selectivity at 433 K as a function of confinement, a) enthalpy of adsorption relative to nC6 for graphite square channels at infinite dilution, b) adsorption selectivity at 100 kPa. Red denotes normal hierarchy, blue reverse hierarchy, the dotted line shows the qualitative behavior of the selectivity.

high interest is CoBDP which combines good selectivity with a high pore volume. The qualitative shape of the isotherms at about 9.3 Å (see subsection 8.10 and 9.4 of the Supporting Information) agrees well with the isotherms obtained for the CoBDP structure. As the results for a smaller spacing appear qualitatively better, it seems possible to optimize the CoBDP structure further by making it slightly smaller. The CoBDP channel is corrugated, because of rotation of the linker molecule, and only approximately rectangular and actually a combination of optimal parts with sub-optimal parts. In the Supporting Information (Section 7) we show results for various modifications of a pseudo-version of CoBDP, created using the Materials Studio Visualizer.[26] We have made the structure rectangular and changed the linker molecule BDP (benzenedipyrazolate) to ADP (acetylenedipyrazolate), BP (bipyrazolate), and BPDP (biphenyldipyrazolate). None of these hypothetical structures are significantly better, indicating that it might be non-trivial to reduce or extend the channel dimensions of crystalline materials by altering the organic linker molecules.

Large-pore MOFs do not show significant alkane selectivity; most of the pore-volume is unused and non-selective. Note that in a square channel, all available pore volume is used. The cylindrical channels we studied are known as carbon nanotubes (CNTs). CNTs are unlikely to be as efficient as the square channels owing to the large amount of unused pore volume. As with a square channel, triangular and honeycomb channel systems would also utilize all of the available pore volume. A honeycomb structure can possibly be made from graphene sheets.[27] Other interesting alkane/carbon-framework systems include mesoporous silica with intraporous nanocarbon.[28]

Our discovery of the unique separation capability of the ZIF-77 would not have been unearthed using a conventional screening study based on, for example, pore size distributions. The reason is that the pores of ZIF-77 are highly non-cylindrical. The pore size distribution of ZIF-77 could be wrongly interpreted as that there are no pores larger than 4.5 Å in diameter. However, this is the shortest distance, and in the other direction the pore is much larger. In fact, linear, mono-branched, and 2,3-di-branched alkanes fit in. Simulations were conducted to compute the self-diffusion coefficients at 433 K and infinite dilution. The hierarchy of diffusivities is linear > mono-branched > 2,3-di-branched ≫ 2,2-di-branched. The 2,2-di-branched is too bulky to enter the pore system. It would be challenging to refine currently used conventional screening methods to be able to detect

systems like ZIF-77. But as we show herein, currently it is feasible to analyze over a 100 structures in full detail, and with current advances in computational efficiency, future screenings could handle many, many more structures.

In conclusion, we have rationalized the adsorption behavior of hexane (and heptane) isomers and our screening study provides a thorough understanding. First, it is an ill-advised endeavor to use large-pore MOFs for alkane separations. Above a certain threshold (depending on the alkane chain-length) the excess pore volume just goes to waste. Below the threshold for selectivity, both branching hierarchies are possible, but the one corresponding to the largest pore volume (the normal hierarchy) is probably most efficient, also because adsorption and diffusion selectivity go hand-in-hand. To properly evaluate a structure at least a 5-component mixture is needed, with both the 2,2-di-branched and the 2,3-di-branched included, as these have usually very different behaviors. The simulated breakthrough curves provide the best way of assessing the efficiency of a structure. The efficiency depends on a) the selectivity, and b) the accessible pore volume. CoBDP provides a very good compromise between the two, but the selectivity of ZIF-77 is so high that this sieve fractionates to yield individual pure components. The screening strategy we presented can be applied to other problems, such as, for example, separating alkane mixtures with C_{10}–C_{18} hydrocarbons[29] and xylene isomers.[30]

Methods Section

The adsorption computations of single and multi-components are performed using the configurational-bias Monte Carlo algorithm in the grand-canonical ensemble. The systems are modeled in full atomistic detail using calibrated classical force fields. Periodic boundary conditions are used to extrapolate the finite system results to macroscopic bulk values. We checked for finite size and hysteresis effects and both were found to be negligible. Using the dual-site Langmuir–Freundlich fits of the pure component isotherms, breakthrough calculations were carried out by solving a set of partial differential equations for each of the species in the gas mixture. The molar loadings of the species at any position along the packed bed and at any time are determined from ideal adsorbed solution theory calculations. Video animations of the breakthrough behavior as a function of time of selected structures are provided as Supporting Information.

Received: June 27, 2012
Published online: October 19, 2012

Keywords: adsorption · alkane separation · metal–organic frameworks · molecular simulations · ZIF-77

[1] R. Banerjee, A. Phan, B. Wang, C. Knobler, H. Furukawa, M. O'Keeffe, O. Yaghi, *Science* **2008**, *319*, 939 – 943.
[2] W. Vermeiren, J.-P. Gilson, *Top. Catal.* **2009**, *52*, 1131 – 1161.
[3] S. C. Stem, W. Evans, United States Patent No. 4855529, **1989**.
[4] S. C. Stem, W. Evans, United States Patent No. 4804802, **1989**.
[5] T. Maesen, T. Harris, United States Patent No. 7037422, **2006**.
[6] T. Maesen, T. Harris, United States Patent No. 7029572, **2006**.
[7] H. Dandekar, G. Funk, R. Gillespie, H. Zinnen, C. McGonegal, M. Kojima, S. Hobbs, United States Patent No. 5763730, **1998**.
[8] H. Dandekar, G. Funk, H. Zinnen, United States Patent No. 6069289, **2000**.
[9] S. Calero, B. Smit, R. Krishna, *Phys. Chem. Chem. Phys.* **2001**, *3*, 4390 – 4398.
[10] M. Eddaoudi, J. Kim, N. Rosi, D. Vodak, J. Wachter, M. O'Keeffe, O. Yaghi, *Science* **2002**, *295*, 469 – 472.
[11] O. M. Yaghi, M. O'Keeffe, N. W. Ockwig, H. K. Chae, M. Eddaoudi, J. Kim, *Nature* **2003**, *423*, 705 – 714.
[12] S. Kitagawa, R. Kitaura, S. Noro, *Angew. Chem.* **2004**, *116*, 2388 – 2430; *Angew. Chem. Int. ed.* **2004**, *43*, 2334 – 2375.
[13] R. Q. Snurr, J. T. Hupp, S. T. Nguyen, *AIChE J.* **2004**, *50*, 1090 – 1095.
[14] U. Mueller, M. Schubert, F. Teich, H. Puetter, K. Schierle-Arndt, J. Pastre, *J. Mater. Chem.* **2006**, *16*, 626 – 636.
[15] G. Férey, *Chem. Soc. Rev.* **2008**, *37*, 191 – 214.
[16] A. Côté, A. Benin, N. Ockwig, M. O. A. Matzger, O. Yaghi, *Science* **2005**, *310*, 1166 – 1170.
[17] H. El-Kaderi, J. Hunt, J. Mendoza-Cortés, A. Côté, R. Taylor, M. O'Keeffe, O. Yaghi, *Science* **2007**, *316*, 268 – 272.
[18] K. Park, Z. Ni, A. Côté, J. Choi, R. Huang, F. Uribe-Romo, H. Chae, M. O'Keeffe, O. Yaghi, *Proc. Natl. Acad. Sci. USA* **2006**, *103*, 10186 – 10191.
[19] C. Wilmer, M. Leaf, C. Lee, O. Farha, B. Hauser, J. Hupp, R. Snurr, *Nat. Chem.* **2012**, *4*, 83 – 89.
[20] E. Haldoupis, S. Nair, D. Sholl, *J. Am. Chem. Soc.* **2012**, *134*, 4313 – 4323.
[21] R. Krishna, B. Smit, S. Calero, *Chem. Soc. Rev.* **2002**, *31*, 185 – 194.
[22] R. Krishna, J. van Baten, *Sep. Purif. Technol.* **2007**, *55*, 246 – 255.
[23] R. Krishna, J. van Baten, *Phys. Chem. Chem. Phys.* **2011**, *13*, 10593 – 10616.
[24] P. Bárcia, D. Guimarães, P. Mendes, J. Silva, V. Guillerm, H. Chevreau, C. Serre, A. Rodrigues, *Microporous Mesoporous Mater.* **2011**, *139*, 67 – 73.
[25] R. Krishna, J. Long, *J. Phys. Chem. C* **2011**, *115*, 12941 – 12950.
[26] Accelrys Materials Studio for materials modeling & simulation, http://accelrys.com/products/materials-studio/.
[27] S. Yin, Y. Zhang, J. Kong, C. Zhou, C. Li, X. Lu, J. Ma, F. Boey, X. Chen, *ACS Nano* **2011**, *5*, 3831 – 3838.
[28] F. de Clippel, A. Harkiolakis, X. Ke, T. Vosch, G. Van Tendeloo, G. V. Baron, P. Jacobs, J. F. M. Denayer, B. F. Sels, *Chem. Commun.* **2010**, *46*, 928 – 930.
[29] S. Raghuram, S. Wilcher, *Sep. Sci. Technol.* **1992**, *27*, 1917 – 1954.
[30] D. Peralta, G. Chaplais, A. Simon-Masseron, K. Barthelet, C. Chizallet, A.-G. Quoineaud, G. Pirngruber, *J. Am. Chem. Soc.* **2012**, *134*, 8115 – 8126.

Angewandte Chemie
Eine Zeitschrift der Gesellschaft Deutscher Chemiker

Supporting Information

69451 Weinheim, Germany

Computer-Assisted Screening of Ordered Crystalline Nanoporous Adsorbents for Separation of Alkane Isomers**

David Dubbeldam, Rajamani Krishna, Sofía Calero, and Ahmet Özgür Yazaydın*

anie_201205040_sm_miscellaneous_information.pdf

Nomenclature

nC4	butane
2mC3	2-methylpropane (isobutane)
nC5	pentane
2MB or 2mC4 or isoC5	2-methylbutane
22dmC3 or neoC5	2,2-dimethylpropane (neopentane)
nC6	hexane
2MP or 2mC5	2-methylpentane
3MP or 3mC5	3-methylpentane
23DMB or 23dmC4	2,3-dimethylbutane
22DMB or 22dmC4	2,2-dimethylbutane
nC7	heptane
2MH or 2mC6	2-methylhexane
3MH or 3mC6	3-methylhexane
23DMP or 23dmC5	2,3-dimethylpentane
22DMP or 22dmC5	2,2-dimethylpentane
SWNT	single wall nanotube
MOF	metal-organic framework
ZIF	zeolitic imidazolate framework
COF	covalent organic framework
ADP	acetylenedipyrazolate
BP	bipyrazolate
BPDP	biphenyldipyrazolate
NDC	2,6-naphthalenedicarboxylate
BPDC	4,4′-biphenyldicarboxylate
BDC	1,4-benzenedicarboxylate
H_2BDC	1,4-benzenedicarboxylate acid
BTC	1,3,5-benzenetricarboxylate
BTB	benzene-1,3,5-tribenzoate
TPDC	[1,1′:4′,1″-terphenyl]-3,3″-dicarboxylate
BTEI	5,5′,5″-(benzene-1,3,5-triyltris(ethyne-2,1-diyl))triisophthalate
PTEI	5,5′-((5′-(4-((3,5-dicarboxylatophenyl)ethynyl)phenyl)-[1,1′:3′,1″-terphenyl]-4,4″-diyl) bis(ethyne-2,1-diyl))diisophthalate
DABCO	1,4-diazabicyclo[2.2.2]octane
DMTRZ	3,5-dimethyl-1,2,4-triazolate
BDP	1,4-benzenedipyrazolate
NDP	naphthalenedipyrazolate
NDC	naphthalenedicarboxylate
DOBDC	2,5-dioxido-1,4-benzene-dicarboxylate
IM	imidazolate
mIM	methylimidazolate
nIM	nitrobenzimidazolate
bIM	benzimidazole
dcIM	4,5-dichloroimidazole
4me5alIM	4-methylimidazole-5-carbaldehyde
4cy5amIM	4-aminoimidazole-5-carbonitrile
mehylIM	4-hydroxymethyl-5-methylimidazole
CBMC	Configurational Bias Monte Carlo
MC	Monte Carlo
MD	Molecular Dynamics
DSLF	dual-site Langmuir-Freundlich
IAST	Ideal Adsorbed Solution Theory

Notation

a, b, c	the crystallographic cell vectors, Å
A	surface area, m^3
$b_{i,A}$	dual-Langmuir-Freundlich constant for species i at adsorption site A, $Pa^{-\nu_i}$
$b_{i,B}$	dual-Langmuir-Freundlich constant for species i at adsorption site B, $Pa^{-\nu_i}$
C_{ads}	adsorption capacity, mol kg^{-1}
D_S	self-diffusion coefficient, m s^{-2}
f_i	partial fugacity in the bulk fluid phase of species i in mixture, Pa
h	Planck constant, 6.626068×10^{-34} m^2 kg s^{-1}
ΔH	enthalpy of adsorption, kJ mol^{-1}
$\mathcal{H}$	the box matrix (has the crystallographic cell vectors a, b, c as columns)
k_B	Boltzmann constant, m^2 kg s^{-2} K^{-1}
L	length of packed bed adsorber, m
m	mass, kg
N	number of molecules, dimensionless
P	pressure of the bulk fluid phase, Pa
q_i	component molar loading of species i, mol kg^{-1}
r	Cartesian atomic position, m
R	gas constant, 8.314464919 J mol^{-1} K^{-1}
s	fractional atomic position, dimensionless
S_{ads}	adsorption selectivity, dimensionless
t	time, s
T	absolute temperature, K
u	superficial gas velocity entering the packed bed, m s^{-1}
U	energy, J=kg m^{-2} s^{-2}
V	volume of the system, $Å^3$
W^{new}, W^{old},W^{IG}	Rosenbluth weights of a new, old, and ideal gas chain respectively, dimensionless
Q	heat of adsorption, kJ mol^{-1}
z	distance along the adsorber, m

Greek letters

α, β, γ	the crystallographic cell angles, degrees
β	inverse temperature, units of inverse energy (βU is dimensionless)
ϵ/k_B	the Lenard-Jones strength parameter, K
ε	voidage of packed bed, dimensionless
$\Lambda = \sqrt{h^2/(2\pi m k_B T)}$	the thermal de Broglie wavelength, m
ν	exponent in dual-Langmuir-Freundlich isotherm, dimensionless
ρ	framework density, kg m^{-3}
σ	the Lennard-Jones size parameter, Å
τ	time, dimensionless
θ, ϕ, χ	bend,torsion,out-of-plane angle, radians
ξ	the helium void fraction, dimensionless

Subscripts

i	referring to component i
t	referring to the total mixture
A	referring to site A
B	referring to site B

Contents

1 Simulation details

1.1 Force field

1.1.1 Introduction

The molecular energy can be described as an Taylor expansion in bonds, bends, torsions, etc.

$$\begin{aligned} U = & \sum_{\text{bonds}} U_r(r) + \sum_{\text{bends}} U_\theta(\theta) + \sum_{\text{torsions}} U_\phi(\phi) + \sum_{\text{out-of-plane bends}} U_\chi(\chi) + \sum_{\text{non-bonded}} U_{nb}(r) \\ & + \sum_{\text{bond-bond}} U_{bb'}(r, r') + \sum_{\text{bond-bend}} U_{b\theta'}(r, \theta) + \sum_{\text{bend-bend}} U_{\theta\theta'}(\theta, \theta') \\ & + \sum_{\text{bond-torsion}} U_{r\phi}(r, \phi, r') + \sum_{\text{bend-torsion}} U_{\theta\phi}(\theta, \phi, \theta') + \dots \end{aligned} \tag{1.1}$$

This expansion is believed to capture all the chemical entities we can think of, such as atoms, bonds, angles, etc, and physical properties like equilibrium structures, vibrational spectra, etc. The cross terms are not ad-hoc functions, but arise naturally from this expansion. For example, bonds and bends interact, as the bend angle becomes smaller the bond lengths tend to increase. Their inclusion leads to two advantages: 1) they increase the accuracy of the force field (especially the vibrational frequencies), and 2) they increase the transferability of the diagonal terms $U_r(r), U_\theta(\theta), U_\phi(\phi), U_\chi(\chi)$. On top of the terms in Eq. 1.1 one can add ad hoc terms, such as hydrogen bonding, that are not adequately accounted for otherwise.

Eq. 1.1 is historically referred to as an *force field*. The name arose from the lowest order approximation using only springs with *force constants*. Force fields have matured and have become quite accurate and many parameters exists for a wide range of structures. These parameters are crucial and determine the quality of the force field.

For more details on molecular simulations in general we refer to: "Statistical Mechanics: Theory and Molecular Simulations" by M. Tuckerman [1], "Computer Simulations of Liquids" by M.P. Allen and D.J. Tildesley [2], "Understanding Molecular Simulations: from Algorithms to Applications" by D. Frenkel and B. Smit [3], "The Art of Molecular Dynamics Simulation" by D.C. Rapaport[4], and "Molecular Modeling: Principles and Applications" by A. Leach [5].

1.1.2 Alkane model

Alkanes are ubiquitous in industrial processes and form the building blocks of biological systems. Alkanes are generally inert to chemical reagents. Carbon-carbon and carbon- hydrogen bonds are strong, and do not break unless heated to high temperatures. Similar electronegativities result in little polarization, so alkanes are generally unaffected by most bases. There are no unshared electrons in alkanes for attack by acids. They

stretch	r_0 [Å]	k_b/k_B [K]
CH_x-CH_x	1.54	96500
bend	θ_0	k_θ/k_B [K]
CH_x-(CH_2)-CH_y	114	62500
CH_x-(CH)-CH_y	112	62500
CH_x-(C)-CH_y	109.47	62500

LJ	ϵ/k_B [K]	σ [Å]
CH_4	158.5	3.72
CH_3	108.0	3.76
CH_2	56.0	3.96
CH	17.0	4.67
C	0.8	6.38

torsion	c_0/k_B [K]	c_1/k_B [K]	c_2/k_B [K]	c_3/k_B [K]
CH_x-(CH_2)-(CH_2)-CH_y	0	335.03	-68.19	791.32
CH_x-(CH_2)-(CH)-CH_y	-251.06	428.73	-111.85	441.27
CH_x-(CH_2)-(C)-CH_y	0	0	0	461.29
CH_x-(CH)-(CH)-CH_y	-251.06	428.73	-111.85	441.27
CH_x-(CH)-(C)-CH_y	0	0	0	1635.7

Table S1: *Stretch, bend, and torsion parameters for alkanes. The parameters are from the TRAPPE force field [6, 7], with the exception of the bond-potential taken from Ref. [9], the (CH)-(C) torsion which is taken from Ref. [10], and the modification of the Lennard-Jones parameters for shifted potentials [11]*

are non-polar and consists of a small number of groups, making them historically the logical starting point for potential model development.

We have used the TraPPE force field by Martin and Siepmann [6, 7]. The force field describes linear alkanes but also mono-branched as well as di-branched alkanes. Despite the fact that the model lumps CH_3, CH_2, and CH into single interaction centers, it very accurately reproduces the experimental phase diagram and critical points. This united atom approach allows for a much longer simulation times and larger systems because each of the CH_x-groups is charge-neutral and charge-charge interaction can be neglected. This order of magnitude gain results in no significant loss in accuracy compared to full-atom models, i.e. deviations from experimental data are comparable to the full-atom TraPPE model [8].

The force field used here is primarily designed to reproduce thermodynamic properties of guest molecules in a host system at minimal computational cost. The internal structure of the guests and the guest-guest interactions are of less importance because the properties are dominated by the strong interaction with the force field exerted by the host. Adsorption in cation-free structures takes place at sites with little or no electric field. For these reasons the united atom model [12] seems the most straightforward choice. We consider the CH_x groups as single, chargeless interaction centers with their own effective potentials. A harmonic cosine bending potential models the bond bending between three neighboring beads, a three-cosine potential controls the torsional angle. The beads in a chain separated by more than three bonds interact with each other through a Lennard-Jones potential. The Lennard-Jones potentials are shifted and cut at 12 Å. Analytical tail-corrections do not apply in nanoporous materials [13]. A truncated and shifted potential is equally suitable to Monte Carlo and Molecular Dynamics. The functional form of the TraPPE-like model is

$$U^{\text{bond}} = \sum_{\text{bonds}} \frac{1}{2} k_b (r - r_0)^2, \tag{1.2}$$

$$U^{\text{bend}} = \sum_{\text{bends}} \frac{1}{2} k_\theta (\theta - \theta_0)^2, \tag{1.3}$$

$$U^{\text{torsion}} = \sum_{\text{torsions}} c_0 + c_1 \left[1 + \cos(\phi)\right] + c_2 \left[1 - \cos(2\phi)\right] + c_3 \left[1 + \cos(3\phi)\right] \tag{1.4}$$

$$U_{ij}^{\text{LJ}} = \sum_{\text{LJ-pairs}} 4\epsilon_{ij} \left[\left(\frac{\sigma_{ij}}{r_{ij}} \right)^{12} - \left(\frac{\sigma_{ij}}{r_{ij}} \right)^{6} \right] - E_{\text{cut}}, \tag{1.5}$$

where k_b is the bond energy constant, r_0 the reference bond length, k_θ the bend energy constant, θ_0 the reference bend angle, ϕ the dihedral angle, c_n/k_B in K denote the four torsion parameters, r_{ij} is the distance between site i and site j, $r_{\text{cut}} = 12.0$ Å, the cutoff radius, E_{cut} the energy at the cut-off radius, and $U_{ij}^{\text{LJ}} = 0$ when $r_{ij} > r_{\text{cut}}$. The Lennard-Jones potential consists of two parameters, σ is the size-parameter, and ϵ is the

	O_{Si}	O_{Al}	Si	Al	CH_4	CH_3	CH_2	CH	C	Na
CH_4	115.00 3.47	115.00 3.47	-	-	158.50 3.72	130.84 3.74	94.21 3.84	51.91 4.20	11.26 5.05	582.17 2.72
CH_3	93.00 3.48	93.00 3.48	-	-	130.84 3.74	108.00 3.76	77.77 3.86	42.85 4.22	9.30 5.07	443.73 2.65
CH_2	60.50 3.58	60.50 3.58	-	-	94.21 3.84	77.77 3.86	56.00 3.96	30.85 4.32	6.69 5.17	310.0 2.95
CH	40.00 3.92	40.00 3.92	-	-	51.91 4.20	42.85 4.22	30.85 4.32	17.00 4.67	3.69 5.53	292.0 2.58
C	10.00 4.56	10.00 4.56	-	-	11.26 5.05	9.30 5.07	6.69 5.17	3.69 5.53	0.8 6.38	126.0 2.71
Na	23.00 3.4	23.00 3.4	-	-	582.17 2.72	443.73 2.65	310.0 2.95	292.0 2.58	126.0 2.71	– –
charge	$q = -1.025$	$q = -1.2$	$q = +2.05$	$q = +1.75$	-	-	-	-	-	$q = +1.0$

Table S2: *Zeolite force field*

strength-parameter. Cross terms between atoms of different types are computed using Lorentz-Berthelot mixing rules

$$\epsilon_{ij} = \sqrt{\epsilon_i \times \epsilon_j} \qquad \sigma_{ij} = \frac{\sigma_i + \sigma_j}{2} \tag{1.6}$$

1.1.3 Zeolite model

Following the work of Bezus et al. [14], the zeolites are modeled as a rigid network of oxygen atoms. This is a very common approximation because the large oxygen atoms essentially shield the much smaller silicon atoms and lattice flexibility is not important for small alkanes in all-silica zeolites [15]. Periodic boundary conditions are commonly applied to overcome the problems of surface effects. The original simulation box, including all the atoms within it, is replicated throughout space. When a molecule in the original box moves, its periodic images in each of the surrounding boxes moves in exactly the same way. If a molecule leaves the central box, one of its images will enter the box through the opposite face. It is not necessary to store the coordinates and momenta of all the images, only the ones in the central box are needed, because the images can be obtained from translation operators. Usually, one imposes the minimum-image convention: the distance between two particles is taken to be the shortest distance between their periodic images. The boundary of the periodic box does not have any physical significance, only the shape and orientation.

In crystallography, the crystal structure is defined by the unit cell (cell lengths a, b, c and angles α, β, γ), and by the fractional coordinates of the atoms within the unit cell. These coordinates form an orthonormal dimensionless $\mathcal{S}$-space. The transformation from $\mathcal{S}$-space to real $\mathcal{R}$-space can be carried out by the matrix $\mathcal{H}$:

$$\mathcal{H} = \begin{pmatrix} a & b\cos(\gamma) & c\cos(\beta) \\ 0 & b\sin(\gamma) & c\zeta \\ 0 & 0 & c\sqrt{1-\cos^2\beta-\zeta^2} \end{pmatrix} \tag{1.7}$$

with

$$\zeta = \frac{\cos\alpha - \cos\gamma\cos\beta}{\sin\gamma} \tag{1.8}$$

Conversely, $\mathcal{H}^{-1}$ transforms real coordinates to fractional coordinates. With the chosen $\mathcal{H}$ the scaled box has a length of 1. Our potential forcefield is defined in real space, therefore it is convenient to store position in $\mathcal{R}$ space, transform them to $\mathcal{S}$ space, apply periodic boundary conditions in $\mathcal{S}$ space, and transform back to $\mathcal{R}$ space to compute distances within the simulation box

$$\begin{aligned} \mathbf{s} &= \mathcal{H}^{-1}\mathbf{r} \\ \mathbf{s}' &= \mathbf{s} - \mathrm{rint}(\mathbf{s}) \\ \mathbf{r}' &= \mathcal{H}\mathbf{s}' \end{aligned} \tag{1.9}$$

where the "rint"-function returns the rounded integer value of its argument. The smallest perpendicular width of the unit cell has to be larger than twice the spherical cutoff in $\mathcal{R}$ space to be consistent with the minimum image convention.

type	ϵ/k_B [K]	σ [Å]
O	48.1581	3.03315
F	36.4834	3.0932
S	173.107	3.59032
H	7.64893	2.84642
Cr	7.54829	2.69319
Cu	2.5161	3.11369
Ti	8.55473	2.8286
Ni	7.54829	2.52481
Ne	21.1352	2.88918
Cd	114.734	2.53728
Al	155.998	3.91105

type	ϵ/k_B [K]	σ [Å]
N	38.9492	3.26256
B	47.8058	3.58141
Cl	142.562	3.51932
Zn	62.3992	2.46155
Fe	6.54185	2.5943
Co	7.04507	2.55866
Sc	9.56117	2.93551
Zr	34.7221	2.78317
Ag	18.1159	2.80455
Sb	225.946	3.93777
Si	155.998	3.80414

type	ϵ/k_B [K]	σ [Å]
C	47.8562	3.47299
P	161.03	3.69723
Br	186.191	3.51905
Be	42.7736	2.44552
Mn	6.54185	2.63795
Ga	208.836	3.90481
V	8.05151	2.80099
Mg	55.8574	2.69141
In	301.428	3.97608
Te	200.281	3.98232

Table S3: *MOF/COF/ZIF/graphite force field.*

When cations such as Na^+ are introduced into the framework, strong and inhomogeneous electric fields are generated. In addition, the negatively charged oxygen atoms form a polarizable environment for adsorbed species. Therefore our model explicitly distinguishes silicon from aluminum with a difference of 0.3 e^- between q_{Si} and q_{Al} [16]. Different charges are used for oxygen atoms bridging two silicon atoms, q_{OSi}, and oxygen atoms bridging one silicon and one aluminum atom q_{OAl}. Using the relation $q_{\text{Si}} + (2\, q_{\text{OSi}}) = 0$ is obtained, making the zeolite neutral in the absence of aluminum, while q_{OAl} is chosen to make the total system charge equal to zero [17, 18].

The forcefield we use does not contain an explicit polarization term. Polarization energies are typically less than 10% to 20% of the total energy, and even less for siliceous zeolites. However, it should be note that the "average" polarization (and also framework flexibility) is included implicitly in the parameterization. The parameters are obtained empirically. For the cation-zeolite interactions we used the approach of Auerbach [16], taking into account the polarization effects by adjusting the partial charges on the oxygen depending whether they are connected to Si or Al. Alkanes are very difficult to polarize and therefore the logical approach is to use effective Lennard-Jones interactions between the cations and the alkanes.

1.1.4 MOF/COF/ZIF/graphite-model

The DREIDING force field [19] is a well-known force field developed to handle a wide range of small organic molecules, including organometallic systems. The small number of adjustable parameters in this force field makes it easy to extend the force field to more complex systems. Van der Waals parameters not found in DREIDING were taken from the universal force field (UFF) [20]. DREIDING and UFF forcefields were designed to be very generic, so that broad coverage of the periodic table, including inorganic compounds, metals, and transition metals, could be achieved. UFF was tailored for simulating molecules containing any combination of elements in the periodic table. All van der Waals parameters used for the MOFs, COF, ZIFs and graphite sheet/channels are listed in Table S3.

MOFs/COFs/ZIFs are more flexible than zeolites. However, also here, little influence of flexibility on adsorption and diffusion has been found [21].

1.2 Methodology

1.2.1 Monte Carlo simulation

In the canonical ensemble, the number of particles N, the temperature T, and the volume V are constant. The partition function is

$$Z_{\text{NVT}} = \frac{1}{\Lambda^{3N} N!} \int e^{-\beta U}\, \mathrm{d}\mathbf{r}^N \tag{1.10}$$

where $\Lambda = \sqrt{h^2/(2\pi m k_B T)}$ is the thermal de Broglie wavelength, h denotes Planck's constant, m is the mass, $\beta = 1/(k_B T)$, with k_B the Boltzmann constant, and $U\left(\mathbf{r}^N\right)$ is the total energy of the system with N

particles at positions $\mathbf{r}^N$. The probability of finding configuration $\mathbf{r}^N$ is given by

$$\mathcal{N}\left(\mathbf{r}^N\right) \propto e^{-\beta U\left(\mathbf{r}^N\right)} \tag{1.11}$$

The average of the variable $A\left(\mathbf{r}^N\right)$ in the NVT ensemble is given by

$$\left\langle A\left(\mathbf{r}^N\right)\right\rangle = \frac{\int A\left(\mathbf{r}^N\right) e^{-\beta U}\, \mathrm{d}\mathbf{r}^N}{\int e^{-\beta U}\, \mathrm{d}\mathbf{r}^N} \tag{1.12}$$

The Markov Chain Monte Carlo method (MCMC) is an important tool to estimate the average properties of systems with a very large number of accessible states. Often the quantity of interest are not the configurational part of the partition function itself, but averages of the type of Eq. 1.12. The ratio $e^{-\beta U}/Z$ is the probability density of finding the system in a configuration around $\mathbf{r}^N$. The Monte Carlo scheme makes use of the fact that only the relative probability of visiting points in configuration space is needed, *not* the absolute probability. To visit points with the correct frequency, the MCMC algorithm generates random trial moves from the current ("old") state (o) to a new state (n). To show that an arbitrary initial distribution eventually relaxes to the equilibrium distribution, it is often convenient to apply the condition of detailed balance (as is used in the original Metropolis scheme). If $P_B(o)$ and $P_B(n)$ denote the probability of finding the system in in state (o) and (n), respectively, and $\alpha(o \to n)$ and $\alpha(n \to o)$ denote the conditional probability to perform a trial move from $o \to n$ and $o \to n$, respectively, then the probability $P_{\text{acc}}(o \to n)$ to accept the trial move from $o \to n$ is related to $P_{\text{acc}}(n \to o)$ by the following

$$P_B(o)\alpha(o \to n)P_{\text{acc}}(o \to n) = P_B(n)\alpha(n \to o)P_{\text{acc}}(n \to o) \tag{1.13}$$

Metropolis et al. assumed that

$$\alpha(o \to n) = \alpha(n \to o) \tag{1.14}$$

and fixed the acceptance probability using

$$P_{\text{acc}}(o \to n) = \min\left(1, \frac{P_B(n)}{P_B(o)}\right) \tag{1.15}$$

1.2.2 Adsorption simulation

In adsorption studies one would like to know the amount of materials adsorbed as a function of pressure and temperature of the reservoir with which the sieve is in contact. Therefore the natural ensemble to use is the grand-canonical ensemble (or μ, V, T ensemble). In this ensemble, the temperature T, the volume V, and the chemical potential μ are fixed. The partition function is given by

$$Z_{\mu\text{VT}} \equiv \sum_{N=0}^{\infty} \frac{e^{\beta\mu N} V^N}{\Lambda^{3N} N!} \int e^{-\beta U(\mathbf{s}^N)}\, \mathrm{d}\mathbf{s}^N \tag{1.16}$$

with a corresponding probability density

$$\mathcal{N}_{\mu\text{VT}} \propto \frac{e^{\beta\mu N} V^N}{\Lambda^{3N} N!} e^{-\beta U(\mathbf{s}^N)} \tag{1.17}$$

The Metropolis algorithm is implemented in the same way as for NVT ensemble, but now we also allow the number of particles to change. We have two additional Monte-Carlo moves. The creation of a particle is accepted with a probability

$$\text{acc}(N \to N+1) = \min\left(1, \frac{V}{\Lambda^3 (N+1)} e^{\beta(\mu - U(N+1) + U(N))}\right) \tag{1.18}$$

and the removal of a particle is accepted with a probability

$$\text{acc}(N \to N-1) = \min\left(1, \frac{\Lambda^3 N}{V} e^{-\beta(\mu + U(N-1) - U(N))}\right) \tag{1.19}$$

The equilibrium conditions are that the temperature and chemical potential of the gas inside and outside the adsorbent must be equal. The imposed chemical potential μ can be related to the fugacity f

$$\beta\mu = \beta\mu^0_{\text{id}} + \ln(\beta f), \tag{1.20}$$

where μ^0_{id} is the reference chemical potential. All information of the reference state drops out, because it simply acts as a shift of the chemical potential that has no effect on the observable thermodynamic properties of the system. The fugacity f_j of component j in the reservoir is defined as the partial pressure of component j in the reservoir under the condition that the reservoir would be an ideal gas. Using the ideal gas law

$$f_j V\beta = N_j \tag{1.21}$$

we obtain for the insertion and deletion of a particle in the system

$$\text{acc}(N \to N+1) = \min\left(1, \frac{V\beta f}{(N+1)} e^{-\beta(U(N+1)-U(N))}\right) \tag{1.22}$$

$$\text{acc}(N \to N-1) = \min\left(1, \frac{N}{V\beta f} e^{-\beta(U(N-1)-U(N))}\right) \tag{1.23}$$

The pressure p is related to the fugacity f by

$$f = \phi p, \tag{1.24}$$

where ϕ is the fugacity coefficient computed directly from the equation of state of the vapor in the reservoir. In our study we have plotted absolute loading versus the fugacity as this is not affected by gas-liquid transitions of the reservoir.

1.2.3 Configurational-Bias Monte Carlo

Conventional Monte Carlo (CBMC) is time-consuming for long chain molecules. The fraction of successful insertions into the sieve is too low. To increase the number of successfully inserted molecules we apply the CBMC technique. In the CBMC scheme it is convenient to split the total potential energy U of a trial site into two parts.

$$U = U^{\text{int}} + U^{\text{ext}}. \tag{1.25}$$

The first part is the internal, bonded potential U^{int} which is used for the generation of trial orientations. The second part of the potential, the external potential U^{ext}, is used to bias the selection of a site from the set of trial sites. This bias is exactly removed by adjusting the acceptance rules. In the CBMC technique a molecule is grown segment-by-segment. For each segment we generate a set of k trial orientations according to the internal energy U^{int} and compute the external energy $U_i^{\text{ext}}(j)$ of each trial position j of segment i. In this work the number of trial positions k is set to 10. We select one of these trial positions with a probability

$$P_i(j) = \frac{e^{-\beta U_i^{\text{ext}}(j)}}{\sum_{l=1}^{k} e^{-\beta U_i^{\text{ext}}(l)}} = \frac{e^{-\beta U_i^{\text{ext}}(j)}}{w(i)}. \tag{1.26}$$

The selected trial orientation is added to the chain and the procedure is repeated until the entire molecule has been grown. For this newly grown molecule we compute the so-called Rosenbluth factor

$$W^{\text{new}} = \prod_i w(i). \tag{1.27}$$

To compute the old Rosenbluth factor W^{old} of an already existing chain, $k-1$ trial orientations are generated for each segment. These orientations, together with the already existing bond, form the set of k trial orientations. In a dynamic scheme, a Markov chain of states is generated. The average of a property is the average of over the elements of the Markov chain. For an infinite Markov chain the expression is exact. Every new configuration is accepted or rejected using an acceptance/rejection rule.

We have defined μ^{ex} as the difference in chemical potential of the interacting alkane and an alkane in the ideal gas state. The Rosenbluth weight $\langle W^{\text{IG}} \rangle$ of the reference state of the ideal gas is needed when comparing with real experimental data. When CBMC is used, it is straightforward to show that $e^{-\beta\Delta U}$ has to be replaced by $\frac{W(\text{new chain})}{W(\text{IG})}$ for inserting a particle and by $\frac{W(\text{IG})}{W(\text{old chain})}$ for the deletion of a particle. Detailed balance is obeyed when W^{IG} is replaced by $\langle W^{\text{IG}} \rangle$, i.e. the *average* Rosenbluth weight of a chain in the reservoir. This implies that $\langle W^{\text{IG}} \rangle$ has to be computed only *once* for a given molecule and temperature.

1.2.4 Monte Carlo moves

Several types of Monte Carlo moves are employed during a simulation.

- Displacement move
  A chain is selected at random and given a random displacement. The maximum displacement is taken such that 50% of the moves is accepted. The acceptance rule is

$$\text{acc}\left(\text{old} \rightarrow \text{new}\right) = \min\left(1, e^{-\beta\left(U^{\text{new}} - U^{\text{old}}\right)}\right). \tag{1.28}$$

  Note that the energy of the new configuration U^{new} and the energy of the old configuration U^{old} only differ in the external energy.

- Rotation move
  A chain is selected at random and given a random rotation. The center of the rotation is the center of mass. The maximum rotation angle is selected such that 50% of the moves are accepted. The acceptance rule is given by Eq. 1.28. Again, the energy of the new configuration U^{new} and the energy of the old configuration U^{old} only differ in the external energy.

- Insertion move
  A chain is grown at a random position. The acceptance rule for insertion of the particle is given by

$$\text{acc}(N \rightarrow N+1) = \min\left(1, \frac{W^{\text{new}}\beta V}{N+1}\frac{f}{\langle W^{\text{IG}}\rangle}\right). \tag{1.29}$$

- Deletion move
  A chain is chosen at a random position and the old Rosenbluth factor is computed. The acceptance rule for deletion of the particle is given by

$$\text{acc}(N \rightarrow N-1) = \min\left(1, \frac{N}{W^{\text{old}}\beta V}\frac{\langle W^{\text{IG}}\rangle}{f}\right). \tag{1.30}$$

- Full reinsertion move
  A chain is selected at random and is completely regrown at a random position. This move is essential for N, V, T to change the internal configuration of a molecule, and during this move data for the average Rosenbluth weight can be collected. The acceptance rule for full reinsertion move is given by

$$\text{acc}\left(\text{old} \rightarrow \text{new}\right) = \min\left(1, \frac{W^{\text{new}}}{W^{\text{old}}}\right). \tag{1.31}$$

- Partial reinsertion move
  A chain is selected at random and part of the molecule is regrown. It is decided at random which part of the chain is regrown and with which segment the regrown is started. The acceptance rule for partial reinsertion is given by Eq. 1.31.

- Identity change move (mixtures)
  The identity-change trial move [22] is called semi-grand ensemble, but it can also be seen as a special case of the Gibbs ensemble. One of the components is selected at random and an attempt is made to change its identity. The acceptance rule is given by [23]

$$\text{acc}\left(\text{A} \rightarrow \text{B}\right) = \min\left(1, \frac{W^{\text{new}} f_B \left\langle W_A^{\text{IG}}\right\rangle N_A}{W^{\text{old}} f_A \left\langle W_B^{\text{IG}}\right\rangle \left(N_B+1\right)}\right), \tag{1.32}$$

  where f_A and f_B are the fugacities of components A and B, and N_A and N_B are the number of particles.

```
Performance of the translation move:
====================================
Component 0 [hexane]
        total        3387324  3386087  3387301
        successful   1694669  1693103  1694731
        accepted     0.500297 0.500018 0.500319
        displacement 0.575638 0.668756 0.444861


Performance of the rotation move:
====================================
Component [hexane] total tried: 10180273 accepted: 338267 (3.322769 [%])

Performance of the swap addition move:
======================================
Component [hexane] total tried: 5094144 successful growth: 954784 (18.742776 [%]) accepted: 19931 (0.391253 [%])

Performance of the swap deletion move:
======================================
Component [hexane] total tried: 5090398 successful growth: 5090398 (100 [%]) accepted: 19932 (0.391561 [%])

Performance of the reinsertion move:
====================================
Component [hexane] total tried: 10185812 successful growth: 2045047 (20.077408 [%]) accepted: 4939 (0.048489 [%])

Performance of the partial reinsertion move:
============================================
Component [hexane] total tried: 10190711 successful growth: 9707965 (95.262882 [%]) accepted: 2348669 (23.047155 [%])
```

Table S4: *Typical statistics of the used Monte-Carlo moves for hexane at a pressure of 100 kPa and 433 K.*

Simulations are performed in cycles. The number of cycles needed for equilibration depends on the number of molecules. We define a cycle to consists of smaller steps proportional to the number number of molecules with 20 as the minimum.

$$N_{\text{cycles}} = \max(20, N) \times N_{\text{steps}}. \tag{1.33}$$

In each step one Monte Carlo move is performed. For single components we used at least 50000 initialization cycles, while 150000 cycles are used to compute the isotherms. For the 5-component mixtures, both initialization and production stages are 5 times longer. The error bars in the isotherms are computed by dividing the simulations results up into five blocks. The error is computed from the standard deviation of the five blocks and corresponds to the 95% confidence interval.

At a pressure of 1 bar, for hexane and the hexane isomer mixture in MFI, we list some typical statistics of the used Monte-Carlo moves in Table S4 and S5.

1.2.5 Self-diffusion coefficients

In MD simulations [2, 3, 4], successive configurations of the system are generated by integrating Newton's laws of motion, which then yields a trajectory that describes the positions, velocities and accelerations of the particles as they vary with time. We used the velocity Verlet integration scheme with a time step of 0.5 fs. The relative energy drift was smaller than 10^{-4}. For temperature control we employed the Nosé-Hoover chain (NHC) method as formulated by Martyna et al. [24].

To prepare the system at the desired temperature in an equilibrium configuration we initialize the system by the following procedure

- N molecules are inserted into the framework at random positions as long as no overlaps occur with the framework or other particles, and as long as the positions are accessible from the main cages and channels.
- During the initializing period we perform an NVT MC simulation to rapidly achieve an equilibrium molecular arrangement.
- After the initialization step, we assign all the atoms velocities from the Maxwell-Boltzmann distribution at the desired average temperature. The total momentum of the system is set to zero. Next, we equilibrate the system further by performing a NVT MD simulation using the NHC thermostat.

```
Performance of the translation move:
=====================================
Component 0 [hexane]                                  Component 1 [2-methylpentane]
       total        2065838  2065649  2063454                 total        2064620  2066692  2065826
       successful   1032817  1034365  1031635                 successful   1032335  1033555  1032436
       accepted     0.499951 0.500746 0.499955                accepted     0.500012 0.500101 0.499769
       displacement 0.689450 0.810975 0.540074                displacement 0.700453 0.830566 0.656879

Component 2 [3-methylpentane]                         Component 3 [22-dimethylbutane]
       total        2065160  2064788  2063660                 total        2061680  2060304  2056641
       successful   1032267  1032456  1031517                 successful   1030345  1030752  1030163
       accepted     0.499848 0.500030 0.499848                accepted     0.499760 0.500291 0.500896
       displacement 0.630632 0.824793 0.608502                displacement 0.643099 0.811360 0.695441

Component 4 [23-dimethylbutane]
       total        2064597  2066051  2063921
       successful   1031762  1032818  1033114
       accepted     0.499740 0.499900 0.500559
       displacement 0.574580 0.706078 0.605981

Performance of the rotation move:
=================================
Component [hexane] total tried: 6207995 accepted: 266210 (4.288180 [%])
Component [2-methylpentane] total tried: 6207627 accepted: 306521 (4.937813 [%])
Component [3-methylpentane] total tried: 6207486 accepted: 338037 (5.445635 [%])
Component [22-dimethylbutane] total tried: 6197096 accepted: 427882 (6.904557 [%])
Component [23-dimethylbutane] total tried: 6205747 accepted: 397111 (6.399085 [%])

Performance of the swap addition move:
======================================
Component [hexane] total tried: 3102165 successful growth: 962310 (31.020594 [%]) accepted: 16819 (0.542170 [%])
Component [2-methylpentane] total tried: 3101853 successful growth: 909006 (29.305257 [%]) accepted: 7115 (0.229379 [%])
Component [3-methylpentane] total tried: 3107340 successful growth: 892311 (28.716233 [%]) accepted: 7092 (0.228234 [%])
Component [22-dimethylbutane] total tried: 3102510 successful growth: 802671 (25.871665 [%]) accepted: 5746 (0.185205 [%])
Component [23-dimethylbutane] total tried: 3105093 successful growth: 758017 (24.412055 [%]) accepted: 4615 (0.148627 [%])

Performance of the swap deletion move:
======================================
Component [hexane] total tried: 3104704 successful growth: 3104704 (100 [%]) accepted: 16947 (0.545849 [%])
Component [2-methylpentane] total tried: 3105836 successful growth: 3105836 (100 [%]) accepted: 7110 (0.228924 [%])
Component [3-methylpentane] total tried: 3102066 successful growth: 3102019 (99.998485 [%]) accepted: 7110 (0.229202 [%])
Component [22-dimethylbutane] total tried: 3102836 successful growth: 3097499 (99.827996 [%]) accepted: 5696 (0.183574 [%])
Component [23-dimethylbutane] total tried: 3103382 successful growth: 3103074 (99.990075 [%]) accepted: 4525 (0.145809 [%])

Performance of the reinsertion move:
====================================
Component [hexane] total tried: 6208990 successful growth: 2011162 (32.391130 [%]) accepted: 7833 (0.126156 [%])
Component [2-methylpentane] total tried: 6207690 successful growth: 1915501 (30.856905 [%]) accepted: 3610 (0.058154 [%])
Component [3-methylpentane] total tried: 6207239 successful growth: 1873936 (30.189525 [%]) accepted: 3499 (0.056370 [%])
Component [22-dimethylbutane] total tried: 6194677 successful growth: 1690318 (27.286620 [%]) accepted: 3730 (0.060213 [%])
Component [23-dimethylbutane] total tried: 6209003 successful growth: 1606368 (25.871593 [%]) accepted: 2274 (0.036624 [%])

Performance of the identity change move:
========================================
Component [hexane]->[hexane] total tried: 1240398 successful growth: 1029989 (83.036977 [%]) accepted: 90971 (7.334017 [%])
Component [hexane]->[2-methylpentane] total tried: 1240684 successful growth: 974256 (78.525716 [%]) accepted: 46323 (3.733666 [%])
Component [hexane]->[3-methylpentane] total tried: 1241749 successful growth: 917685 (73.902616 [%]) accepted: 44932 (3.618445 [%])
Component [hexane]->[22-dimethylbutane] total tried: 1242764 successful growth: 907864 (73.052003 [%]) accepted: 42460 (3.416578 [%])
Component [hexane]->[23-dimethylbutane] total tried: 1241447 successful growth: 829239 (66.796166 [%]) accepted: 30359 (2.445453 [%])
Component [2-methylpentane]->[hexane] total tried: 1239749 successful growth: 1162871 (93.798906 [%]) accepted: 46112 (3.719463 [%])
Component [2-methylpentane]->[2-methylpentane] total tried: 1243330 successful growth: 1186364 (95.418272 [%]) accepted: 84577 (6.802458 [%])
Component [2-methylpentane]->[3-methylpentane] total tried: 1240321 successful growth: 1121362 (90.409015 [%]) accepted: 44842 (3.615354 [%])
Component [2-methylpentane]->[22-dimethylbutane] total tried: 1240975 successful growth: 1186655 (95.622797 [%]) accepted: 88405 (7.123834 [%])
Component [2-methylpentane]->[23-dimethylbutane] total tried: 1241873 successful growth: 1124381 (90.539129 [%]) accepted: 58549 (4.714572 [%])
Component [3-methylpentane]->[hexane] total tried: 1241454 successful growth: 1066854 (85.935846 [%]) accepted: 44726 (3.602711 [%])
Component [3-methylpentane]->[2-methylpentane] total tried: 1242485 successful growth: 1080763 (86.983988 [%]) accepted: 44901 (3.613806 [%])
Component [3-methylpentane]->[3-methylpentane] total tried: 1242054 successful growth: 1019653 (82.094096 [%]) accepted: 83561 (6.727646 [%])
Component [3-methylpentane]->[22-dimethylbutane] total tried: 1241172 successful growth: 1029966 (82.983342 [%]) accepted: 41848 (3.371652 [%])
Component [3-methylpentane]->[23-dimethylbutane] total tried: 1240457 successful growth: 981650 (79.136157 [%]) accepted: 47951 (3.865591 [%])
Component [22-dimethylbutane]->[hexane] total tried: 1240028 successful growth: 1165557 (93.994410 [%]) accepted: 42815 (3.452745 [%])
Component [22-dimethylbutane]->[2-methylpentane] total tried: 1239731 successful growth: 1187572 (95.792716 [%]) accepted: 88275 (7.120496 [%])
Component [22-dimethylbutane]->[3-methylpentane] total tried: 1238798 successful growth: 1126149 (90.906588 [%]) accepted: 41553 (3.354300 [%])
Component [22-dimethylbutane]->[22-dimethylbutane] total tried: 1239067 successful growth: 1195899 (96.516088 [%]) accepted: 108765 (8.777976 [%])
Component [22-dimethylbutane]->[23-dimethylbutane] total tried: 1238215 successful growth: 1132062 (91.426933 [%]) accepted: 69282 (5.595313 [%])
Component [23-dimethylbutane]->[hexane] total tried: 1240795 successful growth: 1153326 (92.950568 [%]) accepted: 30549 (2.462051 [%])
Component [23-dimethylbutane]->[2-methylpentane] total tried: 1240622 successful growth: 1174099 (94.637932 [%]) accepted: 58399 (4.707236 [%])
Component [23-dimethylbutane]->[3-methylpentane] total tried: 1239831 successful growth: 1121319 (90.441278 [%]) accepted: 48121 (3.881255 [%])
Component [23-dimethylbutane]->[22-dimethylbutane] total tried: 1242311 successful growth: 1171384 (94.290721 [%]) accepted: 69160 (5.567044 [%])
Component [23-dimethylbutane]->[23-dimethylbutane] total tried: 1241659 successful growth: 1120126 (90.212047 [%]) accepted: 66688 (5.370879 [%])
```

Table S5: *Typical statistics of the used Monte-Carlo moves for a mixture of hexane isomers at a pressure of 100 kPa and 433 K.*

- The equilibration is completed and during the production run we collect statistics using either the NVE or NVT-ensemble. Following this equilibration procedure, the average temperature using NVE over the entire production period is usually within a few Kelvin of the desired average temperature, while NVT would give the exact desired average temperature if simulated sufficiently long.

The self-diffusion coefficients D_S^α in the direction $\alpha = x, y, z$ are computed by taking the slope of the mean-squared displacement (msd) at long times

$$D_S^\alpha = \frac{1}{2N} \lim_{t\to\infty} \frac{\mathrm{d}}{\mathrm{d}\,t} \left\langle \sum_{i=1}^{N} \left(r_{i\alpha}\left(t\right) - r_{i\alpha}\left(0\right)\right)^2 \right\rangle \tag{1.34}$$

where N is the number of molecules, t the time, and $r_{i\alpha}$ the α-component of the center-of-mass of molecule i.

The calculation of the diffusion coefficients requires much memory and CPU power, especially when fluctuations decay slowly. The order-n algorithm to measure correlations allows us to measure fast and slow dynamics simultaneously at minimal computational cost by using adjustable sampling frequencies [3, 25]. The order-n scheme is equally accurate as the conventional scheme but the saving in memory as well as CPU time is significant for computing the mean-squared displacements at long times.

1.2.6 Heat of adsorption

In molecular simulations, the heat of adsorption in nanoporous materials is often computed using either of the following methods: (1) using the Clausius-Clapeyron equation, which requires the partial derivative of the pressure with respect to temperature at constant loading, (2) using the energy difference between the host with and without a single guest molecule present, and (3) from energy/particle fluctuations in the grand-canonical ensemble.

We can approximate the change in potential energy upon adsorption of a single guest molecule [26, 27]:

$$\left\langle U_{N+1}\right\rangle_{N+1} - \left\langle U_N\right\rangle_N \approx \left(\frac{\partial \left\langle U\right\rangle_\mu}{\partial \left\langle N\right\rangle_\mu}\right)_\beta = \frac{\left(\frac{\partial \left\langle U\right\rangle_\mu}{\partial \mu}\right)_\beta}{\left(\frac{\partial \left\langle N\right\rangle_\mu}{\partial \mu}\right)_\beta} = \frac{\left\langle U\times N\right\rangle_\mu - \left\langle U\right\rangle_\mu \left\langle N\right\rangle_\mu}{\left\langle N^2\right\rangle_\mu - \left\langle N\right\rangle_\mu \left\langle N\right\rangle_\mu} \tag{1.35}$$

where the brackets $\left\langle \cdots \right\rangle_\mu$ denote an average in the grand-canonical ensemble, N is the number of guest molecules, and μ is the chemical potential of the guest molecules. This leads to [26, 27]

$$-Q = \Delta H = \frac{\left\langle U\times N\right\rangle_\mu - \left\langle U\right\rangle_\mu \left\langle N\right\rangle_\mu}{\left\langle N^2\right\rangle_\mu - \left\langle N\right\rangle_\mu \left\langle N\right\rangle_\mu} - \left\langle U_g\right\rangle - \frac{1}{\beta} \tag{1.36}$$

where ΔH is usually defined as the *isosteric enthalpy of adsorption* and Q as *the isosteric heat of adsorption*. It is assumed here that the gas phase is ideal. Eq. 1.36 can be applied at non-zero loading [26].

1.2.7 Surface area, void fraction and pore-size distributions

Surface areas A geometric surface area can be computed using a simple Monte Carlo simulation. Essentially one roles a probe molecule over the surface and in this way calculate the surface area accessible to the probe molecule [28, 29]. Note that the surface area depends on the size of the probe molecule (nitrogen in our case). Experimental surface areas are commonly reported as BET surface areas obtained by applying the theory of Brunauer, Emmett, and Teller (BET) [30] to nitrogen adsorption isotherms measured at 77 K. BET surface areas calculated from simulated isotherms agree very well with the accessible surface areas calculated directly from the crystal structures in a geometric fashion [31], especially over the pressure range identified by established consistency criteria, rather than simply using the "standard" BET pressure range.

Void fraction and pore volume For the pore volume determination, we followed the methodology published by Talu and Myers paper [32]. For consistency with experiment, the pore volume has be determined once using a simulation of a single helium molecule at the reference conditions. Probing the framework

with a nonadsorbing helium molecule using the Widom particle insertion method will give the *helium void fraction* ξ

$$\xi = \int e^{-\beta U}\, \mathbf{dr} \tag{1.37}$$

The pore volume is simply

$$V_{\text{pore}} = \xi V \tag{1.38}$$

Usually a reference temperature of 25°C (298 K) is chosen in experiment for the experimental determination of the helium void volume.

Pore size distribution (PSD) Gelb en Gubbins considered the subvolumes of the system accessible to spheres of different radii [33]. Let $V_{\text{pore}}(r)$ be the volume of the void space "coverable" by spheres of radius r or smaller; a point x is in $V_{\text{pore}}(r)$ only if we can construct a sphere of radius r that overlaps x and does not overlap any substrate atoms. This volume is equivalent to that enclosed by the pore's "Connolly surface". $V_{\text{pore}}(r)$ is a monotonically decreasing function of r and is easily compared with the "cumulative pore volumes" curves often calculated in isotherm-based PSD methods. The derivative $-\mathrm{d}V_{\text{pore}}(r)/\mathrm{d}r$ is the fraction of volume coverable by spheres of radius r but not by spheres of radius $r + \mathrm{d}r$ and is a direct definition of the pore size distribution. The $V_{\text{pore}}(r)$ function can be calculated by a Monte Carlo volume integration.

1.2.8 Definition and calculations of adsorption selectivities and capacities

For a binary mixture the adsorption selectivity is defined as follows

$$S_{\text{ads}} = \frac{q_1/q_2}{f_1/f_2} \tag{1.39}$$

This selectivity definition needs to be adapted for separation of 5-component hexane isomer mixtures of nC6 (= component 1), 2MP (= component 2), 3MP (= component 3), 23DMB (= component 4), and 22DMB (= component 5) with partial fugacities, f_i. Consider first nanoporous materials, such as MFI, Co(BDP) for which the hierarchy is such that the linear nC6 has the strongest adsorption strength. In these cases S_{ads} is defined as follows

$$S_{\text{ads}} = \frac{(q_1 + q_2 + q_3)\,/\,(q_4 + q_5)}{(f_1 + f_2 + f_3)\,/\,(f_4 + f_5)} \tag{1.40}$$

For materials, such as CFI, UiO-66 for which the hierarchy is such that the linear nC6 has the lowest adsorption strength, we define S_{ads} as follows.

$$S_{\text{ads}} = \frac{(q_4 + q_5)\,/\,(q_1 + q_2 + q_3)}{(f_4 + f_5)\,/\,(f_1 + f_2 + f_3)} \tag{1.41}$$

The definition 1.40, 1.41 are direct reflections of the required separations in fixed bed units. The values of S_{ads} can be directly determined from the CBMC mixture simulations, which were performed for equimolar mixtures, i.e. , $f_1 = f_2 = f_3 = f_4 = f_5$.

The corresponding definition of the capacities also needs to be considered carefully. For MFI, Co(BDP), ZIF-77, COF-103, MgMOF-74 with the "normal" hierarchy we define the Capacity as follows

$$C_{\text{ads}} = \frac{(q_1 + q_2 + q_3)}{3} \tag{1.42}$$

For CFI, UiO-66, and MFS with the "reverse" hierarchy we define the Capacity as follows

$$C_{\text{ads}} = \frac{(q_4 + q_5)}{2} \tag{1.43}$$

The division by 3, and 2, respectively in the two scenarios ensures that the values of the Capacities are normalized in the proper manner and that the comparisons are done fairly.

1.2.9 Ideal Adsorbed Solution Theory (IAST)

It is possible to estimate the mixture loading from the pure components using the IAST of Myers and Prausnitz [34]. Briefly, the basic equation of IAST theory is the analogue of Raoult's law for vapour-liquid equilibrium, i.e.

$$P_{y_i} = P_i^0(\pi)\, x_i, \qquad i = 1, 2, \ldots, n \tag{1.44}$$

where x_i is the mol fraction in the adsorbed phase

$$x_i = \frac{q_i}{q_1 + q_2 + \cdots + q_n} \tag{1.45}$$

where q_i is the loading expressed in mol kg^{-1}, and $P_i^0(i\pi)$ is the pressure for the sorption of every pure component i, which yields the same spreading pressure, π as for the mixture. The spreading pressure is defined by the Gibbs adsorption isotherm

$$\frac{\pi A}{k_B T} = \rho \int_{P=0}^{P=P_i^0} \frac{q_i^0(P)}{P}\, \mathrm{d}P \tag{1.46}$$

where A is the surface areas per m^3 of adsorbent, ρ the density of the crystallite expressed in kg m^{-3} and $q_i^0(P)$ the pure component isotherm (emphasized by the superscript 0). The total amount adsorbed is obtained from

$$\begin{aligned} q_{\text{mix}} &\equiv q_1 + q_2 + \cdots + q_n \\ &= \frac{1}{\frac{x_1}{q_1^0(P_1^0)} + \frac{x_2}{q_2^0(P_2^0)} + \cdots + \frac{x_n}{q_n^0(P_n^0)}} \end{aligned} \tag{1.47}$$

The set of Eqs. 1.44,1.45,1.46 and 1.47 need to be solved numerically to obtain the loadings of the individual components in the mixture.

For IAST calculations of component loadings in the 5-component mixture of hexane isomers, used also in the breakthrough calculations, the unary isotherm data on the absolute component loadings, in mol kg^{-1}, nC6, 2MP, 3MP, 23DMB, and 22DMB were fitted with the dual-site Langmuir-Freundlich model:

$$q_i = q_{i,A,\text{sat}} \frac{b_{i,A} f_i^{\nu_i,A}}{1 + b_{i,A} f_i^{\nu_i,A}} + q_{i,B,\text{sat}} \frac{b_{i,B} f_i^{\nu_i,B}}{1 + b_{i,B} f_i^{\nu_i,B}} \tag{1.48}$$

where $q_{i,\text{sat}}$ are the saturation capacities, b_i the Langmuir constants for the two sites A and B.

The fit parameters were determined on the basis of the CBMC simulated isotherms up to a maximum fugacity of 10^6 Pa only because the breakthrough calculations reported are for a total fugacity of 10^5 Pa.

1.2.10 Breakthrough simulations

Using the dual-site Langmuir-Freundlich fits of the pure component hexane isomers, breakthrough calculations were carried out for separation of a 5-component mixture of hexane isomers in a packed bed adsorber for the purposes of demonstrating the separation feasibility in a pressure swing adsorption (PSA) unit. Figure S1 shows a schematic of a packed bed adsorber.

The breakthrough calculations were performed using the methodology described in the paper by Krishna and Long [35]. In the breakthrough calculations the following set of assumptions were made.

1. plug flow of nC6/2MP/3MP/23DMB/22DMB mixture through the fixed bed,
2. the bed is maintained under isothermal conditions at a temperature of 433 K, and
3. the pressure drop across the bed is considered to be negligible, i.e. the total fugacity is maintained constant.

The partial pressures in the gas phase at any position and instant of time are obtained by solving the following set of partial differential equations for each of the species i in the gas mixture.

$$\frac{1}{RT}\varepsilon \frac{\partial p_i}{\partial t} = -\frac{1}{RT}\frac{\partial (u p_i)}{\partial z} - (1-\varepsilon)\rho \frac{\partial q_i}{\partial t}; \qquad i = 1, 2, \ldots, 5 \tag{1.49}$$

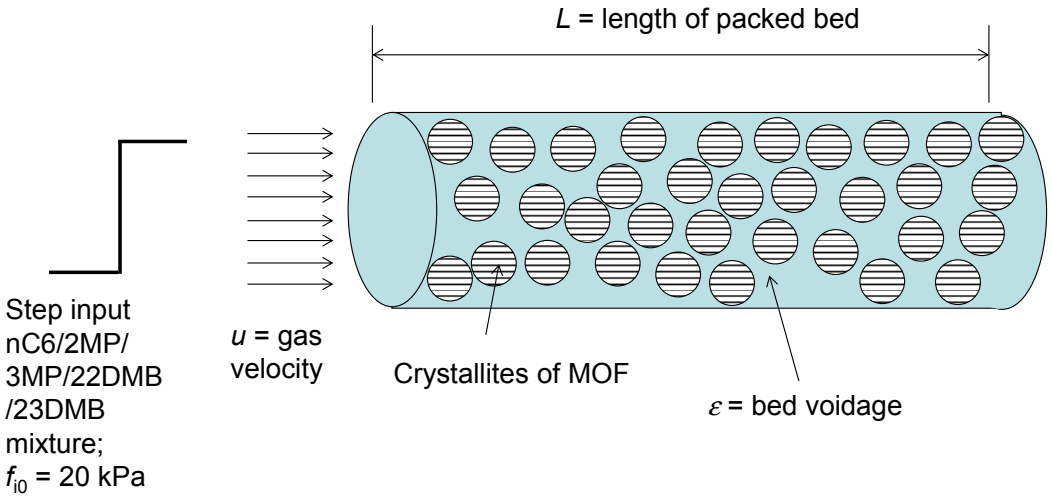

Figure S1: *Schematic of packed bed adsorber.*

In equation 1.49, t is the time, z is the distance along the adsorber, ρ is the framework density, ε is the bed voidage, and u is the superficial gas velocity. The variation of the superficial gas velocity along the length of the adsorber is properly accounted for. The molar loadings of the species i, q_i, at any position z, and time t are determined from IAST calculations. The accuracy of IAST calculations have been established in earlier studies [36, 37]. Typically, the adsorber length L is divided into 100 slices. The number of slices is determined by checking that the obtained breakthrough results do not change on increasing it. In the breakthrough calculations, the pressure drop in the bed is considered to be negligible, and consequently the total pressure remains constant. As a consequence, the velocity u changes along the length of the adsorber due to adsorption into the porous materials. The velocity change is duly accounted for; the value of u at any slice in the adsorber is determined from a material balance across that slice [38]. Combination of the discretized PDEs along with the algebraic IAST equilibrium model, results in a set of differential-algebraic equations (DAEs), which are solved using BESIRK [39]. BESIRK is a sparse matrix solver, based on the semi-implicit Runge-Kutta method originally developed by Michelsen [40], and extended with the Bulirsch-Stoer [41] extrapolation method. Use of BESIRK improves the numerical solution efficiency in solving the set of DAEs. The evaluation of the sparse Jacobian required in the numerical algorithm is largely based on analytic expressions [37]. Further details of the adsorber model, along with the numerical procedures used in this work, are provided in our earlier works [37, 38, 42]. Typical computation times for the 5-component gas mixture breakthrough are less than 500 s. Details of the numerical procedures used are available in earlier works [35, 37, 43]. Specifically, the calculations presented here were performed taking the following parameter values:

- PSA
  $L = 0.3$ m; $\varepsilon = 0.4$; $u = 0.04$ m/s (at inlet); c_{i0} =20000/8.314/433K; all y-axis are c_i/c_{i0},
- pulse
  $L = 1$ m; $\varepsilon = 0.4$; $u = 0.04$ m/s (superficial gas velocity); duration of pulse = $t = 10$ s (real time), so, $\tau = tu/\varepsilon/L = 10 \times 0.04/0.4/1 = 1$; all y-axes are in absolute c_i, mol/m^3 in gas phase.

When comparing different materials, the fractional voidage is held constant at $\varepsilon = 0.4$. This implies the volume of adsorbents used are the same. The total mass of the corresponding adsorbents used is governed by the framework density. All the 5-component mixture breakthrough calculations we carried out for with the inlet gas maintained at partial fugacities $f_1 = f_2 = f_3 = f_4 = f_5 = 20$ kPa at the inlet. In the presented graphs of breakthrough behaviors are presented in terms of the dimensionless outlet concentration, $\frac{c_i}{c_{i,0}} = \frac{f_i}{f_{i0}}$, representing the ratio of the partial fugacities at the outlet gas divided by the partial fugacities at the adsorber inlet, as a function of the dimensionless time, τ, obtained by dividing the actual time, t, by the contact time between the gas and the crystallites, $\varepsilon L/u$. For a given adsorbent, under chosen operating conditions, the breakthrough characteristics are uniquely defined by τ, allowing the results to be presented

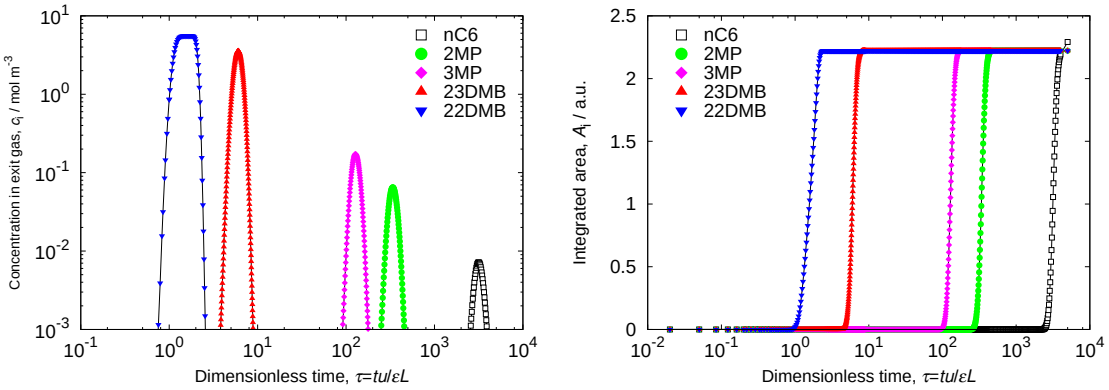

(a) *Simulated pulse breakthrough.*

(b) *The integrated values of the number of moles eluted during the time interval 0-τ using a simple Simpson integration formula.*

Figure S2: *Simulated pulse-type breakthrough of an 5-component equimolar mixture of hexane-isomers in ZIF-77 at 433K and a total fugacity of the bulk fluid phase of 100 kPa. Figure (a) is in log x-axis for pulse chromatography and this can give the false visual impression that the amounts eluted are not the same, but in fact figure (b) shows the integration amounts are the same (as it should be for an equimolar mixture).*

here to be equally applicable to laboratory scale equipment as well as to industrial scale adsorbers. Experimental verification of the PSA breakthrough and pulse chromatographic simulation methodologies have been obtained by comparison with experiments [44, 45, 46].

1.2.11 Visualization

A conventional molecular viewer is able to show the structure of a framework. However, from the atomic positions it is hard to see the shape and size of the pores/cavities of the structure. Often, with the framework present, the adsorbates are hard to see. It is therefore more convenient to view the adsorbates as atoms inside pores/cavities with the framework shown as an "energy landscape". The energy landscape can e.g. be rendered transparent or volume rendered to view the actual shape/size of the pores. The unit cell is divided into $150 \times 150 \times 150$ voxels (volume-elements, not necessarily cubes). At millions of random positions in the unit cell the free energy of a test-particle (helium molecule) is calculated and assigned to the appropriate voxel. To visualize this energy landscape the three-dimensional dataset is volume rendered [47], removing the parts that generate overlap (the zeolite itself) by making it completely transparent. Low energy values are rendered with high transparency, allowing the inside of the cages to be viewed as voids. Higher energy values are rendered less and less transparent until the energy approaches a cutoff energy and is regarded as part of the zeolite wall. Also color is assigned according to the energy value: gold for the inside view of a cage, blue for the outside view of a cage.

The snapshot, framework, and density pictures are made with VTK (the Visualization ToolKit) [47]. The snapshots are single states (hence "snapshots") of the system taken after equilibration. Another visualization technique is to average all the snapshots into a "density". During the grand-canonical Monte Carlo simulation a 3-dimensional histogram of the positions of all united atom alkane beads is collected (per component). The unit cell is divided into 150x150x150 voxels. During the simulation the molecules move around in the box, and every cycle data is collected for the histogram. For every atom the voxel corresponding to its position is incremented. Using atoms shows more structure (position/orientation) than e.g. using only the center of mass. At certain intervals the histogram is written to file so that it can be visualized using VTK. The data is always normalized using the highest occurring voxel value. However, the overall brightness is still influenced by the loading of the specific adsorbate in the mixture.

1.3 Validating the simulations of isotherms and breakthroughs with available experimental data

1.3.1 Zeolites

The alkane-zeolite forcefield by Dubbeldam et al. quantitatively predicts adsorption isotherms [48, 49]. By explicitly fitting to entire adsorption isotherms the proper reproduction of properties such as Henry coefficients, heats of adsorption, adsorption entropies, and saturation loadings is guaranteed. The force field has been extended by Calero et al. to aluminosilicates containing mobile cations [50]. Figure S3 shows some typical cases and in general the predictive power of the model is excellent. The potential parameters are determined through fitting on experimental isotherms with inflection points. The procedure uniquely determines the adsorbent-adsorbate interaction parameters and is very sensitive to the size parameter. Known experimental data was scrutinized and inconsistencies between experiments were removed. A subset of this data was used for calibration, and the remainder used for validation. Very good agreement between experimental and simulated isotherms was found for the studied systems (AFI-, MFI-, TON-, DDR-, and MWW-type zeolites) over a wide range of pressures and temperatures [49].

1.3.2 MOFs/COFs/ZIFs

A force field for alkanes in zeolite is more demanding than for large-pore structure, due to the strong confinement in zeolites. Partly, the accuracy of the zeolite force field stems from the simplicity of the structure (oxygen and silicon). The chemical diversity of MOFs, COFs, and ZIFs is much larger and therefore generic force fields are the best choice here (e.g. DREIDING [19] and UFF [20]). Despite the generic character of the force field, even the early molecular simulations of adsorption in MOFs have shown very good agreement with experiment [28, 51, 52, 53, 54]. Due to the success of this type of modeling on MOFs, ZOFs, COFs, the DREIDING and UFF remain the best choice of force field here.

In Figure S5 we compare the force field to very recent experimental data on methane in MIL-101 [55]. Excellent agreement is obtained. Note that in order to compare to experiments the simulation results are properly converted from absolute loadings to excess loadings.

Recently, Barcia et al. published results for alkane separation in UiO-66 [56]. In Figure S6 we show our modeling corroborates this experimental finding. The results are in qualitatively agreement, but it should be noted that the experimental results are heavily influenced by diffusional effects.

In Figure S7 we show our simulated breakthrough curves *including* diffusional effects for alkane mixtures in ZIF-8 and compare them to the experimental results of [57]. The agreement is qualitatively, but also quantitatively very good. However, our simulation approach allows us to separate adsorption effects from diffusion effects. In experiment, a breakthrough curve is always affected by both.

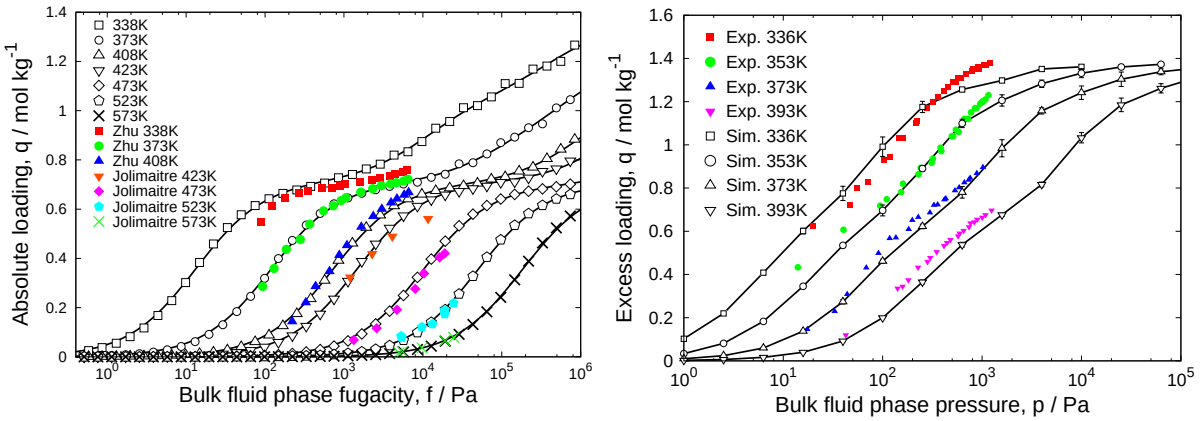

(a) *3MP in MFI at various temperatures.*

(b) *nC6 in MFI at various temperatures.*

Figure S3: *Comparison of simulations with experimental data in zeolites. Figures re-plotted from Refs. [48, 49, 50].*

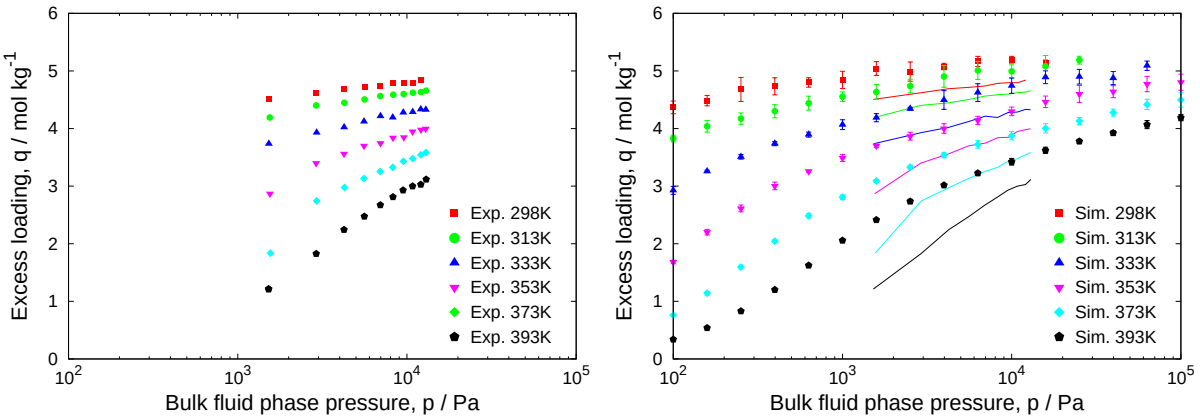

(a) *Experimental data of Lee et al. [58].* **(b)** *points: simulated adsorption data; lines: experimental data.*

Figure S4: *Comparison of simulations with recent experimental adsorption data on hexane in MOF-1 at various temperatures [58].*

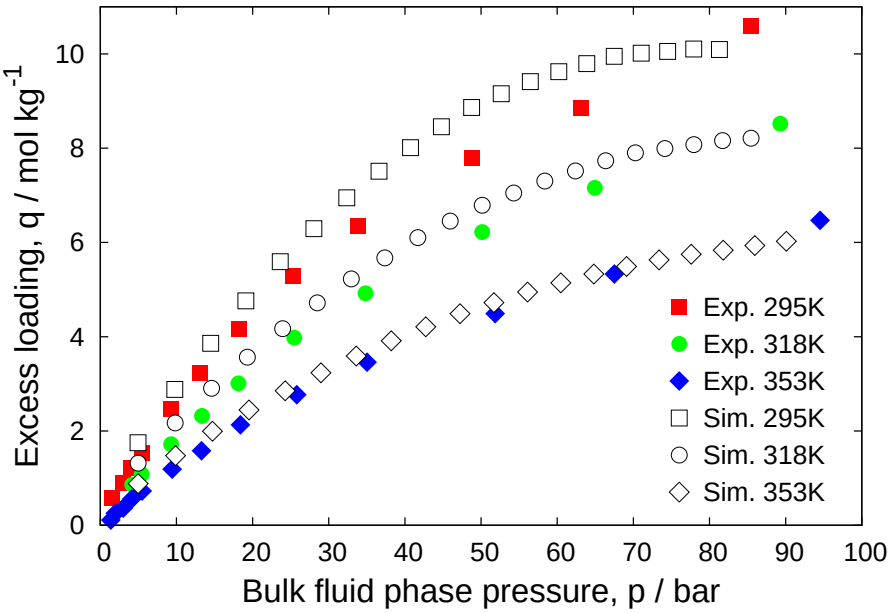

Figure S5: *Comparison of simulations with recent experimental data on methane in MIL-101 [55].*

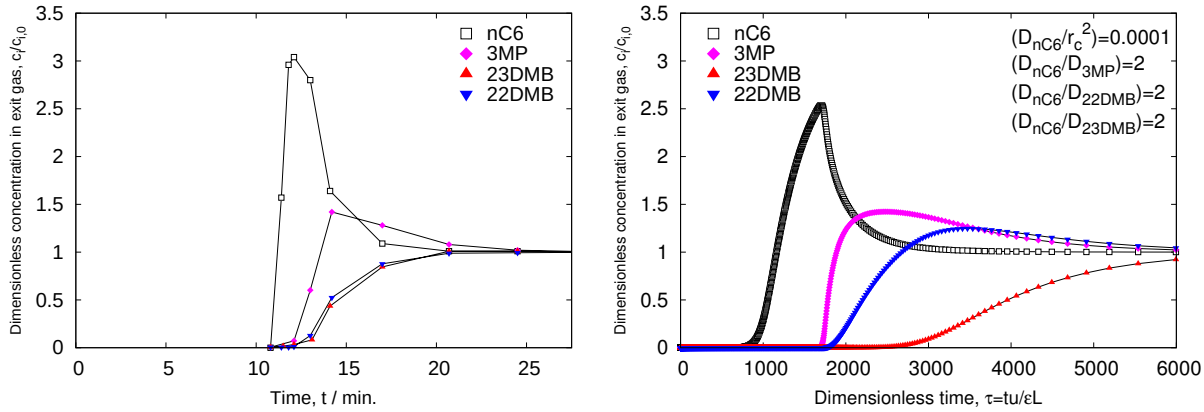

(a) *Bárcia et al. data at 423 K* **(b)** *Simulated breakthrough at 433 K*

Figure S6: *Comparison of simulations with recent experimental breakthrough data on hexane isomers in UiO-66 at a total pressure of 6.3 kPa [56].*

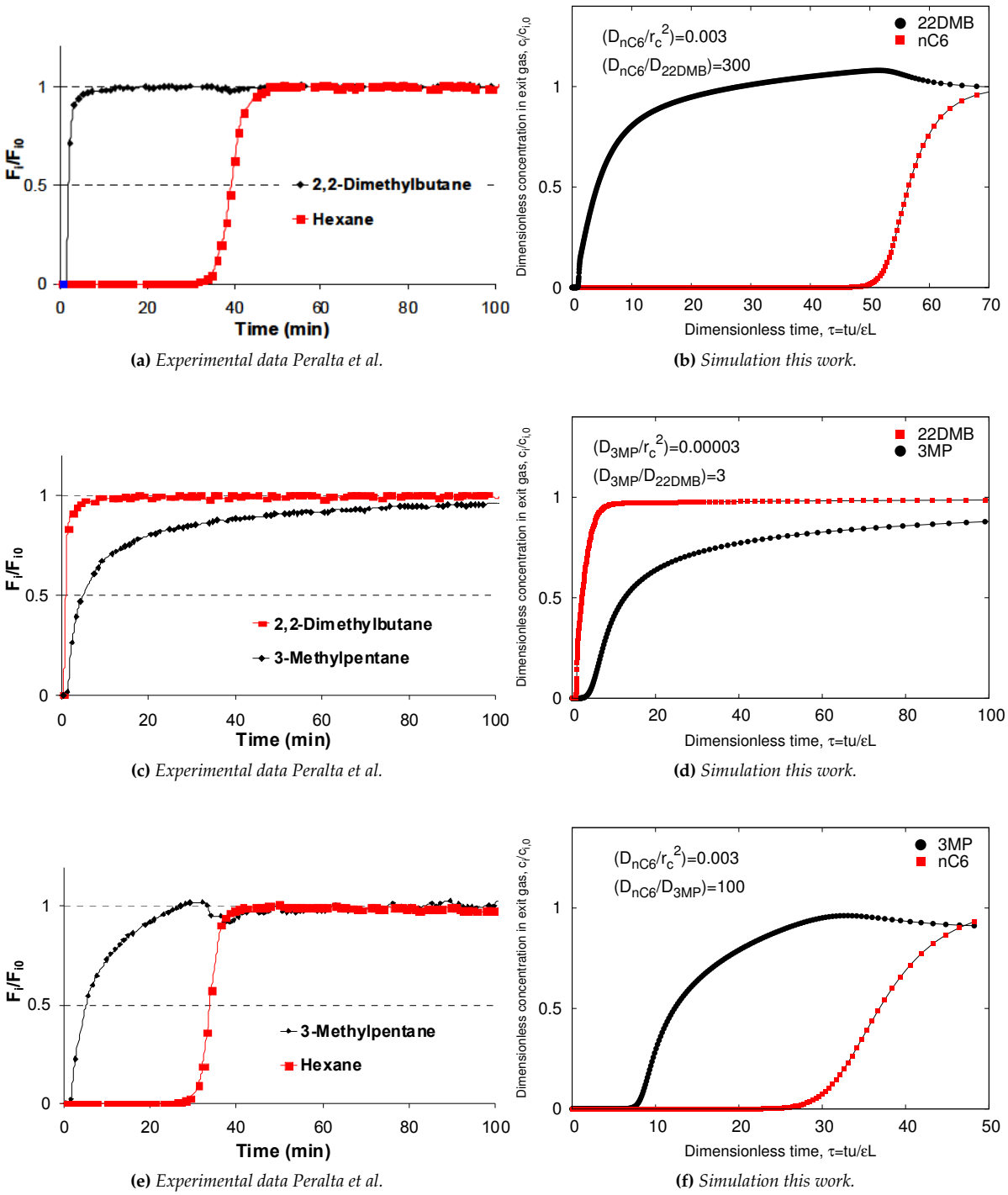

(a) *Experimental data Peralta et al.*

(b) *Simulation this work.*

(c) *Experimental data Peralta et al.*

(d) *Simulation this work.*

(e) *Experimental data Peralta et al.*

(f) *Simulation this work.*

Figure S7: *Comparison of simulations with experimental data in ZIF-8 [57]. The experimental data is at 398K, the simulation data at 433K.*

Short-list of potential adsorbents, selected on the basis of an initial screening of *all* adsorbents, that are deemed to offer practical potential for use in the separation scheme depicted in Fig. S8.

2

Short-list of potential adsorbents

2.1 Separation process and relevant patent literature

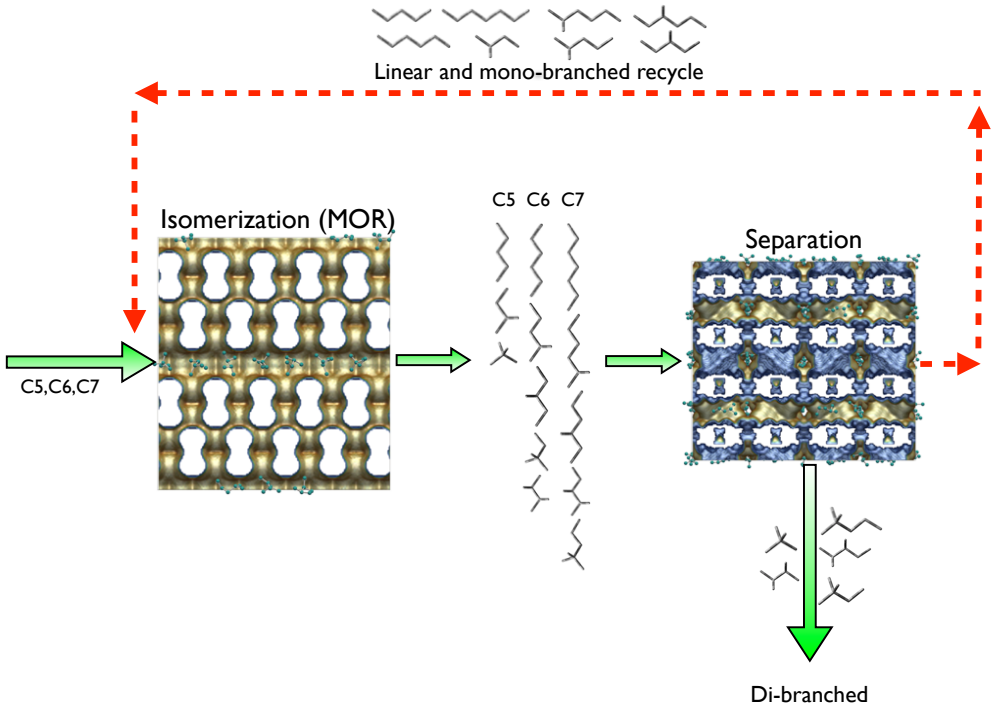

Figure S8: *Schematic of a patented separation process (patent US4717784) to improve upon current technology. The feed consists primarily of linear alkanes. In the first zone linear alkanes are isomerized to branched alkanes. In conventional technology only the linear alkanes would be separated (using LTA-type zeolite). The patent proposes a second zone to separate linear and mono-branched (which are recycled back) from the desired di-branched alkanes (that become the isomerate product blending component). Our study focuses on optimizing this separation process by screening >100 nanoporous materials for their hexane separation efficiency. In this chapter we present a selection of the best candidates and study them in considerably greater detail.*

UOP	5763730	1998	Process for alkane isomerization using reactive chromatography
UOP	6069289	2000	Process for separating and recovering multimethyl-branched alkanes
UOP	4455444	1984	Low temperature process for separating hydrocarbons
UOP	4486618	1984	Process for separating C_6 olefin hydrocarbons
UOP	5326925	1994	Isomerization process for 2,3-dimethylbutane production
UOP	4367364	1983	Process for separating normal paraffins using silicalite adsorbent
Shell	4804802	1989	Isomerization process with recycle of mono-methyl-branched paraffins and normal paraffins
Shell	4717784	1988	Total isomerization process with mono-methyl-branched plus normal paraffin recycle stream
Shell	4855529	1989	Isomerization process with preliminary normal paraffin and mono-methyl paraffin feed capture step
Shell	5073667	1991	Process for the isomerization of a hydrocarbon feed
Chevron	7029572	2006	Process for producing high RON gasoline using ATS zeolite
Chevron	7037422	2006	Process for producing high RON gasoline using CFI zeolite
VUB	7435865	2006	Method for separating hydrocarbons and use of a zeolite therefor
IFP	2968656	2010	Procede de separation de paraffines multibranchees utilisant un adsorbant de la famille des ZIF de type structural SOD

Table S1: *Selection of patents on the hexane isomer separation process. The use of ATS-, CFI-, MFI-zeolite and ZIF-8 as a means to increase the Research Octane Number (RON) is patented.*

2.2 MFI

2.2.1 Energy landscapes

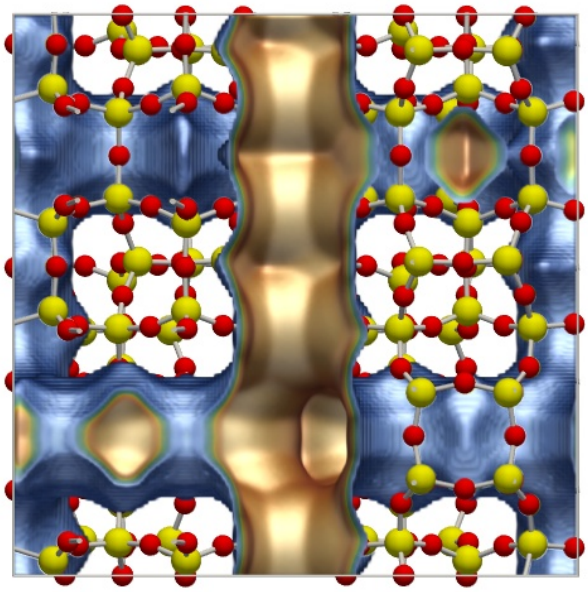

(a) *MFI (single unit cell); XY-view.*

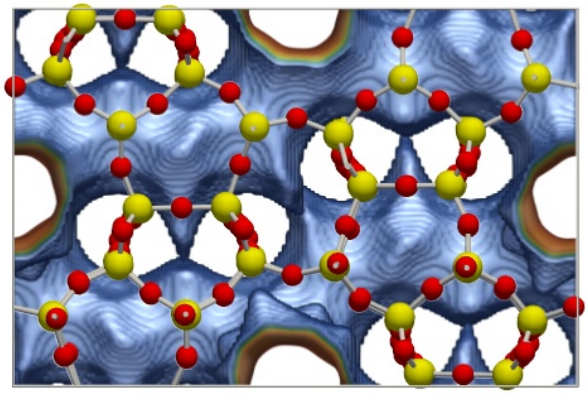

(b) *MFI (single unit cell); XZ-view*

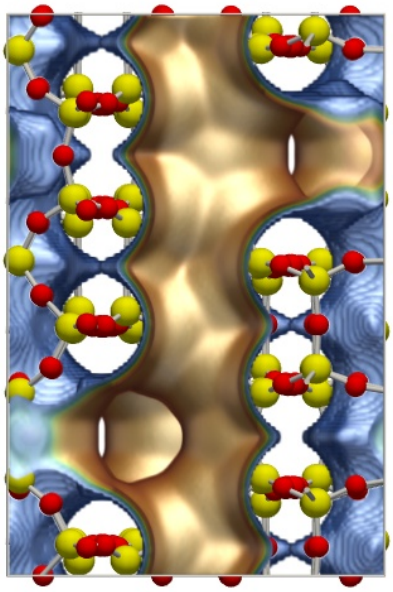

(c) *MFI (single unit cell); YZ-view*

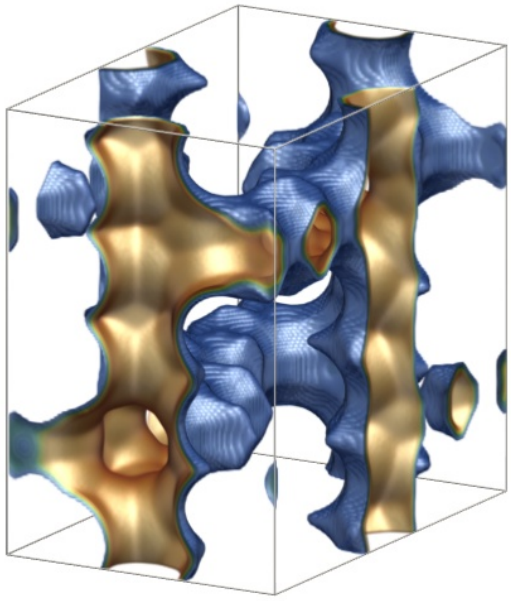

(d) *MFI (single unit cell); XYZ-view*

Figure S9: *Energy landscape of MFI. The MFI unit cell has edge lengths $a = 20.022$ Å, $b = 19.899$ Å, and $c = 13.383$ Å, with cell angles $\alpha = \beta = \gamma = 90°$. The MFI pore system consists of straight channels running in the c-direction which are connected via 'zig-zag' channels. About 29% of the structure is void. Color code: oxygen (red), silicon (yellow).*

2.2.2 Simulation snapshots

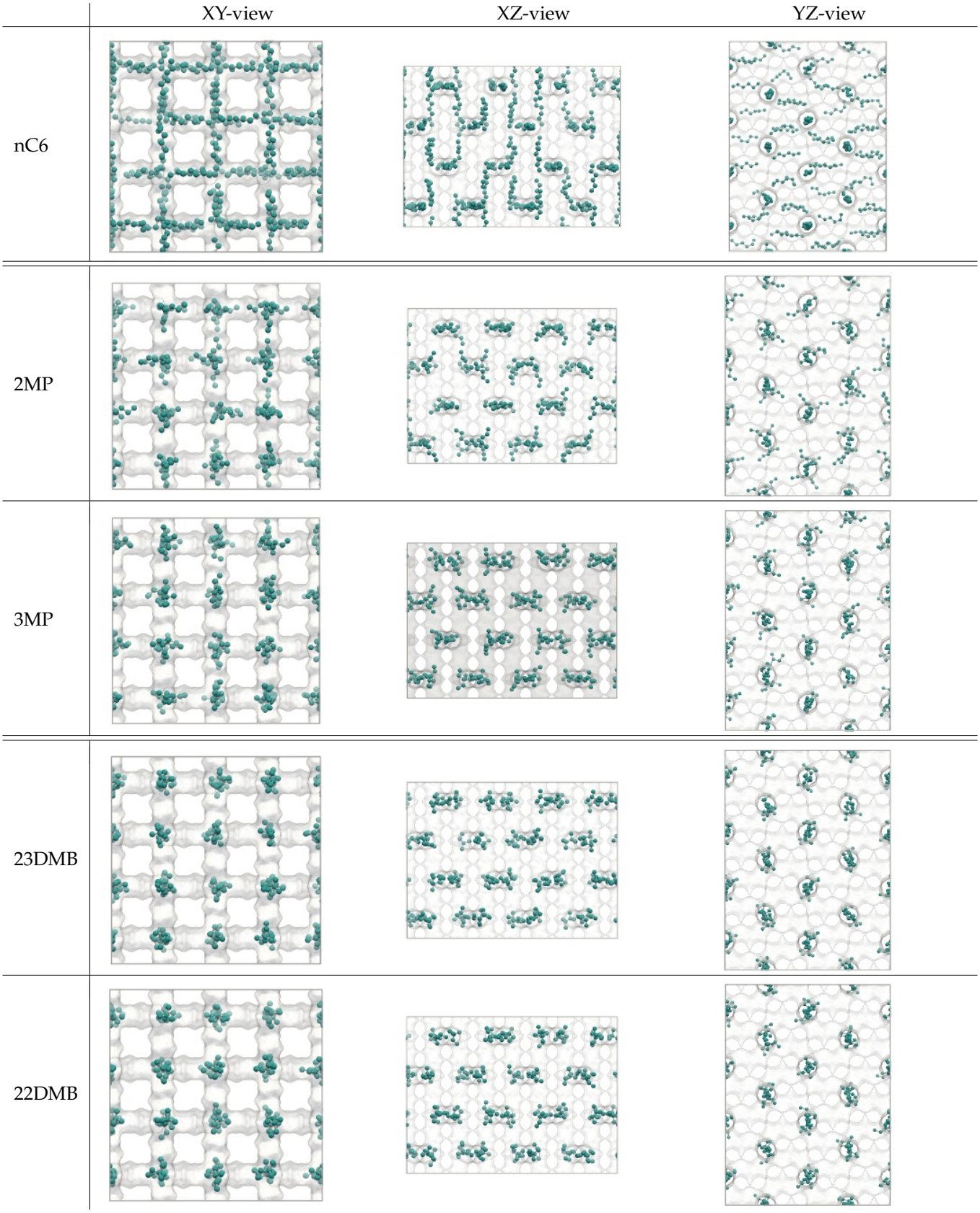

Figure S10: *Simulation snapshots of hexane isomers in MFI (2 × 2 × 4 unit cells) at 433K and 100 kPa.*

2.2.3 Simulation adsorbate densities

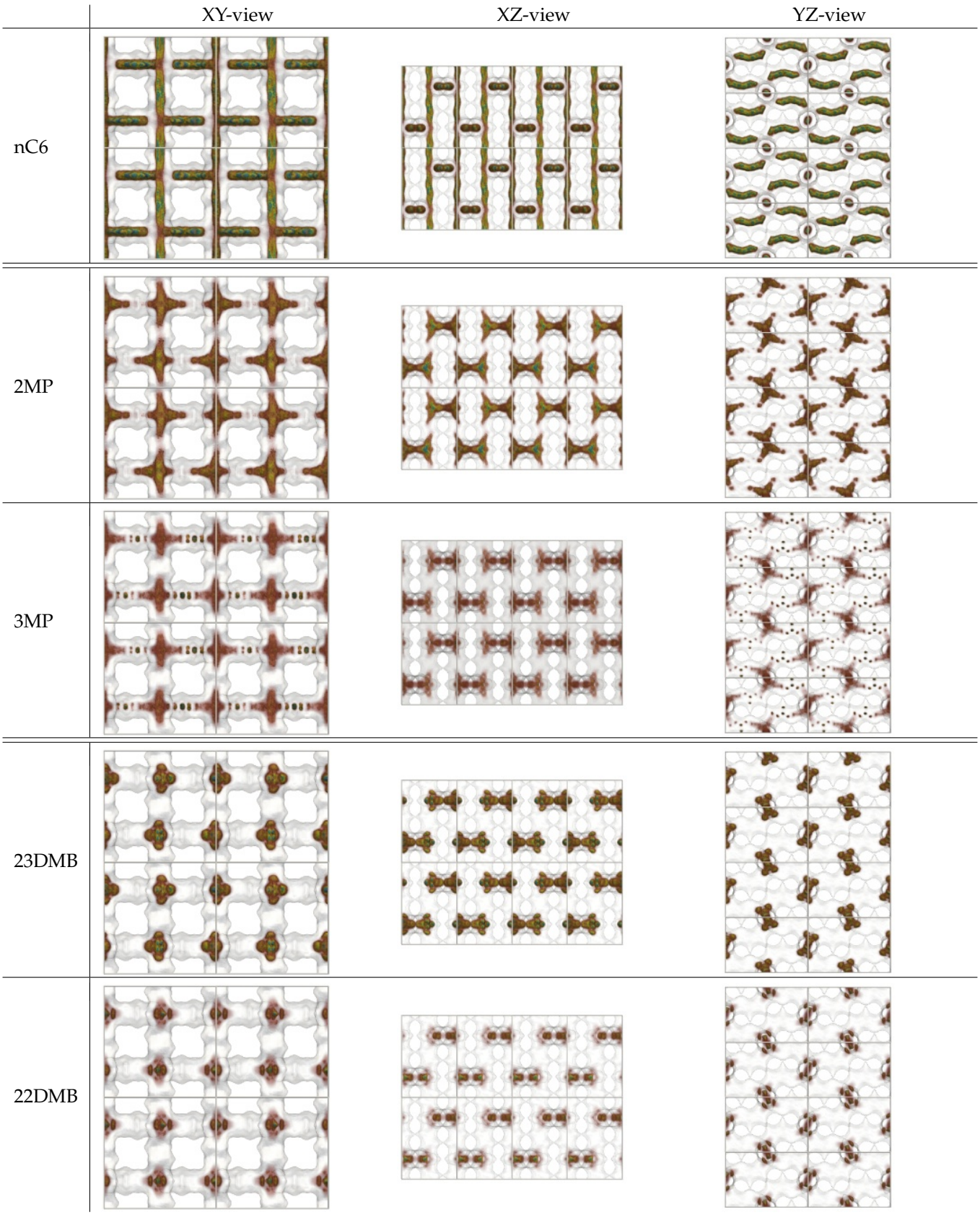

Figure S11: *Probability densities of hexane isomers in MFI ($2 \times 2 \times 4$ unit cells) at 433K and 100 kPa.*

2.2.4 Single component adsorption

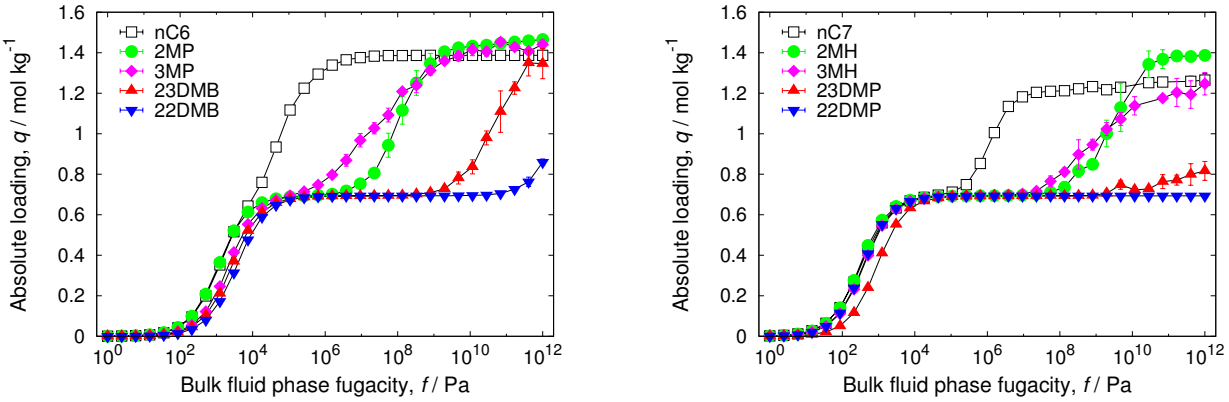

Figure S12: *Single component isotherms of hexane and heptane isomers in MFI at 433K.*

2.2.5 Heats of adsorption

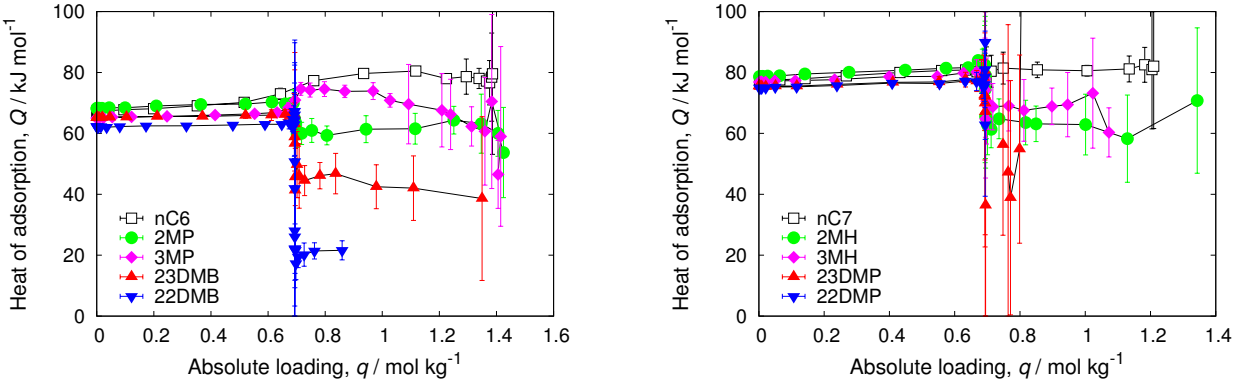

Figure S13: *Heat of adsorption of hexane and heptane isomers in MFI at 433K.*

2.2.6 Mixture adsorption

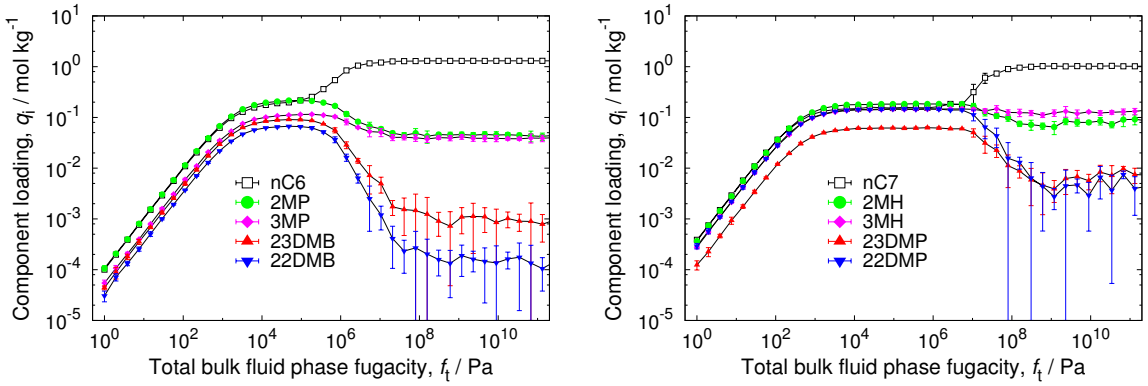

Figure S14: *Equimolar mixture isotherms of hexane and heptane isomers in MFI at 433K.*

2.2.7 IAST

	site A			site B		
	$q_{i,A,\text{sat}}$ [mol kg^{-1}]	$b_{i,A}$ [Pa$^{-\nu_{i,A}}$]	$\nu_{i,A}$ [-]	$q_{i,B,\text{sat}}$ [mol kg^{-1}]	$b_{i,B}$ [Pa$^{-\nu_{i,B}}$]	$\nu_{i,B}$ [-]
nC6	0.6935	1.34×10^{-5}	1	0.6935	7.86×10^{-4}	1
2MP	0.6935	8.52×10^{-4}	1			
3MP	0.6935	4.49×10^{-4}	1	0.1734	1.03×10^{-6}	1
23DMB	0.6935	4.99×10^{-4}	1			
22DMB	0.6935	2.75×10^{-4}	1			

Table S2: *Dual-site Langmuir-Freundlich parameters for pure component hexane isomers at 433 K in MFI.*

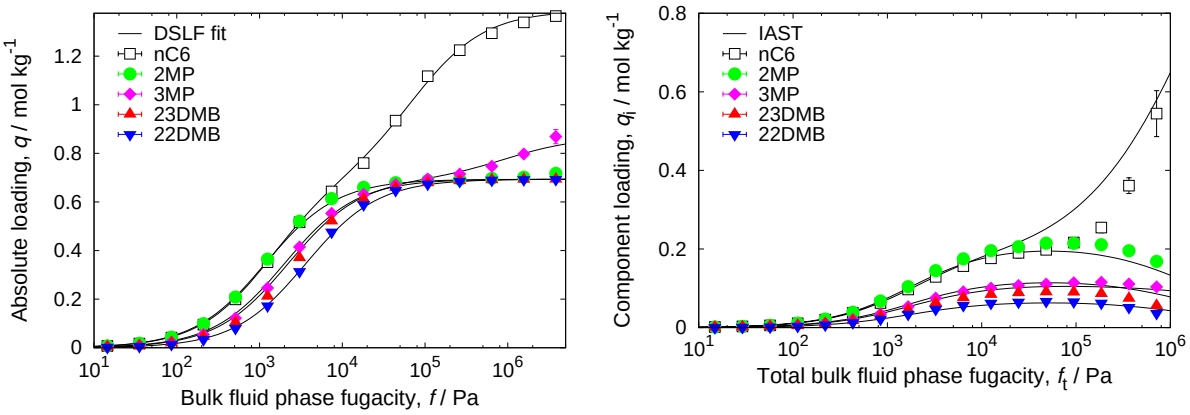

(a) *Lines are dual-site Langmuir-Freundlich fits of the pure components, points are the pure component isotherms.*

(b) *Lines are the IAST prediction of the mixture isotherms, points are the mixture isotherms.*

Figure S15: *Validation of IAST for equimolar hexane isomer mixtures in MFI at 433K.*

2.2.8 Breakthrough simulations

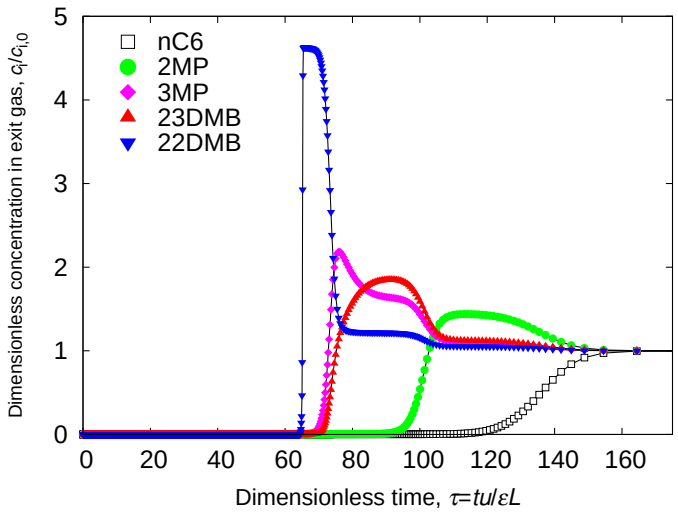

Figure S16: *Simulated step-type breakthrough of hexane isomers in MFI at 433K and a total fugacity of the bulk fluid phase of 100 kPa. Video animations of the breakthrough behavior as a function of time are provided as Supplementary information.*

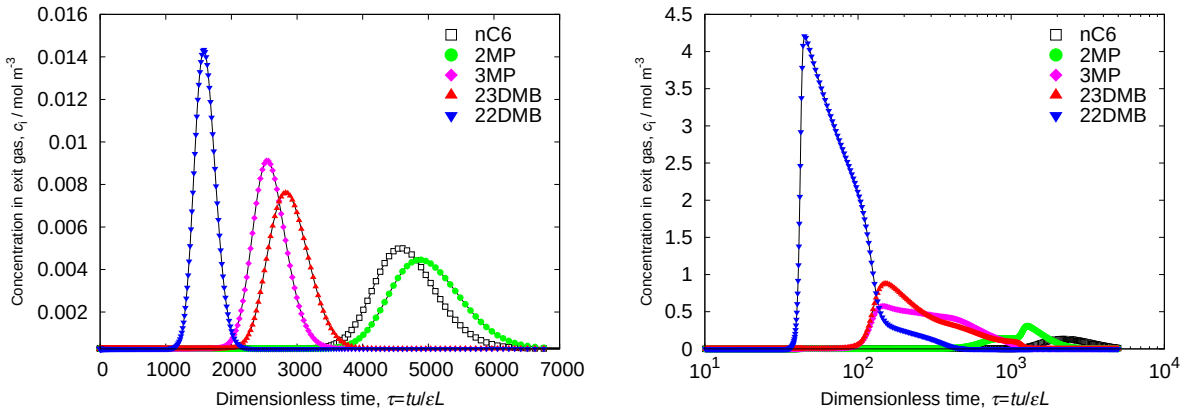

(a) *Total fugacity 100 kPa.*

(b) *Total fugacity 5 Mpa.*

Figure S17: *Simulated pulse-type breakthrough of hexane isomers in MFI at 433K.*

2.2.9 Performance discussion

Figure	description and remarks
S9	The MFI channel system: 3D channel system with intersections. There are 2 straight and 2 zig-zag channels per unit cell, and 4 intersections per unit cell.
S10,S11	Linear molecules are adsorbing everywhere, but branched molecules adsorb mostly at the intersection. At high pressures the branched molecules are forced into the zig-zag and linear channels.
S12	The isotherms show inflections related to the location of adsorption. The plateau value of the inflection corresponds to 4 molecules per unit cell. Branched molecules adsorb preferentially at the intersections. It takes additional pressure to push them into the linear and zig-zag channels.
S13	The heats of adsorption of the linear and mono-branched are slightly higher at low loading because they have a tighter fit than the dibranched at the intersection. The heats show a jump at 4 molecules per unit cell, at which the the molecules are also forced into less favorable sites.
S14	Branched molecules are driven out of the system at high pressures.
S15	The single components isotherms can be fitted very well with the Langmuir-Freundlich model (the fitted values can be found in Table S2). IAST describes the mixture well for this system.
S16	MFI does not work very well as a hexane isomer separation device at 100 kPa. However, at high pressures/loading its efficiency is outstanding.
S17	At 100 kPa only 22DMB can be separated in its pure form; At 5 MPa all components can be separated.

2.3 CFI

2.3.1 Energy landscapes

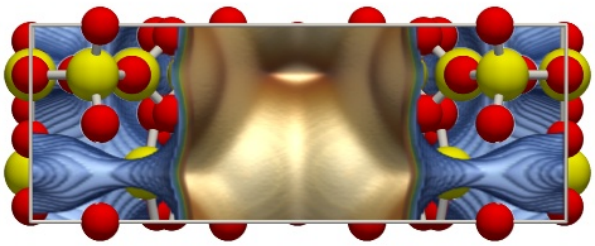

(a) *CFI (single unit cell); XY-view.*

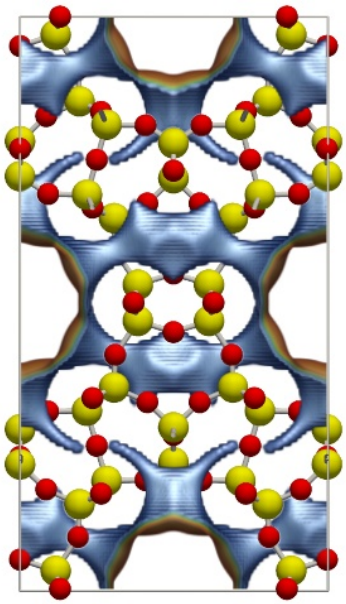

(b) *CFI (single unit cell); XZ-view.*

(c) *CFI (single unit cell); YZ-view.*

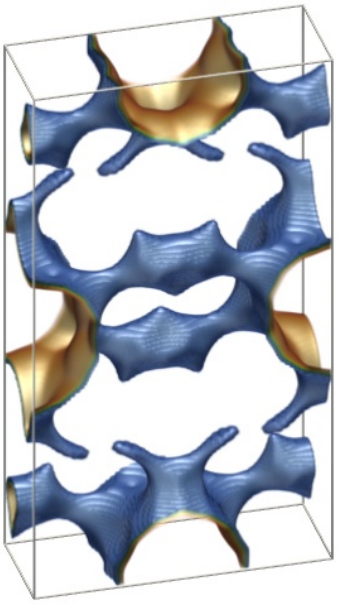

(d) *CFI (single unit cell); XYZ-view.*

Figure S18: *Energy landscape of CFI. The CFI unit cell has edge lengths* $a = 13.695$ *Å,* $b = 5.021$*Å, and* $c = 25.497$ *Å, with cell angles* $\alpha = \beta = \gamma = 90°$*. The CFI pore system consists of channels running in the b-direction. The side-pockets are too small to allow alkanes to cross from channel to channel. There are 2 uni-dimensional channels per unit cell. About 26% of the structure is void. Color code: oxygen (red), silicon (yellow).*

2.3.2 Simulation snapshots

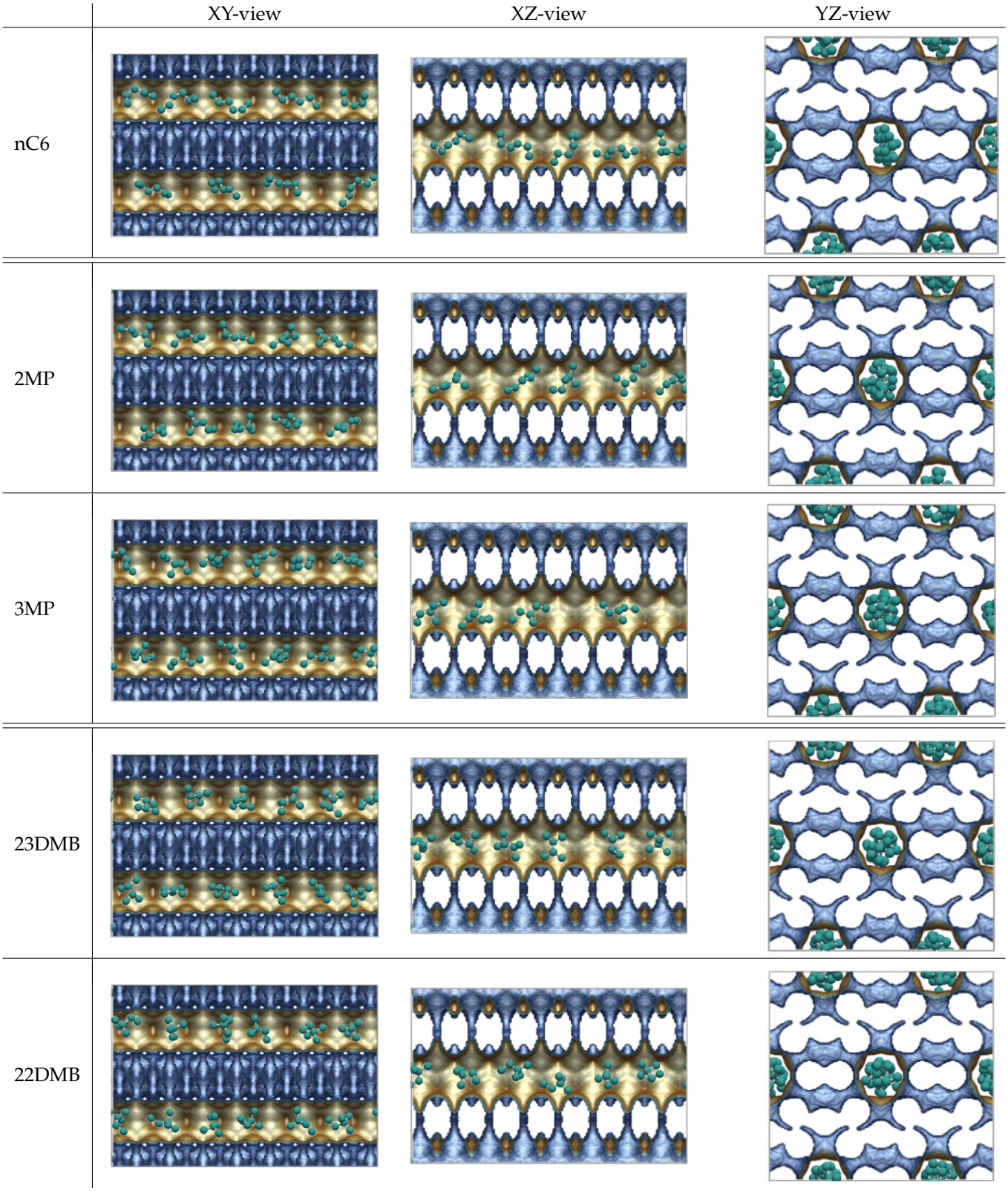

Figure S19: *Simulation snapshots of hexane isomers in CFI ($2 \times 5 \times 1$ unit cells) at 433K and 100 kPa.*

2.3.3 Single component adsorption

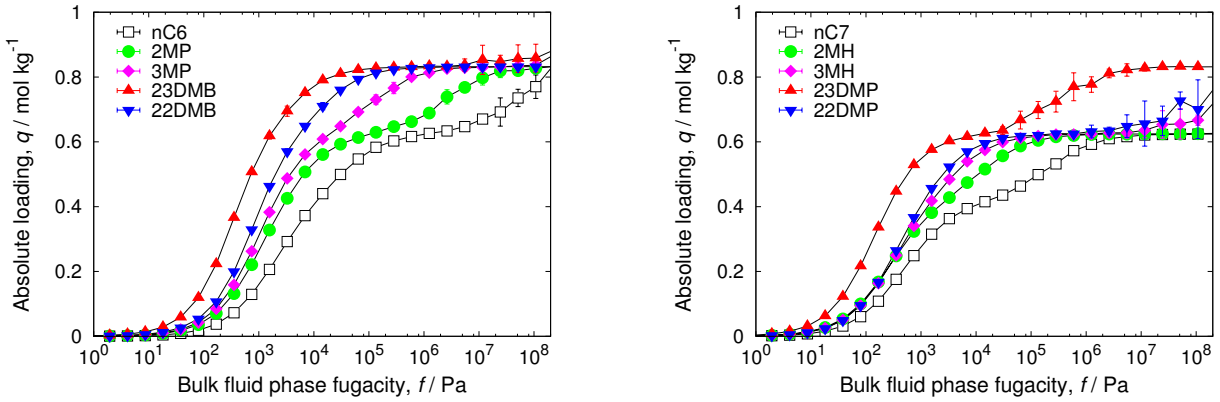

Figure S20: *Single component isotherms of hexane and heptane isomers in CFI at 433K.*

2.3.4 Heats of adsorption

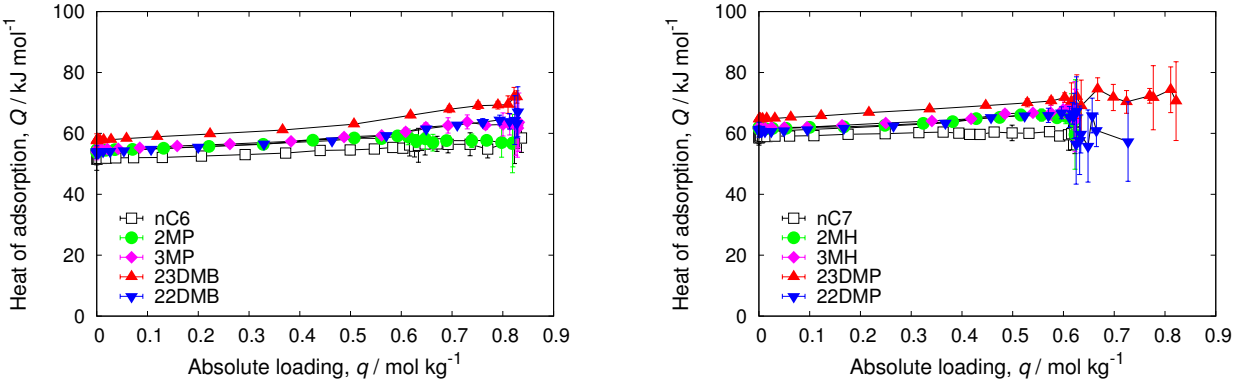

Figure S21: *Heat of adsorption of hexane and heptane isomers in CFI at 433K.*

2.3.5 Mixture adsorption

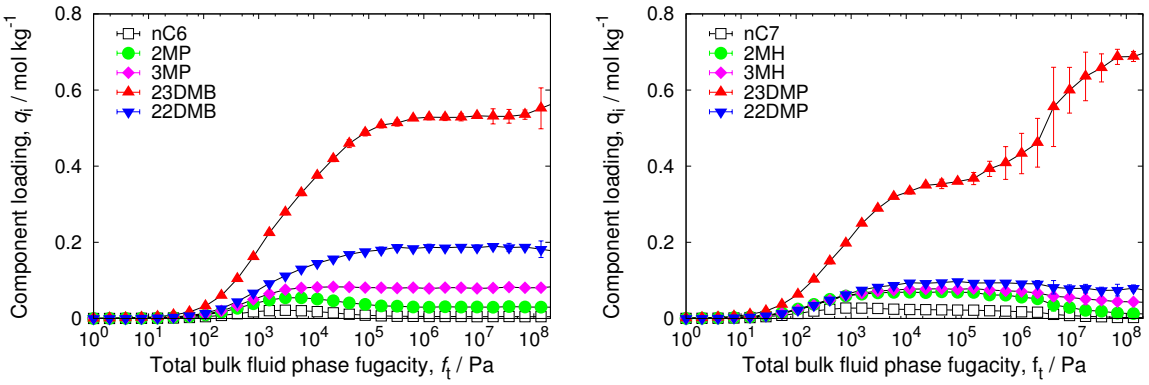

Figure S22: *Equimolar mixture isotherms of hexane and heptane isomers in CFI at 433K.*

2.3.6 IAST

	site A			site B		
	$q_{i,A,\text{sat}}$ [mol kg^{-1}]	$b_{i,A}$ [Pa$^{-\nu_{i,A}}$]	$\nu_{i,A}$ [-]	$q_{i,B,\text{sat}}$ [mol kg^{-1}]	$b_{i,B}$ [Pa$^{-\nu_{i,B}}$]	$\nu_{i,B}$ [-]
nC6	0.25	2.92×10^{-8}	1	0.59	3.41×10^{-4}	1
2MP	0.22	5.07×10^{-7}	1	0.61	7.71×10^{-4}	1
3MP	0.18	7.59×10^{-6}	1	0.65	8.03×10^{-4}	1
23DMB	0.83	1.96×10^{-3}	1			
22DMB	0.11	2.65×10^{-5}	1	0.73	1.02×10^{-3}	1

Table S3: *Dual-site Langmuir-Freundlich parameters for pure component hexane isomers at 433 K in CFI.*

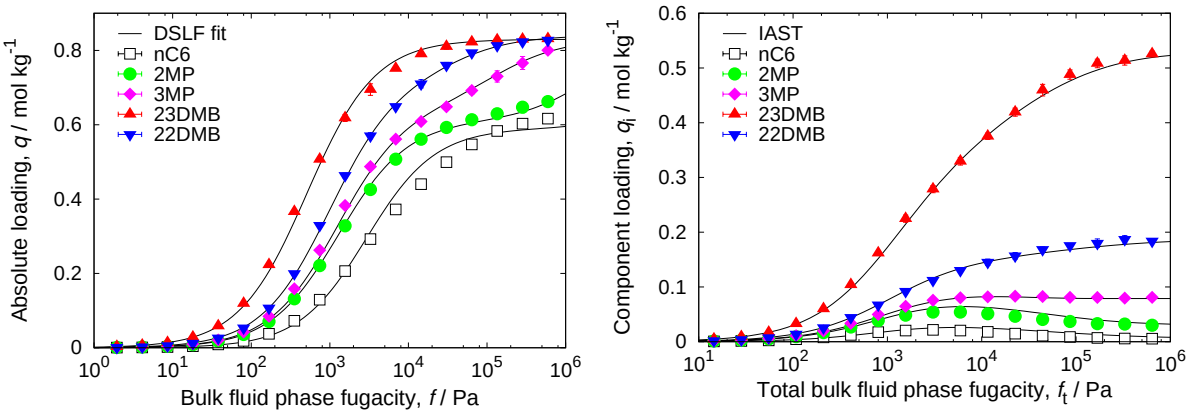

(a) *Lines are dual-site Langmuir-Freundlich fits of the pure components, points are the pure component isotherms.*

(b) *Lines are the IAST prediction of the mixture isotherms, points are the mixture isotherms.*

Figure S23: *Validation of IAST for equimolar hexane isomer mixtures in CFI at 433K.*

2.3.7 Breakthrough simulations

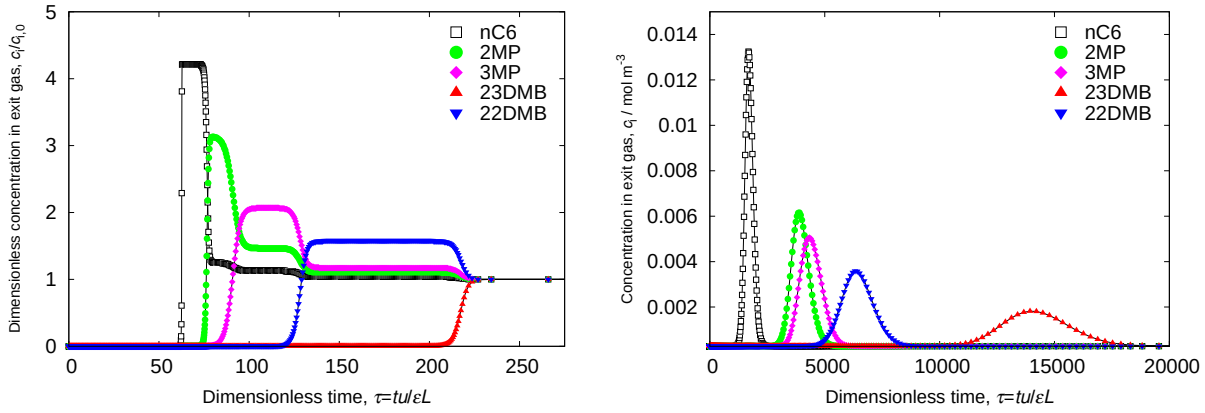

(a) *Step-type breakthrough.*

(b) *Pulse-type breakthrough.*

Figure S24: *Simulated breakthrough of hexane isomers in CFI at 433K and a total fugacity of the bulk fluid phase of 0.1 MPa. Video animations of the breakthrough behavior as a function of time are provided as Supplementary information.*

2.3.8 Performance discussion

Figure	description and remarks
S18	The CFI channel system is an uni-dimensional channel system. There are 2 channels per unit cell.
S19	The channels are slightly tortuous and show alternating corrugations. The dibranched molecules are more commensurate with the corrugations than the linear molecules.
S20	The isotherms show inflections which indicate several possible adsorption sites that differ in energy and packing effects.
S21	The higher heat of adsorption of the di-branched molecules is evidence of their better fit in the channels.
S22	For hexane isomers there is a clear separation for linear, mono-and di-branched alkanes. For heptane isomers the separation is much reduced.
S23	The single components isotherms can be fitted very well with the Langmuir-Freundlich model (the fitted values can be found in Table S3). IAST describes the mixture very well for this system.
S24(a)	CFI works very well as a hexane isomer separation device at 100 kPa.
S24(b)	23DMB can be nicely separated from 22DMB with CFI. Also excellent separation of nC6 in pure form.

2.4 ATS

2.4.1 Energy landscapes

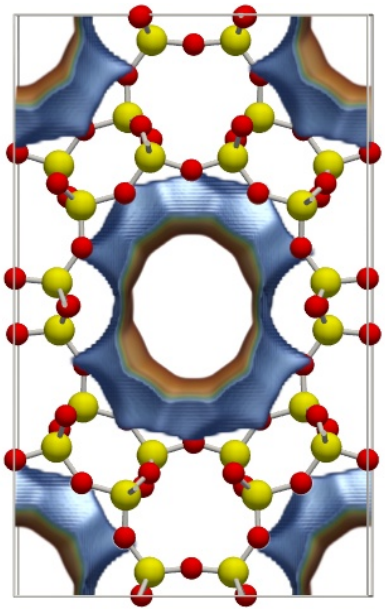

(a) *ATS (single unit cell); XY-view.*

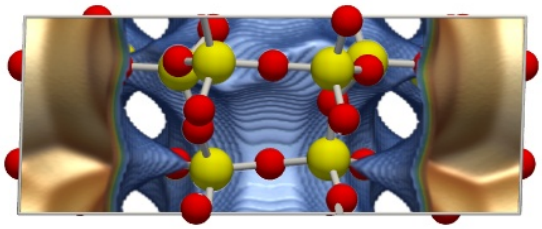

(b) *ATS (single unit cell); XZ-view.*

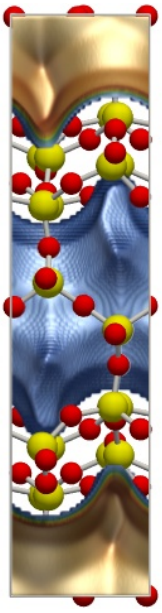

(c) *ATS (single unit cell); YZ-view.*

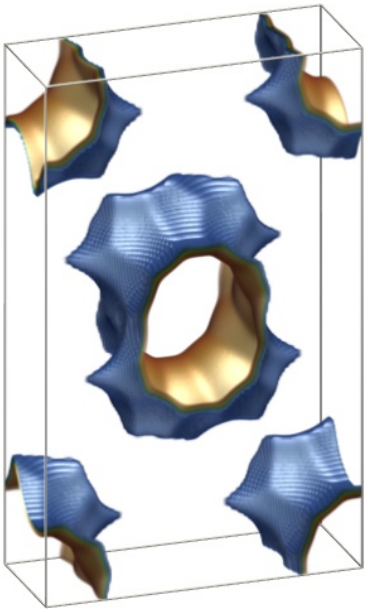

(d) *ATS (single unit cell); XYZ-view.*

Figure S25: *Energy landscape of ATS. The CFI unit cell has edge lengths $a = 13.1483$ Å, $b = 21.5771$ Å, and $c = 5.1639$ Å, with cell angles $\alpha = 90°$, $\beta = 91.84°$, and $\gamma = 90°$. The ATS pore system consists of channels running in the c-direction. There are 2 uni-dimensional channels per unit cell. About 30% of the structure is void. Color code: oxygen (red), silicon (yellow).*

2.4.2 Simulation snapshots

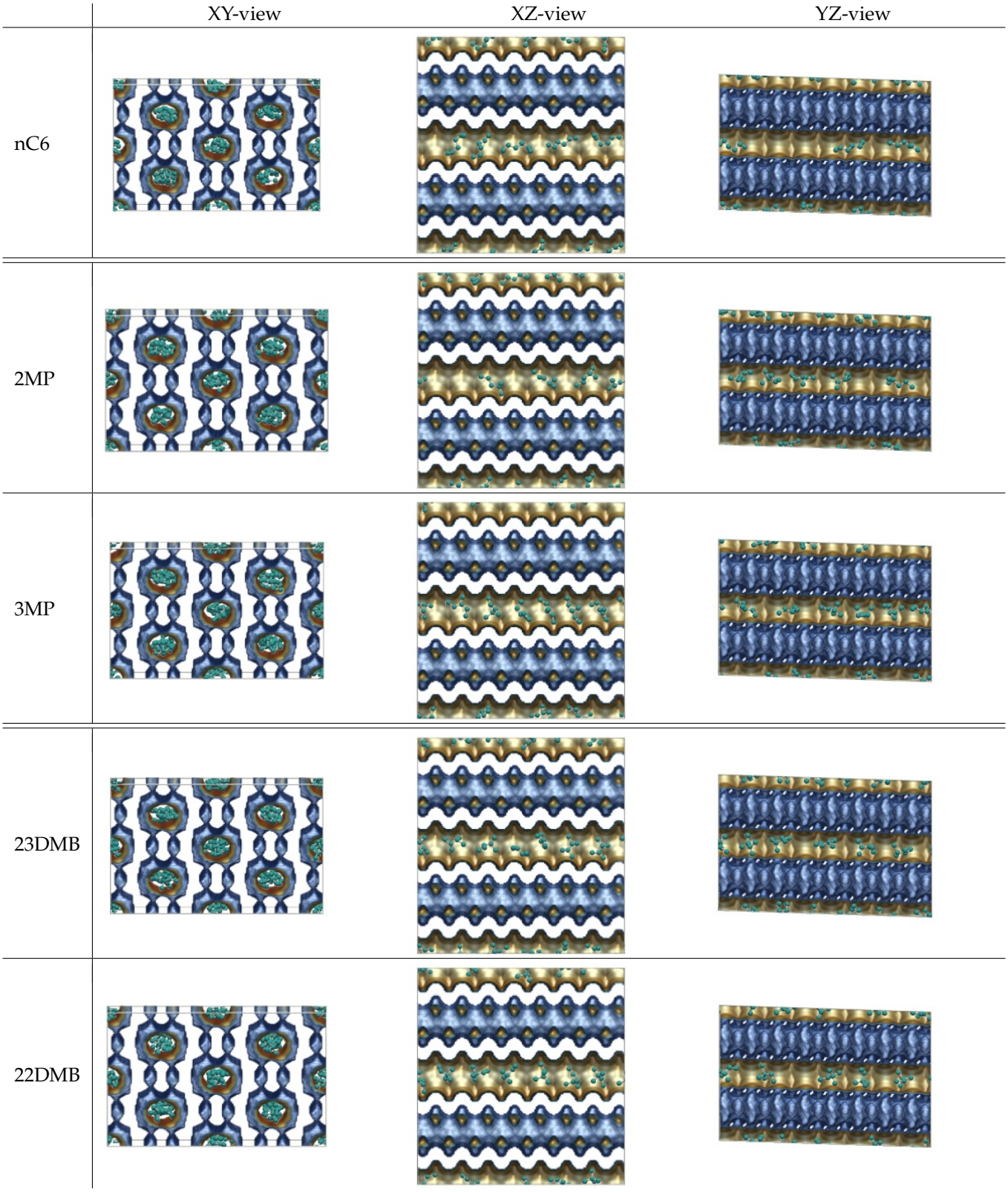

Figure S26: *Simulation snapshots of hexane isomers in ATS at 433K and 100 kPa.*

2.4.3 Single component adsorption

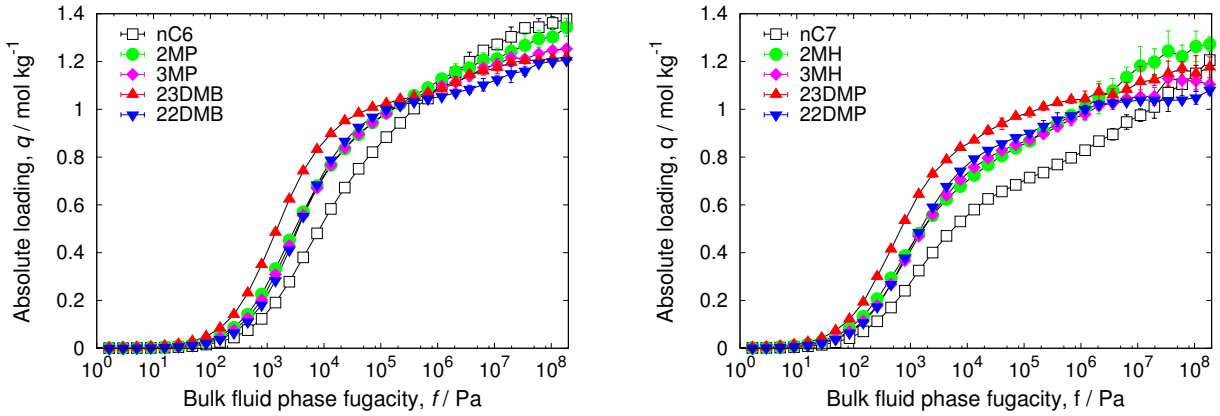

Figure S27: *Single component isotherms of hexane and heptane isomers in ATS at 433K.*

2.4.4 Heats of adsorption

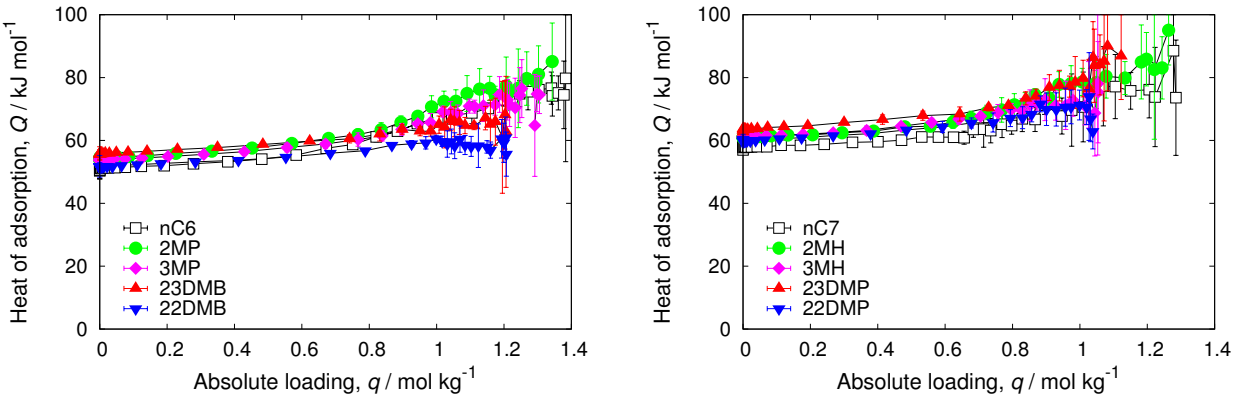

Figure S28: *Heat of adsorption of hexane and heptane isomers in ATS at 433K.*

2.4.5 Mixture adsorption

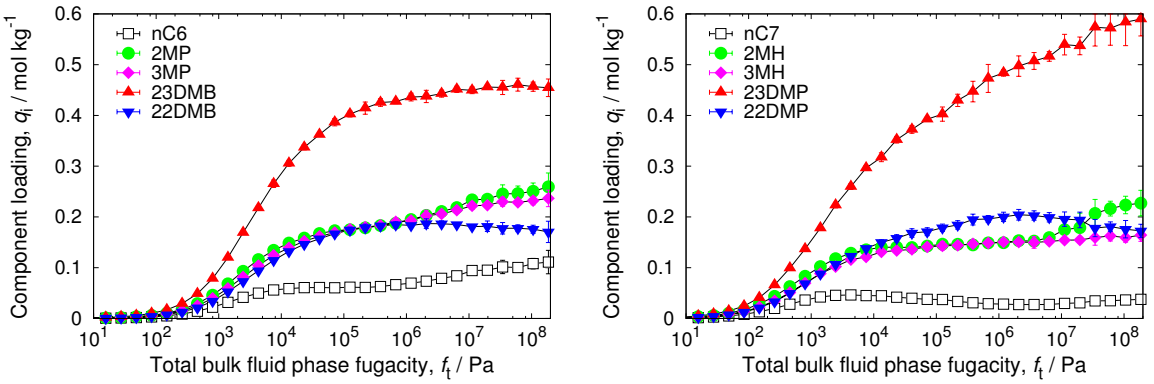

Figure S29: *Equimolar mixture isotherms of hexane and heptane isomers in ATS at 433K.*

2.4.6 IAST

	site A			site B		
	$q_{i,A,\text{sat}}$ [mol kg^{-1}]	$b_{i,A}$ [Pa$^{-\nu_{i,A}}$]	$\nu_{i,A}$ [-]	$q_{i,B,\text{sat}}$ [mol kg^{-1}]	$b_{i,B}$ [Pa$^{-\nu_{i,B}}$]	$\nu_{i,B}$ [-]
nC6	0.82	2.21×10^{-4}	1	0.54	9.78×10^{-7}	1
2MP	0.95	3.82×10^{-4}	1	0.37	6.41×10^{-7}	1
3MP	0.98	3.17×10^{-4}	1	0.285	4.34×10^{-7}	1
23DMB	1.03	5.91×10^{-4}	1	0.2	3.11×10^{-7}	1
22DMB	1.03	2.57×10^{-4}	1	0.18	1.1×10^{-7}	1

Table S4: *Dual-site Langmuir-Freundlich parameters for pure component hexane isomers at 433 K in ATS.*

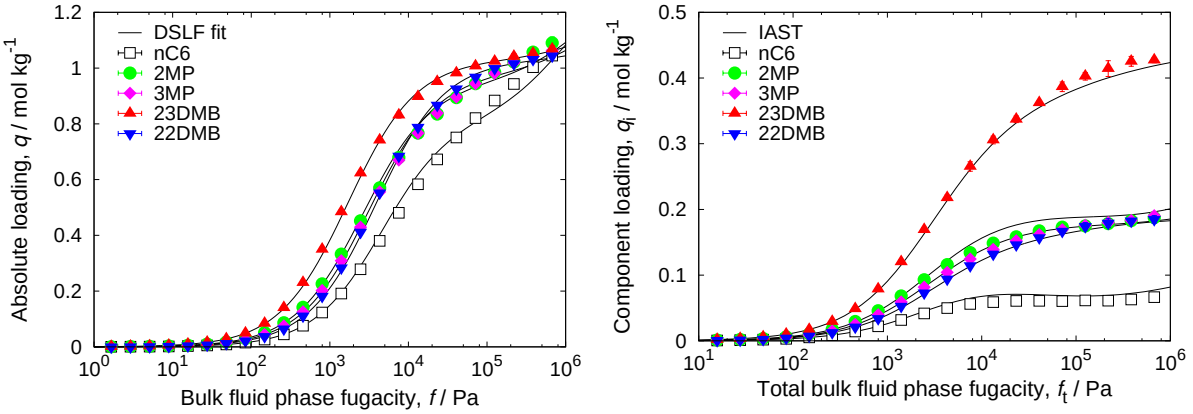

(a) *Lines are dual-site Langmuir-Freundlich fits of the pure components, points are the pure component isotherms.*

(b) *Lines are the IAST prediction of the mixture isotherms, points are the mixture isotherms.*

Figure S30: *Validation of IAST for equimolar hexane isomer mixtures in ATS at 433K.*

2.4.7 Breakthrough simulations

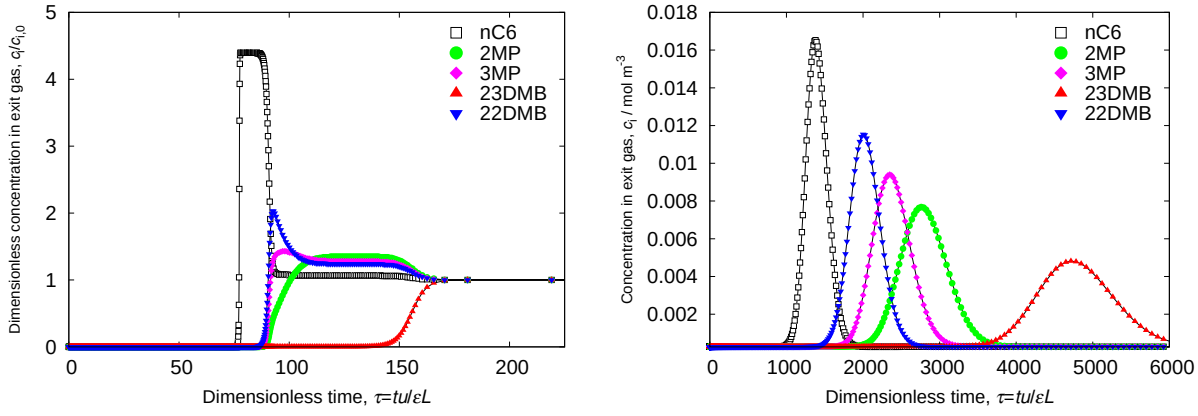

(a) *Step-type breakthrough.*

(b) *Pulse-type breakthrough.*

Figure S31: *Simulated breakthrough of hexane isomers in ATS at 433K and a total fugacity of the bulk fluid phase of 100 kPa. Video animations of the breakthrough behavior as a function of time are provided as Supplementary information.*

2.4.8 Performance discussion

Figure	description and remarks
S25	The ATS channel system consists of 2 uni-dimensional channels per unit cell.
S26	The channels are slightly tortuous and show alternating corrugations. The 2,3-dibranched molecules are more commensurate with the corrugations than the linear molecules.
S27	The 23DMB adsorbs the best, the linear the worst, but there is no clear difference between 2MP, 3MP, and 22DMB.
S28	The heat of adsorption is in the same order as the single components isotherms.
S29	The mixture is not able to differentiate between 2MP, 3MP, and 22DMB up to fairly high pressure.
S30	The single components isotherms can be fitted very well with the Langmuir-Freundlich model (the fitted values can be found in Table S4). IAST describes the mixture very well for this system.
S31(a)	Only the linear alkane and the 2,2-dibranched molecule can be separated of the remainder. We would not have selected this structure if it were not for the Chevron-patent.
S31(b)	Only 23DMB can be separated in pure form. We have to concluded, based on the simulations, that despite the patent for this structure, ATS seems to be a mediocre separation device for hexane isomers.

2.5 MgMOF-74

2.5.1 Energy landscapes

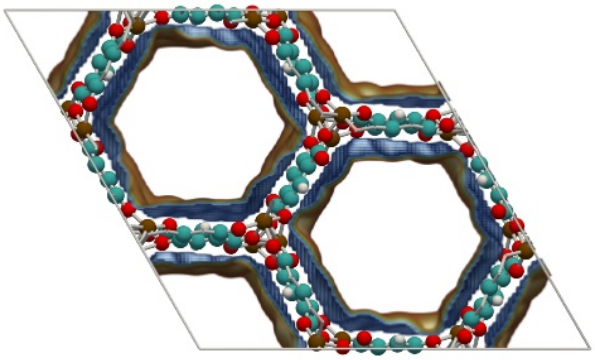

(a) *MgMOF-74 (single unit cell); XY-view.*

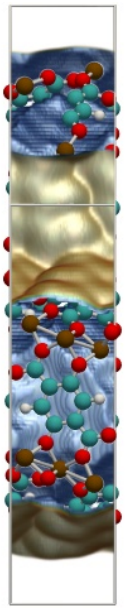

(b) *MgMOF-74 (single unit cell); XZ-view.*

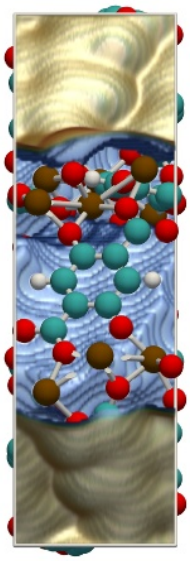

(c) *MgMOF-74 (single unit cell); YZ-view.*

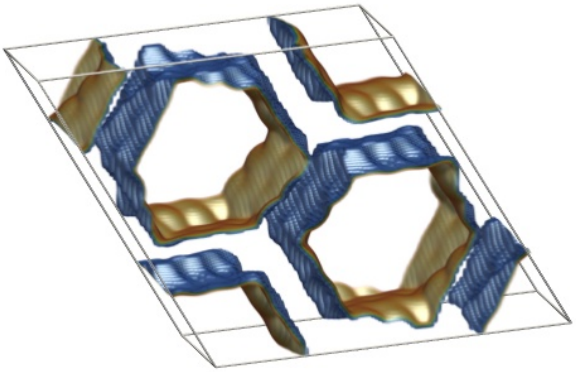

(d) *MgMOF-74 (single unit cell); XYZ-view.*

Figure S32: *Energy landscape of MgMOF-74. The MgMOF-74 unit cell has edge lengths* $a = 25.8765$ *Å,* $b = 25.8765$ *Å, and* $c = 6.7856$ *Å, with cell angles* $\alpha = \beta = 90.0°$*, and* $\gamma = 120°$*. The MgMOF-74 pore system consists of channels running in the c-direction (two per unit cell). About 78% of the structure is void. Color code: magnesium (ochre), oxygen (red), nitrogen (blue), carbon (cyan), hydrogen (white).*

2.5.2 Simulation snapshots

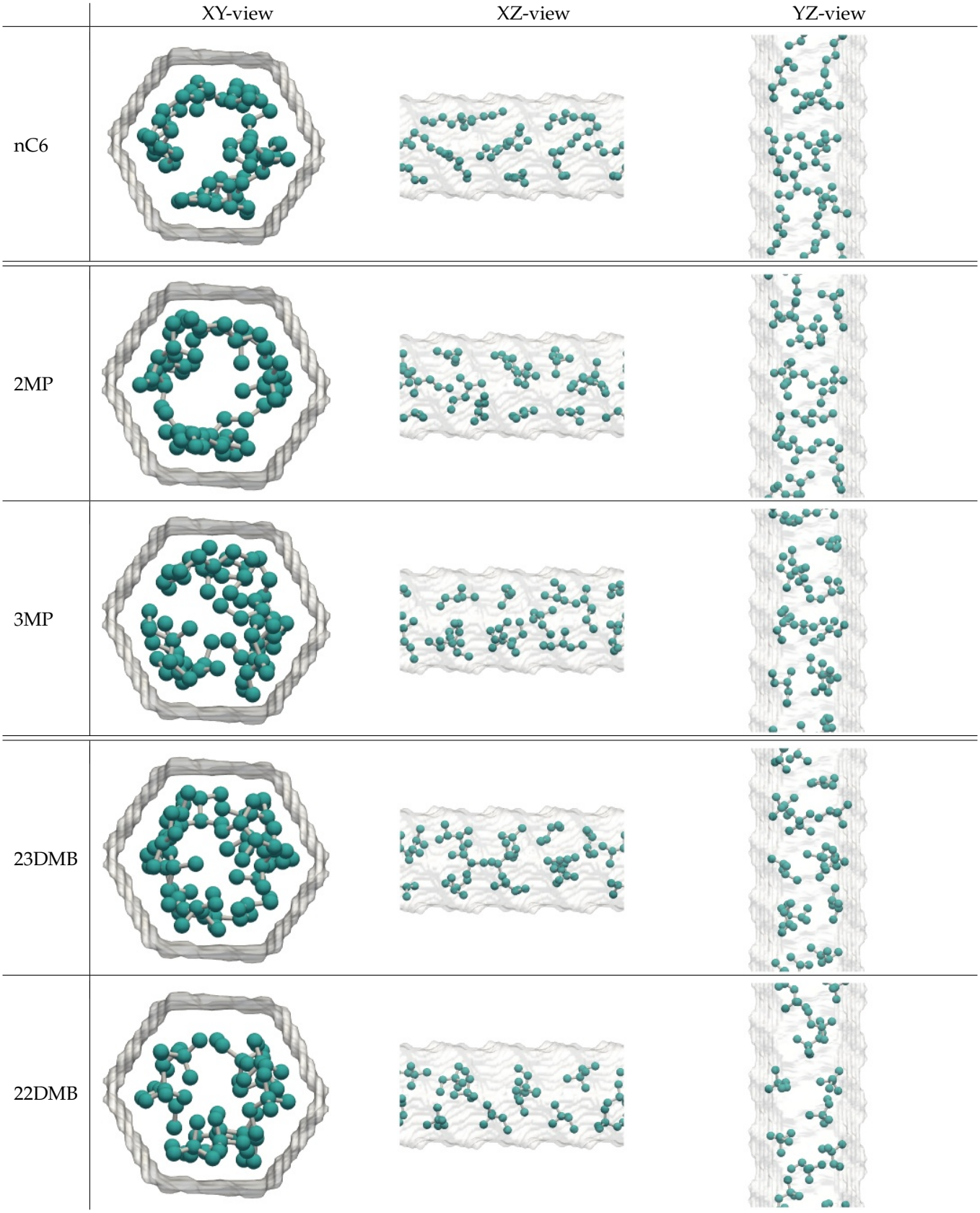

Figure S33: *Simulation snapshots of hexane isomers in MgMOF-74 at 433K and 100 kPa.*

2.5.3 Single component adsorption

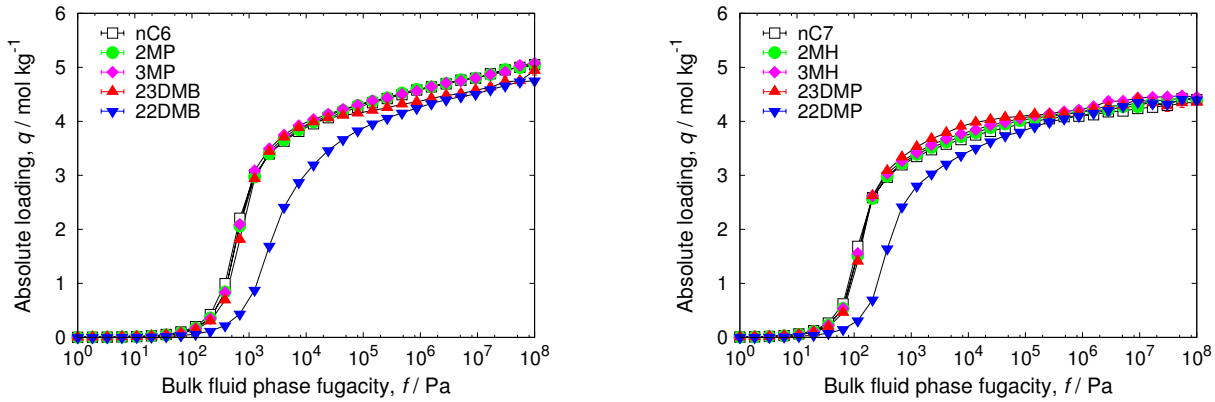

Figure S34: *Single component isotherms of hexane and heptane isomers in MgMOF-74 at 433K.*

2.5.4 Heats of adsorption

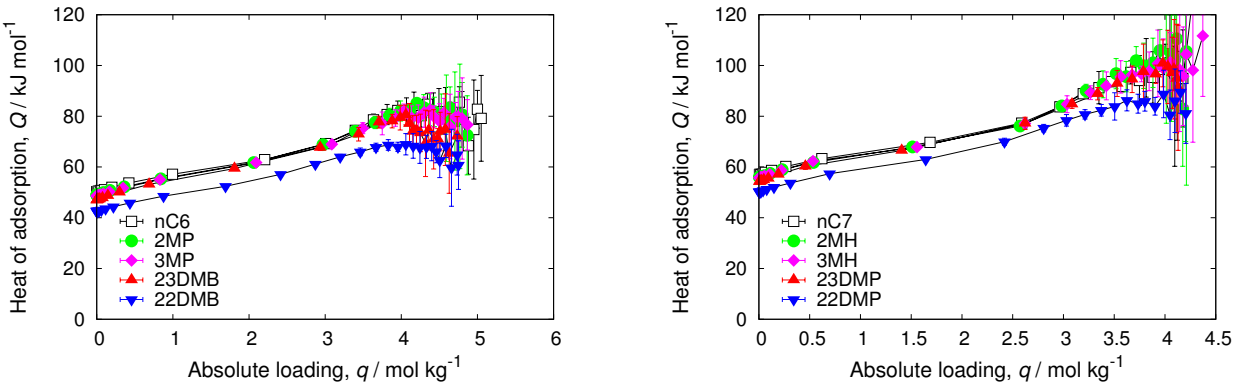

Figure S35: *Heat of adsorption of hexane and heptane isomers in MgMOF-74 at 433K.*

2.5.5 Mixture adsorption

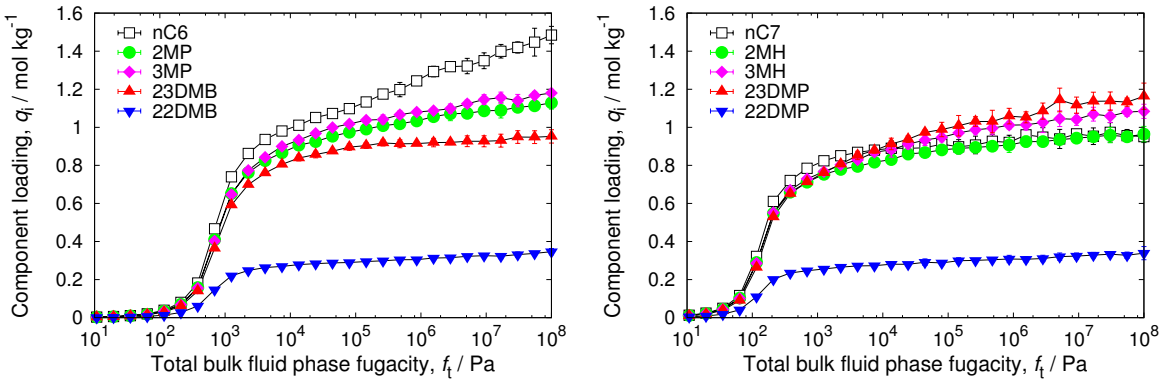

Figure S36: *Equimolar mixture isotherms of hexane and heptane isomers in MgMOF-74 at 433K.*

2.5.6 IAST

	site A			site B		
	$q_{i,A,\text{sat}}$ [mol kg^{-1}]	$b_{i,A}$ [Pa$^{-\nu_{i,A}}$]	$\nu_{i,A}$ [-]	$q_{i,B,\text{sat}}$ [mol kg^{-1}]	$b_{i,B}$ [Pa$^{-\nu_{i,B}}$]	$\nu_{i,B}$ [-]
nC6	3.95	1.98×10^{-5}	1.66	1.1	1.41×10^{-3}	0.5
2MP	3.84	1.85×10^{-5}	1.66	1.2	1.39×10^{-3}	0.52
3MP	3.95	1.81×10^{-5}	1.66	1.1	1.43×10^{-3}	0.5
23DMB	3.9	9.94×10^{-6}	1.73	1.04	1.57×10^{-3}	0.45
22DMB	3.5	4.0×10^{-5}	1.3	1.2	5.0×10^{-4}	0.6

Table S5: *Dual-site Langmuir-Freundlich parameters for pure component hexane isomers at 433 K in MgMOF-74.*

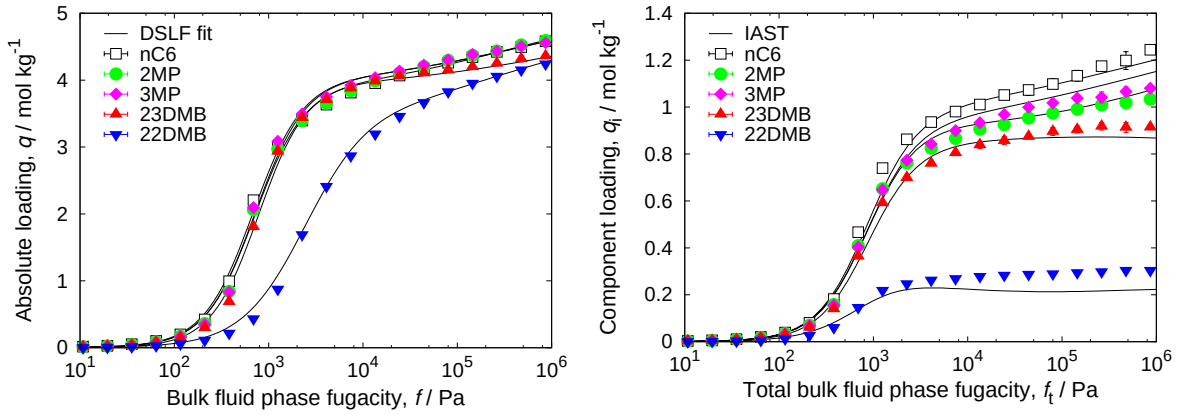

(a) *Lines are dual-site Langmuir-Freundlich fits of the pure components, points are the pure component isotherms.*

(b) *Lines are the IAST prediction of the mixture isotherms, points are the mixture isotherms.*

Figure S37: *Validation of IAST for equimolar hexane isomer mixtures in MgMOF-74 at 433K.*

2.5.7 Breakthrough simulations

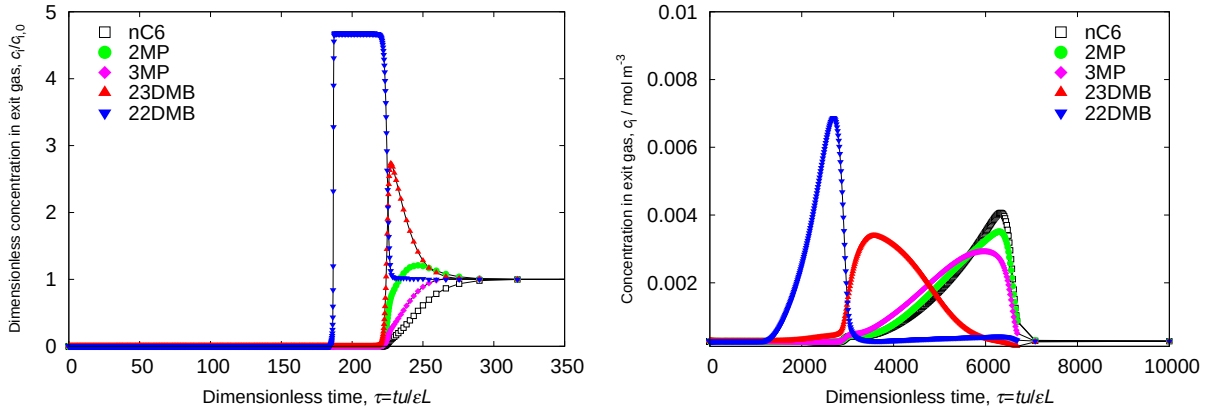

(a) *Step-type breakthrough.*

(b) *Pulse-type breakthrough.*

Figure S38: *Simulated breakthrough of hexane isomers in MgMOF-74 at 433K and a total fugacity of the bulk fluid phase of 100 kPa. Video animations of the breakthrough behavior as a function of time are provided as Supplementary information.*

2.5.8 Performance discussion

Figure	description and remarks
S32	The MgMOF-74 channel system consists of 3 uni-dimensional hexagonal channels per unit cell.
S33	The linear molecules are most commensurate with the structure; they can pack efficiently both parallel and perpendicular along the grooves inside the honeycomb channels.
S34	The single component isotherms are very similar, only the 2,2-dibranched stands out.
S35	The heat of adsorption is in the same order as the single components isotherms.
S36	The MgMOF-74 is sensitive to the length of the alkanes, the hexane isomers show the normal adsorption hierarchy, but the heptane isomers do not. The mixture shows a much larger discrimination of the hexane isomers than the single components which indicates competitive adsorption.
S37	The single components isotherms can be fitted very well with the Langmuir-Freundlich model (the fitted values can be found in Table S5). IAST describes the mixture very well for this system.
S38	The MgMOF-74 structure meets the process requirement: for hexane isomers it is possible to separate the linear and mono-branched from the dibranched.

2.6 CoBDP

2.6.1 Energy landscapes

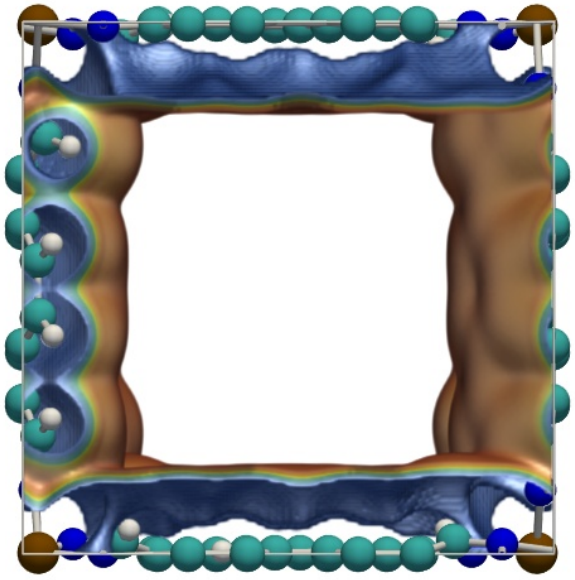

(a) *CoBDP (single unit cell); XY-view.*

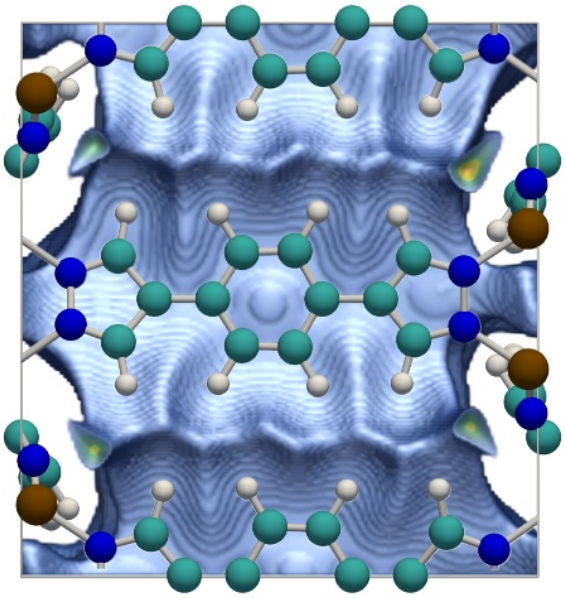

(b) *CoBDP (single unit cell); XZ-view.*

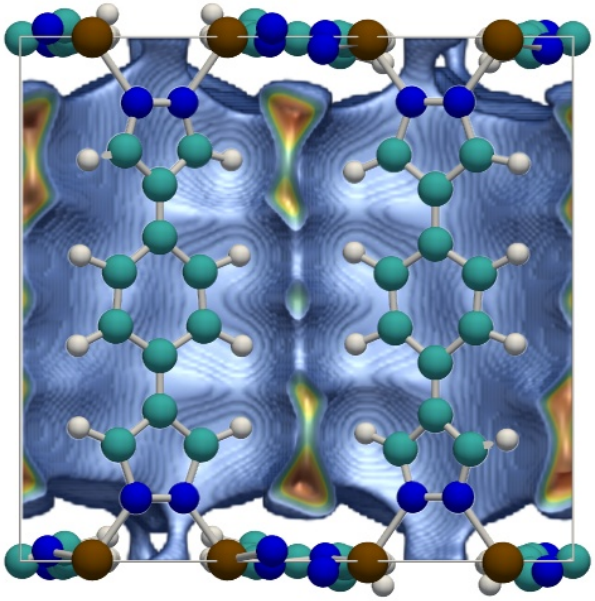

(c) *CoBDP (single unit cell); YZ-view.*

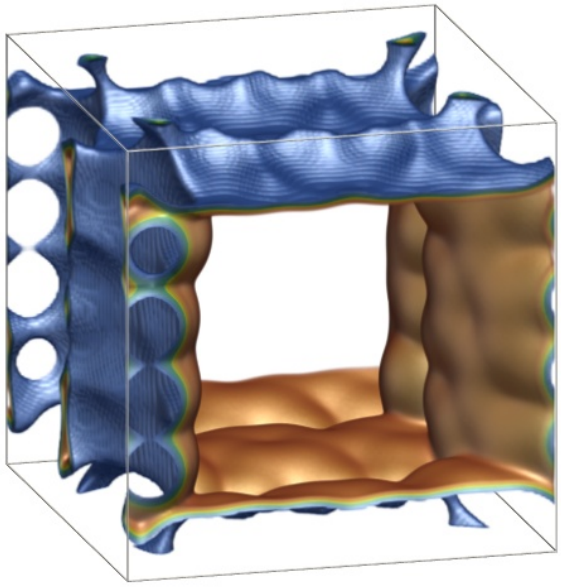

(d) *CoBDP (single unit cell); XYZ-view.*

Figure S39: *Energy landscape of CoBDP. The CoBDP unit cell has edge lengths* $a = 13.2529$ *Å,* $b = 13.253$ *Å, and* $c = 13.995$ *Å, with cell angles* $\alpha = \beta = \gamma = 90°$*. The CoBDP pore system consists of approximately rectangular channels running in the c-direction. There is 1 uni-dimensional channel per unit cell. About 66% of the structure is void. Color code: cobalt (ochre), oxygen (red), nitrogen (blue), carbon (cyan), hydrogen (white).*

2.6.2 Simulation snapshots

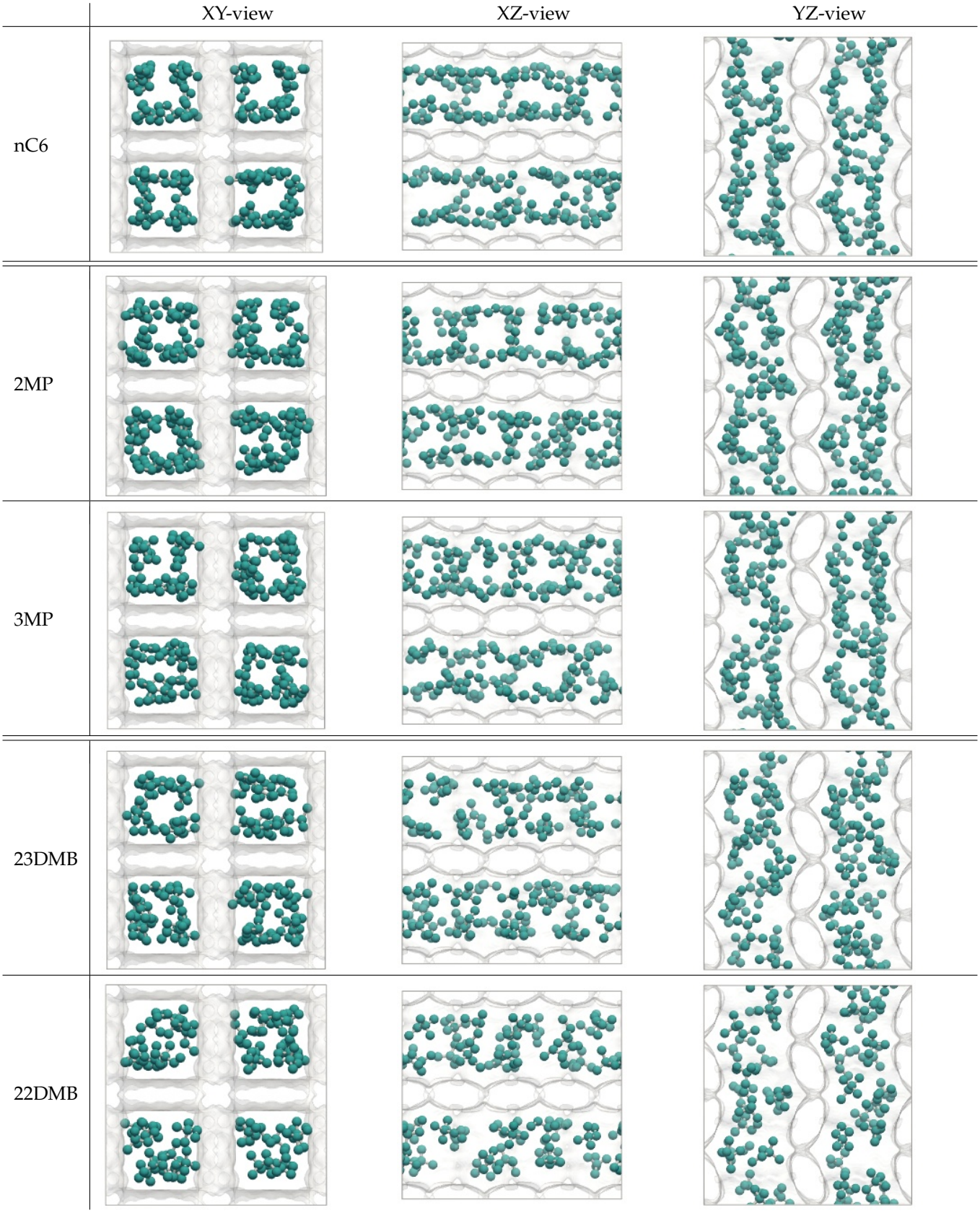

Figure S40: *Simulation snapshots of hexane isomers in CoBDP at 433K and 100 kPa.*

2.6.3 Single component adsorption

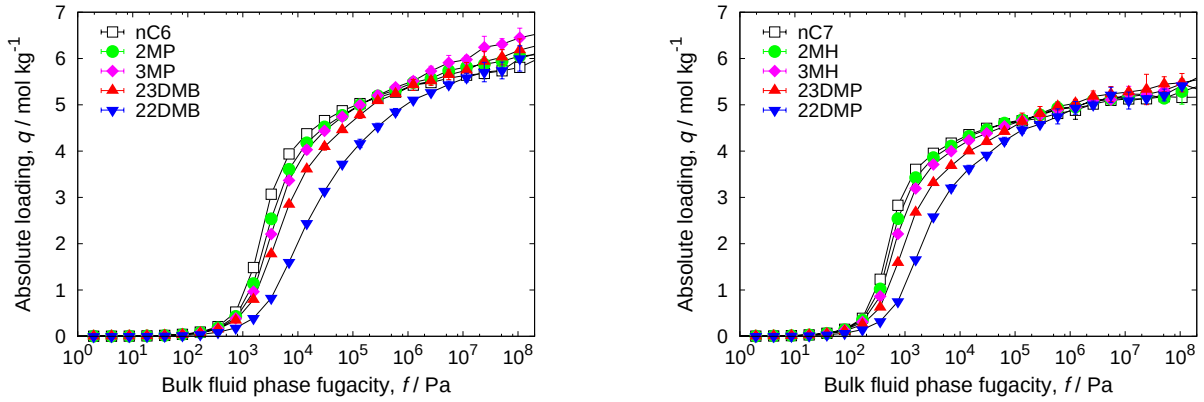

Figure S41: *Single component isotherms of hexane and heptane isomers in CoBDP at 433K.*

2.6.4 Heats of adsorption

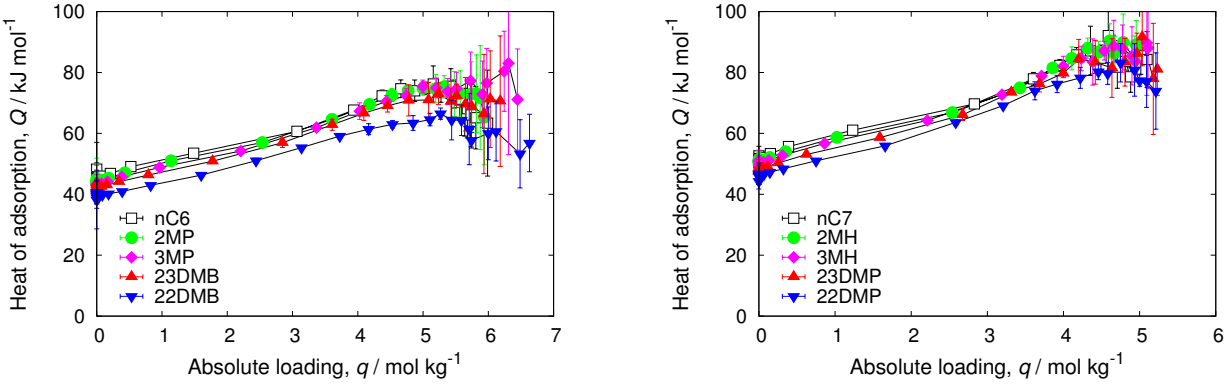

Figure S42: *Heat of adsorption of hexane and heptane isomers in CoBDP at 433K.*

2.6.5 Mixture adsorption

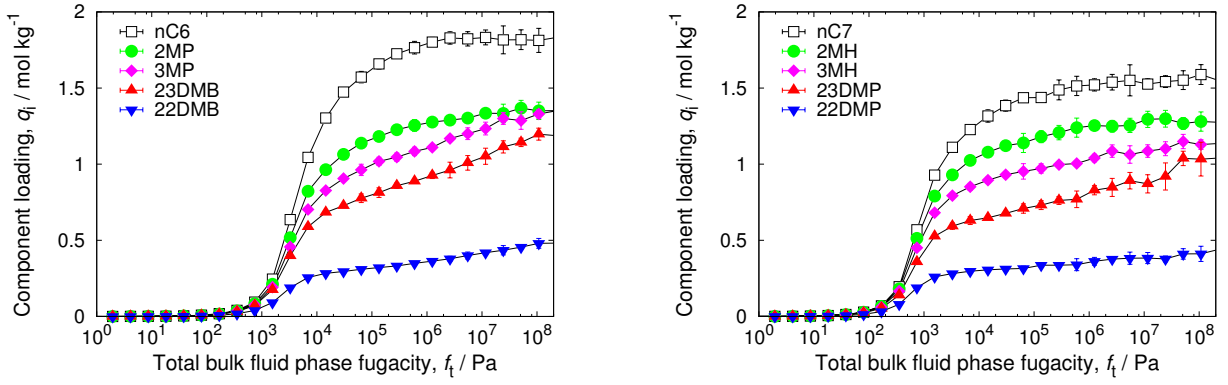

Figure S43: *Equimolar mixture isotherms of hexane and heptane isomers in CoBDP at 433K.*

2.6.6 IAST

	site A			site B		
	$q_{i,A,\text{sat}}$ [mol kg^{-1}]	$b_{i,A}$ [Pa$^{-\nu_{i,A}}$]	$\nu_{i,A}$ [-]	$q_{i,B,\text{sat}}$ [mol kg^{-1}]	$b_{i,B}$ [Pa$^{-\nu_{i,B}}$]	$\nu_{i,B}$ [-]
nC6	1.1	2.14×10^{-4}	0.6	4.8	2.39×10^{-5}	1.35
2MP	1.4	1.68×10^{-4}	0.6	4.8	3.3×10^{-5}	1.26
3MP	1.75	1.14×10^{-4}	0.62	4.8	3.22×10^{-5}	1.24
23DMB	1.5	8.31×10^{-5}	0.63	4.8	5.46×10^{-5}	1.13
22DMB	1.74	5.65×10^{-6}	0.72	4.8	4.3×10^{-5}	1.04

Table S6: *Dual-site Langmuir-Freundlich parameters for pure component hexane isomers at 433 K in CoBDP.*

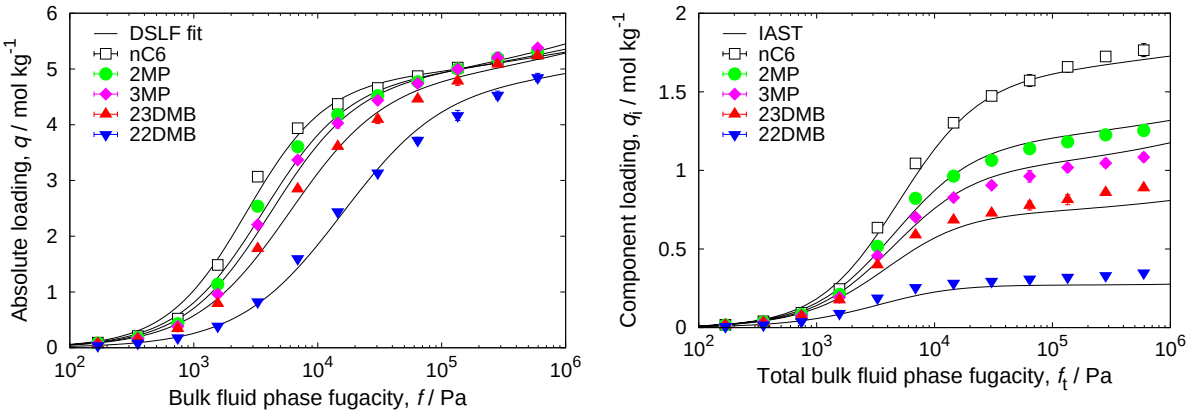

(a) *Lines are dual-site Langmuir-Freundlich fits of the pure components, points are the pure component isotherms.*

(b) *Lines are the IAST prediction of the mixture isotherms, points are the mixture isotherms.*

Figure S44: *Validation of IAST for equimolar hexane isomer mixtures in CoBDP at 433K.*

2.6.7 Breakthrough simulations

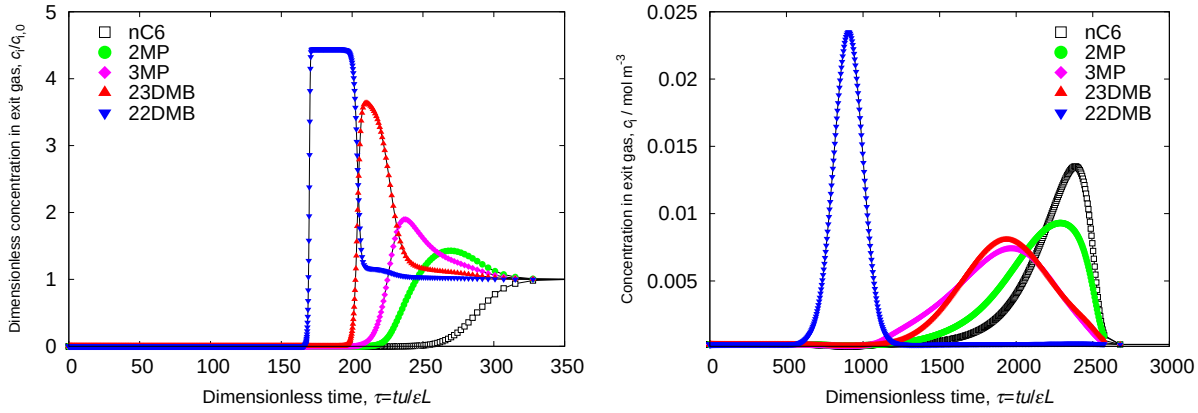

(a) *Step-type breakthrough.*

(b) *Pulse-type breakthrough.*

Figure S45: *Simulated breakthrough of hexane isomers in CoBDP at 433K and a total fugacity of the bulk fluid phase of 100 kPa. Video animations of the breakthrough behavior as a function of time are provided as Supplementary information.*

2.6.8 Performance discussion

Figure	description and remarks
S39	The CoBDP channel system consists of 1 uni-dimensional rectangular-like channel per unit cell.
S40	The rectangular shape is only an approximation; the channels are tortuous in shape with a varying diameter. At the smaller distances the molecules can be aligned from wall to opposite wall.
S41	The single component isotherms show a qualitative similar behavior to a graphite sheet and rectangular channel of 8-9 Å in free diameter.
S42	The heat of adsorption are in the same order as found in the isotherms.
S43	The difference between components is much more pronounced than the single components, which indicates competitive adsorption.
S44	The single components isotherms can be fitted very well with the Langmuir-Freundlich model (the fitted values can be found in Table S6). IAST describes the mixture well for this system.
S45	The CoBDP structure seems very suitable for hexane separation. The efficiency could be further improved by making the structure slightly smaller in effective diameter.
S45	Only 22DMB can be separated in pure form.

2.7 UiO-66

2.7.1 Energy landscapes

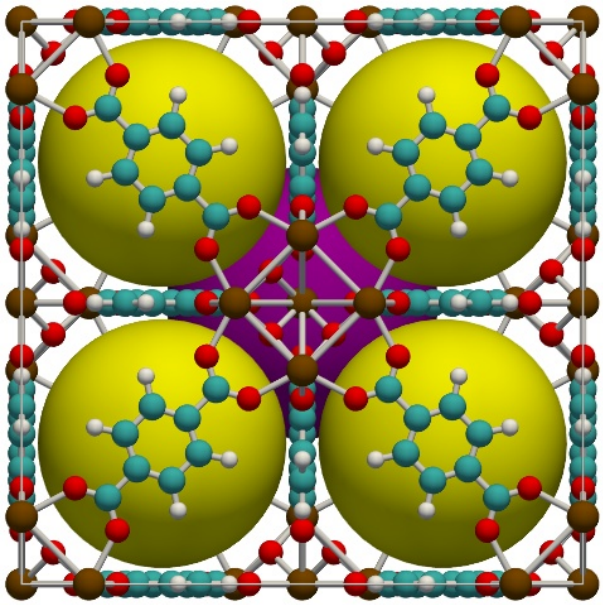

(a) *UiO-66 (single unit cell); XY-view.*

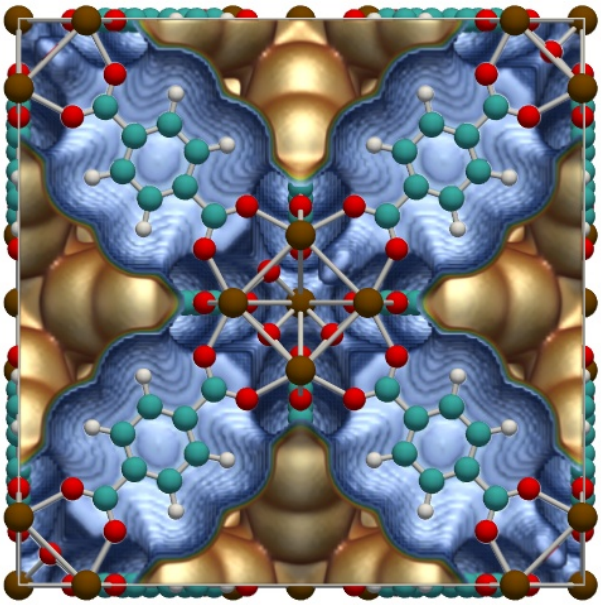

(b) *UiO-66 (single unit cell); XZ-view.*

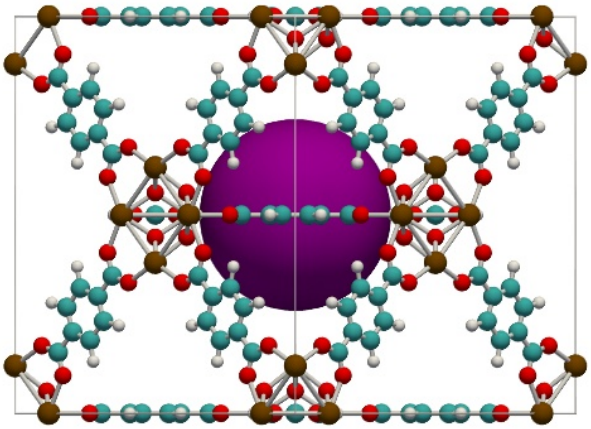

(c) *UiO-66 (single unit cell); YZ-view.*

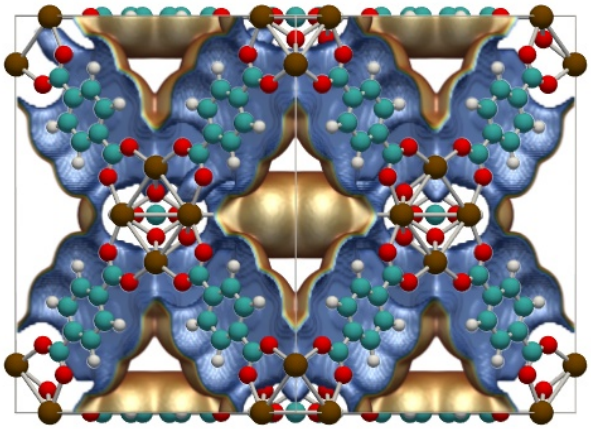

(d) *UiO-66 (single unit cell); XYZ-view.*

Figure S46: *Energy landscape of UiO-66. The UiO-66 unit cell has edge lengths* $a = b = c = 20.7004$ *Å, with cell angles* $\alpha = \beta = \gamma = 90°$*. UiO-66 has a cubic rigid 3D pores structure consisting of an array of octahedral cavities of diameter 11 Å (purple sphere) and tetrahedral cavities of diameter 8 Å (yellow spheres), connected through narrow triangular windows (approximately 6 Å). There are 4 octahedral cages and 8 tetrahedral cages per unit cell. About 49% of the structure is void. Color code: Zirconium (ochre), oxygen (red), carbon (cyan), and hydrogen (white).*

2.7.2 Simulation snapshots

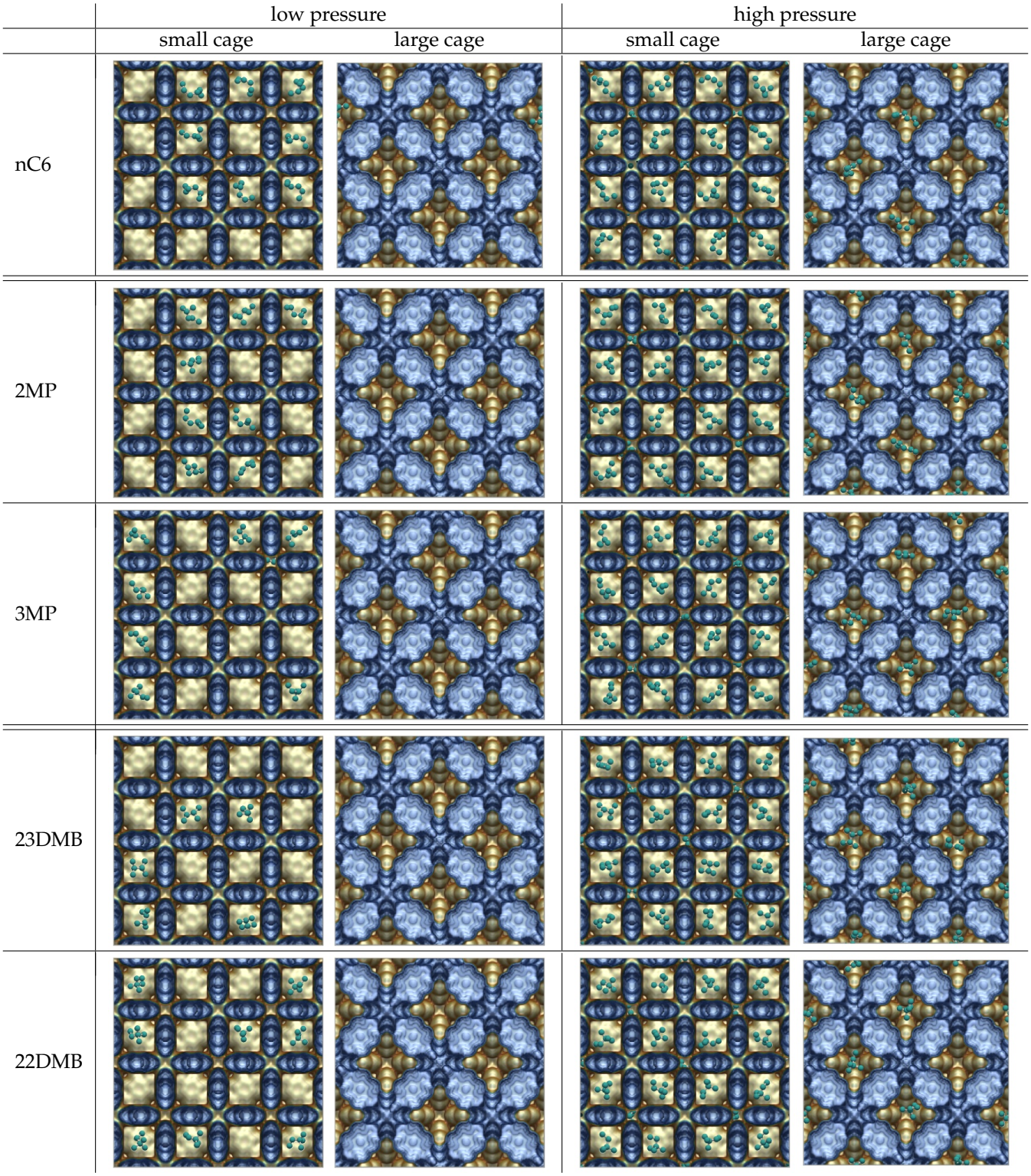

Figure S47: *Simulation snapshots of hexane isomers in UiO-66 at 433K and low and high pressure. High pressure is 100 kPa (i.e. maximum loading), low pressure is chosen such that the fraction loading is approximately 25%.*

2.7.3 Single component adsorption

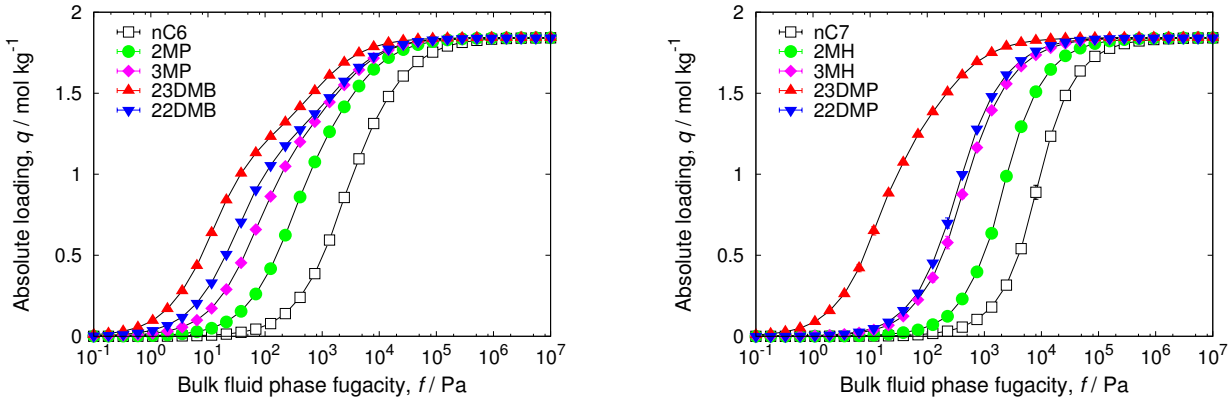

Figure S48: *Single component isotherms of hexane and heptane isomers in UiO-66 at 433K.*

2.7.4 Heats of adsorption

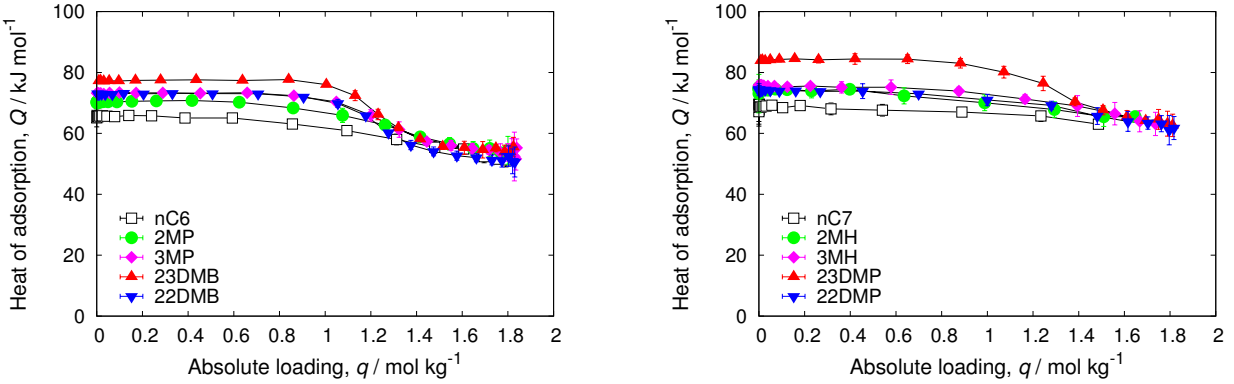

Figure S49: *Heat of adsorption of hexane and heptane isomers in UiO-66 at 433K.*

2.7.5 Mixture adsorption

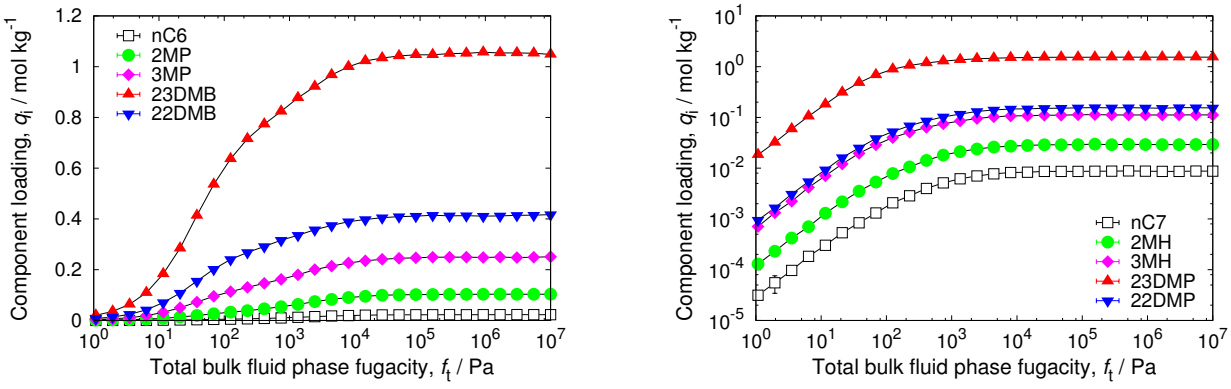

Figure S50: *Single component isotherms of hexane and heptane isomers in UiO-66 at 433K.*

2.7.6 IAST solution

	site A			site B		
	$q_{i,A,\text{sat}}$ [mol kg^{-1}]	$b_{i,A}$ [Pa$^{-\nu_{i,A}}$]	$\nu_{i,A}$ [-]	$q_{i,B,\text{sat}}$ [mol kg^{-1}]	$b_{i,B}$ [Pa$^{-\nu_{i,B}}$]	$\nu_{i,B}$ [-]
nC6	1.82	3.63×10^{-4}	1			
2MP	1.56	2.72×10^{-3}	1	0.28	1.57×10^{-4}	1
3MP	1.45	1.1×10^{-2}	1	0.4	2.44×10^{-4}	1
23DMB	1.33	7.14×10^{-2}	1	0.52	9.11×10^{-4}	1
22DMB	1.35	2.67×10^{-2}	1	0.49	3.87×10^{-4}	1

Table S7: *Dual-site Langmuir-Freundlich parameters for pure component hexane isomers at 433 K in UiO-66.*

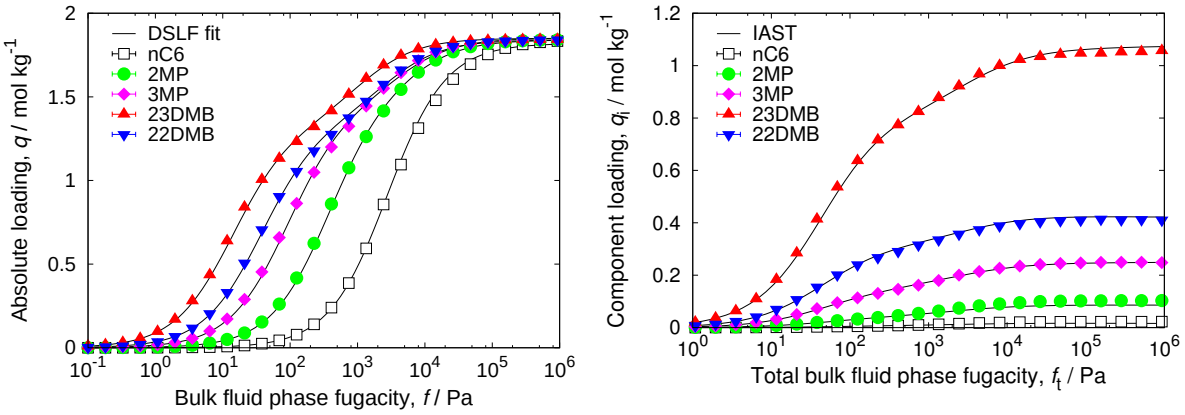

(a) *Lines are dual-site Langmuir-Freundlich fits of the pure components, points are the pure component isotherms.*

(b) *Lines are the IAST prediction of the mixture isotherms, points are the mixture isotherms.*

Figure S51: *Validation of IAST for equimolar hexane isomer mixtures in UiO-66 at 433K.*

2.7.7 Breakthrough simulations

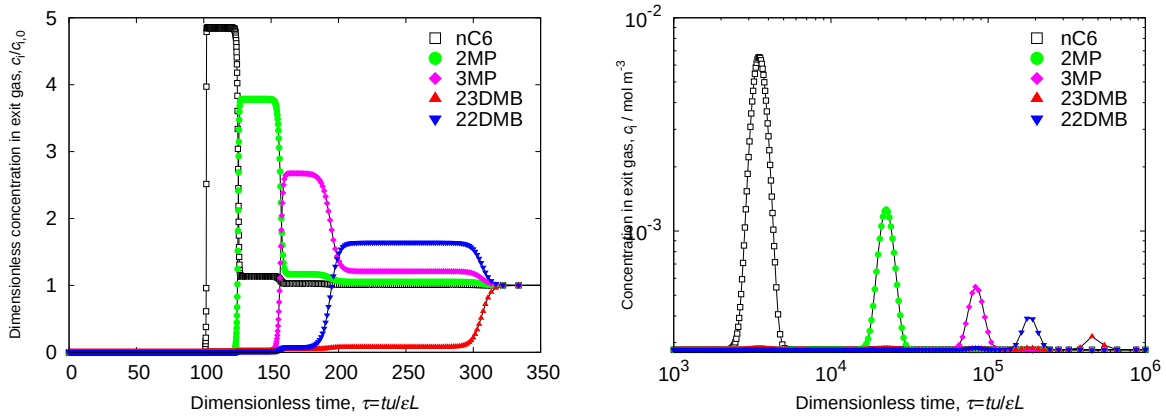

(a) *Step-type breakthrough.*

(b) *Pulse-type breakthrough.*

Figure S52: *Simulated breakthrough of hexane isomers in UiO-66 at 433K and a total fugacity of the bulk fluid phase of 100 kPa. Video animations of the breakthrough behavior as a function of time are provided as Supplementary information.*

2.7.8 Performance discussion

Figure	description and remarks
S46	The UiO-66 channel system: 3D channel system with two types of cage: octahedral cavities of diameter 11 Å and tetrahedral cavities of diameter 8 Å, connected through narrow triangular windows (approximately 6 Å).
S47	Linear and branches molecules are adsorbing everywhere, but in the mixture the linear molecules are driven out of the tetrahedral cavities because branched molecule fit more snugly.
S48	The isotherms show mild inflections related to the location of adsorption.
S49	The heats of adsorption of branched molecules (at low loading) are higher, which is related to their tight fit in the tetrahedral cavities.
S50	Linear molecules are driven out of the system at high pressures.
S51	The single components isotherms can be fitted very well with the Langmuir-Freundlich model (the fitted values can be found in Table S7). IAST describes the mixture very well for this system.
S52(a)	UiO-66 performs very well as a hexane isomer separation device at 100 kPa, but is limited to hexane molecules or smaller (due to the limited tetrahedral cavity space).
S52(b)	It appears from the breakthrough curves, that all components can be separated in pure form. But this conclusion is not correct because diffusion effects do not go hand in hand with adsorption. Due to diffusional limitations, the curves will tend to come together. This is evidenced in the experiments of Barcia et al., Figure S6.

2.8 ZIF-77

2.8.1 Energy landscapes

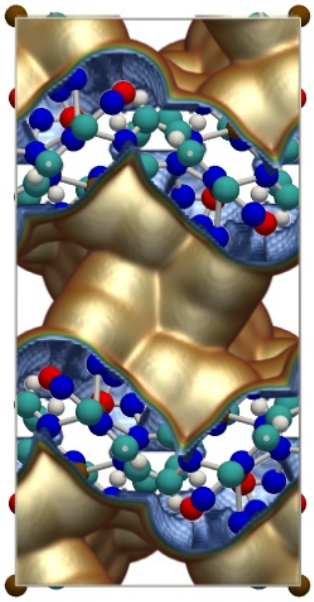

(a) *ZIF-77 (single unit cell); XY-view.*

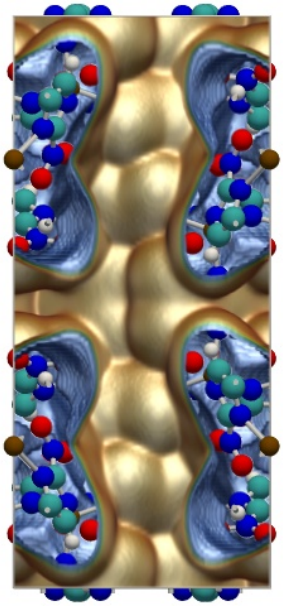

(b) *ZIF-77 (single unit cell); XZ-view.*

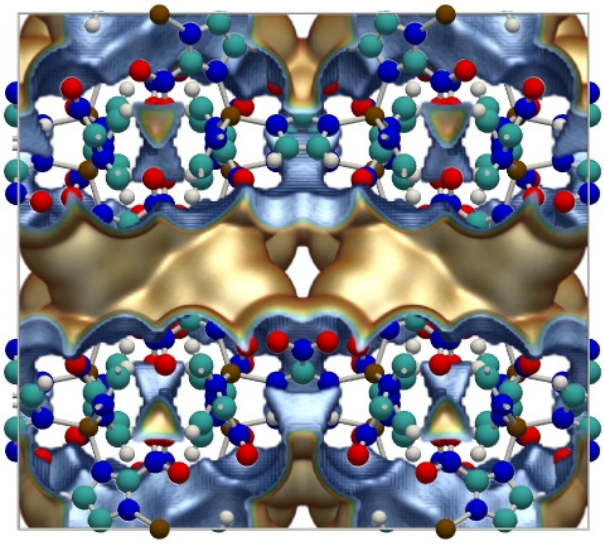

(c) *ZIF-77 (single unit cell); YZ-view.*

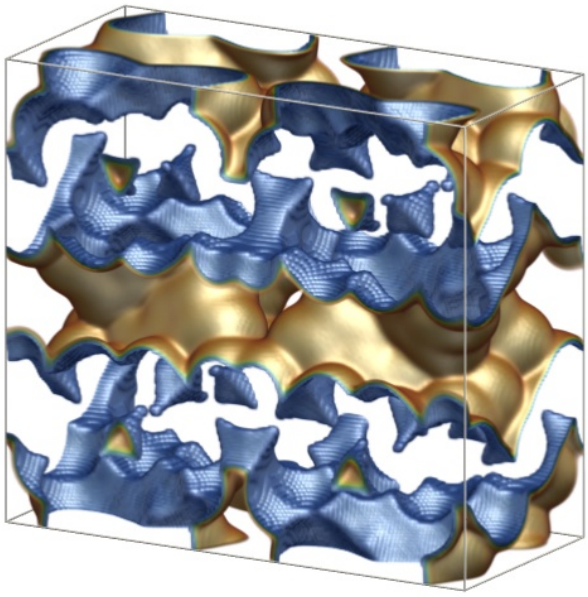

(d) *ZIF-77 (single unit cell); XYZ-view.*

Figure S53: *Energy landscape of ZIF-77. The ZIF-776 unit cell has edge lengths* $a = 11.1248$, $b = 22.3469$, *and* $c = 24.9087$ *Å, Color code: Zinc (ochre), oxygen (red), carbon (cyan), nitrogen (blue), and hydrogen (white).*

2.8.2 Simulation snapshots

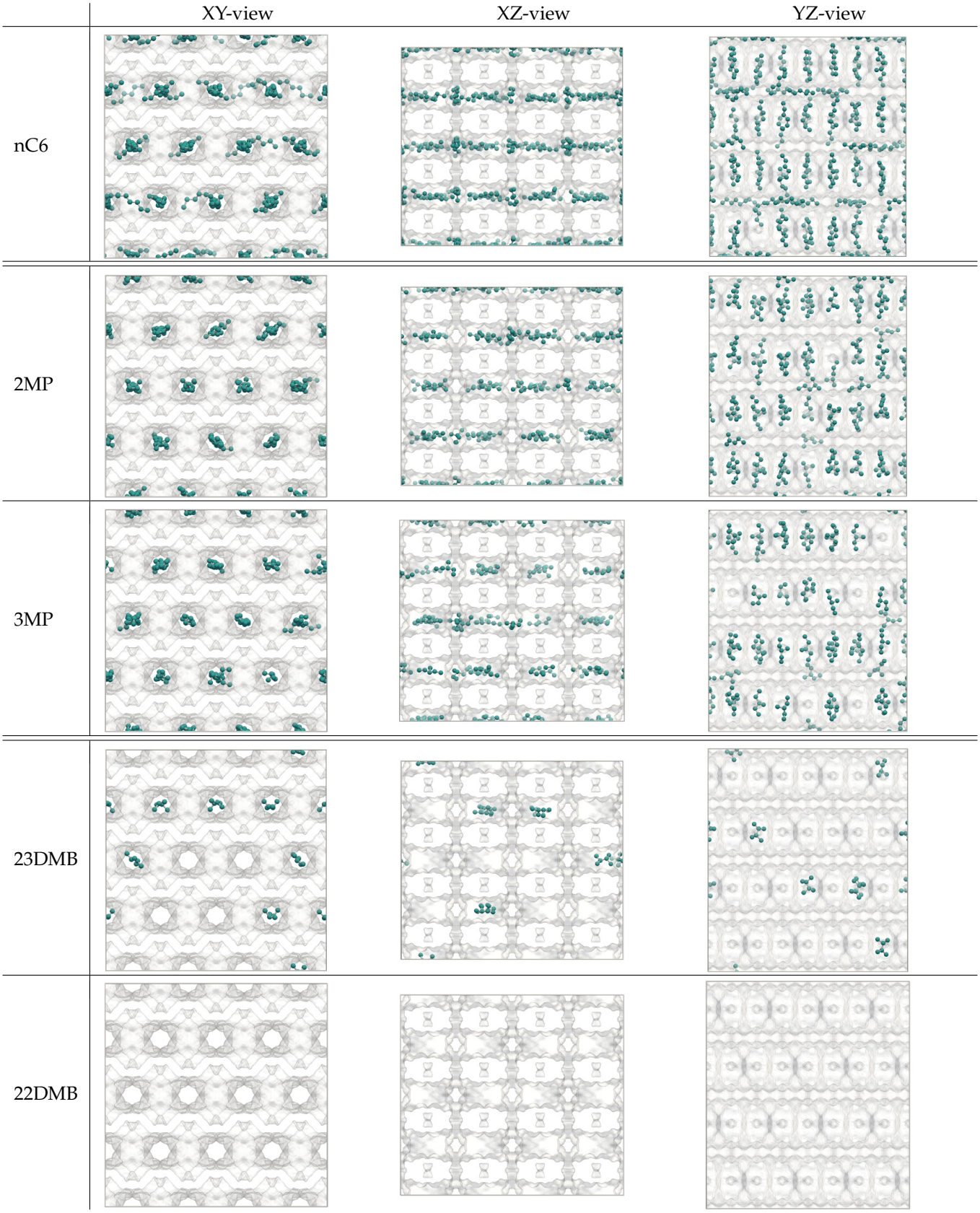

Figure S54: *Simulation snapshots of hexane isomers in ZIF-77 at 433K and 100 kPa.*

2.8.3 Simulation adsorbate densities

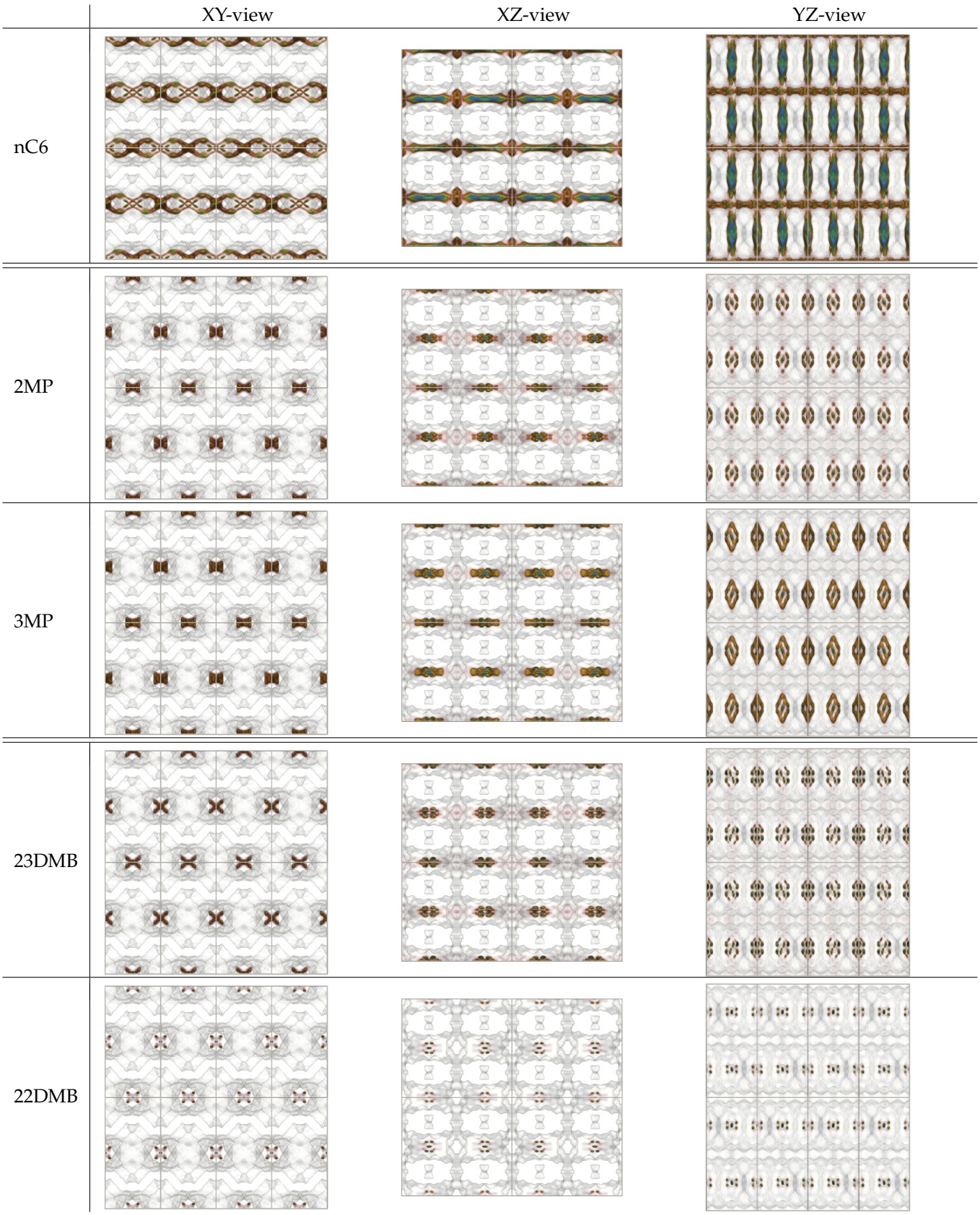

Figure S55: *Probability densities of hexane isomers in ZIF-77 at 433K and 100 kPa.*

2.8.4 Single component adsorption

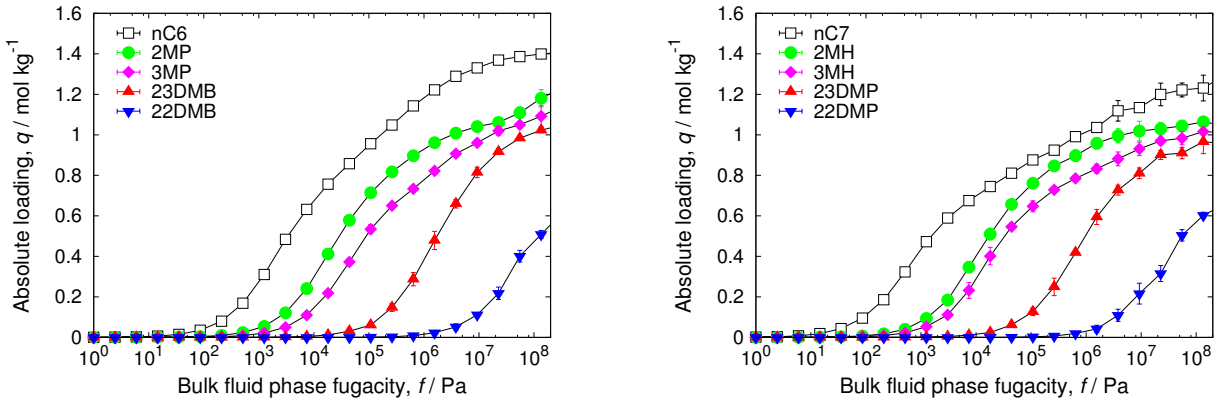

Figure S56: *Single component isotherms of hexane and heptane isomers in ZIF-77 at 433K.*

2.8.5 Heats of adsorption

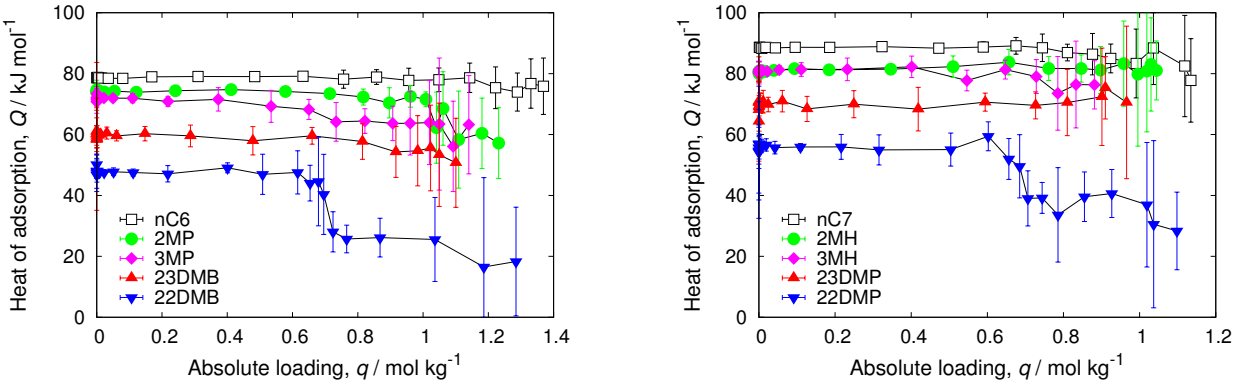

Figure S57: *Heat of adsorption of hexane and heptane isomers in ZIF-77 at 433K.*

2.8.6 Mixture adsorption

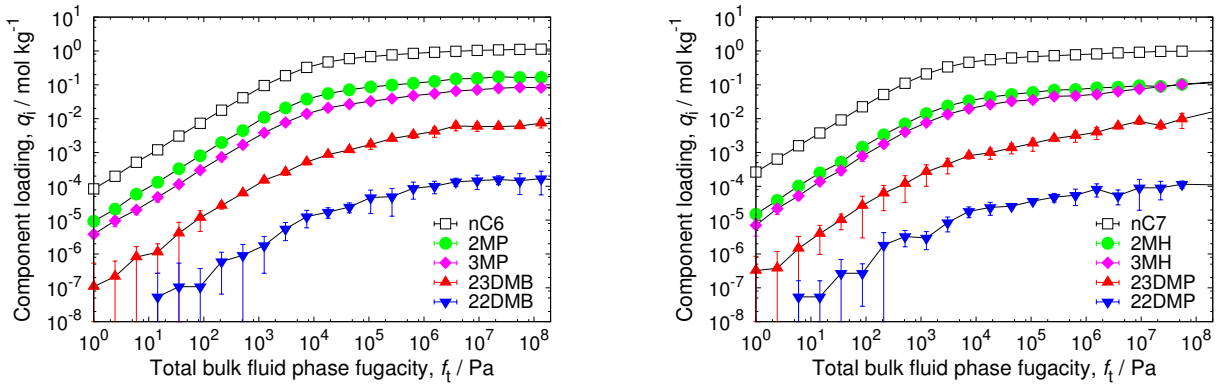

Figure S58: *Equimolar mixture isotherms of hexane and heptane isomers in ZIF-77 at 433K.*

2.8.7 IAST

	site A			site B		
	$q_{i,A,\text{sat}}$ [mol kg^{-1}]	$b_{i,A}$ [Pa$^{-\nu_{i,A}}$]	$\nu_{i,A}$ [-]	$q_{i,B,\text{sat}}$ [mol kg^{-1}]	$b_{i,B}$ [Pa$^{-\nu_{i,B}}$]	$\nu_{i,B}$ [-]
nC6	0.81	5.25×10^{-4}	1	0.59	2.24×10^{-6}	1
2MP	0.92	4.95×10^{-5}	1	0.43	1.66×10^{-8}	1
3MP	0.8	2.15×10^{-5}	1	0.4	5.15×10^{-8}	1
23DMB	0.96	6.31×10^{-7}	1	0.2	3.65×10^{-9}	1
22DMB	0.7	2.1×10^{-8}	1			

Table S8: *Dual-site Langmuir-Freundlich parameters for pure component hexane isomers at 433 K in ZIF-77.*

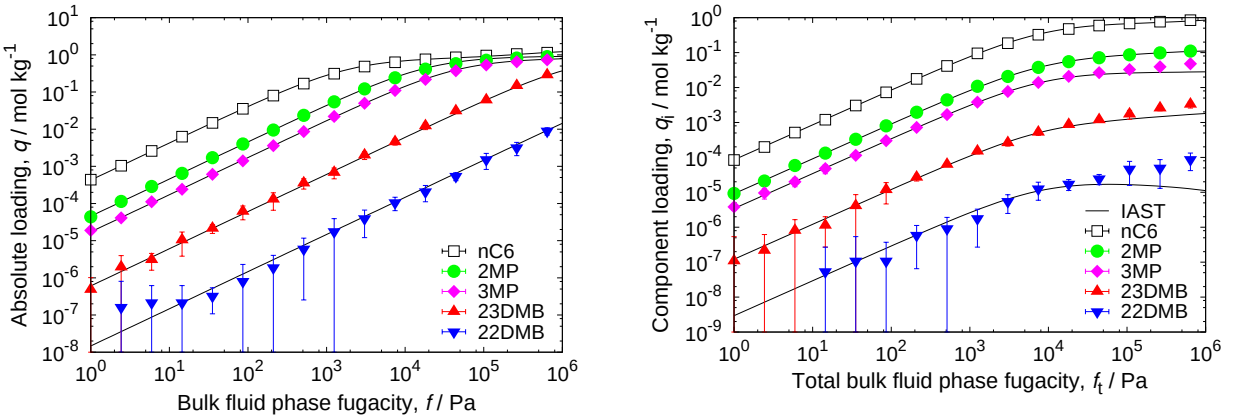

(a) *Lines are dual-site Langmuir-Freundlich fits of the pure components, points are the pure component isotherms.*

(b) *Lines are the IAST prediction of the mixture isotherms, points are the mixture isotherms.*

Figure S59: *Validation of IAST for equimolar hexane isomer mixtures in ZIF-77 at 433K.*

2.8.8 Breakthrough simulations

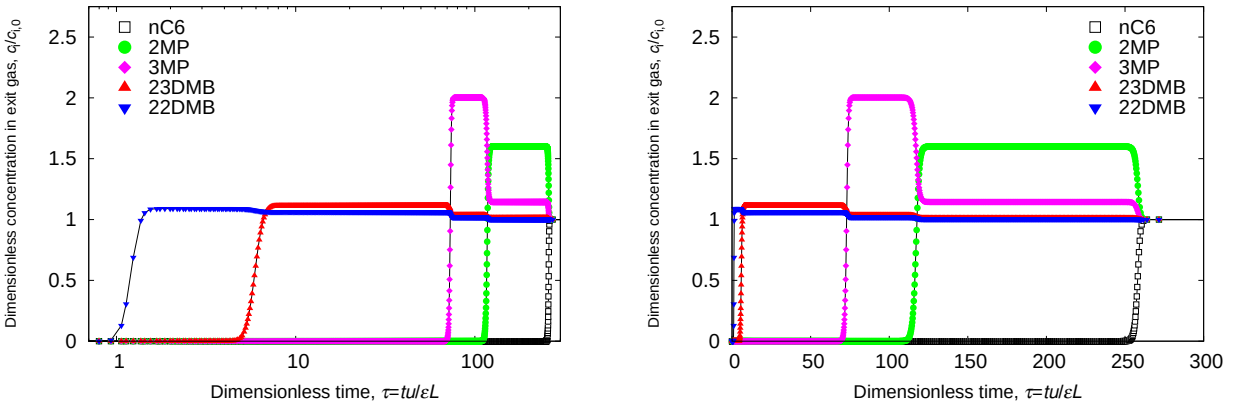

Figure S60: *Simulated step-type breakthrough of hexane isomers in ZIF-77 at 433K and a total fugacity of the bulk fluid phase of 100 kPa in log-and linear scale, respectively. Video animations of the breakthrough behavior as a function of time are provided as Supplementary information.*

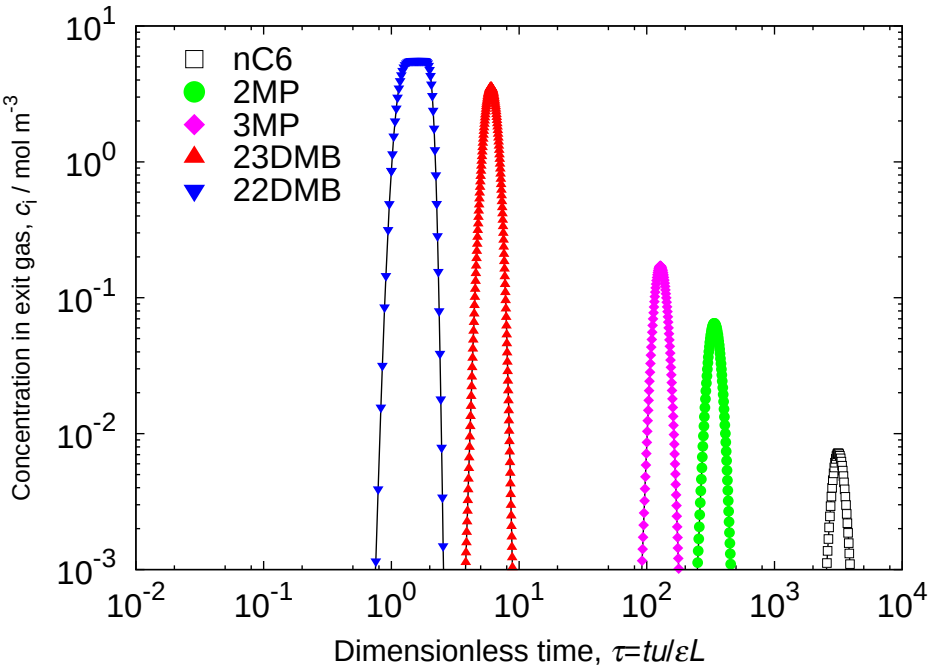

Figure S61: *Simulated pulse-type breakthrough of hexane isomers in ZIF-77 at 433K and a total fugacity of the bulk fluid phase of 100 kPa. Video animations of the breakthrough behavior as a function of time are provided as Supplementary information.*

2.8.9 Self-diffusion coefficients

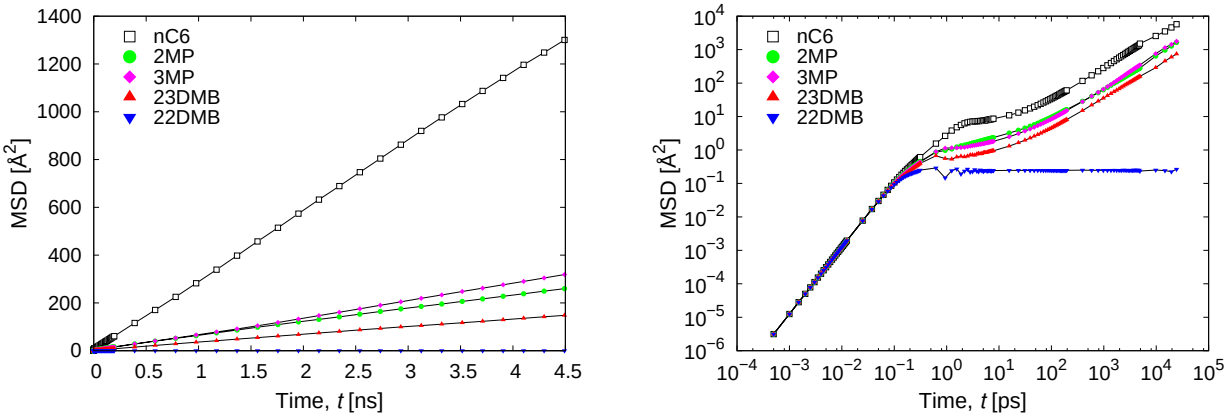

Figure S62: *Mean-squared displacements of hexane isomers at infinite dilution in ZIF-77 at 433K.*

adsorbate	D_s [m^2/s]	D_s^x [m^2/s]	D_s^y [m^2/s]	D_s^z [m^2/s]
nC6	4.93×10^{-10}	1.48×10^{-11}	-	1.46×10^{-9}
2MP	9.20×10^{-11}	-	-	2.76×10^{-10}
3MP	1.22×10^{-10}	-	-	3.65×10^{-10}
23DMB	5.28×10^{-11}	-	-	1.58×10^{-10}
22DMB	-	-	-	-

Table S9: *Self-diffusion coefficients of hexane isomers at infinite dilution in ZIF-77 at 433K. The self-diffusion D_s is defined as $D_s = \frac{1}{3}\left(D_s^x + D_s^y + D_s^z\right)$; '-' means to low to be computable by conventional MD.*

2.8.10 Performance discussion

Figure	description and remarks
S53	The ZIF-77 structure forms a 2D-channel system for linear alkanes, and a 1D-channel system for mono-and dibranched alkanes.
S54, S55	The ZIF-77 is a 2D channel system with larger main channels and smaller side channels. The larger main channels are size-excluding the di-branched molecules, while the smaller channels are size-excluding the mono-branched. The linear molecules fit snugly in both the main and side channels and are the dominantly adsorbed species.
S56	The single components show a normal adsorption hierarchy over the full pressure range.
S57	The linear molecules have a more favorable interaction with the structure compared to mono-and di-branched.
S58	The tight fit discriminates on the degree of branching and leads to the highest adsorption selectivity of all examined structures (one to two orders of magnitude higher).
S59	The single components isotherms can be fitted very well with the Langmuir-Freundlich model (the fitted values can be found in Table S8). IAST describes the mixture well for this system.
S60	ZIF-77 work extremely well as a hexane isomer separation device at all pressures. The break-through curves proof the components can be separated in turn.
S61	Each individual component can be separated into its pure form.
Table S9	The 22DMB fits in the cages, but are unable to diffuse through. The 23DMB is able to enter the structure. The adsorption selectivity is enhanced when diffusion is taken into account.
Remark	A patent for ZIF-77 as an alkane-separation device is pending: “Process for separating mixtures containing straight-chain and branched alkanes” Inventors: David Dubbeldam, Rajamani Krishna. European Patent Office, Application No./12165907.2-2103, Filed by Universiteit van Amsterdam, 27 April 2012.

2.9 ZIF-77: a generic alkane separation device

2.9.1 Simulation snapshots C4-C7 isomers

Figure S63: *Simulation snapshots of (single-component) C4, C5, C6 and C7 isomers in ZIF-77 at 433K and 100 kPa. The structure is shown as a top-view of a single 2D layer of a* $4 \times 2 \times 2$ *super cell. The main channels run top to bottom; the smaller side channels run from left to right and are only accessible to linear alkanes.*

2.9.2 Single component adsorption

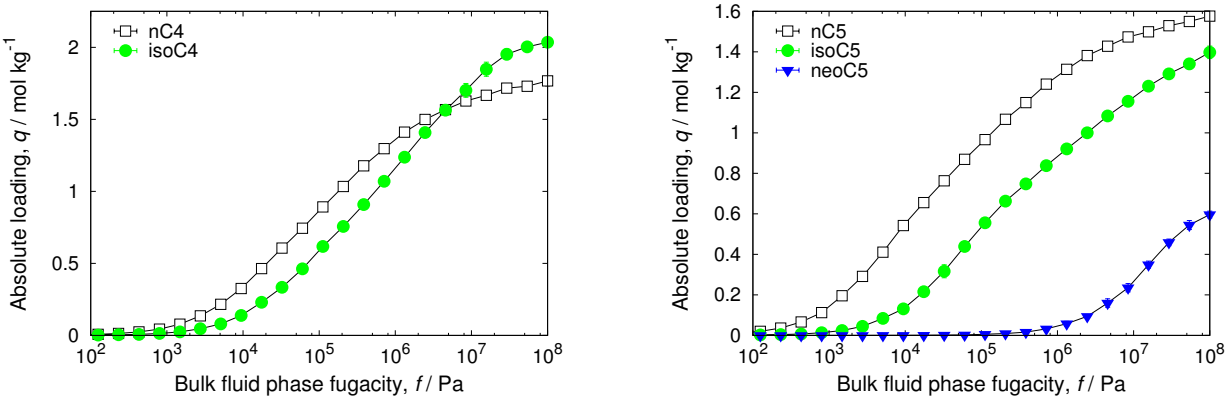

Figure S64: *Single component isotherms of butane and pentane isomers in ZIF-77 at 433K.*

2.9.3 Heats of adsorption

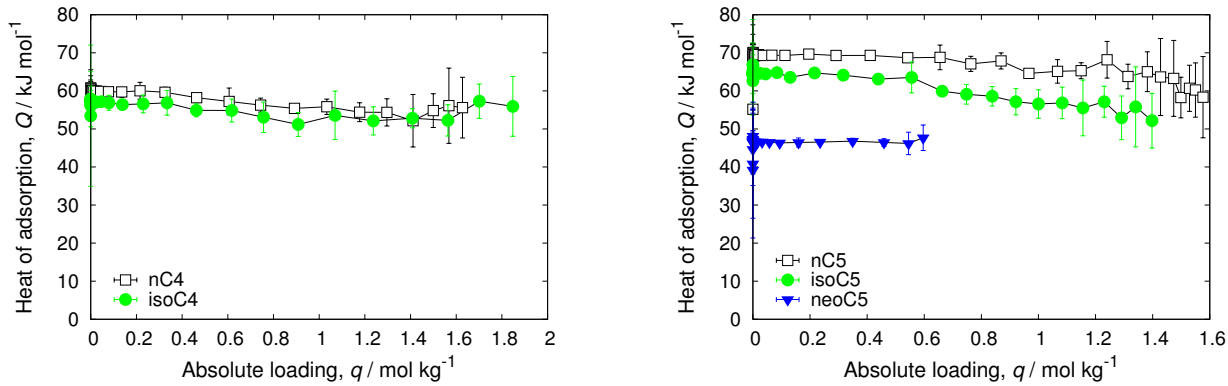

Figure S65: *Heat of adsorption of butane and pentane isomers in ZIF-77 at 433K.*

2.9.4 Mixture adsorption

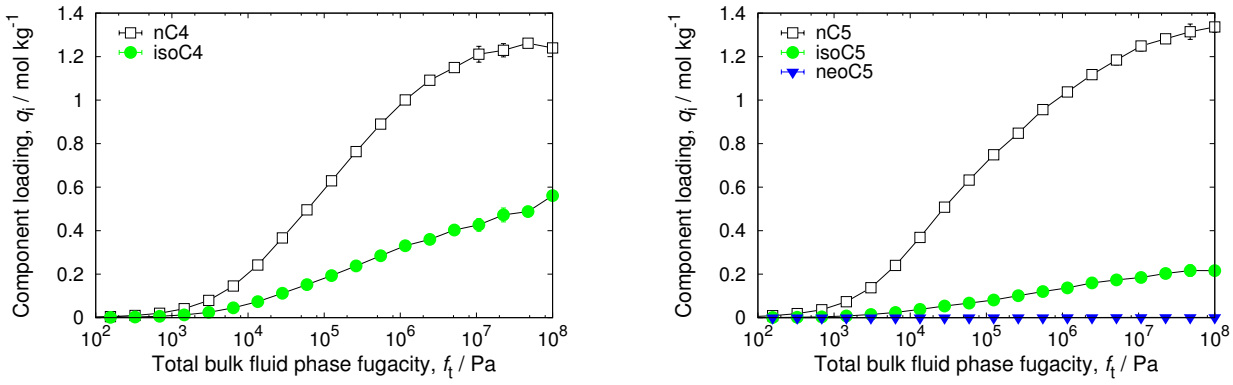

Figure S66: *Equimolar mixture isotherms of butane and pentane isomers in ZIF-77 at 433K.*

2.9.5 IAST

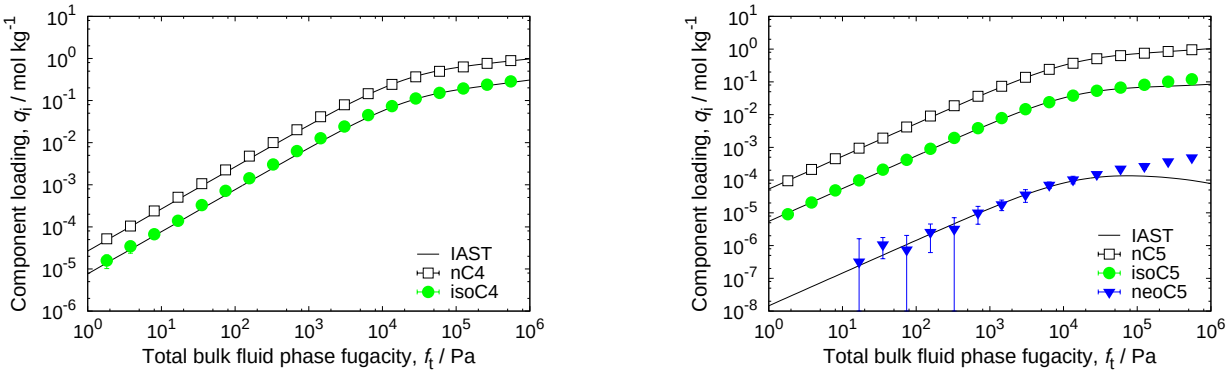

Figure S67: *Validation of IAST for equimolar butane and pentane isomer mixtures in ZIF-77 at 433K. Lines are the IAST prediction of the mixture isotherms, points are the mixture isotherms.*

2.9.6 Breakthrough simulations

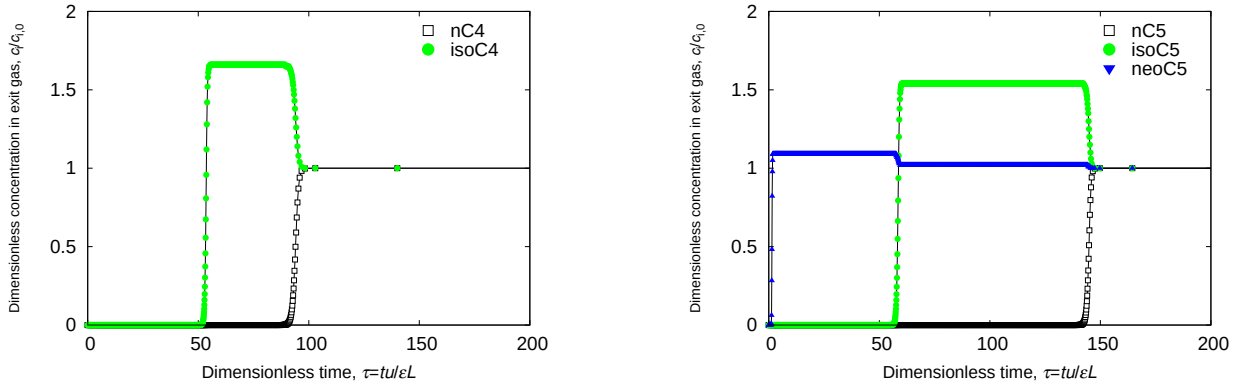

Figure S68: *Simulated step-type breakthrough of butane and pentane isomers in ZIF-77 at 433K and a total fugacity of the bulk fluid phase of 100 kPa. Video animations of the breakthrough behavior as a function of time are provided as Supplementary information.*

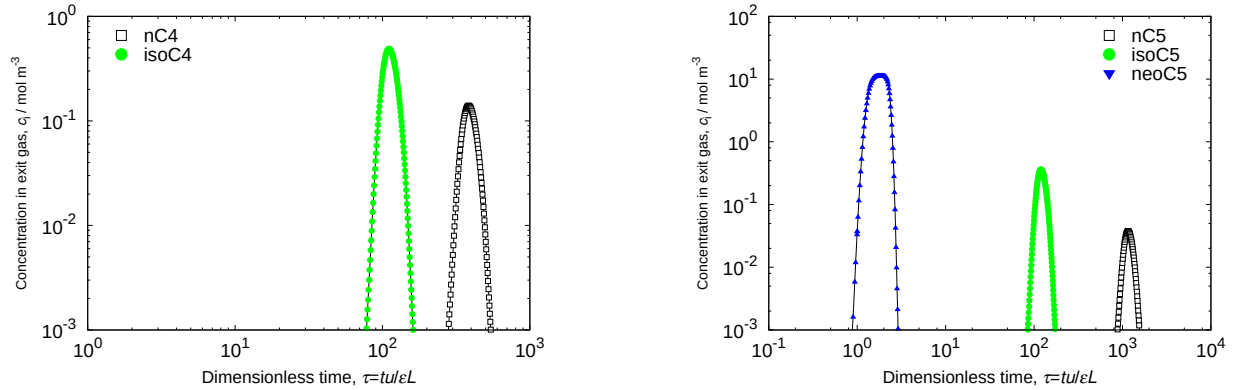

Figure S69: *Simulated pulse-type breakthrough of butane and pentane isomers in ZIF-77 at 433K and a total fugacity of the bulk fluid phase of 100 kPa. Video animations of the breakthrough behavior as a function of time are provided as Supplementary information.*

2.9.7 13- and 15-component mixtures

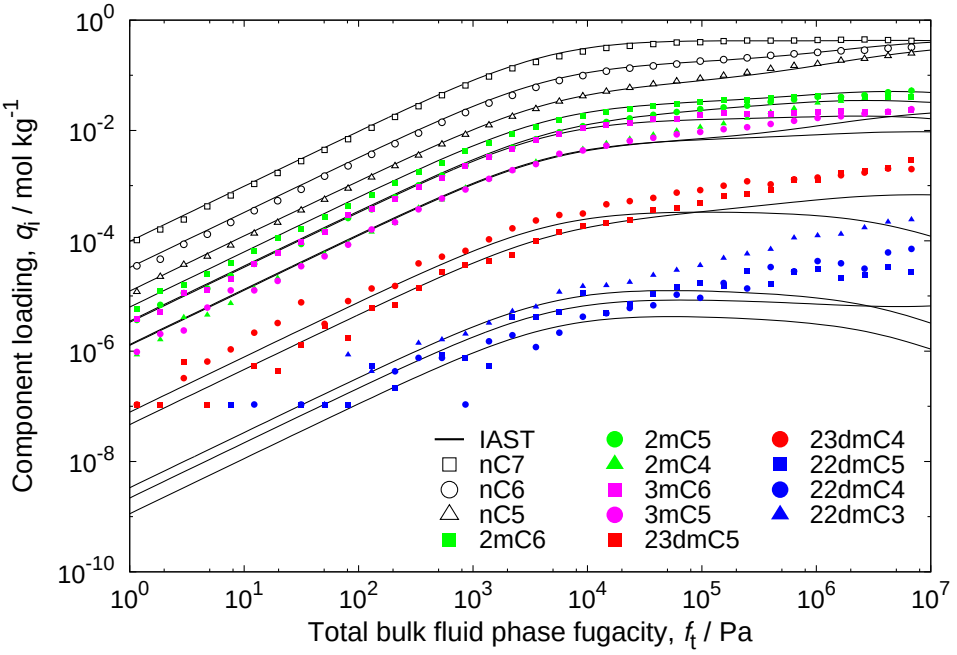

Figure S70: *13-component equimolar mixture of C5-, C6-, and C7-isomers at 433K in ZIF-77. Although not perfect, IAST describes the mixture well (note the log-scale; the loadings of the mono-branched and especially the di-branched alkanes is very low). Color code: linear alkane (white), 2-methyl alkane (green), 3-methyl alkane (purple), 23-dimethyl alkane (red), 22-dimethyl alkane (blue).*

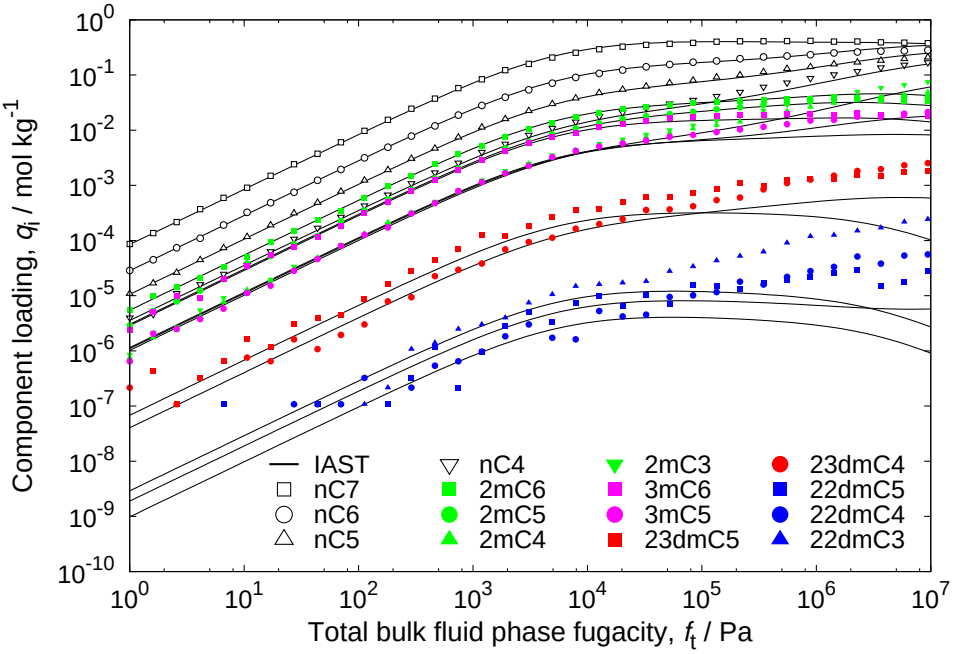

Figure S71: *15-component equimolar mixture of C4-, C5-, C6-, and C7-isomers at 433K in ZIF-77. Although not perfect, IAST describes the mixture well (note the log-scale; the loadings of the mono-branched and especially the di-branched alkanes is very low). Color code: linear alkane (white), 2-methyl alkane (green), 3-methyl alkane (purple), 23-dimethyl alkane (red), 22-dimethyl alkane (blue).*

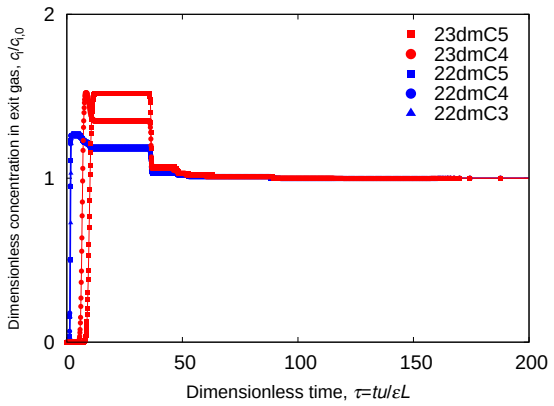

(a) *The di-branched molecules breakthrough at the start of the run.*

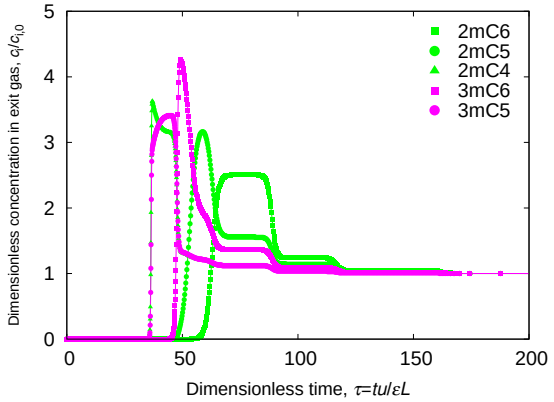

(b) *The mono-branched breakthrough during the middle of the run.*

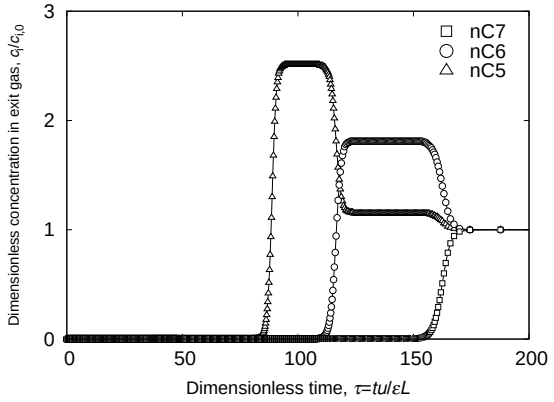

(c) *The linear molecules breakthrough at the end of the run.*

Figure S72: *Simulated step-type breakthrough of a 13-component equimolar mixture of C5-, C6-, and C7-isomers in ZIF-77 at 433K and partial fugacities of the bulk fluid phase of 20 kPa.*

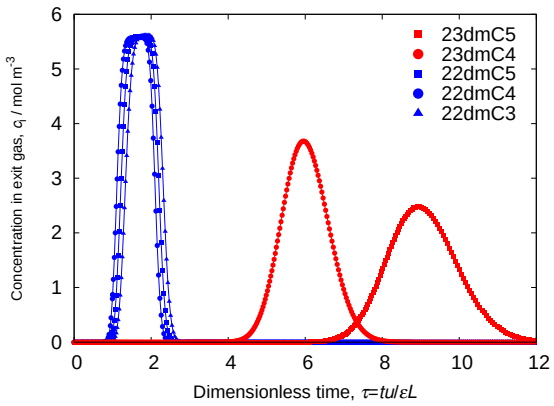

(a) *The di-branched molecules breakthrough at the start of the run.*

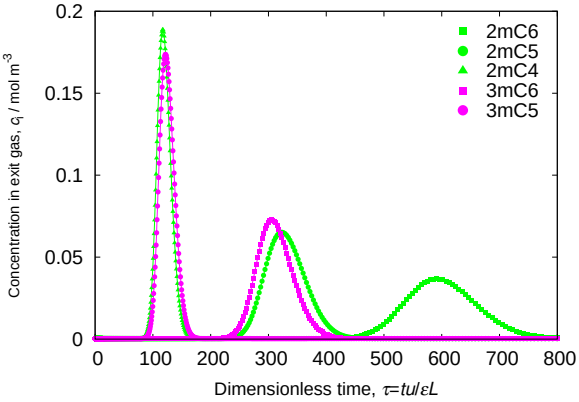

(b) *The mono-branched breakthrough during the middle of the run.*

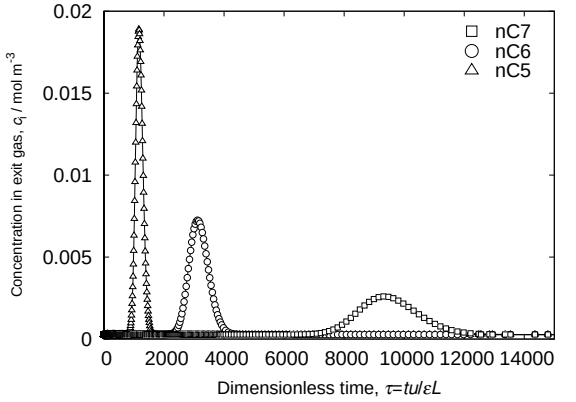

(c) *The linear molecules breakthrough at the end of the run.*

Figure S73: *Simulated pulse-type breakthrough of a 13-component equimolar mixture of C5-, C6-, and C7-isomers in ZIF-77 at 433K and partial fugacities of the bulk fluid phase of 20 kPa.*

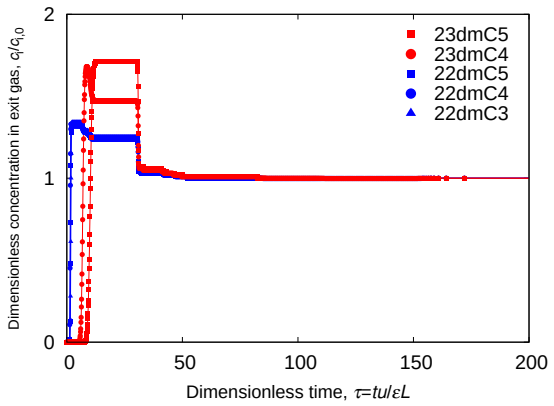

(a) *The di-branched molecules breakthrough at the start of the run.*

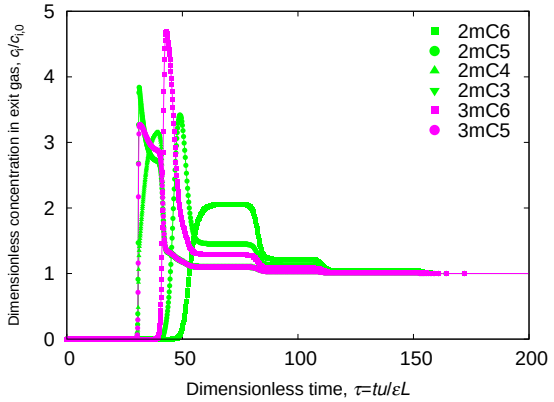

(b) *The mono-branched breakthrough during the middle of the run.*

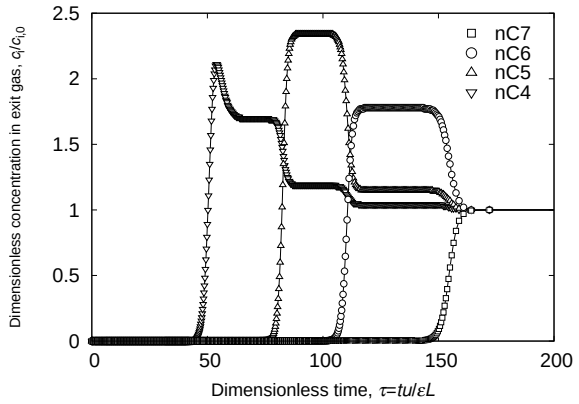

(c) *The linear molecules breakthrough at the end of the run.*

Figure S74: *Simulated step-type breakthrough of a 15-component equimolar mixture of C4-, C5-, C6-, and C7-isomers in ZIF-77 at 433K and partial fugacities of the bulk fluid phase of 20 kPa.*

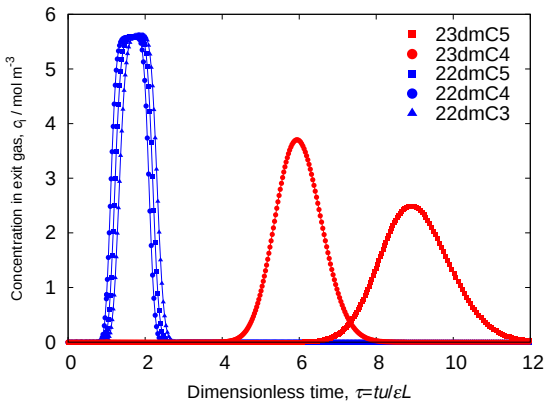

(a) *The di-branched molecules breakthrough at the start of the run.*

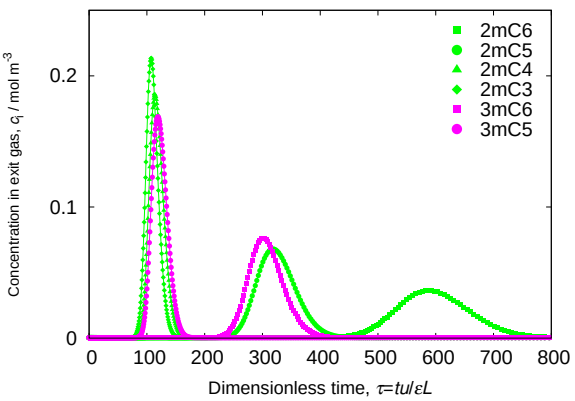

(b) *The mono-branched breakthrough during the middle of the run.*

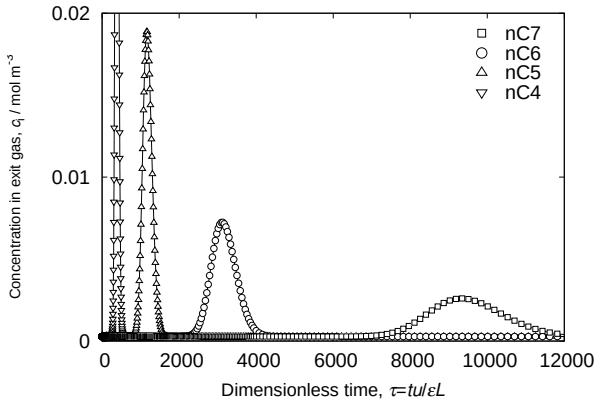

(c) *The linear molecules breakthrough at the end of the run.*

Figure S75: *Simulated pulse-type breakthrough of a 15-component equimolar mixture of C4-, C5-, C6-, and C7-isomers in ZIF-77 at 433K and partial fugacities of the bulk fluid phase of 20 kPa.*

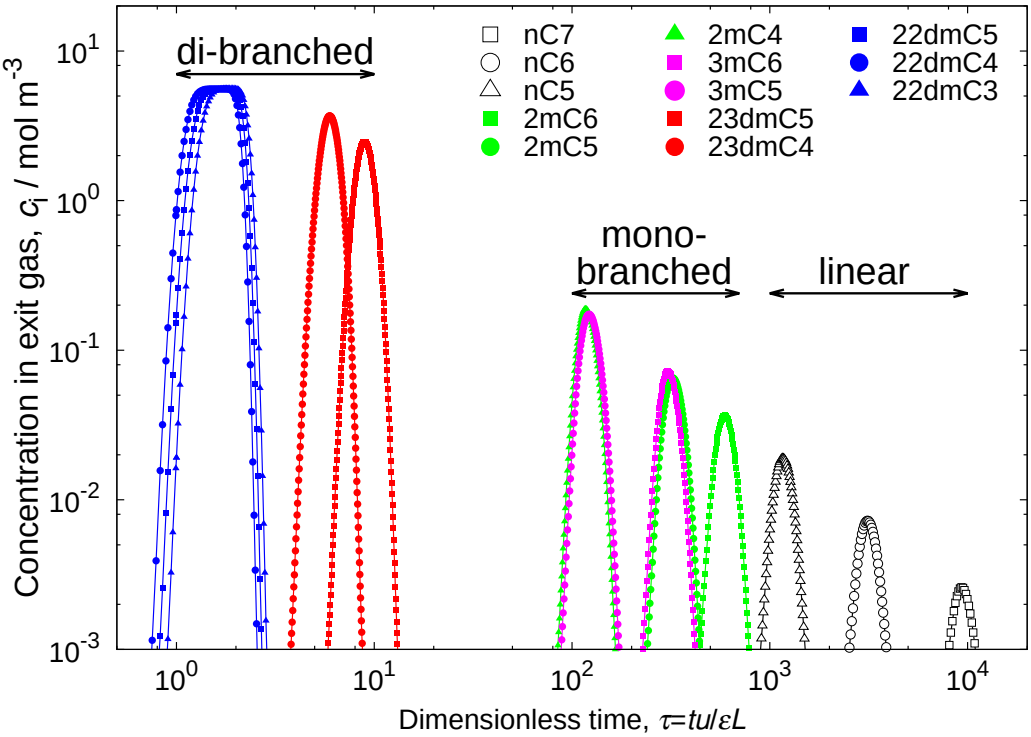

Figure S76: *Simulated pulse-type breakthrough of a 13-component equimolar mixture of C5-, C6-, and C7-isomers in ZIF-77 at 433K and partial fugacities of the bulk fluid phase of 20 kPa.*

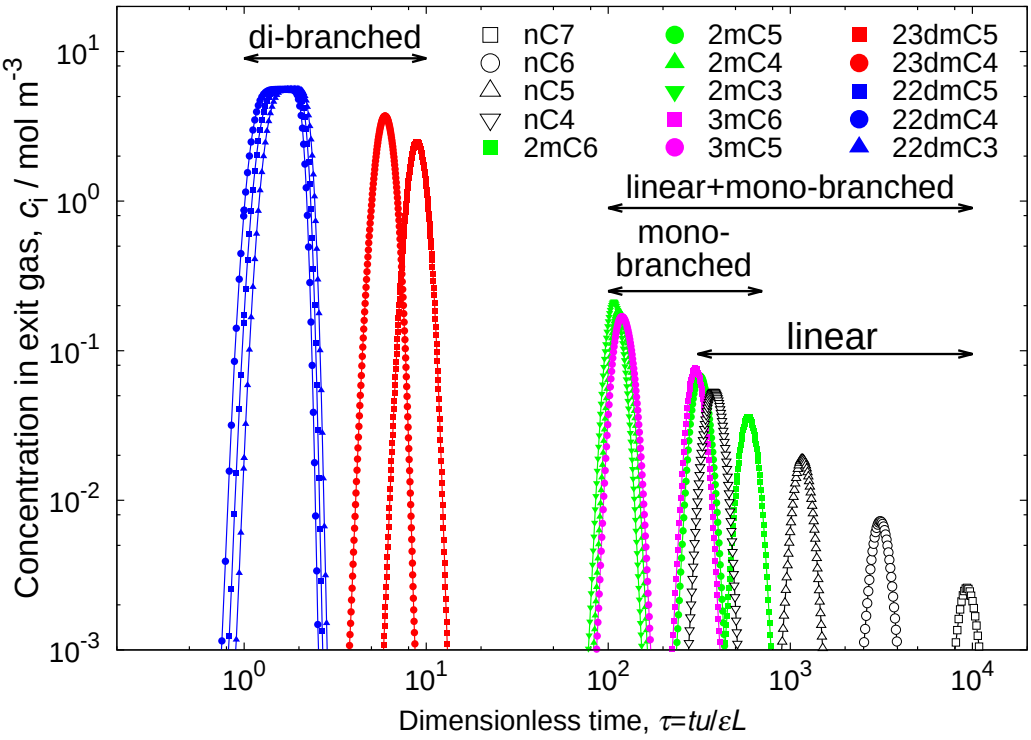

Figure S77: *Simulated pulse-type breakthrough of a 15-component equimolar mixture of C4-, C5-, C6-, and C7-isomers in ZIF-77 at 433K and partial fugacities of the bulk fluid phase of 20 kPa.*

2.10 Comparison of structures

	nC6 [kJ/mol]	2MP [kJ/mol]	3MP [kJ/mol]	23DMB [kJ/mol]	22DMB [kJ/mol]
ZIF-77	-77.8 ± 0.1	-73.4 ± 0.3	-71.3 ± 0.3	-59.4 ± 0.4	-47.2 ± 0.2
MFI	-66.5 ± 0.1	-67.5 ± 0.1	-64.3 ± 0.1	-64.4 ± 0.1	-61.4 ± 0.1
MgMOF-74	-49.5 ± 0.1	-48.3 ± 0.1	-47.8 ± 0.1	-46.3 ± 0.1	-41.8 ± 0.1
CoBDP	-44.5 ± 0.1	-43.3 ± 0.1	-42.3 ± 0.1	-41.3 ± 0.1	-38.5 ± 0.1
COF-103	-30.0 ± 0.1	-29.5 ± 0.1	-29.1 ± 0.1	-28.5 ± 0.1	-26.7 ± 0.1
UiO-66	-64.9 ± 0.1	-69.6 ± 0.1	-72.4 ± 0.1	-76.5 ± 0.1	-72.2 ± 0.1
MFS	-65.9 ± 0.1	-69.5 ± 0.1	-66.8 ± 0.1	-69.0 ± 0.1	-64.5 ± 0.1
STF	-54.7 ± 0.1	-59.1 ± 0.1	-60.3 ± 0.1	-63.8 ± 0.1	-59.1 ± 0.1
CFI	-51.0 ± 0.1	-53.7 ± 0.1	-53.9 ± 0.1	-56.9 ± 0.1	-53.2 ± 0.1
ATS	-50.5 ± 0.1	-53.6 ± 0.1	-53.0 ± 0.1	-55.0 ± 0.1	-50.9 ± 0.1

Table S10: *Heats of adsorption of the 'shortlist'-structures at 433K and infinite dilution.*

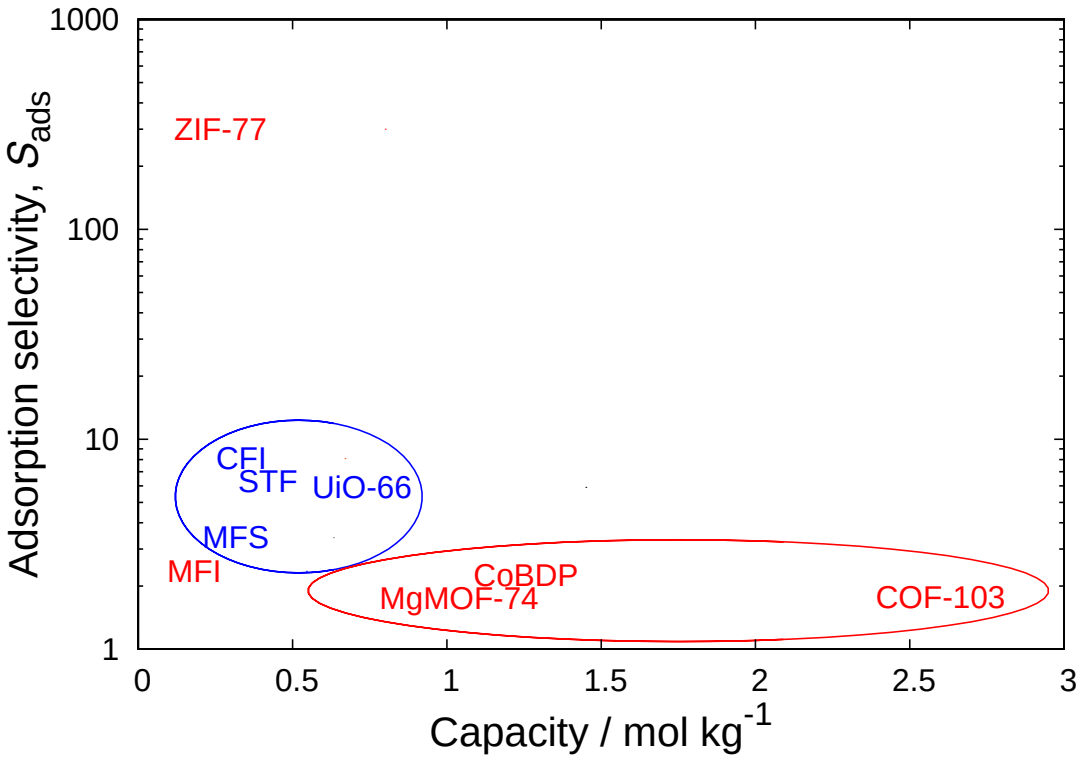

Figure S78: *Adsorption selectivity plotted against the capacity for hexane isomers at a total fugacity of the bulk fluid phase of 100 kPa and 433 K. For materials showing the normal hierarchy (red color) the capacity is defined as the averaged loadings of linear and mono-branched isomers. For materials with a reverse hierarchy (blue color), we define the capacity as the averaged loading of the di-branched isomers. We have omitted COF-102 from the figure, because COF-102 overlaps with COF-103.*

Zeolites are three-dimensional, microporous, crystalline solids with well-defined structures that contain aluminum, silicon, and oxygen. Their regular frameworks have void spaces (cavities or channels) that can host cations, water, or other molecules. The first zeolite was discovered by Cronstedt in 1756 who found that the mineral rapidly loses water on heating and seemed to boil. The name "zeolite" comes from the Greek words zeo (to boil) and lithos (stone). The framework aluminum and silicon are bound to each other through shared oxygen atoms. The SiO_4 units are neutral: Si_4^+/O_4^- but the AlO_4 results in a net negative charge: Al_3^+/O_4^-. The net negative charge is balanced by cations that are present during the synthesis. These cations are highly mobile and can be exchanged for other cationic species. According to the so-called Löwenstein rule, Al-O-Al linkages in zeolitic frameworks are forbidden. The picture shows the LTL-type zeolite.

3
Zeolites

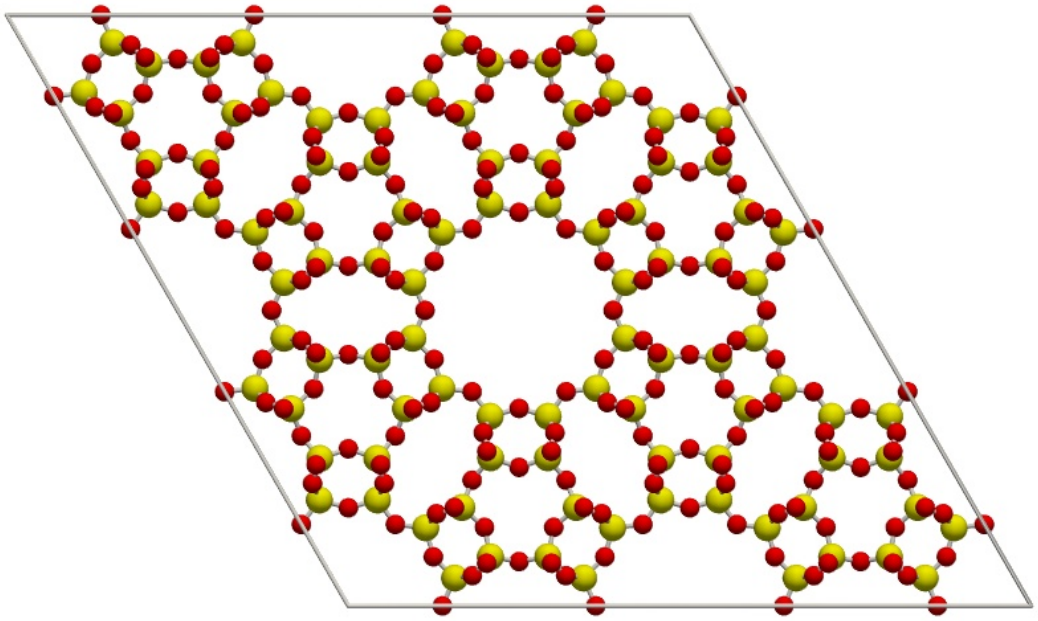

3.1 AEL

unit cell size	$a = 33.29$ [Å], $b = 14.7036$ [Å], $c = 8.3863$ [Å]
unit cell angles	$\alpha = \beta = \gamma = 90[^\circ]$
description	10-ring channel in the [001]-direction, free diameter 4.0×6.5 Å
crystallographic data	ref. [59]
framework density	1749.99 [kg/m^3]
void fraction	0.271512 [-]
accessible pore volume	0.1552 [cm^3/g]
nitrogen surface area	507 [m^2/g], 887 [m^2/cm^3]

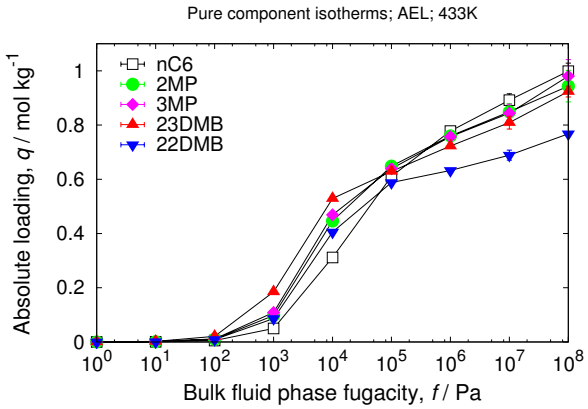

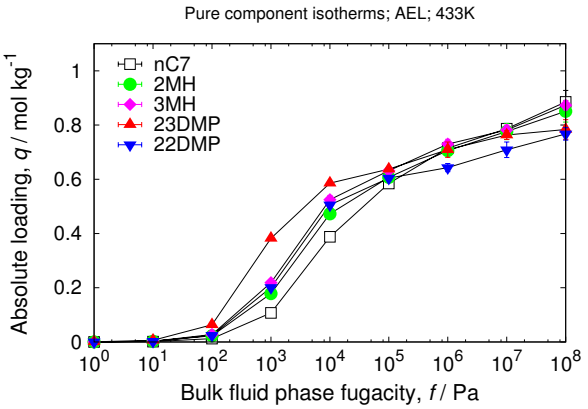

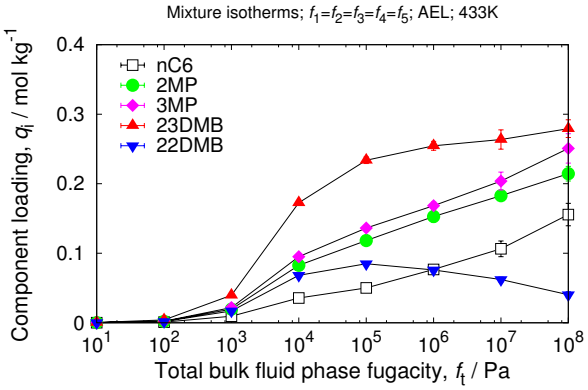

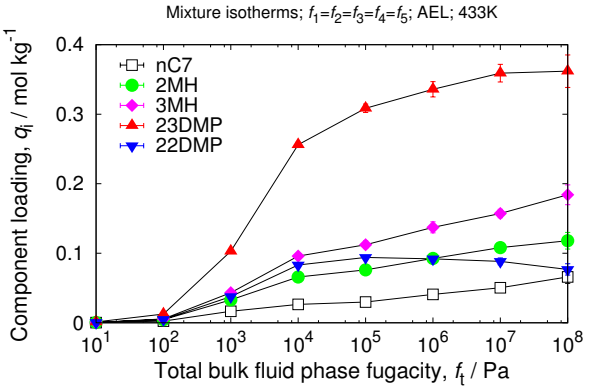

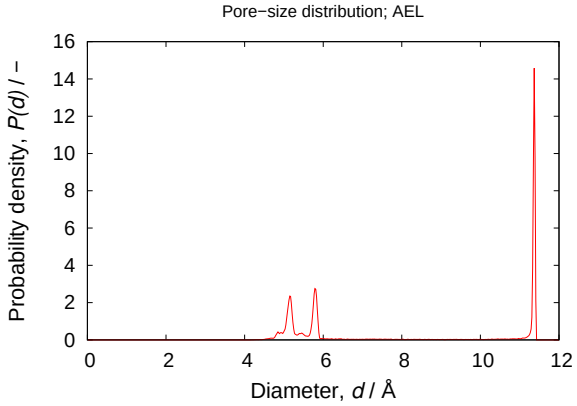

3.2 ATS

unit cell size	$a = 13.1483$ [Å], $b = 21.5771$ [Å], $c = 5.1639$ [Å]
unit cell angles	$\alpha = 90[^\circ]$, $\beta = 91.84[^\circ]$, $\gamma = 90[^\circ]$
description	12-ring channel in the [001]-direction, free diameter 6.5×7.5 Å
crystallographic data	ref. [60]
framework density	1635.33 [kg/m^3]
void fraction	0.297 [-]
accessible pore volume	0.1817 [cm^3/g]
nitrogen surface area	762 [m^2/g], 1247 [m^2/cm^3]

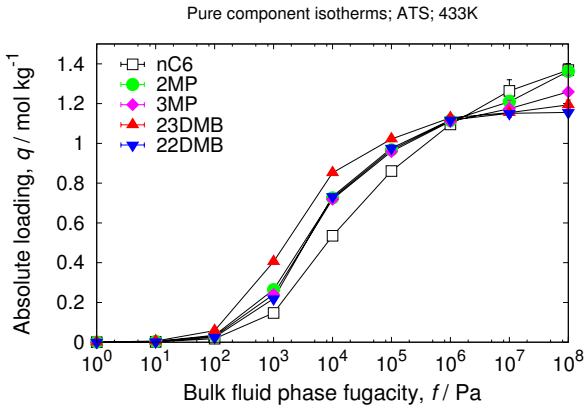

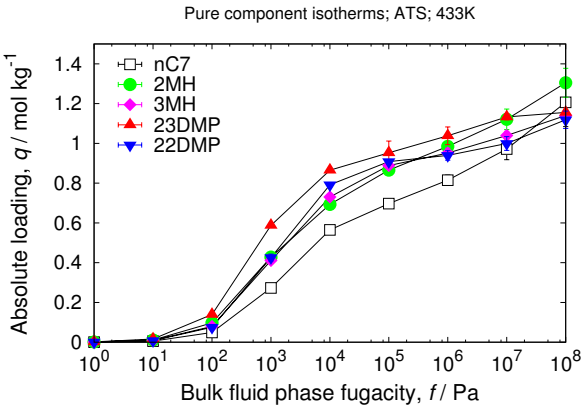

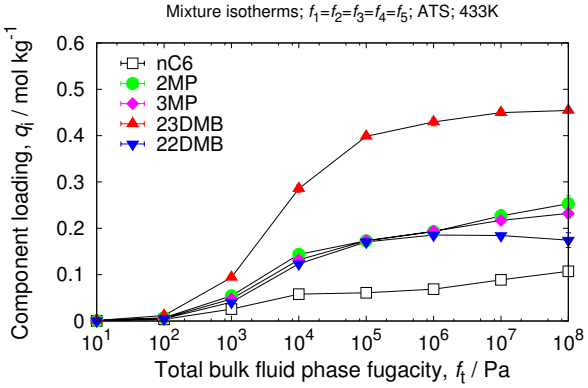

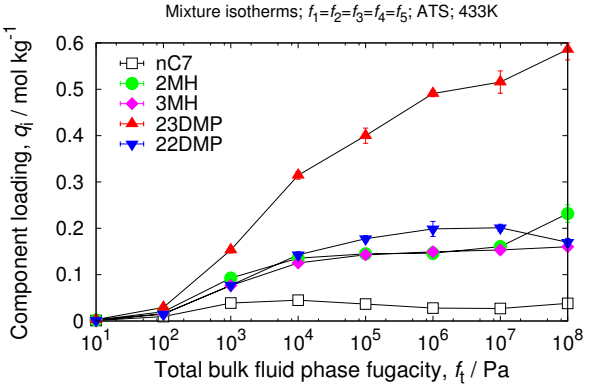

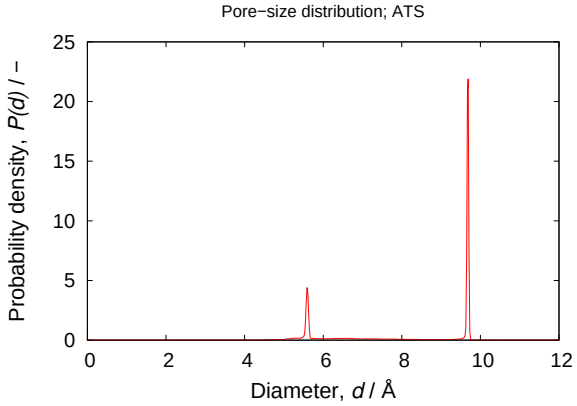

3.3 BEA

unit cell size	$a = 12.661$ [Å], $b = 12.661$ [Å], $c = 26.406$ [Å]
unit cell angles	$\alpha = \beta = \gamma = 90[^\circ]$
description	12-ring channel in the [100]-direction, free diameter 6.6×6.7 Å
	12-ring channel in the [001]-direction, free diameter 5.6×5.6 Å
crystallographic data	ref. [61]
framework density	1508.52 [kg/m^3]
void fraction	0.415 [-]
accessible pore volume	0.2749 [cm^3/g]
nitrogen surface area	1080 [m^2/g], 1630 [m^2/cm^3]

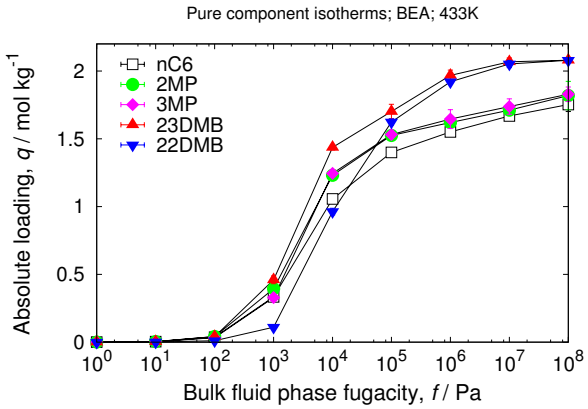

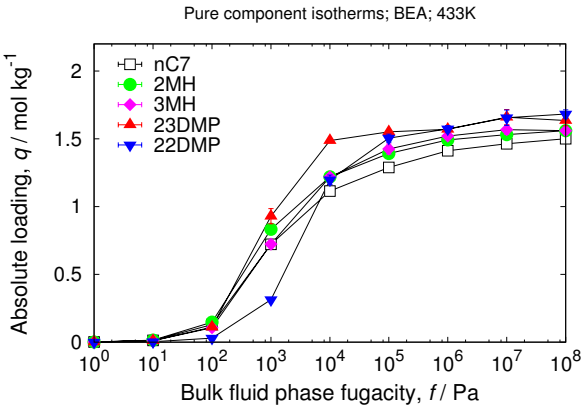

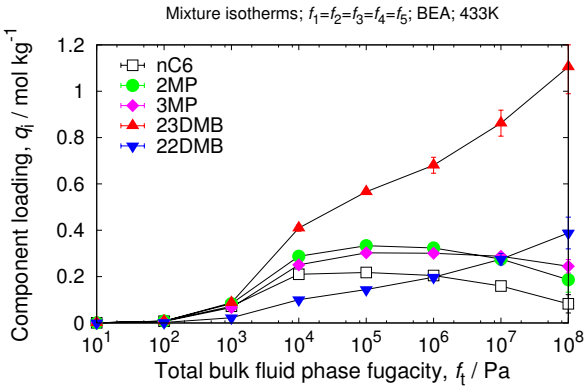

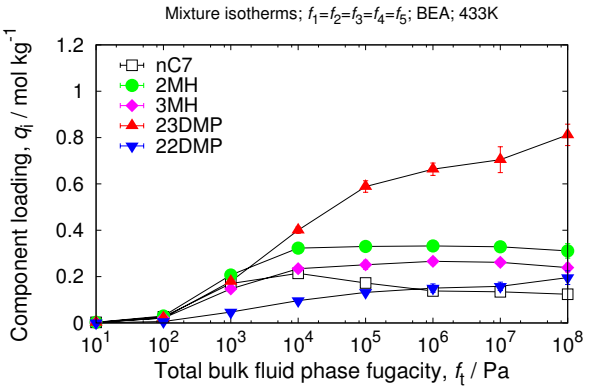

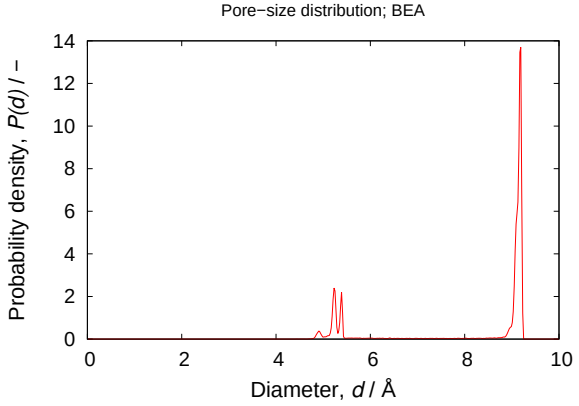

3.4 BOG

unit cell size	$a = 20.236$ [Å], $b = 23.798$ [Å], $c = 12.798$ [Å]
unit cell angles	$\alpha = \beta = \gamma = 90[^\circ]$
description	12-ring channel in the [100]-direction, free diameter 7.0×7.0 Å
	10-ring channel in the [010]-direction, free diameter 5.5×5.8 Å
crystallographic data	ref. [62]
framework density	1554.08 [kg/m^3]
void fraction	0.372 [-]
accessible pore volume	0.2392 [cm^3/g]
nitrogen surface area	928 [m^2/g], 1442 [m^2/cm^3]

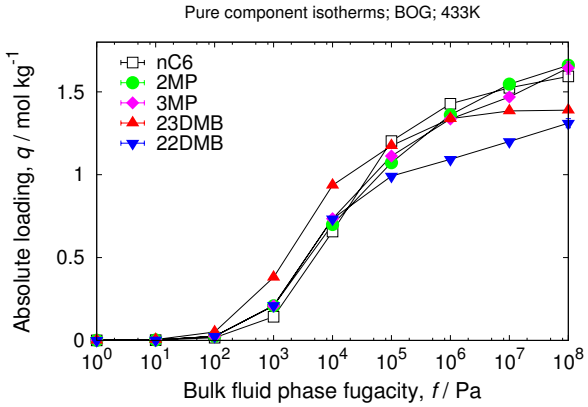

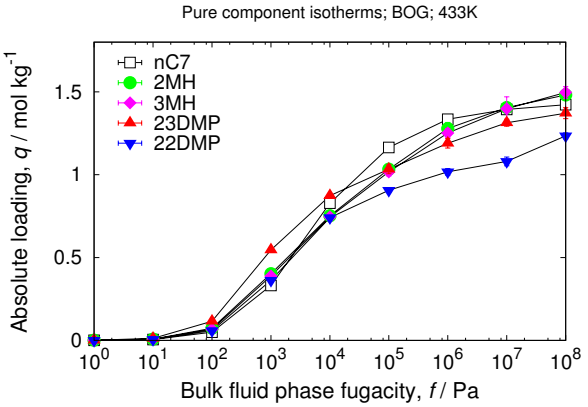

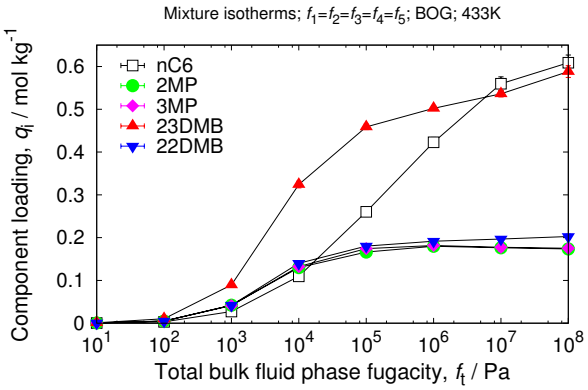

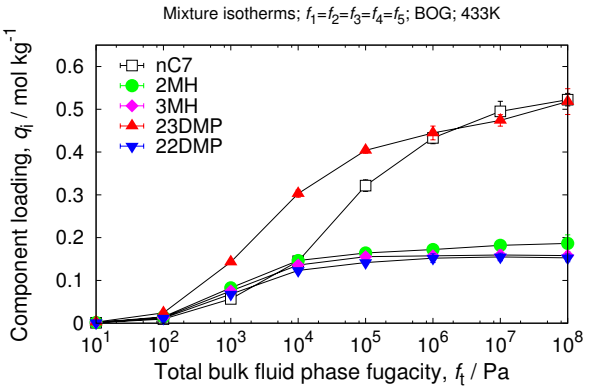

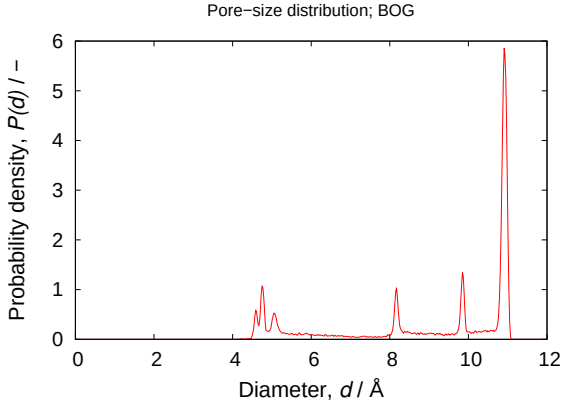

3.5 CFI

unit cell size	$a = 13.695$ [Å], $b = 5.021$ [Å], $c = 25.497$ [Å]
unit cell angles	$\alpha = \beta = \gamma = 90[^\circ]$
description	14-ring channel in the [010]-direction, free diameter 7.2×7.5 Å
crystallographic data	ref. [63]
framework density	1821.03 [kg/m^3]
void fraction	0.261 [-]
accessible pore volume	0.1432 [cm^3/g]
nitrogen surface area	527 [m^2/g], 959 [m^2/cm^3]

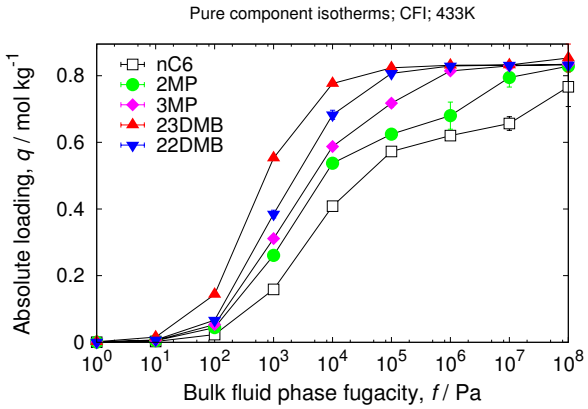

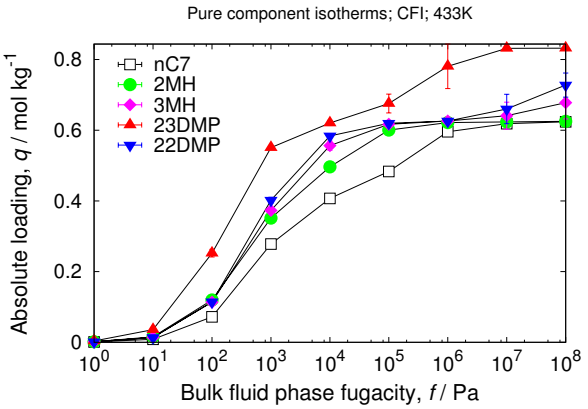

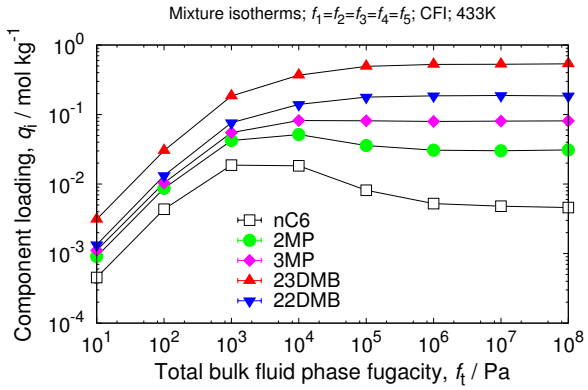

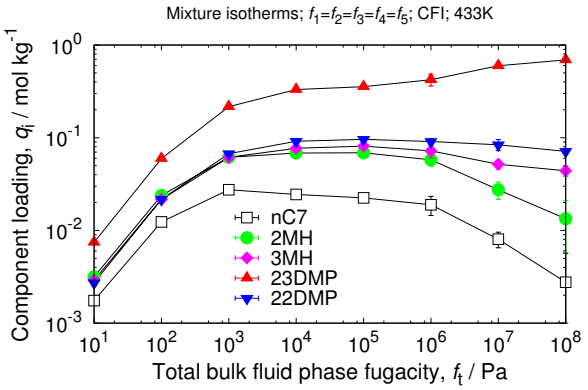

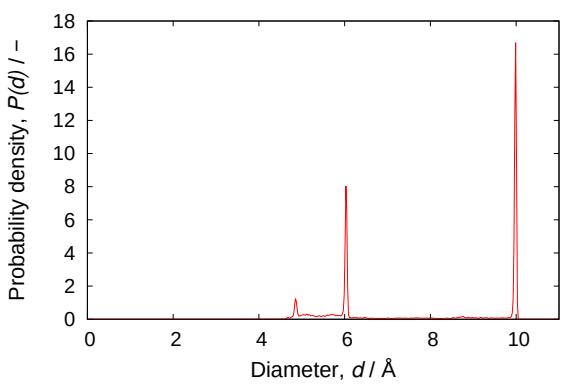

3.6 CON

unit cell size	$a = 22.6242$ [Å], $b = 13.3503$ [Å], $c = 12.3642$ [Å]
unit cell angles	$\alpha = 90[^\circ]$, $\beta = 68.913[^\circ]$, $\gamma = 90[^\circ]$
description	12-ring channel in the [001]-direction, free diameter 6.4×7.0 Å 12-ring channel in the [100]-direction, free diameter 7.0×5.9 Å 10-ring channel in the [010]-direction, free diameter 5.1×4.5 Å
crystallographic data	ref. [64]
framework density	1603.50 [kg/m^3]
void fraction	0.395 [-]
accessible pore volume	0.2461 [cm^3/g]
nitrogen surface area	987 [m^2/g], 1582 [m^2/cm^3]

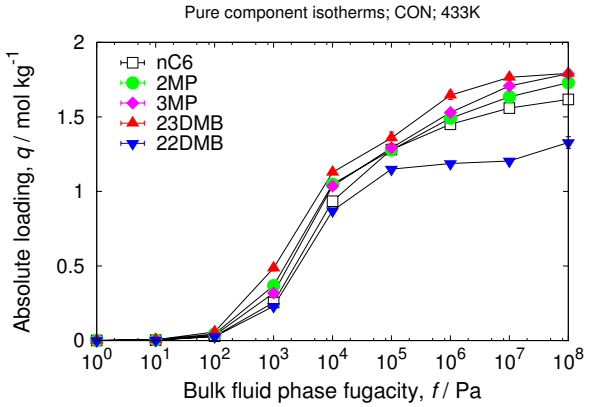

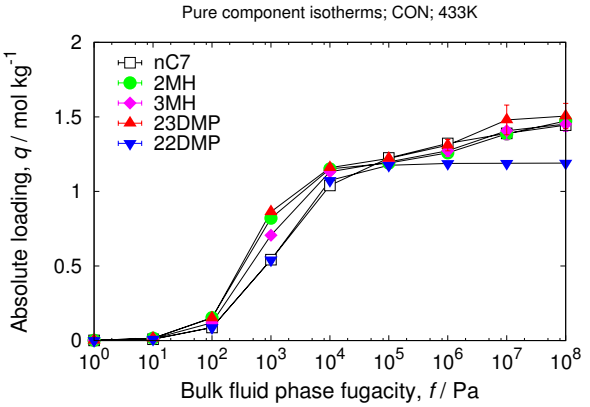

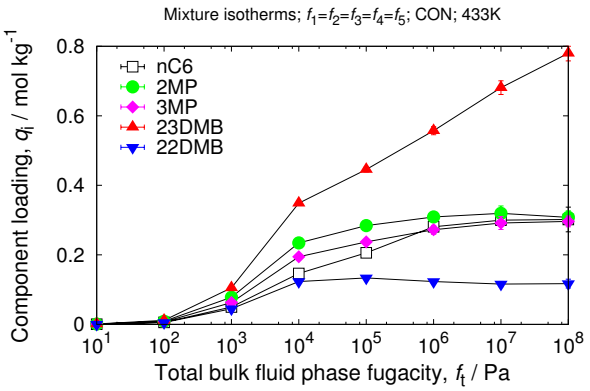

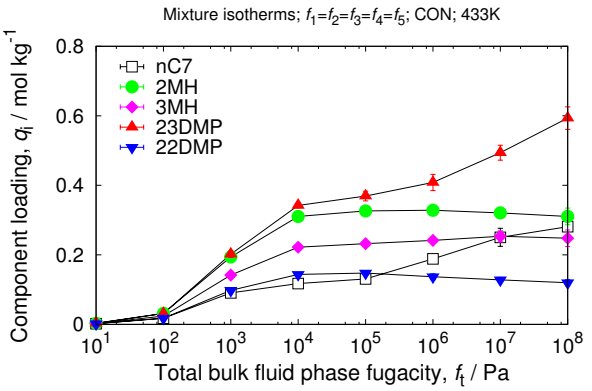

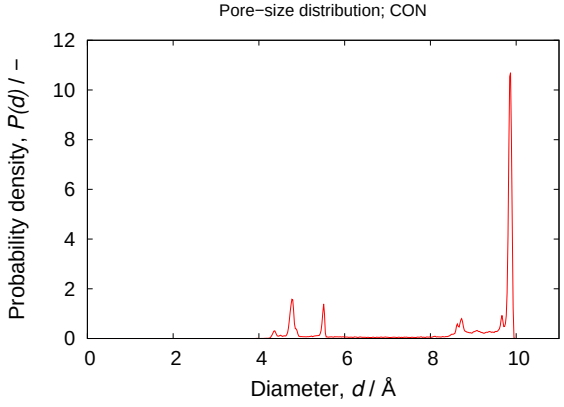

3.7 DON

unit cell size	$a = 14.9701$ [Å], $b = 8.4761$ [Å], $c = 30.0278$ [Å]
unit cell angles	$\alpha = 90[^\circ]$, $\beta = 102.65[^\circ]$, $\gamma = 90[^\circ]$
description	14-ring channel in the [010]-direction, free diameter 8.1×8.2 Å
crystallographic data	ref. [65]
framework density	1717.58 [kg/m^3]
void fraction	0.285 [-]
accessible pore volume	0.1659 [cm^3/g]
nitrogen surface area	559 [m^2/g], 960 [m^2/cm^3]

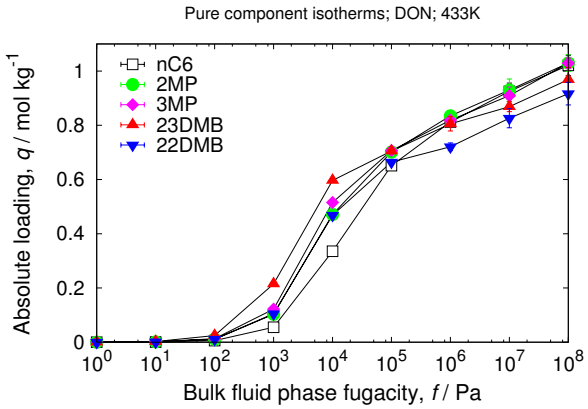

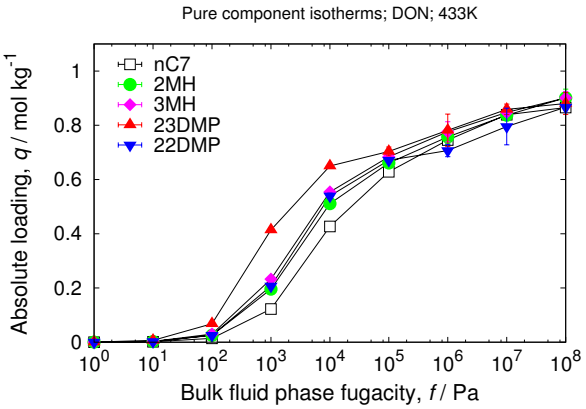

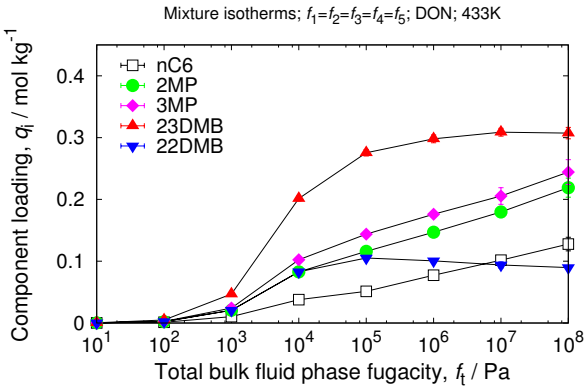

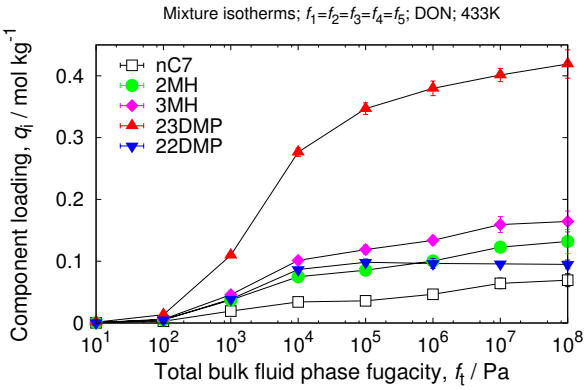

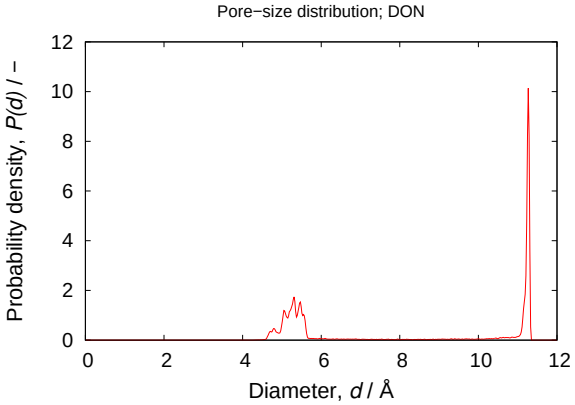

3.8 EMT

unit cell size	$a = 17.3864$ [Å], $b = 17.3864$ [Å], $c = 28.3459$ [Å]
unit cell angles	$\alpha = \beta = 90[^\circ]$, $\gamma = 120[^\circ]$
description	12-ring channel in the [001]-direction, free diameter 7.3×7.3 Å 12-ring channel in the $\perp$[001]-direction, free diameter 6.5×7.5 Å
crystallographic data	ref. [66]
framework density	1290.75 [kg/m^3]
void fraction	0.475 [-]
accessible pore volume	0.3681 [cm^3/g]
nitrogen surface area	1238 [m^2/g], 1597 [m^2/cm^3]

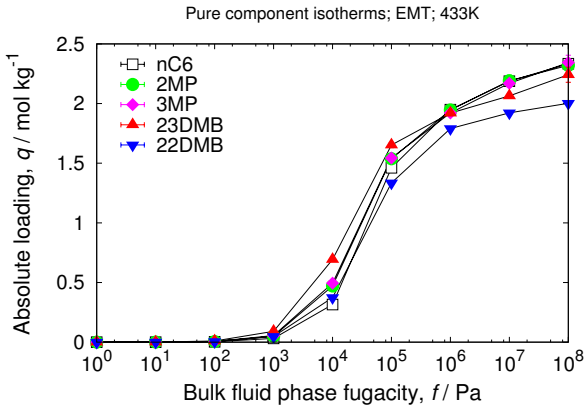

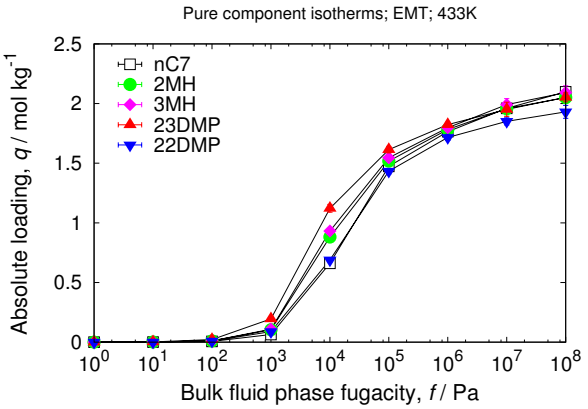

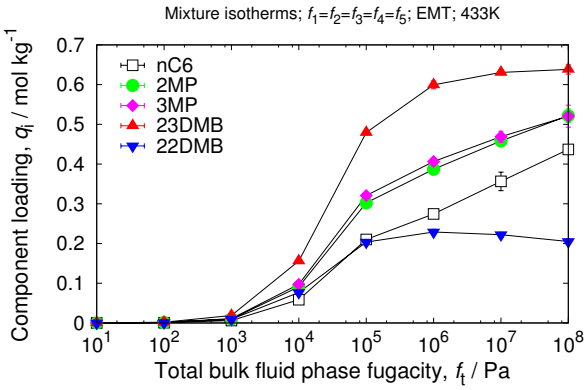

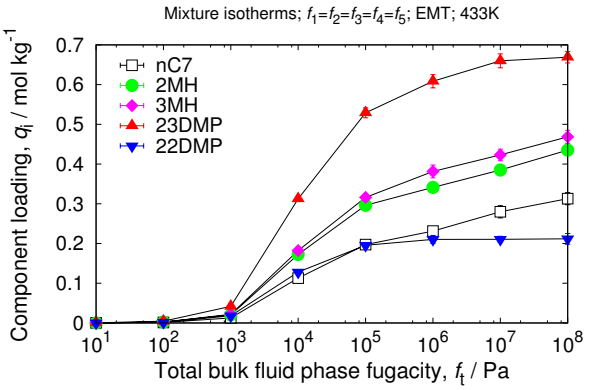

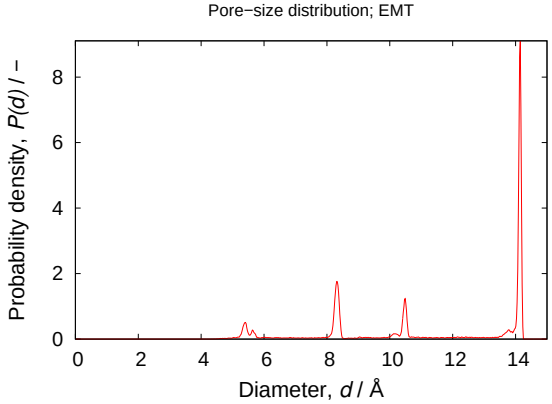

3.9 FAU

unit cell size	$a = 24.2576$ [Å], $b = 24.2576$ [Å], $c = 24.2576$ [Å]
unit cell angles	$\alpha = \beta = \gamma = 90[^\circ]$
description	12-ring channel in the [111]-direction, free diameter 7.4×7.4 Å
crystallographic data	ref. [67]
framework density	1342.05 [kg/m^3]
void fraction	0.444 [-]
accessible pore volume	0.3309 [cm^3/g]
nitrogen surface area	1199 [m^2/g], 1609 [m^2/cm^3]

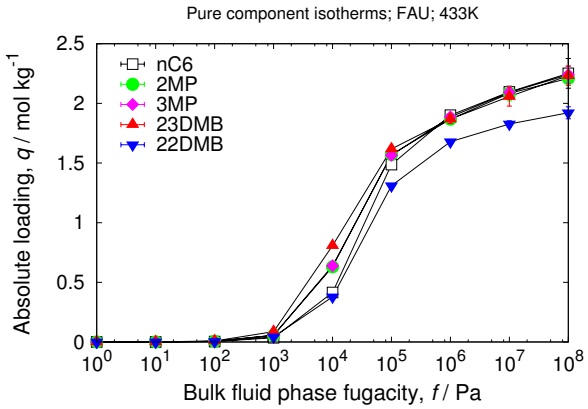

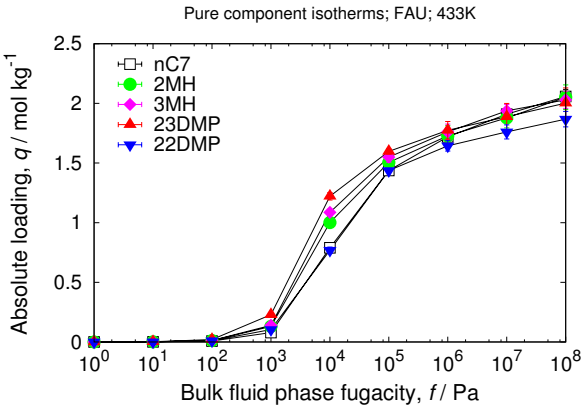

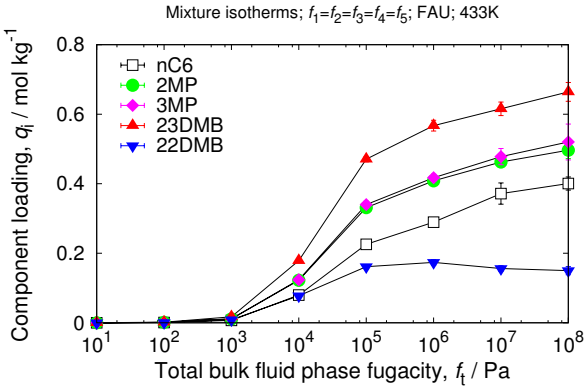

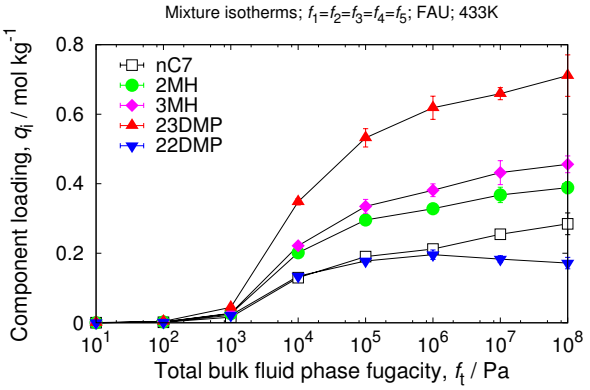

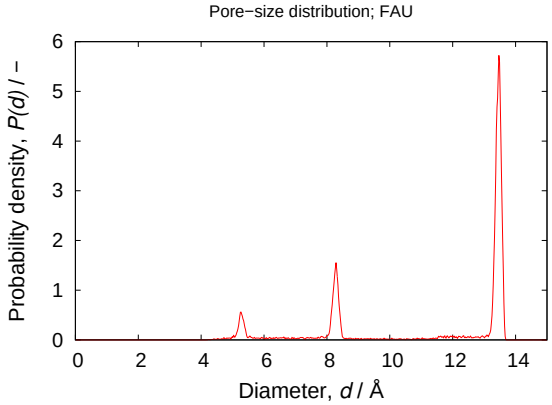

3.10 NaY

unit cell size	$a = 25.099$ [Å], $b = 25.099$ [Å], $c = 25.099$ [Å]
unit cell angles	$\alpha = \beta = \gamma = 90[^\circ]$
description	12-ring channel in the [111]-direction, free diameter 7.4×7.4 Å
crystallographic data	ref. [68]
framework density	1344.86 [kg/m^3]
void fraction	0.435 [-]
accessible pore volume	0.3235 [cm^3/g]

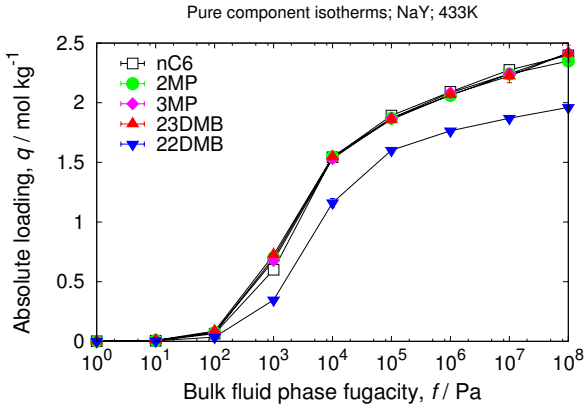

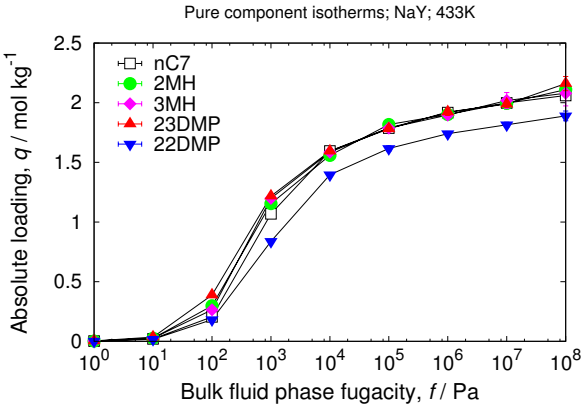

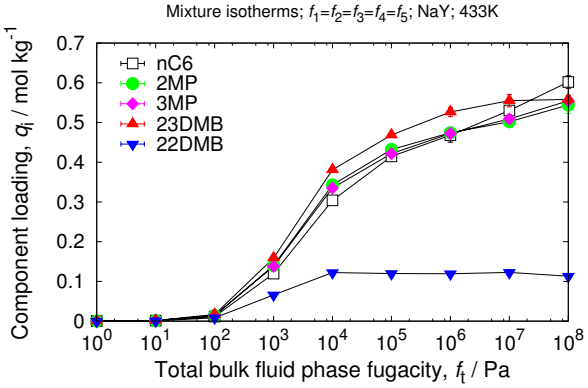

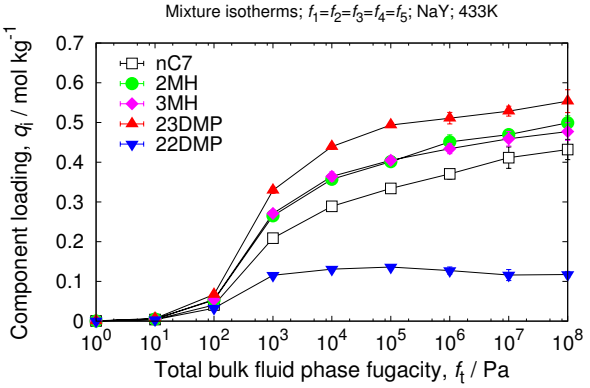

3.11 NaX

unit cell size	$a = 25.099$ [Å], $b = 25.099$ [Å], $c = 25.099$ [Å]
unit cell angles	$\alpha = \beta = \gamma = 90[^\circ]$
description	12-ring channel in the [111]-direction, free diameter 7.4×7.4 Å
crystallographic data	ref. [68]
framework density	1409.22 [kg/m^3]
void fraction	0.435 [-]
accessible pore volume	0.3087 [cm^3/g]

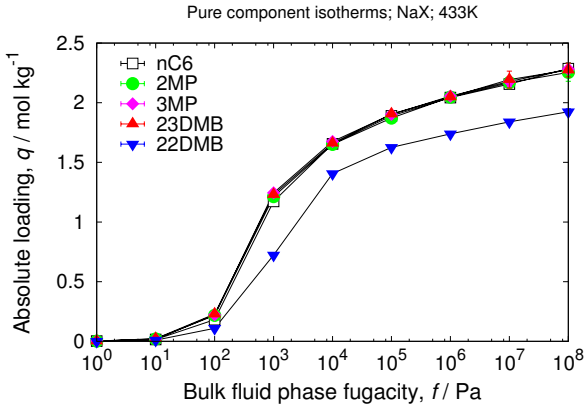

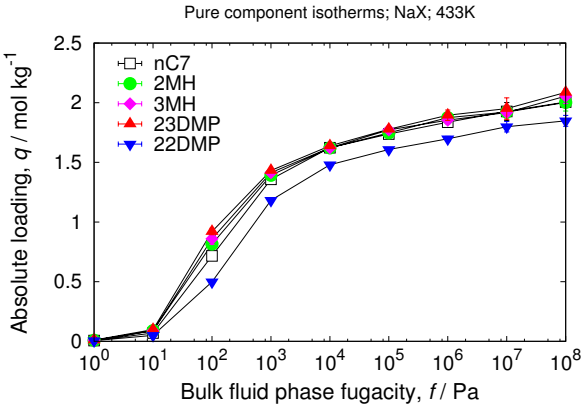

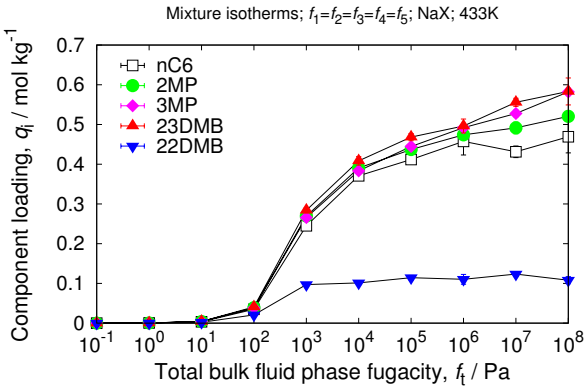

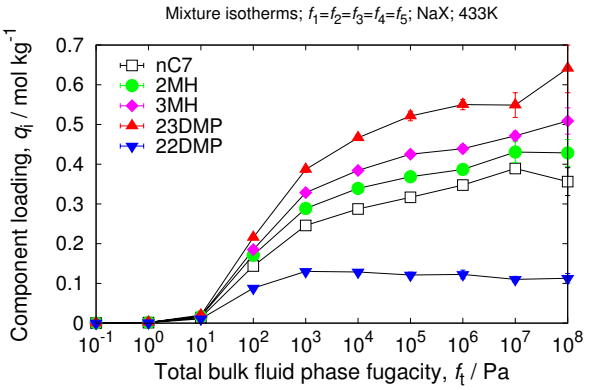

3.12 FER

unit cell size	$a = 18.7202$ [Å], $b = 14.0702$ [Å], $c = 7.41971$ [Å]
unit cell angles	$\alpha = \beta = \gamma = 90[^\circ]$
description	10-ring channel in the [001]-direction, free diameter 4.2×5.4 Å
	8-ring channel in the [010]-direction, free diameter 3.5×4.8 Å
crystallographic data	ref. [69]
framework density	1837.87 [kg/m^3]
void fraction	0.2358 [-]
accessible pore volume	0.1283 [cm^3/g]
nitrogen surface area	558 [m^2/g], 1025 [m^2/cm^3]

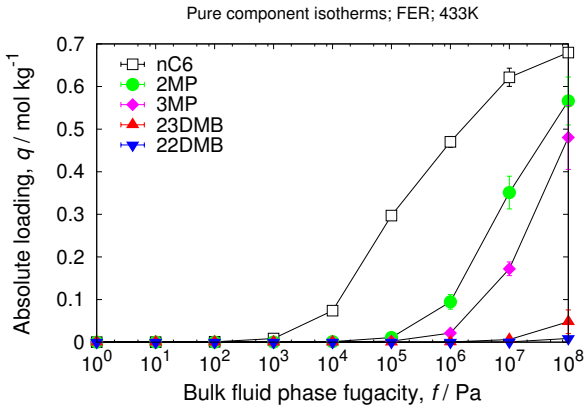

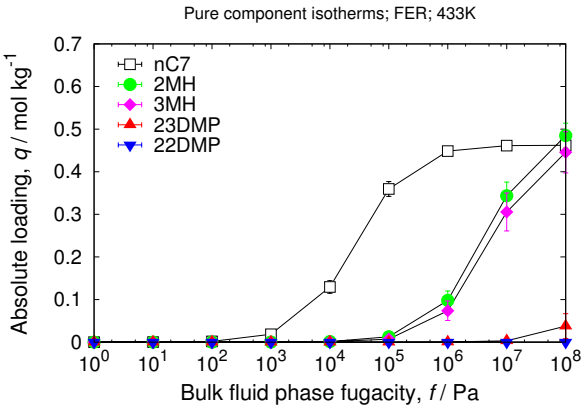

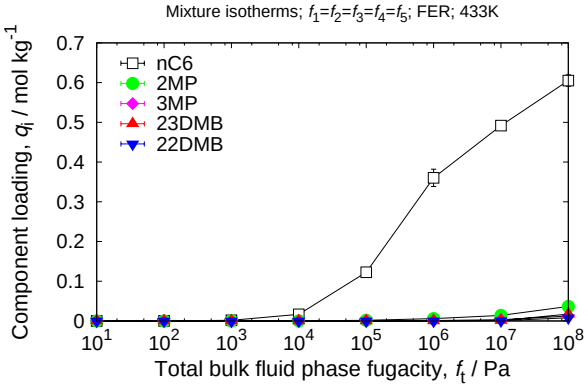

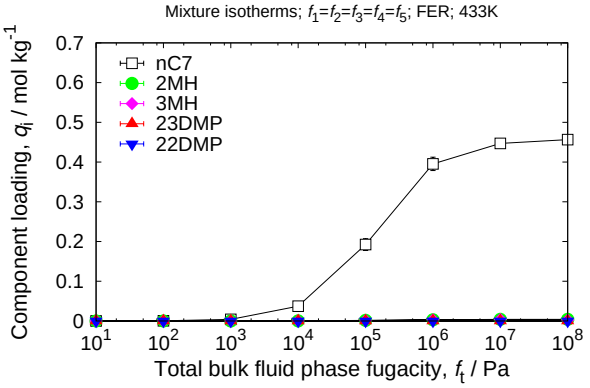

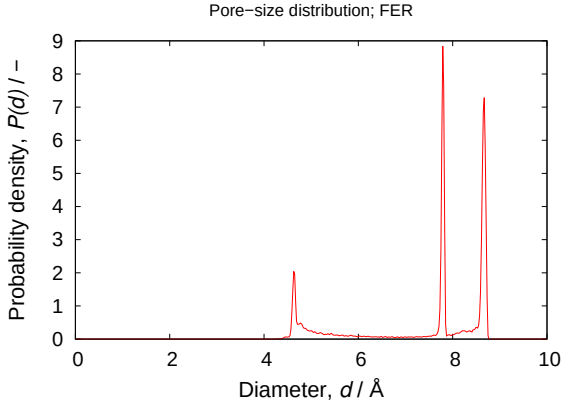

3.13 GME

unit cell size	$a = 13.75$ [Å], $b = 13.75$ [Å], $c = 10.05$ [Å]
unit cell angles	$\alpha = \beta = 90[^\circ]$, $\gamma = 120[^\circ]$
description	12-ring channel in the [001]-direction, free diameter 7.0×7.0 Å
	8-ring channel in the $\perp$[001]-direction, free diameter 3.6×3.9 Å
crystallographic data	ref. [70]
framework density	1455.18 [kg/m^3]
void fraction	0.338 [-]
accessible pore volume	0.2322 [cm^3/g]
nitrogen surface area	1097 [m^2/g], 1596 [m^2/cm^3]
note	results need further detailed analysis to check blocking issues

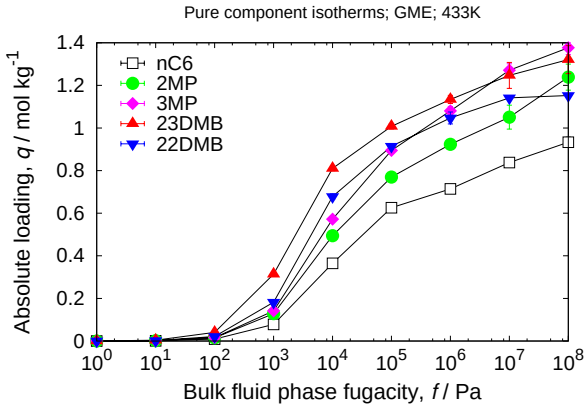

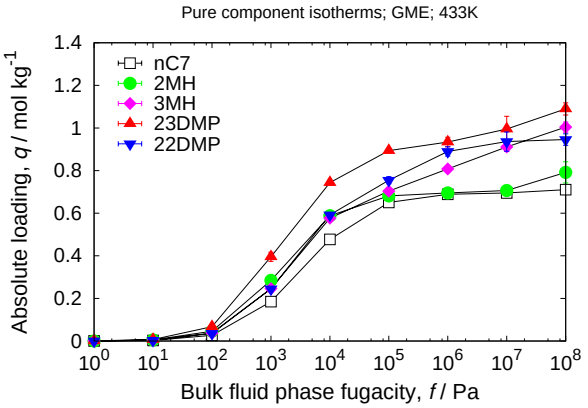

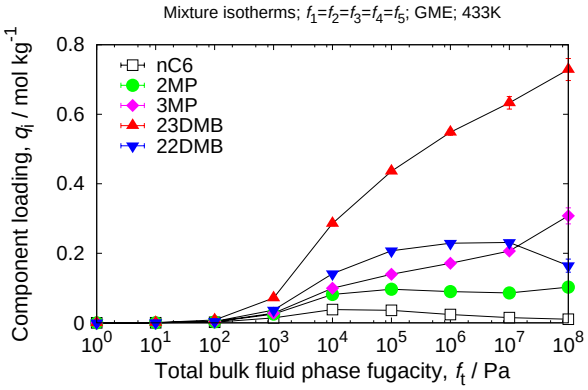

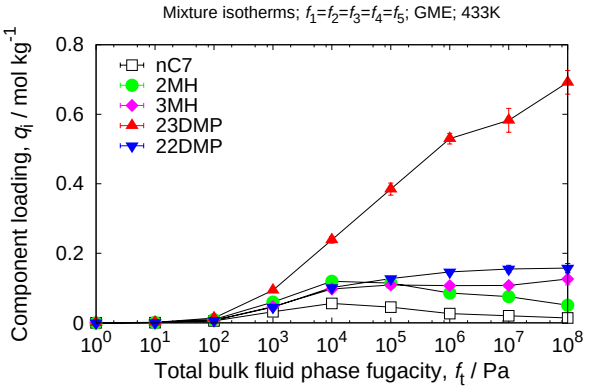

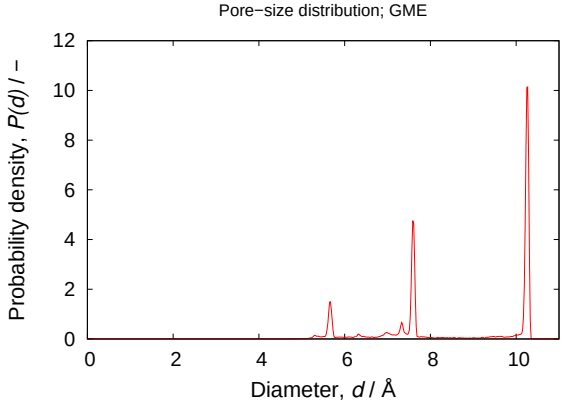

3.14 ISV

unit cell size	$a = 12.8528$ [Å], $b = 12.8528$ [Å], $c = 25.2136$ [Å]
unit cell angles	$\alpha = \beta = \gamma = 90[^\circ]$
description	12-ring channel in the [100]-direction, free diameter 6.1×6.5 Å 12-ring channel in the [001]-direction, free diameter 5.9×6.6 Å
crystallographic data	ref. [71]
framework density	1533.06 [kg/m^3]
void fraction	0.437 [-]
accessible pore volume	0.2850 [cm^3/g]
nitrogen surface area	1063 [m^2/g], 1630 [m^2/cm^3]

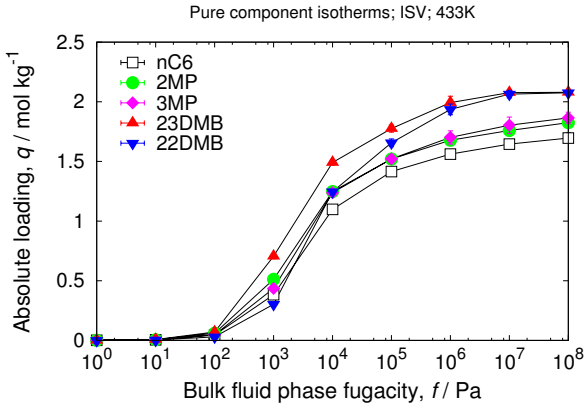

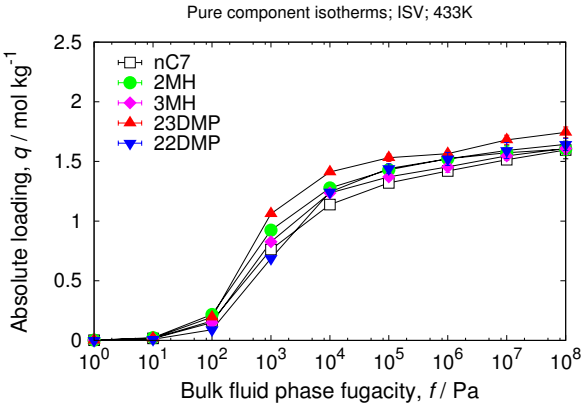

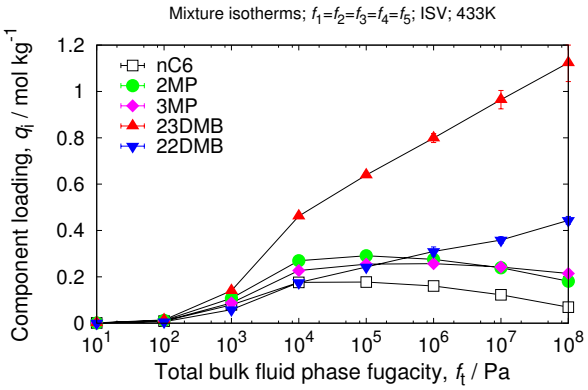

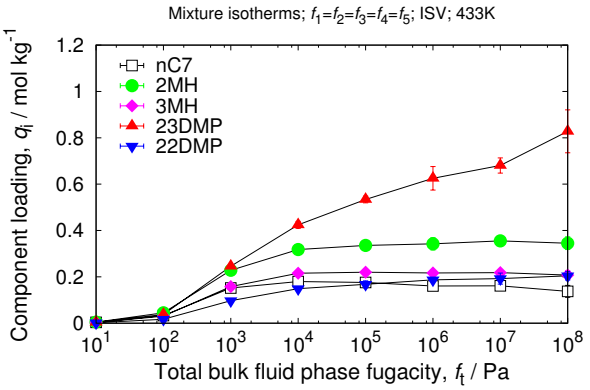

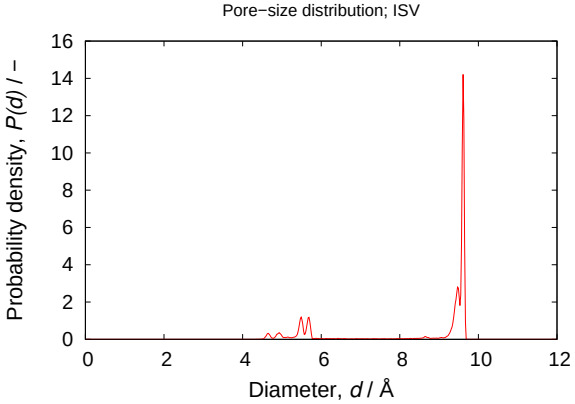

3.15 LAU

unit cell size	$a = 14.8538$ [Å], $b = 13.1695$ [Å], $c = 7.5421$ [Å]
unit cell angles	$\alpha = 90[^\circ]$, $\beta = 110.323[^\circ]$, $\gamma = 90[^\circ]$
description	10-ring channel in the [100]-direction, free diameter 4.0×5.3 Å
crystallographic data	ref. [72]
framework density	1720.15 [kg/m^3]
void fraction	0.229 [-]
accessible pore volume	0.1332 [cm^3/g]
nitrogen surface area	611 [m^2/g], 1051 [m^2/cm^3]

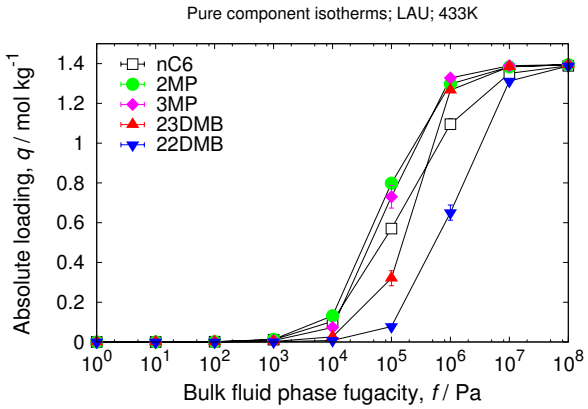

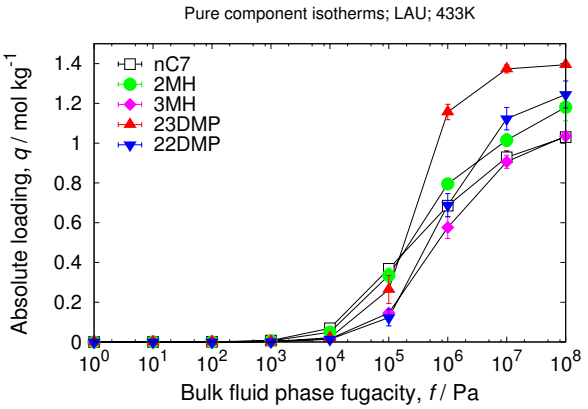

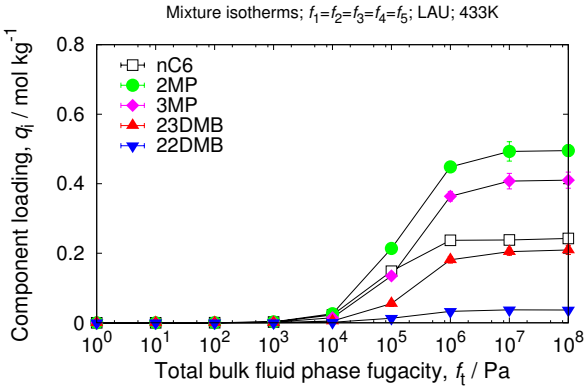

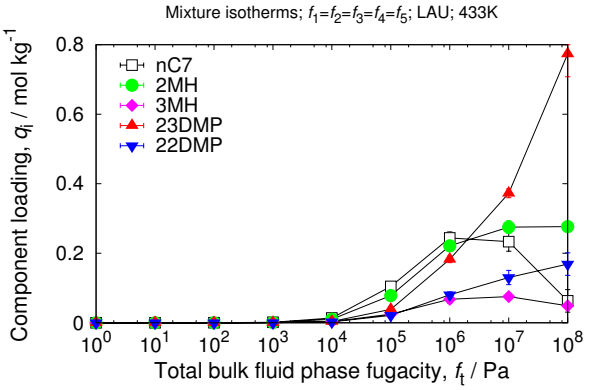

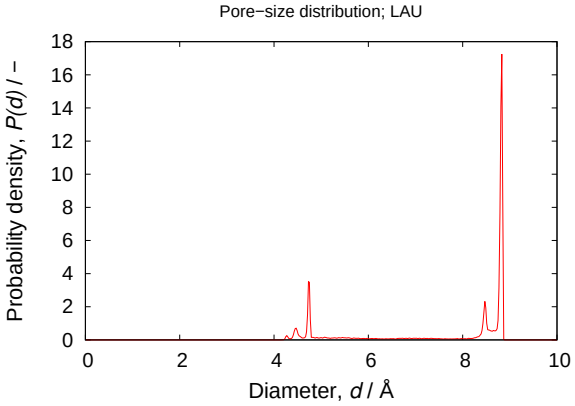

3.16 LTL

unit cell size	$a = 18.466$ [Å], $b = 18.466$ [Å], $c = 7.4763$ [Å]
unit cell angles	$\alpha = \beta = 90[^\circ]$, $\gamma = 120[^\circ]$
description	12-ring channel in the [001]-direction, free diameter 7.1×7.1 Å
crystallographic data	ref. [73]
framework density	1626.86 [kg/m^3]
void fraction	0.273 [-]
accessible pore volume	0.1677 [cm^3/g]
nitrogen surface area	609 [m^2/g], 990 [m^2/cm^3]

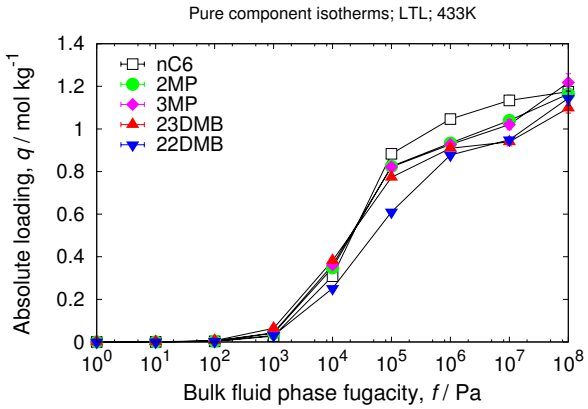

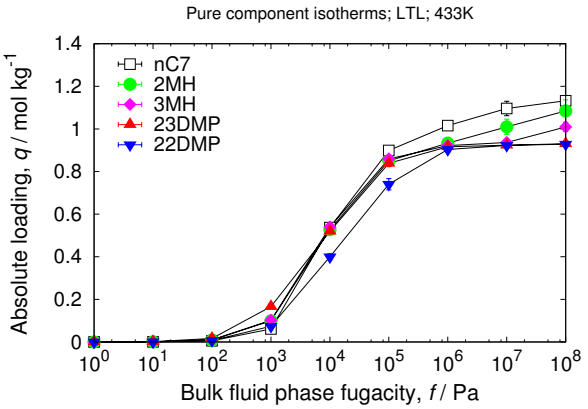

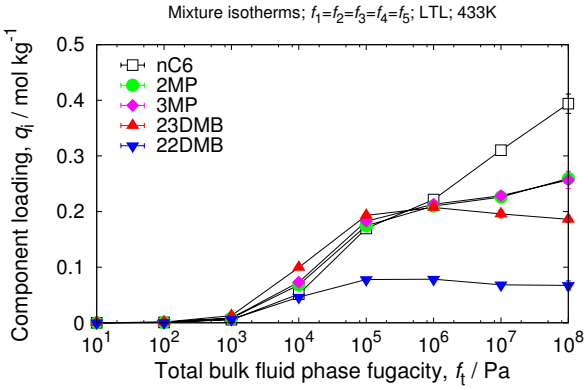

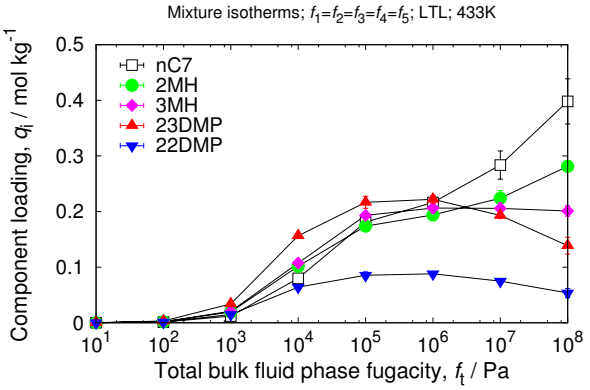

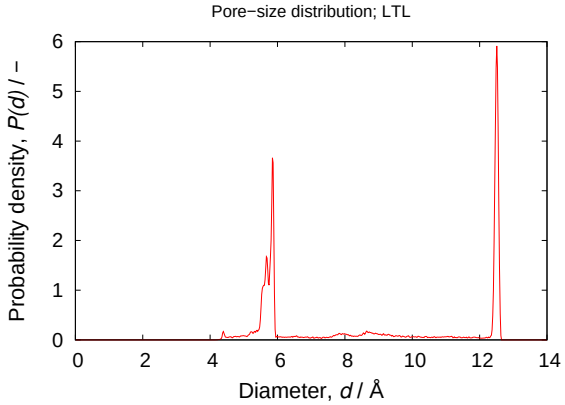

3.17 MAZ

unit cell size	$a = 18.392$ [Å], $b = 18.392$ [Å], $c = 7.646$ [Å]
unit cell angles	$\alpha = \beta = 90[^\circ]$, $\gamma = 120[^\circ]$
description	12-ring channel in the [001]-direction, free diameter 7.4×7.4 Å
	8-ring channel in the [001]-direction, free diameter 3.1×3.1 Å
crystallographic data	ref. [74]
framework density	1603.58 [kg/m^3]
void fraction	0.274 [-]
accessible pore volume	0.1709 [cm^3/g]
nitrogen surface area	698 [m^2/g], 1120 [m^2/cm^3]

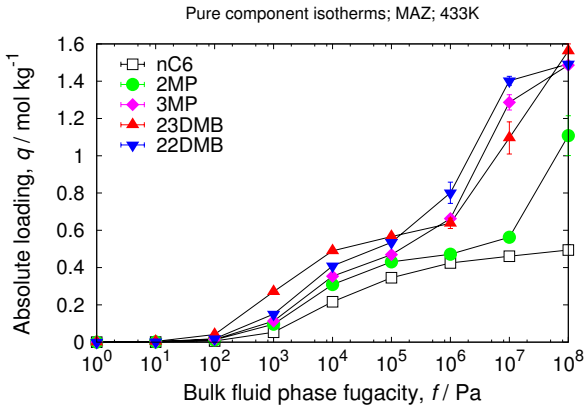

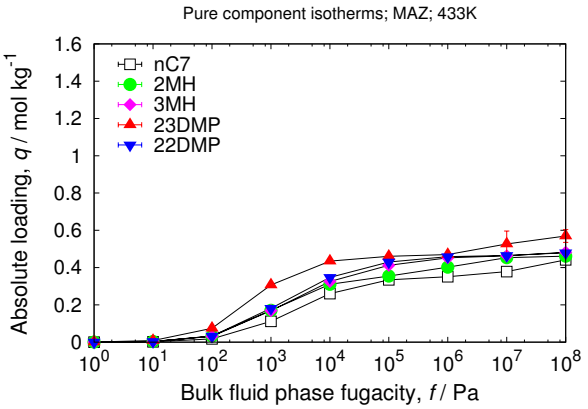

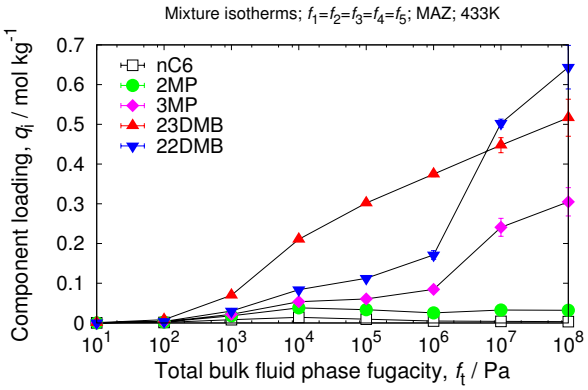

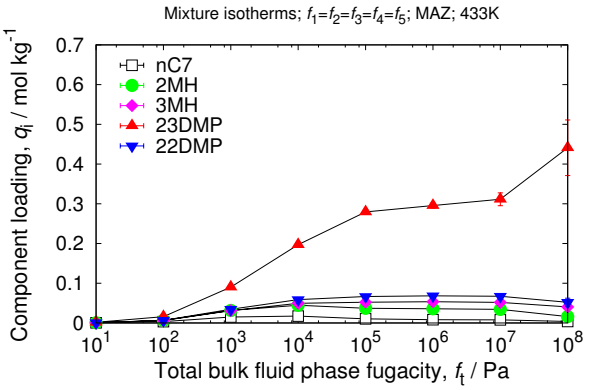

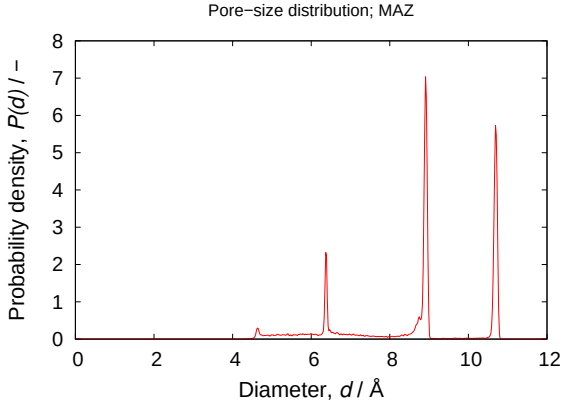

3.18 MEI

unit cell size	$a = 13.175$ [Å], $b = 13.175$ [Å], $c = 15.848$ [Å]
unit cell angles	$\alpha = \beta = 90[^\circ]$, $\gamma = 120[^\circ]$
description	12-ring channel in the [001]-direction, free diameter 6.9×6.9 Å
	7-ring channel in the $\perp$[001]-direction, free diameter 3.2×3.5 Å
crystallographic data	ref. [75]
framework density	1423.91 [kg/m^3]
void fraction	0.413 [-]
accessible pore volume	0.2899 [cm^3/g]
nitrogen surface area	1173 [m^2/g], 1670 [m^2/cm^3]

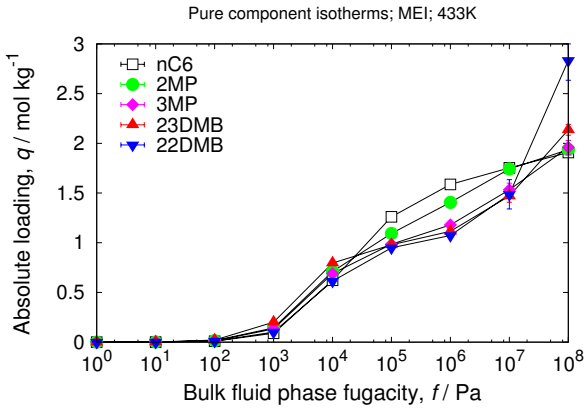

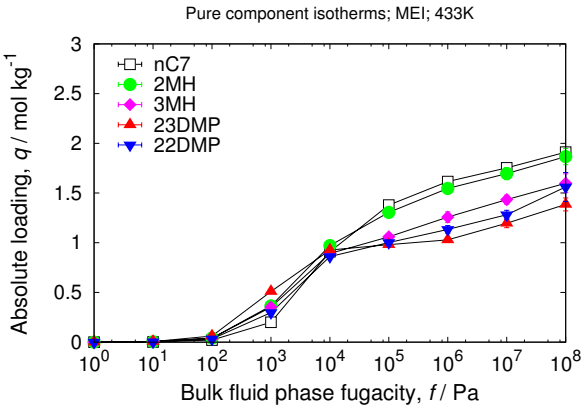

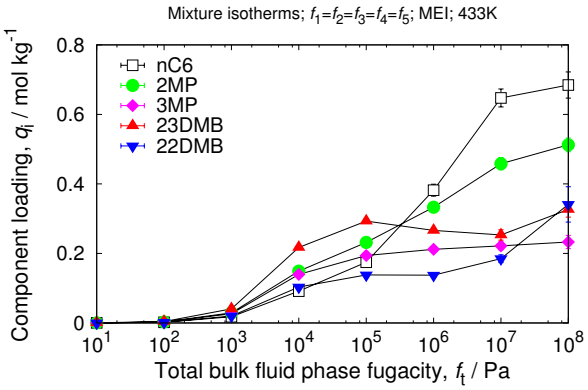

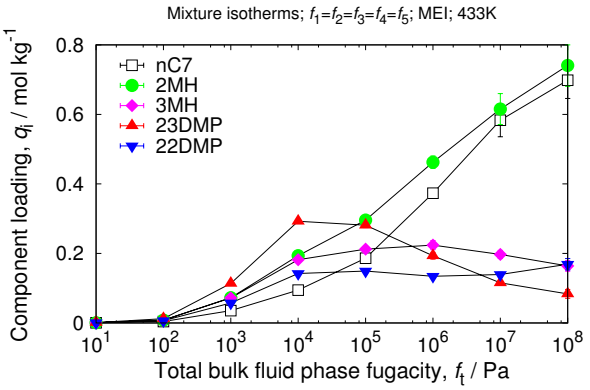

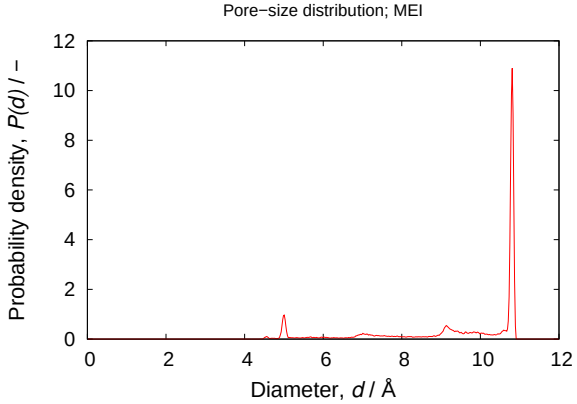

3.19 MEL

unit cell size	$a = 20.067$ [Å], $b = 20.067$ [Å], $c = 13.411$ [Å]
unit cell angles	$\alpha = \beta = \gamma = 90[^\circ]$
description	10-ring channel in the [100]-direction, free diameter 5.3×5.4 Å
crystallographic data	ref. [76]
framework density	1773.60 [kg/m^3]
void fraction	0.272 [-]
accessible pore volume	0.1535 [cm^3/g]
nitrogen surface area	664 [m^2/g], 1177 [m^2/cm^3]

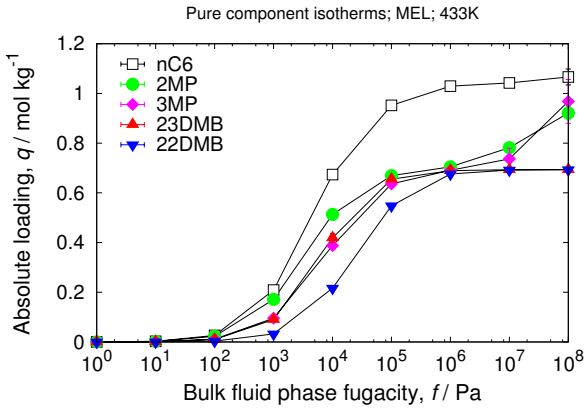

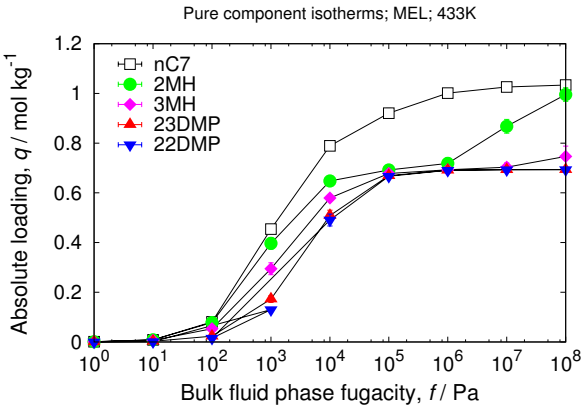

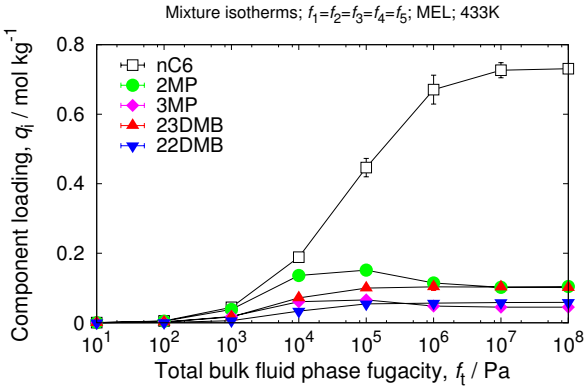

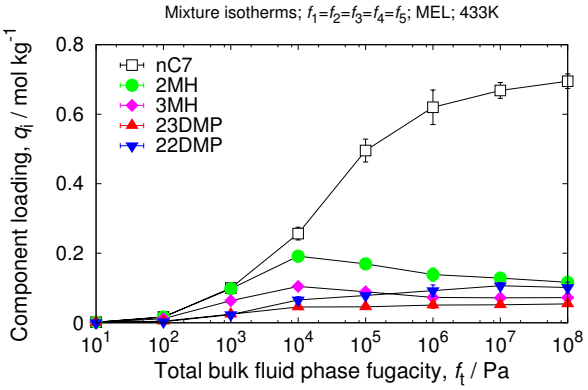

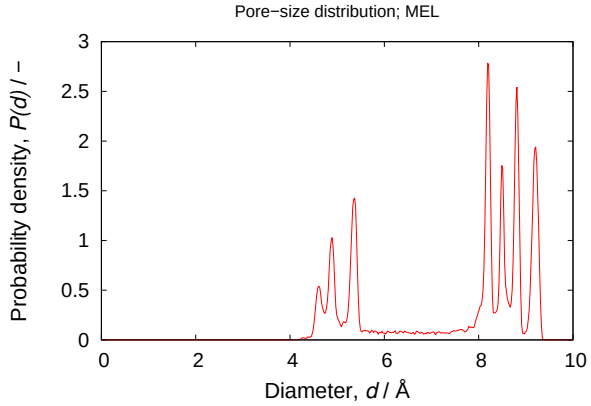

3.20 MFI

unit cell size	$a = 20.022$ [Å], $b = 19.899$ [Å], $c = 13.383$ [Å]
unit cell angles	$\alpha = \beta = \gamma = 90[^\circ]$
description	10-ring channel in the [100]-direction, free diameter 5.1×5.5 Å
	10-ring channel in the [010]-direction, free diameter 5.3×5.6 Å
crystallographic data	ref. [77]
framework density	1796.34 [kg/m^3]
void fraction	0.292 [-]
accessible pore volume	0.1626 [cm^3/g]
nitrogen surface area	658 [m^2/g], 1183 [m^2/cm^3]

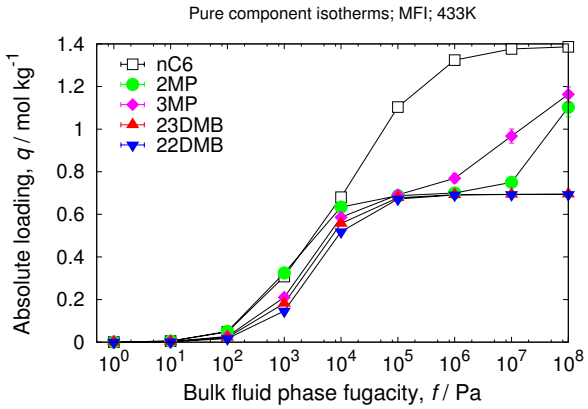

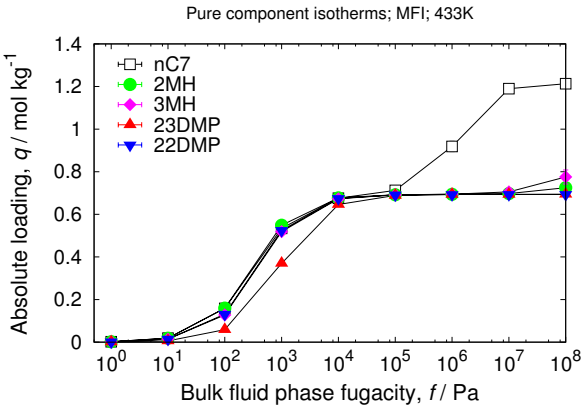

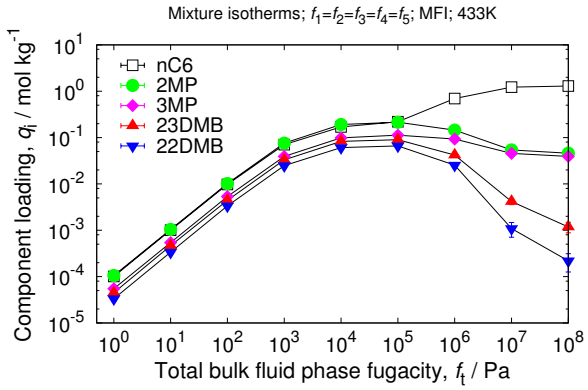

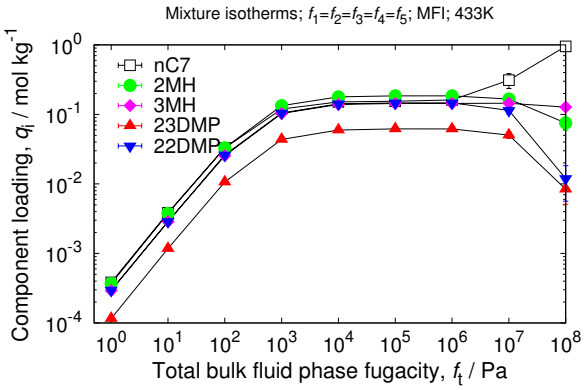

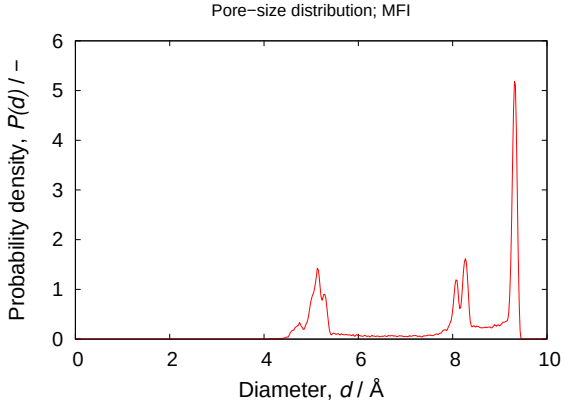

3.21 MFS

unit cell size	$a = 7.451$ [Å], $b = 14.1711$ [Å], $c = 18.767$ [Å]
unit cell angles	$\alpha = \beta = \gamma = 90[^\circ]$
description	10-ring channel in the [100]-direction, free diameter 5.1×5.4 Å 8-ring channel in the [010]-direction, free diameter 3.3×4.8 Å
crystallographic data	ref. [78]
framework density	1812.59 [kg/m^3]
void fraction	0.238 [-]
accessible pore volume	0.1312 [cm^3/g]
nitrogen surface area	534 [m^2/g], 968 [m^2/cm^3]

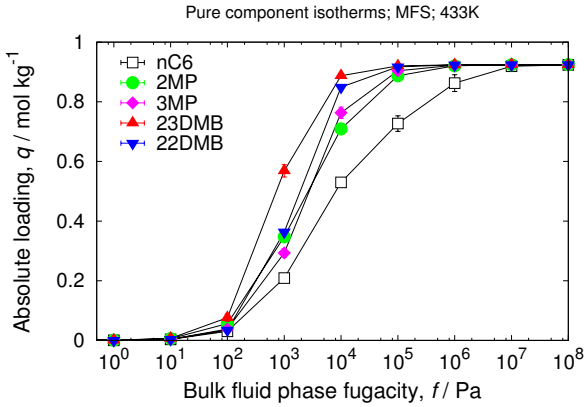

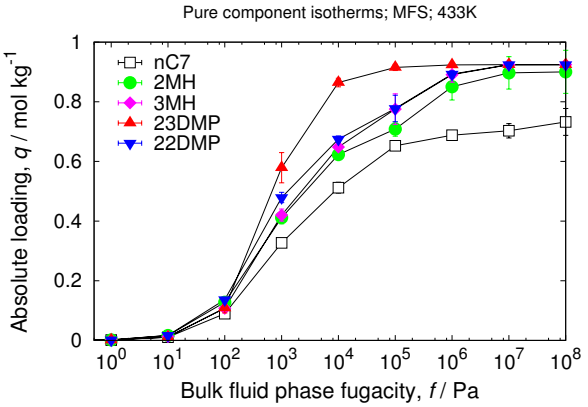

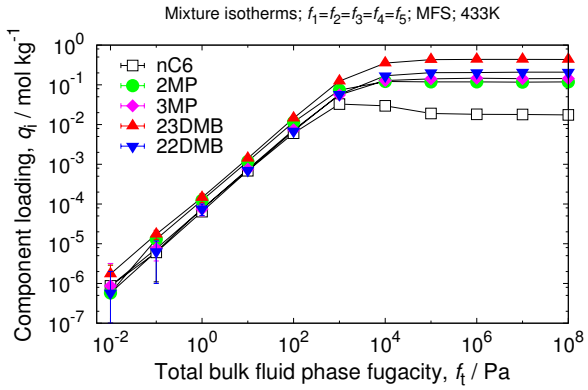

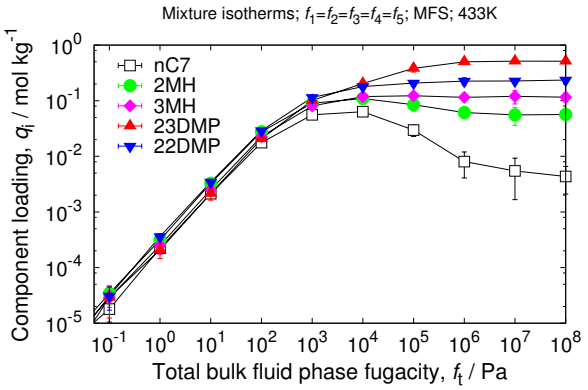

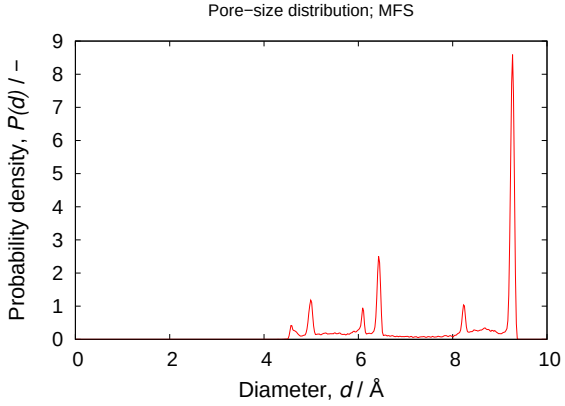

3.22 MOR

unit cell size	$a = 18.11$ [Å], $b = 20.53$ [Å], $c = 7.528$ [Å]
unit cell angles	$\alpha = \beta = \gamma = 90[^\circ]$
description	12-ring channel in the [001]-direction, free diameter 6.5×7.0 Å
	8-ring channel in the [010]-direction, free diameter 3.4×4.8 Å
	8-ring channel in the [001]-direction, free diameter 2.6×5.7 Å
crystallographic data	ref. [79]
framework density	1711.06 [kg/m^3]
void fraction	0.254 [-]
accessible pore volume	0.1485 [cm^3/g]
nitrogen surface area	634 [m^2/g], 1084 [m^2/cm^3]

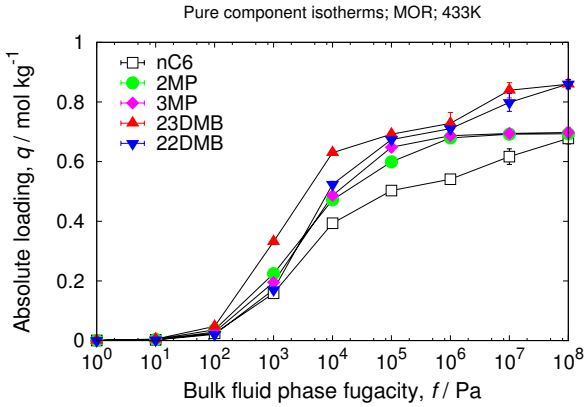

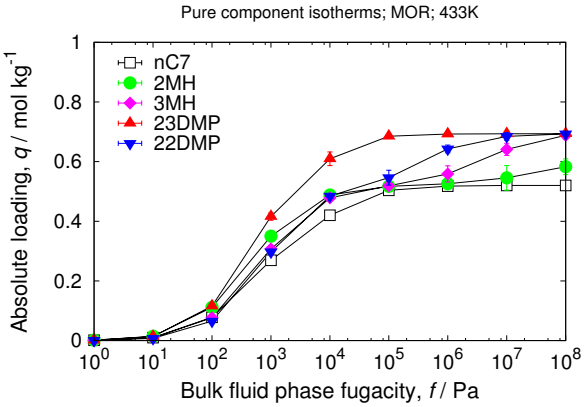

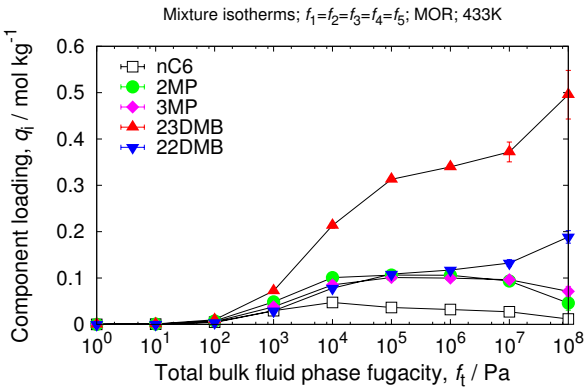

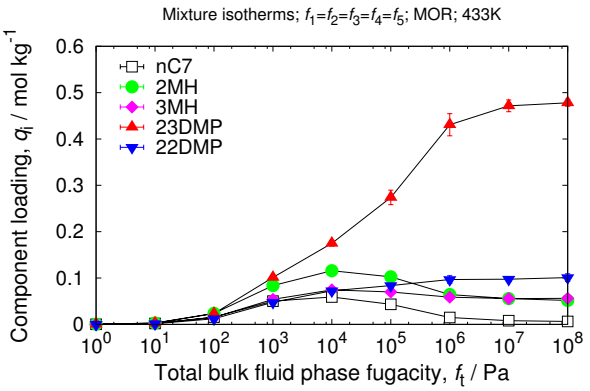

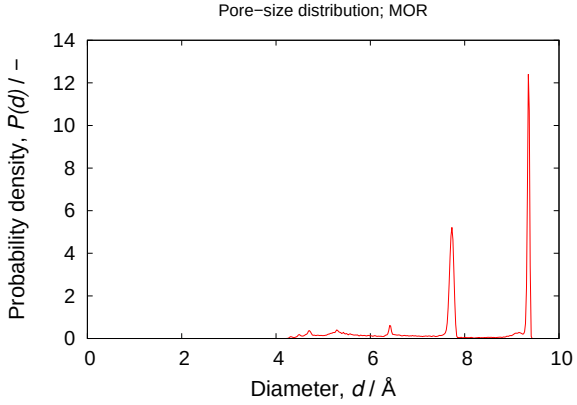

3.23 MTW

unit cell size	$a = 24.8633$ [Å], $b = 5.01238$ [Å], $c = 24.3275$ [Å]
unit cell angles	$\alpha = 90[^\circ]$, $\beta = 107.722[^\circ]$, $\gamma = 120[^\circ]$
description	12-ring channel in the [010]-direction, free diameter 5.6×6.0 Å
crystallographic data	ref. [80]
framework density	1934.69 [kg/m^3]
void fraction	0.213 [-]
accessible pore volume	0.1101 [cm^3/g]
nitrogen surface area	435 [m^2/g], 842 [m^2/cm^3]

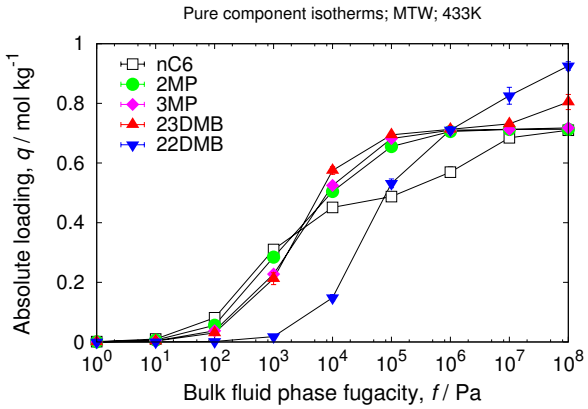

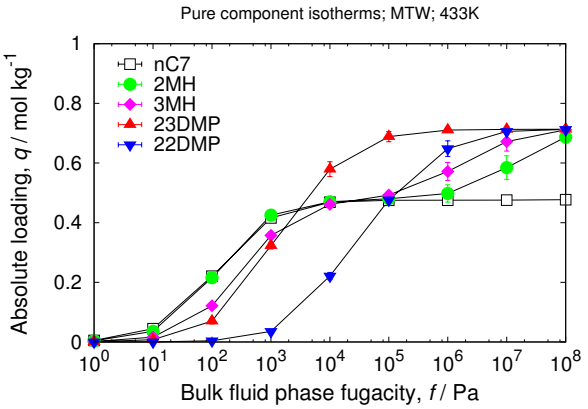

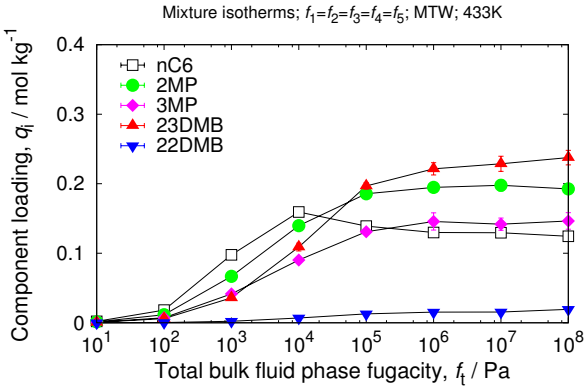

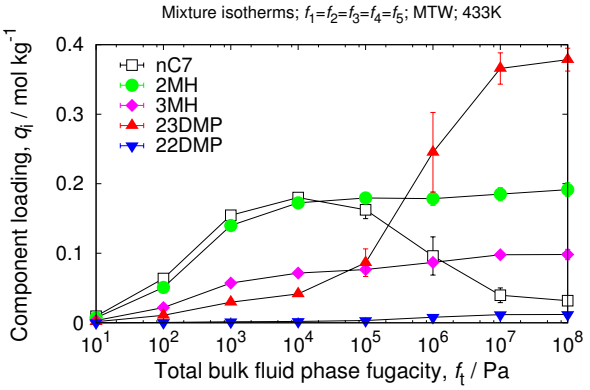

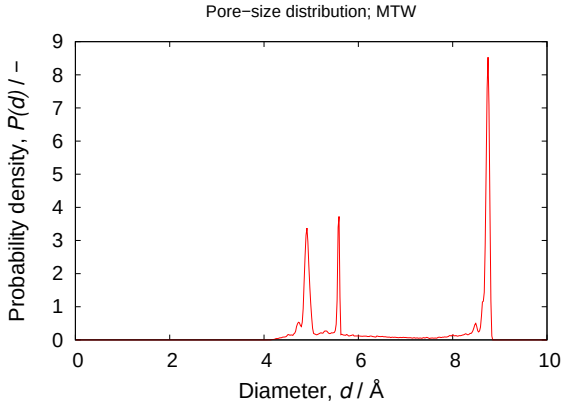

3.24 MWW (also known as ITQ-1 or MCM-22)

unit cell size	$a = 14.2081$ [Å], $b = 14.2081$ [Å], $c = 24.945$ [Å]
unit cell angles	$\alpha = \beta = 90[^\circ]$, $\gamma = 120[^\circ]$
description	MWW structures have two independent 10-ring pore systems, a large cavity (7.1 Å × 18 Å) pore system, and a channel-type (4 Å × 5.5 Å) pore system
crystallographic data	ref. [81]
framework density	1647.24 [kg/m^3]
void fraction	0.357 [-]
accessible pore volume	0.2168 [cm^3/g]
nitrogen surface area	871.8 [m^2/g], 1436.0 [m^2/cm^3]

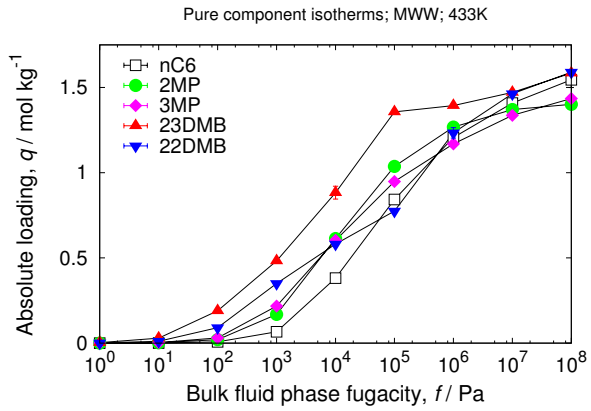

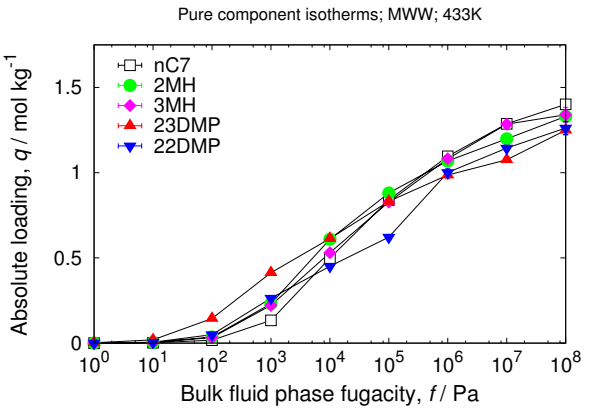

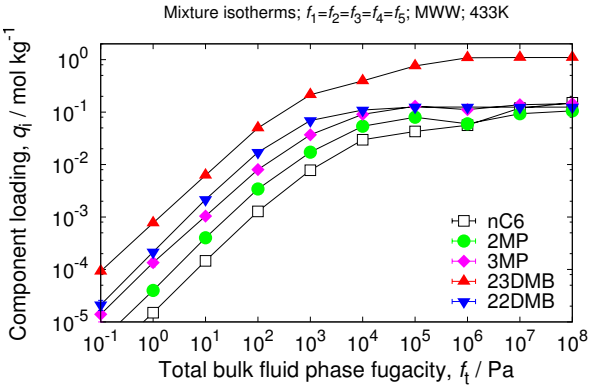

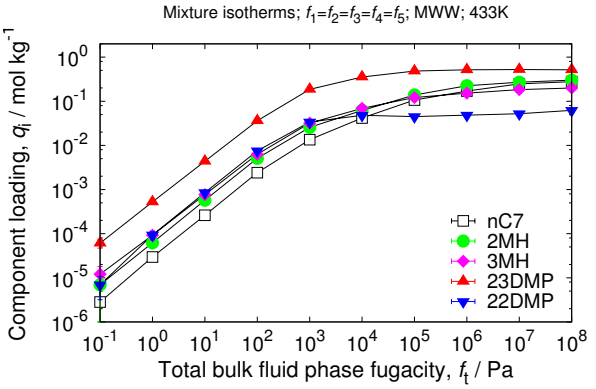

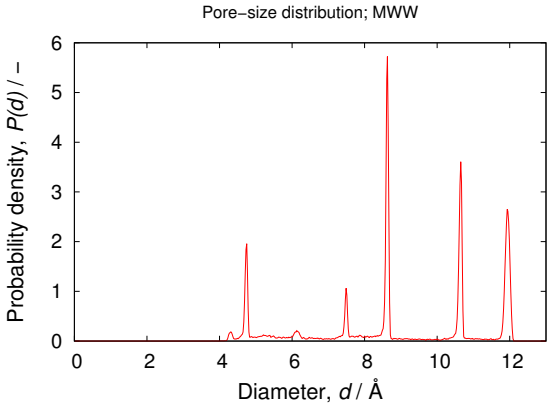

3.25 OFF

unit cell size	$a = 13.331$ [Å], $b = 13.291$ [Å], $c = 7.593$ [Å]
unit cell angles	$\alpha = \beta = 90[^\circ]$, $\gamma = 120[^\circ]$
description	12-ring channel in the [001]-direction, free diameter 6.7×6.8 Å
	8-ring channel in the $\perp$[001]-direction, free diameter 3.6×4.9 Å
crystallographic data	ref. [82]
framework density	1541.41 [kg/m^3]
void fraction	0.332 [-]
accessible pore volume	0.2156 [cm^3/g]
nitrogen surface area	913 [m^2/g], 1407 [m^2/cm^3]

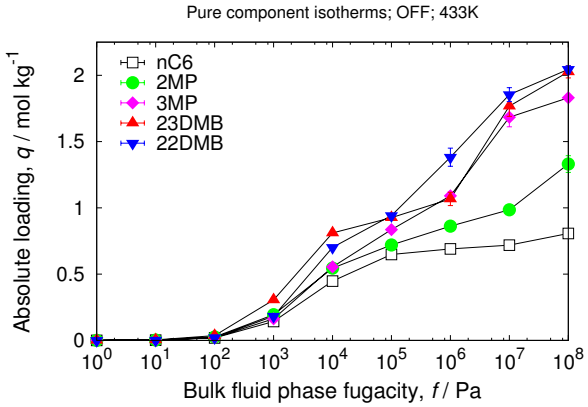

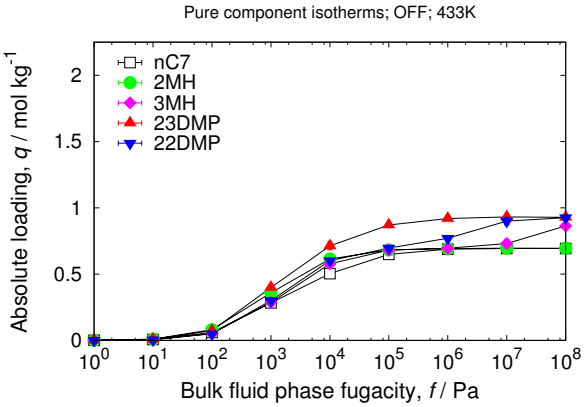

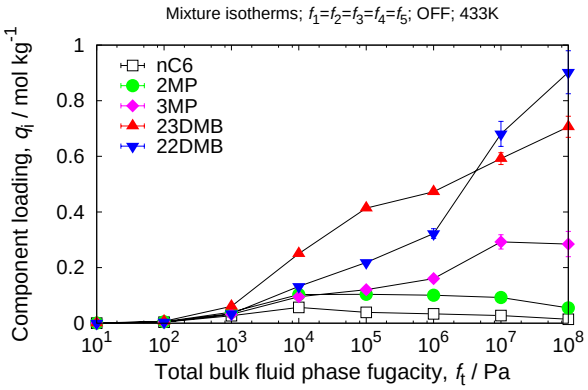

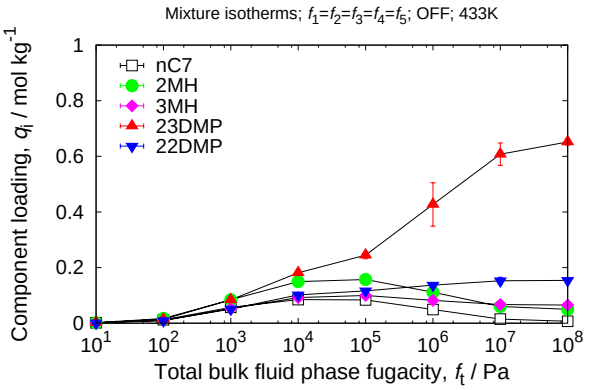

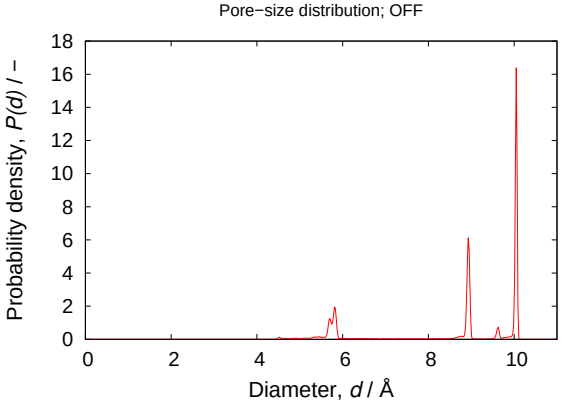

3.26 SFF

unit cell size	$a = 11.4853$ [Å], $b = 21.9458$ [Å], $c = 7.3881$ [Å]
unit cell angles	$\alpha = 90[^\circ]$, $\beta = 94.702[^\circ]$, $\gamma = 90[^\circ]$
description	10-ring channel in the [001]-direction, free diameter 5.4×5.7 Å
crystallographic data	ref. [83]
framework density	1720.27 [kg/m^3]
void fraction	0.348 [-]
accessible pore volume	0.2024 [cm^3/g]
nitrogen surface area	751 [m^2/g], 1292 [m^2/cm^3]

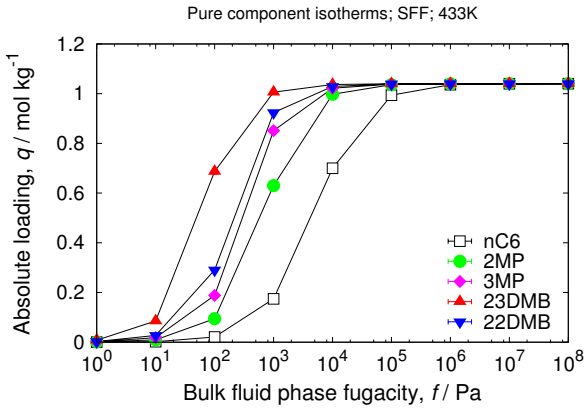

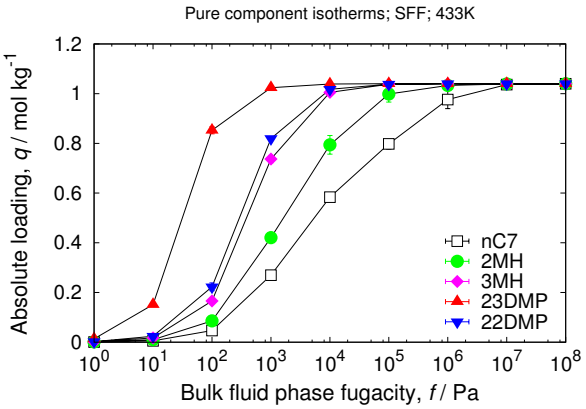

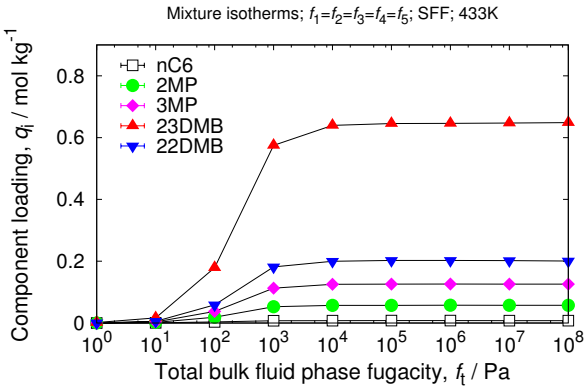

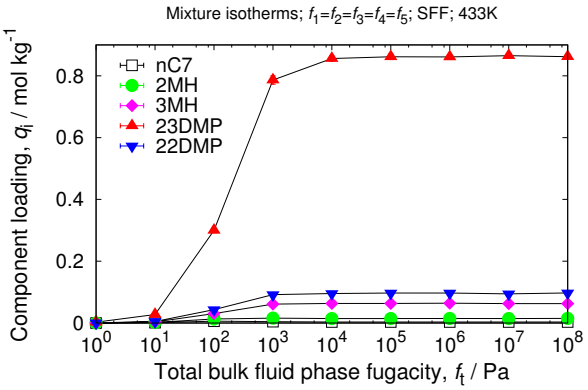

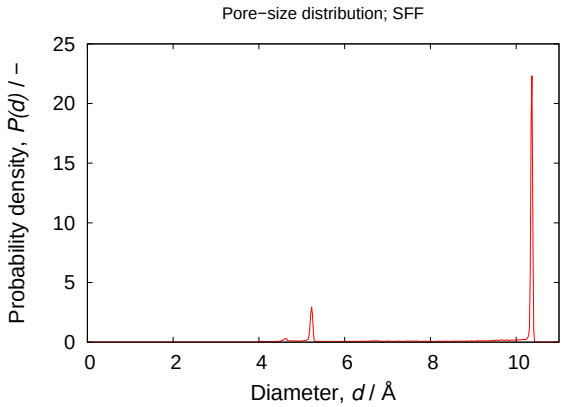

3.27 STF

unit cell size	$a = 11.4114$ [Å], $b = 11.5268$ [Å], $c = 7.377$ [Å]
unit cell angles	$\alpha = 94.661[^\circ]$, $\beta = 96.206[^\circ]$, $\gamma = 104.892[^\circ]$
description	10-ring channel in the [001]-direction, free diameter 5.4×5.7 Å
crystallographic data	ref. [83]
framework density	1723.49 [kg/m^3]
void fraction	0.346 [-]
accessible pore volume	0.2005 [cm^3/g]
nitrogen surface area	740 [m^2/g], 1276 [m^2/cm^3]

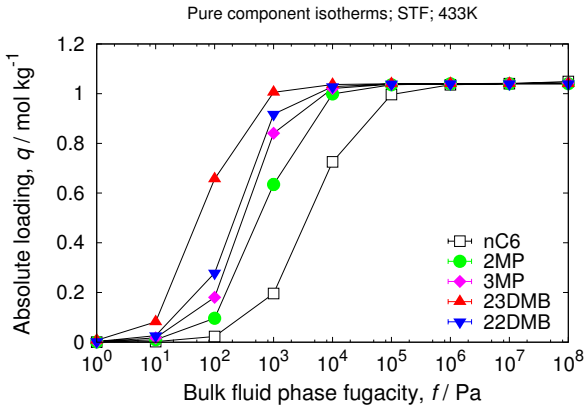

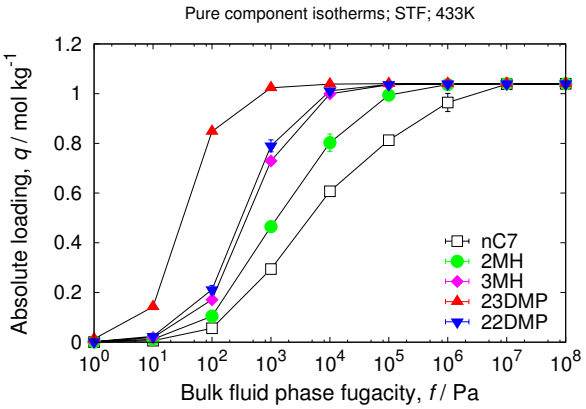

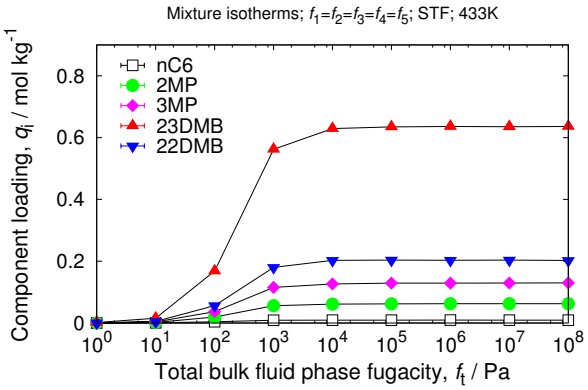

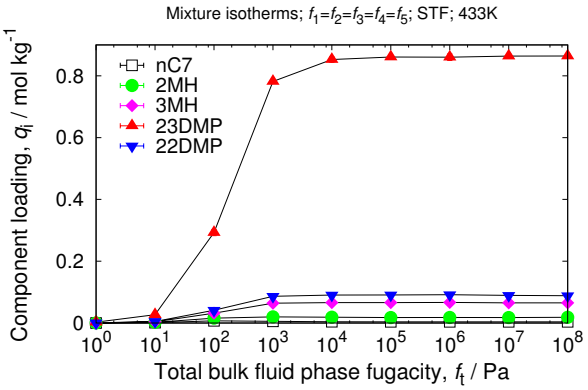

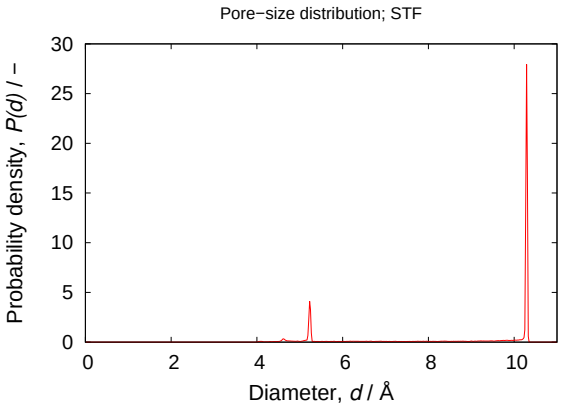

3.28 VFI

unit cell size	$a = 18.9752$ [Å], $b = 18.9752$ [Å], $c = 8.1044$ [Å]
unit cell angles	$\alpha = \beta = 90[^\circ]$, $\gamma = 120[^\circ]$
description	18-ring channel in the [001]-direction, free diameter 12.7×12.7 Å
crystallographic data	ref. [84]
framework density	1442.41 [kg/m^3]
void fraction	0.426 [-]
accessible pore volume	0.2956 [cm^3/g]
nitrogen surface area	810 [m^2/g], 1169 [m^2/cm^3]

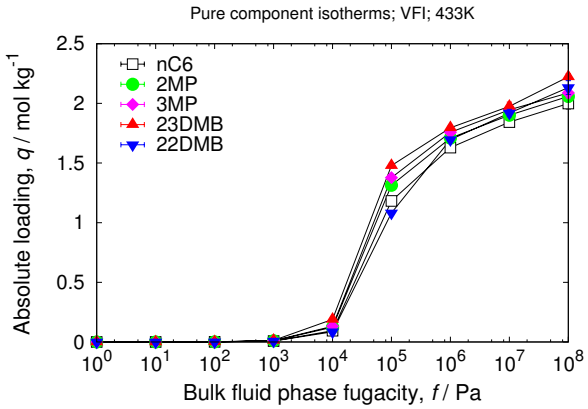

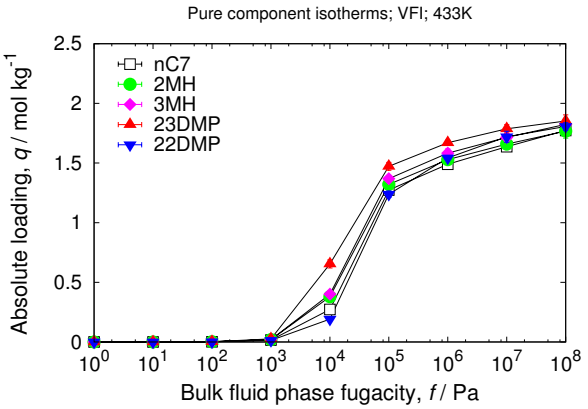

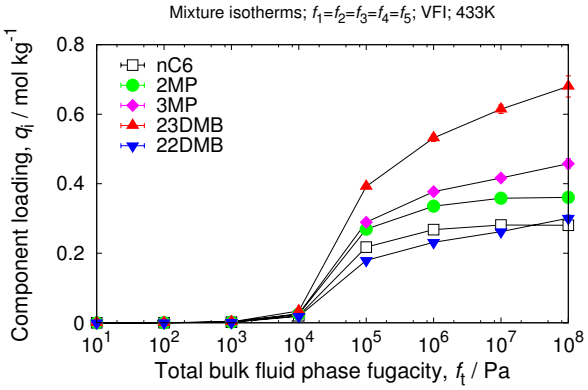

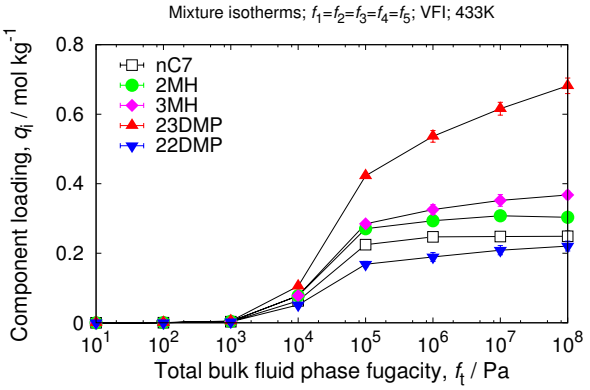

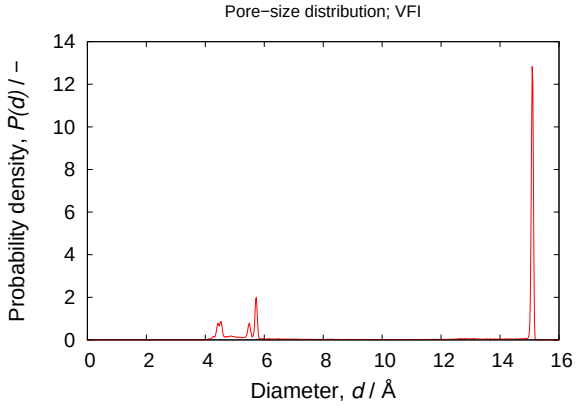

Metal-organic frameworks (MOFs) are a new class of nanoporous materials that have good stability, high void volumes, and well defined tailorable cavities of uniform size. MOFs generally consist of metal or metal oxide vertices interconnected by rigid or semirigid organic molecules. A large variety of MOFs has been produced by various research groups, featuring different linker molecules and chemistries for the bonding of vertices with linkers. The pores of MOFs can be systematically varied by a judicious choice of linker molecules and/or metal-corners. MOFs have much higher void volumes in comparison to for example zeolites. The picture shows the pore landscape of the MIL-101 unit cell (89 Å×89 Å×89 Å), containing 14416 atoms.

4
MOFs

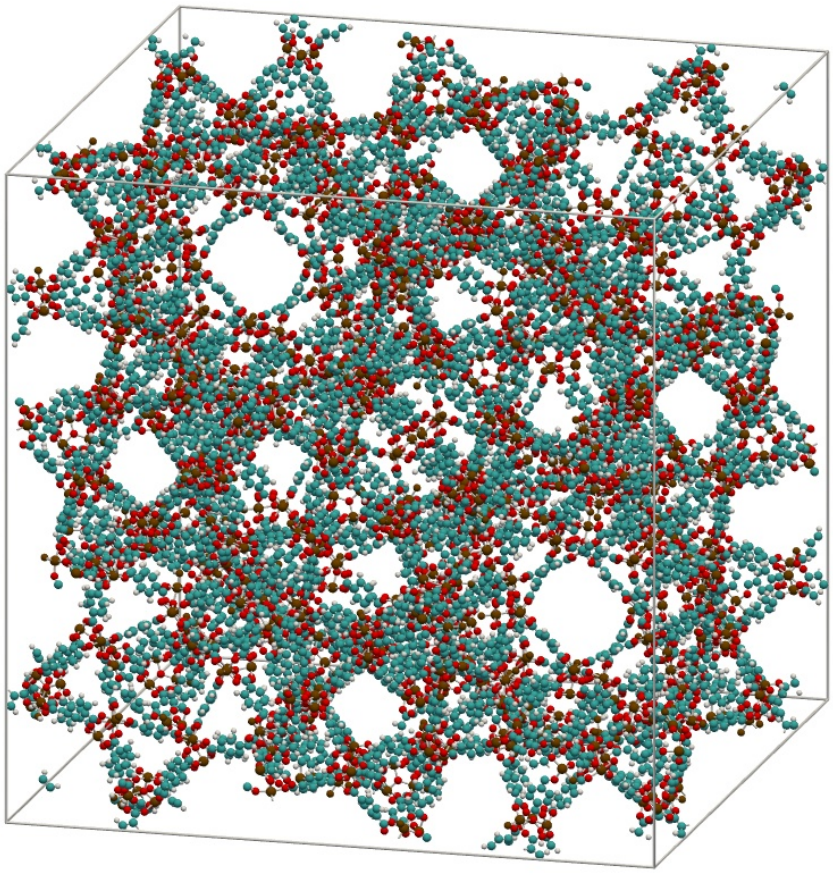

4.1 IRMOF-1

unit cell size	$a = 25.832$ [Å], $b = 25.832$ [Å], $c = 25.832$ [Å]
unit cell angles	$\alpha = \beta = \gamma = 90[^\circ]$
description	$Zn_4O(BDC)_3$
crystallographic data	ref. [85]
framework density	593.40 [kg/m^3]
void fraction	0.802 [-]
accessible pore volume	1.3514 [cm^3/g]
nitrogen surface area	3684 [m^2/g], 2186 [m^2/cm^3]

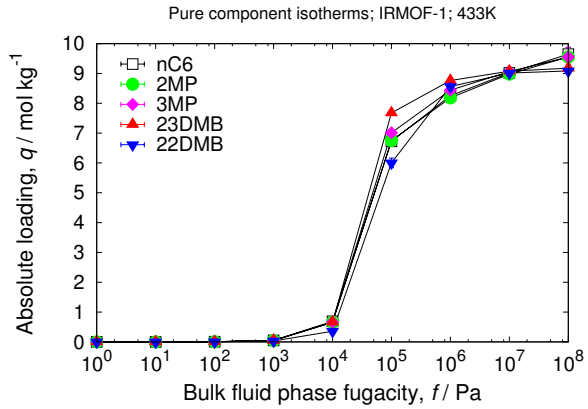

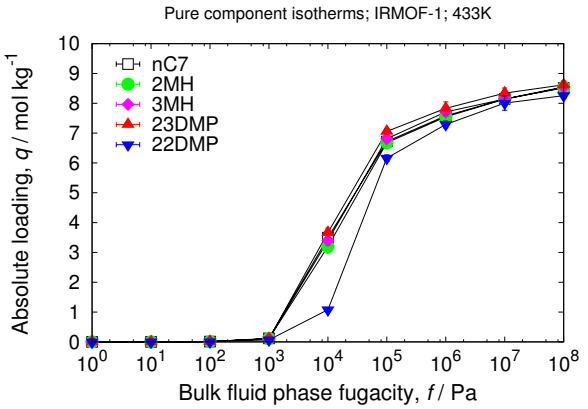

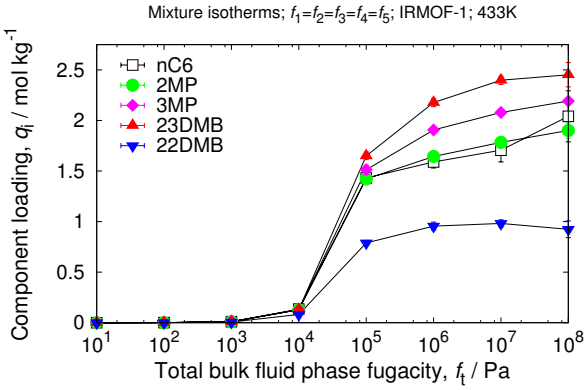

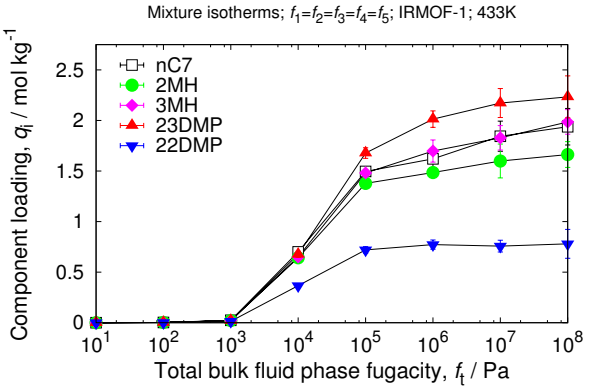

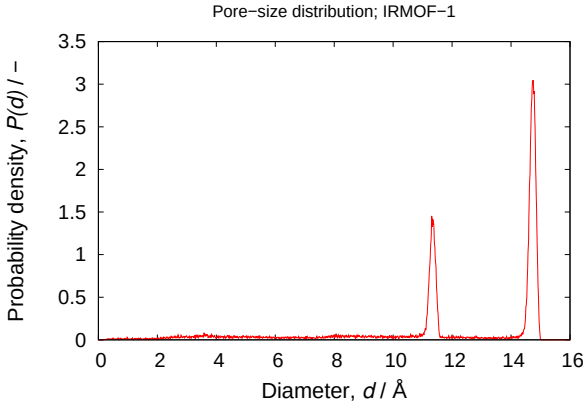

4.2 IRMOF-9

unit cell size	$a = 17.1469$ [Å], $b = 23.3222$ [Å], $c = 25.2552$ [Å]
unit cell angles	$\alpha = \beta = \gamma = 90[^\circ]$
description	interpenetrated $Zn_4O(BPDC)_3$
crystallographic data	ref. [85]
framework density	656.52 [kg/m^3]
void fraction	0.749 [-]
accessible pore volume	1.1403 [cm^3/g]
nitrogen surface area	3592 [m^2/g], 2358 [m^2/cm^3]

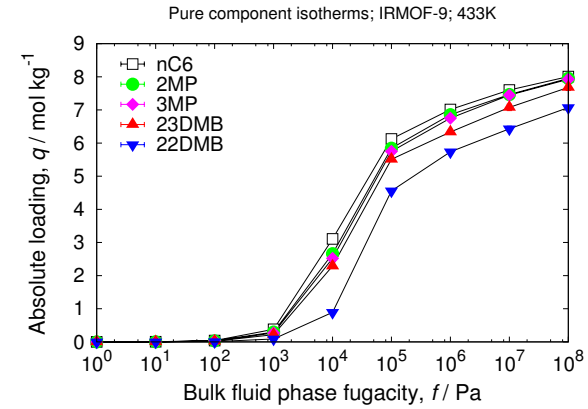

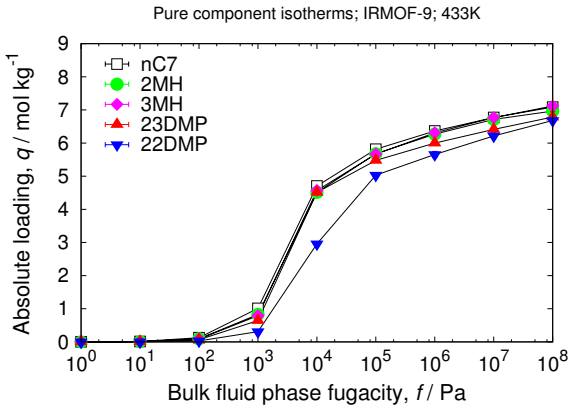

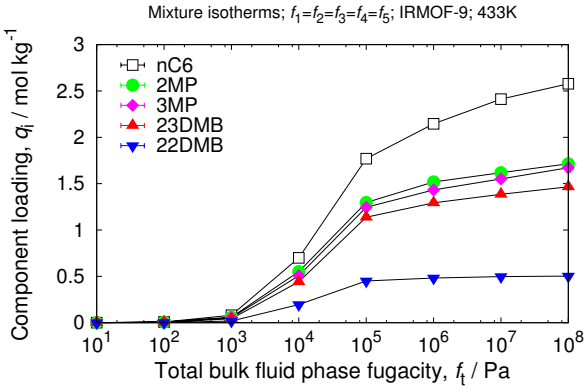

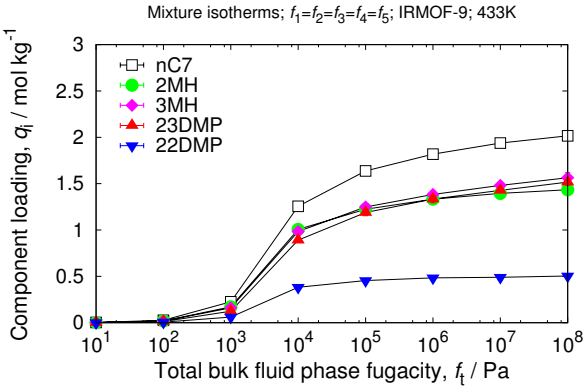

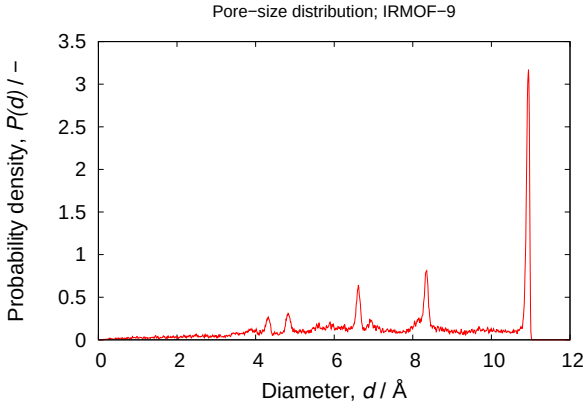

4.3 IRMOF-10

unit cell size	$a = 34.2807$ [Å], $b = 34.2807$ [Å], $c = 34.2807$ [Å]
unit cell angles	$\alpha = \beta = \gamma = 90[^\circ]$
description	$Zn_4O(BPDC)_3$
crystallographic data	ref. [85]
framework density	329.18 [kg/m^3]
void fraction	0.883 [-]
accessible pore volume	2.6834 [cm^3/g]
nitrogen surface area	4963 [m^2/g], 1634 [m^2/cm^3]

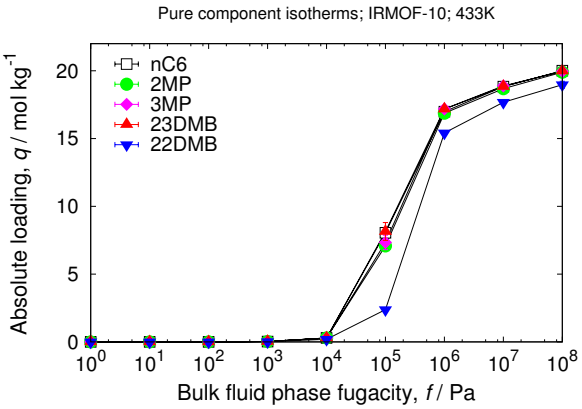

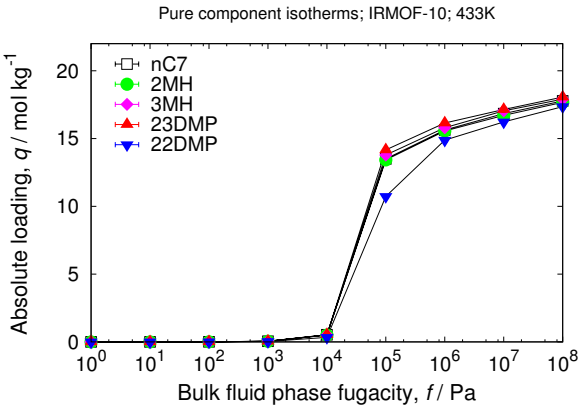

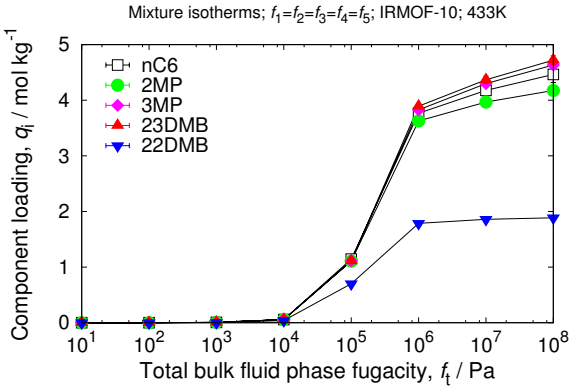

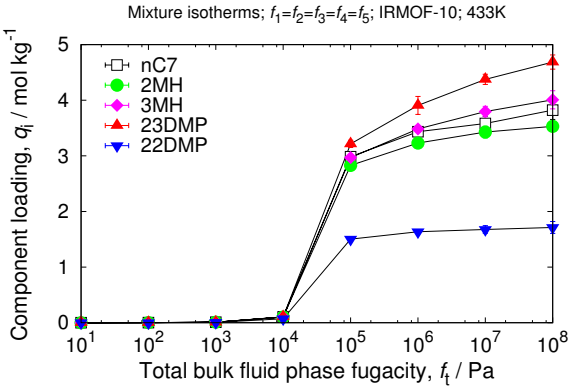

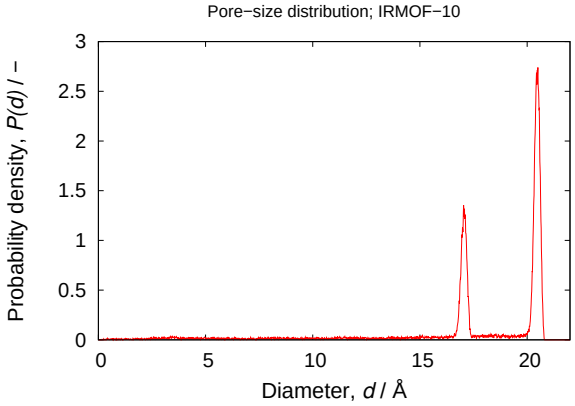

4.4 IRMOF-15

unit cell size	$a = 21.4594$ [Å], $b = 21.4594$ [Å], $c = 21.4594$ [Å]
unit cell angles	$\alpha = \beta = \gamma = 90[^\circ]$
description	interpenetrated $Zn_4O(TPDC)_3$
crystallographic data	ref. [85]
framework density	412.21 [kg/m^3]
void fraction	0.837 [-]
accessible pore volume	2.0305 [cm^3/g]
nitrogen surface area	6060 [m^2/g], 2498 [m^2/cm^3]

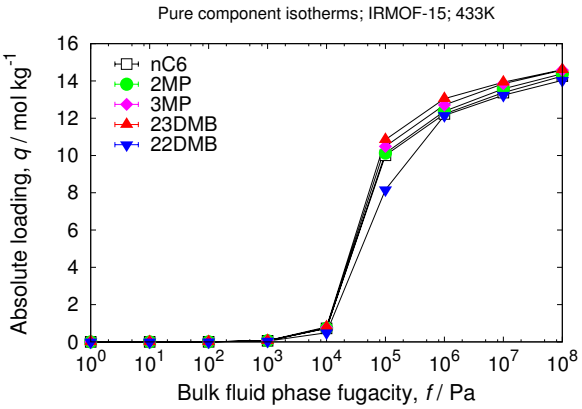

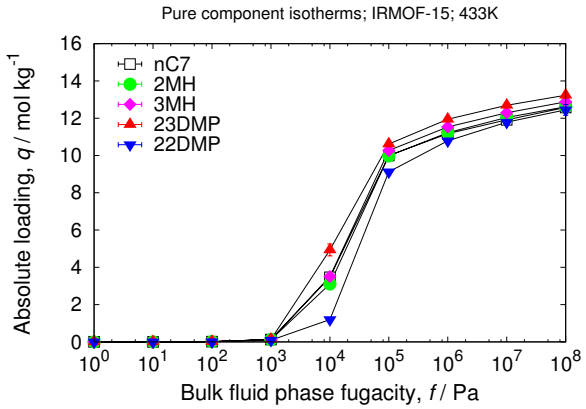

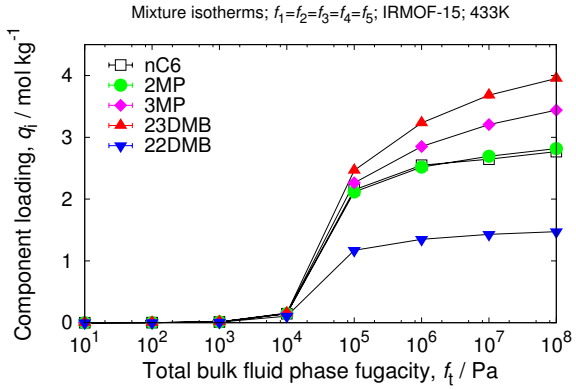

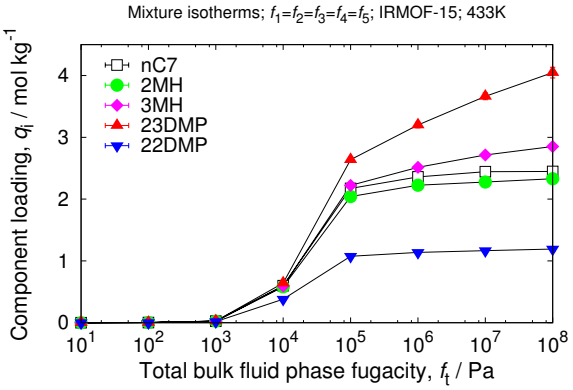

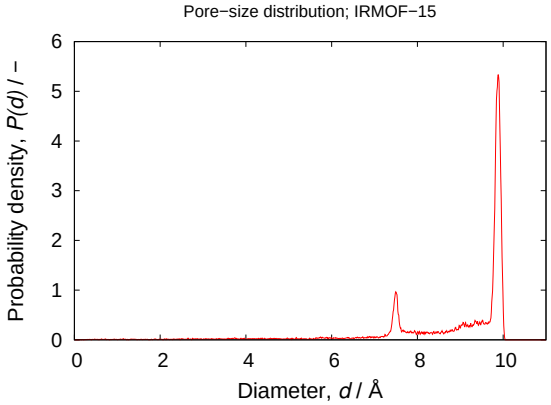

4.5 IRMOF-16

unit cell size	$a = 42.9806$ [Å], $b = 42.9806$ [Å], $c = 42.9806$ [Å]
unit cell angles	$\alpha = \beta = \gamma = 90[^\circ]$
description	$Zn_4O(TPDC)_3$
crystallographic data	ref. [85]
framework density	205.22 [kg/m^3]
void fraction	0.919 [-]
accessible pore volume	4.4762 [cm^3/g]
nitrogen surface area	6045 [m^2/g], 1241 [m^2/cm^3]

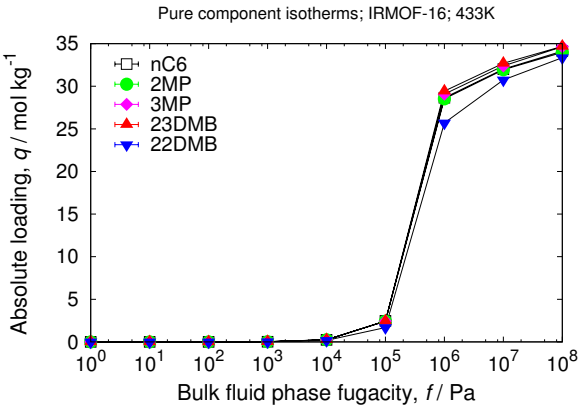

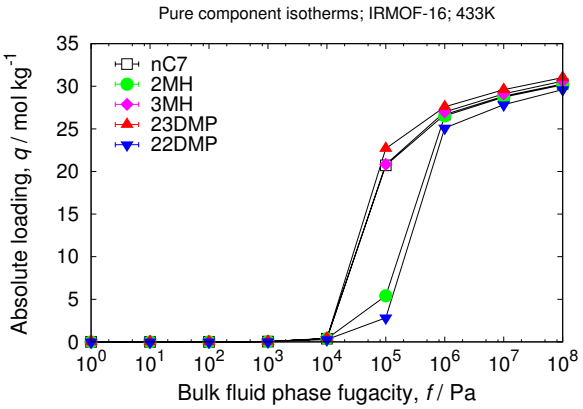

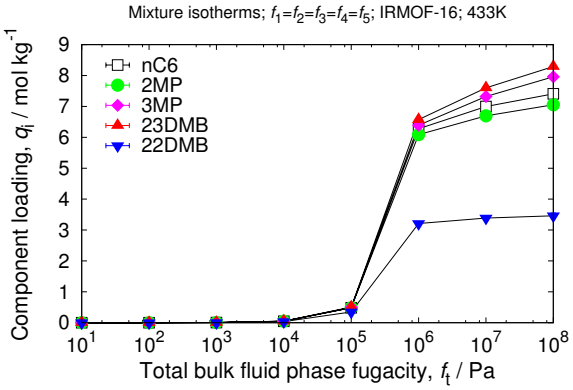

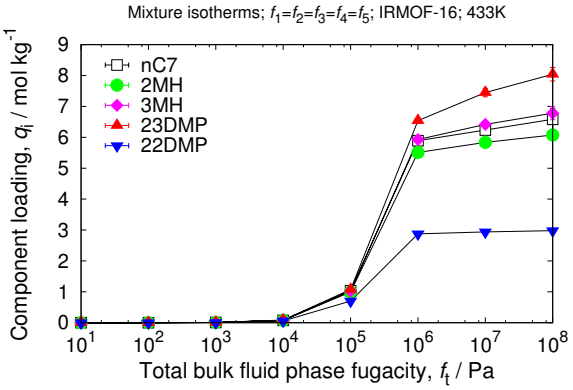

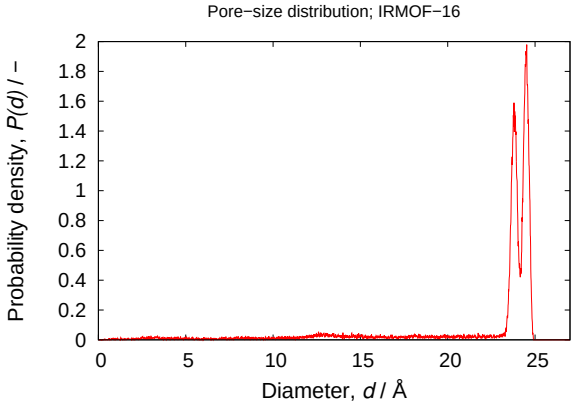

4.6 MOF-69c

unit cell size	$a = 17.664$ [Å], $b = 14.848$ [Å], $c = 18.129$ [Å]
unit cell angles	$\alpha = 90[^\circ]$, $\beta = 112.14[^\circ]$, $\gamma = 90[^\circ]$
framework density	1263.38 [kg/m^3]
description	$Zn_3(OH)_2(BDC)_2$
crystallographic data	ref. [86]
void fraction	0.513 [-]
accessible pore volume	0.4064 [cm^3/g]
nitrogen surface area	1178 [m^2/g], 1488 [m^2/cm^3]

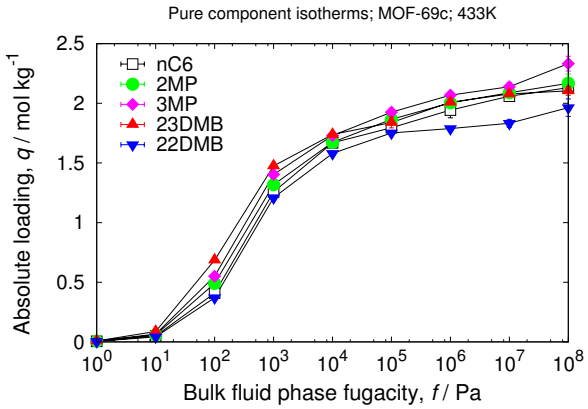

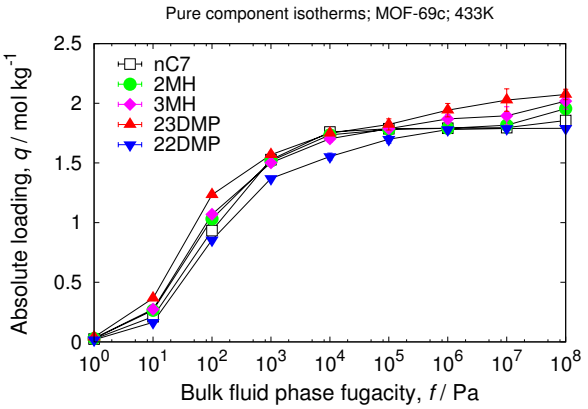

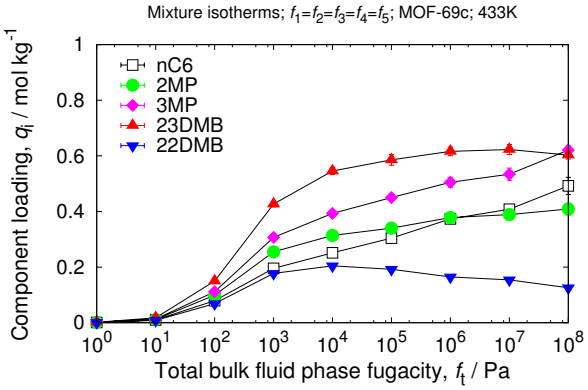

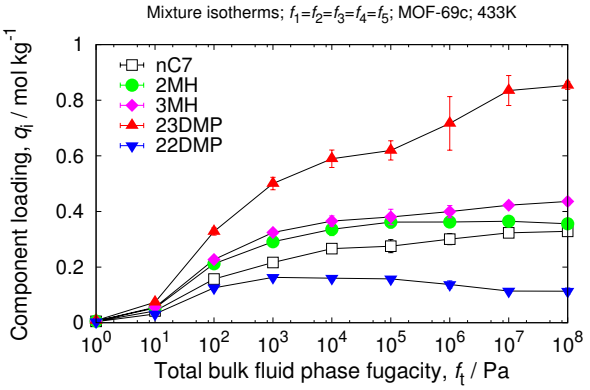

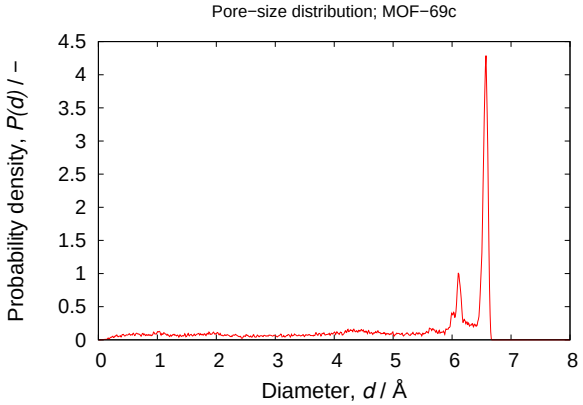

4.7 MOF-70

unit cell size	$a = 8.3639$ [Å], $b = 17.9914$ [Å], $c = 9.9617$ [Å]
unit cell angles	$\alpha = 90[^\circ]$, $\beta = 102.687[^\circ]$, $\gamma = 90[^\circ]$
framework density	1686.55 [kg/m^3]
description	Pb(BDC)
crystallographic data	ref. [86]
void fraction	0.506 [-]
accessible pore volume	0.3002 [cm^3/g]
nitrogen surface area	817 [m^2/g], 1378 [m^2/cm^3]

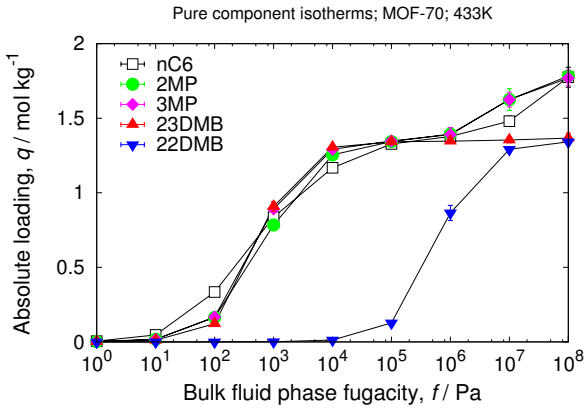

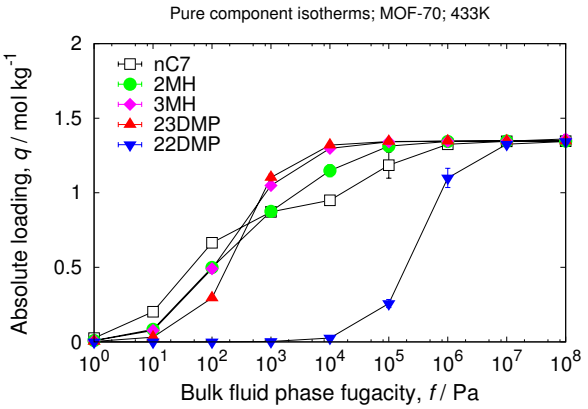

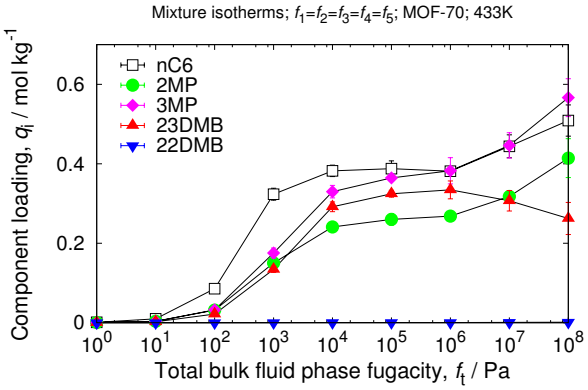

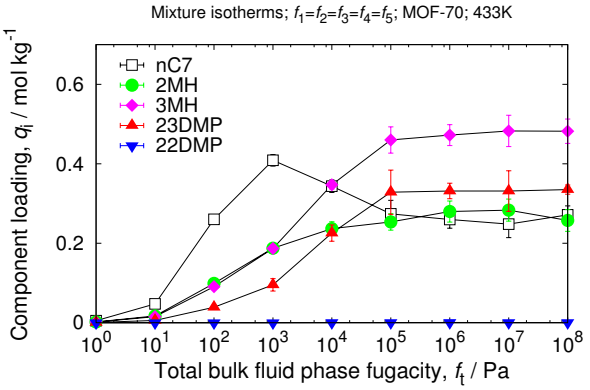

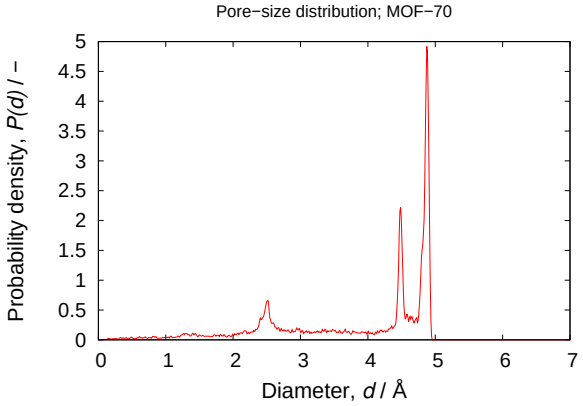

4.8 MOF-177

unit cell size	$a = 37.072$ [Å], $b = 37.072$ [Å], $c = 30.0333$ [Å]
unit cell angles	$\alpha = \beta = 90[^\circ]$, $\gamma = 120[^\circ]$
framework density	426.80 [kg/m^3]
description	$Zn_4O(BTB)_2$
crystallographic data	ref. [87]
void fraction	0.833 [-]
accessible pore volume	1.9526 [cm^3/g]
nitrogen surface area	4850 [m^2/g], 2070 [m^2/cm^3]

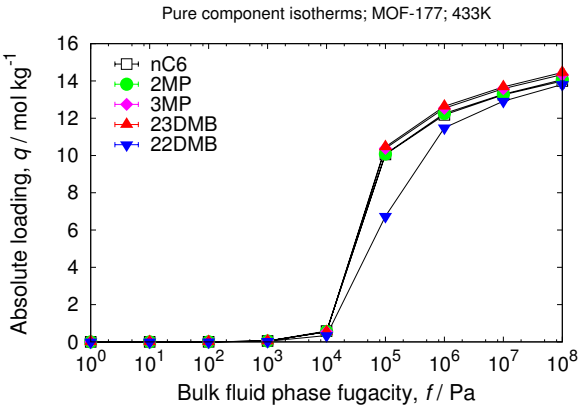

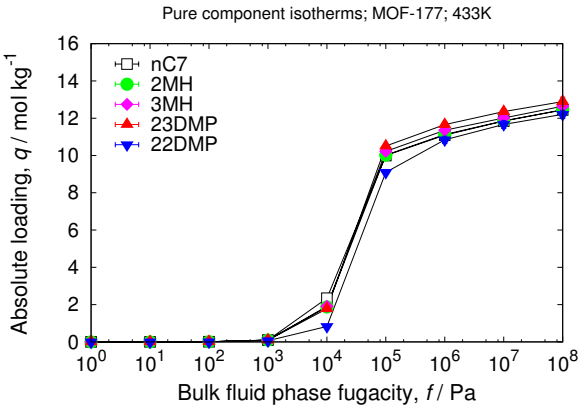

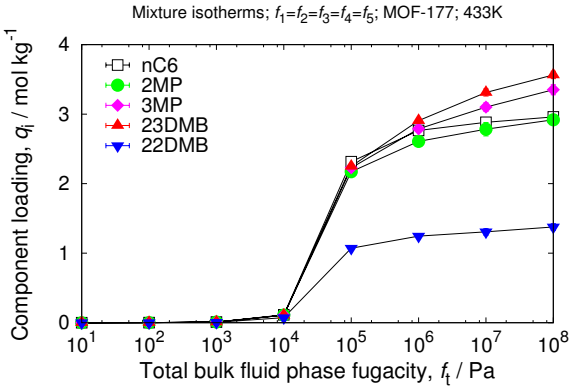

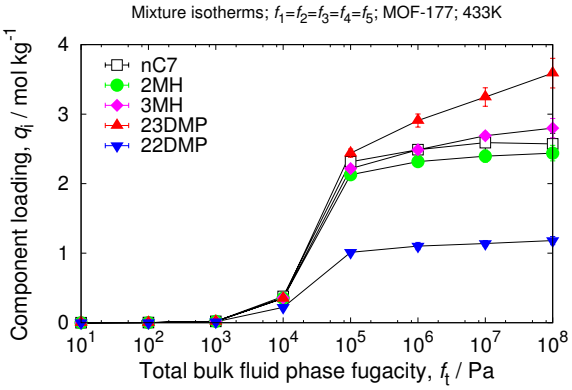

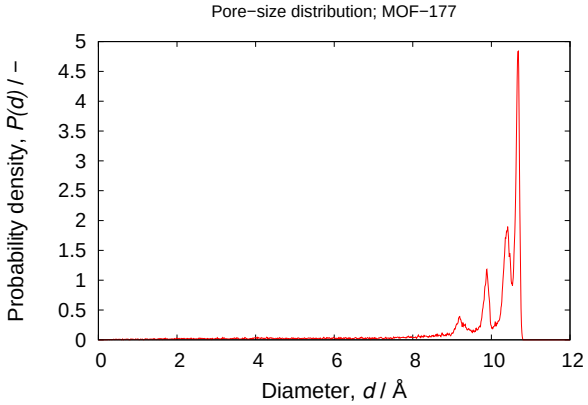

4.9 MOF-200

unit cell size	$a = 52.022$ [Å], $b = 52.022$ [Å], $c = 42.316$ [Å]
unit cell angles	$\alpha = \beta = 90[^\circ]$, $\gamma = 120[^\circ]$
framework density	214.97 [kg/m^3]
description	$Zn_4O(BBC)_2$
crystallographic data	ref. [88]
void fraction	0.904 [-]
accessible pore volume	4.2048 [cm^3/g]
nitrogen surface area	6195 [m^2/g], 1332 [m^2/cm^3]

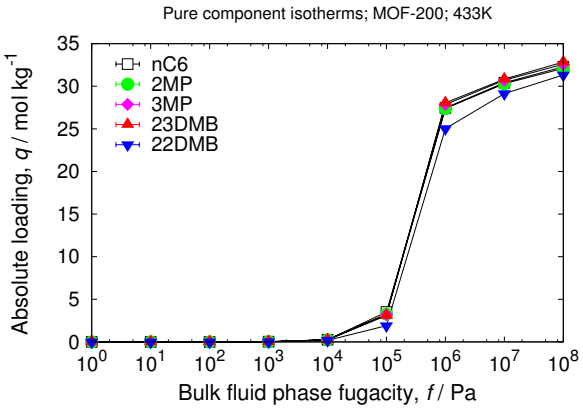

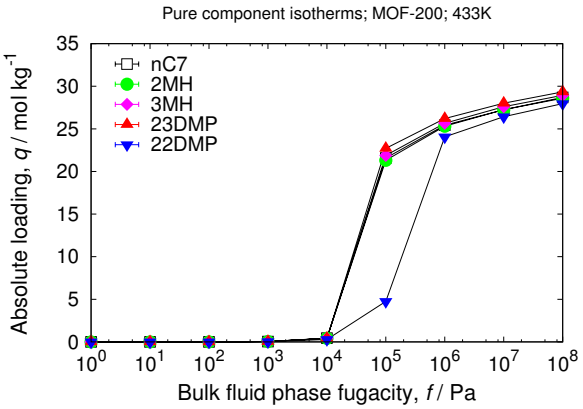

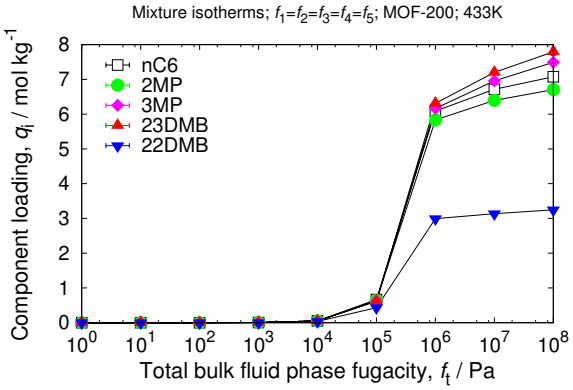

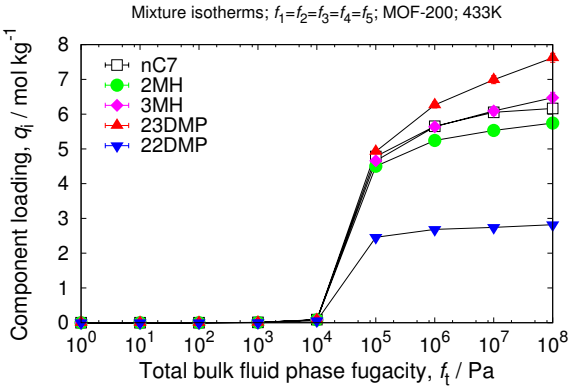

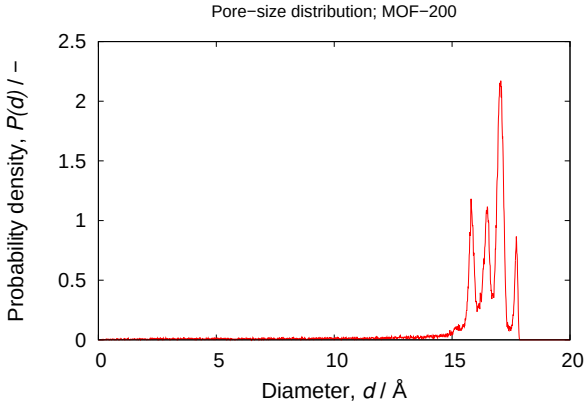

4.10 MOF-205

unit cell size	$a = 30.353$ [Å], $b = 30.353$ [Å], $c = 30.353$ [Å]
unit cell angles	$\alpha = \beta = \gamma = 90[^\circ]$
framework density	382.06 [kg/m^3]
description	$Zn_4O(BTB)_{4/3}(NDC)$
crystallographic data	ref. [88]
void fraction	0.869 [-]
accessible pore volume	2.2750 [cm^3/g]
nitrogen surface area	4726 [m^2/g], 1806 [m^2/cm^3]

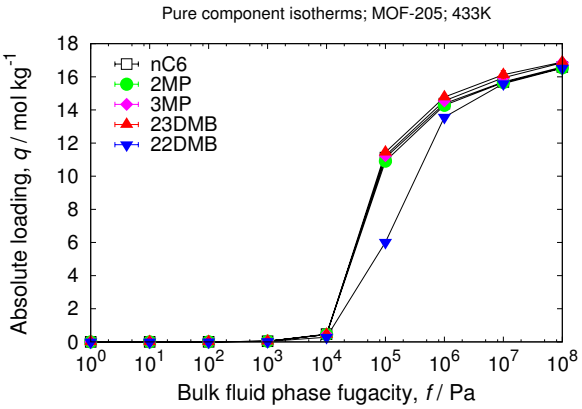

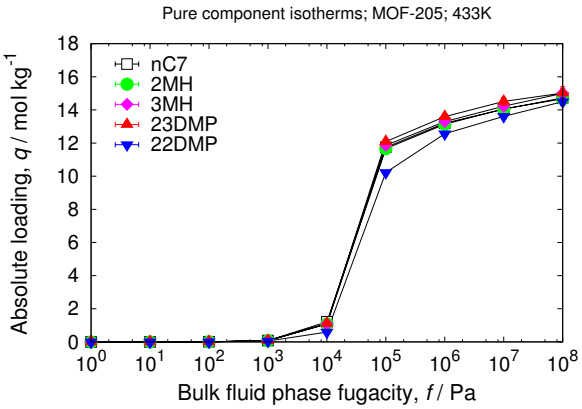

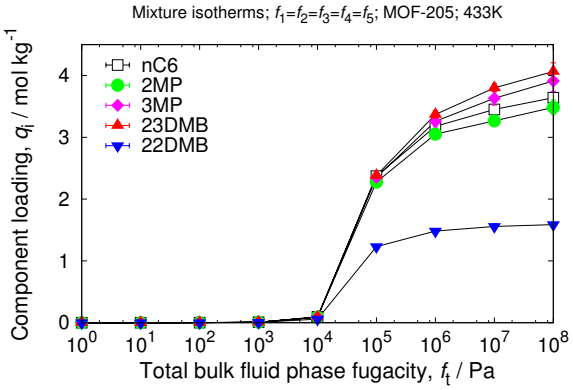

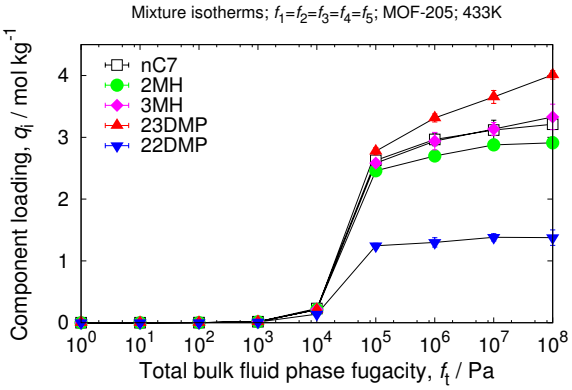

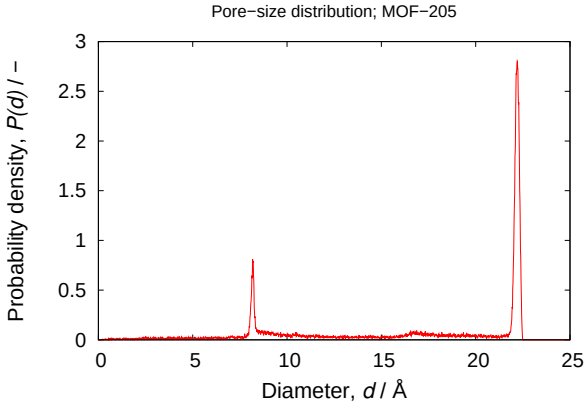

4.11 MOF-210

unit cell size	$a = 50.745$ [Å], $b = 50.745$ [Å], $c = 194.256$ [Å]
unit cell angles	$\alpha = \beta = 90[^\circ]$, $\gamma = 120[^\circ]$
framework density	246.83 [kg/m^3]
description	$Zn_4O(BTE)_{4/3}(BPDC)$
crystallographic data	ref. [88]
void fraction	0.905 [-]
accessible pore volume	3.6662 [cm^3/g]
nitrogen surface area	5790 [m^2/g], 1429 [m^2/cm^3]

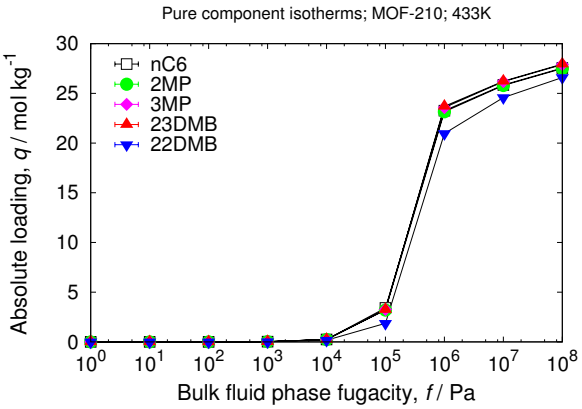

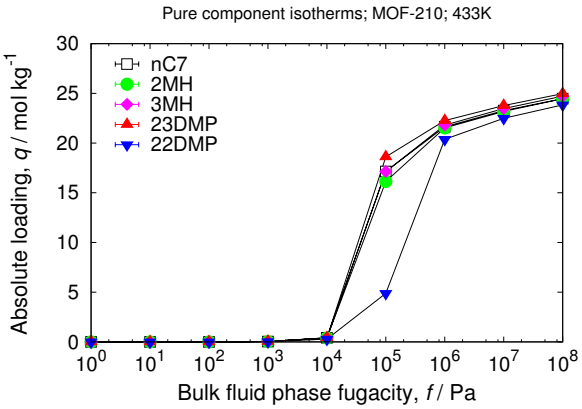

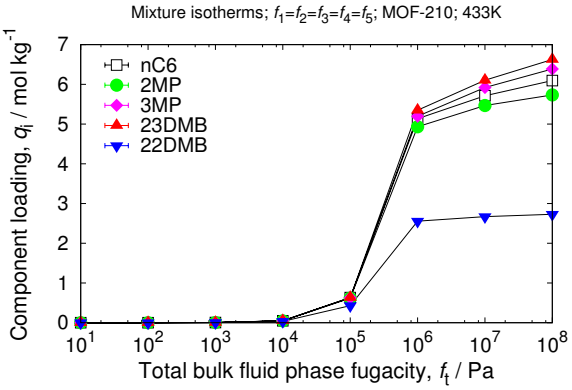

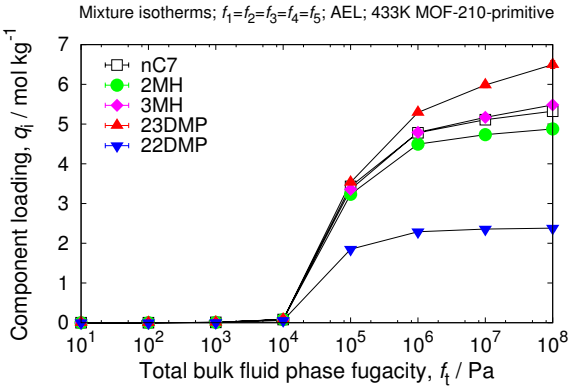

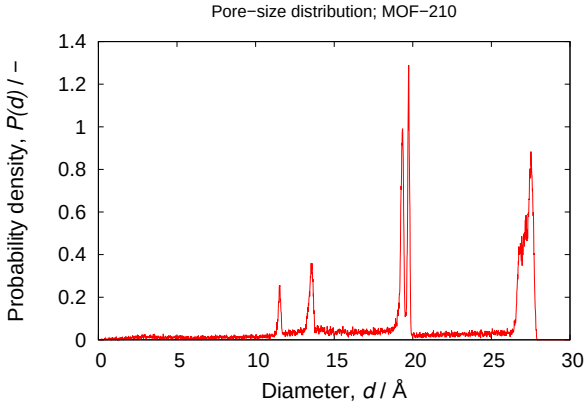

4.12 NU-108(Cu)

unit cell size	$a = 63.515$ [Å], $b = 63.515$ [Å], $c = 63.515$ [Å]
unit cell angles	$\alpha = \beta = \gamma = 90[^\circ]$
crystallographic data	ref. [89]
framework density	266.21 [kg/m^3]
void fraction	0.904 [-]
accessible pore volume	3.3944 [cm^3/g]
nitrogen surface area	5842 [m^2/g], 1555 [m^2/cm^3]

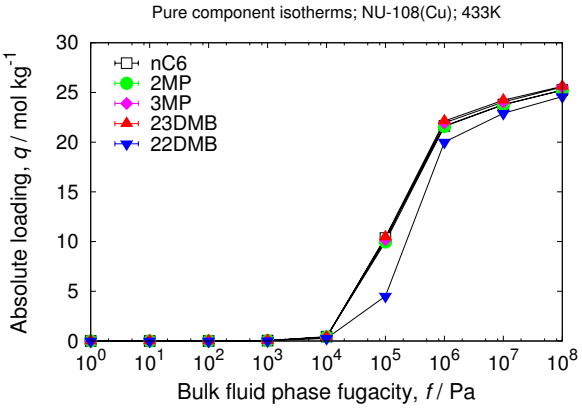

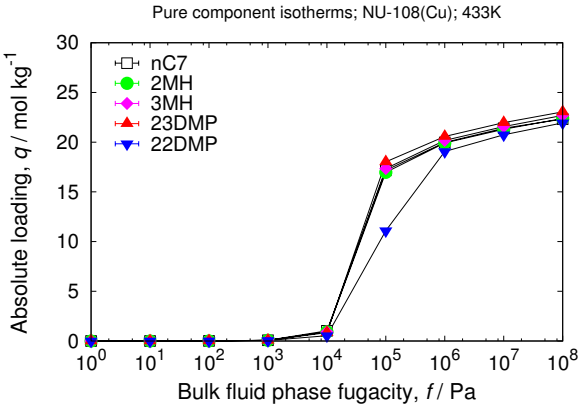

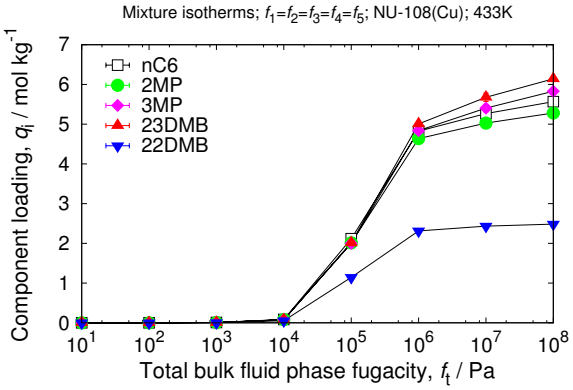

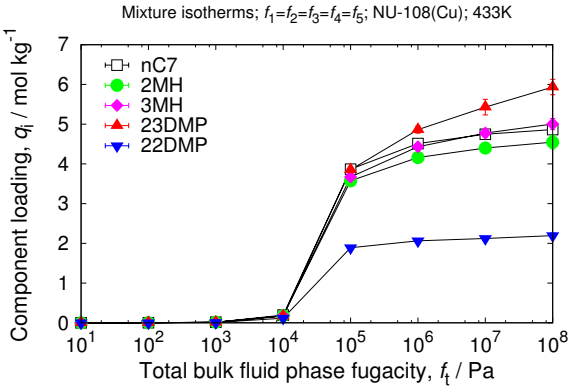

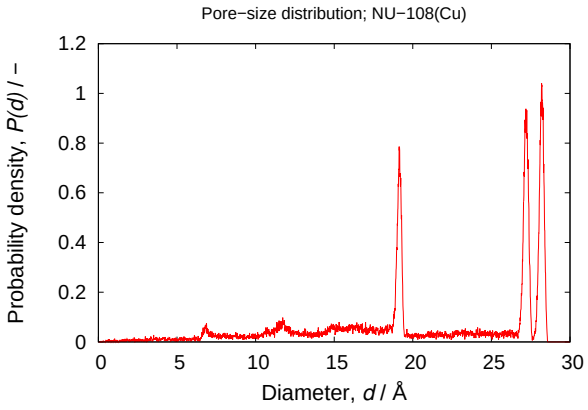

4.13 NU-108(Zn)

unit cell size	$a = 24.527$ [Å], $b = 24.527$ [Å], $c = 71.355$ [Å]
unit cell angles	$\alpha = \beta = 90[^\circ]$, $\gamma = 120[^\circ]$
crystallographic data	ref. [89]
framework density	367.36 [kg/m^3]
void fraction	0.863 [-]
accessible pore volume	2.3494 [cm^3/g]
nitrogen surface area	5439 [m^2/g], 1998 [m^2/cm^3]

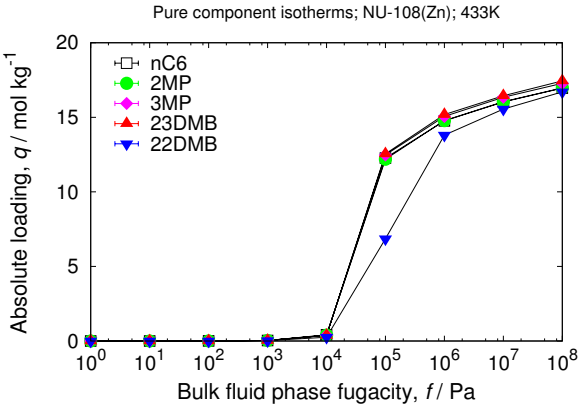

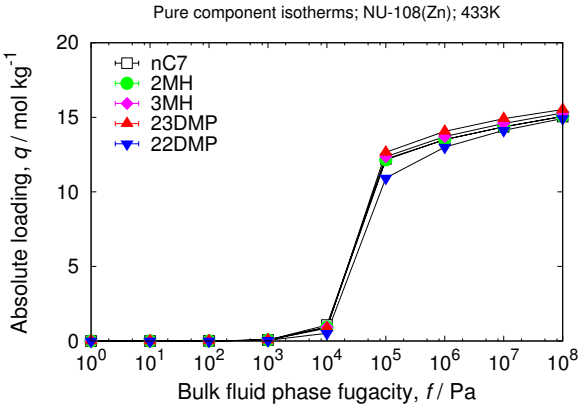

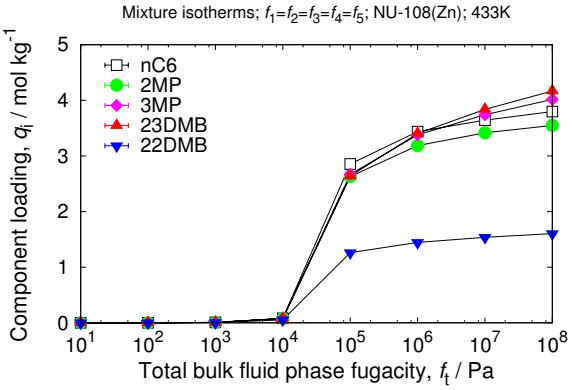

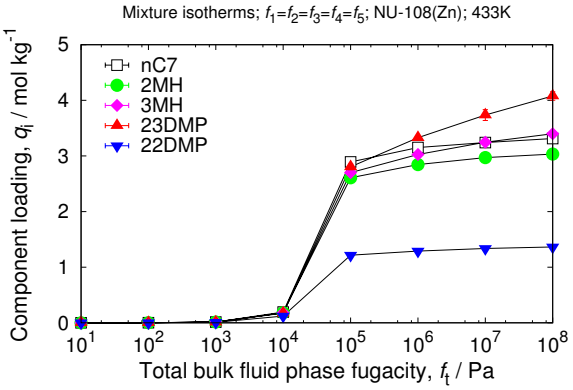

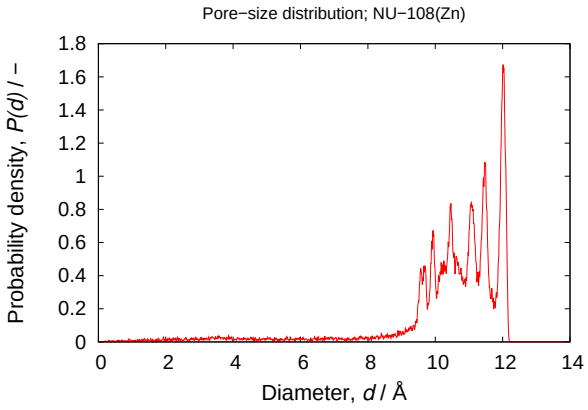

4.14 NU-100

unit cell size	$a = 59.872$ [Å], $b = 59.872$ [Å], $c = 59.872$ [Å]
unit cell angles	$\alpha = \beta = \gamma = 90[^\circ]$
framework density	279.15 [kg/m^3]
description	Cu_3(TTEI)
crystallographic data	ref. [90]
void fraction	0.895 [-]
accessible pore volume	3.2072 [cm^3/g]
nitrogen surface area	5850 [m^2/g], 1633 [m^2/cm^3]

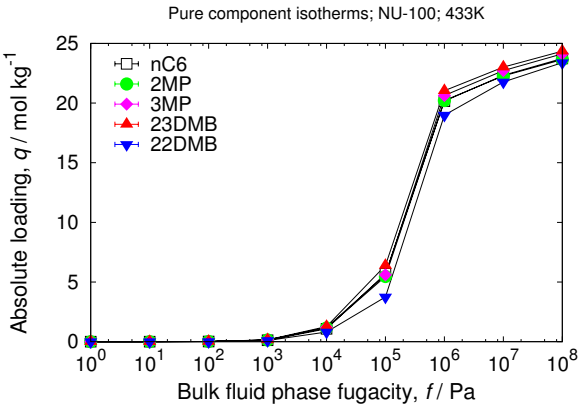

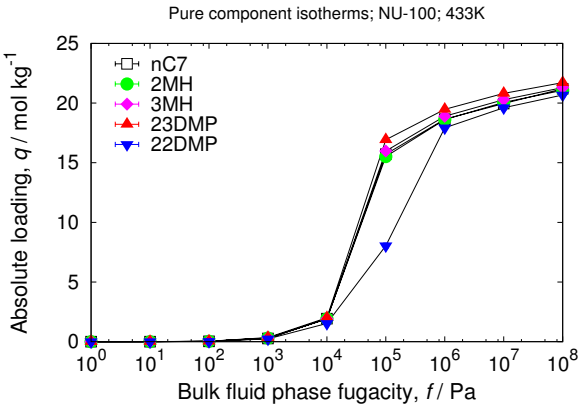

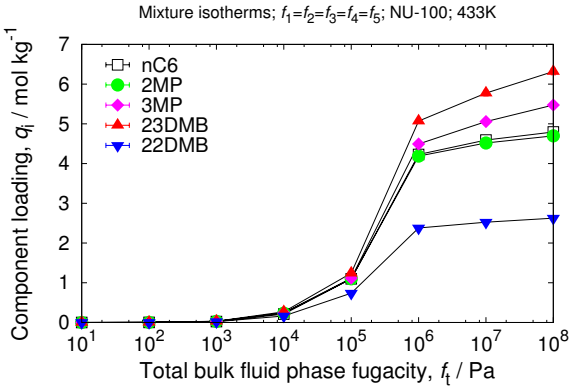

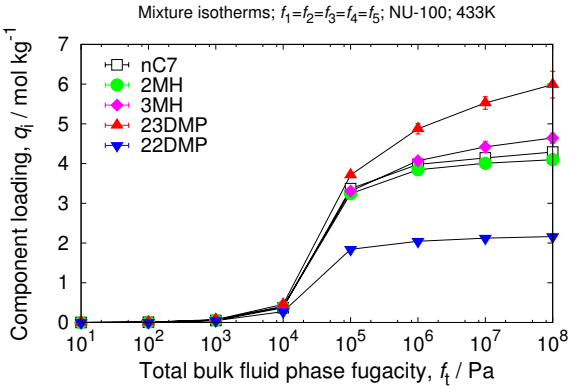

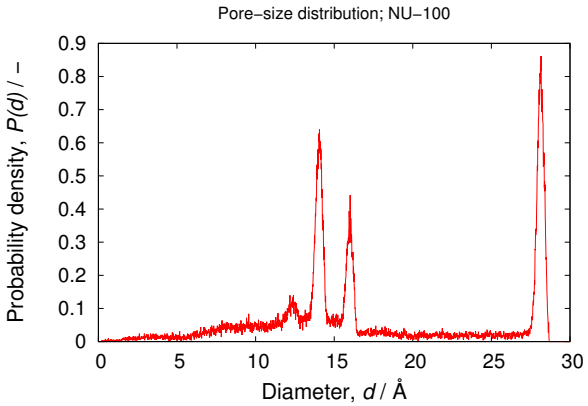

4.15 MIL-47

unit cell size	$a = 6.8179$ [Å], $b = 16.143$ [Å], $c = 13.939$ [Å]
unit cell angles	$\alpha = \beta = \gamma = 90[^\circ]$
framework density	1000.37 [kg/m^3]
description	V(O)(BDC)
crystallographic data	ref. [91]
void fraction	0.606 [-]
accessible pore volume	0.6057 [cm^3/g]
nitrogen surface area	1655 [m^2/g], 1655 [m^2/cm^3]

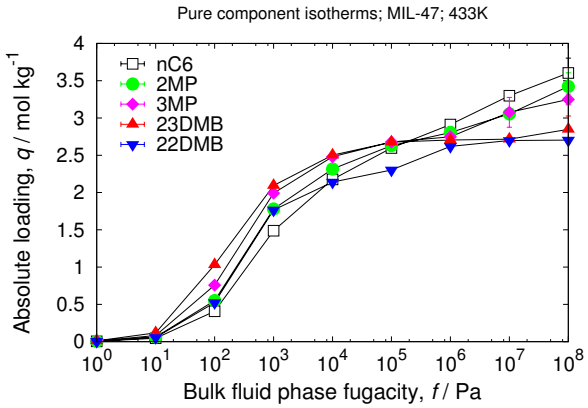

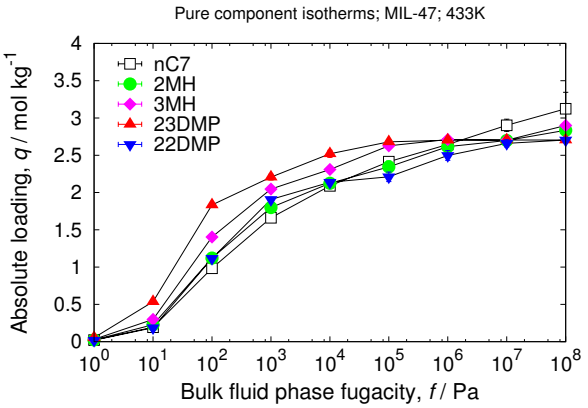

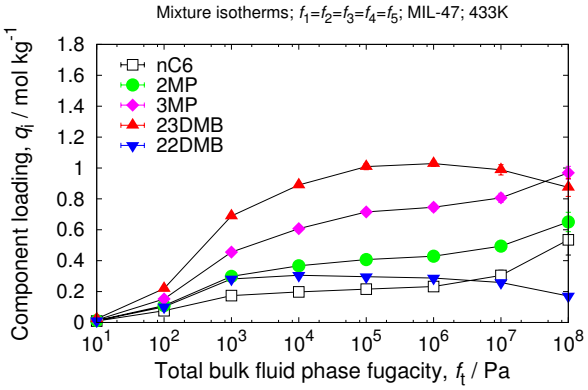

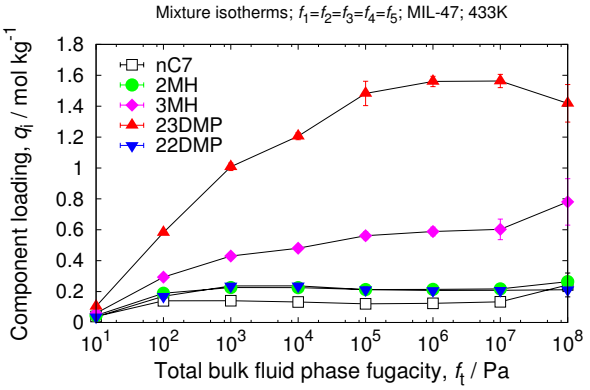

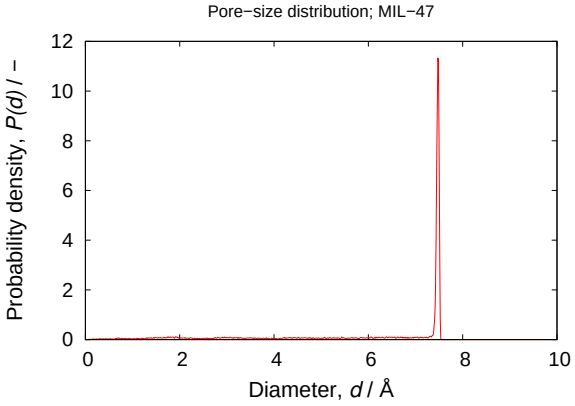

4.16 MIL-53(Cr)

unit cell size	$a = 16.733$ [Å], $b = 13.038$ [Å], $c = 6.812$ [Å]
unit cell angles	$\alpha = \beta = \gamma = 90[^\circ]$
framework density	1041.90 [kg/m^3]
description	Cr(OH)(BDC)
crystallographic data	ref. [92]
void fraction	0.548 [-]
accessible pore volume	0.5259 [cm^3/g]
nitrogen surface area	1438 [m^2/g], 1498 [m^2/cm^3]

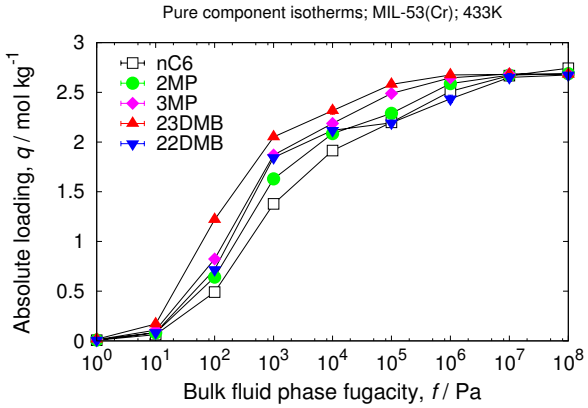

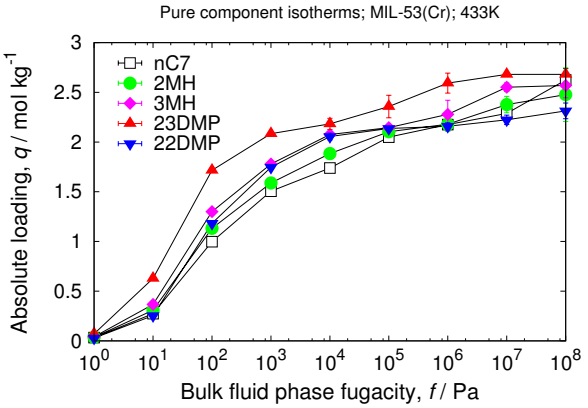

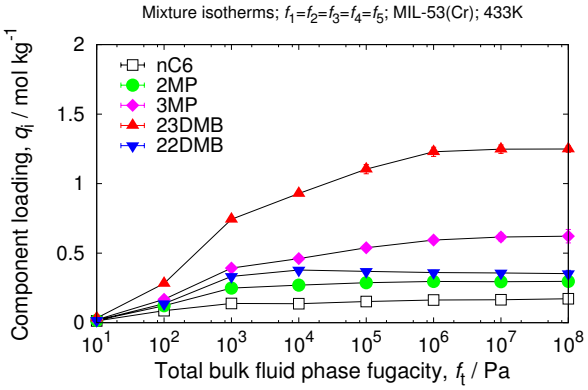

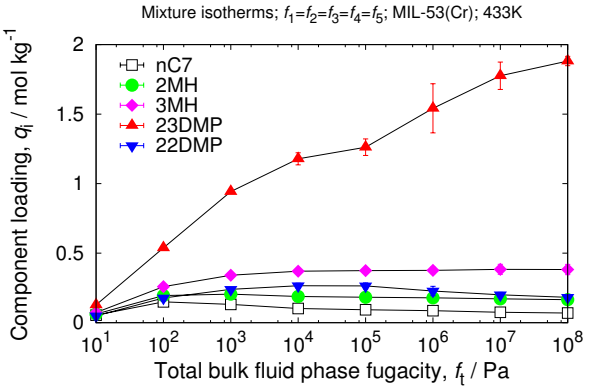

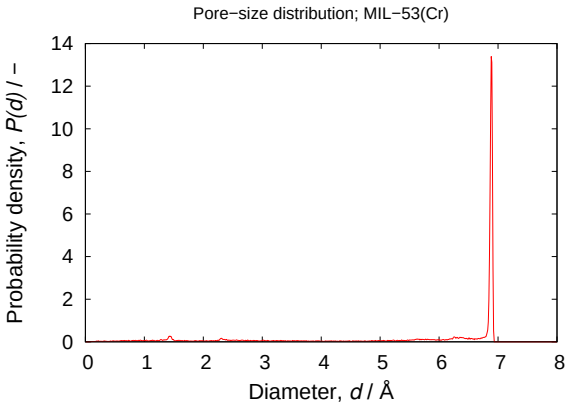

4.17 MIL-88A(open)

unit cell size	$a = 13.8711$ [Å], $b = 13.8711$ [Å], $c = 12.663$ [Å]
unit cell angles	$\alpha = \beta = 90[^\circ]$, $\gamma = 120[^\circ]$
framework density	902.98 [kg/m^3]
description	Fe_3O(fumarate)$_3$
crystallographic data	ref. [93]
void fraction	0.599 [-]
accessible pore volume	0.6629 [cm^3/g]
nitrogen surface area	2554 [m^2/g], 2306 [m^2/cm^3]

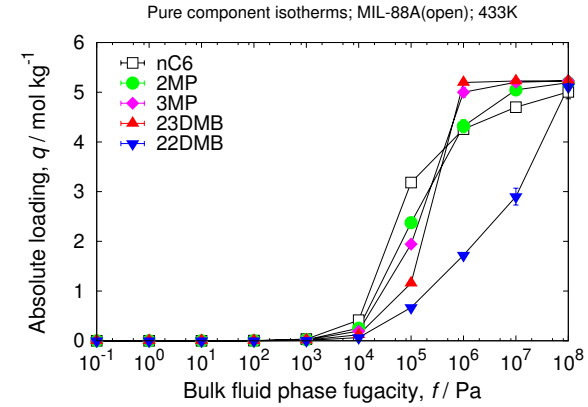

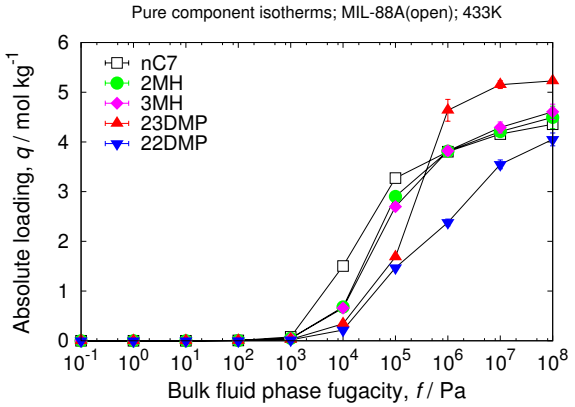

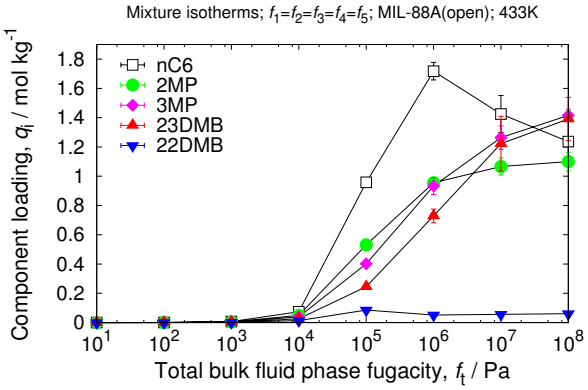

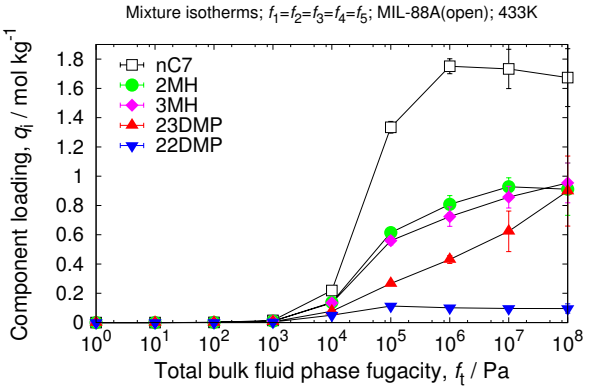

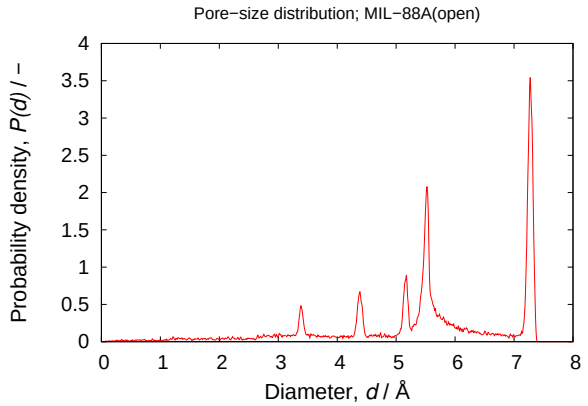

4.18 MIL-88B(open)

unit cell size	$a = 15.6261$ [Å], $b = 15.6261$ [Å], $c = 15.9604$ [Å]
unit cell angles	$\alpha = \beta = 90[^\circ]$, $\gamma = 120[^\circ]$
framework density	700.95 [kg/m^3]
description	$Cr_3O(BDC)_3$
crystallographic data	ref. [93]
void fraction	0.688 [-]
accessible pore volume	0.9821 [cm^3/g]
nitrogen surface area	3190 [m^2/g], 2236 [m^2/cm^3]

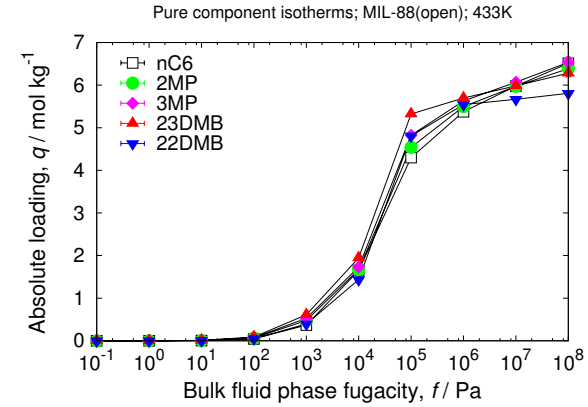

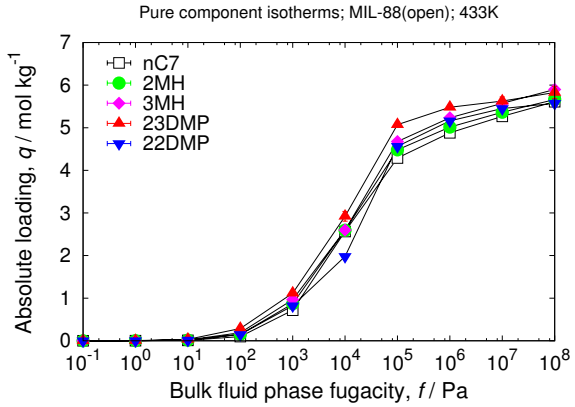

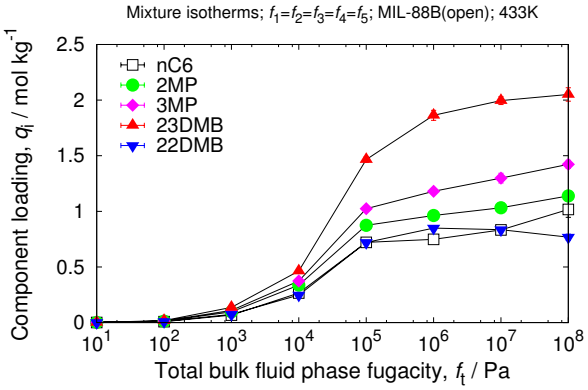

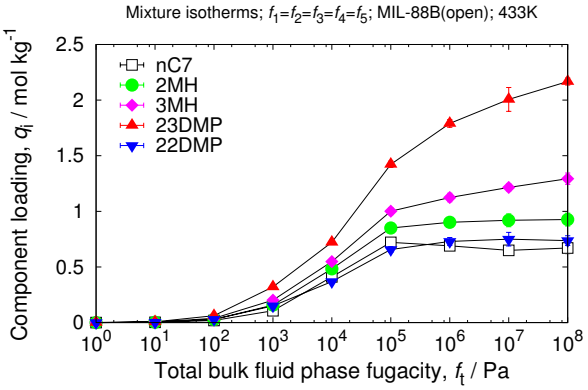

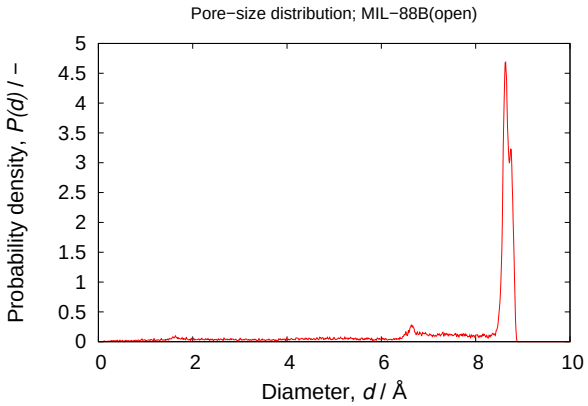

4.19 MIL-88C(open)

unit cell size	$a = 18.7529$ [Å], $b = 18.7529$ [Å], $c = 18.7425$ [Å]
unit cell angles	$\alpha = \beta = 90[^\circ]$, $\gamma = 120[^\circ]$
framework density	508.54 [kg/m^3]
description	$Fe_3O(NDC)_3$
crystallographic data	ref. [93]
void fraction	0.766 [-]
accessible pore volume	1.5061 [cm^3/g]
nitrogen surface area	3867 [m^2/g], 1966 [m^2/cm^3]

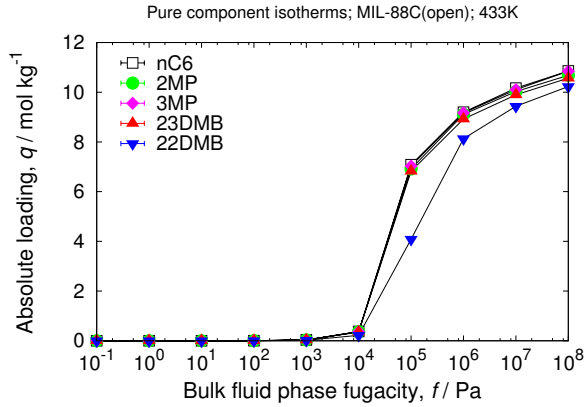

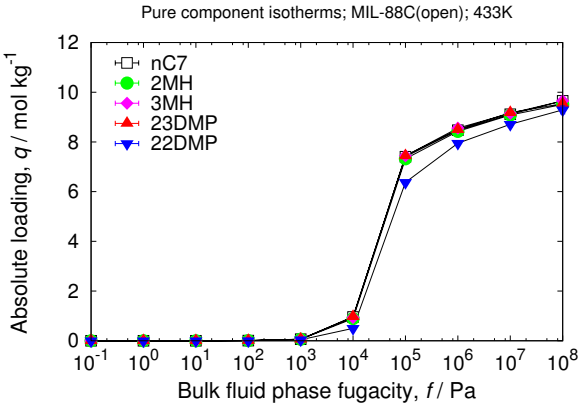

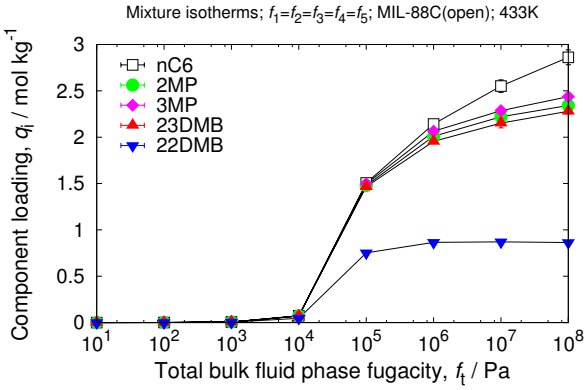

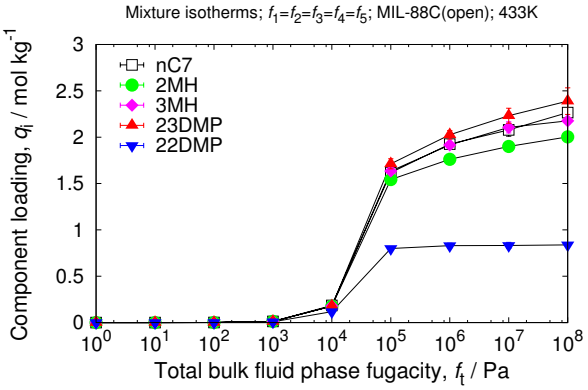

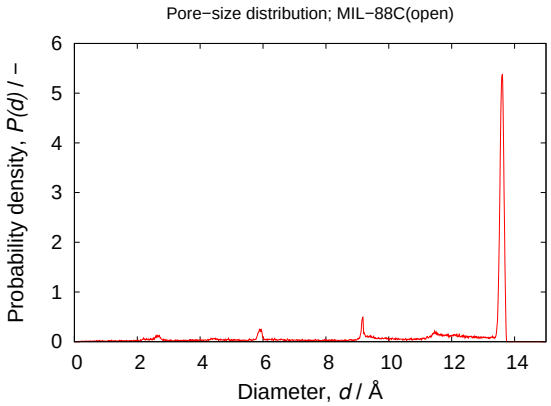

4.20 MIL-88D(open)

unit cell size	$a = 19.6235$ [Å], $b = 19.6235$ [Å], $c = 23.2614$ [Å]
unit cell angles	$\alpha = \beta = 90[^\circ]$, $\gamma = 120[^\circ]$
framework density	402.69 [kg/m^3]
description	$Cr_3O(BPDC)_3$
crystallographic data	ref. [93]
void fraction	0.800 [-]
accessible pore volume	1.9859 [cm^3/g]
nitrogen surface area	4880 [m^2/g], 1965 [m^2/cm^3]

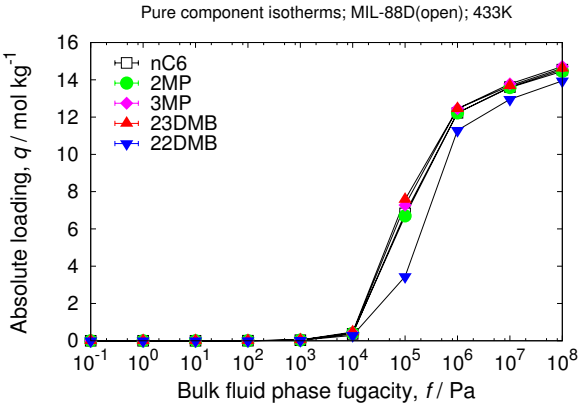

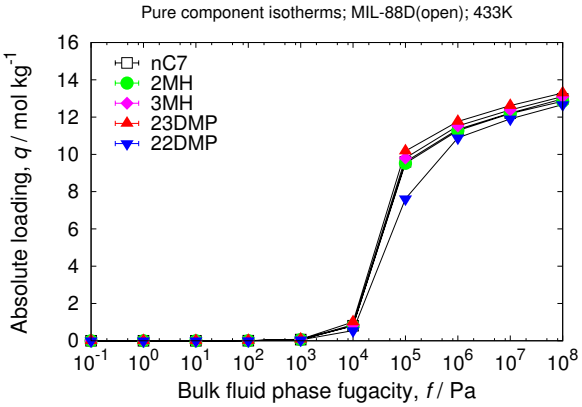

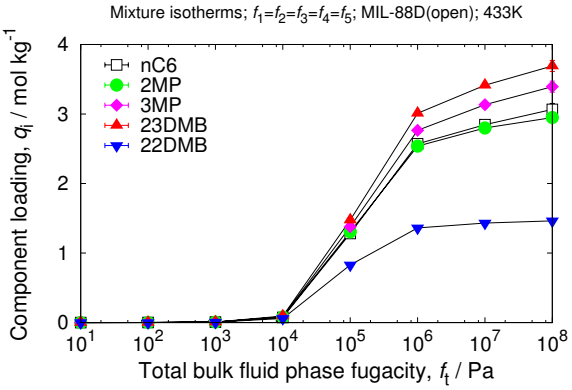

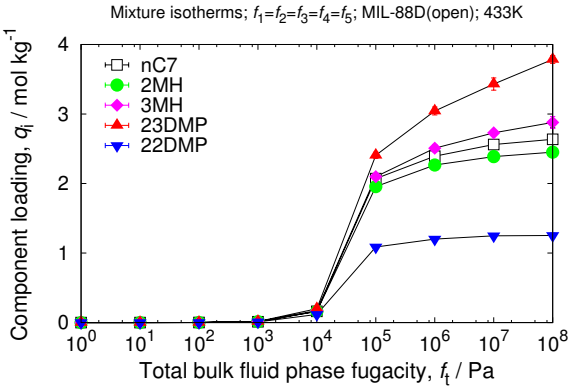

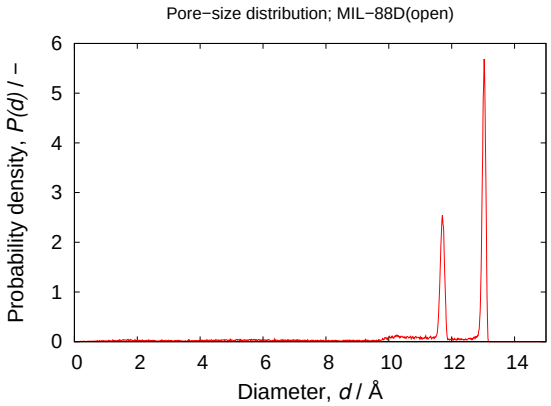

4.21 MIL-100

unit cell size	$a = 72.9057$ [Å], $b = 72.9057$ [Å], $c = 72.9057$ [Å]
unit cell angles	$\alpha = \beta = \gamma = 90[^\circ]$
description	$CrOF(BTC)_2$
framework density	705.42 [kg/m^3]
crystallographic data	ref. [94]
void fraction	0.711 [-]
accessible pore volume	1.0099 [cm^3/g]
nitrogen surface area	2075 [m^2/g], 1464 [m^2/cm^3]

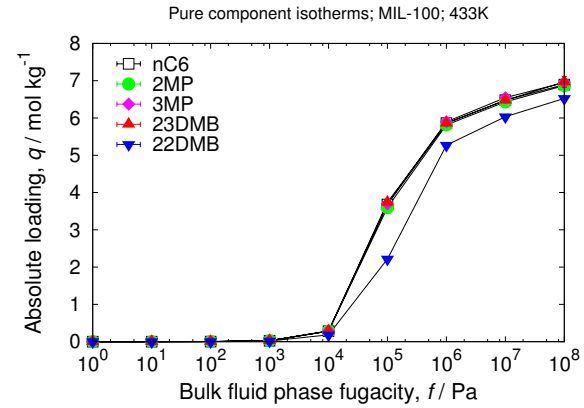

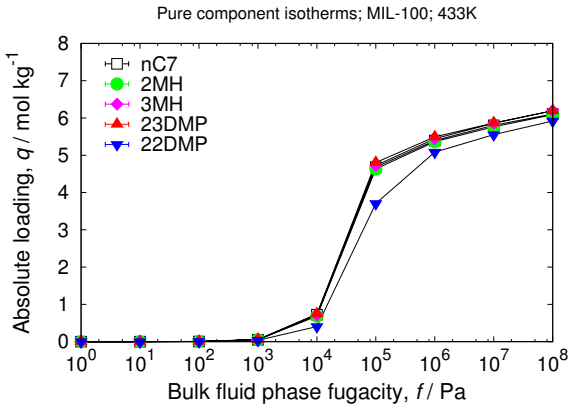

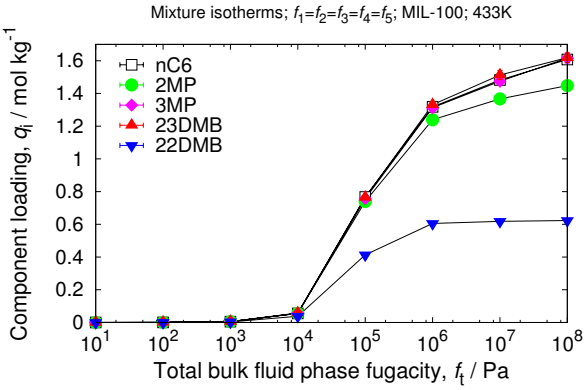

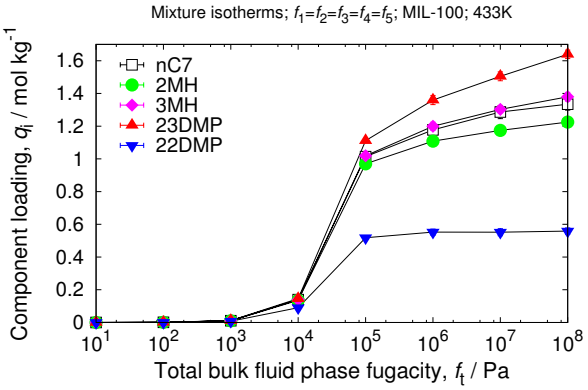

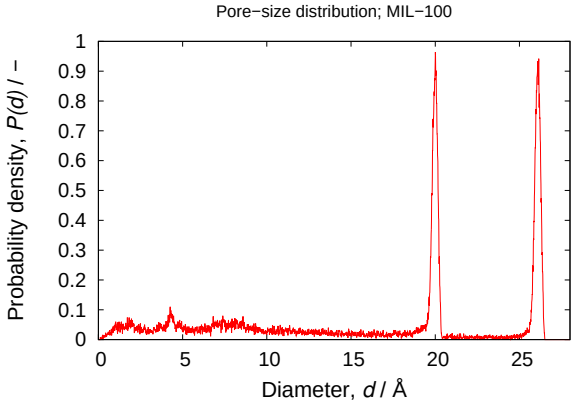

4.22 MIL-101

unit cell size	$a = 88.869$ [Å], $b = 88.869$ [Å], $c = 88.869$ [Å]
unit cell angles	$\alpha = \beta = \gamma = 90[^\circ]$
description	$CrOF(BDC)_2$
framework density	439.74 [kg/m^3]
crystallographic data	ref. [95]
void fraction	0.809 [-]
accessible pore volume	1.8394 [cm^3/g]
nitrogen surface area	3134 [m^2/g], 1378 [m^2/cm^3]

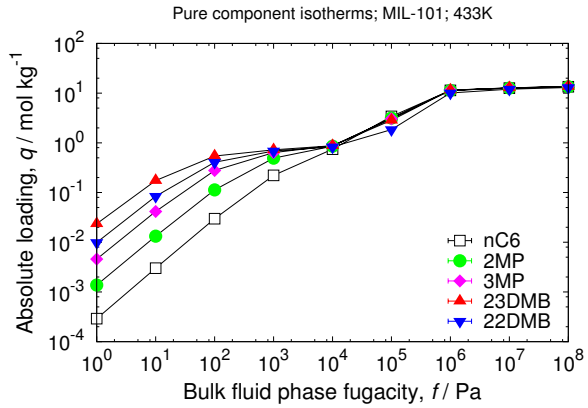

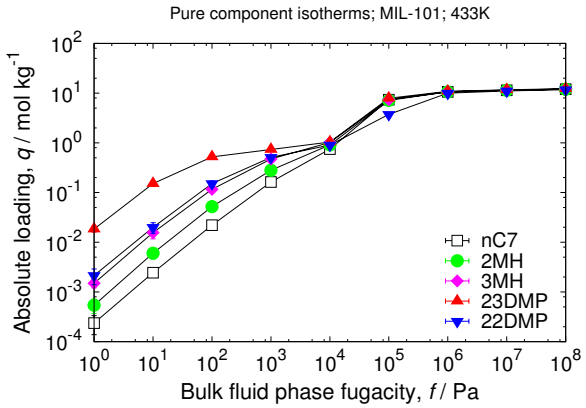

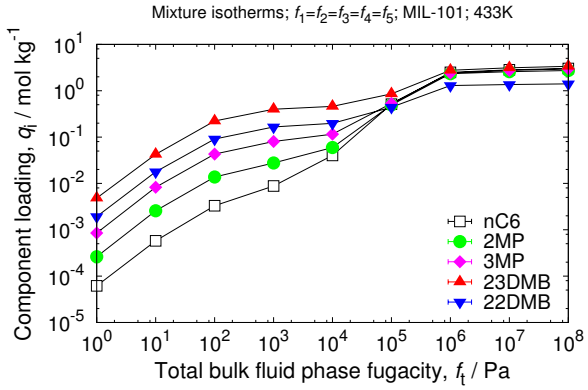

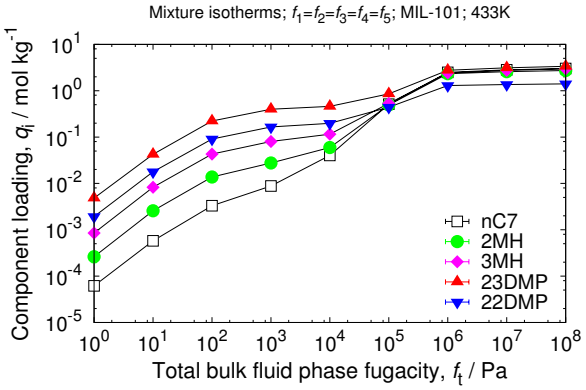

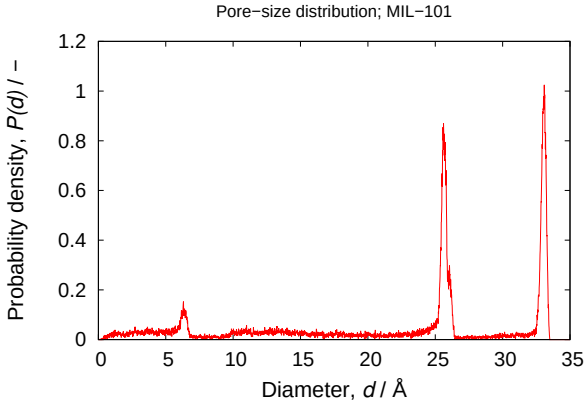

4.23 MIL-140A

unit cell size	$a = 23.8688$ [Å], $b = 11.1968$ [Å], $c = 7.8252$ [Å]
unit cell angles	$\alpha = 90[^\circ]$, $\beta = 95.475[^\circ]$, $\gamma = 90[^\circ]$
description	$ZrO[O_2C\text{-}C_6H_4\text{-}CO_2]$
framework density	1731.47 [kg/m^3]
crystallographic data	ref. [96]
void fraction	0.168 [-]
accessible pore volume	0.0970 [cm^3/g]
nitrogen surface area	9.0 [m^2/g], 15.7 [m^2/cm^3]

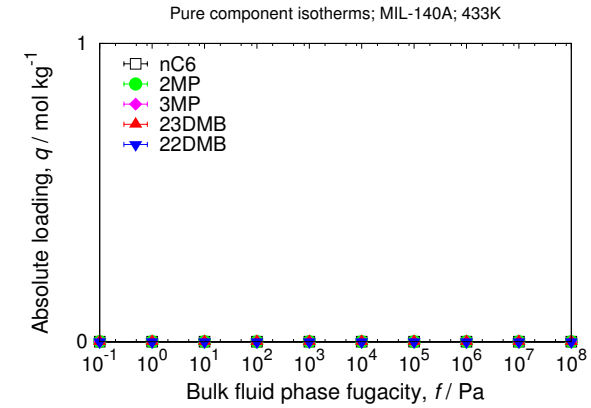

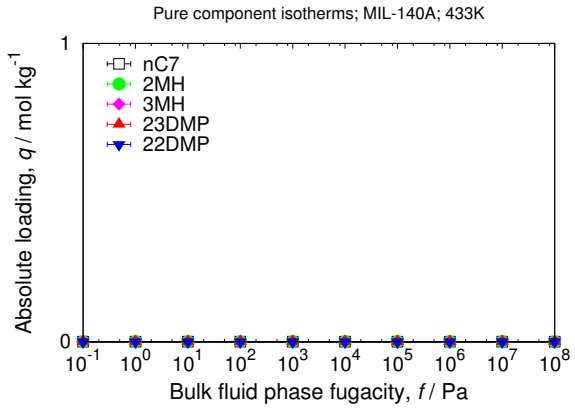

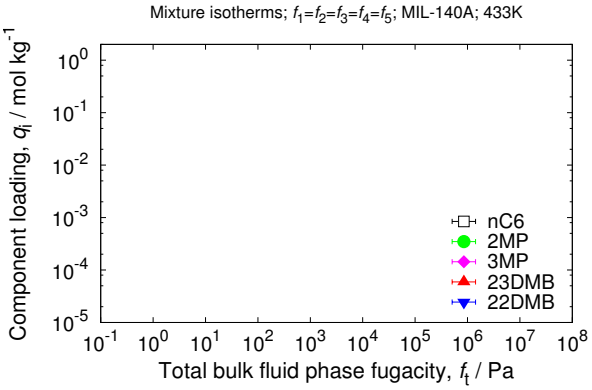

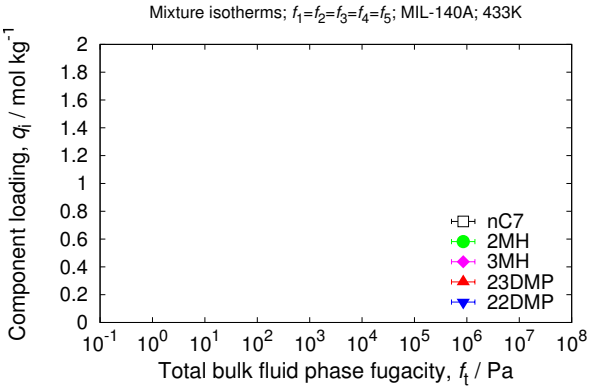

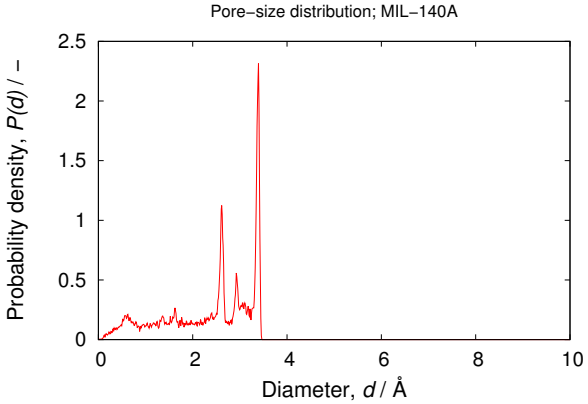

4.24 MIL-140B

unit cell size	$a = 28.1582$ [Å], $b = 13.4675$ [Å], $c = 7.889$ [Å]
unit cell angles	$\alpha = 90[^\circ]$, $\beta = 93.43[^\circ]$, $\gamma = 90[^\circ]$
description	ZrO[O_2C-$C_{10}H_6$-CO_2]
framework density	1429.70 [kg/m^3]
crystallographic data	ref. [96]
void fraction	0.288 [-]
accessible pore volume	0.2017 [cm^3/g]
nitrogen surface area	359 [m^2/g], 513 [m^2/cm^3]

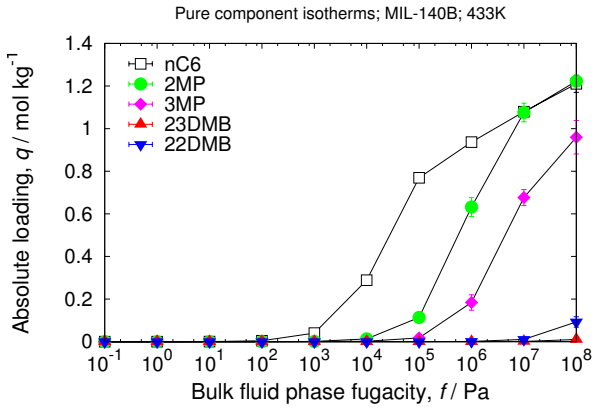

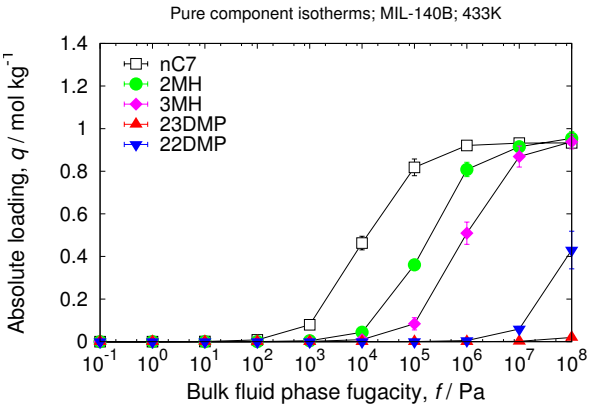

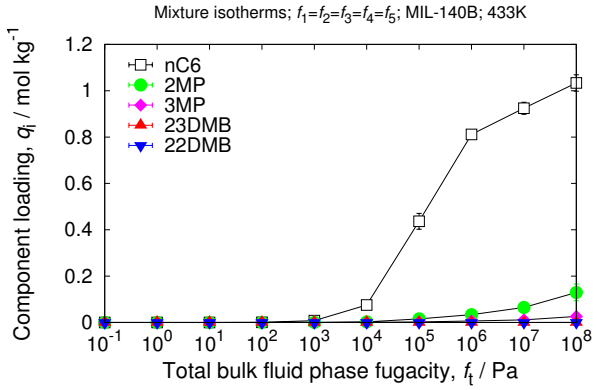

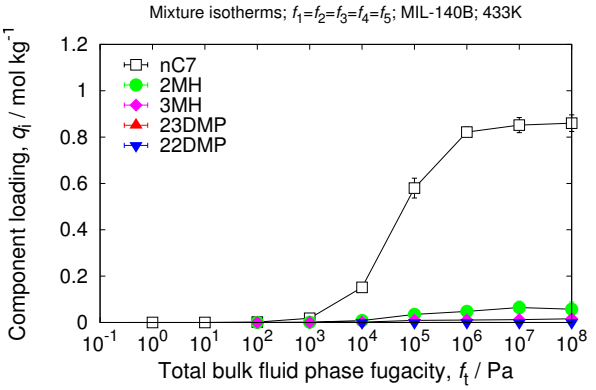

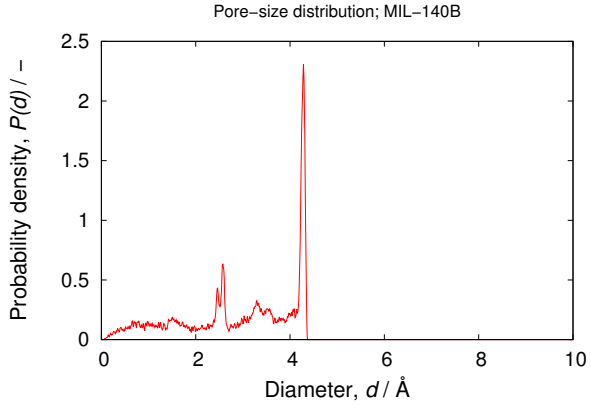

4.25 MIL-140C

unit cell size	$a = 31.8931$ [Å], $b = 15.6099$ [Å], $c = 7.9348$ [Å]
unit cell angles	$\alpha = 90[^\circ]$, $\beta = 84.83[^\circ]$, $\gamma = 90[^\circ]$
description	$ZrO[O_2C\text{-}C_{12}H_8\text{-}CO_2]$
framework density	1173.14 [kg/m^3]
crystallographic data	ref. [96]
void fraction	0.398 [-]
accessible pore volume	0.3398 [cm^3/g]
nitrogen surface area	1011 [m^2/g], 1186 [m^2/cm^3]

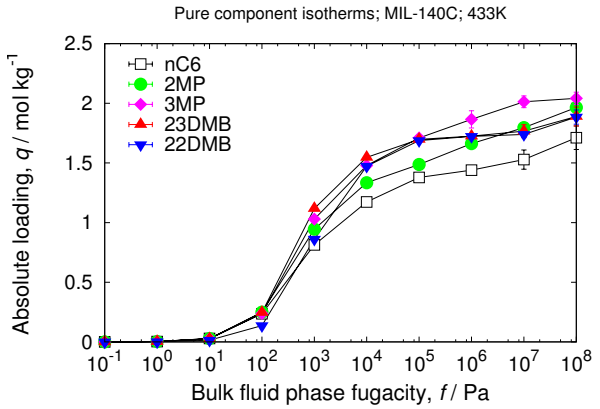

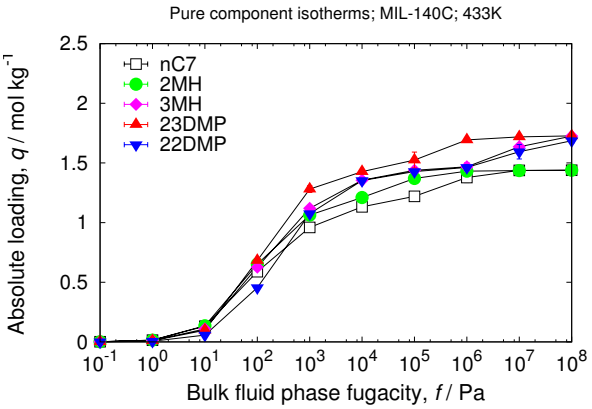

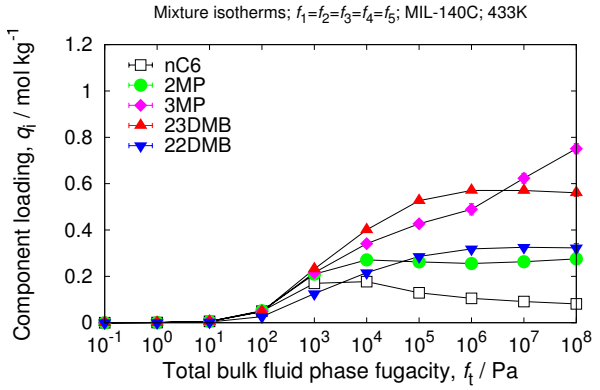

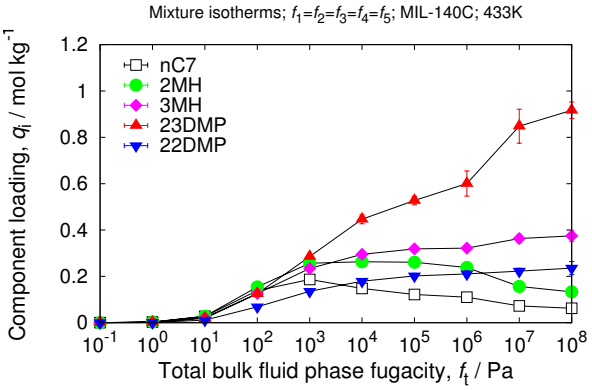

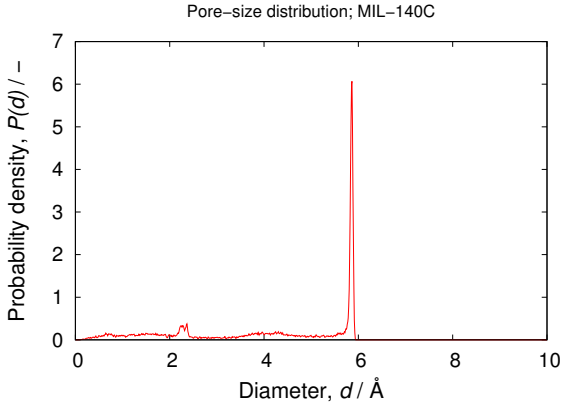

4.26 MIL-140D

unit cell size	$a = 34.8613$ [Å], $b = 17.4795$ [Å], $c = 7.8598$ [Å]
unit cell angles	$\alpha = 90[^\circ]$, $\beta = 90.27[^\circ]$, $\gamma = 90[^\circ]$
description	$ZrO[O_2C\text{-}C_{12}N_2H_6Cl_2\text{-}CO_2]$
framework density	1163.32 [kg/m^3]
crystallographic data	ref. [96]
void fraction	0.423 [-]
accessible pore volume	0.3634 [cm^3/g]
nitrogen surface area	1029 [m^2/g], 1268 [m^2/cm^3]

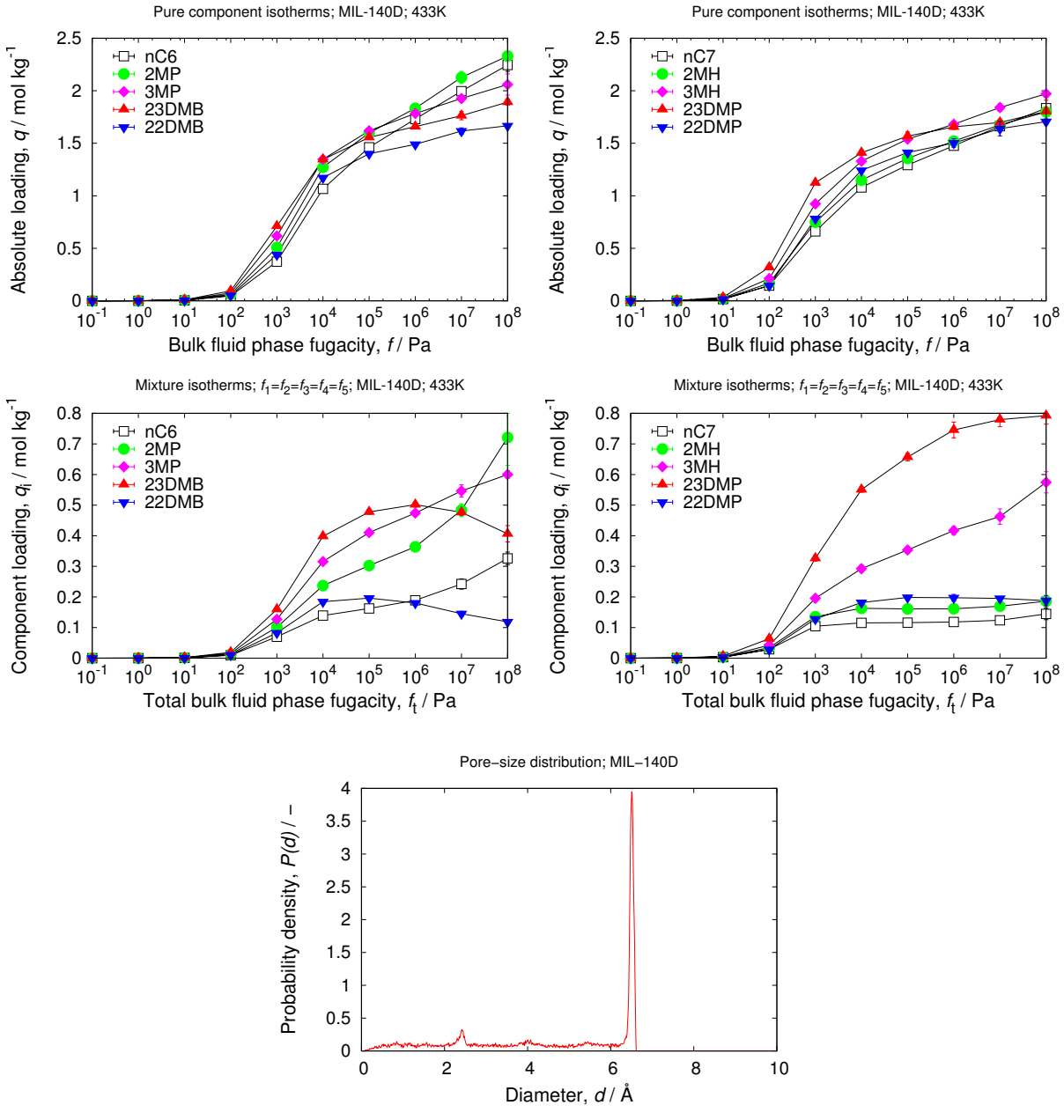

4.27 ZnBDC

unit cell size	$a = 6.723$ [Å], $b = 15.481$ [Å], $c = 12.435$ [Å]
unit cell angles	$\alpha = 90[^\circ]$, $\beta = 102.825[^\circ]$, $\gamma = 90[^\circ]$
framework density	1208.10 [kg/m^3]
description	Zn(BDC)
crystallographic data	ref. [97]
void fraction	0.5160 [-]
accessible pore volume	0.4271 [cm^3/g]
nitrogen surface area	1145 [m^2/g], 1383 [m^2/cm^3]

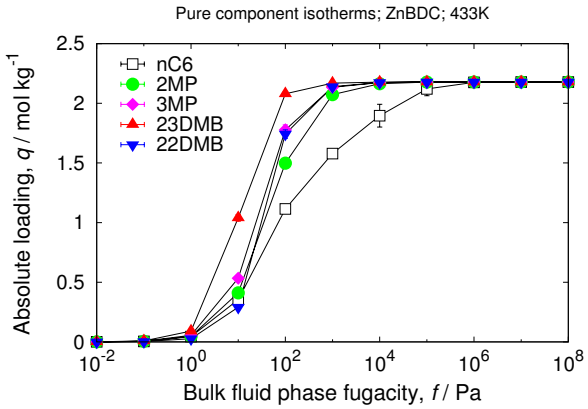

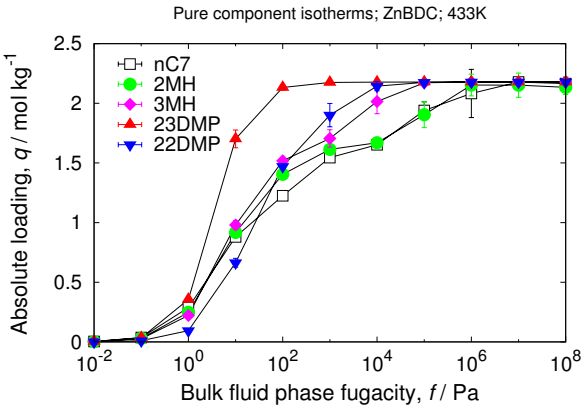

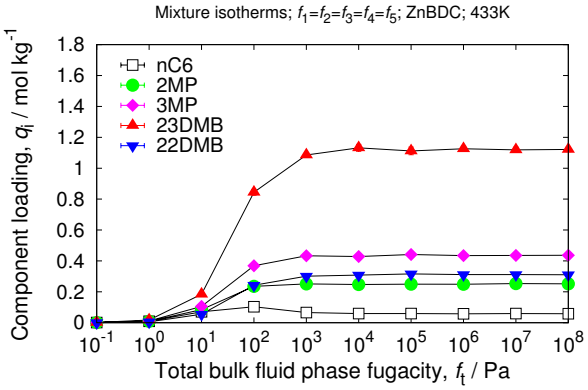

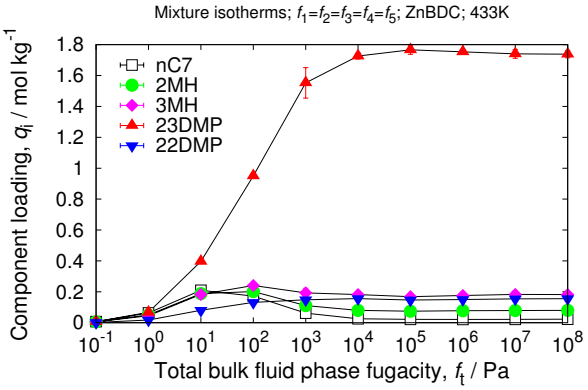

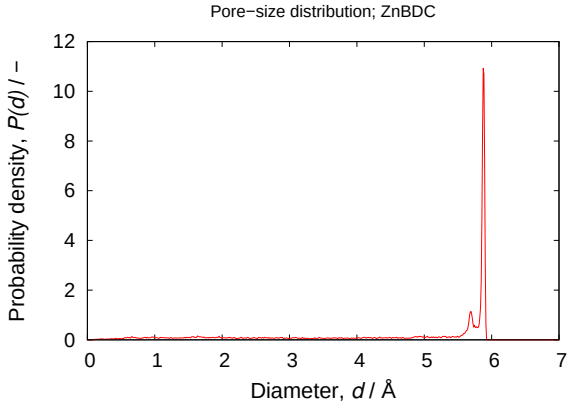

4.28 ZnBDCdabco

unit cell size	$a = 10.9288$ [Å], $b = 10.9288$ [Å], $c = 9.6084$ [Å]
unit cell angles	$\alpha = \beta = \gamma = 90[^\circ]$
framework density	826.53 [kg/m^3]
description	$Zn_2(BDC)_2(DABCO)$
crystallographic data	ref. [98]
void fraction	0.627 [-]
accessible pore volume	0.7587 [cm^3/g]
nitrogen surface area	2110 [m^2/g], 1744 [m^2/cm^3]

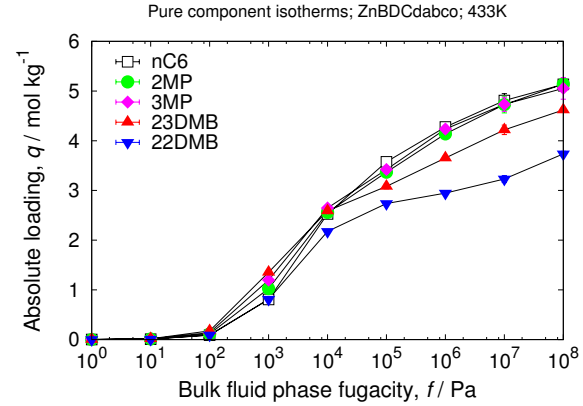

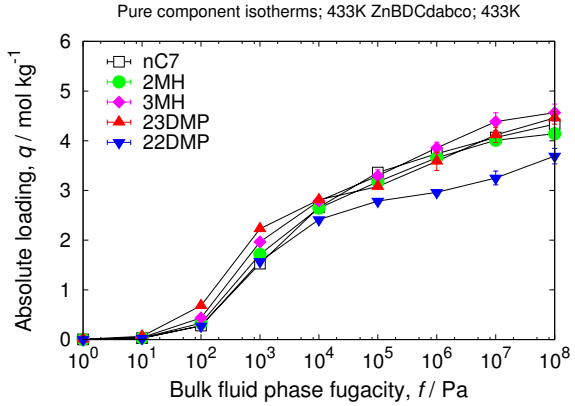

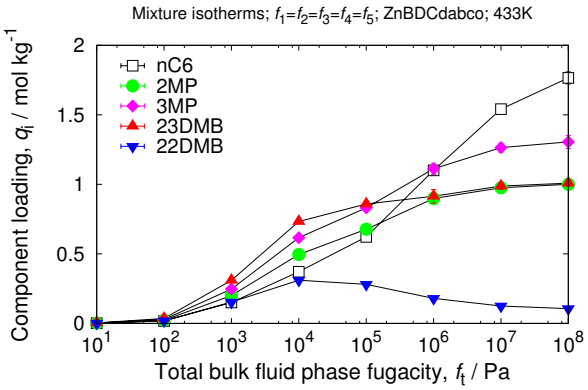

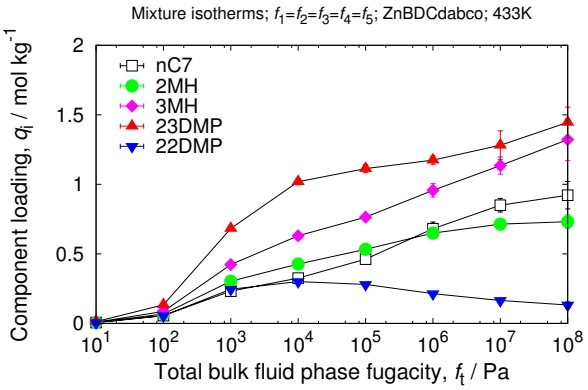

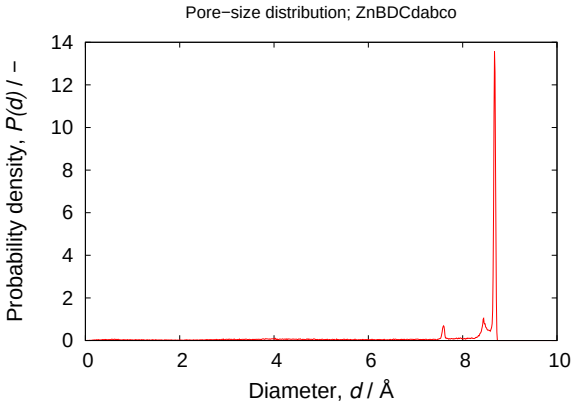

4.29 ZnHBDC

unit cell size	$a = 21.222$ [Å], $b = 17.716$ [Å], $c = 14.376$ [Å]
unit cell angles	$\alpha = 90, [^\circ]$ $\beta = 127.821[^\circ]$, $\gamma = 90[^\circ]$
framework density	866.81 [kg/m^3]
description	$Zn_2(HBDC)_2(DMTRZ)_2$
crystallographic data	ref. [99]
void fraction	0.625 [-]
accessible pore volume	0.7207 [cm^3/g]
nitrogen surface area	1907 [m^2/g], 1653 [m^2/cm^3]

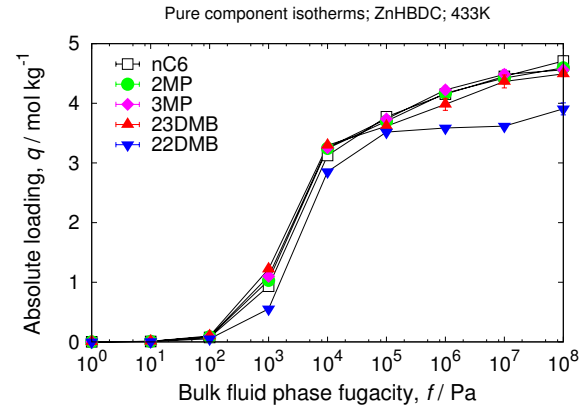

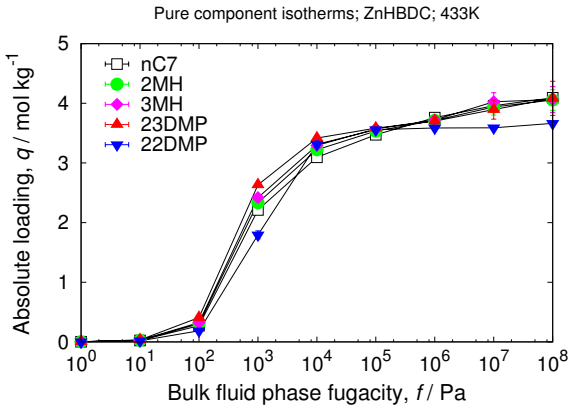

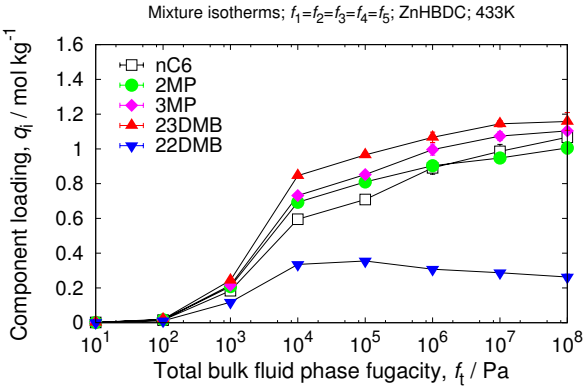

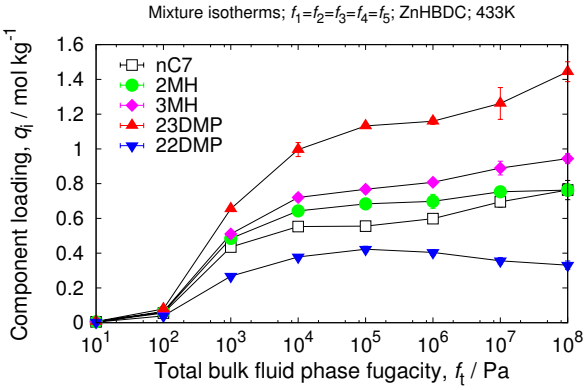

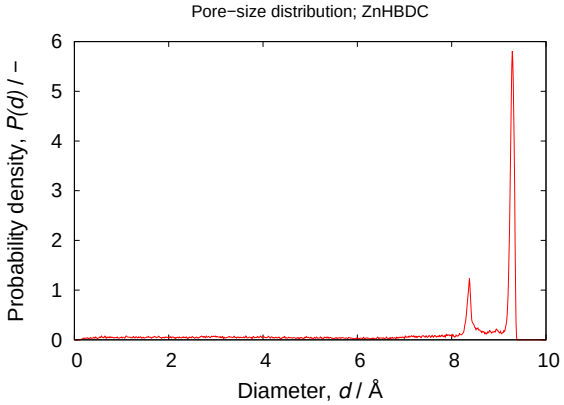

4.30 CoBDP

unit cell size	$a = 13.2529$ [Å], $b = 13.253$ [Å], $c = 13.995$ [Å]
unit cell angles	$\alpha = \beta = \gamma = 90[^\circ]$
framework density	721.89 [kg/m^3]
description	Co(BDP)
crystallographic data	ref. [100]
void fraction	0.657366 [-]
accessible pore volume	0.9106 [cm^3/g]
nitrogen surface area	2267 [m^2/g], 1637 [m^2/cm^3]

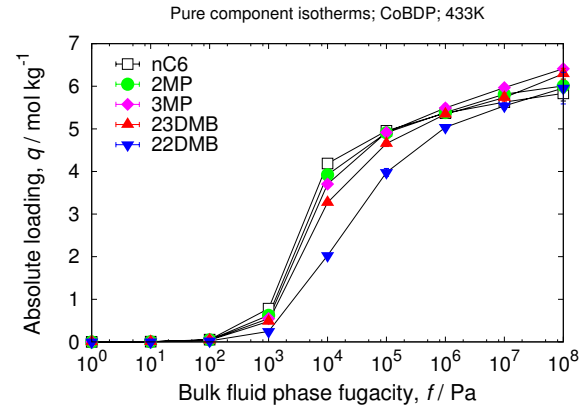

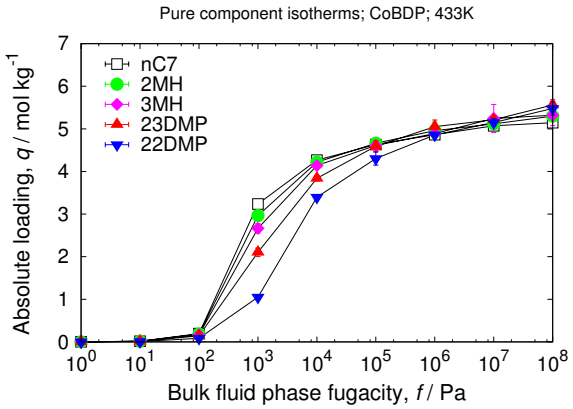

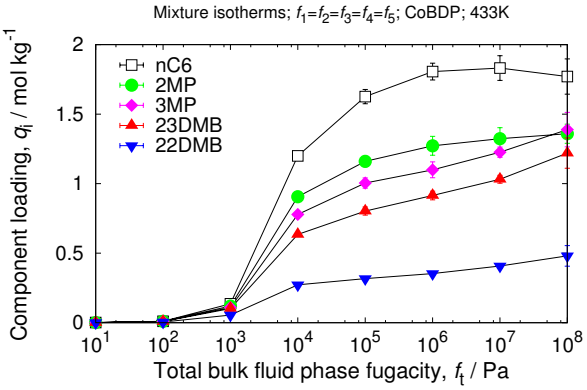

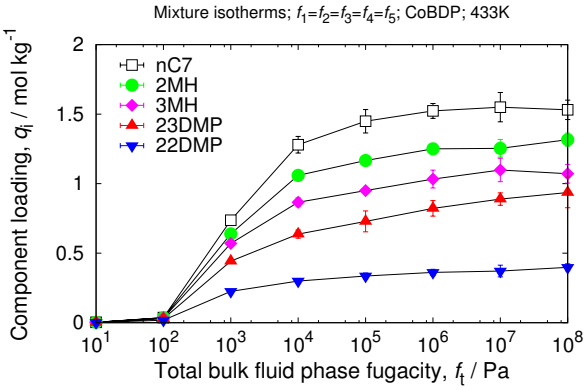

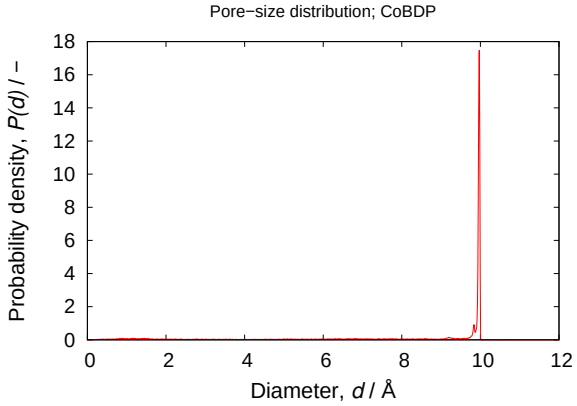

4.31 PCN-60

unit cell size	$a = 42.8434$ [Å], $b = 42.8434$ [Å], $c = 42.8434$ [Å]
unit cell angles	$\alpha = \beta = \gamma = 90[^\circ]$
framework density	562.65 [kg/m^3]
description	Zn_3(BTEI)
crystallographic data	ref. [101]
void fraction	0.822 [-]
accessible pore volume	1.4617 [cm^3/g]
nitrogen surface area	3817 [m^2/g], 2148 [m^2/cm^3]

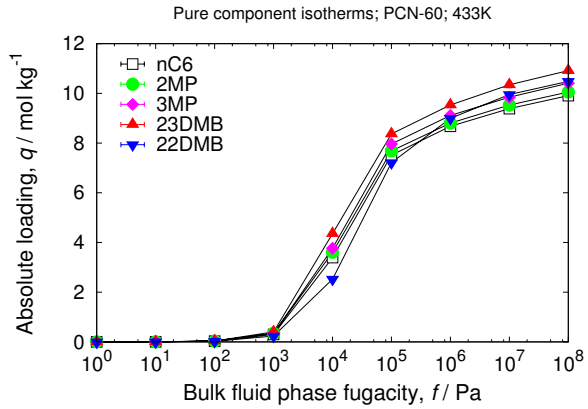

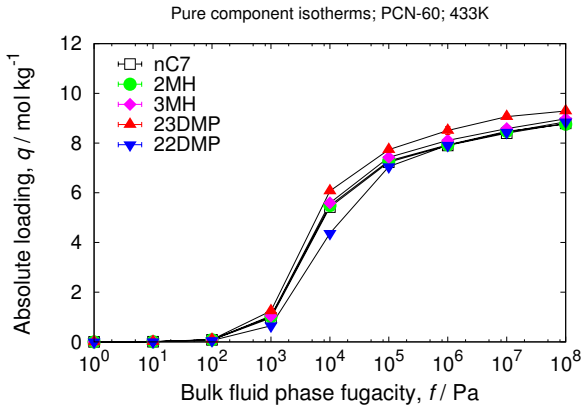

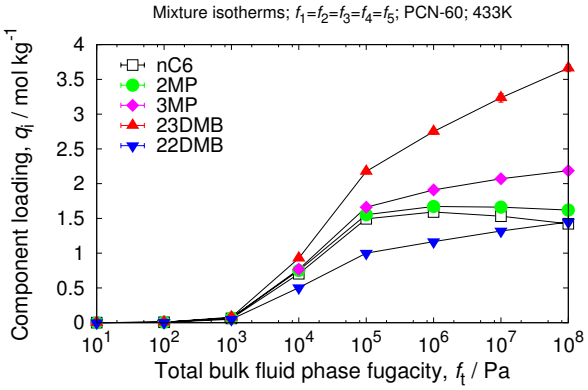

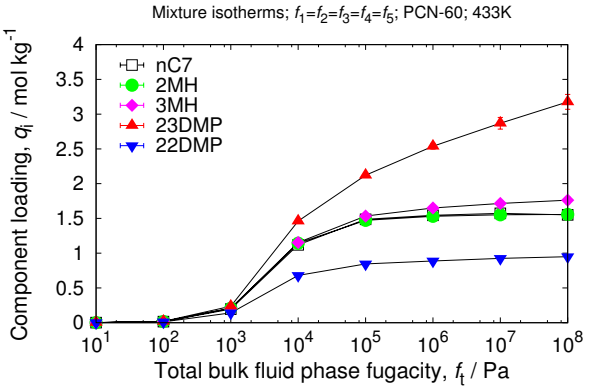

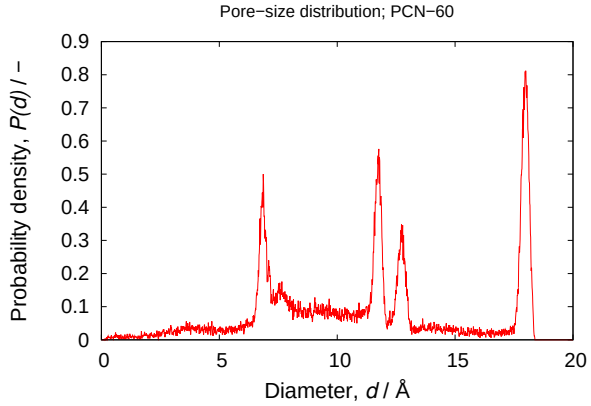

4.32 PCN-61

unit cell size	$a = 42.7958$ [Å], $b = 42.7958$ [Å], $c = 42.7958$ [Å]
unit cell angles	$\alpha = \beta = \gamma = 90[^\circ]$
framework density	560.74 [kg/m^3]
description	Cu_3(BTEI)
crystallographic data	ref. [101]
void fraction	0.817 [-]
accessible pore volume	1.4576 [cm^3/g]
nitrogen surface area	3852 [m^2/g], 2160 [m^2/cm^3]

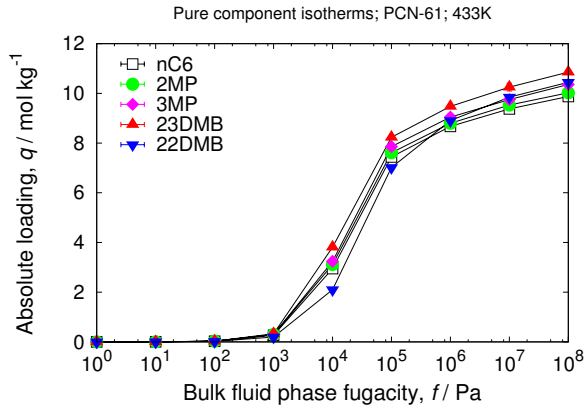

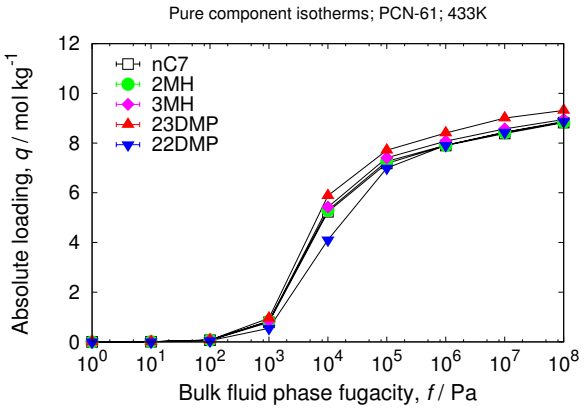

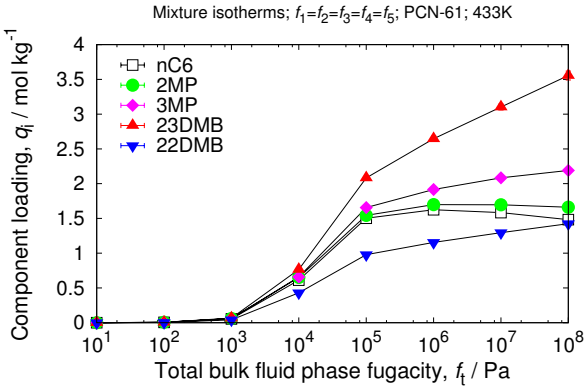

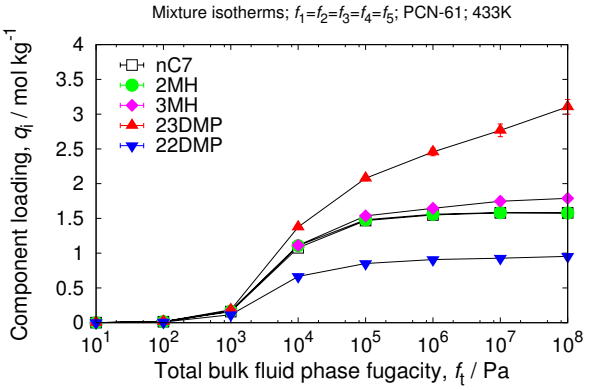

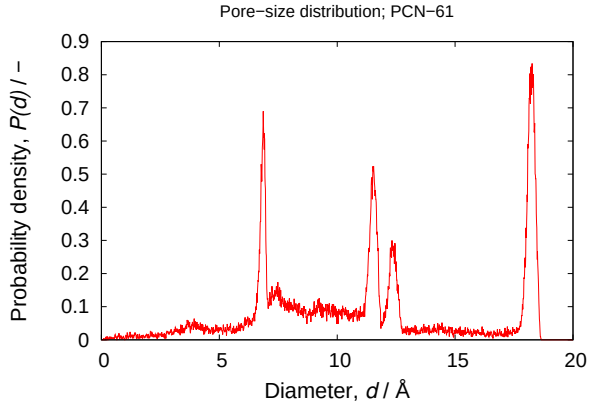

4.33 PCN-68

unit cell size	$a = 59.153$ [Å], $b = 59.153$ [Å], $c = 59.153$ [Å]
unit cell angles	$\alpha = \beta = \gamma = 90[^\circ]$
framework density	289.45 [kg/m^3]
description	Cu_3(PTEI)
crystallographic data	ref. [102]
void fraction	0.890 [-]
accessible pore volume	3.0747 [cm^3/g]
nitrogen surface area	5823 [m^2/g], 1685 [m^2/cm^3]

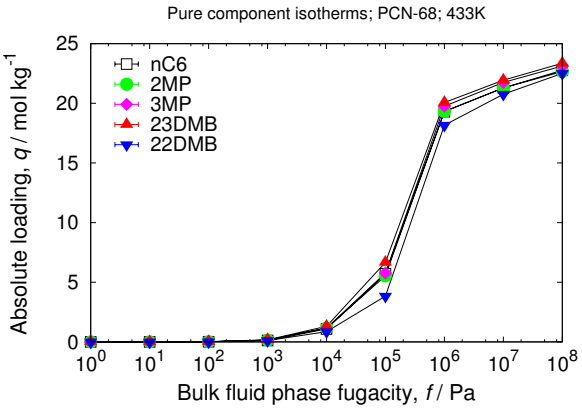

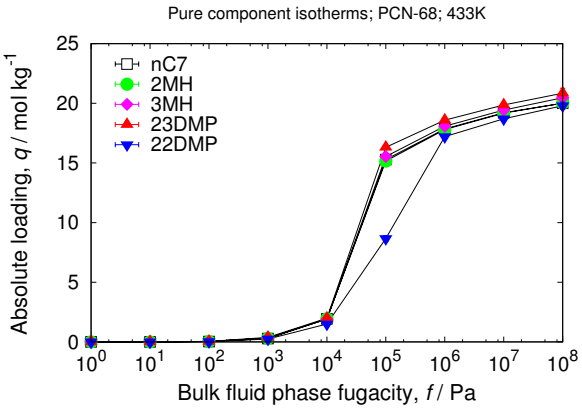

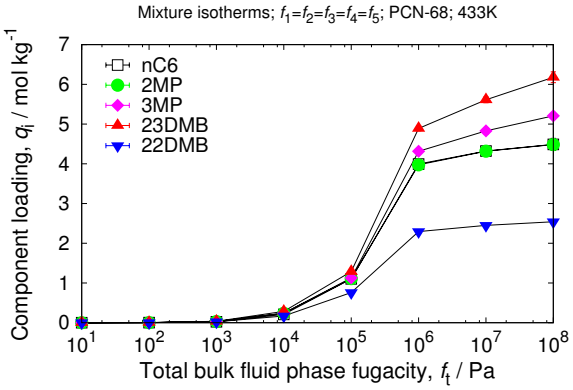

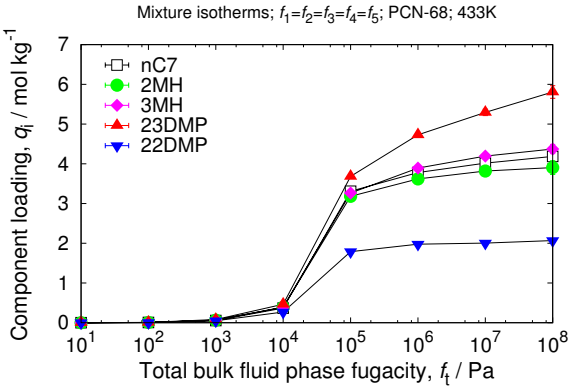

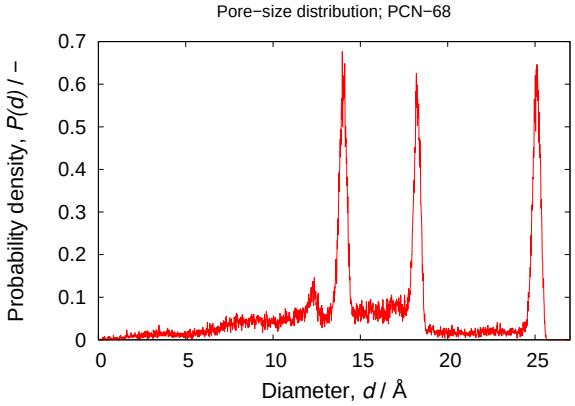

4.34 UiO-66

unit cell size	$a = 20.7004$ [Å], $b = 20.7004$ [Å], $c = 20.7004$ [Å]
unit cell angles	$\alpha = \beta = \gamma = 90[^\circ]$
framework density	1219.09 [kg/m^3]
description	ZrO(BDC)
crystallographic data	ref. [103]
void fraction	0.494 [-]
accessible pore volume	0.4053 [cm^3/g]
nitrogen surface area	1116 [m^2/g], 1360 [m^2/cm^3]

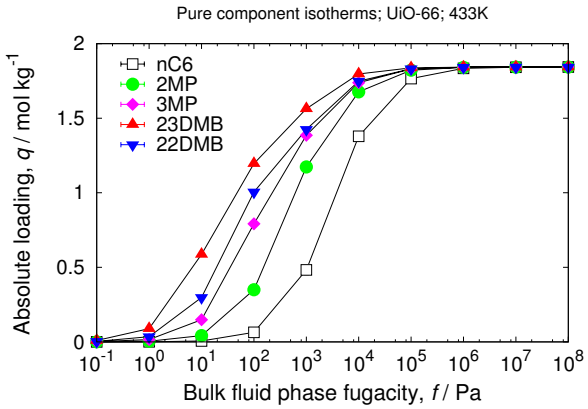

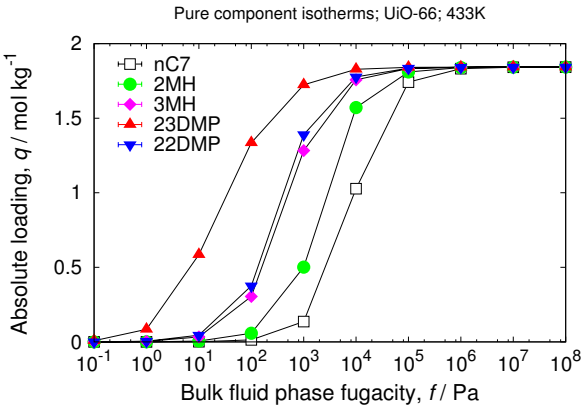

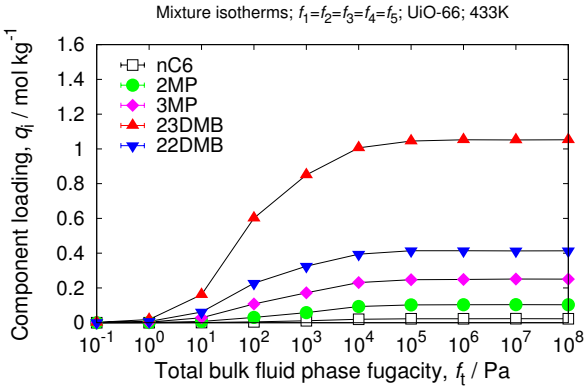

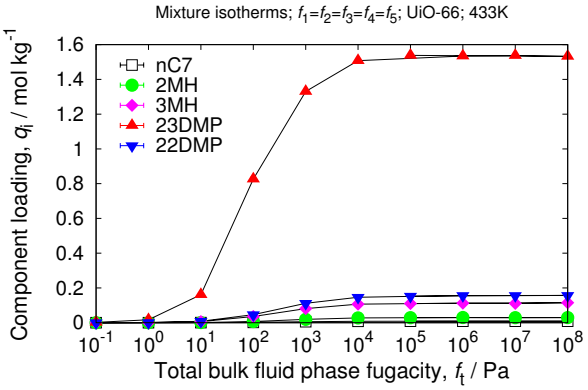

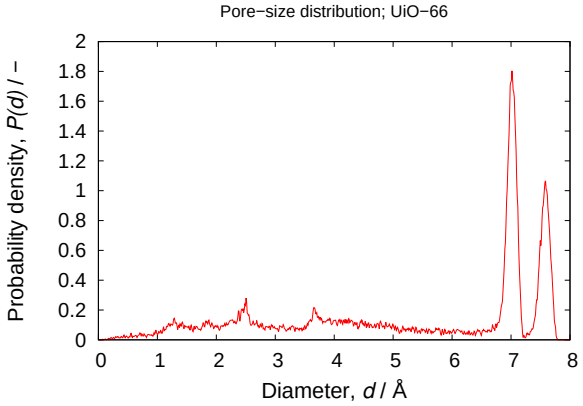

4.35 Zr-TPDC

unit cell size	$a = 32.7767$ [Å], $b = 32.7767$ [Å], $c = 32.7767$ [Å]
unit cell angles	$\alpha = \beta = \gamma = 90[^\circ]$
framework density	485.38 [kg/m^3]
description	ZrO(TPDC)
crystallographic data	ref. [104]
void fraction	0.762 [-]
accessible pore volume	1.5705 [cm^3/g]
nitrogen surface area	4531 [m^2/g], 2199 [m^2/cm^3]

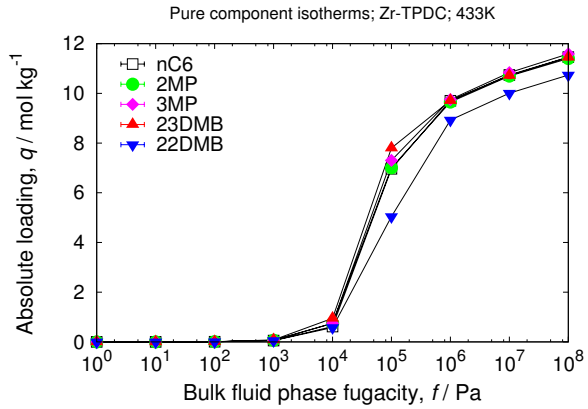

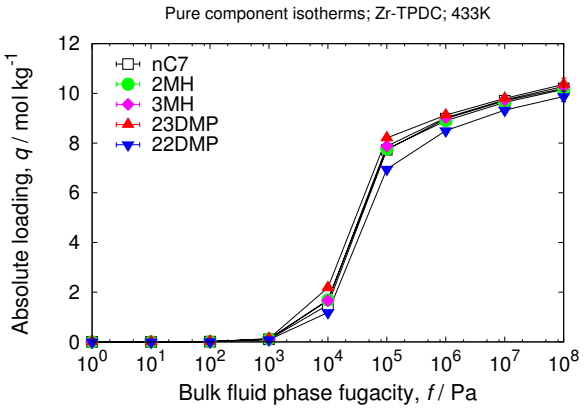

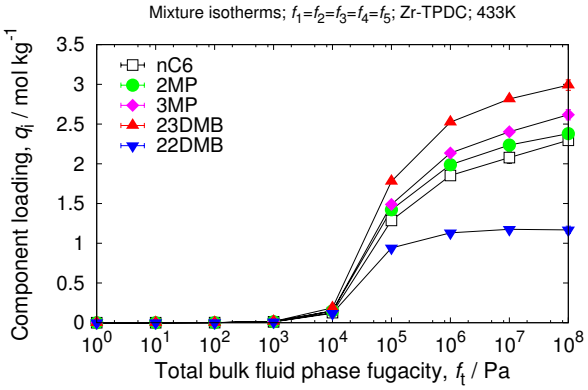

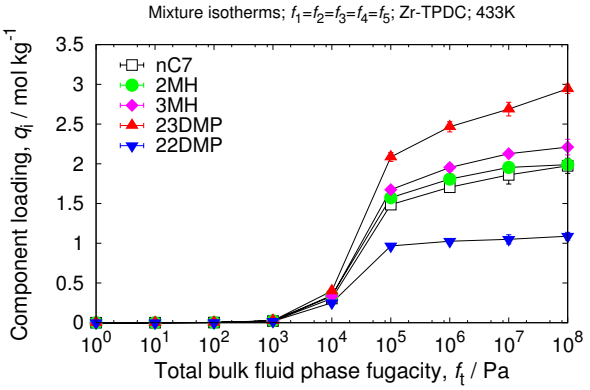

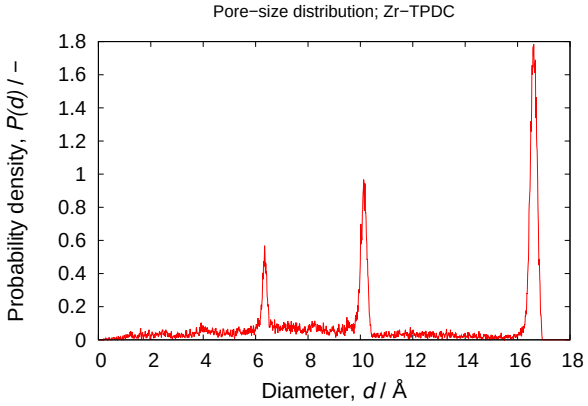

4.36 Mg-DOBDC (also known as MgMOF-74 and CPO-27-Mg)

unit cell size	$a = 25.8765$ [Å], $b = 25.8765$ [Å], $c = 6.7856$ [Å]
unit cell angles	$\alpha = \beta = 90[^\circ]$, $\gamma = 120[^\circ]$
framework density	921.82 [kg/m^3]
description	Mg_2(DOBDC)]
crystallographic data	ref. [105]
void fraction	0.723 [-]
accessible pore volume	0.7845 [cm^3/g]
nitrogen surface area	1708 [m^2/g], 1575 [m^2/cm^3]

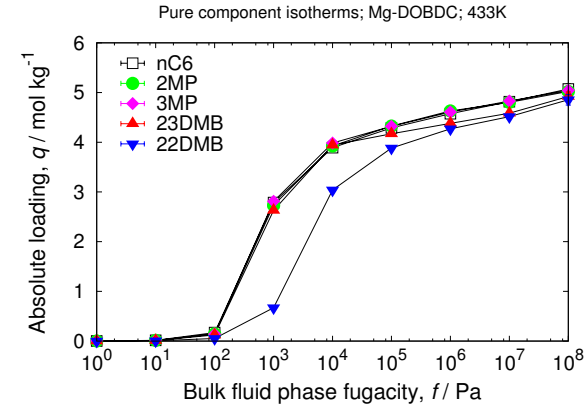

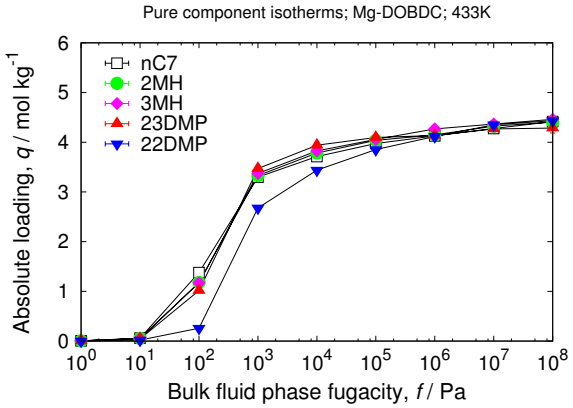

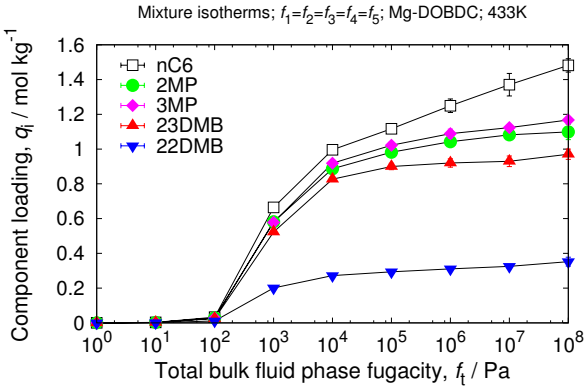

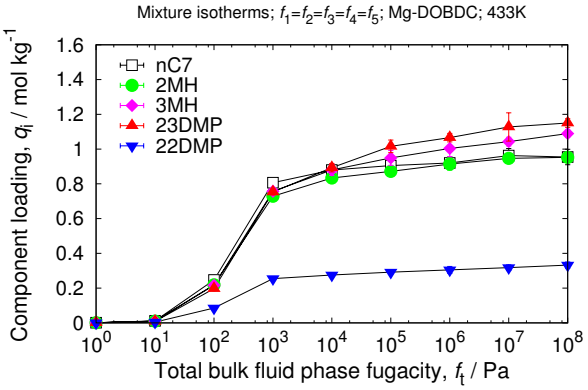

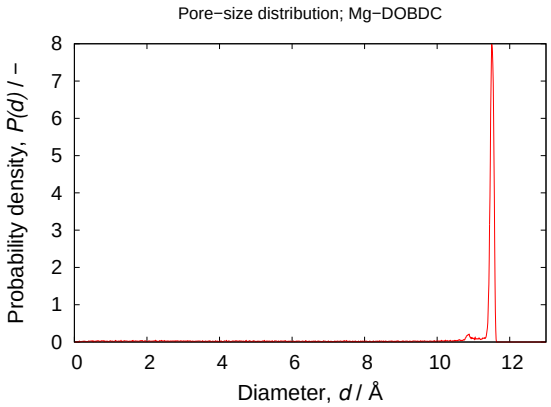

4.37 Ni-DOBDC (also known as NiMOF-74 and CPO-27-Ni)

unit cell size	$a = 25.7856$ [Å], $b = 25.7856$ [Å], $c = 6.7701$ [Å]
unit cell angles	$\alpha = \beta = 90[^\circ]$, $\gamma = 120[^\circ]$
framework density	1194.12 [kg/m^3]
description	Ni_2(DOBDC)]
crystallographic data	ref. [105]
void fraction	0.692 [-]
accessible pore volume	0.5799 [cm^3/g]
nitrogen surface area	1312 [m^2/g], 1567 [m^2/cm^3]

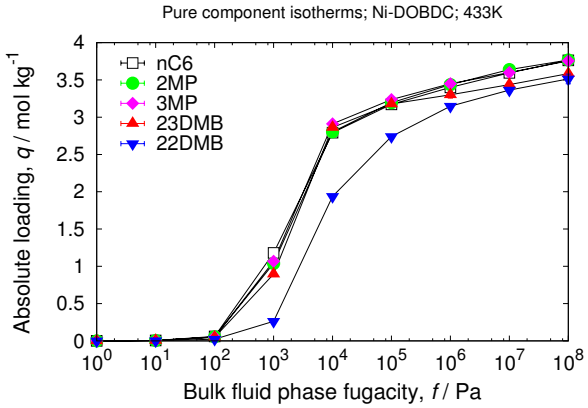

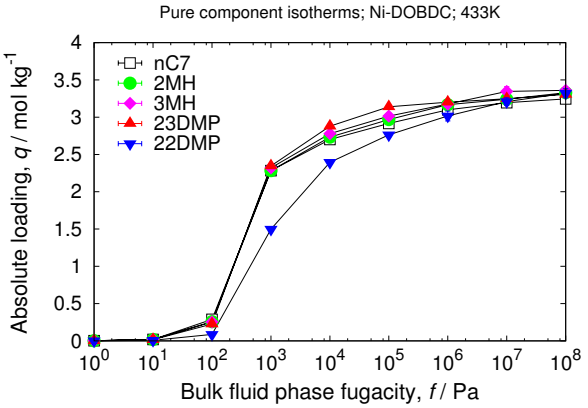

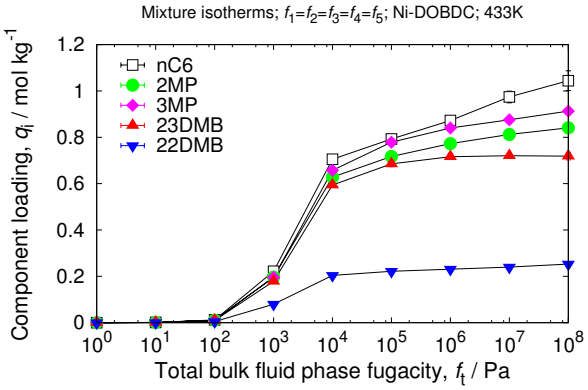

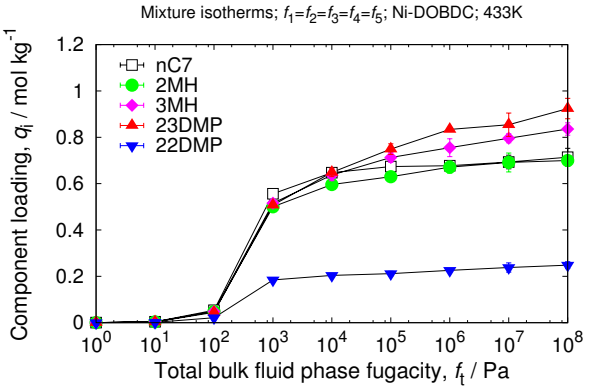

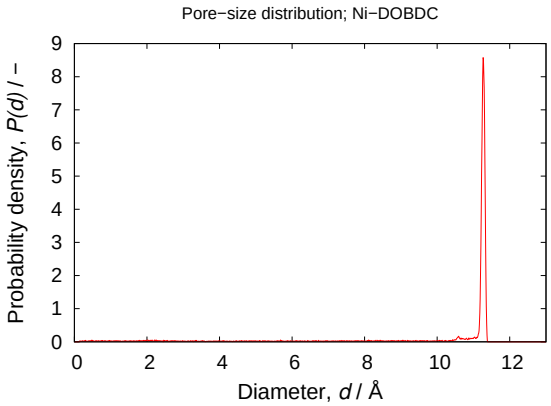

4.38 Zn-DOBDC (also known as ZnMOF-74 and CPO-27-Zn)

unit cell size	$a = 25.9322$ [Å], $b = 25.9322$ [Å], $c = 6.8365$ [Å]
unit cell angles	$\alpha = \beta = 90[^\circ]$, $\gamma = 120[^\circ]$
framework density	1219.60 [kg/m^3]
description	Zn_2(DOBDC)]
crystallographic data	ref. [86, 105]
void fraction	0.717 [-]
accessible pore volume	0.5880 [cm^3/g]
nitrogen surface area	1290 [m^2/g], 1573 [m^2/cm^3]

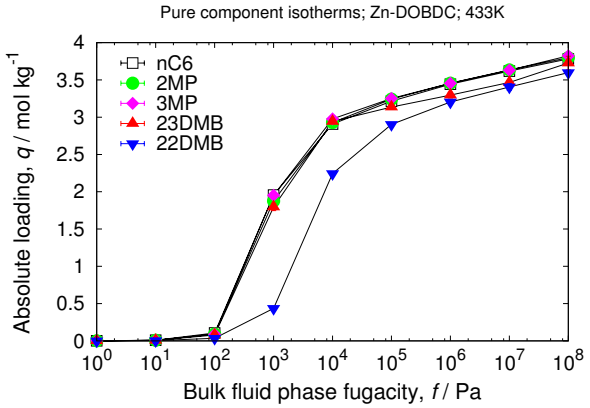

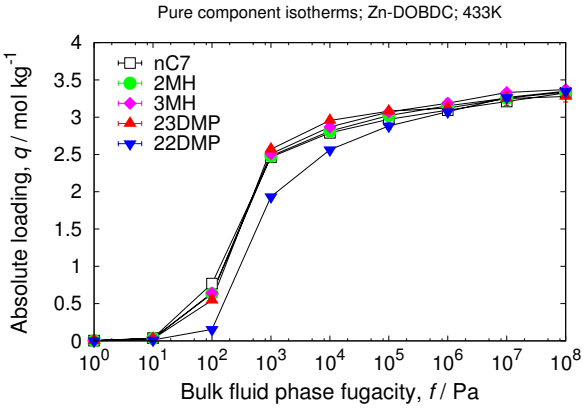

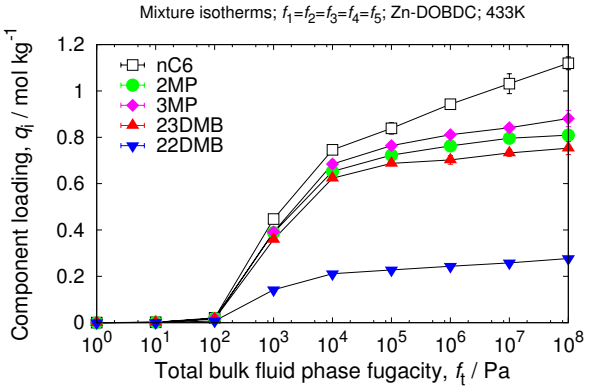

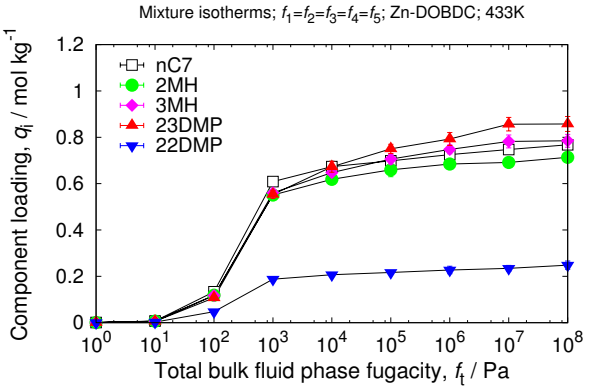

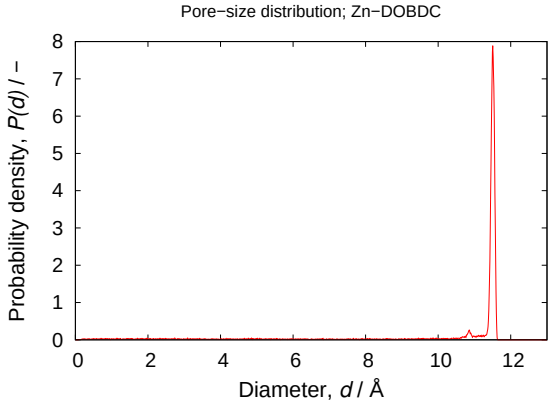

4.39 Co-DOBDC (also known as CoMOF-74 and CPO-27-Co)

unit cell size	$a = 25.885$ [Å], $b = 25.885$ [Å], $c = 6.8058$ [Å]
unit cell angles	$\alpha = \beta = 90[^\circ]$, $\gamma = 120[^\circ]$
framework density	1180.57 [kg/m^3]
description	Co_2(DOBDC)
crystallographic data	ref. [105]
void fraction	0.704 [-]
accessible pore volume	0.596 [cm^3/g]
nitrogen surface area	1340 [m^2/g], 1582 [m^2/cm^3]

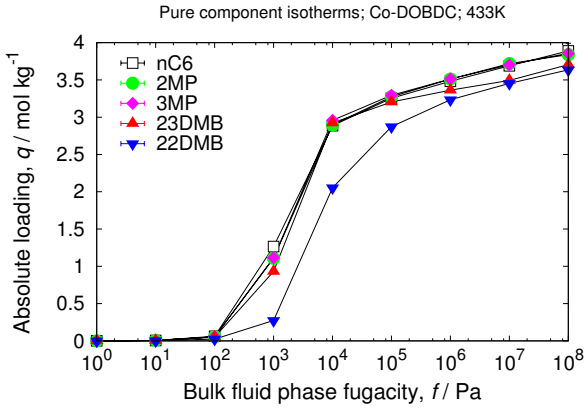

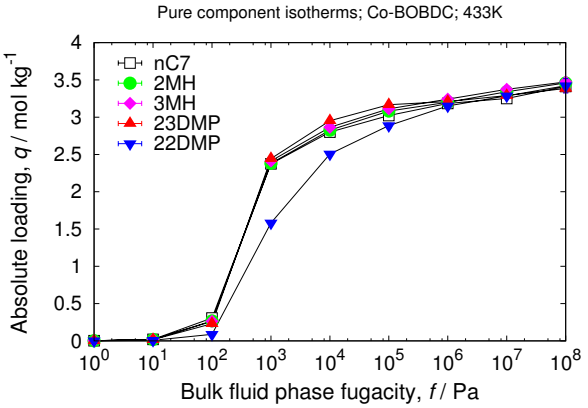

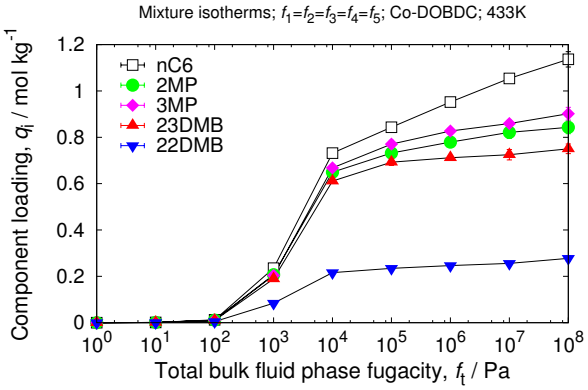

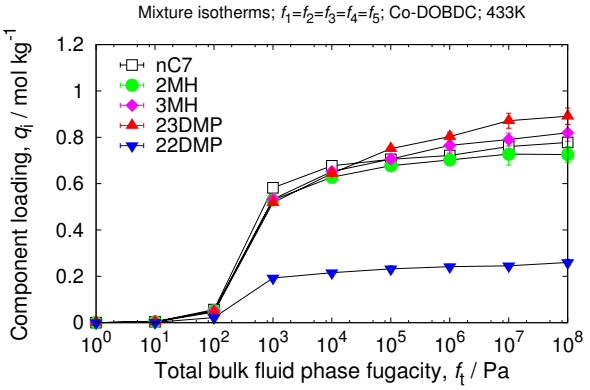

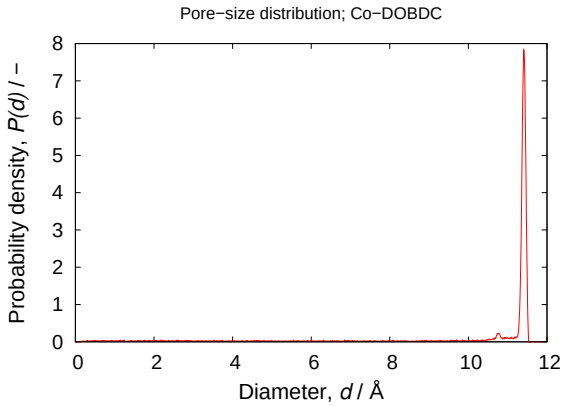

4.40 Cd_3BTB_2

unit cell size	$a = 10.4595$ [Å], $b = 14.392$ [Å], $c = 14.7634$ [Å]
unit cell angles	$\alpha = 69.608[^\circ]$, $\beta = 82.476[^\circ]$, $\gamma = 88.043[^\circ]$
framework density	971.43 [kg/m^3]
description	Cd_3BTB_2
crystallographic data	ref. [106]
void fraction	0.597 [-]
accessible pore volume	0.6150 [cm^3/g]
nitrogen surface area	2091 [m^2/g], 2031 [m^2/cm^3]

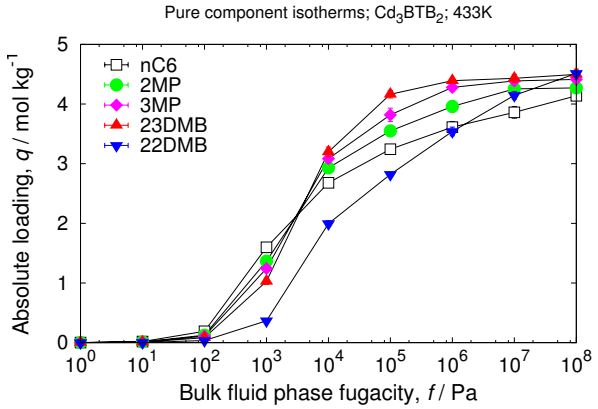

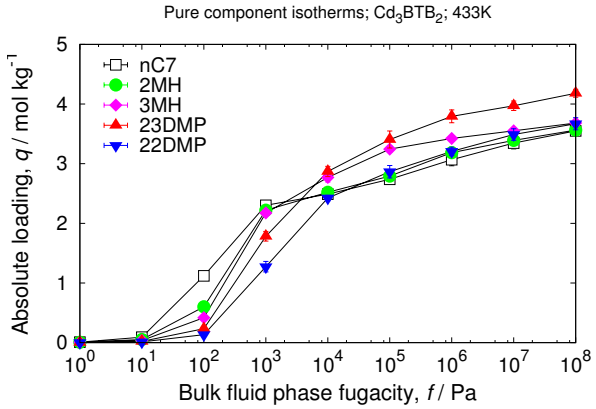

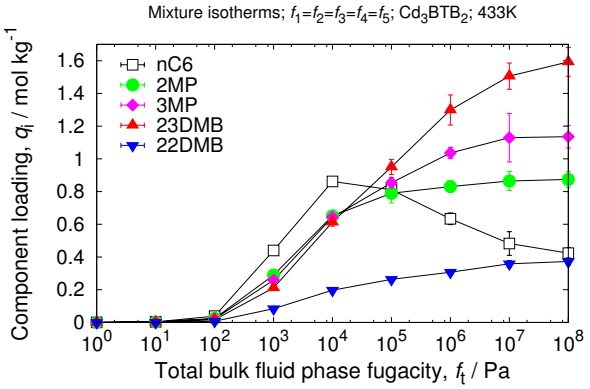

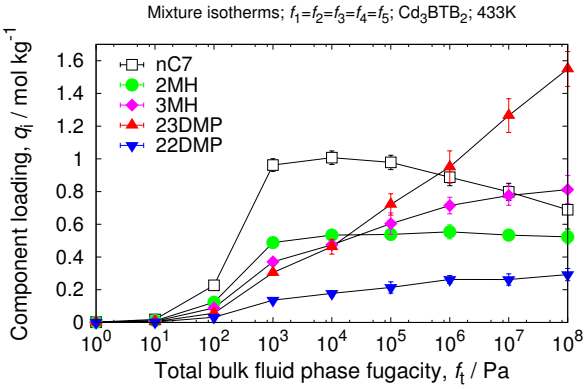

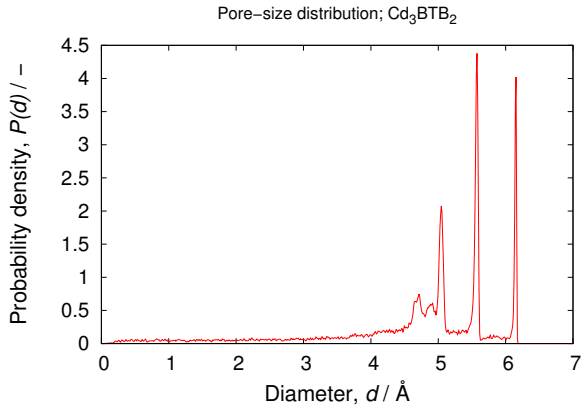

4.41 UMCM-1

unit cell size	$a = 41.5262$ [Å], $b = 41.5262$ [Å], $c = 17.4916$ [Å]
unit cell angles	$\alpha = \beta = 90[^\circ]$, $\gamma = 120[^\circ]$
framework density	389.91 [kg/m^3]
description	$Zn_4O(BDC)(BTB)_{4/3}$
crystallographic data	ref. [107]
void fraction	0.865 [-]
accessible pore volume	2.2186 [cm^3/g]
nitrogen surface area	4476 [m^2/g], 1745 [m^2/cm^3]

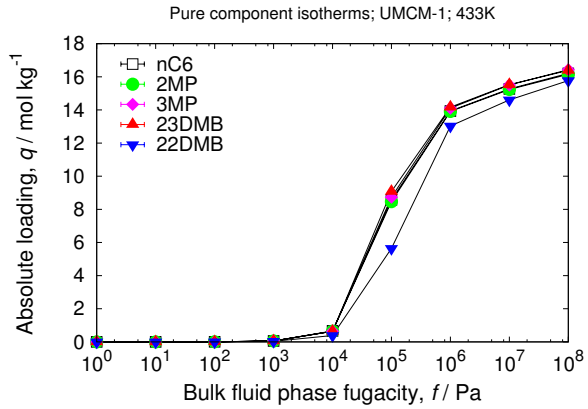

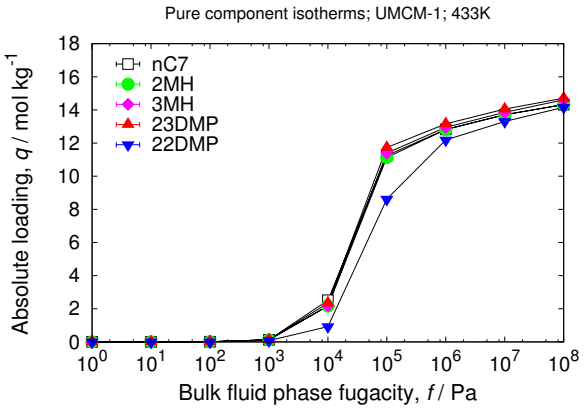

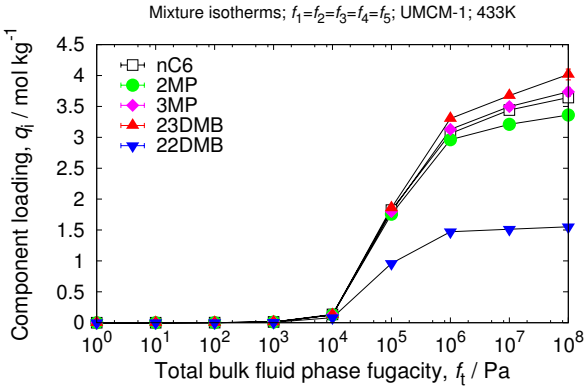

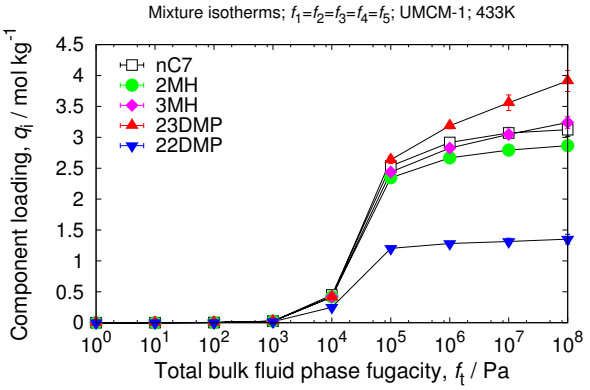

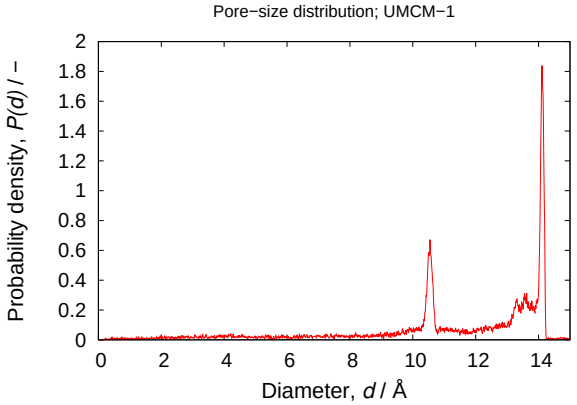

Covalent organic frameworks (COFs) are based on organic building units connected by covalent bonds. These materials retain the attractive characteristics of MOFs but have even lower crystal densities. Unlike MOFs, COFs are entirely composed of light elements (H, B, C, and O) that are linked by strong covalent bonds (B-O, C-C, and B-C) to make a highly porous class of materials. Indeed, one member of this class has the highest pore volume ever reported for a crystalline solid (5.4592 [cm3/g] for COF-108 shown below).

5
COFs

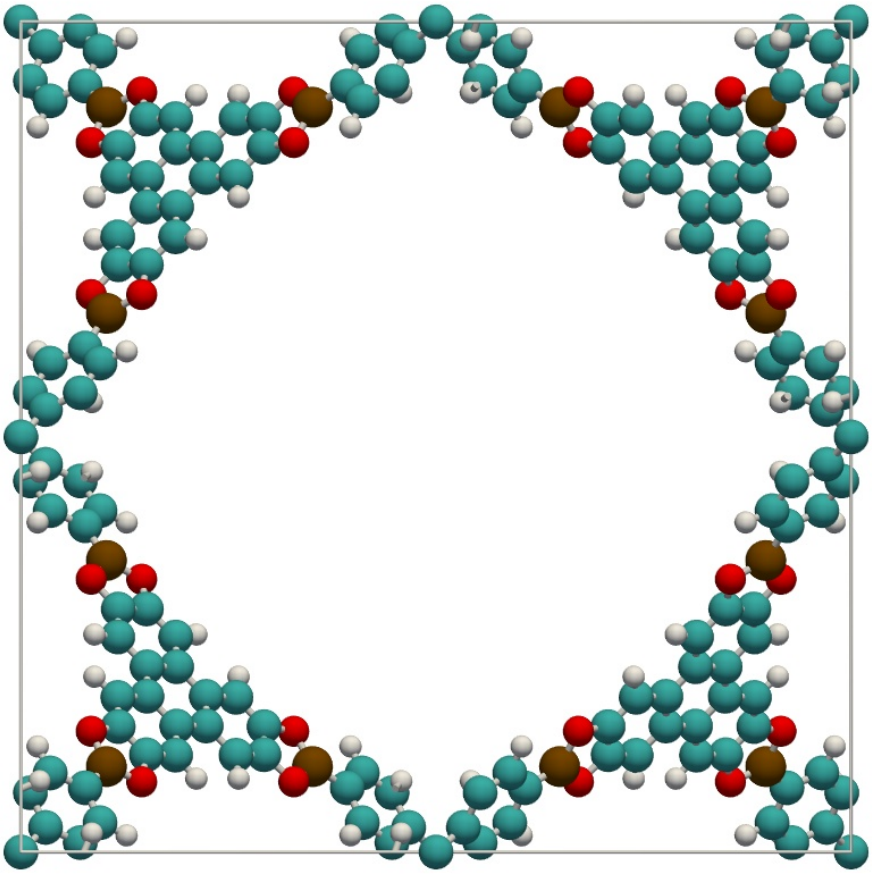

5.1 COF-1

unit cell size	$a = 15.6529$ [Å], $b = 15.6529$ [Å], $c = 6.7005$ [Å]
unit cell angles	$\alpha = \beta = 90[^\circ]$, $\gamma = 120[^\circ]$
framework density	909.01 [kg/m^3]
description	$(C_3H_2BO)_6 \cdot (C_9H_{12})_1$
crystallographic data	ref. [108]
void fraction	0.335 [-]
accessible pore volume	0.3682 [cm^3/g]
nitrogen surface area	948 [m^2/g], 861 [m^2/cm^3]

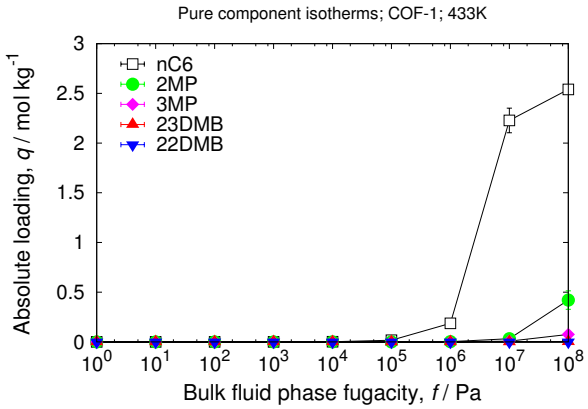

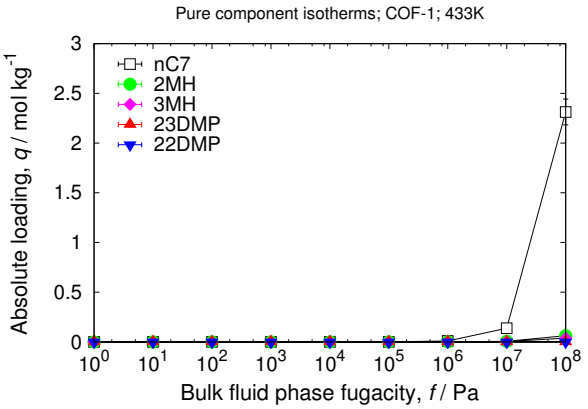

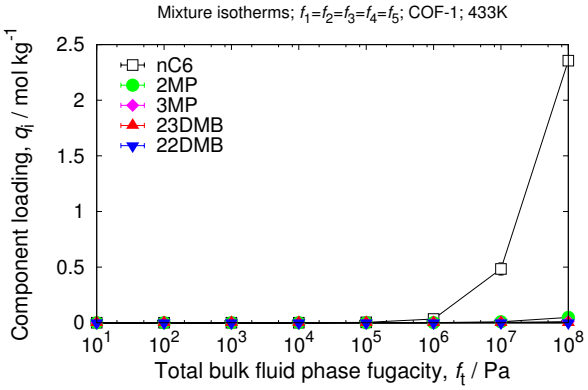

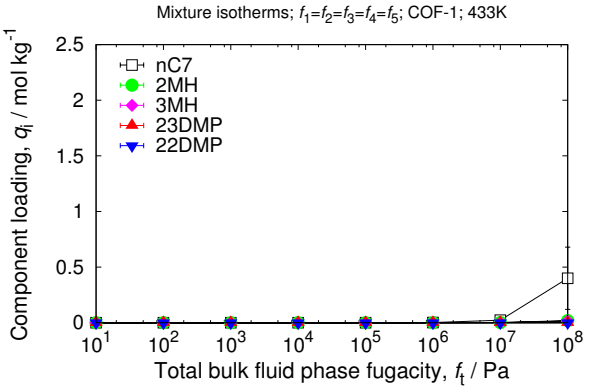

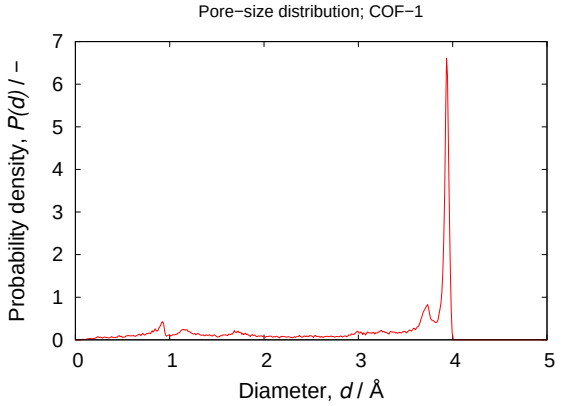

5.2 COF-5

unit cell size	$a = 30.0198$ [Å], $b = 30.0198$ [Å], $c = 3.404$ [Å]
unit cell angles	$\alpha = \beta = 90[^\circ], \gamma = 120[^\circ]$
framework density	581.06 [kg/m^3]
description	$C_9H_4BO_2$
crystallographic data	ref. [108]
void fraction	0.679 [-]
accessible pore volume	1.1688 [cm^3/g]
nitrogen surface area	2159 [m^2/g], 1255 [m^2/cm^3]

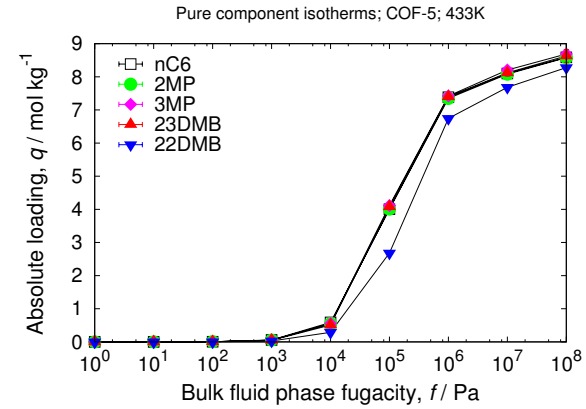

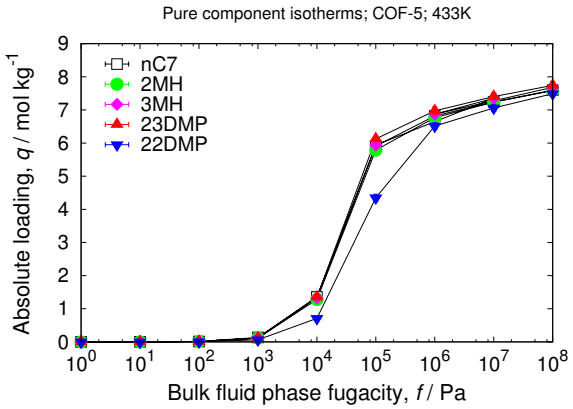

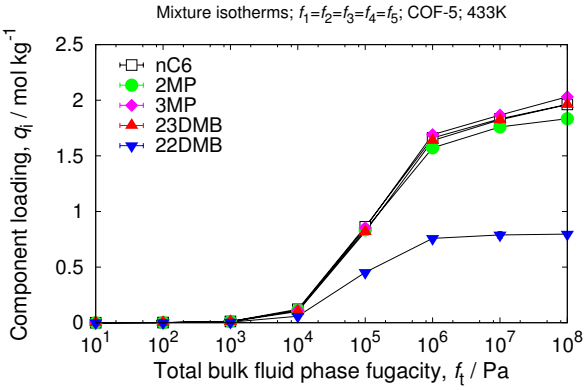

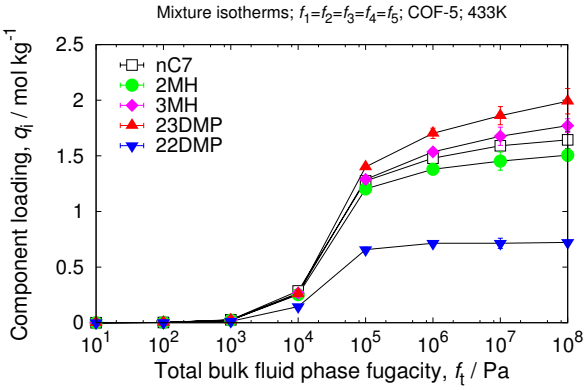

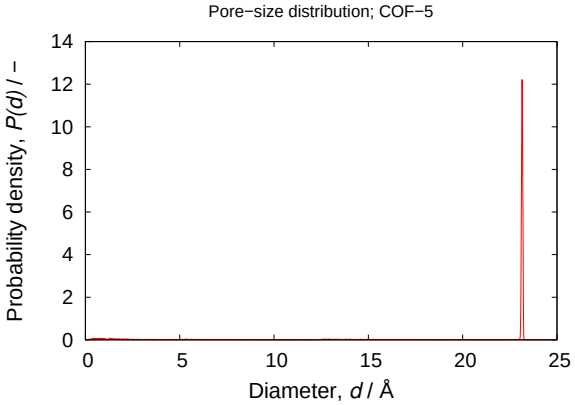

5.3 COF-102

unit cell size	$a = 27.1771$ [Å], $b = 27.1771$ [Å], $c = 27.1771$ [Å]
unit cell angles	$\alpha = \beta = \gamma = 90[^\circ]$
framework density	420.55 [kg/m^3]
description	$C_{25}H_{16}B_4O_4$
crystallographic data	ref. [109]
void fraction	0.795 [-]
accessible pore volume	1.8906 [cm^3/g]
nitrogen surface area	5159 [m^2/g], 2170 [m^2/cm^3]

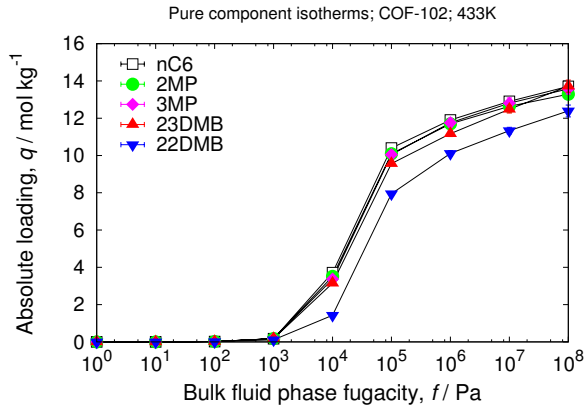

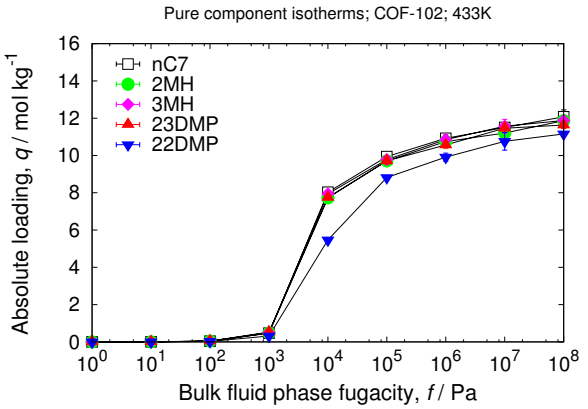

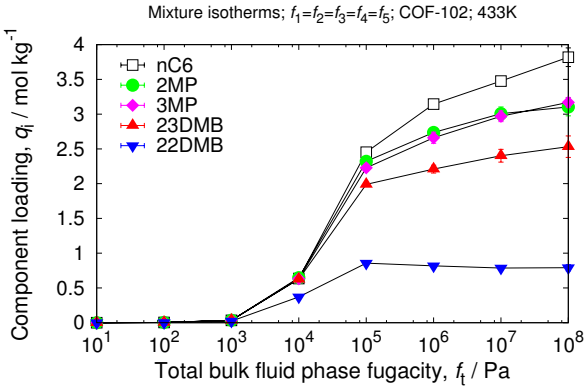

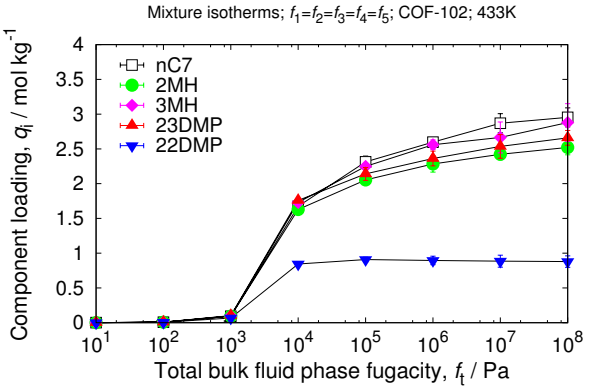

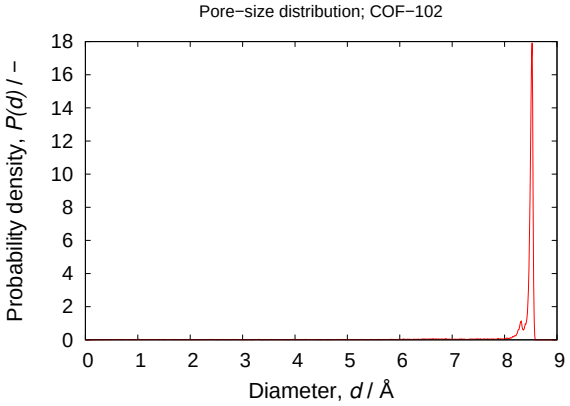

5.4 COF-103

unit cell size	$a = 28.2477$ [Å], $b = 28.2477$ [Å], $c = 28.2477$ [Å]
unit cell angles	$\alpha = \beta = \gamma 90[^\circ]$
framework density	388.73 [kg/m^3]
description	$C_{24}H_{16}B_4O_4Si$
crystallographic data	ref. [109]
void fraction	0.810 [-]
accessible pore volume	2.0845 [cm^3/g]
nitrogen surface area	5330 [m^2/g], 2072 [m^2/cm^3]

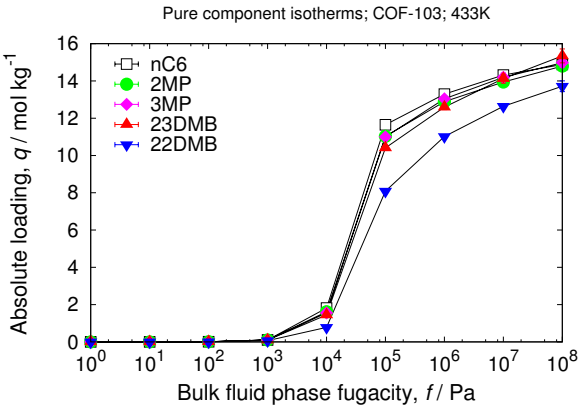

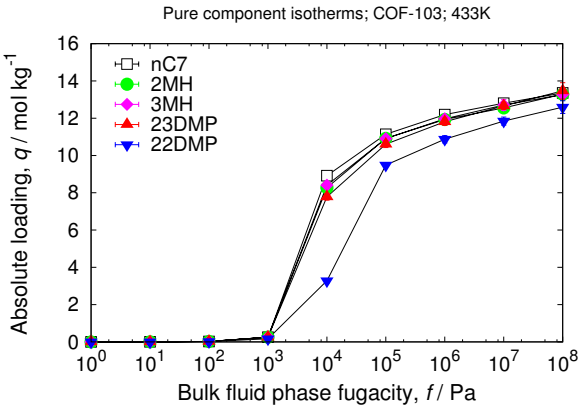

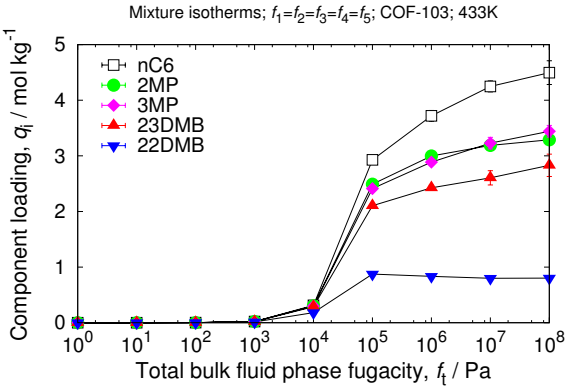

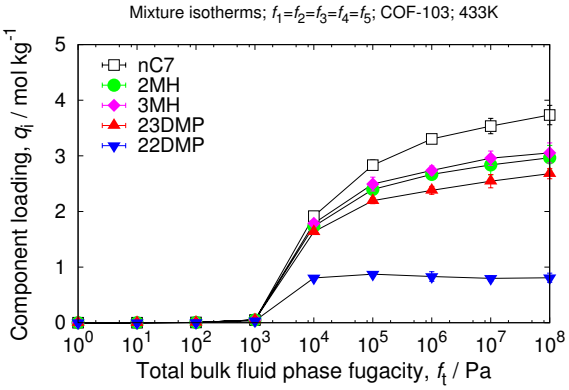

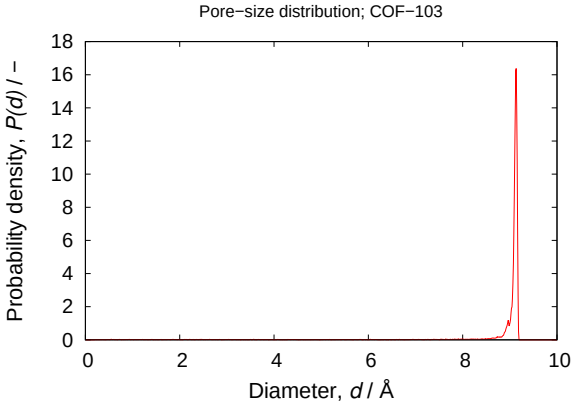

5.5 COF-105

unit cell size	$a = 44.886$ [Å], $b = 44.886$ [Å], $c = 44.886$ [Å]
unit cell angles	$\alpha = \beta = \gamma = 90[^\circ]$
framework density	176.28 [kg/m^3]
description	$C_{48}H_{24}B_4O_8Si$
crystallographic data	ref. [109]
void fraction	0.923 [-]
accessible pore volume	5.2338 [cm^3/g]
nitrogen surface area	6739 [m^2/g], 1188 [m^2/cm^3]

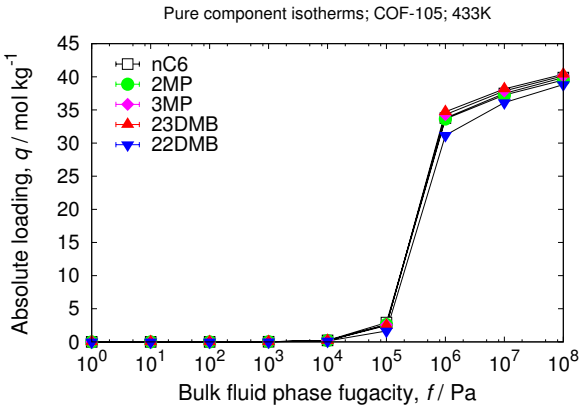

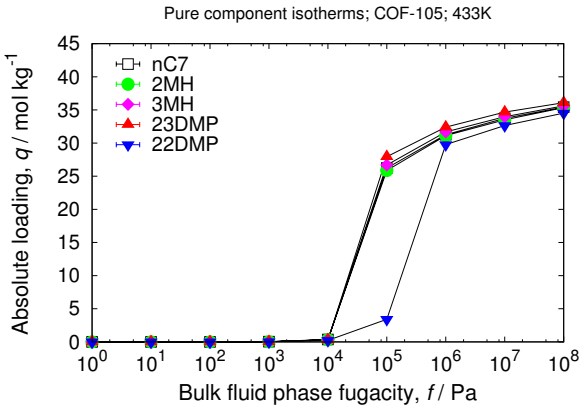

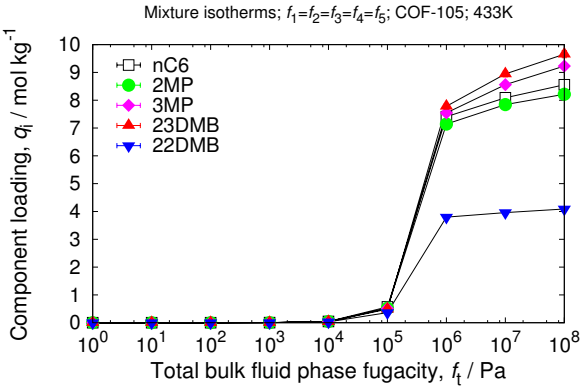

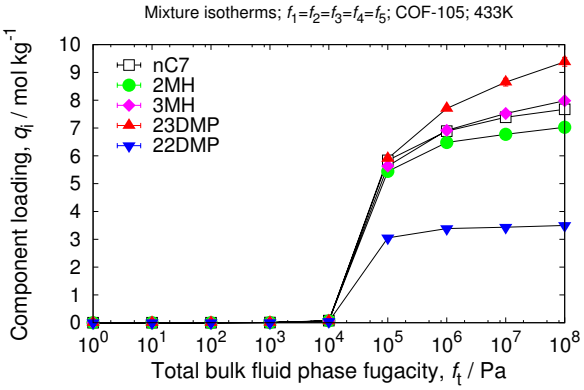

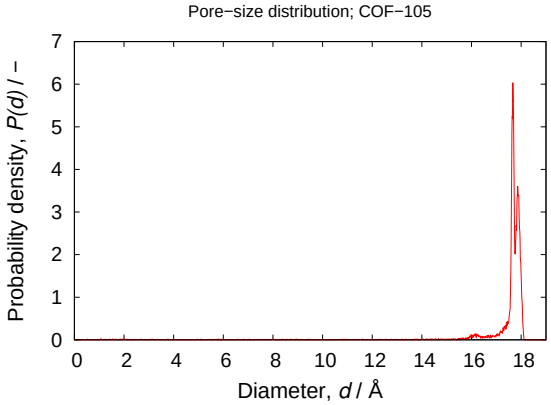

5.6 COF-108

unit cell size	$a = 28.401$ [Å], $b = 28.401$ [Å], $c = 28.401$ [Å]
unit cell angles	$\alpha = \beta = \gamma = 90[^\circ]$
framework density	170.48 [kg/m^3]
description	$C_{147}H_{72}B_{12}O_{24}$
crystallographic data	ref. [109]
void fraction	0.931 [-]
accessible pore volume	5.4592 [cm^3/g]
nitrogen surface area	6490 [m^2/g], 1106 [m^2/cm^3]

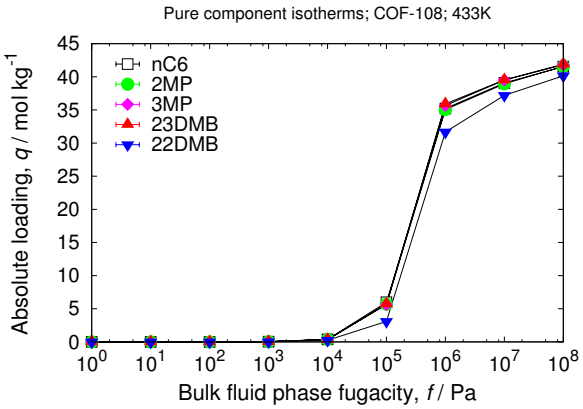

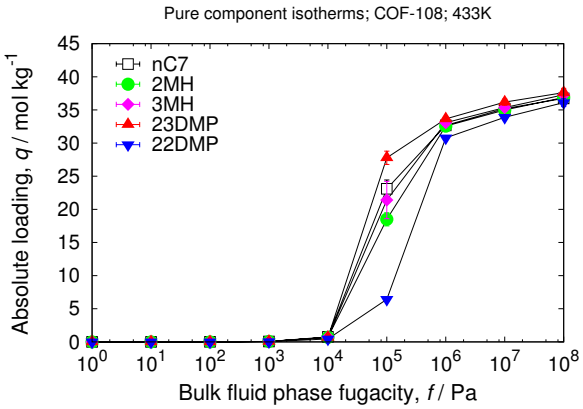

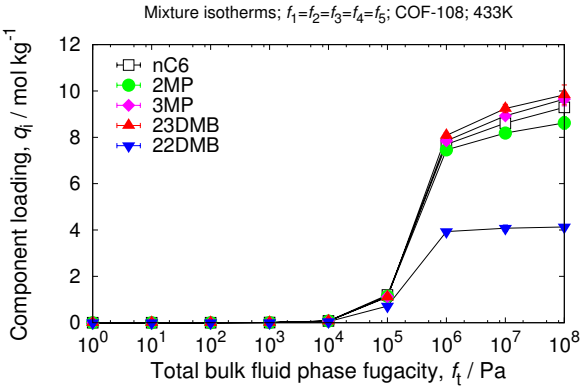

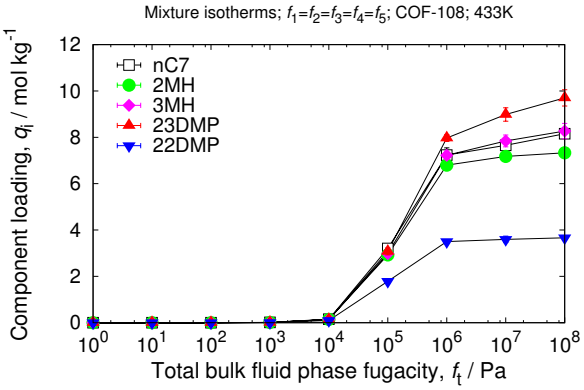

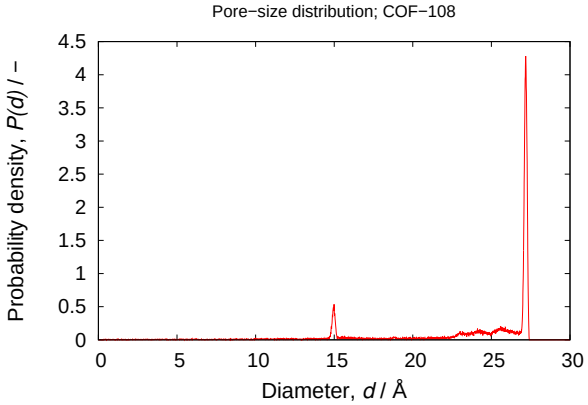

5.7 COF-202

unit cell size	$a = 30.1051$ [Å], $b = 30.1051$ [Å], $c = 30.1051$ [Å]
unit cell angles	$\alpha = \beta = \gamma = 90[^\circ]$
framework density	471.31 [kg/m^3]
description	$C_{107}H_{120}B_{12}O_{24}Si_8$
crystallographic data	ref. [110]
void fraction	0.639 [-]
accessible pore volume	1.3563 [cm^3/g]
nitrogen surface area	4781 [m^2/g], 2253 [m^2/cm^3]

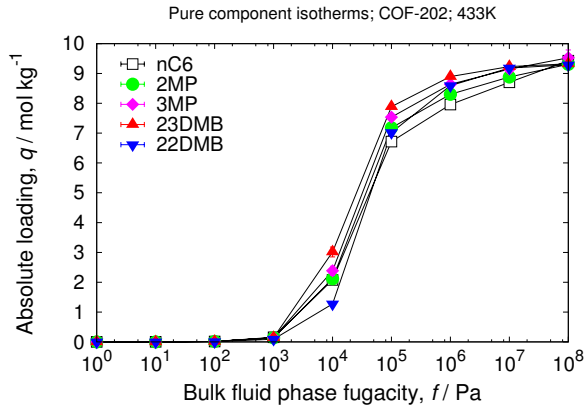

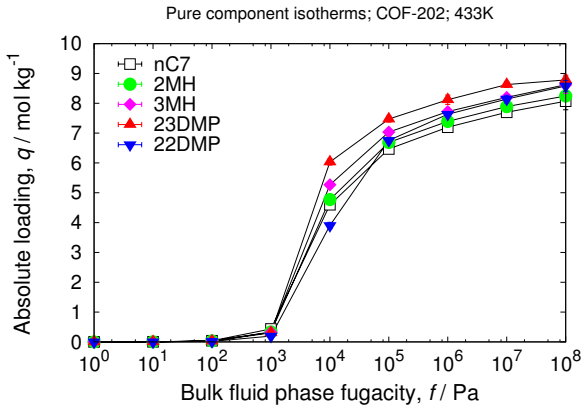

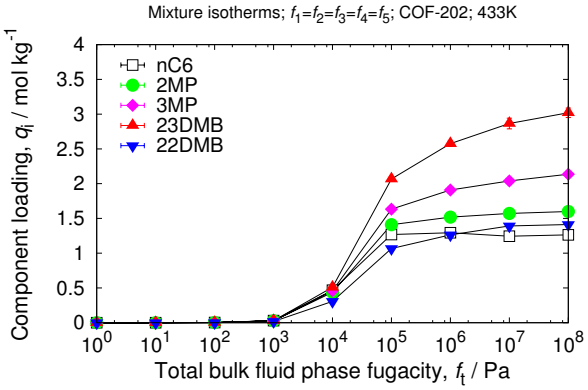

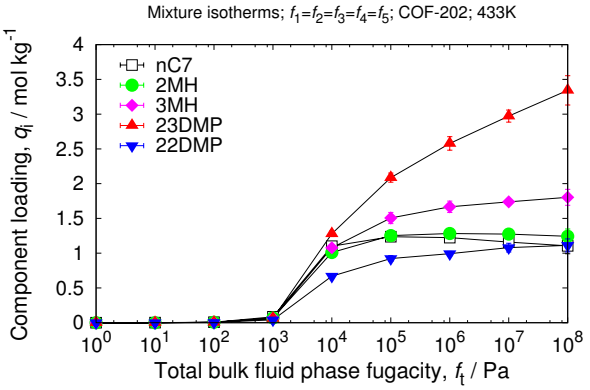

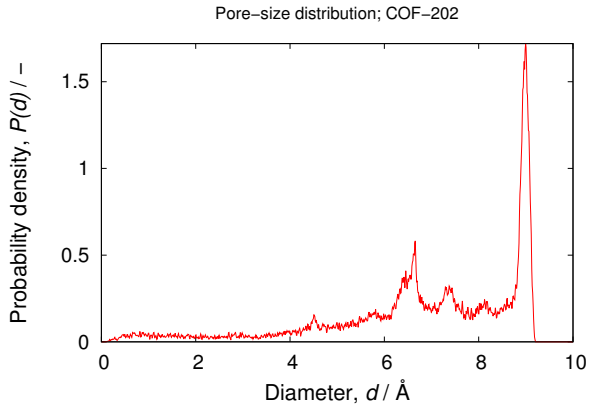

5.8 COF-300

unit cell size	$a = 28.127$ [Å], $b = 28.127$ [Å], $c = 8.879$ [Å]
unit cell angles	$\alpha = \beta = \gamma = 90[^\circ]$
framework density	545.306 [kg/m^3]
description	$C_{41}H_{28}N_4$
crystallographic data	ref. [111]
void fraction	0.637 [-]
accessible pore volume	1.1683 [cm^3/g]
nitrogen surface area	3453 [m^2/g], 1883 [m^2/cm^3]

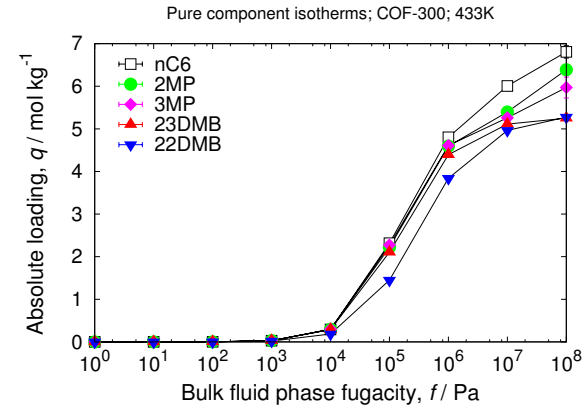

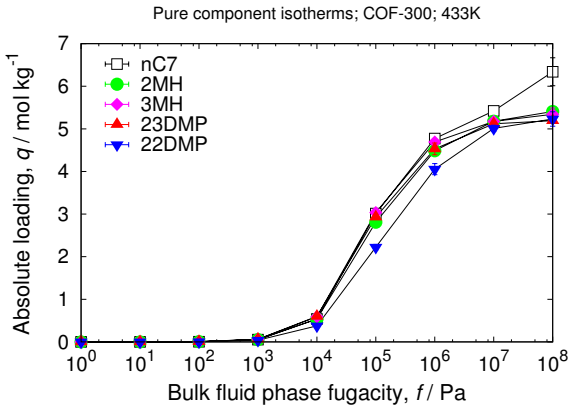

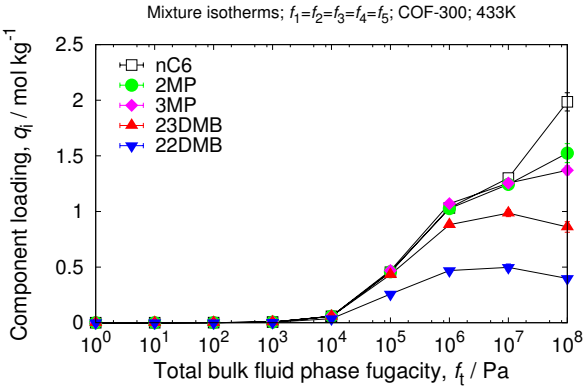

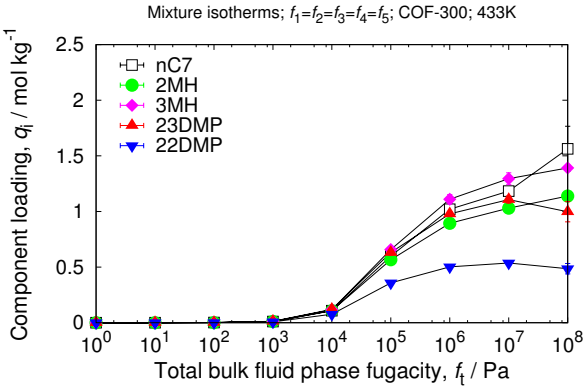

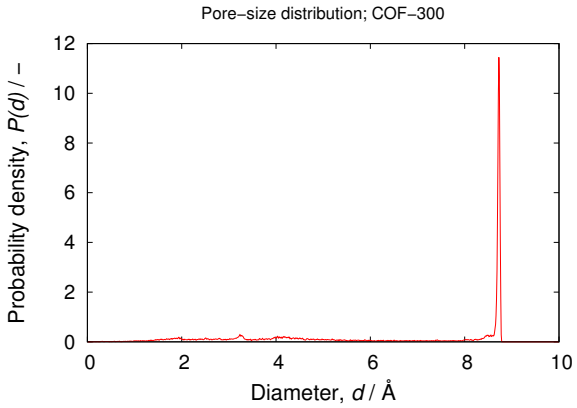

Zeolitic imidazolate frameworks (ZIFs) adopt crystalline architectures, where typically Zn^{2+} ions play the role of silicon and the imidazolate anions form bridges that mimic the role of oxygen in zeolites. Currently many distinct ZIFs have been synthesised, a subset of which possess the same framework topologies as zeolites. Most of the known ZIFs contain Zn or Co ions in combination with imidazolate or functionalized imidazolate anions. The picture shows the ZIF-69 structure.

6 ZIFs

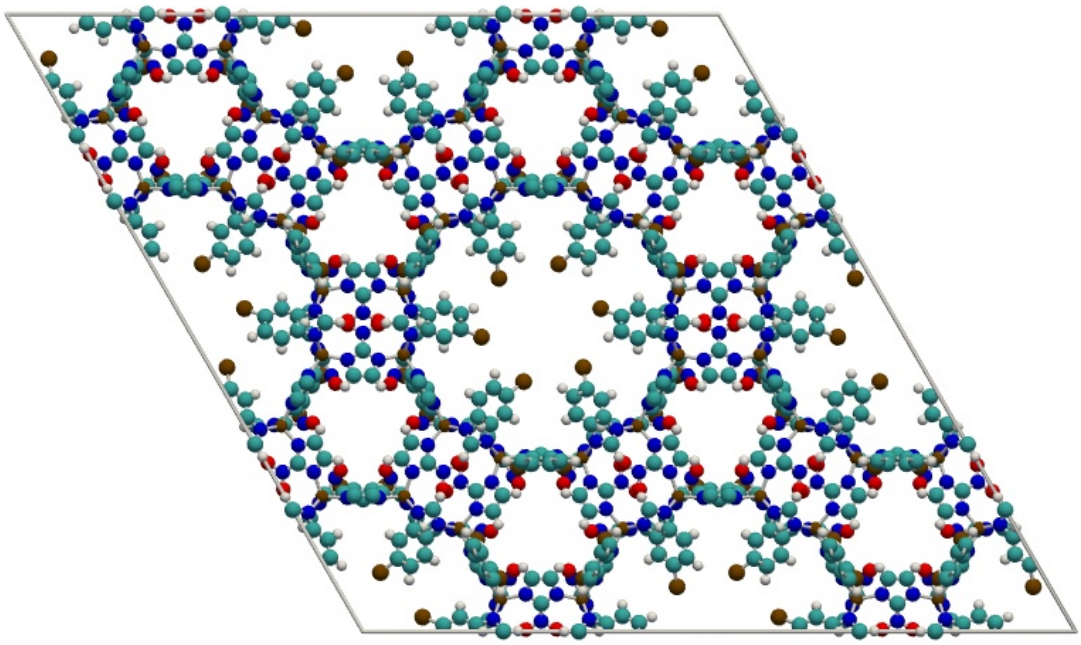

6.1 ZIF-8

unit cell size	$a = 16.991$ [Å], $b = 16.991$ [Å], $c = 16.991$ [Å]
unit cell angles	$\alpha = \beta = \gamma = 90[^\circ]$
framework density	924.59 [kg/m^3]
description	Zn(mIM)$_2$
crystallographic data	ref. [112]
void fraction	0.483 [-]
accessible pore volume	0.5222 [cm^3/g]
nitrogen surface area	1405 [m^2/g], 1299 [m^2/cm^3]

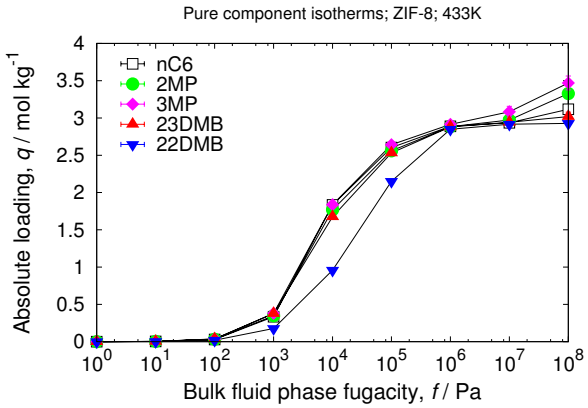

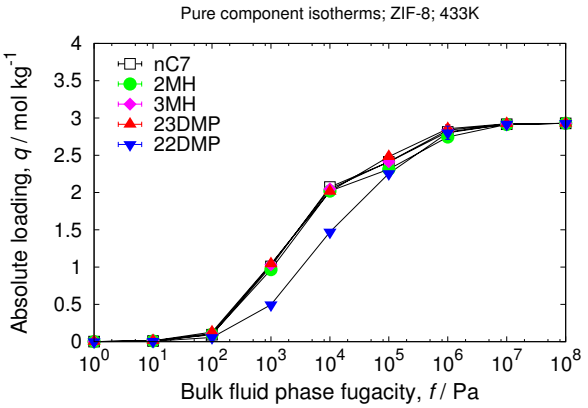

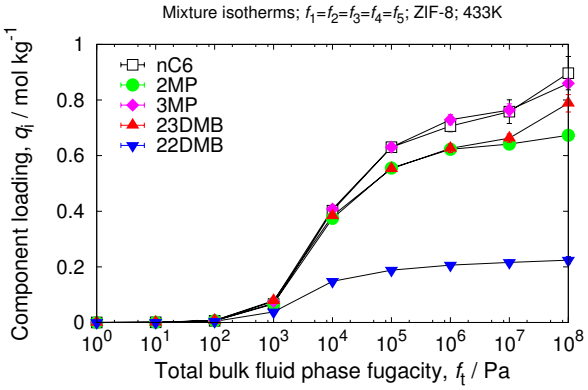

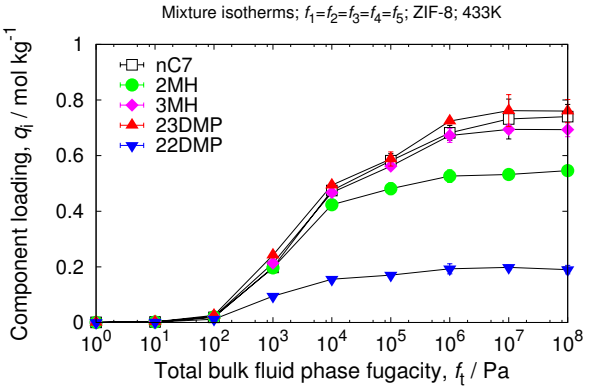

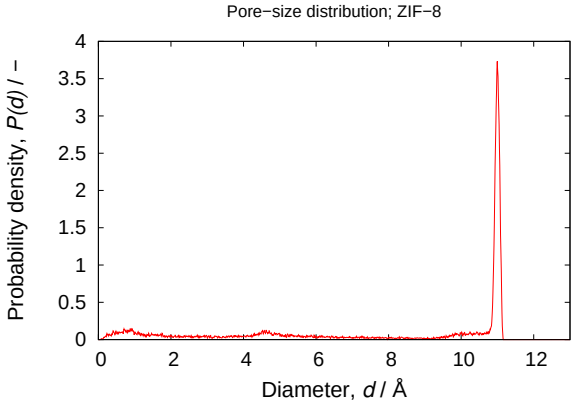

6.2 ZIF-10

unit cell size	$a = 27.0608$ [Å], $b = 27.0608$ [Å], $c = 19.406$ [Å]
unit cell angles	$\alpha = \beta = \gamma = 90[^\circ]$
framework density	746.15 [kg/m^3]
description	$Zn(IM)_2$
crystallographic data	ref. [112]
void fraction	0.594 [-]
accessible pore volume	0.796 [cm^3/g]
nitrogen surface area	2465 [m^2/g], 1840 [m^2/cm^3]

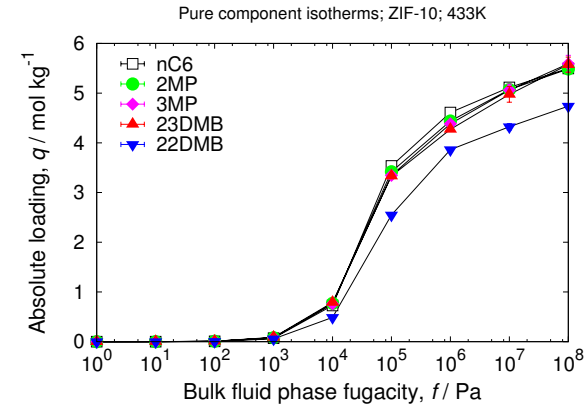

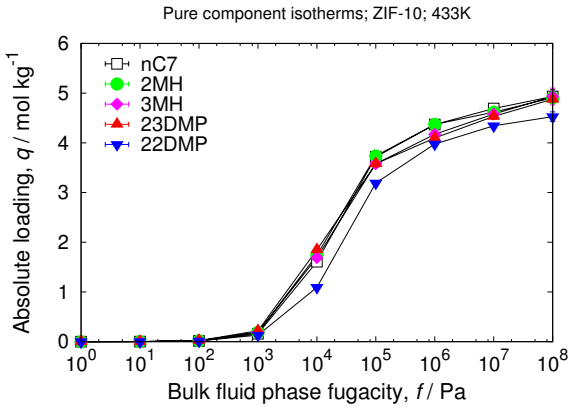

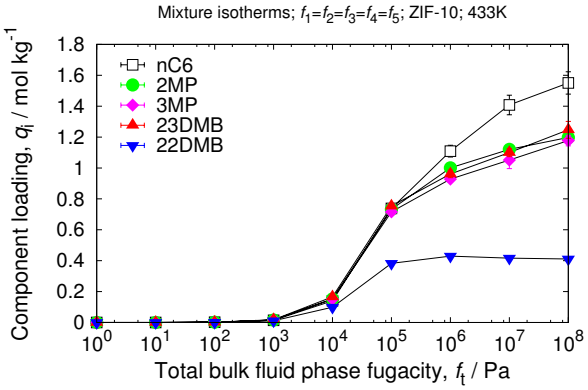

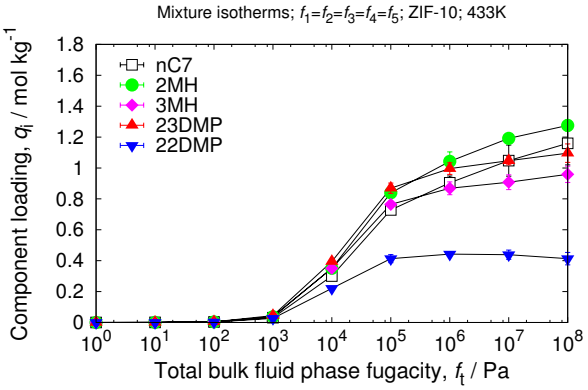

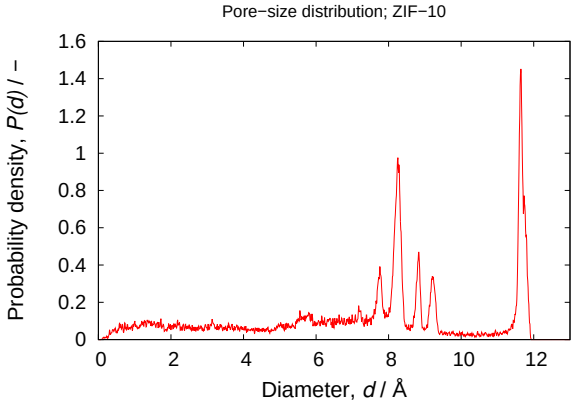

6.3 ZIF-20

unit cell size	$a = 45.4725$ [Å], $b = 45.4725$ [Å], $c = 45.4725$ [Å]
unit cell angles	$\alpha = \beta = \gamma = 90[^\circ]$
framework density	1029.51 [kg/m^3]
description	Zn(purinate)$_2$
crystallographic data	ref. [113]
void fraction	0.480 [-]
accessible pore volume	0.4660 [cm^3/g]
nitrogen surface area	1212 [m^2/g], 1247 [m^2/cm^3]

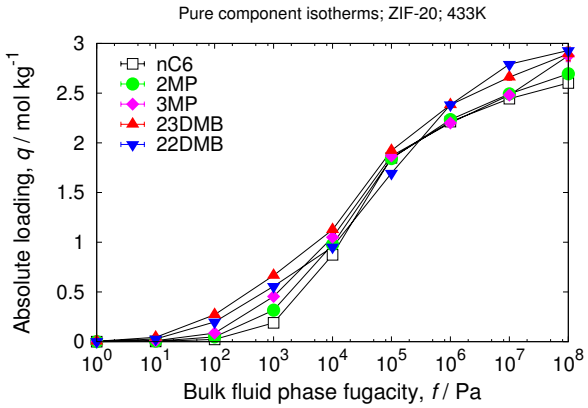

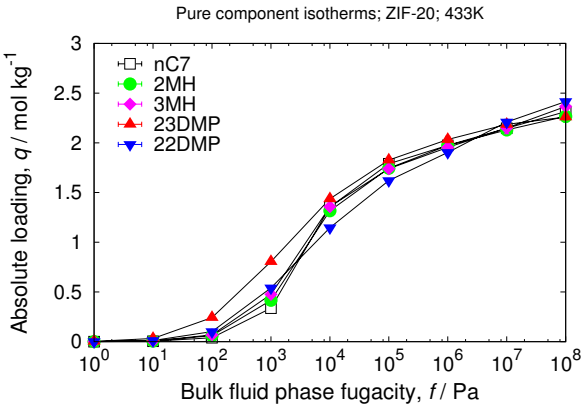

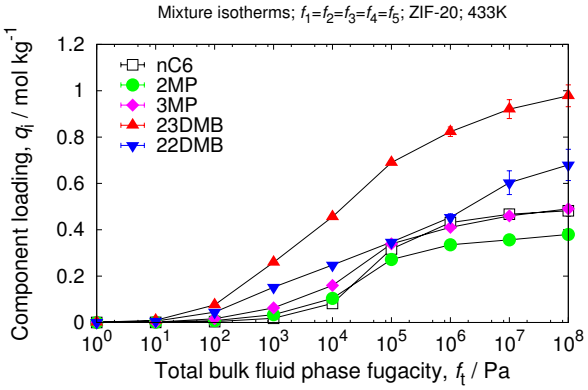

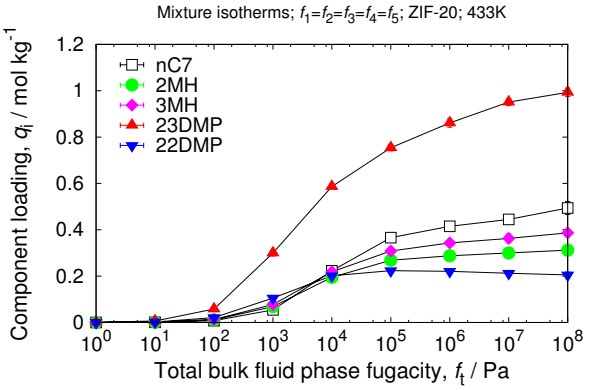

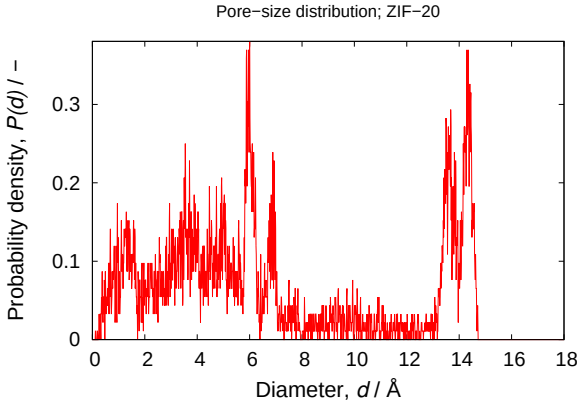

6.4 ZIF-68

unit cell size	$a = 26.6407$ [Å], $b = 26.6407$ [Å], $c = 18.4882$ [Å]
unit cell angles	$\alpha = \beta = 90[^\circ]$, $\gamma = 120[^\circ]$
framework density	1033.20 [kg/m^3]
description	Zn(bIM)(nIM)
crystallographic data	ref. [114]
void fraction	0.455 [-]
accessible pore volume	0.4408 [cm^3/g]
nitrogen surface area	1226 [m^2/g], 1266 [m^2/cm^3]

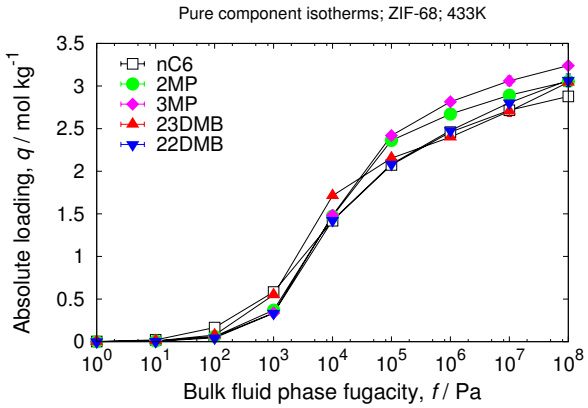

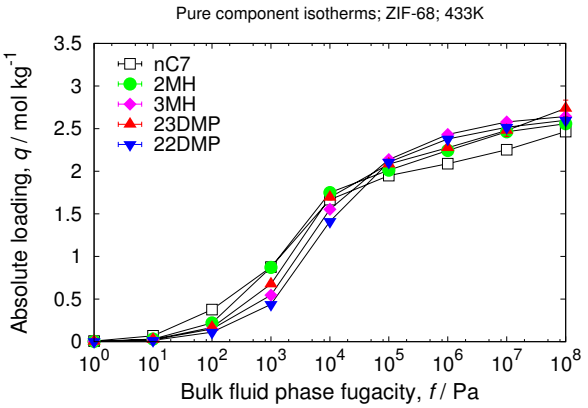

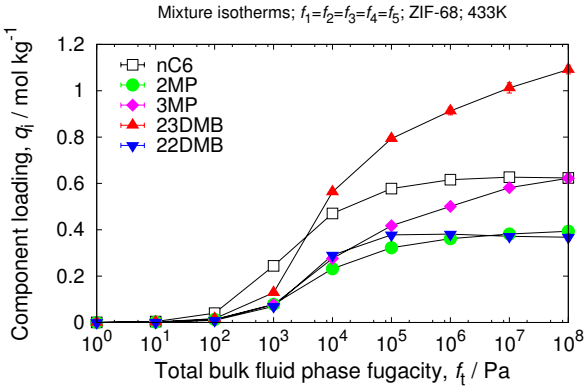

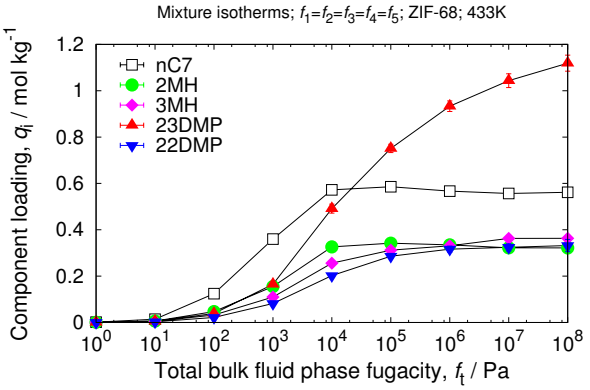

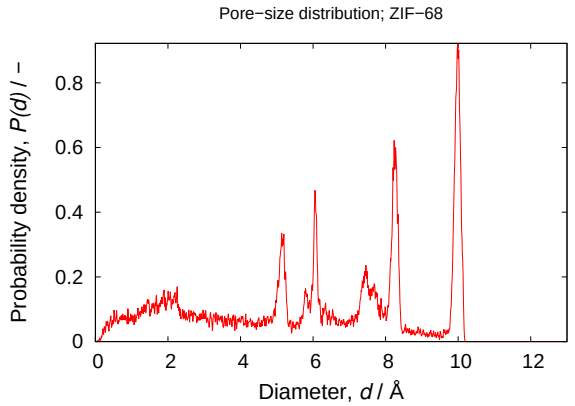

6.5 ZIF-69

unit cell size	$a = 26.084$ [Å], $b = 26.084$ [Å], $c = 19.4082$ [Å]
unit cell angles	$\alpha = \beta = 90[^\circ]$, $\gamma = 120[^\circ]$
framework density	1103.28 [kg/m^3]
description	Zn(cbIM)(nIM)
crystallographic data	ref. [114]
void fraction	0.408 [-]
accessible pore volume	0.3701 [cm^3/g]
nitrogen surface area	1075 [m^2/g], 1232 [m^2/cm^3]

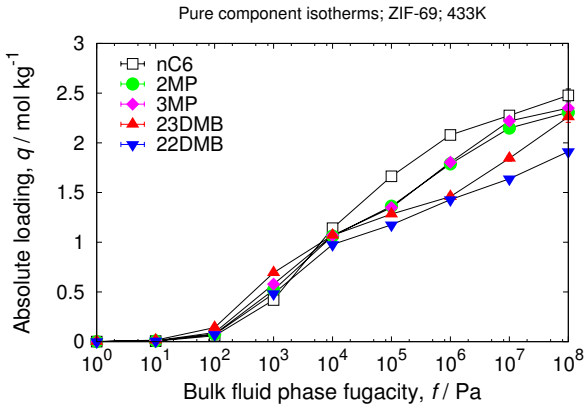

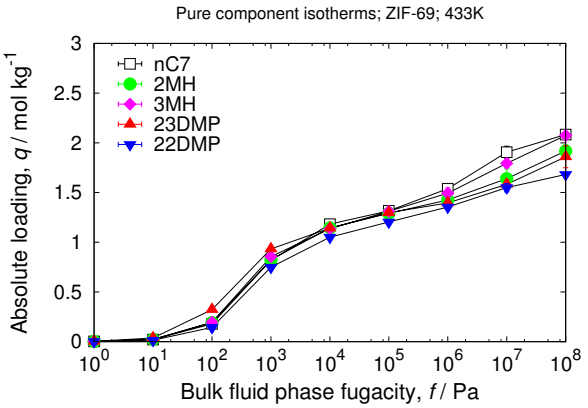

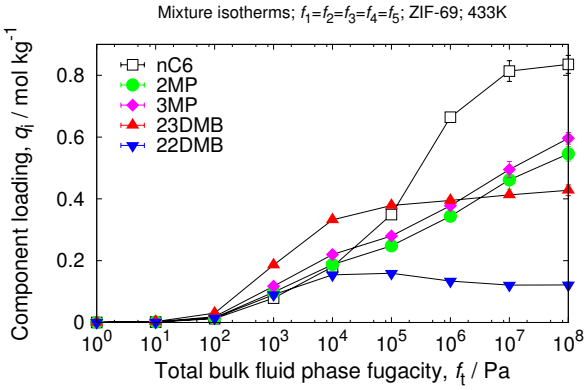

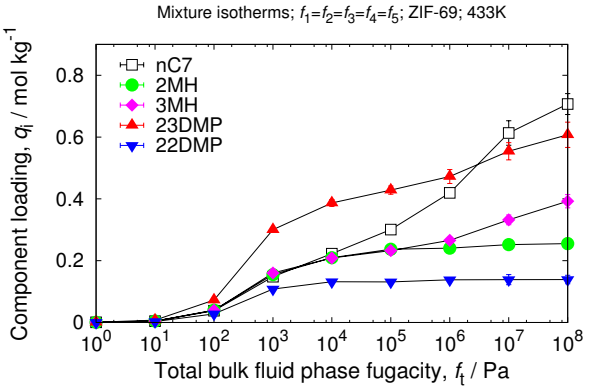

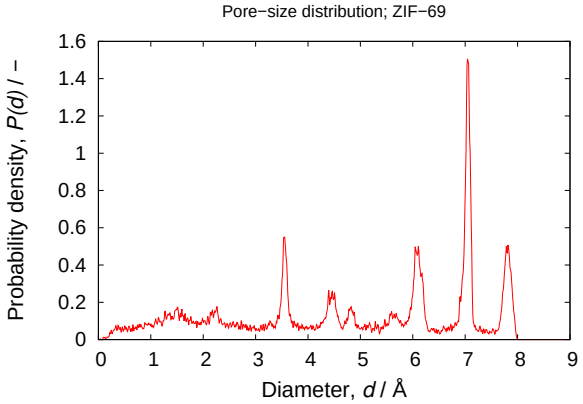

6.6 ZIF-71

unit cell size	$a = 28.5539$ [Å], $b = 28.5539$ [Å], $c = 28.5539$ [Å]
unit cell angles	$\alpha = \beta = \gamma = 90[^\circ]$
framework density	984.22 [kg/m^3]
description	Zn(dcIM)$_2$
crystallographic data	ref. [114]
void fraction	0.494 [-]
accessible pore volume	0.5019 [cm^3/g]
nitrogen surface area	1131 [m^2/g], 1306 [m^2/cm^3]

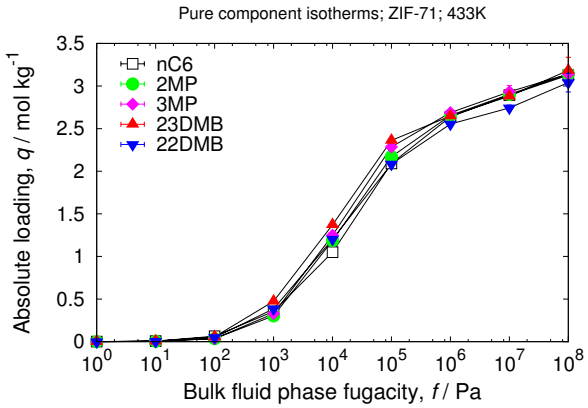

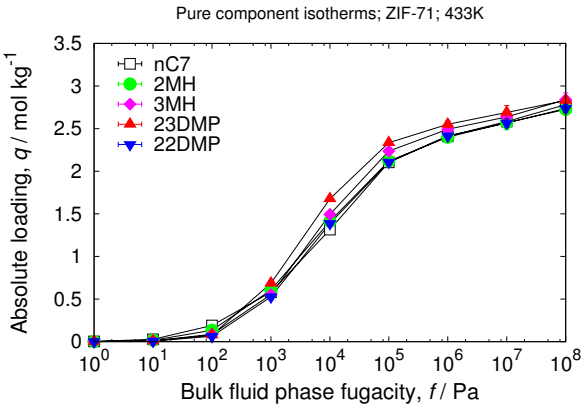

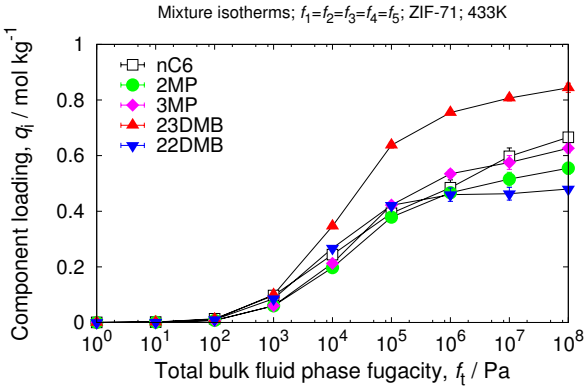

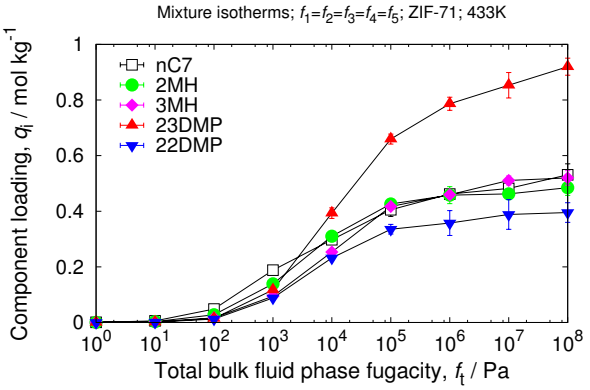

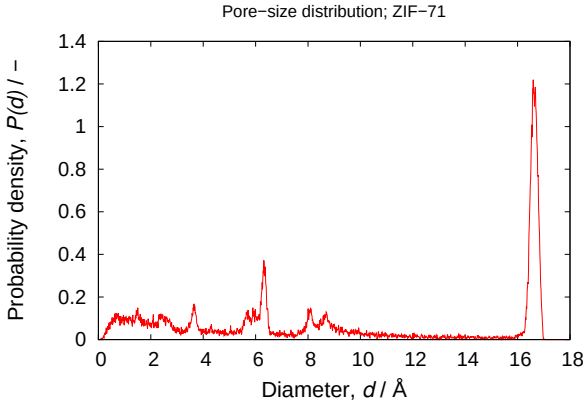

6.7 ZIF-77

unit cell size	$a = 11.1248$ [Å], $b = 22.3469$ [Å], $c = 24.9087$ [Å]
unit cell angles	$\alpha = \beta = \gamma = 90[^\circ]$
framework density	1552.86 [kg/m^3]
crystallographic data	ref. [114]
description	$Zn(nIM)_2$
void fraction	0.293 [-]
accessible pore volume	0.1889 [cm^3/g]
nitrogen surface area	541 [m^2/g], 841 [m^2/cm^3]

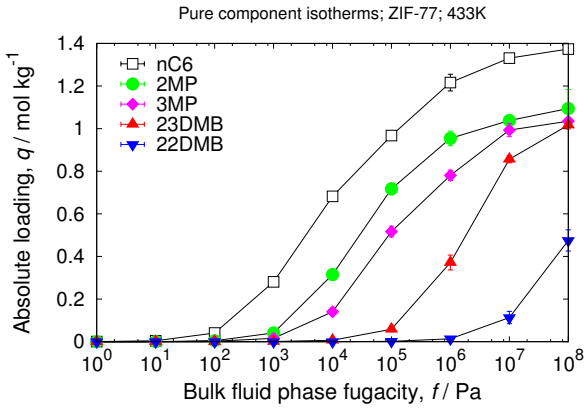

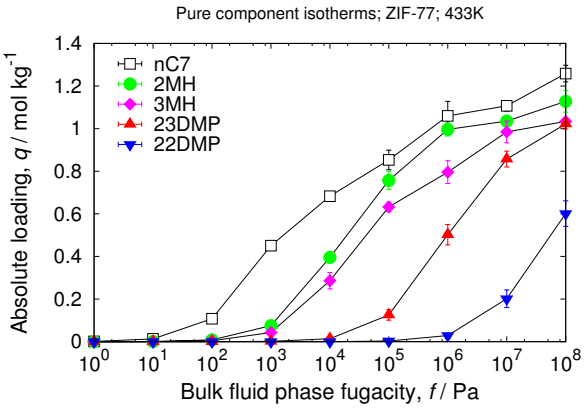

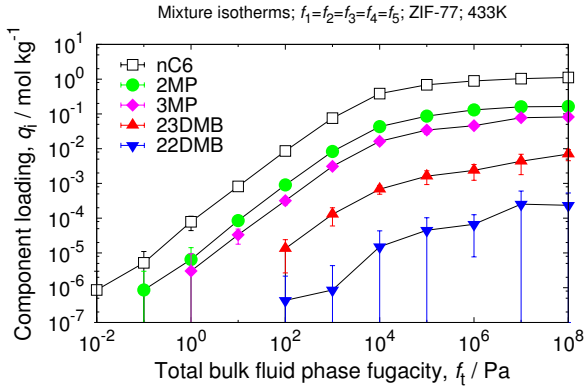

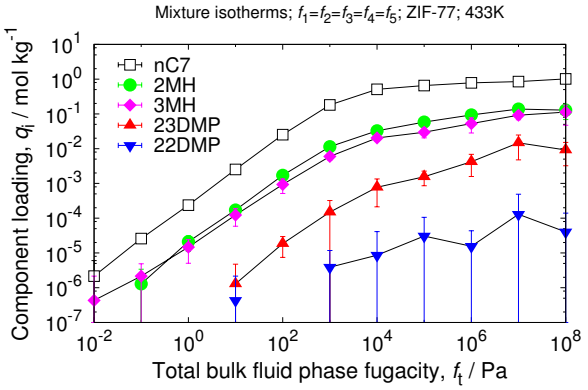

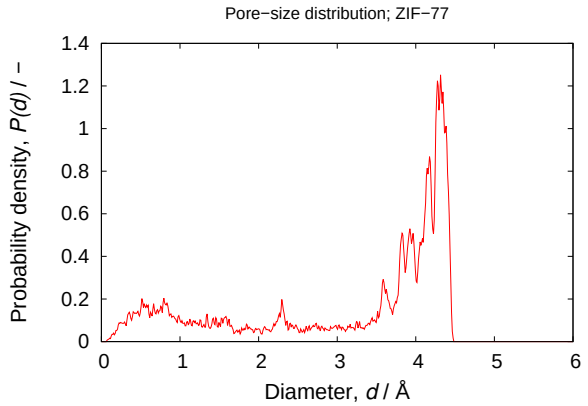

6.8 ZIF-80

unit cell size	$a = 26.307$ [Å], $b = 26.307$ [Å], $c = 19.361$ [Å]
unit cell angles	$\alpha = \beta = 90[^\circ]$, $\gamma = 120[^\circ]$
framework density	990.87 [kg/m^3]
crystallographic data	ref. [115]
description	Zn(dcIM)(nIM)
crystallographic data	ref. [116]
void fraction	0.495 [-]
accessible pore volume	0.4993 [cm^3/g]
nitrogen surface area	1374 [m^2/g], 1479 [m^2/cm^3]

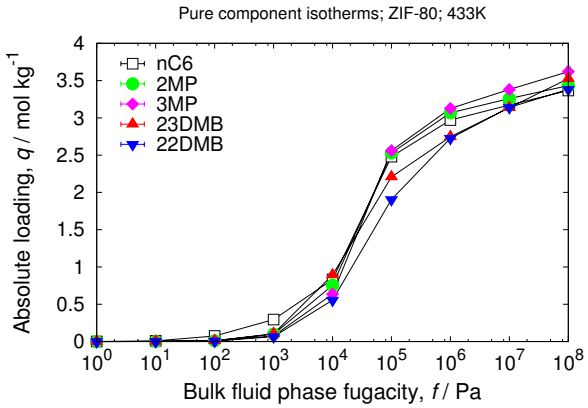

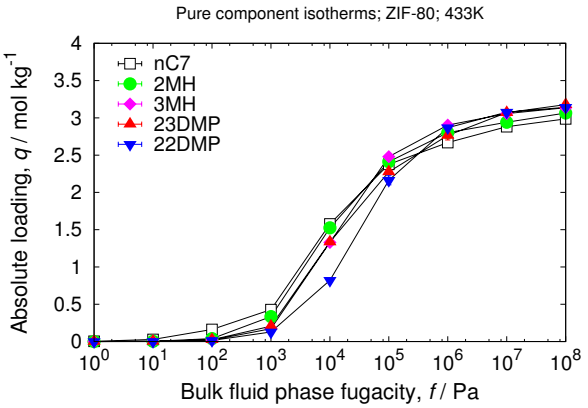

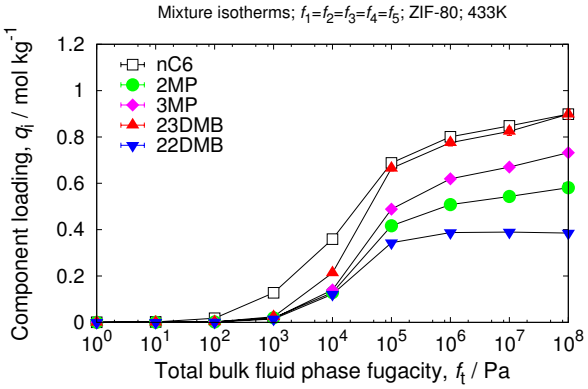

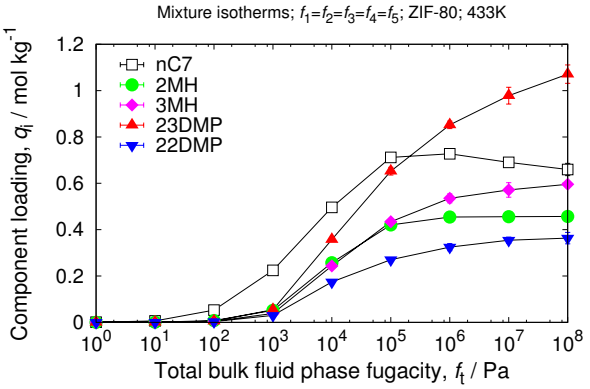

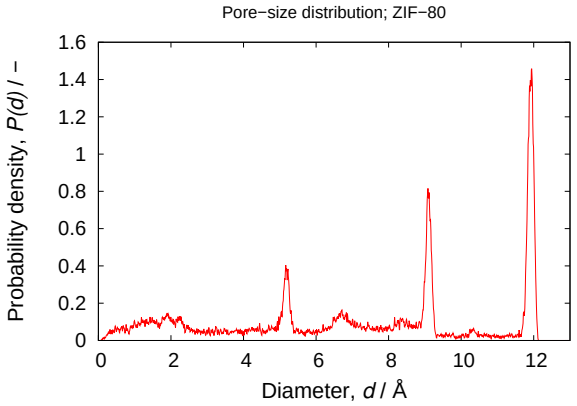

6.9 ZIF-93

unit cell size	$a = 28.3565$ [Å], $b = 28.3565$ [Å], $c = 28.3565$ [Å]
unit cell angles	$\alpha = \beta = \gamma = 90[^\circ]$
framework density	991.45 [kg/m^3]
description	Zn(4me5alIM)$_2$
crystallographic data	ref. [115]
void fraction	0.417 [-]
accessible pore volume	0.4203 [cm^3/g]
nitrogen surface area	1046 [m^2/g], 1037 [m^2/cm^3]

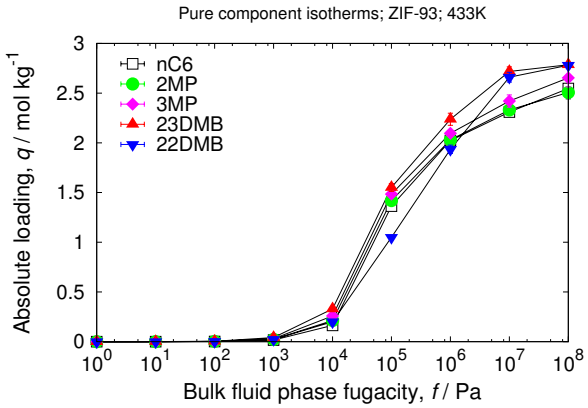

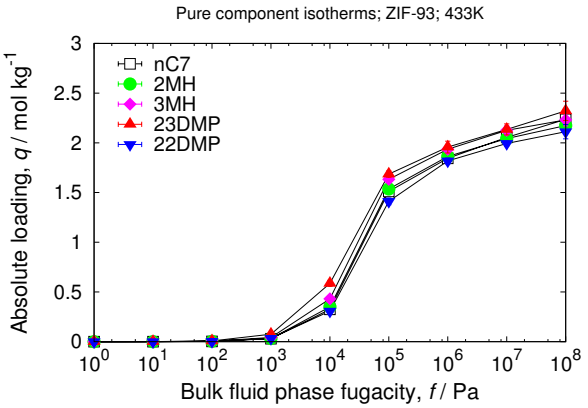

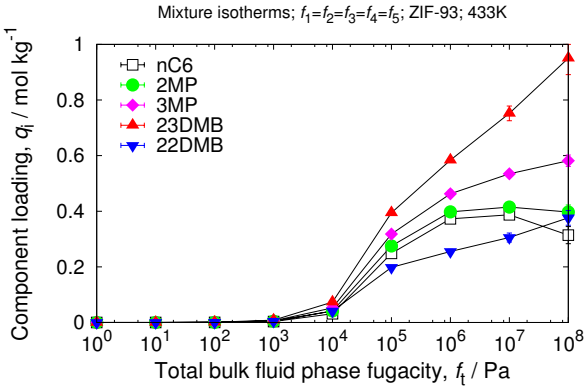

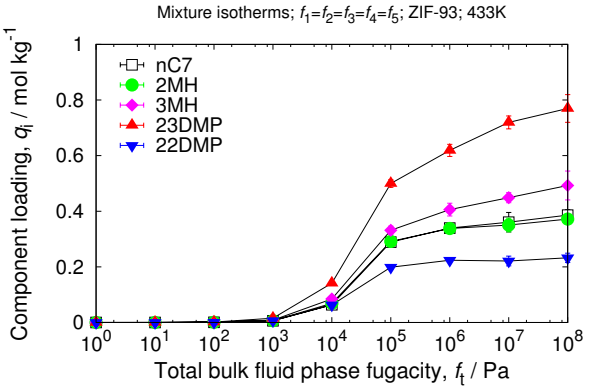

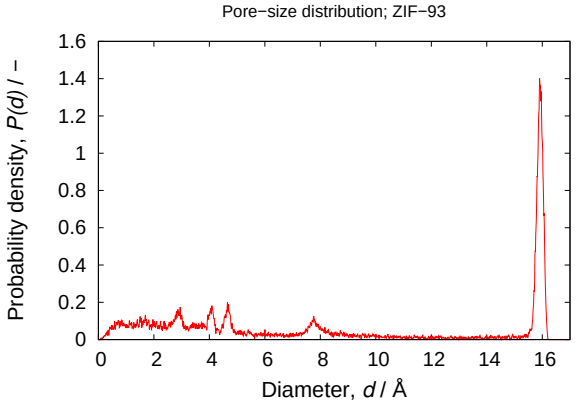

6.10 ZIF-96

unit cell size	$a = 28.3564$ [Å], $b = 28.3564$ [Å], $c = 28.3564$ [Å]
unit cell angles	$\alpha = \beta = \gamma = 90[^\circ]$
framework density	977.39 [kg/m^3]
description	Zn(4cy5amIM)$_2$
crystallographic data	ref. [115]
void fraction	0.469 [-]
accessible pore volume	0.4796 [cm^3/g]
nitrogen surface area	1279 [m^2/g], 1250 [m^2/cm^3]

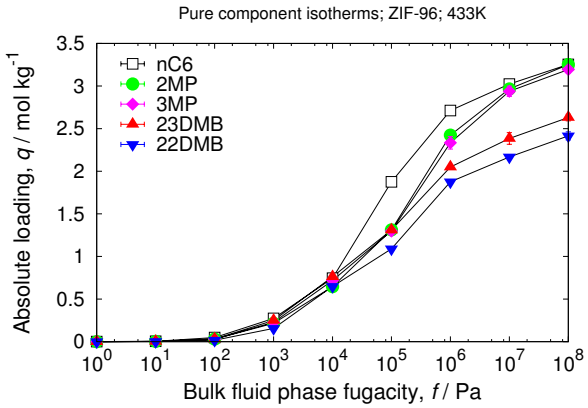

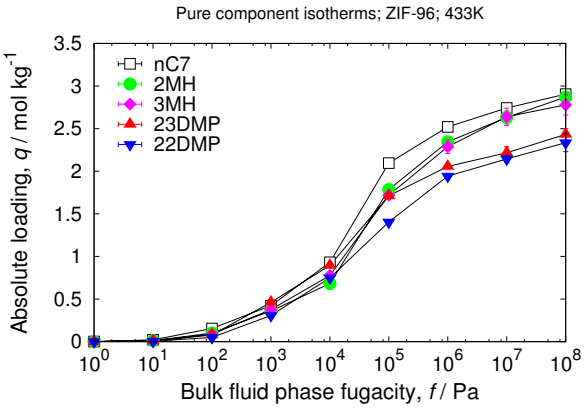

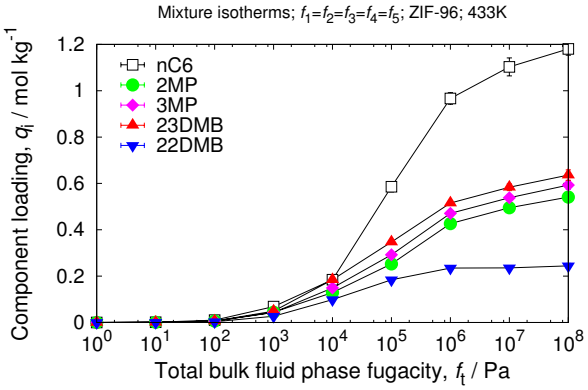

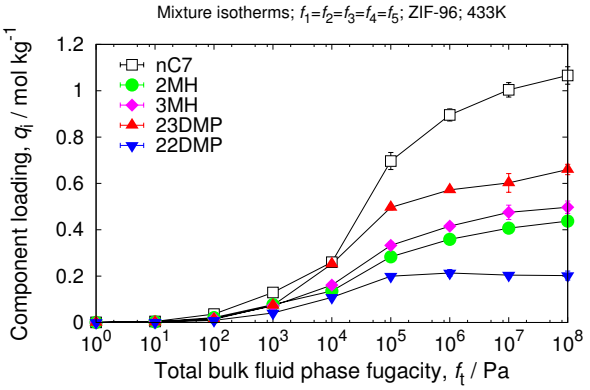

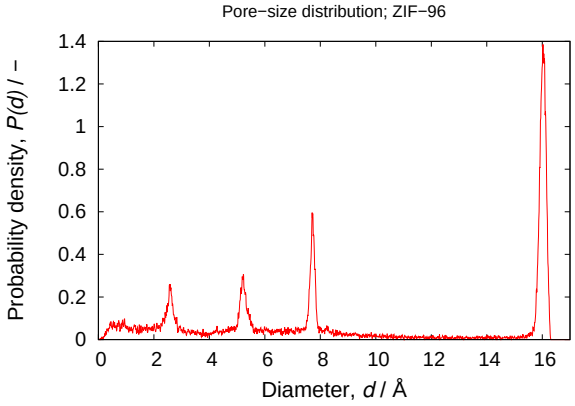

6.11 ZIF-97

unit cell size	$a = 28.4319$ [Å], $b = 28.4319$ [Å], $c = 28.4319$ [Å]
unit cell angles	$\alpha = \beta = \gamma = 90[^\circ]$
framework density	977.57 [kg/m^3]
description	Zn(mehylIM)$_2$
crystallographic data	ref. [115]
void fraction	0.367 [-]
accessible pore volume	0.3675 [cm^3/g]
nitrogen surface area	896 [m^2/g], 893 [m^2/cm^3]

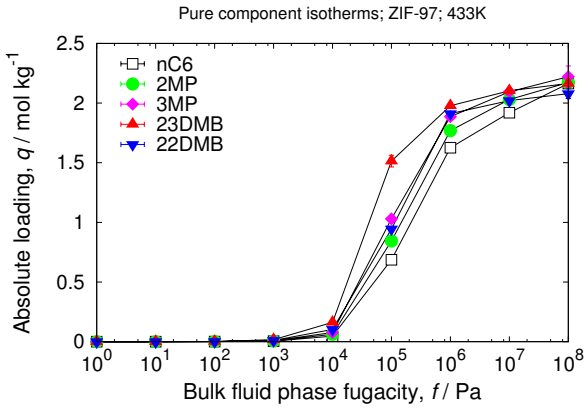

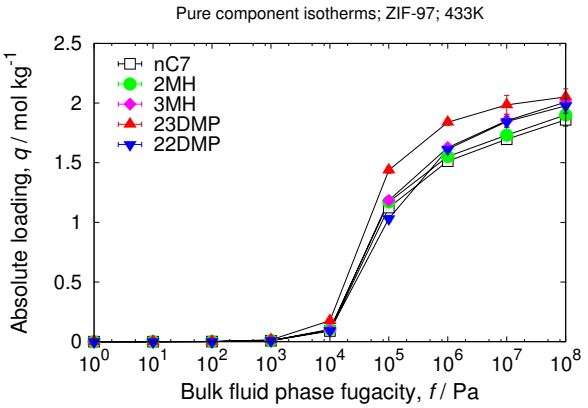

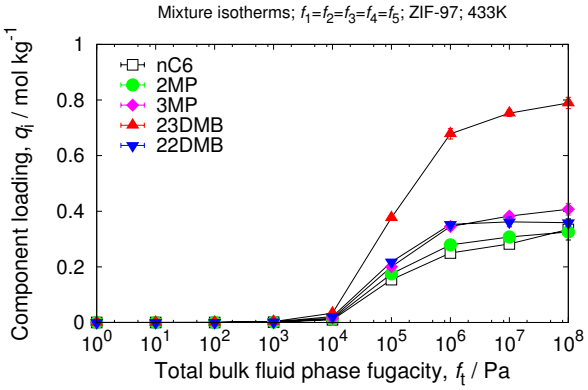

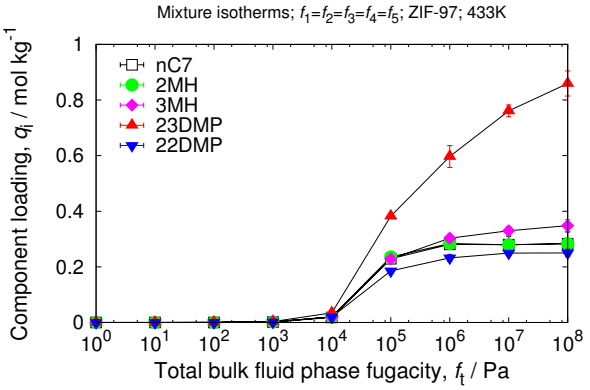

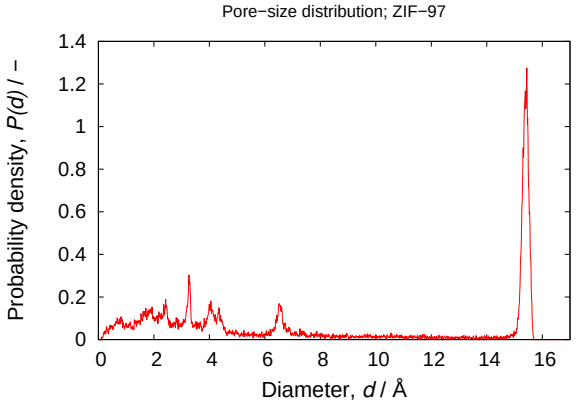

CoBDP is modified; all linker molecules are set orthogonal to the channel. Four linker molecules are chosen to vary the channel dimension: BP (bipyrazolate), ADP (acetylenedipyrazolate), BDP (benzenedipyrazolate), and BPDP (biphenyldipyrazolate).

7 CoBDP analogues

CoBP (pseudo)

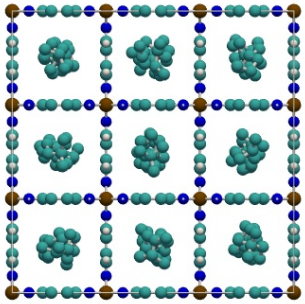

CoADP (pseudo)

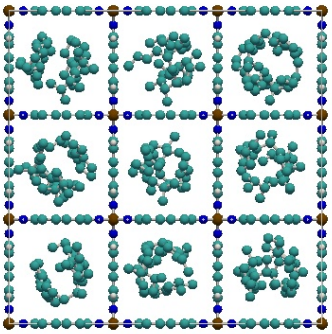

CoBDP (pseudo)

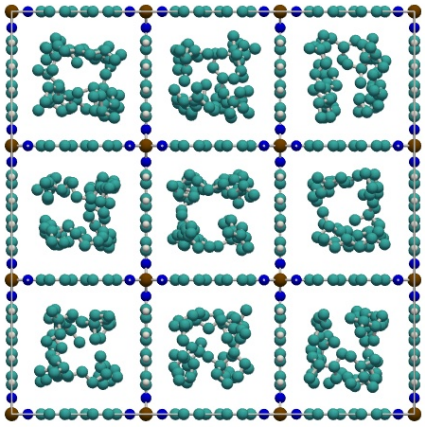

CoBPDP (pseudo)

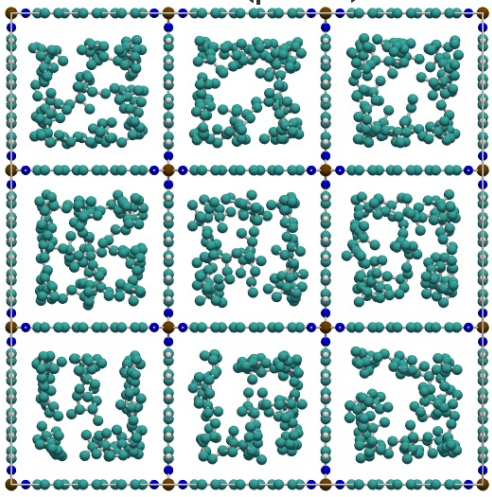

7.1 CoBP (pseudo)

unit cell size	$a = 9.086$ [Å], $b = 9.086$ [Å], $c = 13.995$ [Å]
unit cell angles	$\alpha = \beta = \gamma = 90[^\circ]$
framework density	1098.38 [kg/m^3]
description	Co(BP)
void fraction	0.507 [-]
accessible pore volume	0.4616 [cm^3/g]
nitrogen surface area	1273 [m^2/g], 1399 [m^2/cm^3]

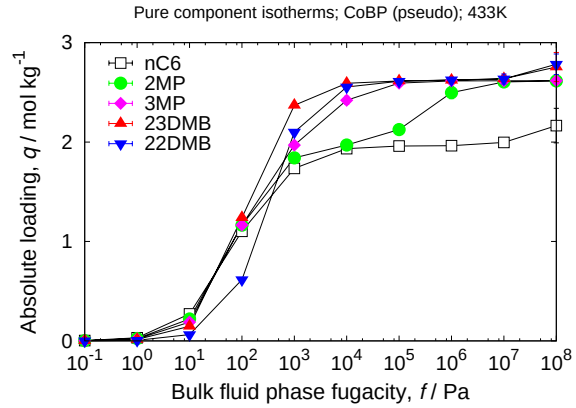

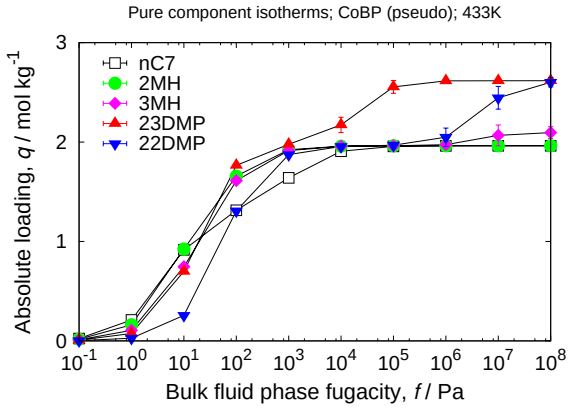

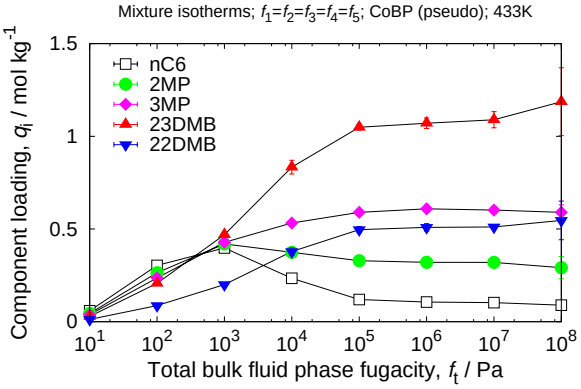

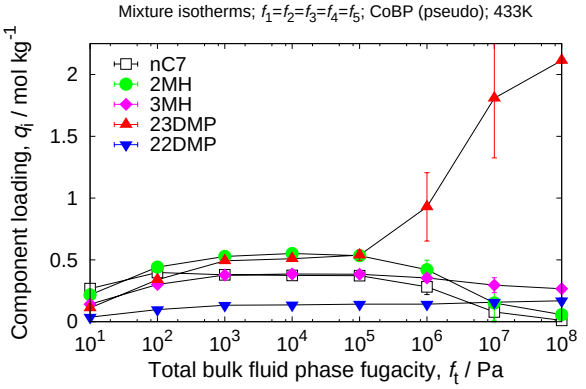

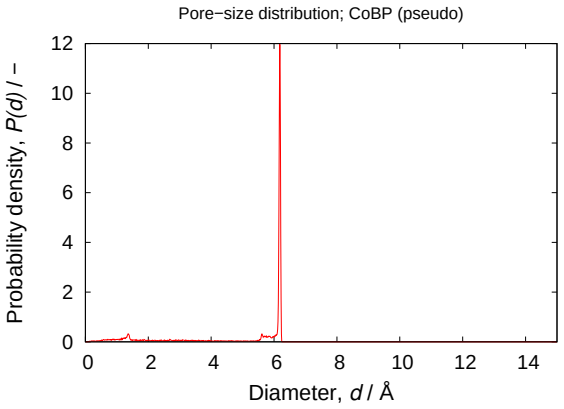

```
data_CoBP_pseudo

_audit_creation_method RASPA-1.0
_audit_creation_date 2012-4-1
_audit_author_name 'Ozgur Yazaydin'

_cell_length_a    9.086
_cell_length_b    9.086
_cell_length_c    13.995
_cell_angle_alpha 90
_cell_angle_beta  90
_cell_angle_gamma 90
_cell_volume      1155.36

_symmetry_cell_setting          orthorhombic
_symmetry_space_group_name_Hall 'P 2c 2'
_symmetry_space_group_name_H-M  'P 2 2 21'
_symmetry_Int_Tables_number     17

loop_
_symmetry_equiv_pos_as_xyz
 'x,y,z'
 '-x,-y,z+1/2'
 '-x,y,-z+1/2'
 'x,-y,-z'

loop_
_atom_site_label
_atom_site_type_symbol
_atom_site_fract_x
_atom_site_fract_y
_atom_site_fract_z
N1       N     0.17813      0            0.05002
N2       N     0.82187      0            0.05002
C3       C     0.32473      0            0.08096
C4       C     0.67527      0            0.08096
Co5      Co    0            0            0.12747
N6       N     0            0.17813      0.19996
N7       N     0            0.82187      0.19996
C8       C     0            0.32473      0.16902
C9       C     0            0.67527      0.16895
H10      H     0.34646      0            0.14739
H11      H     0.65355      0            0.14736
H12      H     0            0.34645      0.1026
H13      H     0            0.65363      0.10255
C14      C     0.4152       0            0
C15      C     0.5848       0            0
C18      C     0            0.4152       0.25
C19      C     0            0.5848       0.25
```

7.2 CoADP (pseudo)

unit cell size	$a = 11.826$ [Å], $b = 11.826$ [Å], $c = 13.995$ [Å]
unit cell angles	$\alpha = \beta = \gamma = 90[^\circ]$
framework density	729.89 [kg/m^3]
description	Co(ADP)
void fraction	0.653 [-]
accessible pore volume	0.8947 [cm^3/g]
nitrogen surface area	2515 [m^2/g], 1836 [m^2/cm^3]

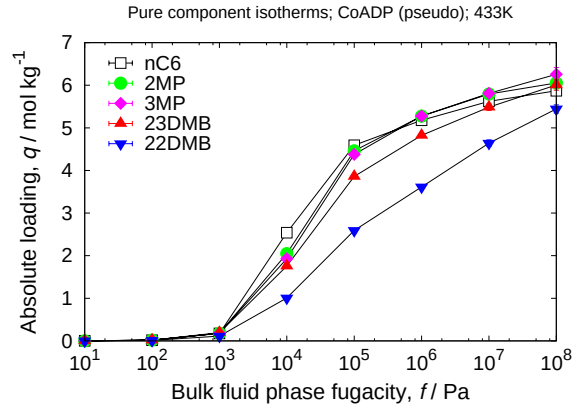

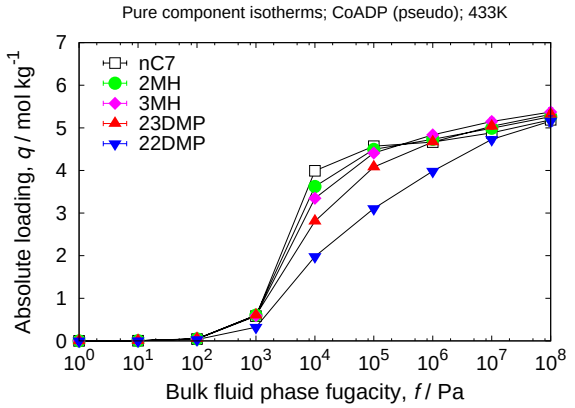

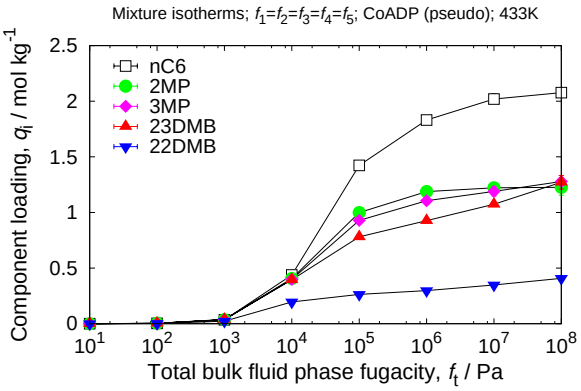

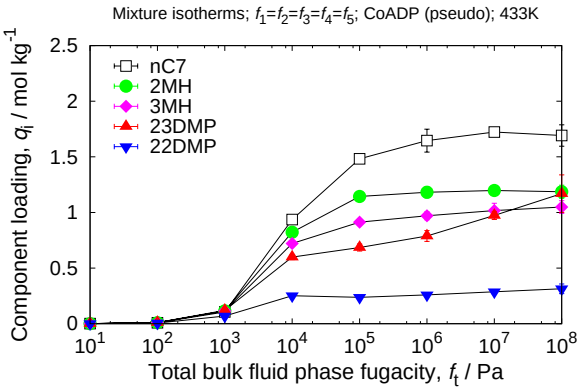

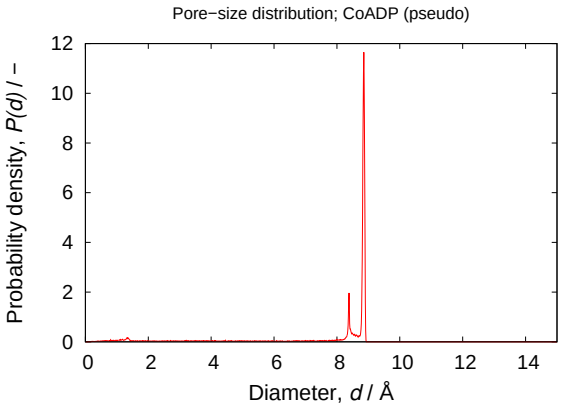

```
data_CoADP_pseudo

_audit_creation_method RASPA-1.0
_audit_creation_date 2012-4-1
_audit_author_name 'Ozgur Yazaydin'

_cell_length_a    11.826
_cell_length_b    11.826
_cell_length_c    13.995
_cell_angle_alpha 90
_cell_angle_beta  90
_cell_angle_gamma 90
_cell_volume      1957.26

_symmetry_cell_setting          orthorhombic
_symmetry_space_group_name_Hall 'P 2c 2'
_symmetry_space_group_name_H-M  'P 2 2 21'
_symmetry_Int_Tables_number     17

loop_
_symmetry_equiv_pos_as_xyz
 'x,y,z'
 '-x,-y,z+1/2'
 '-x,y,-z+1/2'
 'x,-y,-z'

loop_
_atom_site_label
_atom_site_type_symbol
_atom_site_fract_x
_atom_site_fract_y
_atom_site_fract_z
N1       N     0.13686      0            0.05002
N2       N     0.86314      0            0.05002
C3       C     0.24949      0            0.08096
C4       C     0.75051      0            0.08096
Co5      Co    0            0            0.12747
N6       N     0            0.13686      0.19996
N7       N     0            0.86314      0.19996
C8       C     0            0.24949      0.16902
C9       C     0            0.75051      0.16895
H10      H     0.26619      0            0.14739
H11      H     0.73382      0            0.14736
H12      H     0            0.26618      0.1026
H13      H     0            0.73388      0.10255
C14      C     0.319        0            0
C15      C     0.681        0            0
C16      C     0.44926      0            0
C17      C     0.55074      0            0
C18      C     0            0.319        0.25
C19      C     0            0.681        0.25
C20      C     0            0.55074      0.25
C21      C     0            0.44926      0.25
```

7.3 CoBDP (pseudo)

unit cell size	$a = 13.426$ [Å], $b = 13.426$ [Å], $c = 13.995$ [Å]
unit cell angles	$\alpha = \beta = \gamma = 90[^\circ]$
framework density	703.40 [kg/m^3]
description	Co(BDP)
void fraction	0.681 [-]
accessible pore volume	0.9678 [cm^3/g]
nitrogen surface area	2356 [m^2/g], 1658 [m^2/cm^3]

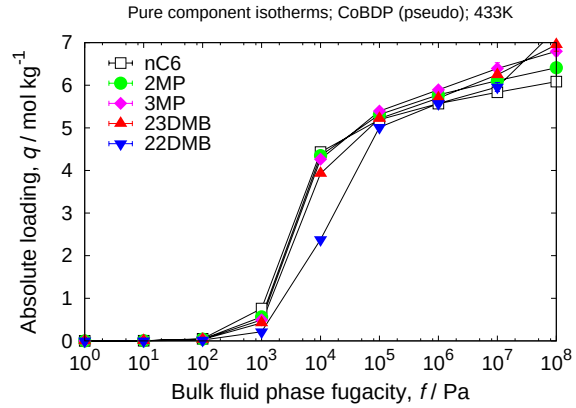

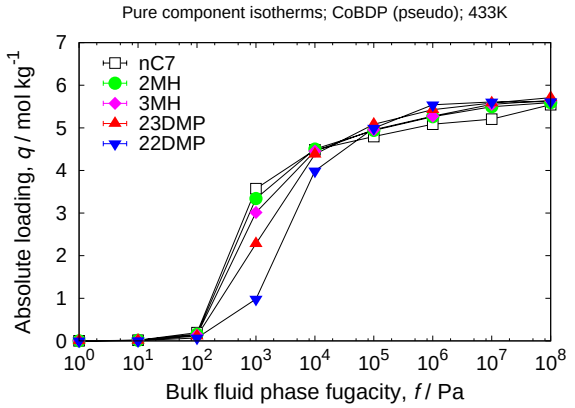

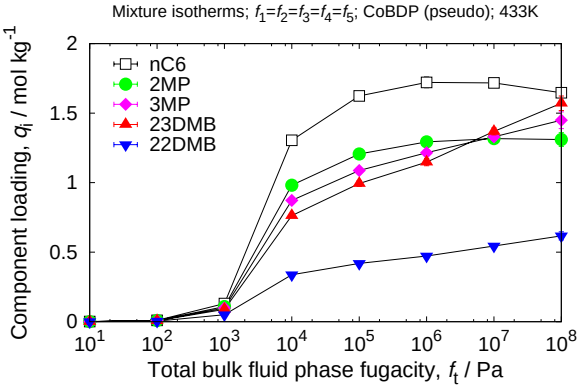

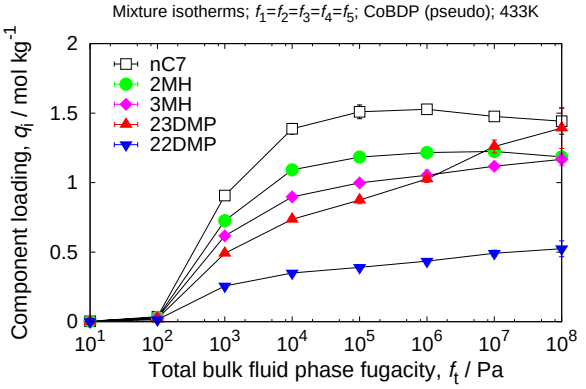

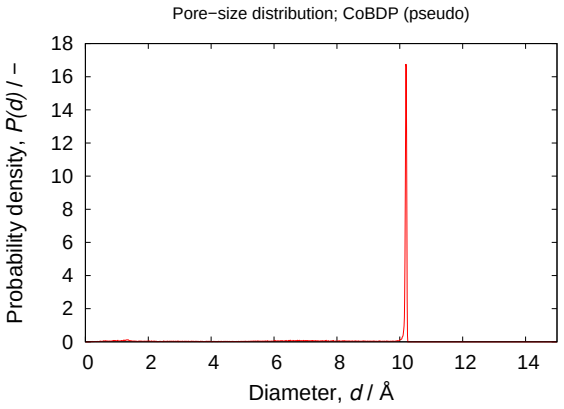

```
data_CoBDP_pseudo

_audit_creation_method RASPA-1.0
_audit_creation_date 2012-4-1
_audit_author_name 'Ozgur Yazaydin'

_cell_length_a    13.426
_cell_length_b    13.426
_cell_length_c    13.995
_cell_angle_alpha 90
_cell_angle_beta  90
_cell_angle_gamma 90
_cell_volume      2522.7

_symmetry_cell_setting          orthorhombic
_symmetry_space_group_name_Hall 'P 2c 2'
_symmetry_space_group_name_H-M  'P 2 2 21'
_symmetry_Int_Tables_number     17

loop_
_symmetry_equiv_pos_as_xyz
 'x,y,z'
 '-x,-y,z+1/2'
 '-x,y,-z+1/2'
 'x,-y,-z'

loop_
_atom_site_label
_atom_site_type_symbol
_atom_site_fract_x
_atom_site_fract_y
_atom_site_fract_z
N1       N     0.12055      0            0.05002
N2       N     0.87945      0            0.05002
C3       C     0.44783      0            0.08664
C4       C     0.5521       0            0.08664
C5       C     0.21976      0            0.08096
C6       C     0.78024      0            0.08096
Co7      Co    0            0            0.12747
N8       N     0            0.12055      0.19996
N9       N     0            0.87945      0.19996
C10      C     0            0.21976      0.16902
C11      C     0            0.78024      0.16895
C12      C     0            0.44783      0.16342
C13      C     0            0.5521       0.16342
H14      H     0.41245      0            0.14542
H15      H     0.58749      0            0.14545
H16      H     0.23447      0            0.14739
H17      H     0.76554      0            0.14736
H18      H     0            0.23446      0.1026
H19      H     0            0.76559      0.10255
H20      H     0            0.41246      0.10462
H21      H     0            0.58747      0.10464
C22      C     0.28098      0            0
C23      C     0.71902      0            0
C24      C     0.60431      0            0
C25      C     0.39569      0            0
C26      C     0            0.28098      0.25
C27      C     0            0.71902      0.25
C28      C     0            0.39569      0.25
C29      C     0            0.60431      0.25
```

7.4 CoBPDP (pseudo)

unit cell size	$a = 17.766$ [Å], $b = 17.766$ [Å], $c = 13.995$ [Å]
unit cell angles	$\alpha = \beta = \gamma = 90[^\circ]$
framework density	516.14 [kg/m^3]
description	Co(BPDP)
void fraction	0.765 [-]
accessible pore volume	1.4822 [cm^3/g]
nitrogen surface area	2961 [m^2/g], 1528 [m^2/cm^3]

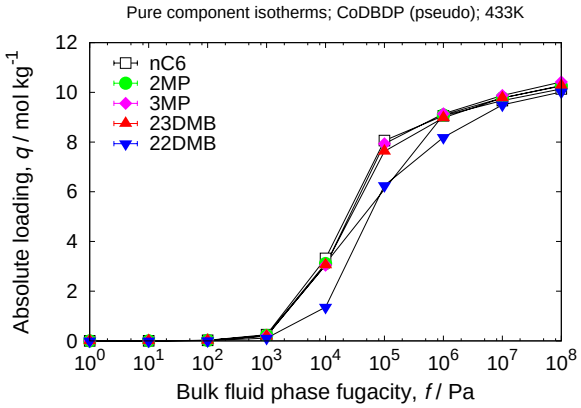

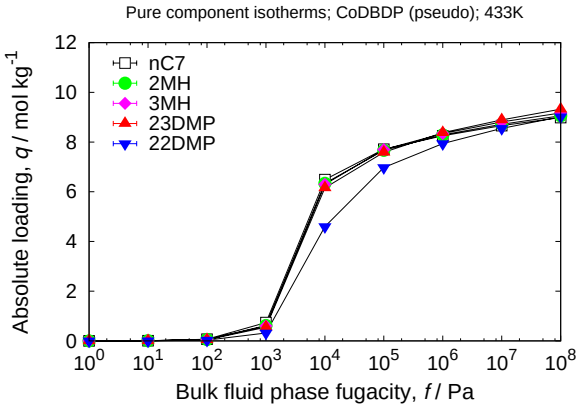

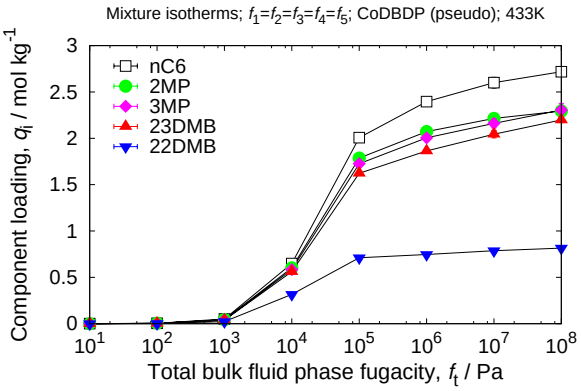

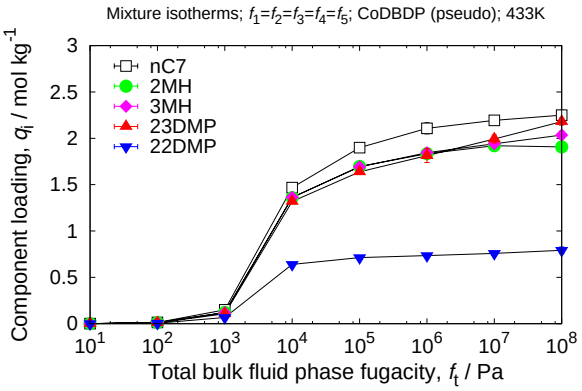

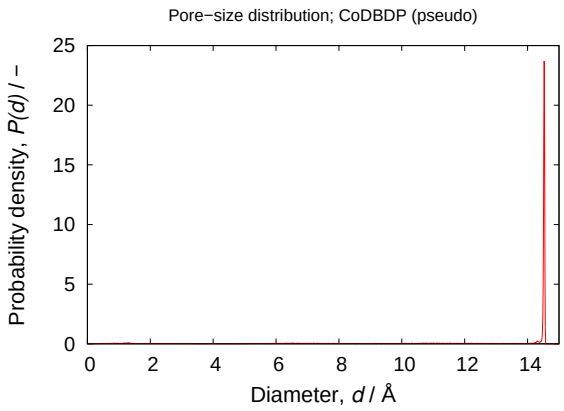

```
data_CoBPDP_pseudo

_audit_creation_method RASPA-1.0
_audit_creation_date 2012-4-1
_audit_author_name 'Ozgur Yazaydin'

_cell_length_a    17.766
_cell_length_b    17.766
_cell_length_c    13.995
_cell_angle_alpha 90
_cell_angle_beta  90
_cell_angle_gamma 90
_cell_volume      4417.25

_symmetry_cell_setting          orthorhombic
_symmetry_space_group_name_Hall 'P 2c 2'
_symmetry_space_group_name_H-M  'P 2 2 21'
_symmetry_Int_Tables_number     17

loop_
_symmetry_equiv_pos_as_xyz
 'x,y,z'
 '-x,-y,z+1/2'
 '-x,y,-z+1/2'
 'x,-y,-z'

loop_
_atom_site_label
_atom_site_type_symbol
_atom_site_fract_x
_atom_site_fract_y
_atom_site_fract_z
N1       N     0.0911       0            0.05002
N2       N     0.9089       0            0.05002
C3       C     0.33843      0            0.08664
C4       C     0.41723      0            0.08664
C5       C     0.16608      0            0.08096
C6       C     0.83392      0            0.08096
Co7      Co    0            0            0.12747
N8       N     0            0.0911       0.19996
N9       N     0            0.9089       0.19996
C10      C     0            0.16608      0.16902
C11      C     0            0.83392      0.16895
C12      C     0            0.33843      0.16342
C13      C     0            0.41723      0.16342
H14      H     0.31169      0            0.14542
H15      H     0.44397      0            0.14545
H16      H     0.17719      0            0.14739
H17      H     0.82282      0            0.14736
H18      H     0            0.17718      0.1026
H19      H     0            0.82285      0.10255
H20      H     0            0.3117       0.10462
H21      H     0            0.44396      0.10464
C22      C     0.58271      0            0.08664
C23      C     0.66152      0            0.08664
C24      C     0            0.58271      0.16342
```

C25	C	0	0.66152	0.16342
H26	H	1	0.55595	0.39539
H27	H	1	0.68822	0.39542
H28	H	0.44405	1	0.6454
H29	H	0.31176	1	0.64548
C30	C	0.21234	0	0
C31	C	0.78766	0	0
C32	C	0.45668	0	0
C33	C	0.29903	0	0
C34	C	0.54337	0	0
C35	C	0.70097	0	0
C36	C	0	0.21234	0.25
C37	C	0	0.78766	0.25
C38	C	0	0.29903	0.25
C39	C	0	0.45668	0.25
C40	C	0	0.54337	0.25
C41	C	0	0.70097	0.25

Graphite slits with a fixed layer spacing. The slit pore has walls made of a single layer of graphitic carbon. The edges of the simulation cell are treated with periodic boundary conditions. Picture shows the equimolar C6 isomer mixture in graphite sheets of 6.5 Å in effective diameter at a total fugacity of the bulk fluid phase of 100 kPa and 433K.

8

Graphite sheets

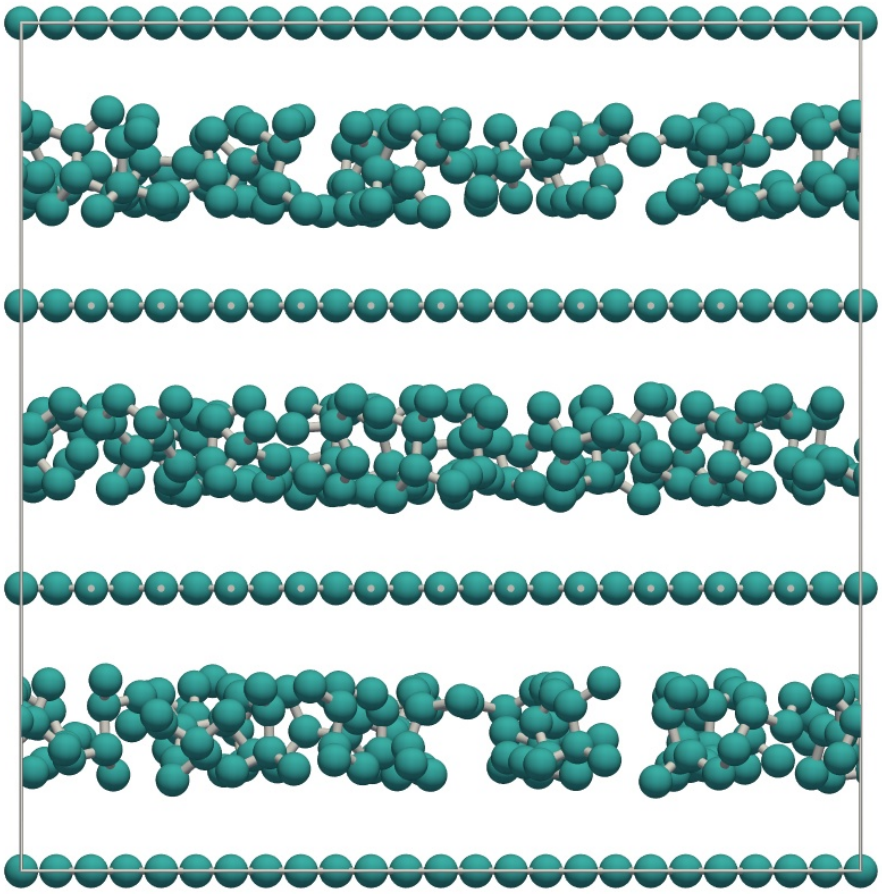

8.1 Sheet: free spacing 5.047 Å

cell size	$a = 39.36$ [Å], $b = 25.56$ [Å], $c = 25.56$ [Å]
volume	25714.42 [Å^3]
framework density	893.50 [kg/m^3]
sheet-sheet distance	8.52 [Å]

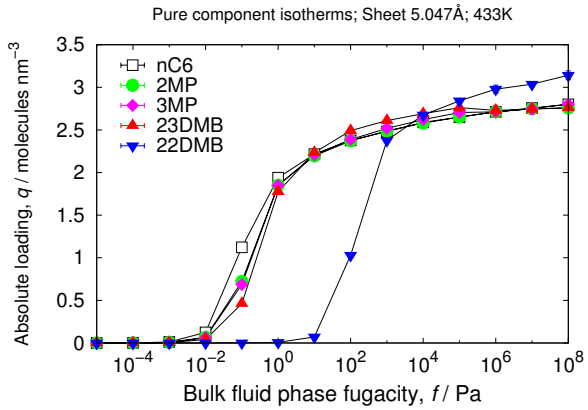

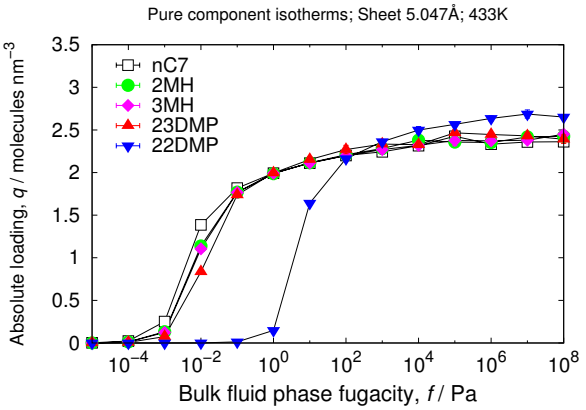

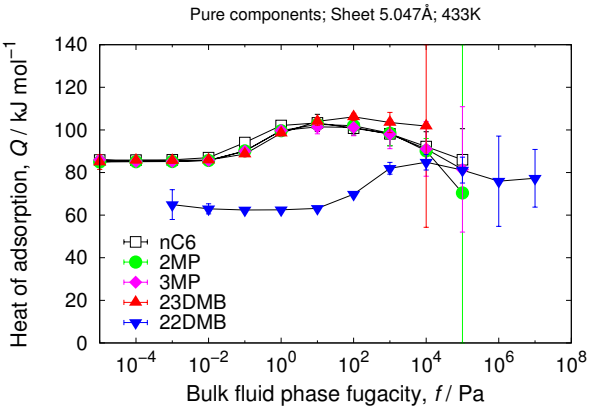

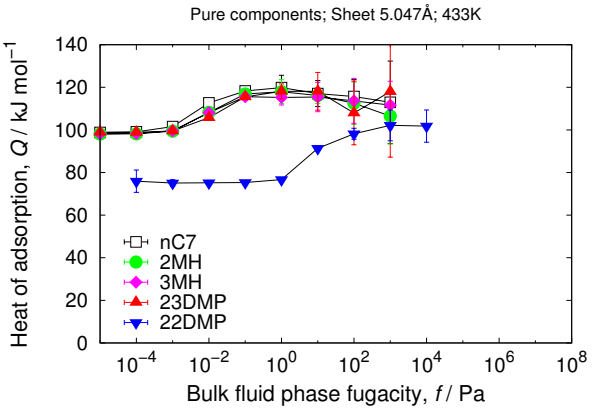

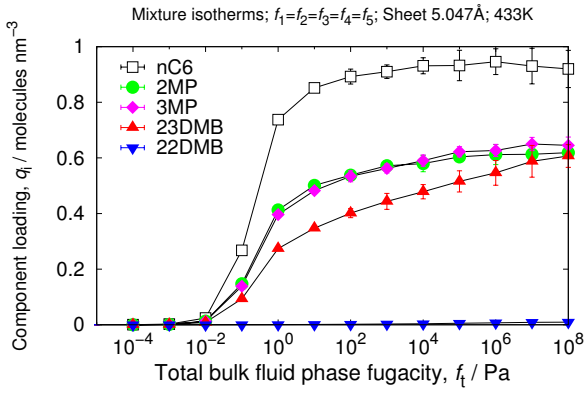

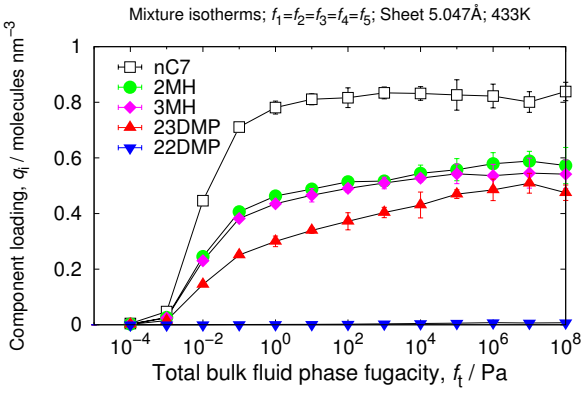

8.2 Sheet: free spacing 5.527 Å

cell size	$a = 29.52$ [Å], $b = 29.82$ [Å], $c = 27.0$ [Å]
volume	23767.73 [Å^3]
framework density	845.85 [kg/m^3]
sheet-sheet distance	9.0 [Å]

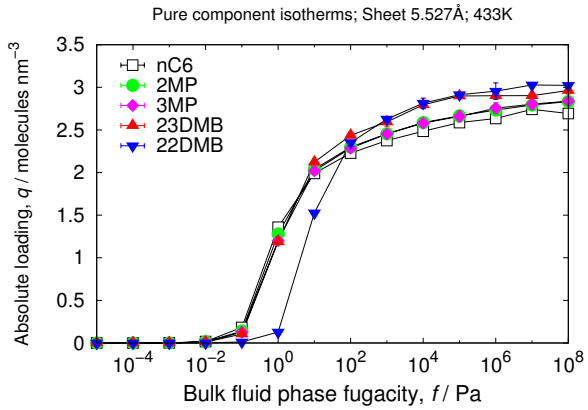

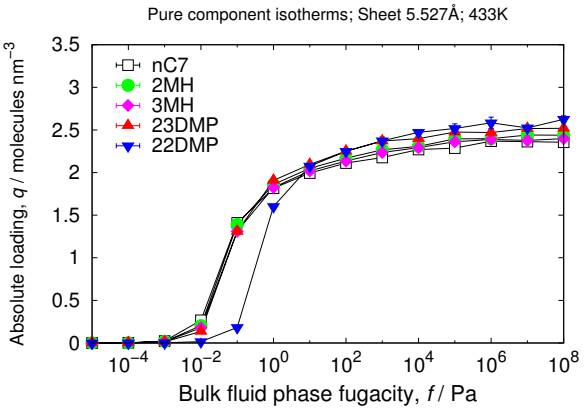

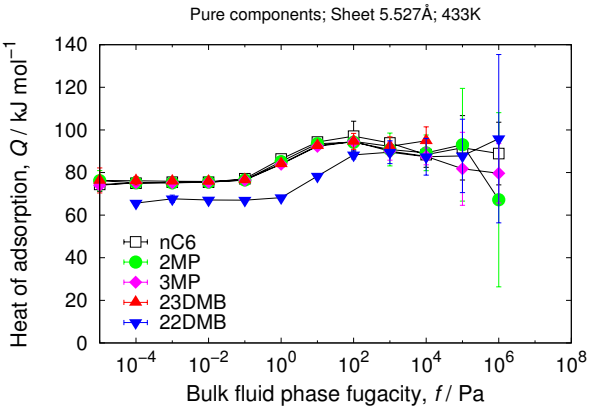

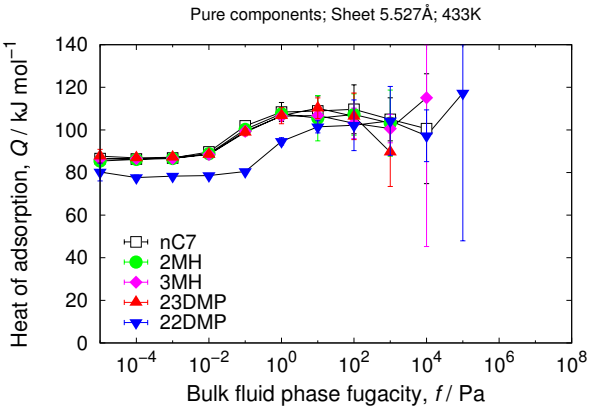

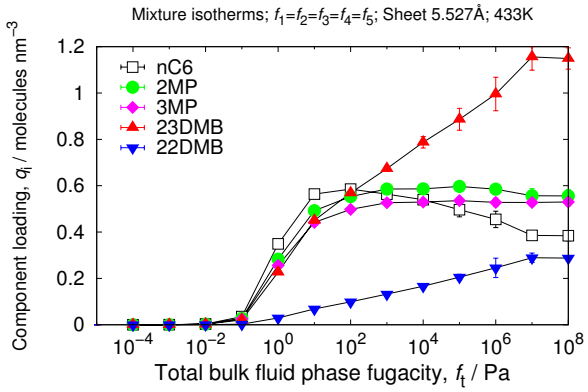

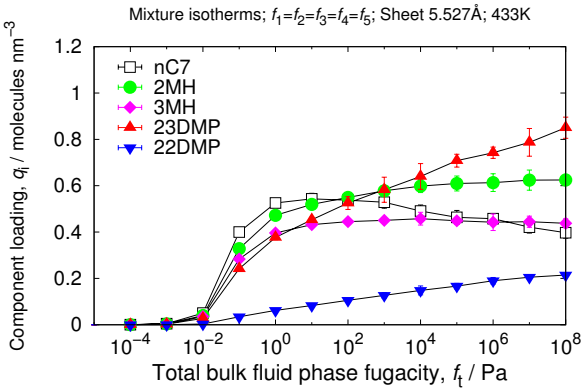

8.3 Sheet: free spacing 6.027 Å

cell size	$a = 29.52$ [Å], $b = 29.82$ [Å], $c = 28.5$ [Å]
volume	25088.16 [Å^3]
framework density	801.33 [kg/m^3]
sheet-sheet distance	9.5 [Å]

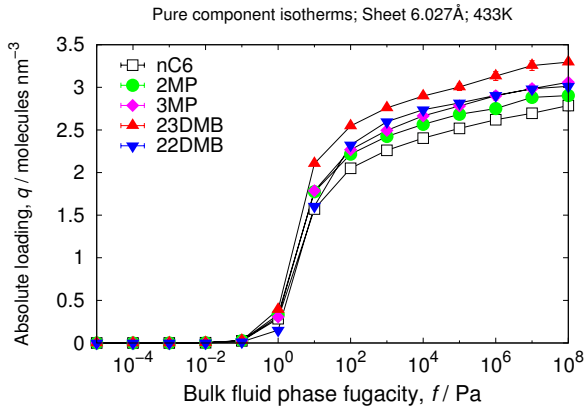

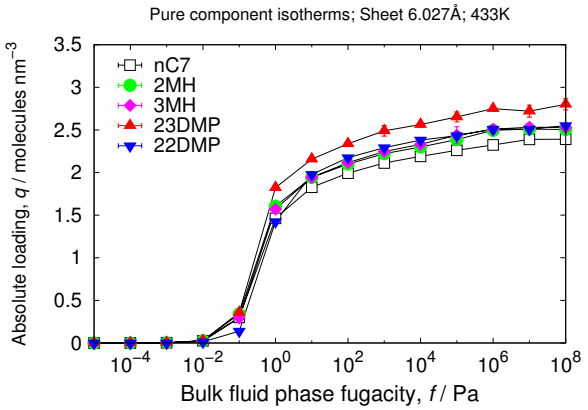

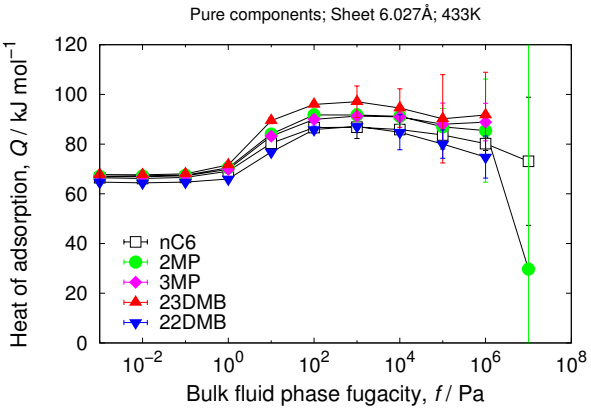

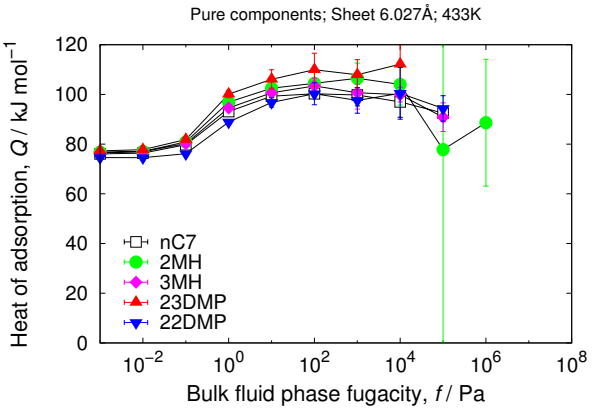

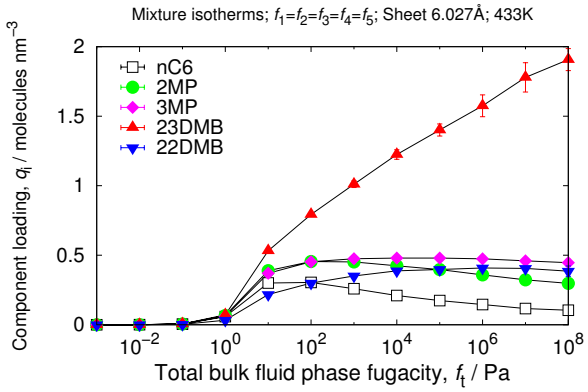

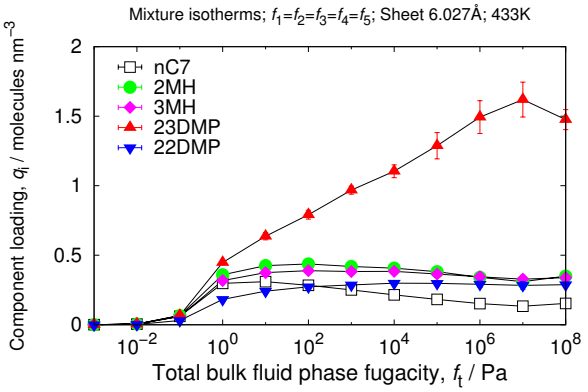

8.4 Sheet: free spacing 6.467 Å

cell size	$a = 29.52$ [Å], $b = 29.82$ [Å], $c = 29.82$ [Å]
volume	26250.14 [Å^3]
framework density	765.86 [kg/m^3]
sheet-sheet distance	9.94 [Å]

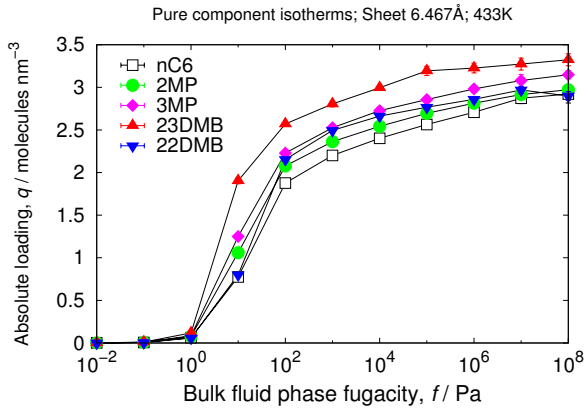

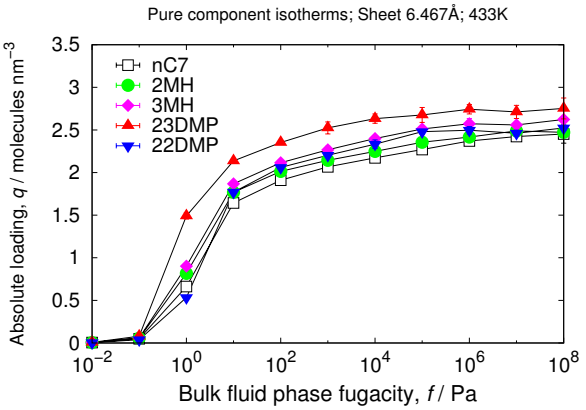

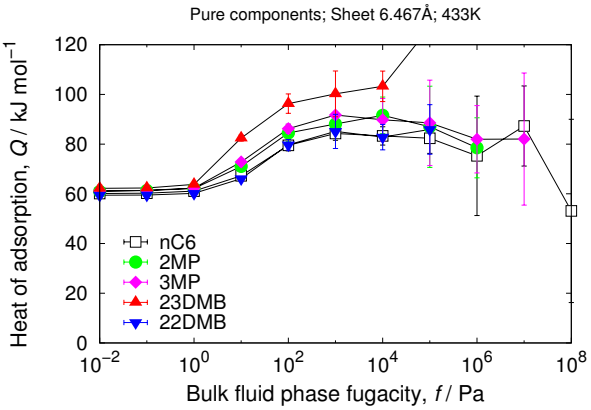

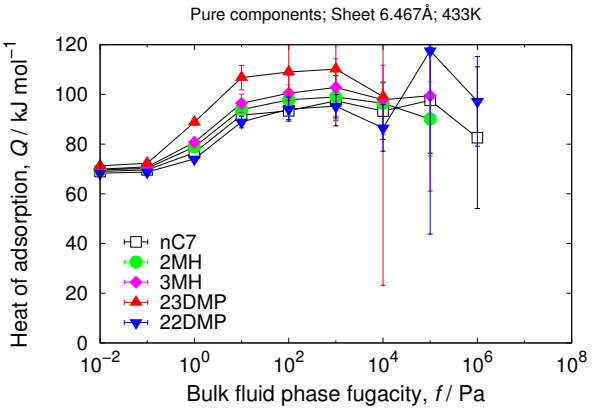

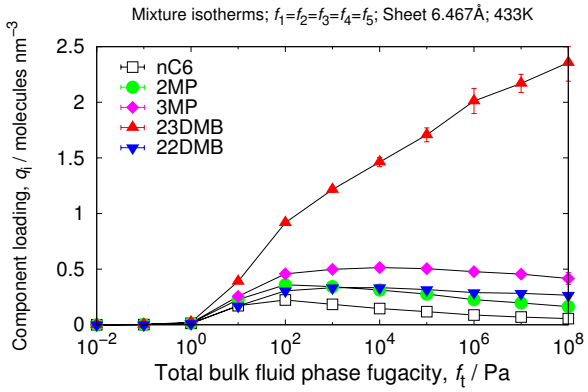

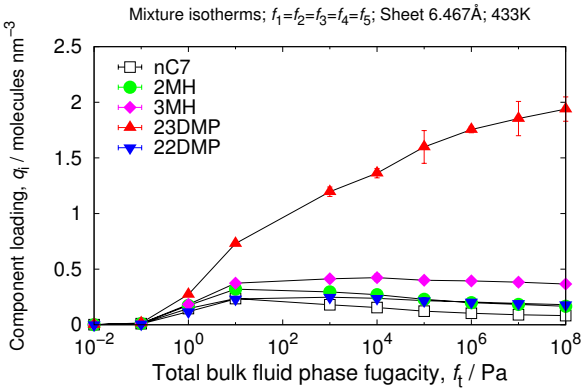

8.5 Sheet: free spacing 6.777 Å

cell size	$a = 29.52$ [Å], $b = 29.82$ [Å], $c = 30.75$ [Å]
volume	27068.80680 [Å^3]
framework density	742.69 [kg/m^3]
sheet-sheet distance	10.25 [Å]

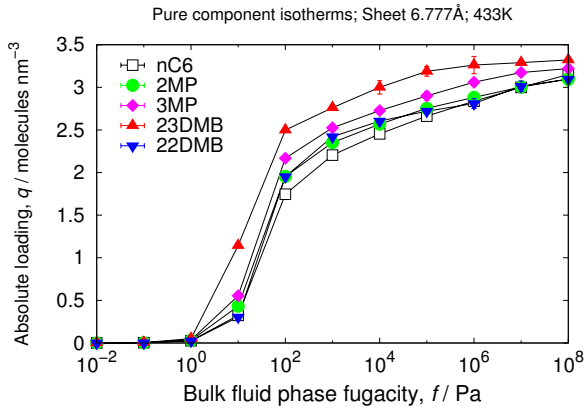

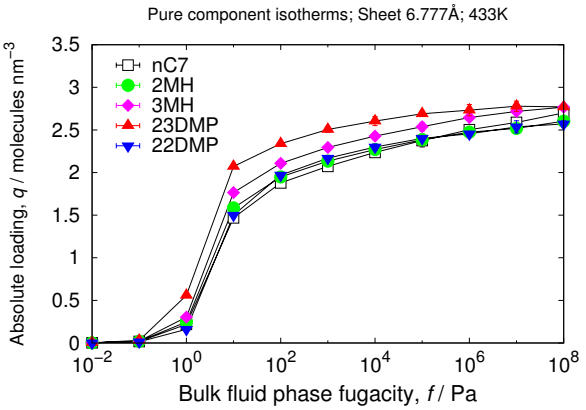

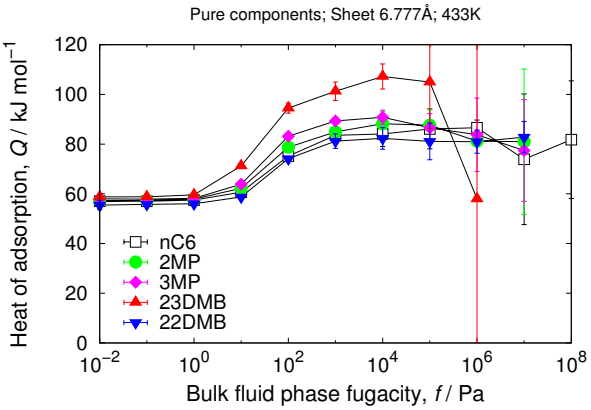

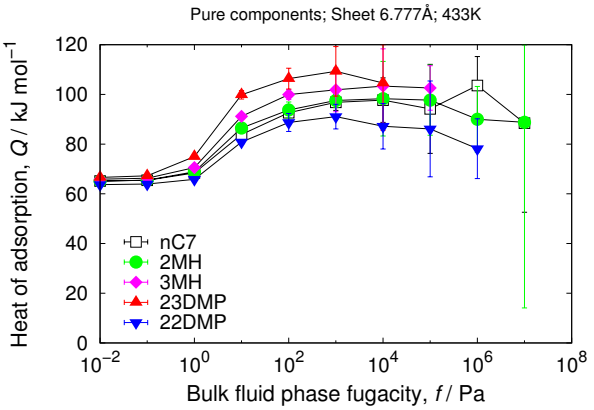

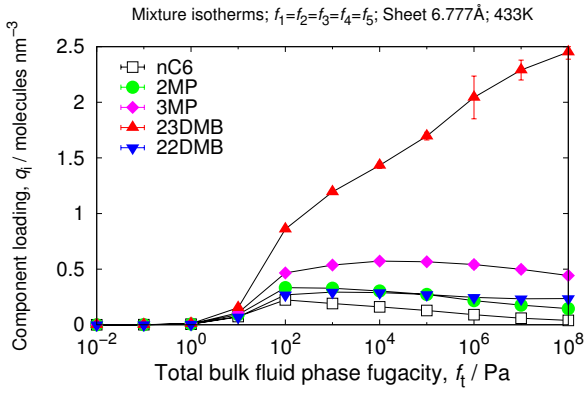

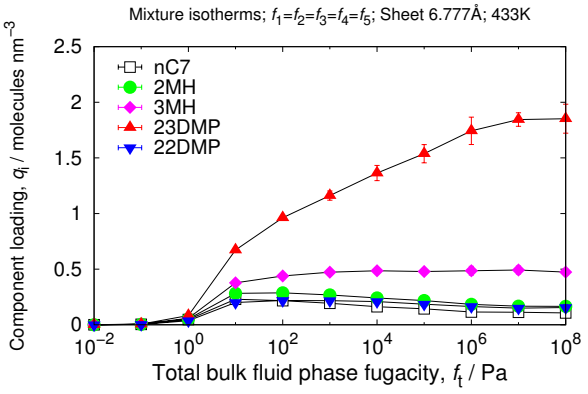

8.6 Sheet: free spacing 7.177 Å

cell size	$a = 29.52$ [Å], $b = 29.82$ [Å], $c = 31.95$ [Å]
volume	28125.15 [Å^3]
framework density	714.80 [kg/m^3]
sheet-sheet distance	10.65 [Å]

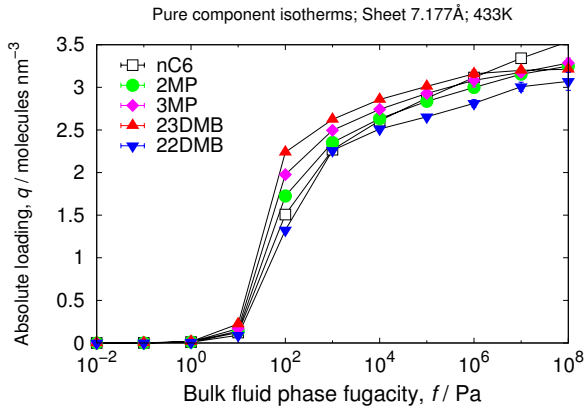

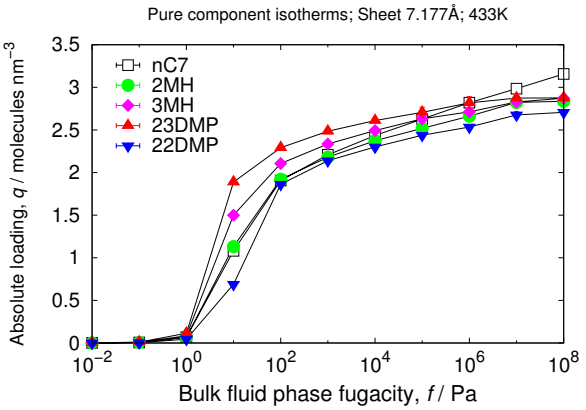

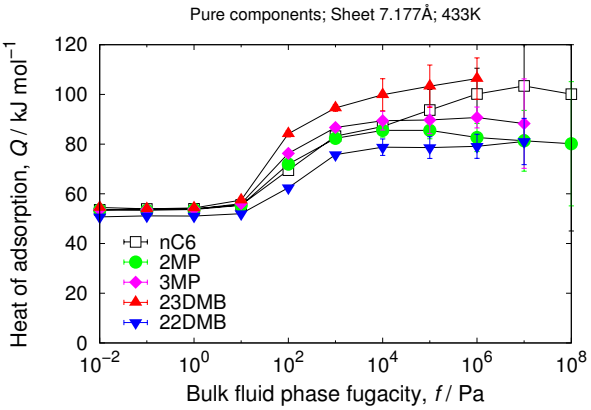

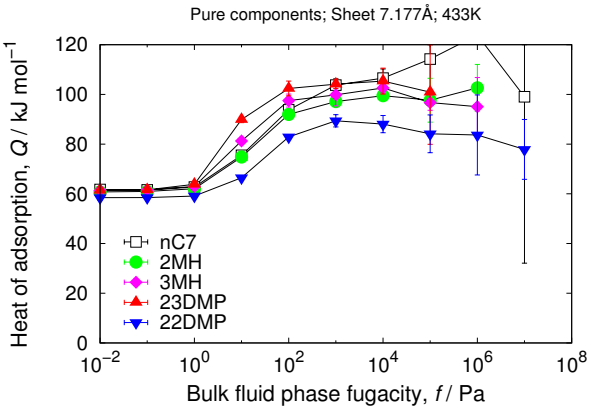

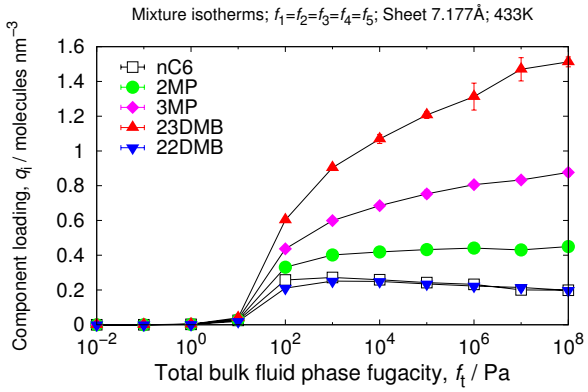

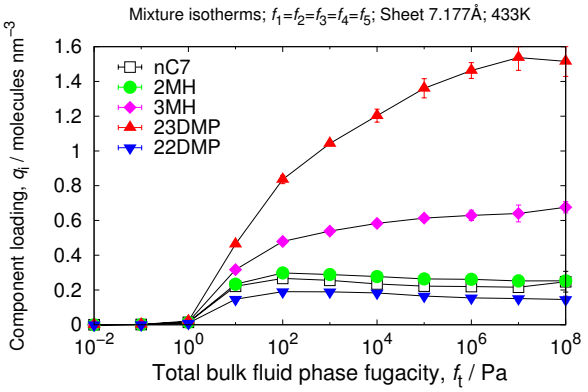

8.7 Sheet: free spacing 7.527 Å

cell size	$a = 29.52$ [Å], $b = 29.82$ [Å], $c = 33.0$ [Å]
volume	29049.45 [Å^3]
framework density	692.06 [kg/m^3]
sheet-sheet distance	11.0 [Å]

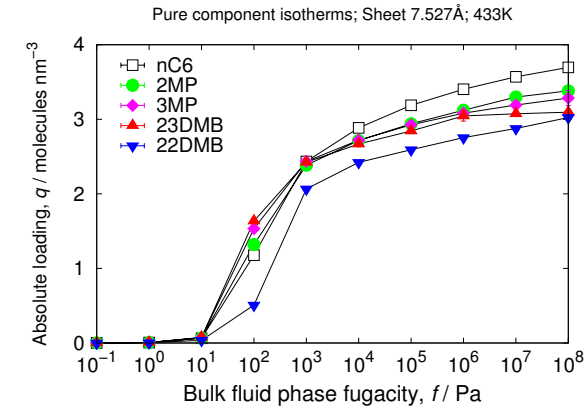

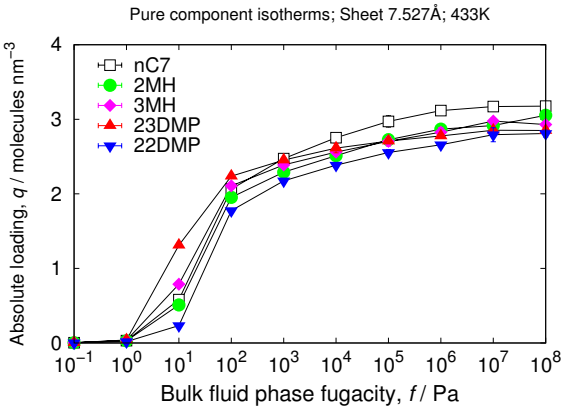

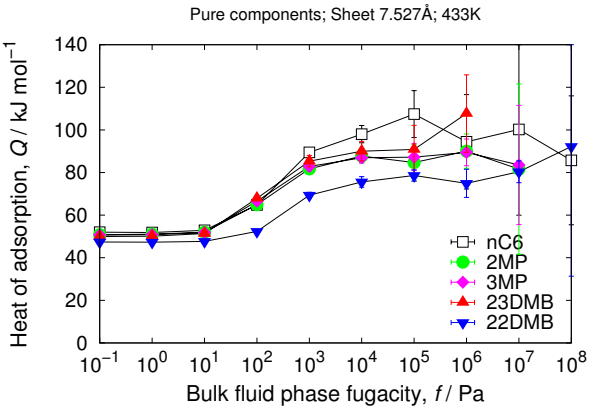

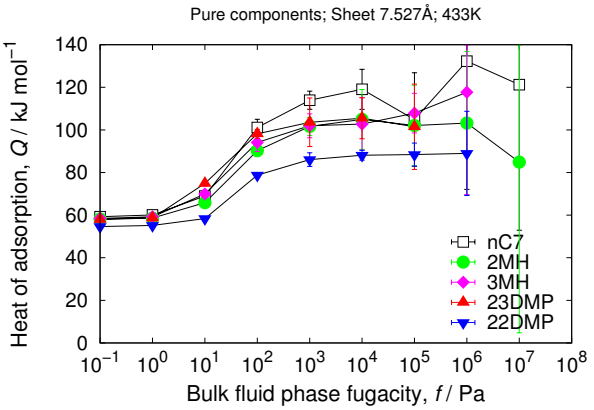

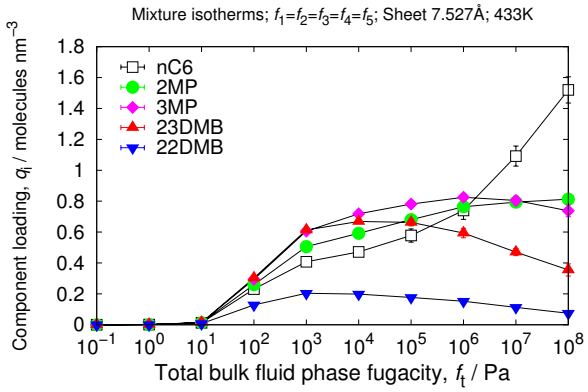

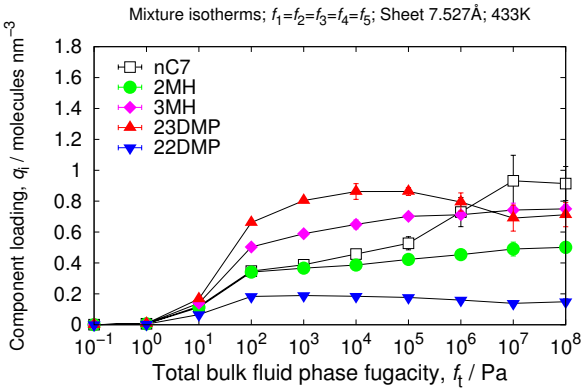

8.8 Sheet: free spacing 7.887 Å

cell size	$a = 29.52$ [Å], $b = 29.82$ [Å], $c = 34.08$ [Å]
volume	30000.16 [Å^3]
framework density	670.12 [kg/m^3]
sheet-sheet distance	11.36 [Å]

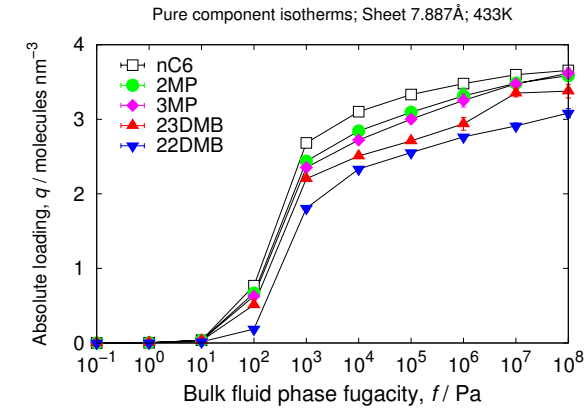

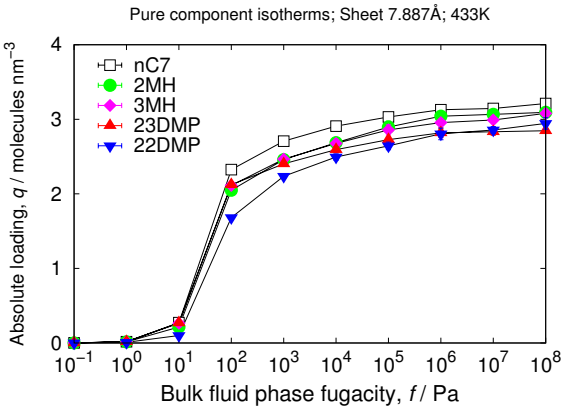

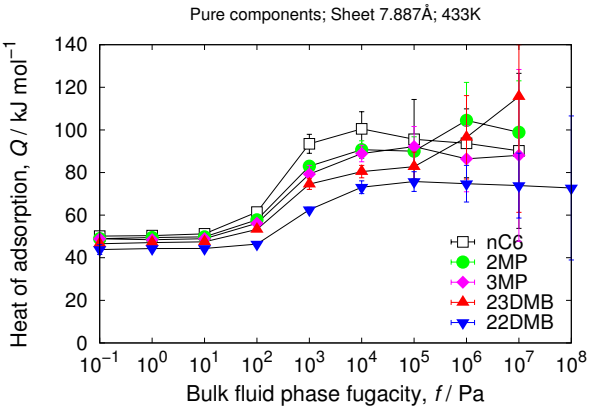

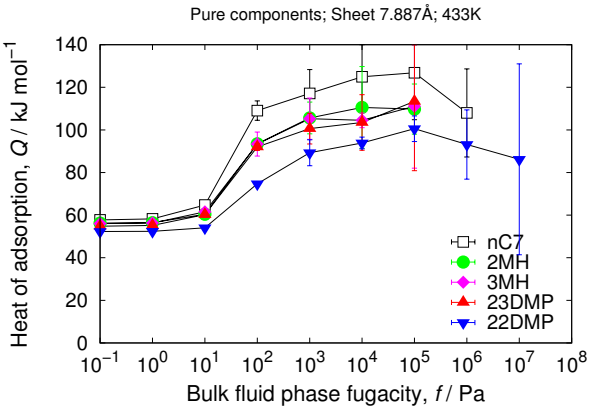

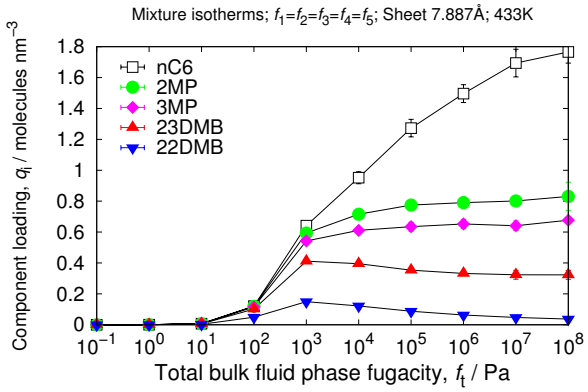

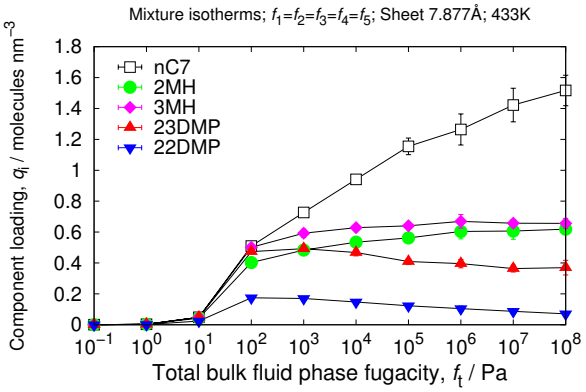

8.9 Sheet: free spacing 8.527 Å

cell size	$a = 29.52$ [Å], $b = 29.82$ [Å], $c = 36.0$ [Å]
volume	31690.31040 [Å^3]
framework density	634.38 [kg/m^3]
sheet-sheet distance	12.0 [Å]

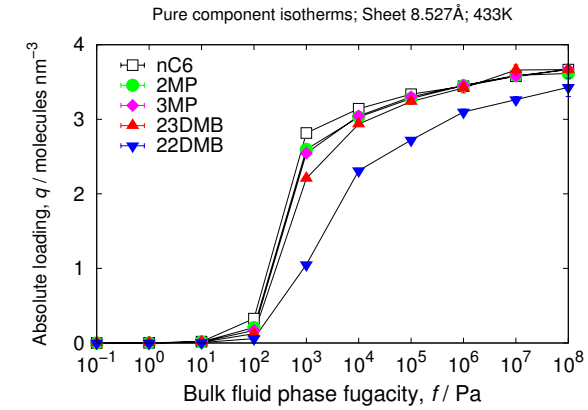

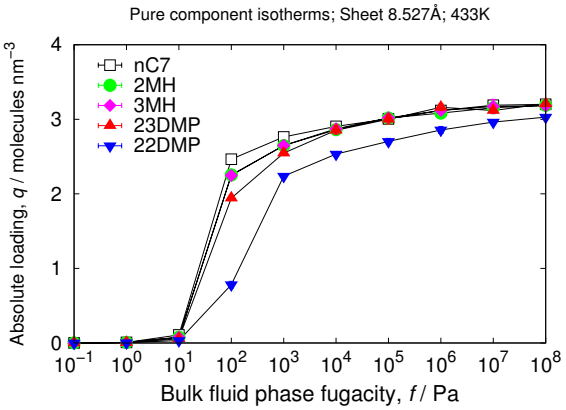

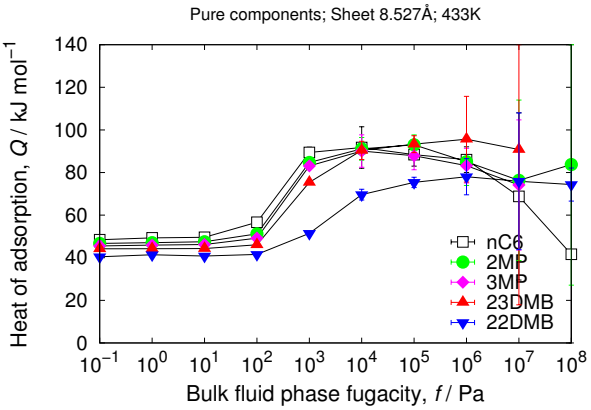

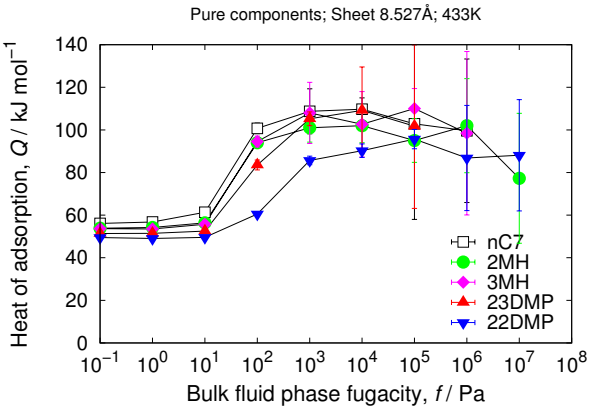

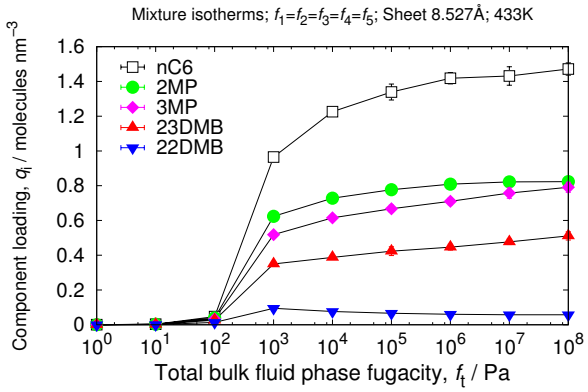

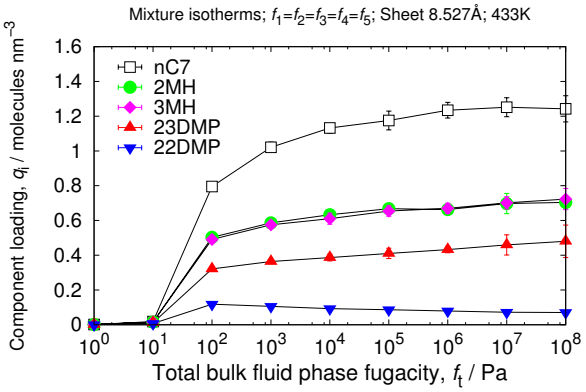

8.10 Sheet: free spacing 9.307 Å

cell size	$a = 29.52$ [Å], $b = 29.82$ [Å], $c = 38.34$ [Å]
volume	33750.18 [Å^3]
framework density	595.67 [kg/m^3]
sheet-sheet distance	12.78 [Å]

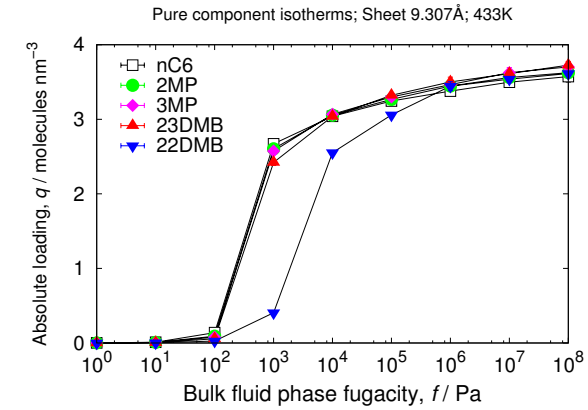

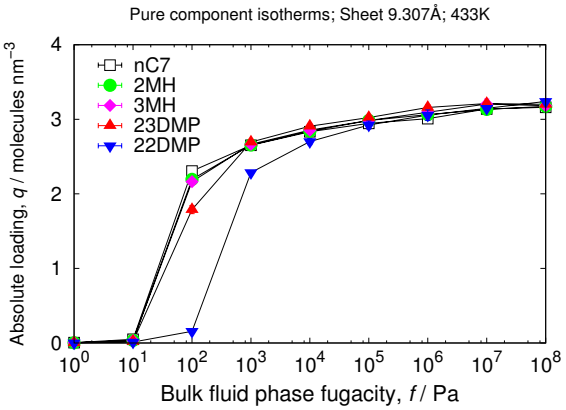

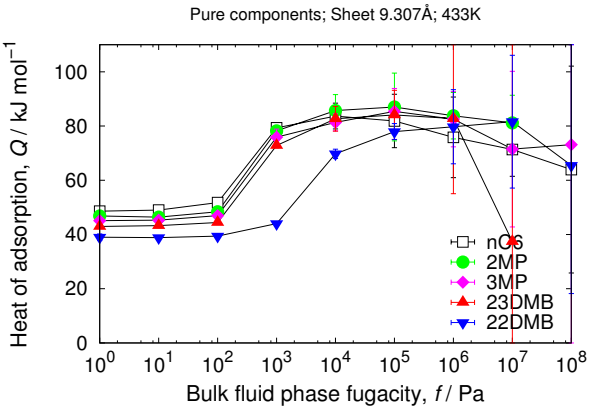

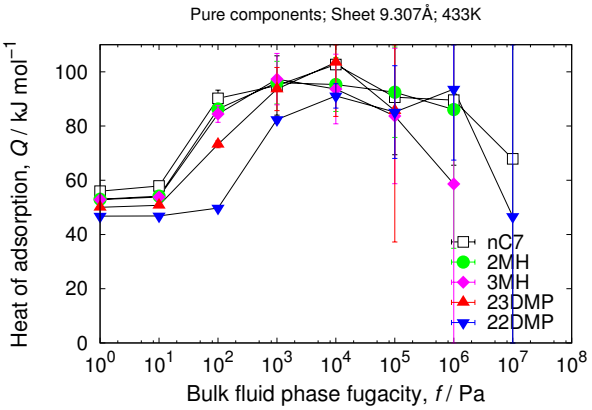

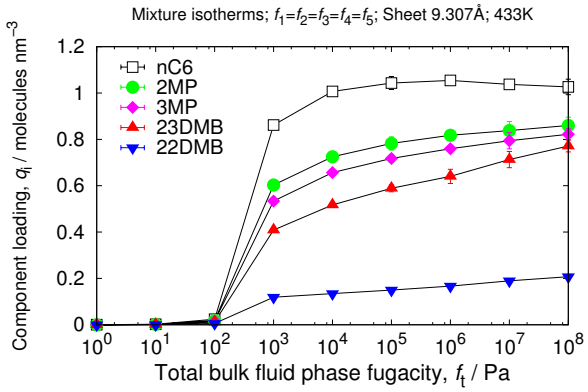

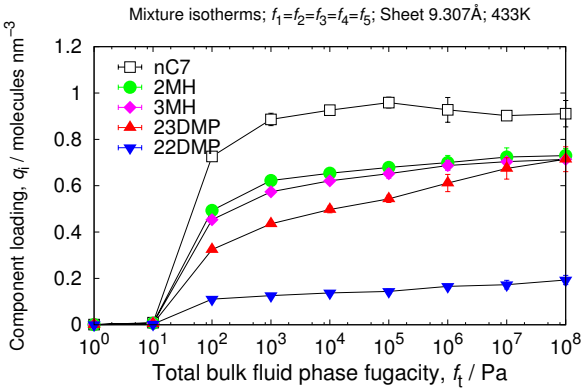

8.11 Sheet: free spacing 10.727 Å

cell size	$a = 29.52$ [Å], $b = 29.82$ [Å], $c = 42.6$ [Å]
volume	37500.20 [Å^3]
framework density	536.10 [kg/m^3]
sheet-sheet distance	14.2 [Å]

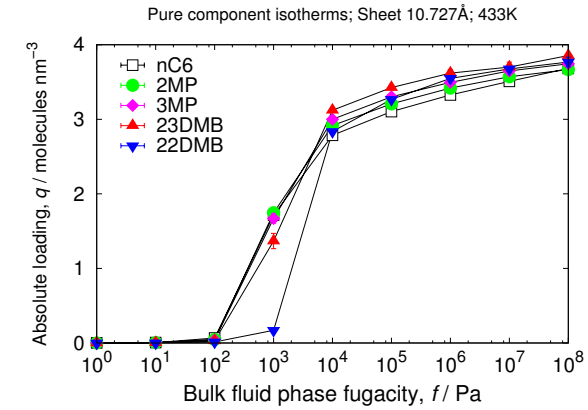

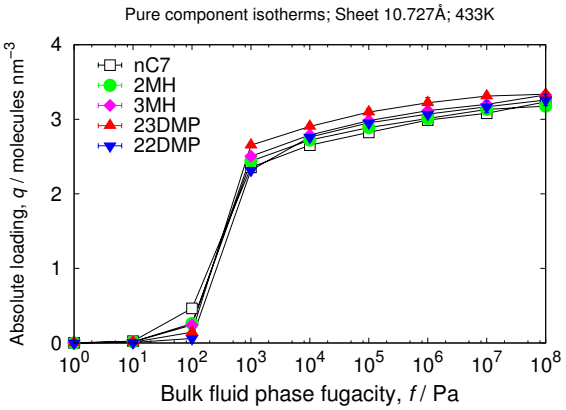

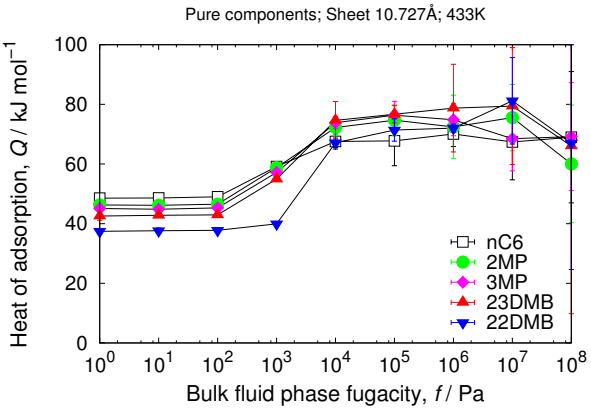

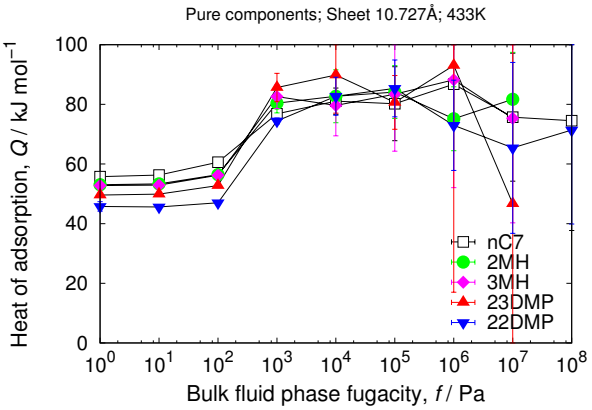

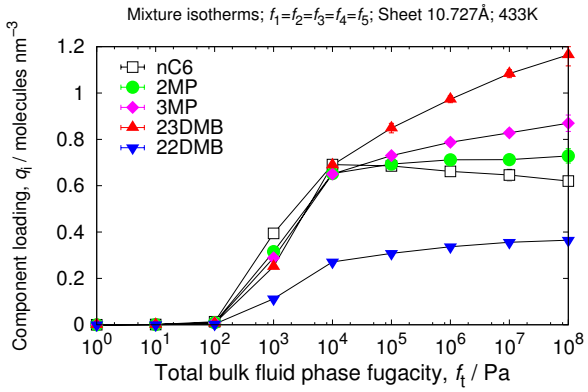

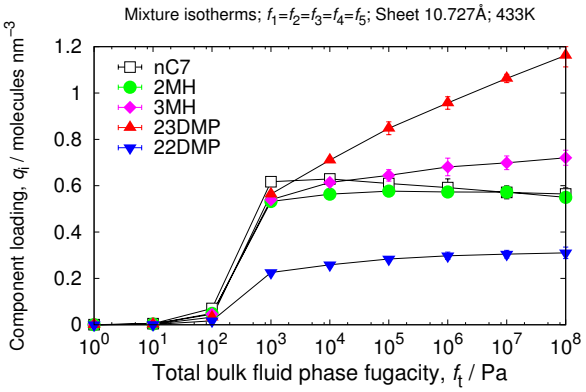

8.12 Sheet: free spacing 12.147 Å

cell size	$a = 29.52$ [Å], $b = 29.82$ [Å], $c = 46.86$ [Å]
volume	41250.22 [Å^3]
framework density	487.36 [kg/m^3]
sheet-sheet distance	15.62 [Å]

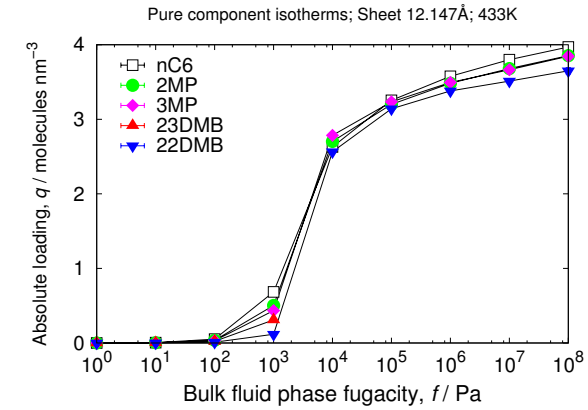

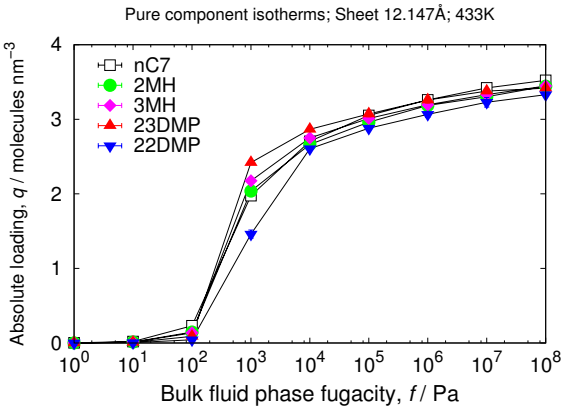

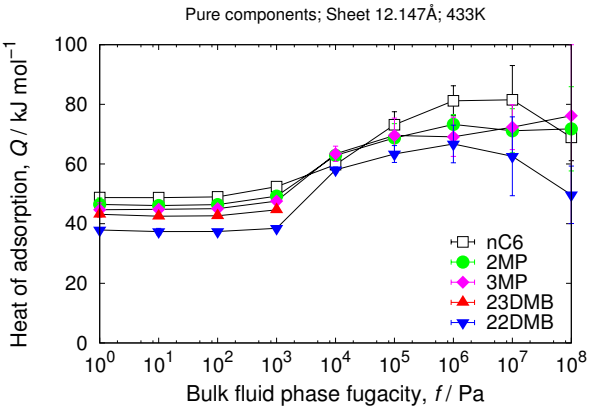

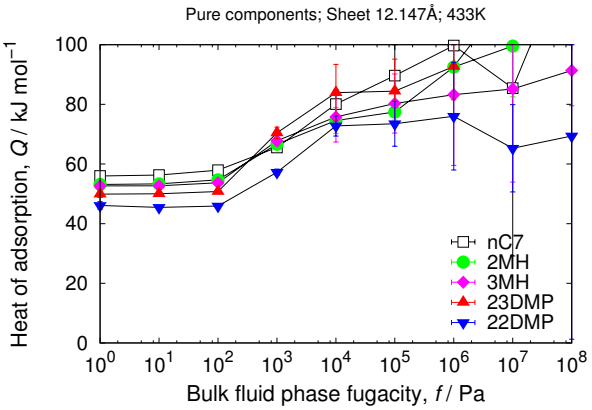

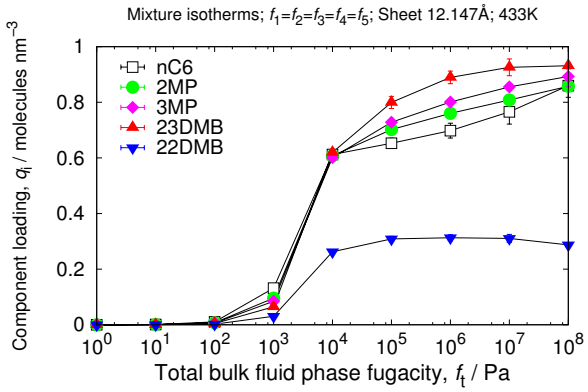

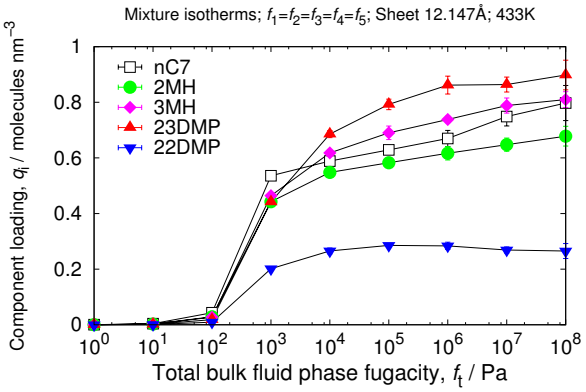

8.13 Sheet: free spacing 13.567 Å

cell size	$a = 39.36$ [Å], $b = 51.12$ [Å], $c = 51.12$ [Å]
volume	102857.69 [Å^3]
framework density	446.75 [kg/m^3]
sheet-sheet distance	17.04 [Å]

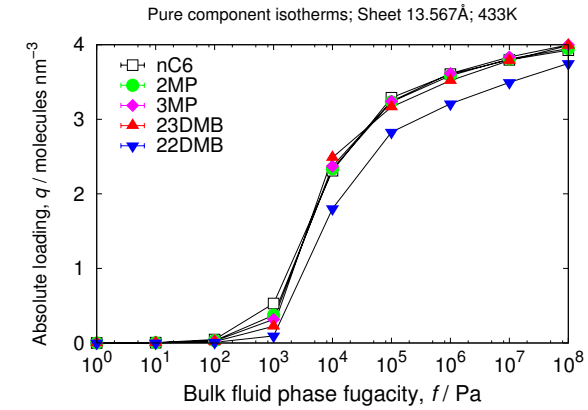

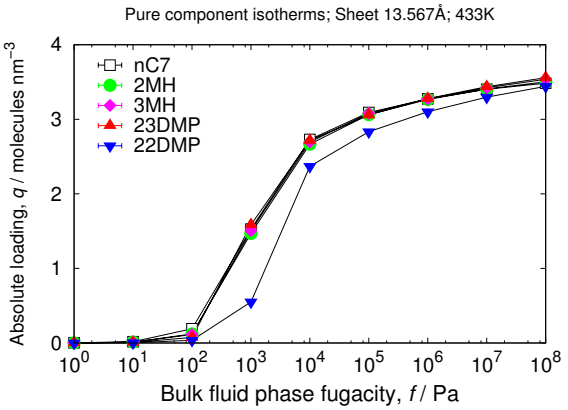

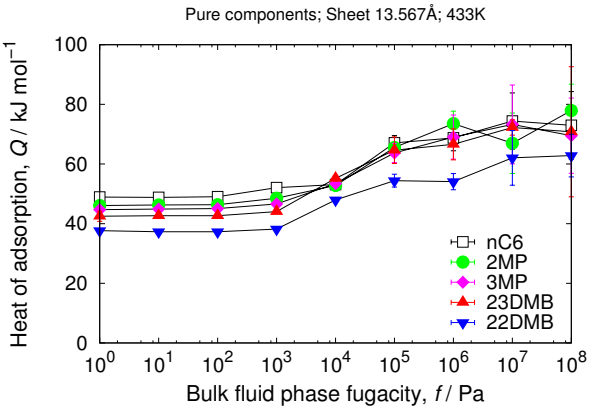

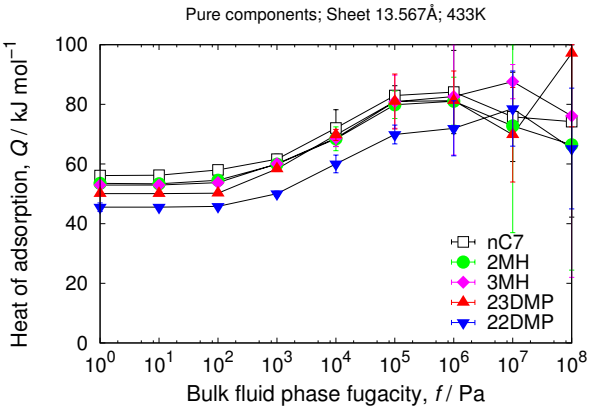

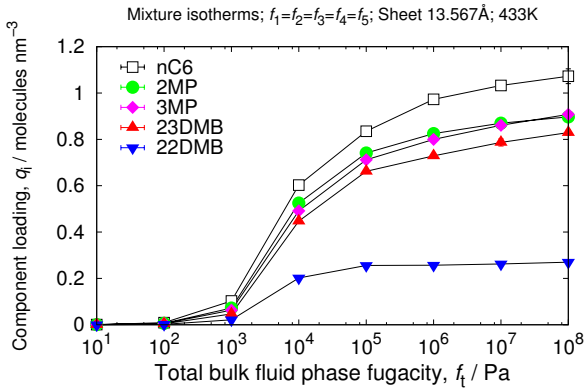

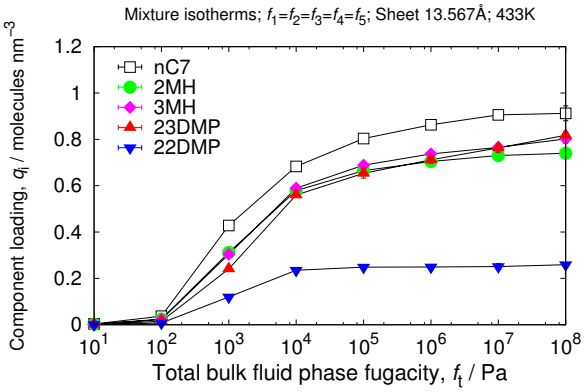

8.14 Sheet: free spacing 14.987 Å

cell size	$a = 39.36$ [Å], $b = 55.38$ [Å], $c = 55.38$ [Å]
volume	120714.9 [Å^3]
framework density	412.38 [kg/m^3]
sheet-sheet distance	18.46 [Å]

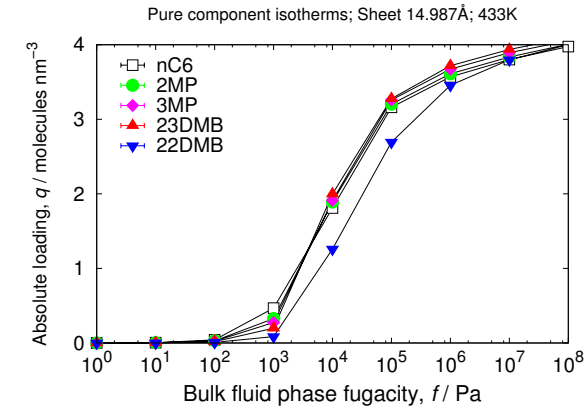

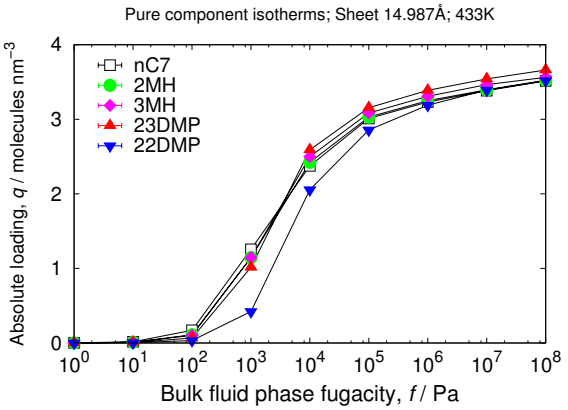

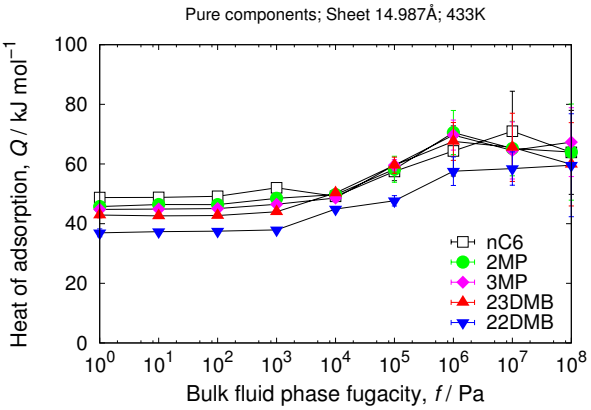

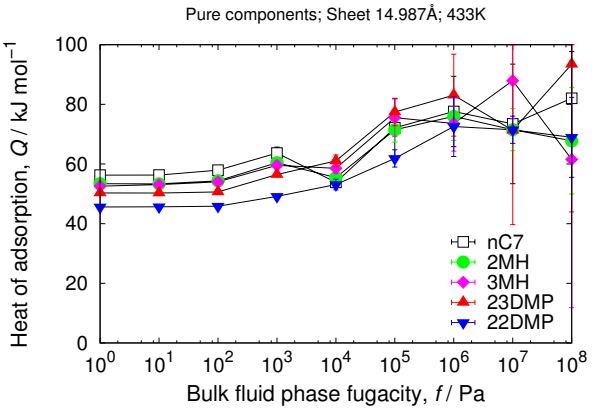

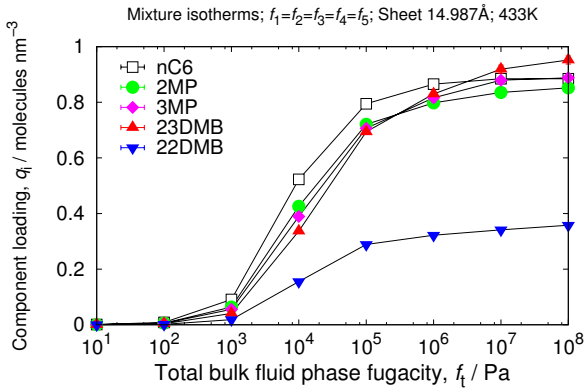

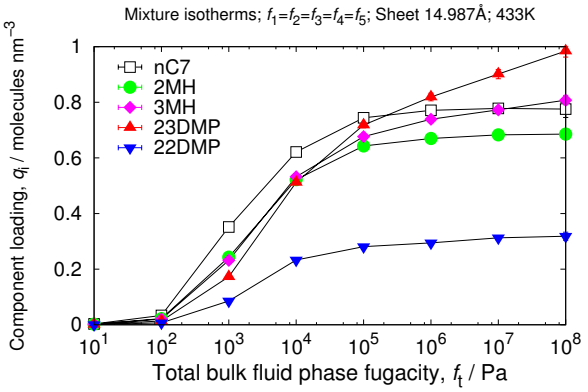

8.15 Sheet: free spacing 16.407 Å

cell size	$a = 39.36$ [Å], $b = 59.64$ [Å], $c = 59.64$ [Å]
volume	140000.7 [Å^3]
framework density	382.93 [kg/m^3]
sheet-sheet distance	19.88 [Å]

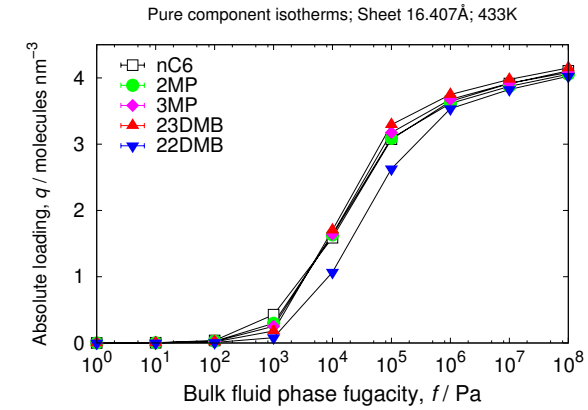

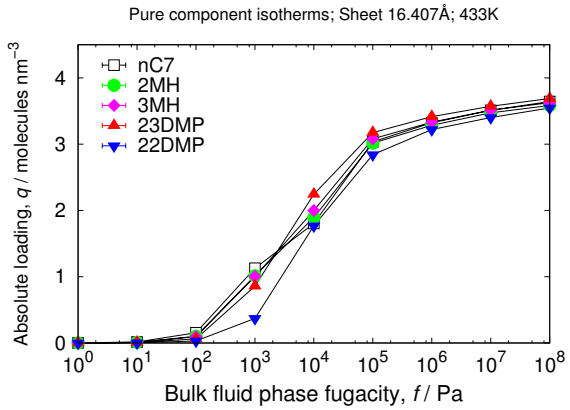

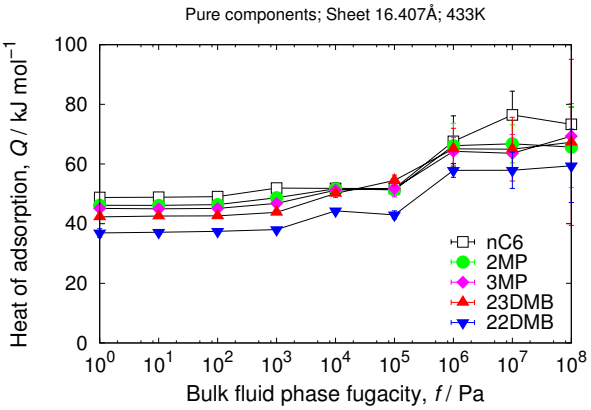

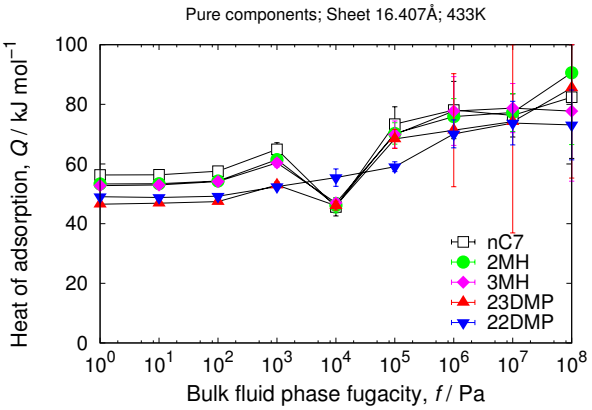

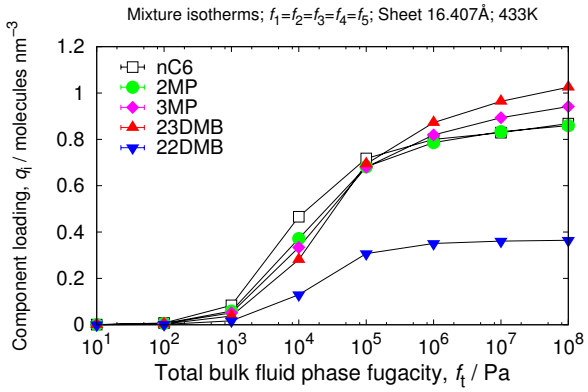

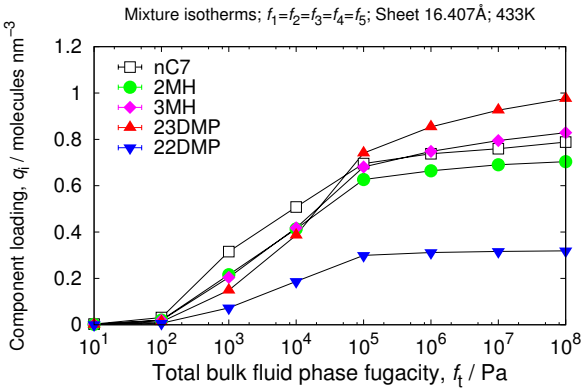

8.16 Heat of adsorption as a function of spacing

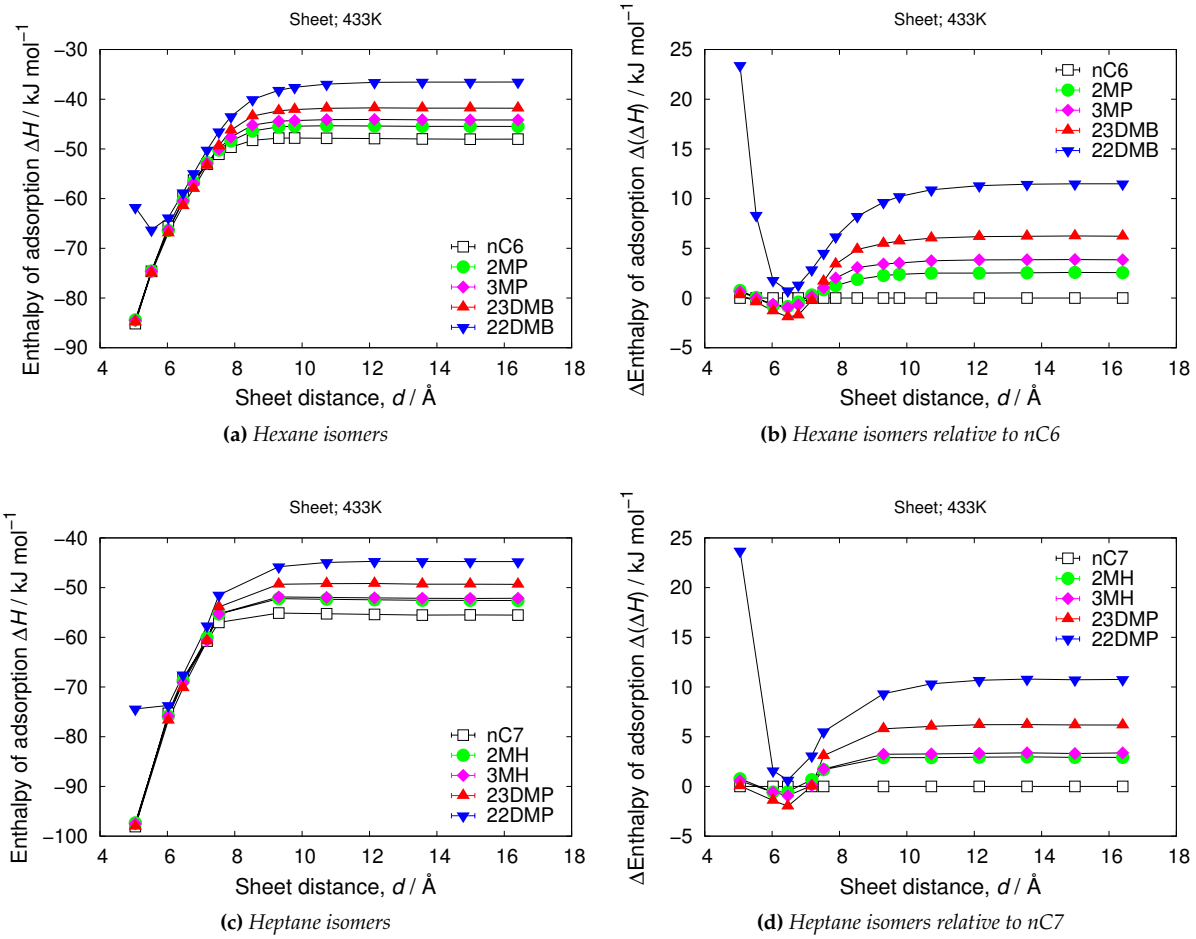

(a) *Hexane isomers*

(b) *Hexane isomers relative to nC6*

(c) *Heptane isomers*

(d) *Heptane isomers relative to nC7*

Figure S79: *Enthalpy of adsorption of hexane and heptane isomers in graphite sheets at 433K and infinite dilution.*

Graphite square channel with a fixed channel dimension. The walls are made up of a single layer of graphitic carbon. The edges of the simulation cell are treated with periodic boundary conditions. Picture shows the equimolar C6 isomer mixture in square channels of 9.3 Å in effective diameter at a total fugacity of the bulk fluid phase of 100 kPa and 433K.

9

Square graphite channels

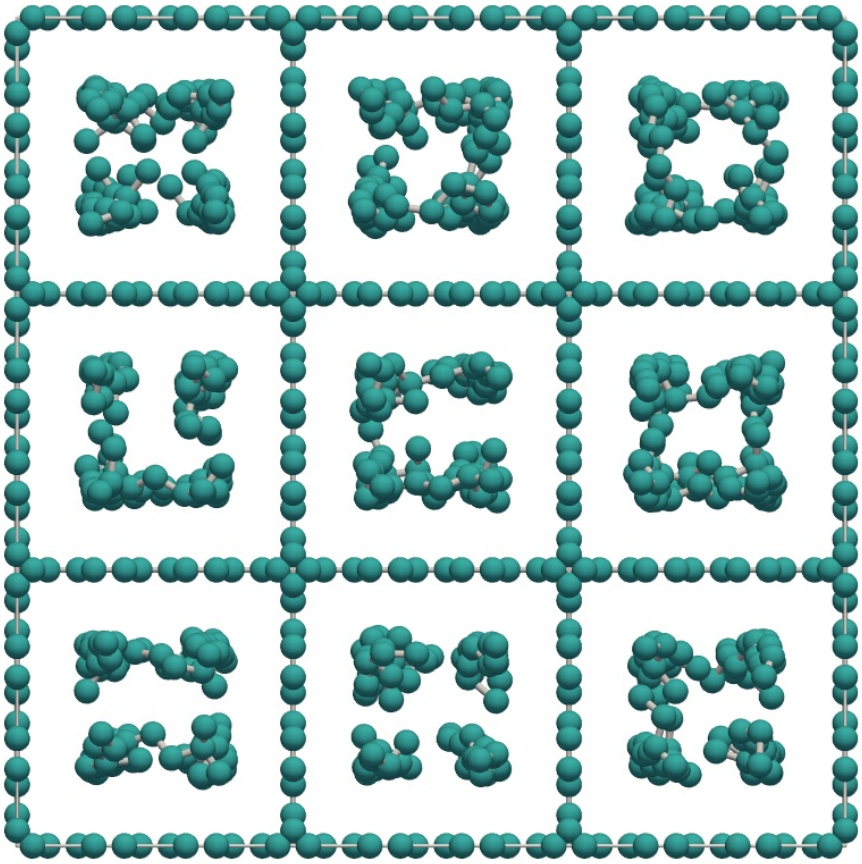

9.1 Channel: free dimension 5.047 Å

cell size	$a = 39.36$ [Å], $b = 25.56$ [Å], $c = 25.56$ [Å]
volume	25714.42 [Å^3]
framework density	1787.00 [kg/m^3]
sheet-sheet distance	8.52 [Å]

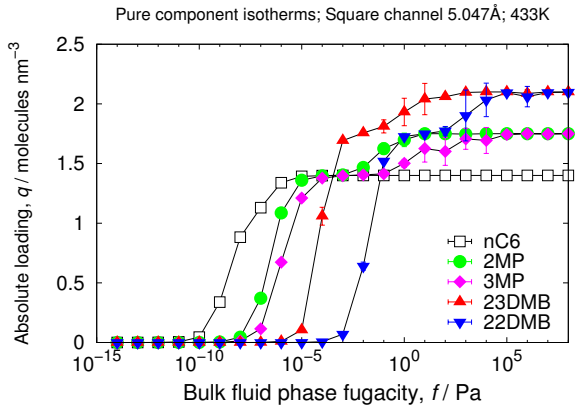

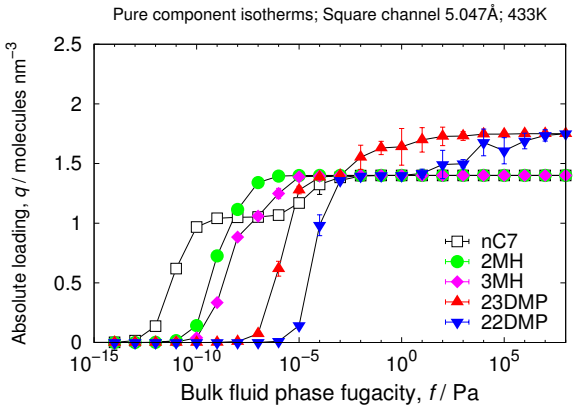

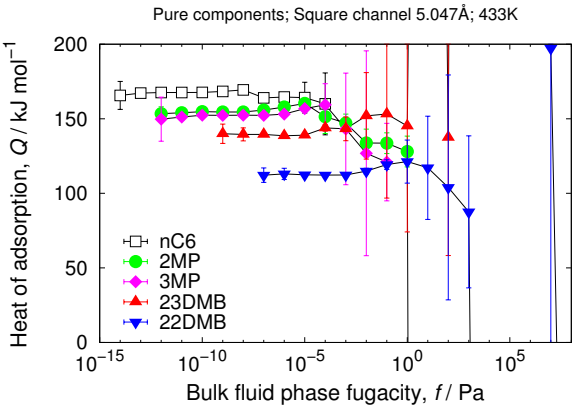

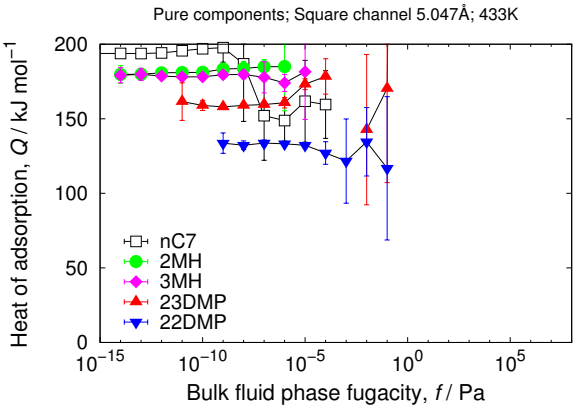

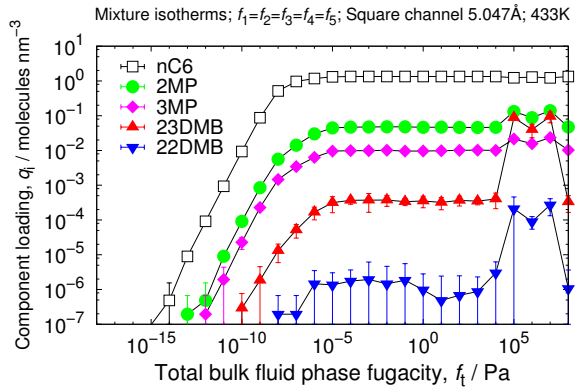

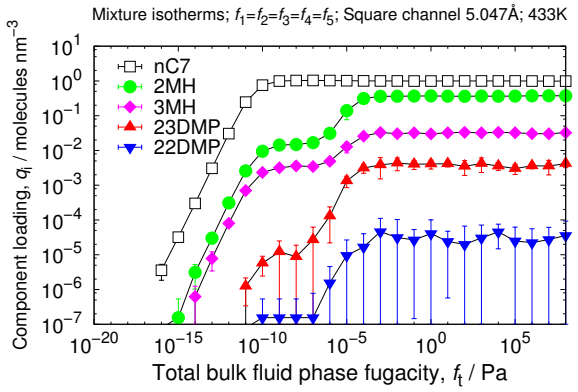

9.2 Channel: free dimension 6.467 Å

cell size	$a = 39.36$ [Å], $b = 29.82$ [Å], $c = 29.82$ [Å]
volume	35000.19 [Å^3]
framework density	1495.24 [kg/m^3]
sheet-sheet distance	9.94 [Å]

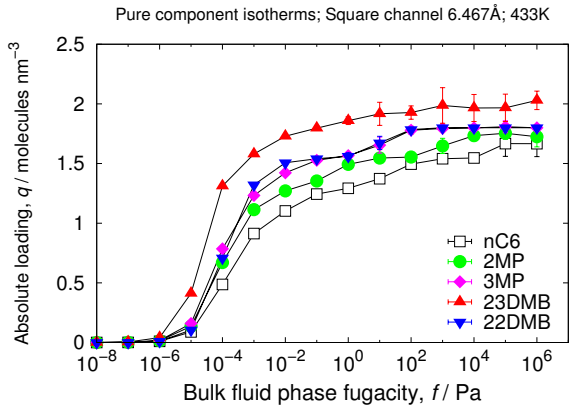

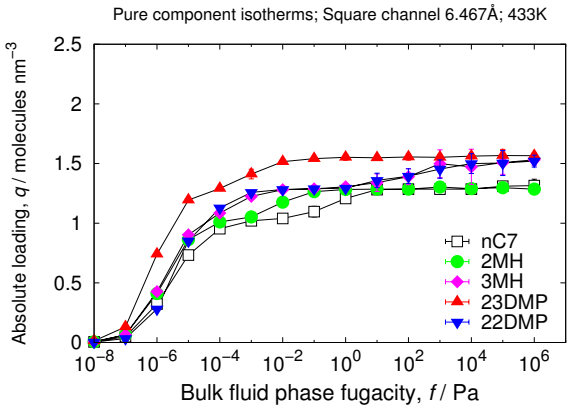

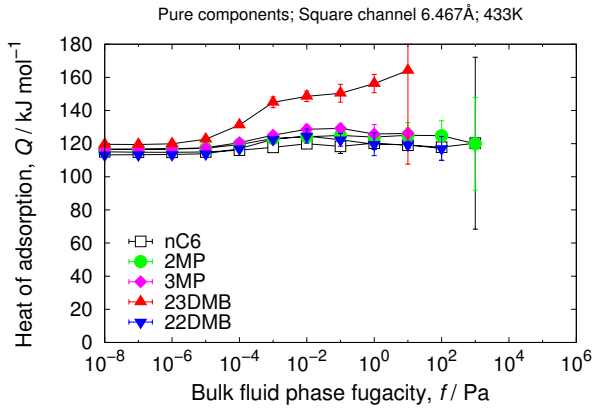

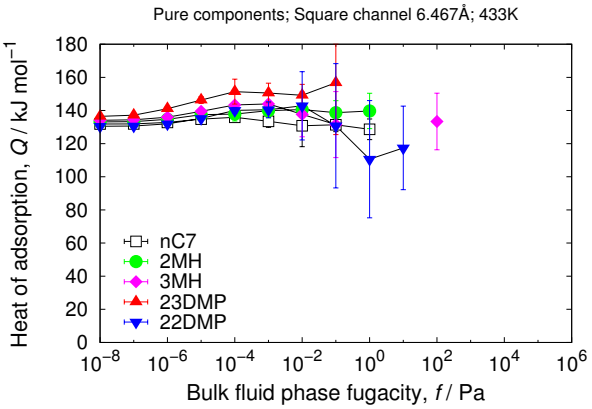

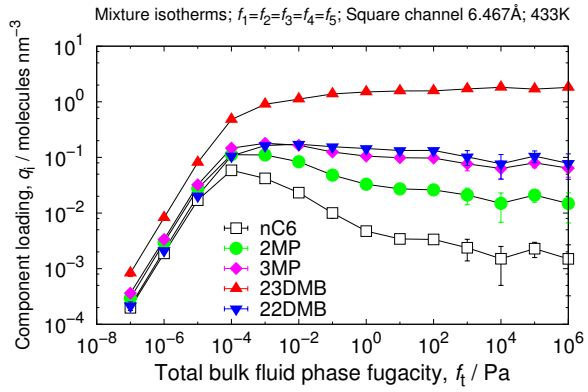

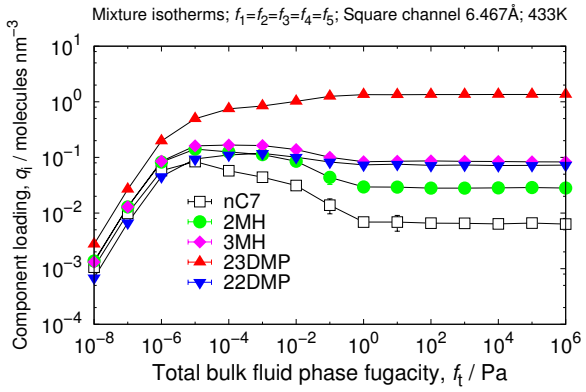

9.3 Channel: free dimension 7.887 Å

cell size	$a = 39.36$ [Å], $b = 34.08$ [Å], $c = 34.08$ [Å]
volume	45714.53 [Å^3]
framework density	1312.33 [kg/m^3]
sheet-sheet distance	11.36 [Å]

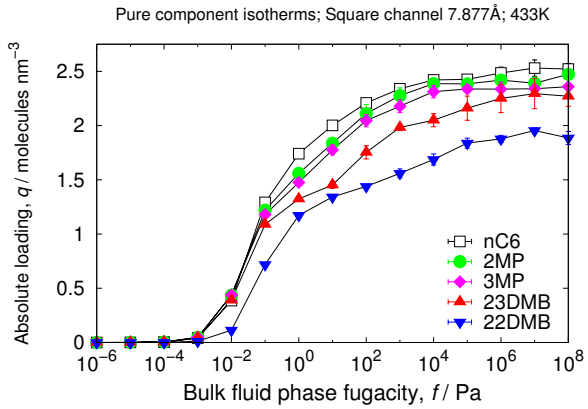

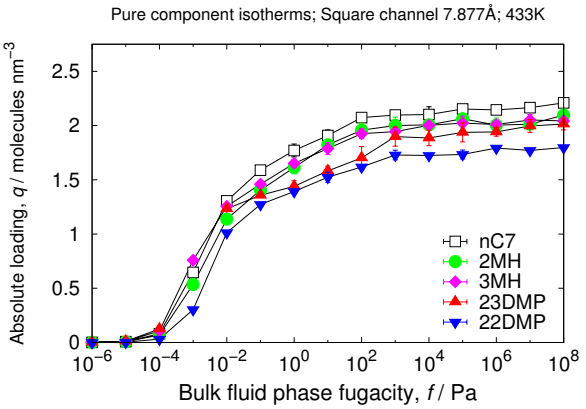

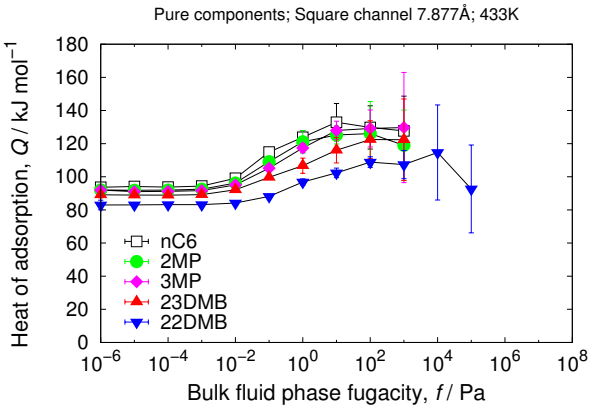

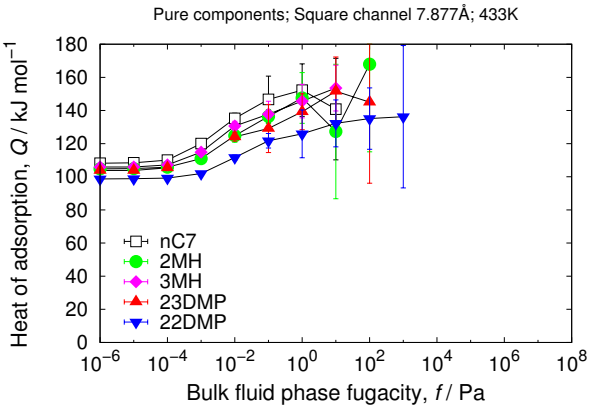

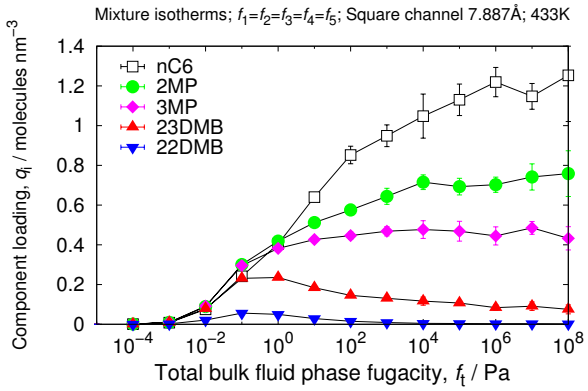

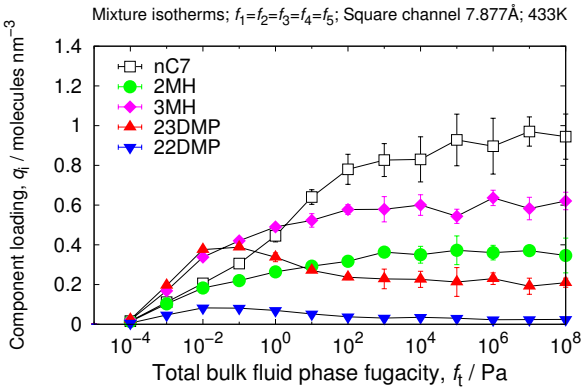

9.4 Channel: free dimension 9.307 Å

cell size	$a = 39.36$ [Å], $b = 38.34$ [Å], $c = 38.34$ [Å]
volume	57857.45 [Å^3]
framework density	1191.33 [kg/m^3]
sheet-sheet distance	12.78 [Å]

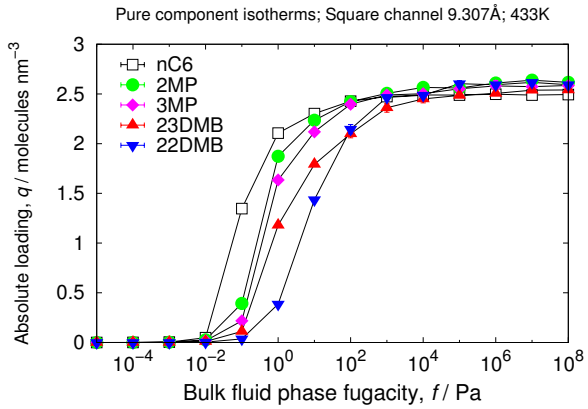

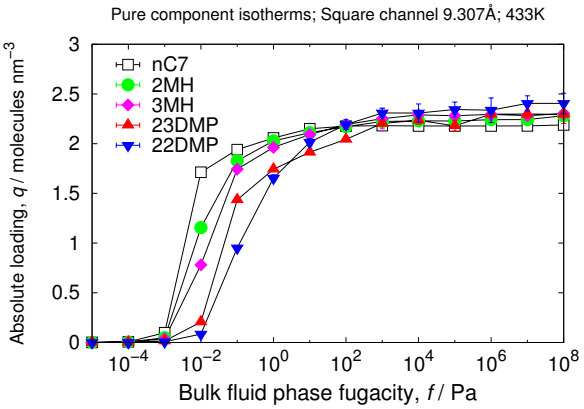

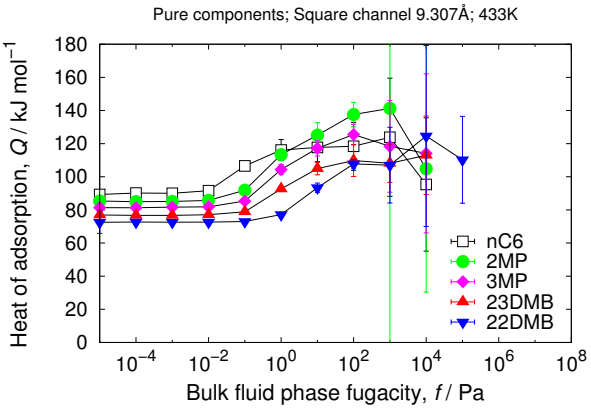

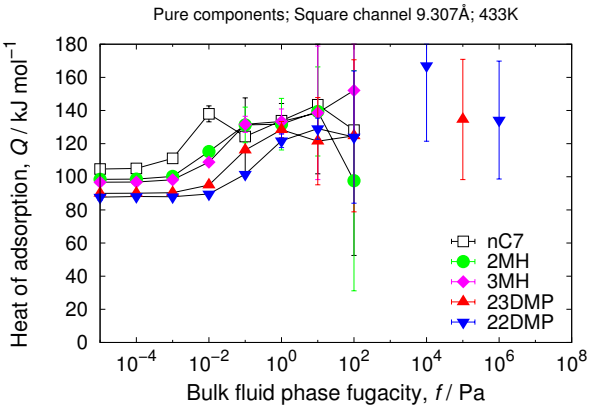

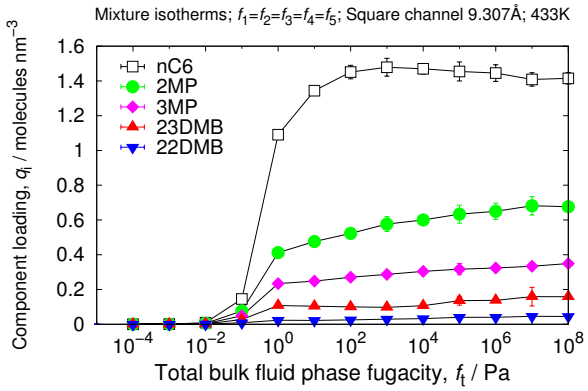

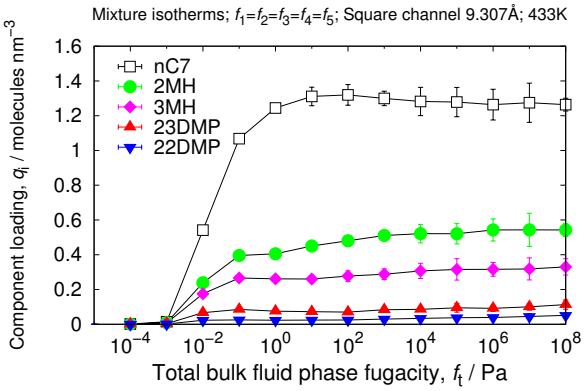

9.5 Channel: free dimension 10.727 Å

cell size	$a = 39.36$ [Å], $b = 42.6$ [Å], $c = 42.6$ [Å]
volume	71428.95 [Å^3]
framework density	1054.33 [kg/m^3]
sheet-sheet distance	14.2 [Å]

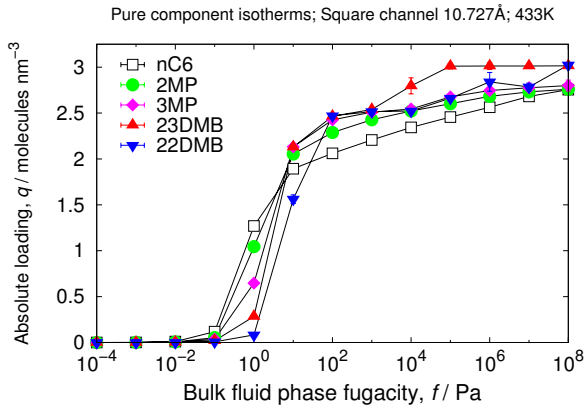

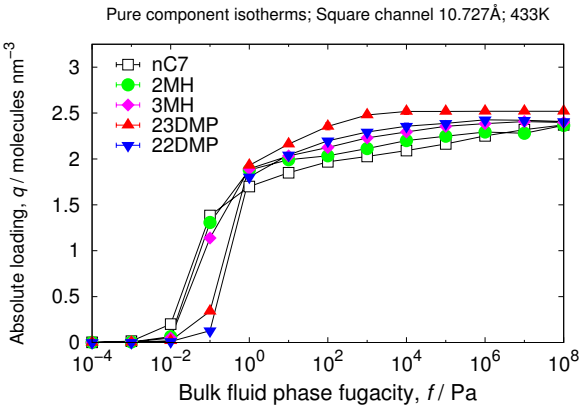

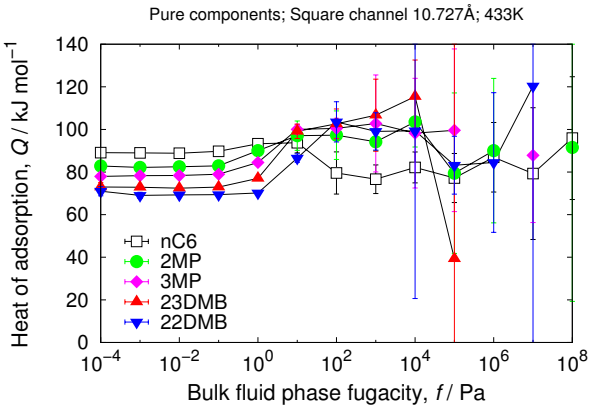

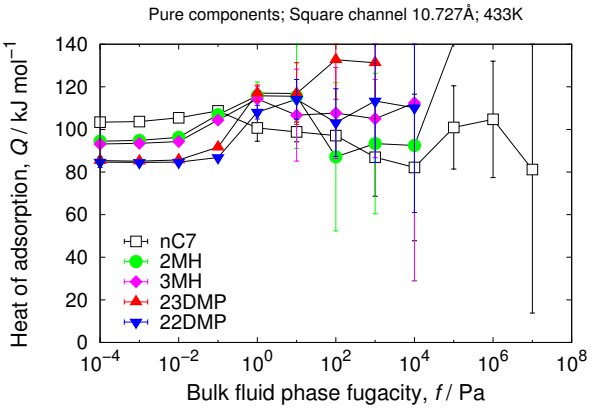

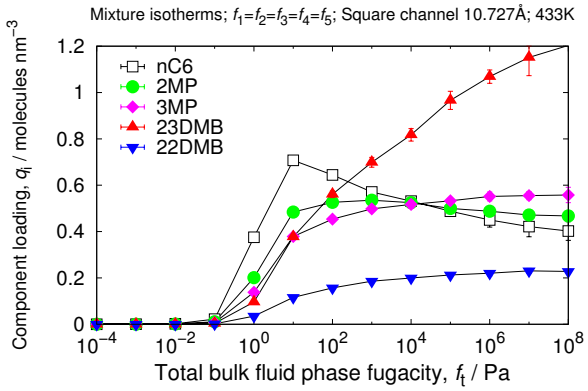

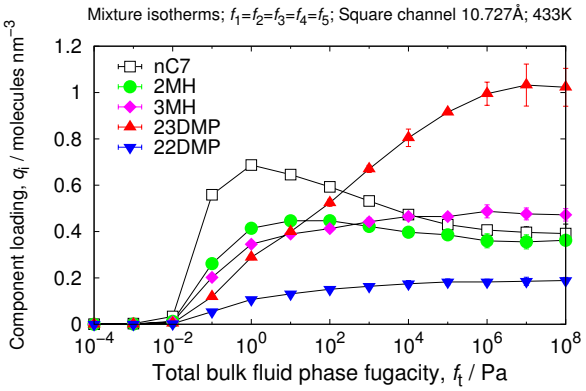

9.6 Channel: free dimension 12.147 Å

cell size	$a = 39.36$ [Å], $b = 46.86$ [Å], $c = 46.86$ [Å]
volume	86429.03 [Å^3]
framework density	959.96 [kg/m^3]
sheet-sheet distance	15.62 [Å]

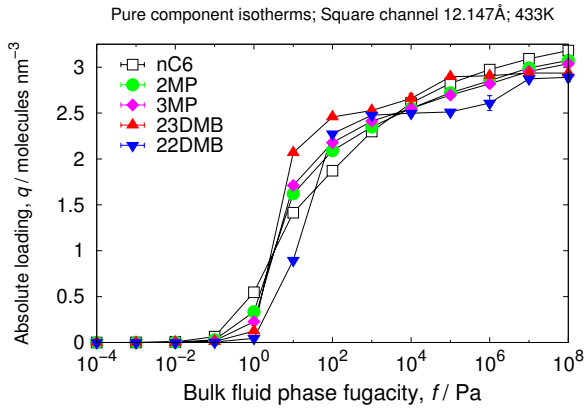

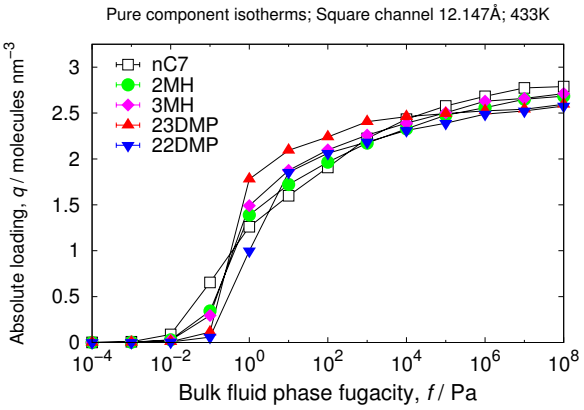

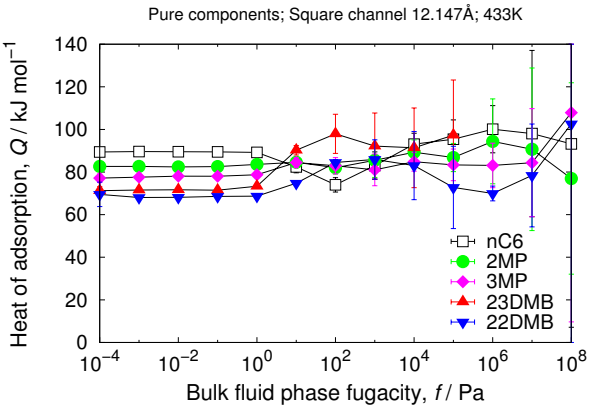

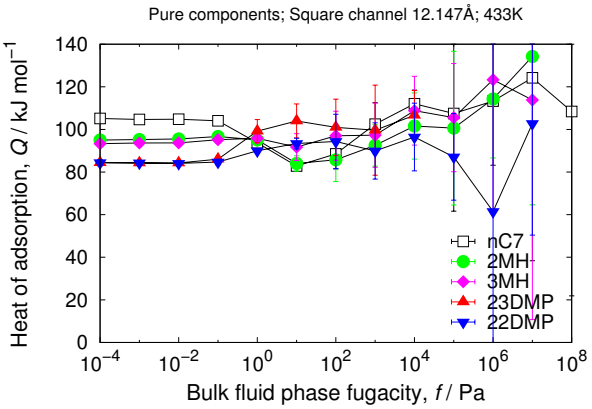

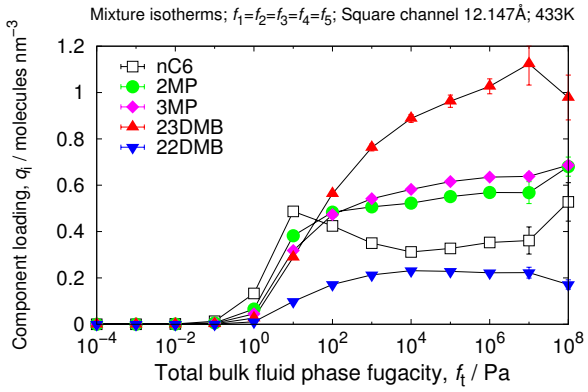

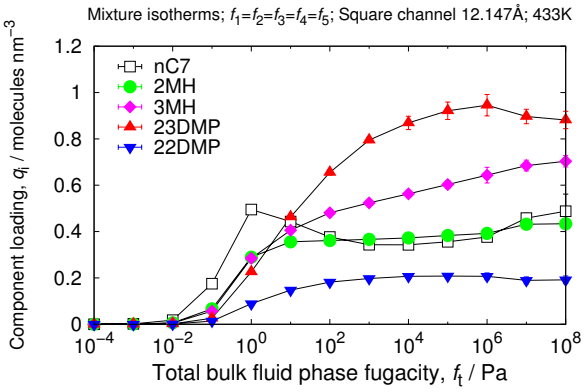

9.7 Channel: free dimension 13.567 Å

cell size	$a = 39.36$ [Å], $b = 51.12$ [Å], $c = 51.12$ [Å]
volume	102857.69 [Å^3]
framework density	893.50 [kg/m^3]
sheet-sheet distance	17.04 [Å]

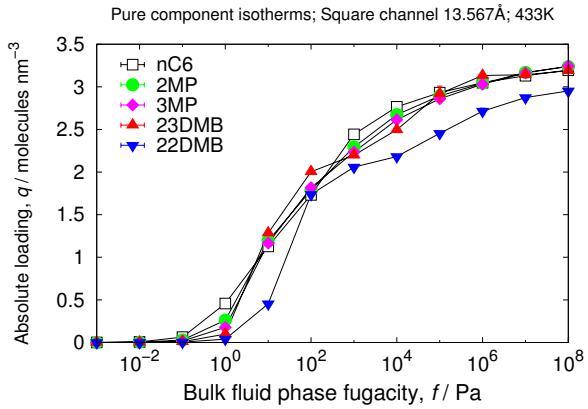

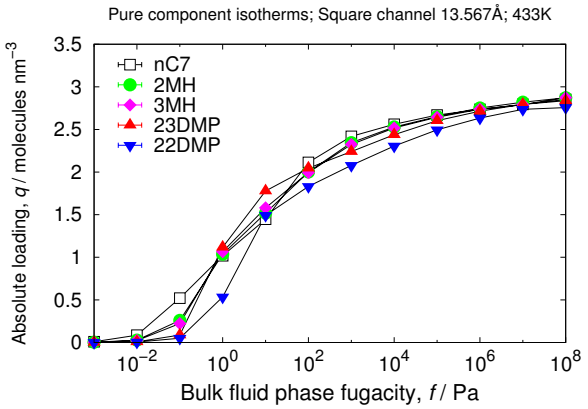

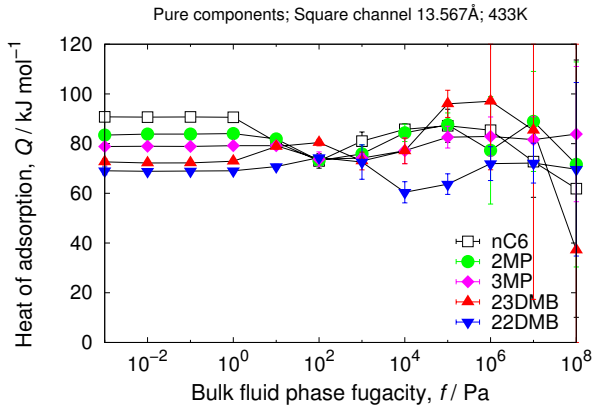

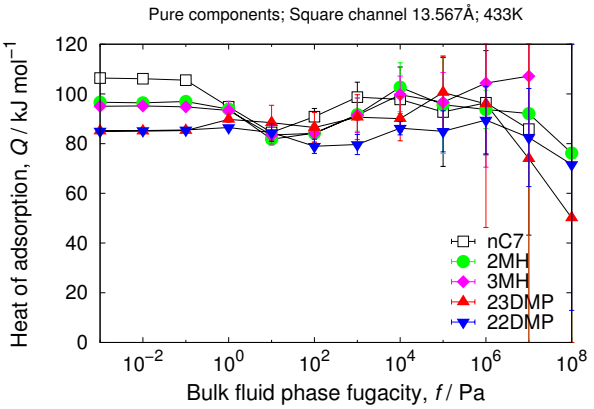

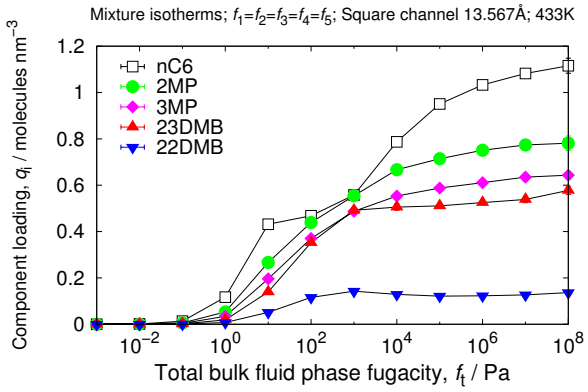

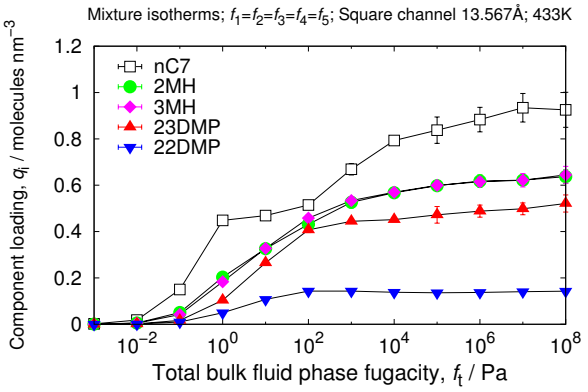

9.8 Channel: free dimension 14.987 Å

cell size	$a = 39.36$ [Å], $b = 55.38$ [Å], $c = 55.38$ [Å]
volume	120714.93 [Å^3]
framework density	814.19 [kg/m^3]
sheet-sheet distance	18.46 [Å]

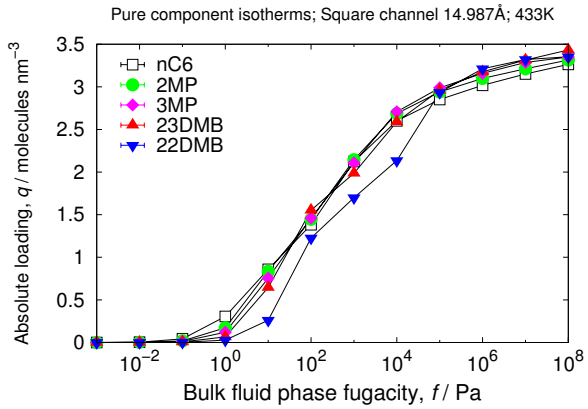

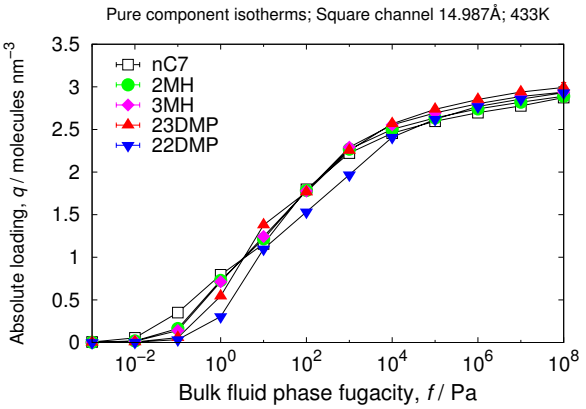

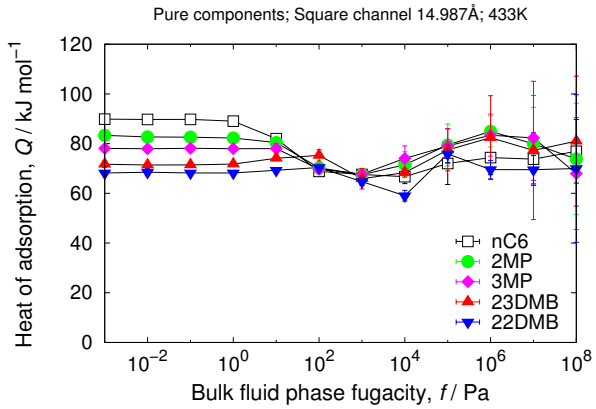

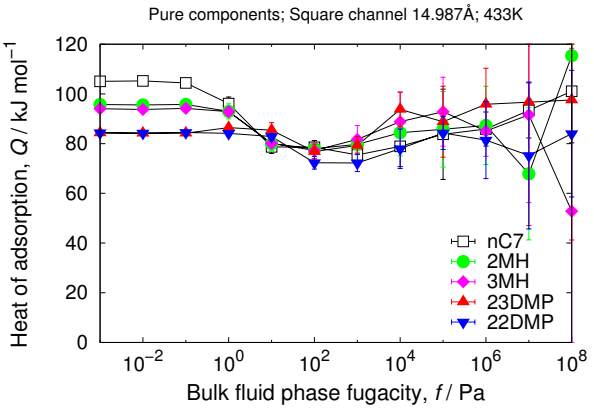

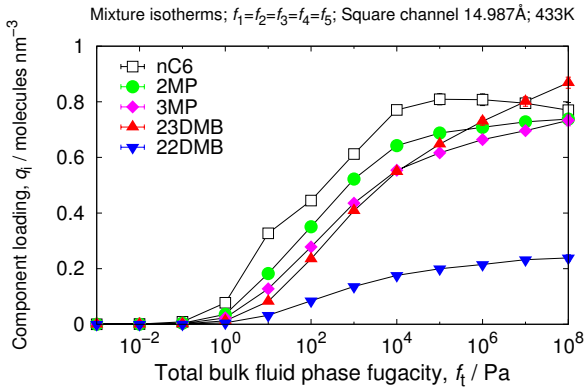

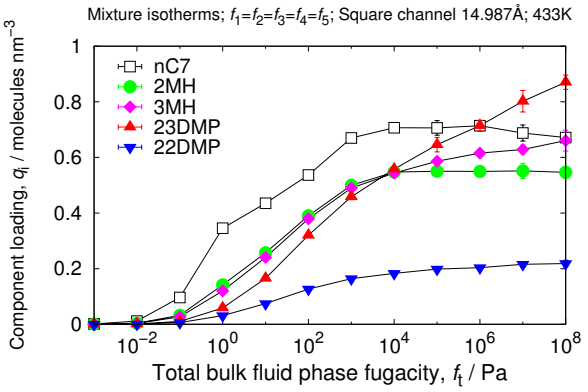

9.9 Channel: free dimension 16.407 Å

cell size	$a = 39.36$ [Å], $b = 59.64$ [Å], $c = 59.64$ [Å]
volume	140000.75 [Å^3]
framework density	756.74 [kg/m^3]
sheet-sheet distance	19.88 [Å]

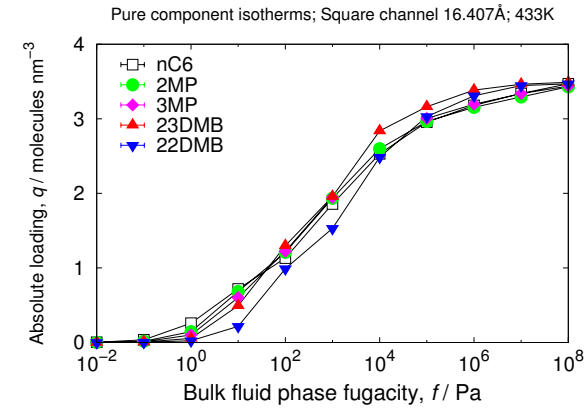

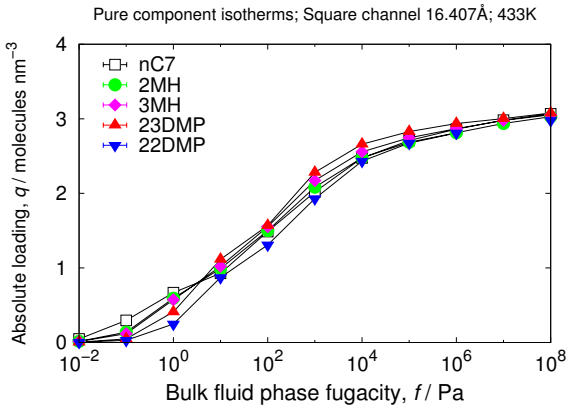

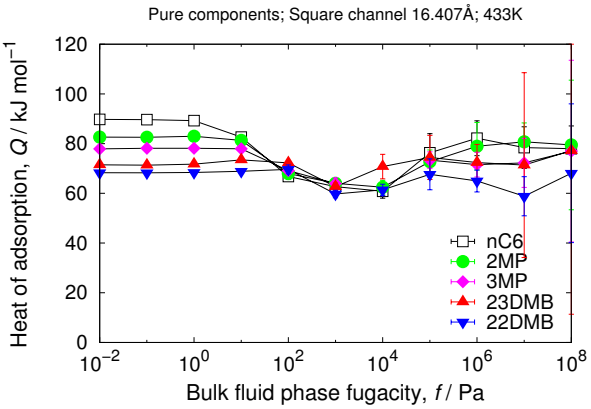

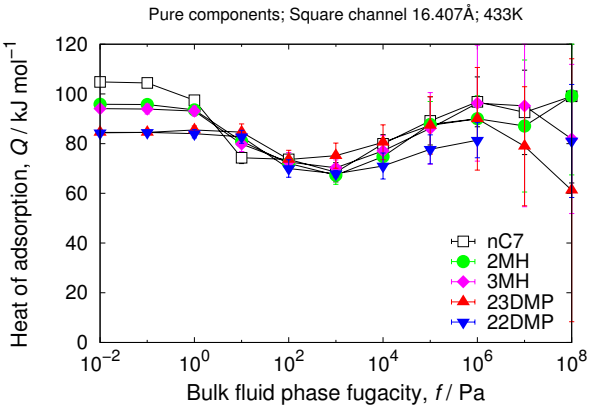

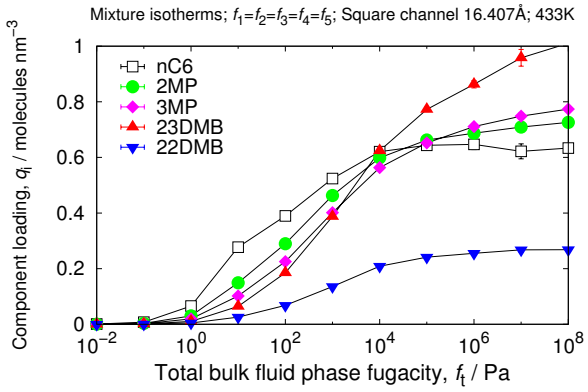

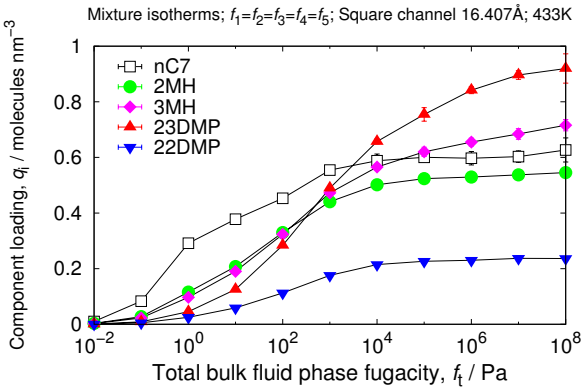

9.10 Heat of adsorption as a function of spacing

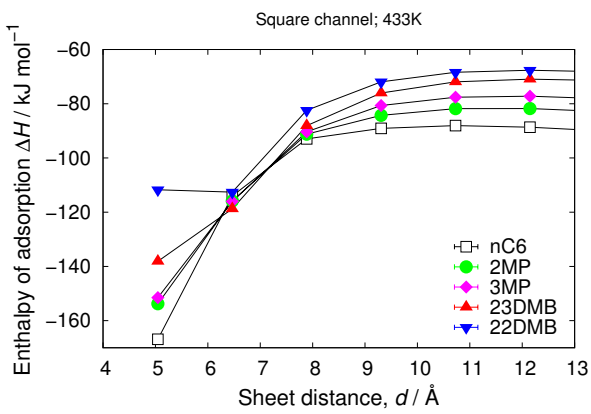

(a) *Hexane isomers*

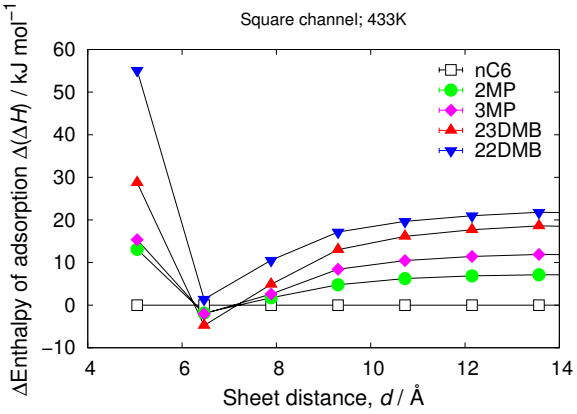

(b) *Hexane isomers relative to nC6*

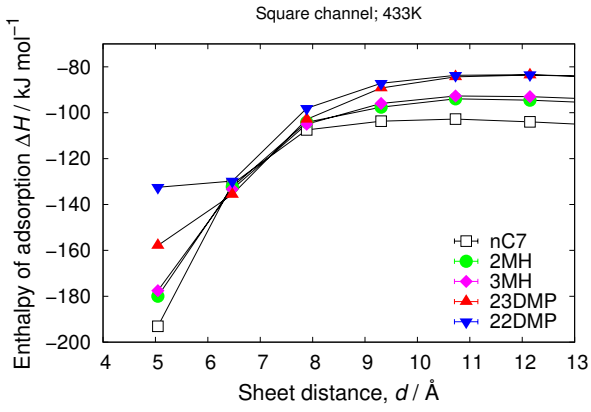

(c) *Heptane isomers*

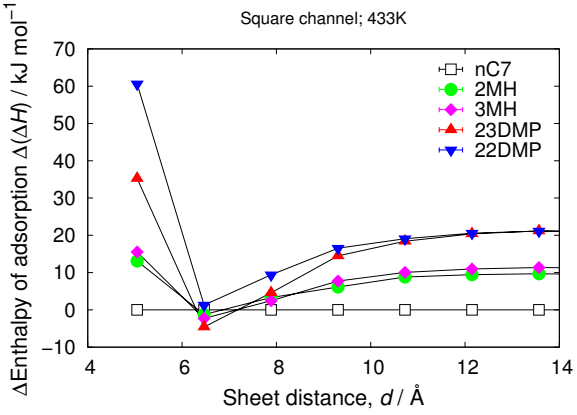

(d) *Heptane isomers relative to nC7*

Figure S80: *Enthalpy of adsorption of hexane and heptane isomers in square graphite-channels at 433K and infinite dilution.*

Graphite cylindrical channel with a fixed channel dimension. The walls are made up of a single layer of graphitic carbon. The edges of the simulation cell are treated with periodic boundary conditions. Picture shows the equimolar C6 isomer mixture in CNT(n=4,m=14), effective diameter of 9.3 Å, at a total fugacity of the bulk fluid phase of 100 kPa and 433K.

10

Cylindrical graphite channels (Carbon Nanotubes)

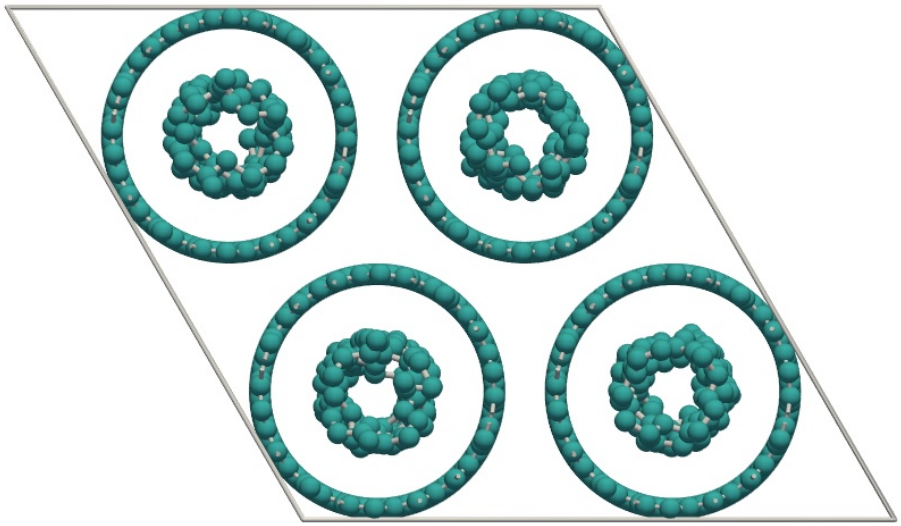

10.1 Channel: free dimension 4.997 Å (CNT: $n = 3, m = 9$)

cell size	$a = 23.6304$ [Å], $b = 23.6304$ [Å], $c = 61.4384$ [Å]
unit cell angles	$\alpha = \beta = 90[^\circ]$, $\gamma = 120[^\circ]$
framework density	1675.52 [kg/m^3]
volume	29710.68 [Å^3]
void fraction	0.589 [-]
sheet-sheet distance	8.47 [Å]
LJ cutoff	10 Å

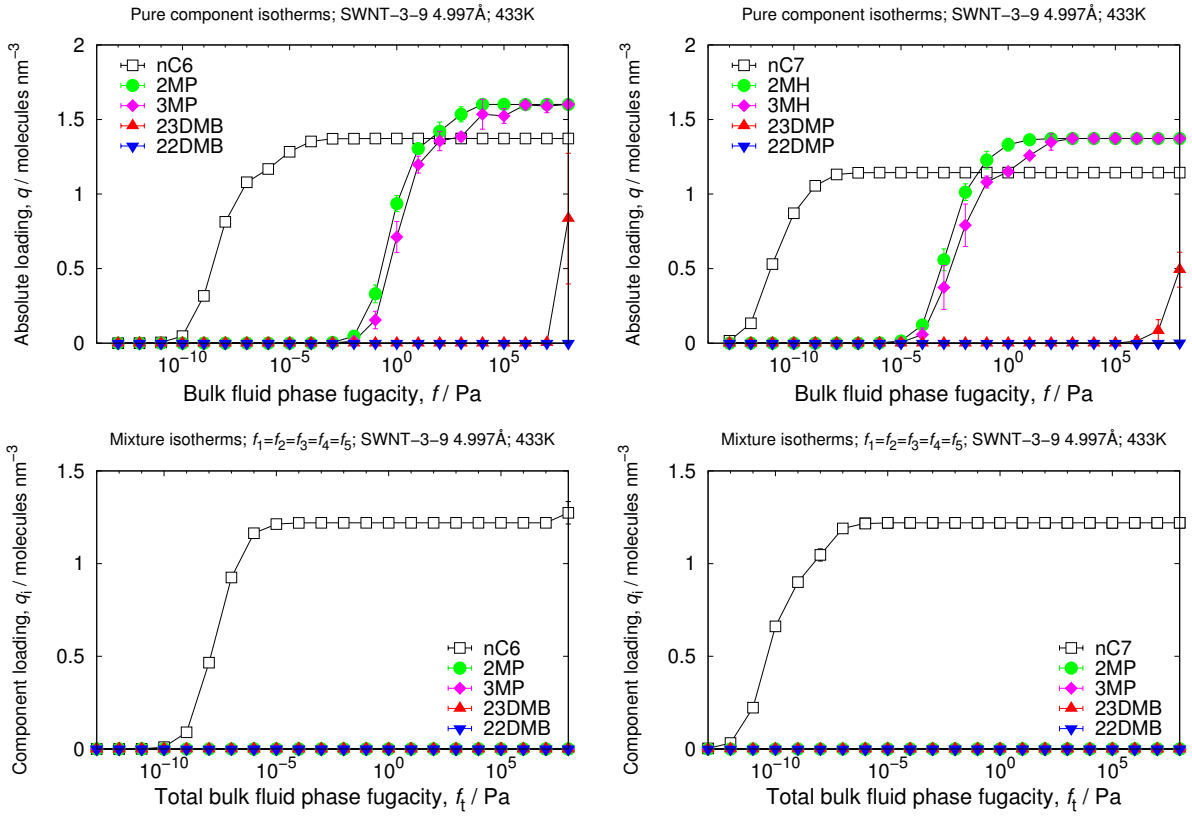

10.2 Channel: free dimension 6.527 Å (CNT: $n = 3, m = 11$)

cell size	$a = 26.6844$ [Å], $b = 26.6844$ [Å], $c = 54.388$ [Å]
unit cell angles	$\alpha = \beta = 90[^\circ]$, $\gamma = 120[^\circ]$
volume	33538.88 [Å^3]
void fraction	0.680 [-]
framework density	1550.88 [kg/m^3]
sheet-sheet distance	10.0 [Å]

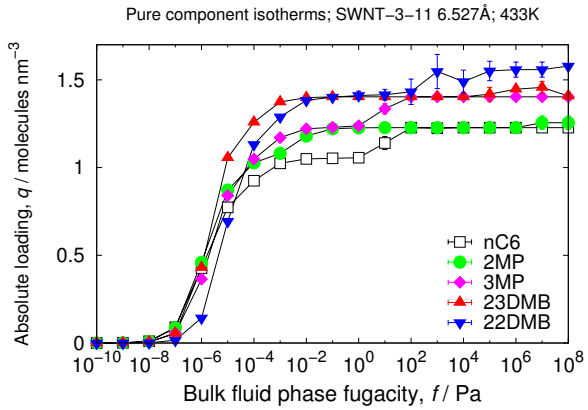

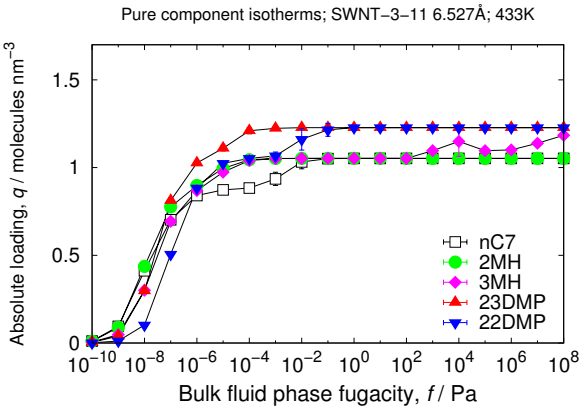

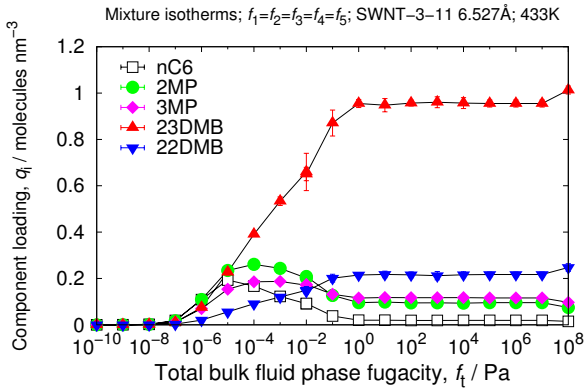

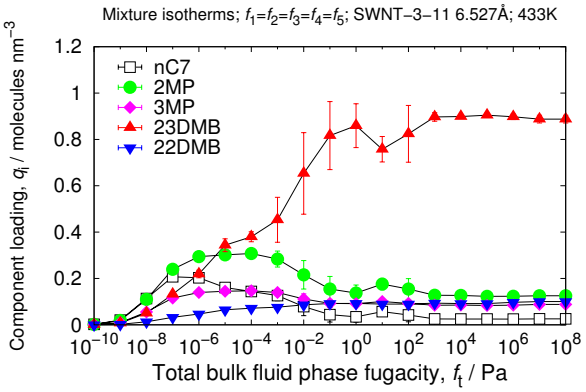

10.3 Channel: free dimension 7.897 Å (CNT: $n = 1, m = 14$)

cell size	$a = 29.4382$ [Å], $b = 29.4382$ [Å], $c = 61.8801$ [Å]
unit cell angles	$\alpha = \beta = 90[^\circ]$, $\gamma = 120[^\circ]$
volume	46441.28 [Å^3]
void fraction	0.712 [-]
framework density	1449.83 [kg/m^3]
sheet-sheet distance	11.37 [Å]

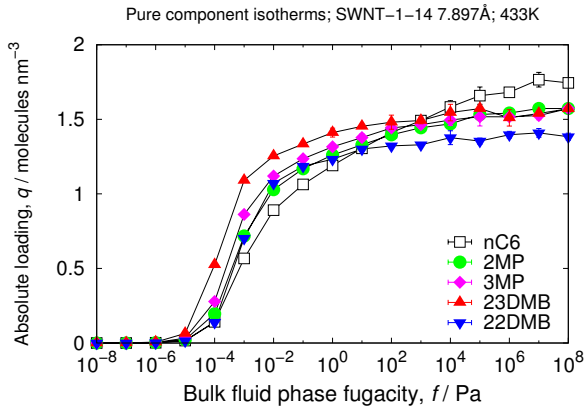

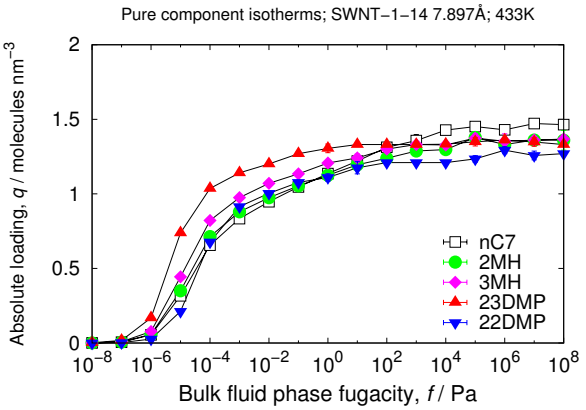

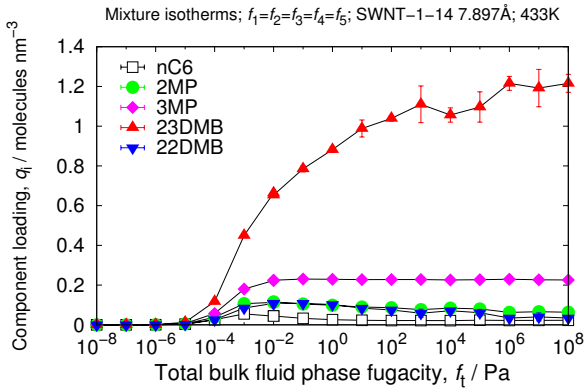

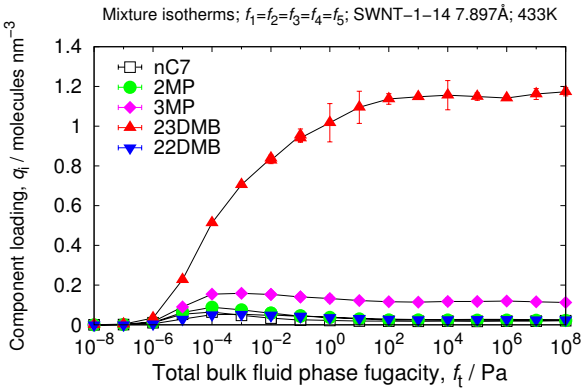

10.4 Channel: free dimension 9.347 Å (CNT: $n = 4, m = 14$)

cell size	$a = 32.3268$ [Å], $b = 32.3268$ [Å], $c = 69.7392$ [Å]
unit cell angles	$\alpha = \beta = 90[^\circ]$, $\gamma = 120[^\circ]$
volume	63115.06 [Å^3]
void fraction	0.734 [-]
framework density	1355.00 [kg/m^3]
sheet-sheet distance	12.82 [Å]

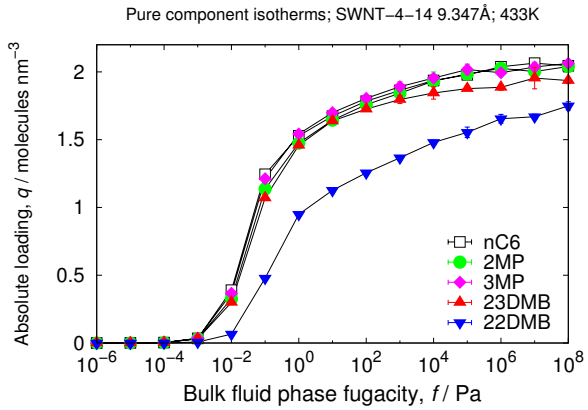

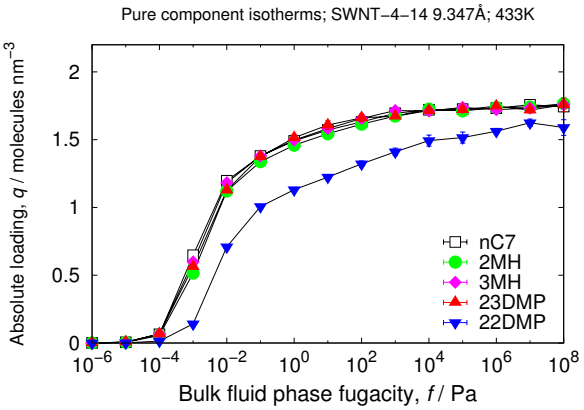

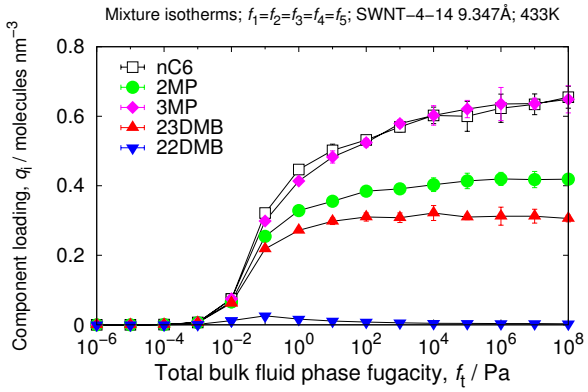

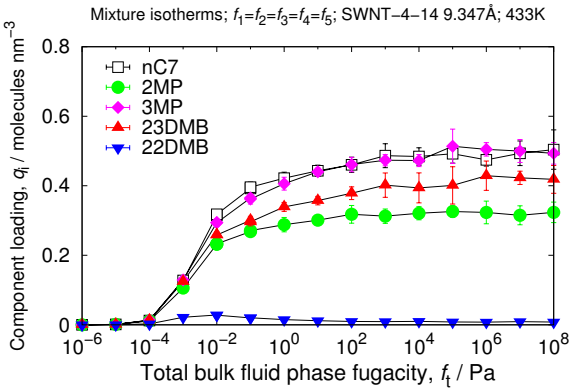

10.5 Channel: free dimension 10.767 Å (CNT: $n = 10, m = 11$)

cell size	$a = 35.1808$ [Å], $b = 35.1808$ [Å], $c = 77.5039$ [Å]
unit cell angles	$\alpha = \beta = 90[^\circ]$, $\gamma = 120[^\circ]$
volume	83074.09 [Å^3]
void fraction	0.757 [-]
framework density	1271.45 [kg/m^3]
sheet-sheet distance	14.24 [Å]

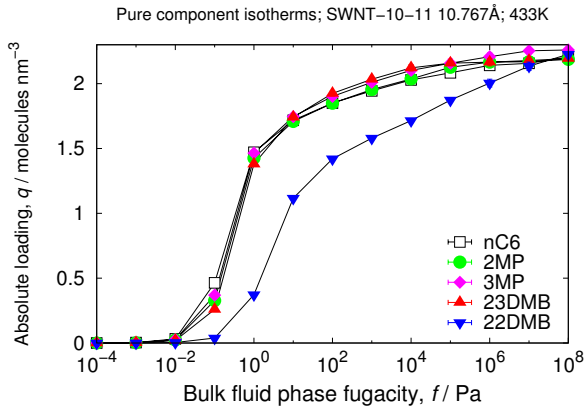

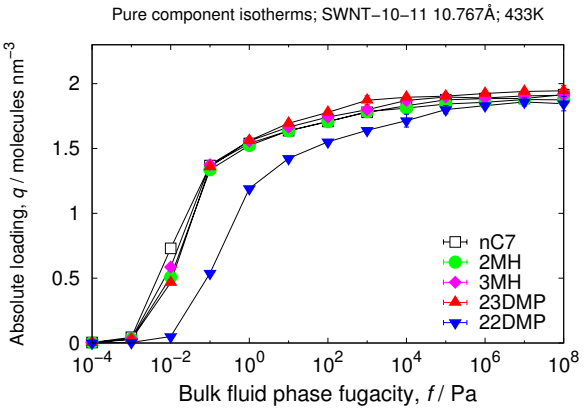

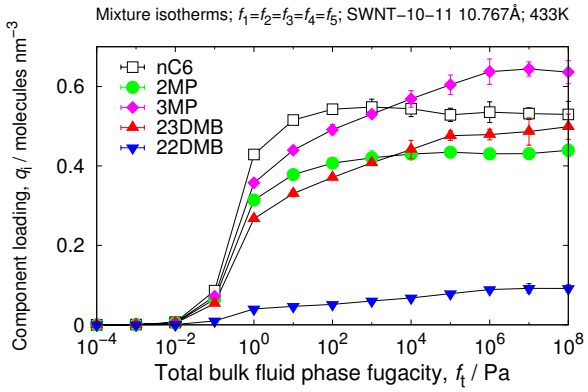

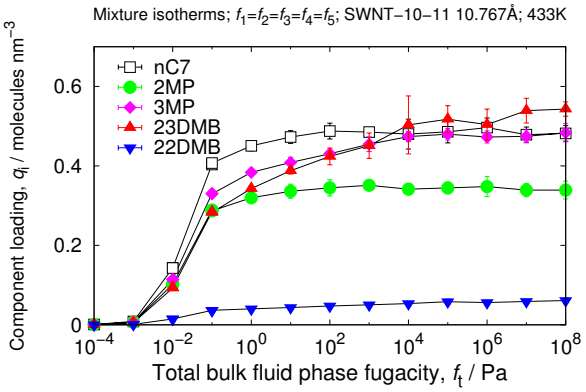

10.6 Channel: free dimension 12.167 Å (CNT: $n = 10, m = 13$)

cell size	$a = 37.9704$ [Å], $b = 37.9704$ [Å], $c = 85.0934$ [Å]
unit cell angles	$\alpha = \beta = 90[^\circ]$, $\gamma = 120[^\circ]$
volume	106247.04 [Å^3]
void fraction	0.774 [-]
framework density	1198.38 [kg/m^3]
sheet-sheet distance	15.64 [Å]

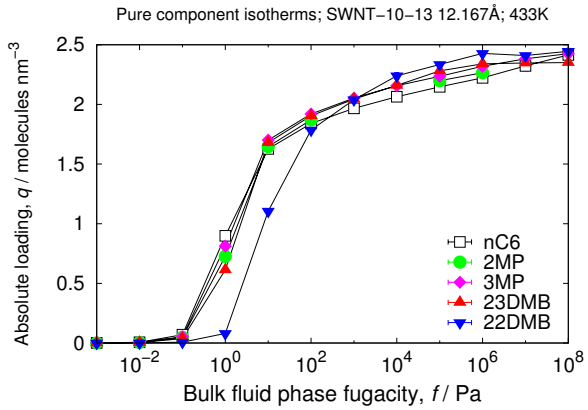

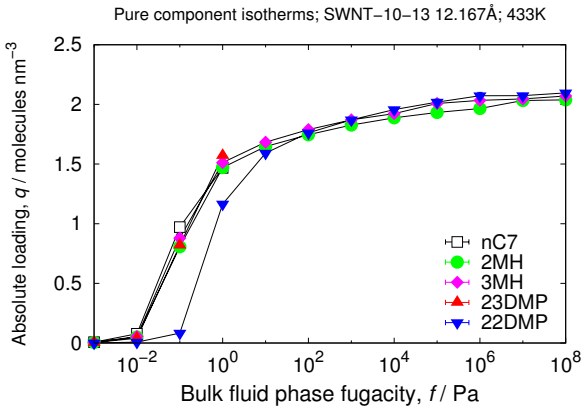

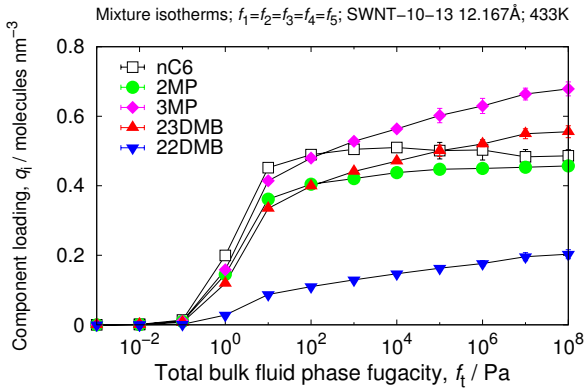

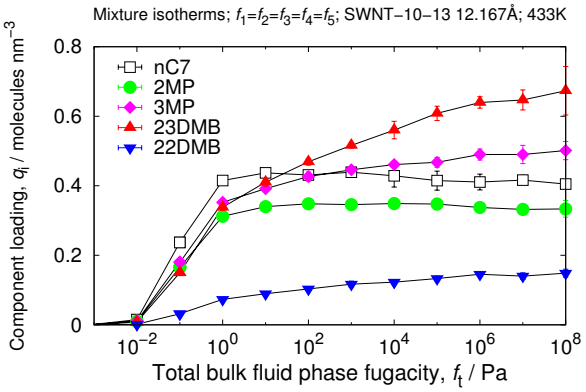

10.7 Heat of adsorption as a function of spacing

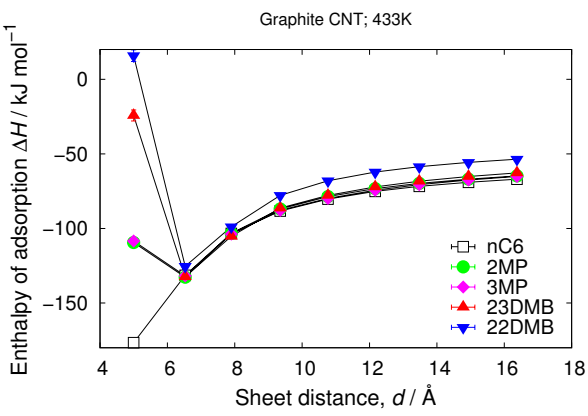

(a) *Hexane isomers*

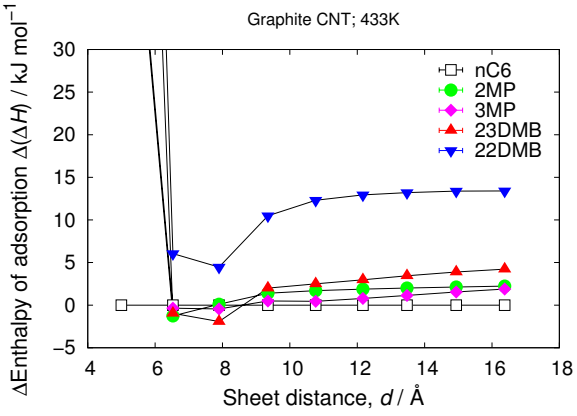

(b) *Hexane isomers relative to nC6*

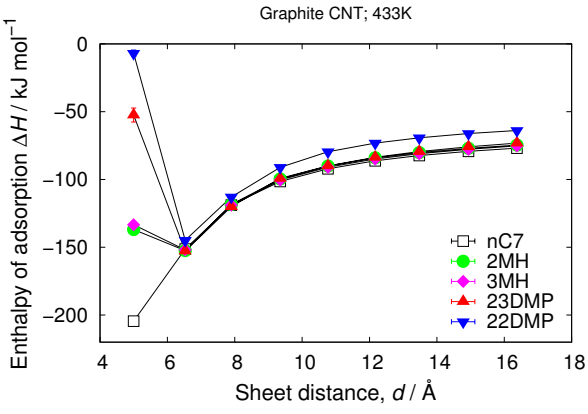

(c) *Heptane isomers*

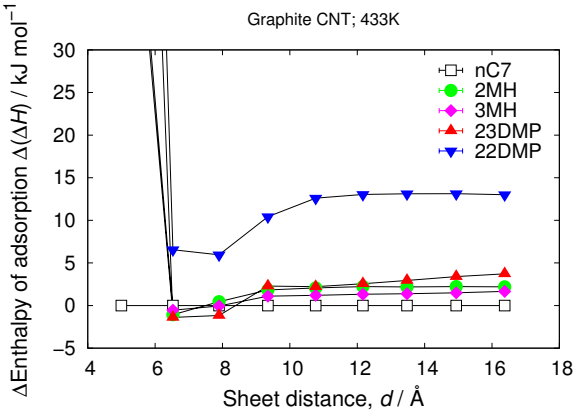

(d) *Heptane isomers relative to nC7*

Figure S81: *Enthalpy of adsorption of hexane and heptane isomers in graphite cylinders at 433K and infinite dilution.*

Acknowledgments

We thank Jasper van Baten, Said Hamad Gomez, Tina Düren and Randall Snurr for help with various structure-cif-files.

List of video animations included as Supporting Information

MFI step breakthrough video animation of step breakthrough dynamics of an equimolar 5-component mixture of nC6/2MP/3MP/23DMB/22DMB in adsorbers packed with MFI zeolite at 433 K and 100 kPa of total pressure (20 kPa partial pressure).

CFI step breakthrough video animation of step breakthrough dynamics of an equimolar 5-component mixture of nC6/2MP/3MP/23DMB/22DMB in adsorbers packed with CFI zeolite at 433 K and 100 kPa of total pressure (20 kPa partial pressure).

MgMOF-74 step breakthrough video animation of step breakthrough dynamics of an equimolar 5-component mixture of nC6/2MP/3MP/23DMB/22DMB in adsorbers packed with MgMOF-74 at 433 K and 100 kPa of total pressure (20 kPa partial pressure).

CoBDP step breakthrough video animation of step breakthrough dynamics of an equimolar 5-component mixture of nC6/2MP/3MP/23DMB/22DMB in adsorbers packed with CoBDP at 433 K and 100 kPa of total pressure (20 kPa partial pressure).

UiO-66 step breakthrough video animation of step breakthrough dynamics of an equimolar 5-component mixture of nC6/2MP/3MP/23DMB/22DMB in adsorbers packed with UiO-66 at 433 K and 100 kPa of total pressure (20 kPa partial pressure).

ZIF-77 step breakthrough video animation of step breakthrough dynamics of an equimolar 5-component mixture of nC6/2MP/3MP/23DMB/22DMB in adsorbers packed with ZIF-77 at 433 K and 100 kPa of total pressure (20 kPa partial pressure).

MFI pulse breakthrough video animation of pulse breakthrough dynamics of an equimolar 5-component mixture of nC6/2MP/3MP/23DMB/22DMB in adsorbers packed with MFI zeolite at 433 K and 100 kPa of total pressure (20 kPa partial pressure).

CFI pulse breakthrough video animation of pulse breakthrough dynamics of an equimolar 5-component mixture of nC6/2MP/3MP/23DMB/22DMB in adsorbers packed with CFI zeolite at 433 K and 100 kPa of total pressure (20 kPa partial pressure).

MgMOF-74 pulse breakthrough video animation of pulse breakthrough dynamics of an equimolar 5-component mixture of nC6/2MP/3MP/23DMB/22DMB in adsorbers packed with MgMOF-74 at 433 K and 100 kPa of total pressure (20 kPa partial pressure).

CoBDP pulse breakthrough video animation of pulse breakthrough dynamics of an equimolar 5-component mixture of nC6/2MP/3MP/23DMB/22DMB in adsorbers packed with CoBDP at 433 K and 100 kPa of total pressure (20 kPa partial pressure).

UiO-66 pulse breakthrough video animation of pulse breakthrough dynamics of an equimolar 5-component mixture of nC6/2MP/3MP/23DMB/22DMB in adsorbers packed with UiO-66 at 433 K and 100 kPa of total pressure (20 kPa partial pressure).

ZIF-77 pulse breakthrough video animation of pulse breakthrough dynamics of an equimolar 5-component mixture of nC6/2MP/3MP/23DMB/22DMB in adsorbers packed with ZIF-77 at 433 K and 100 kPa of total pressure (20 kPa partial pressure).

ZIF-8 pulse breakthrough video animation of pulse breakthrough dynamics of an equimolar 5-component mixture of nC6/2MP/3MP/23DMB/22DMB in adsorbers packed with ZIF-8 at 433 K and 100 kPa of total pressure (20 kPa partial pressure).

ZIF-77 pulse breakthrough (13 components) video animation of pulse breakthrough dynamics of an equimolar 13-component mixture of C5/C6/C7 isomers in adsorbers packed with ZIF-77 at 433 K and 260 kPa of total pressure (20 kPa partial pressure).

ZIF-77 pulse breakthrough (15 components) video animation of pulse breakthrough dynamics of an equimolar 15-component mixture of C4/C5/C6/C7 isomers in adsorbers packed with ZIF-77 at 433 K and 300 kPa of total pressure (20 kPa partial pressure).

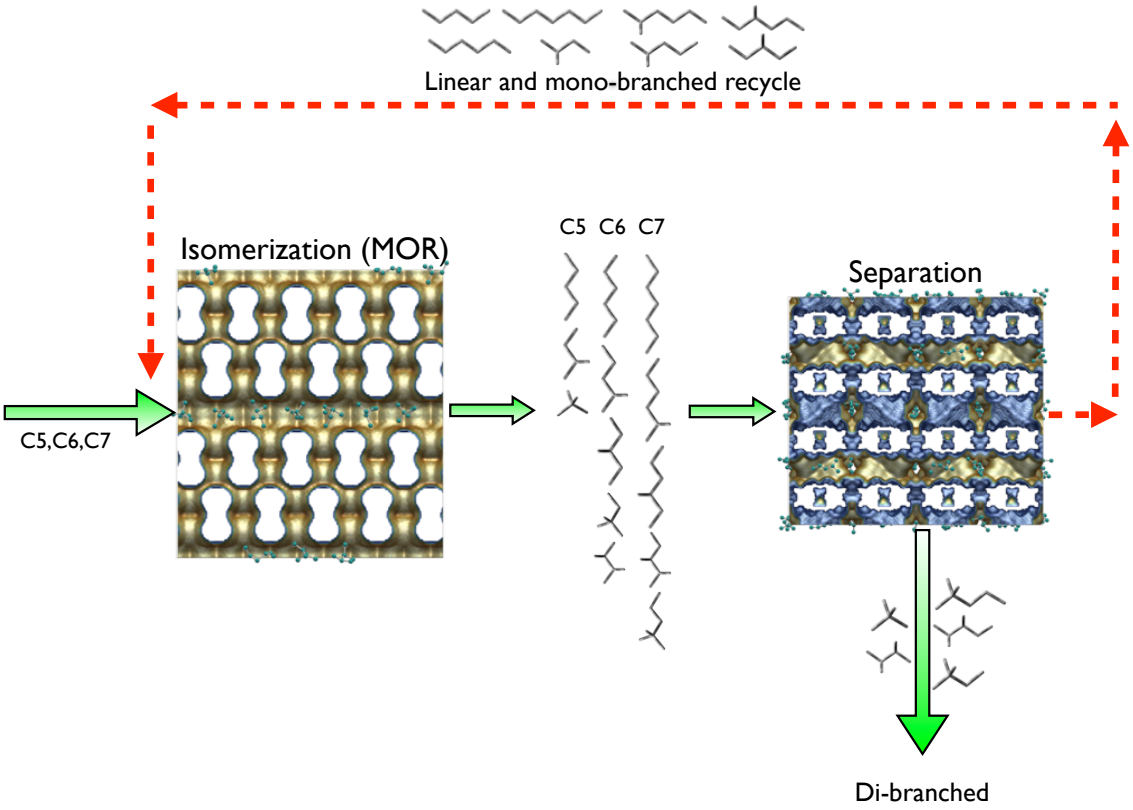

Figure 1: *Schematic of the separation process. The feed consists of mostly linear alkanes. In the first zone linear alkanes are isomerized to branched alkanes, usually using MOR-zeolite which is first converted into the acid form and then acid-leached to increase the silica/alumina ratio. The second zone separates linear and mono-branched (which are recycled back) from the desired di-branched alkanes (that become the isomerate product blending component). Our study focuses on optimizing this separation process by screening >100 nanoporous materials for their hexane separation efficiency. A recently synthesized material, ZIF-77, is shown to have superior selectivity, compared to current technology.*

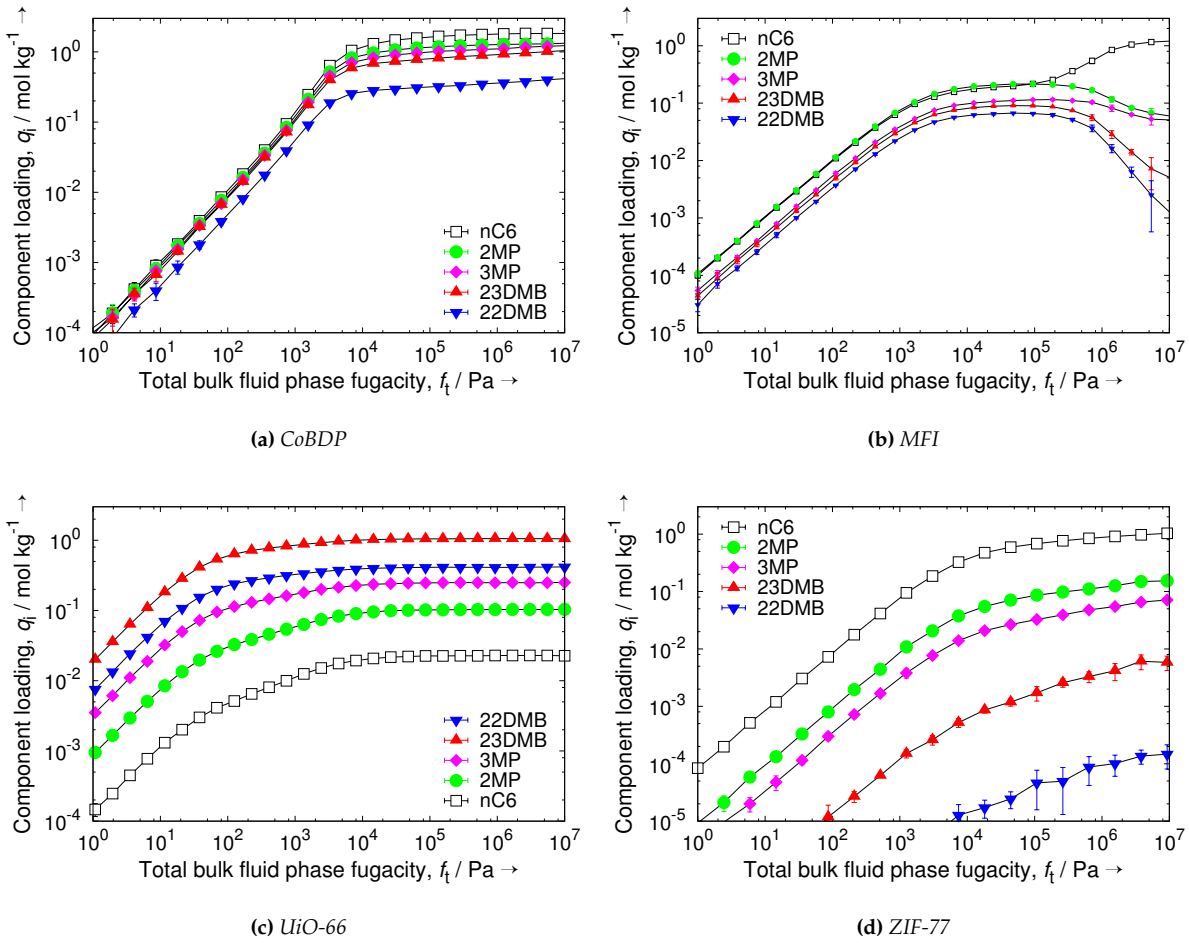

(a) *CoBDP* **(b)** *MFI*

(c) *UiO-66* **(d)** *ZIF-77*

Figure 2: *Equimolar mixture isotherms of C6 isomers in (a) CoBDP, (b) MFI, (c) UiO-66, and (d) ZIF-77 at 433K.*

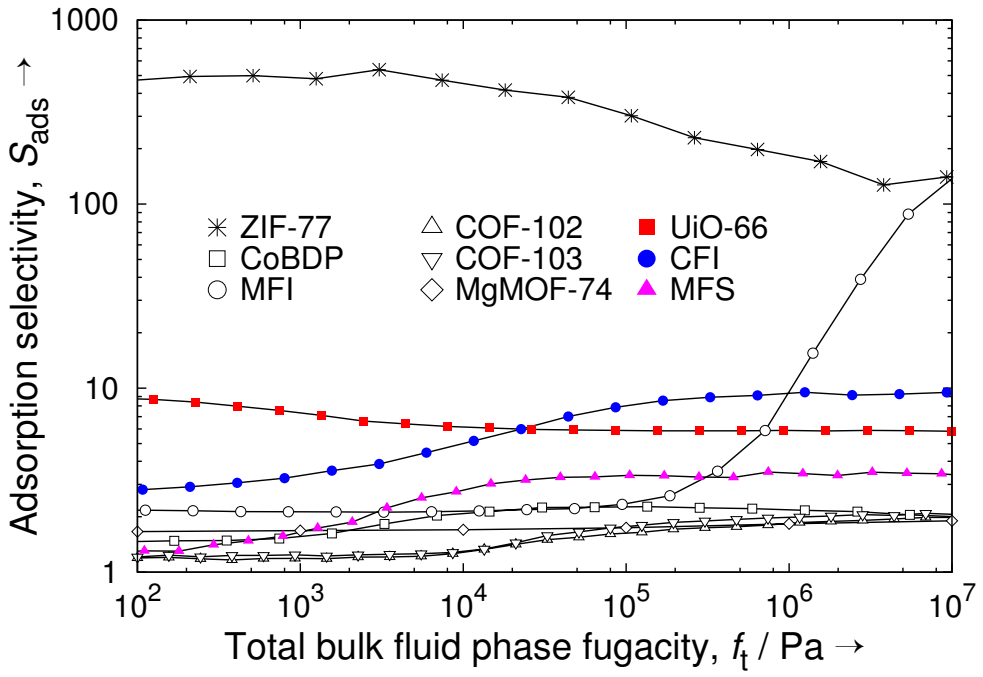

(a)

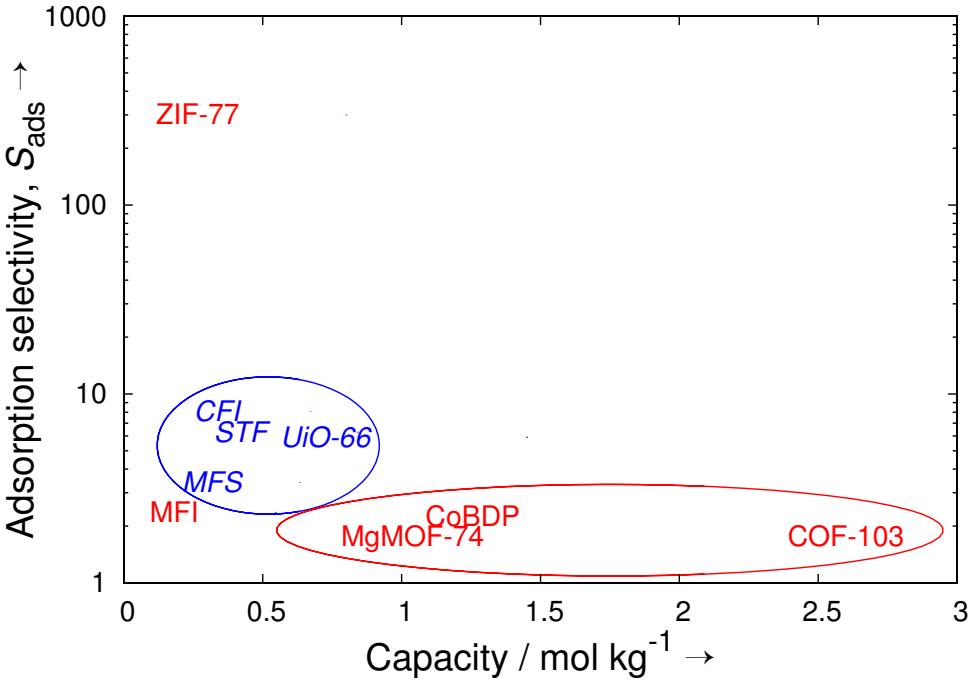

(b)

Figure 3: *Summary of the screening results: the adsorption selectivity S_{ads} (a) as a function of the total bulk fluid phase fugacity at 433 K, and (b) versus capacity for promising structures at 100 kPa. Typical operational reactor pressures are above atmospheric (above 10^5 Pa fugacity). Consider the separation of 5-component hexane isomer mixtures of nC6 (= component 1), 2MP (= component 2), 3MP (= component 3), 23DMB (= component 4), and 22DMB (= component 5) with partial fugacities, f_i, and corresponding loadings, q_i. For materials showing the normal hierarchy (star and open symbols in (a), red color in (b)), S_{ads} is defined as $S_{ads} = \frac{(q_1+q_2+q_3)/(q_4+q_5)}{(f_1+f_2+f_3)/(f_4+f_5)}$, and the capacity as the averaged loadings of linear and mono-branched isomers. For materials with a reverse adsorption hierarchy (closed symbols in (a), blue color in (b)), we defined $S_{ads} = \frac{(q_4+q_5)/(q_1+q_2+q_3)}{(f_4+f_5)/(f_1+f_2+f_3)}$, and capacity as the averaged loadings of the di-branched isomers.*

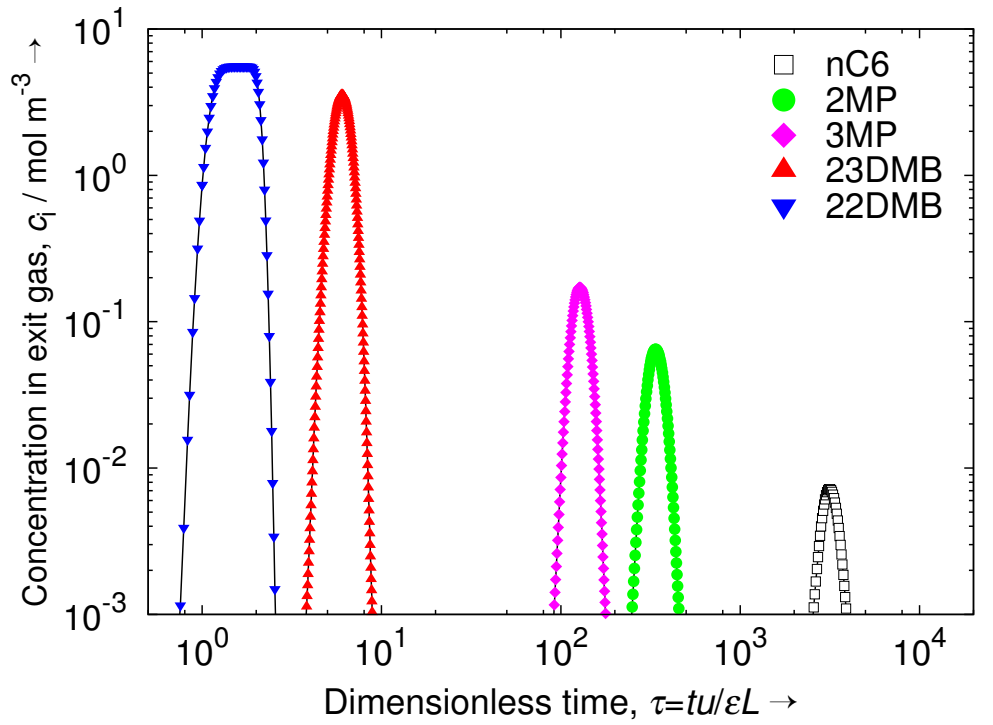

(a)

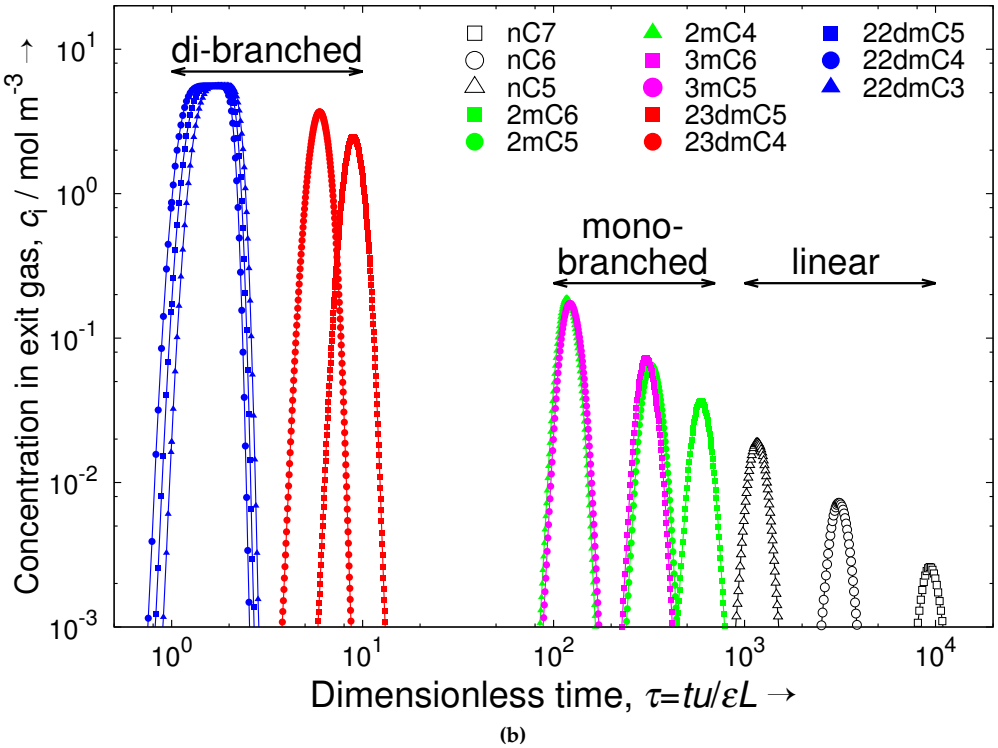

(b)

Figure 4: *Simulated pulse-style breakthrough curves of (a) C6 isomers, (b) C5/C6/C7 isomers in ZIF-77 at partial fugacities of the bulk fluid phase of 20 kPa and 433 K. The pulse-style breakthrough clearly shows that ZIF-77 is able to fractionate the individual components of a C6 mixture, and when it is fed an alkane mixture differing in chain length it is still able to fractionate the mixture into linear, mono-branched, and di-branched components. Video animations of the breakthrough behavior as a function of time of ZIF-77 and other selected structures are provided as Supporting Information.*

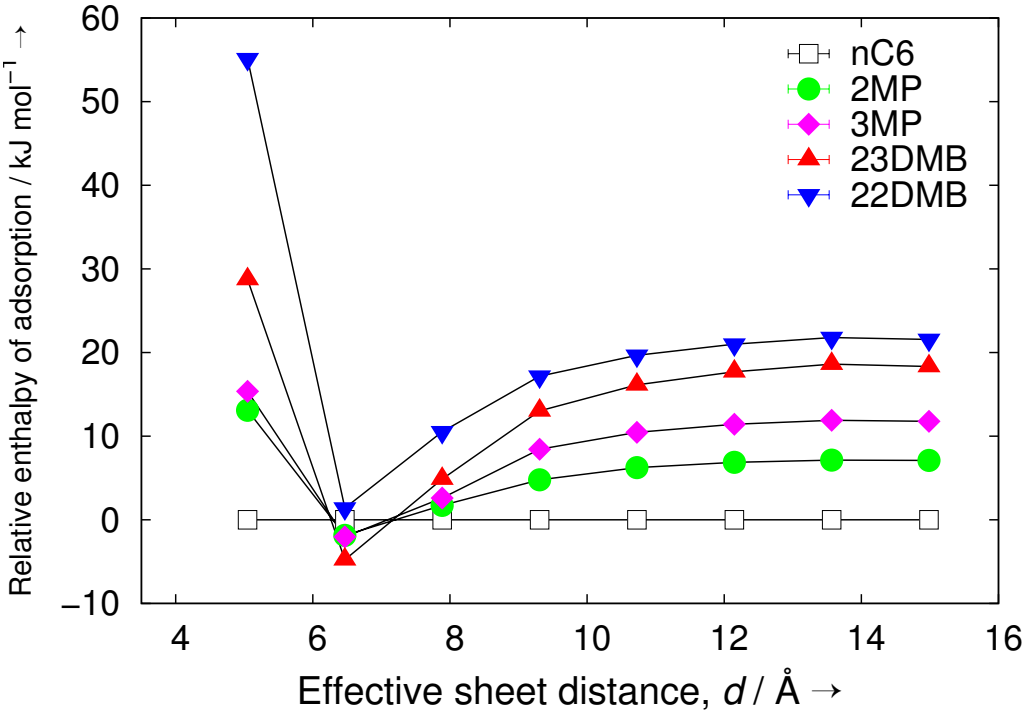

(a)

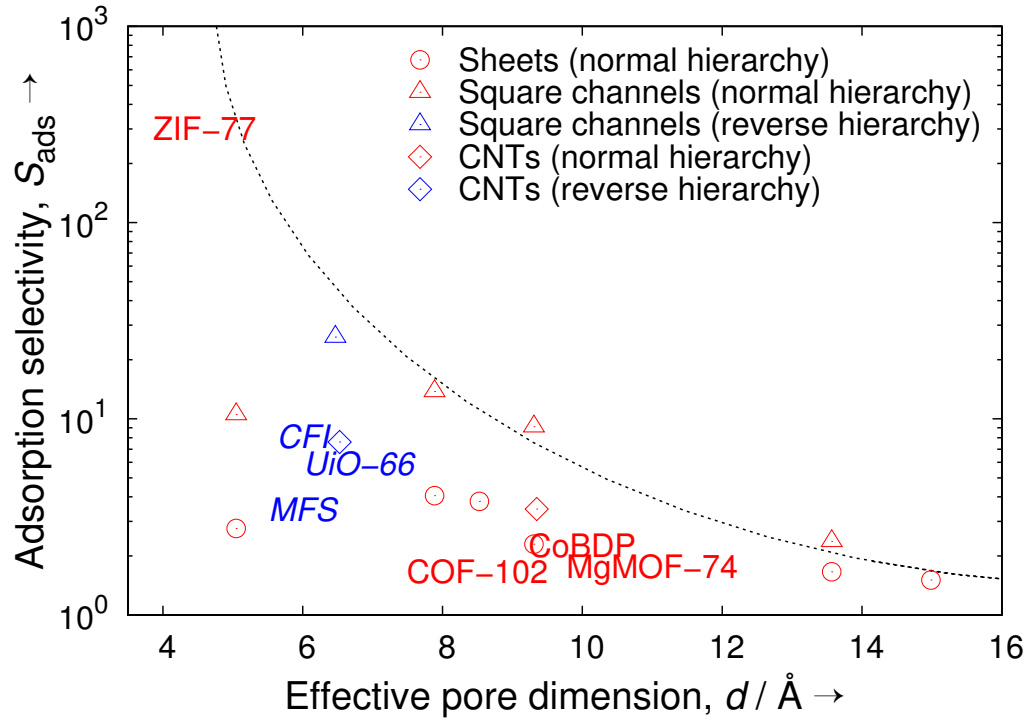

(b)

Figure 5: *Hexane isomer selectivity at 433K as a function of confinement, (a) enthalpy of adsorption relative to nC6 for graphite square channels at infinite dilution, (b) adsorption selectivity at 100 kPa. Red color denotes normal hierarchy, blue color reverse hierarchy, the dotted line shows the qualitative behavior of the selectivity.*

Bibliography

[1] M. Tuckerman, *Statistical Mechanics: Theory and Molecular Simulations*, Oxford University Press, New York, **2010**.

[2] M. Allen, D. Tildesley, *Computer Simulation of Liquids*, Clarendon Press, Oxford, **1987**.

[3] D. Frenkel, B. Smit, *Understanding Molecular Simulation 2nd Edition*, Academic Press, London, UK, **2002**.

[4] D. Rapaport, *The Art of Molecular Dynamics Simulation 2nd Edition*, Cambridge University Press, Cambridge, **2004**.

[5] A. Leach, *Molecular Modelling: Principles and Applications*, Prentice Hall, Longman, Essex, England, 2nd ed., **2001**.

[6] M. Martin, J. Siepmann, *J. Chem. Phys.* **1998**, *102*, 2569–2577.

[7] M. Martin, J. Siepmann, *J. Phys. Chem. B.* **1999**, *103*, 4508–4517.

[8] B. Chen, J. Siepmann, *J. Phys. Chem. B.* **1999**, *103*, 5370–5379.

[9] S. Nath, F. Escobedo, J. de Pablo, *J. Chem. Phys.* **1998**, *108*, 9905–9911.

[10] S. Natha, R. Khare, *J. Chem. Phys.* **2001**, *115*, 10837–10844.

[11] M. Martin, A. Thompson, T. Nenoff, *J. Chem. Phys.* **2001**, *114*, 7174–7181.

[12] J. Ryckaert, A. Bellemans, *Faraday Dicuss. Chem. Soc.* **1978**, *66*, 95–106.

[13] M. Macedonia, E. Maginn, *Mol. Phys.* **1999**, *96*, 1375–1390.

[14] A. Bezus, A. Kiselev, A. Lopatkin, P. Du, *J. Chem. Soc. Faraday Trans. II* **1978**, *74*, 367–379.

[15] T. Vlugt, M. Schenk, *J. Phys. Chem. B.* **2002**, *106*, 12757–12763.

[16] E. Jaramillo, S. Auerbach, *J. Phys. Chem. B* **1999**, *103*, 9589–9594.

[17] E. Beerdsen, B. Smit, S. Calero, *J. Phys. Chem. B* **2002**, *106*, 10659–10667.

[18] E. Beerdsen, D. Dubbeldam, B. Smit, T. Vlugt, S. Calero, *J. Phys. Chem. B* **2003**, *107*, 12088–12096.

[19] S. Mayo, B. Olafson, W. Goddard, *J. Phys. Chem.* **1990**, *94*, 8897–8909.

[20] A. Rappé, C. Casewit, K. Colwell, W. Goddard, W. Skiff, *J. Am. Chem. Soc.* **1992**, *114*, 10024–10035.

[21] D. Ford, D. Dubbeldam, R. Snurr, *Diffusion Fundamentals III* **2009**, *11*, 1–8.

[22] M. Martin, J. Siepmann, *J. Am. Chem. Soc.* **1997**, *119*, 8921–8924.

[23] A. Panagiotopoulos, *Int. J. Thermophys.* **1989**, *10*, 447–457.

[24] G. Martyna, M. Tuckerman, D. Tobias, M. Klein, *Mol. Phys.* **1996**, *87*, 1117–1157.

[25] D. Dubbeldam, D. Ford, D. Ellis, R. Snurr, *Mol. Sim.* **2009**, *35*, 1084–1097.

[26] F. Karavias, A. Myers, *Langmuir* **1991**, *7*, 3118–3126.

[27] T. Vlugt, E. Garcia-Perez, D. Dubbeldam, S. Ban, S. Calero, *J. Theory and Comput.* **2008**, *7*, 1107–1118.

[28] T. Duren, L. Sarkisov, O. Yaghi, R. Snurr, *Langmuir* **2004**, *20*, 2683–2689.

[29] T. Duren, F. Millange, G. Ferey, K. Walton, R. Snurr, *J. Phys. Chem. C* **2007**, *111*, 15350–15356.

[30] S. Brunauer, P. Emmett, E. Teller, *J. Am. Chem. Soc.* **1938**, *60*, 309–319.

[31] K. Walton, R. Snurr, *J. Am. Chem. Soc.* **2007**, *129*, 8852–8556.

[32] O. Talu, A. L. Myers, *AIChE. J.* **2001**, *47*, 1160–1168.

[33] L. Gelb, K. Gubbins, *Langmuir* **1999**, *15*, 305–308.

[34] A. Myers, J. Prausnitz, *AIChE J.* **1965**, *11*, 121–127.

[35] R. Krishna, J. Long, *J. Phys. Chem. C* **2011**, *115*, 12941–12950.

[36] R. Krishna, S. Calero, B. Smit, *Chem. Eng. J.* **2002**, *88*, 81–94.

[37] R. Krishna, R. Baur, *Sep. Purif. Technol.* **2008**, *33*, 213–253.

[38] R. Krishna, R. Baur, *University of Amsterdam* **2003**.

[39] H. Kooijman, R. Taylor, *AIChE J.* **1995**, *41*, 1852–1863.

[40] M. Michelsen, *AIChE J.* **1976**, *22*, 594–597.

[41] R. Bulirsch, J. Stoer, *Numer. Math.* **1966**, *8*, 1–14.

[42] R. Krishna, J. van Baten, *J. Membr. Sci.* **2011**, *377*, 249–260.

[43] K. Walton, M. LeVan, *Ind. Eng. Chem. Res.* **2003**, *42*, 6938–6948.

[44] E. Bloch, W. Queen, R. Krishna, J. Zadrozny, C. Brown, J. Long, *Science* **2012**, *335*, 1606–1610.

[45] Y. He, R. Krishna, B. Chen, *Energy Environ. Sci.* **2012**, *5*, 9107–9120.

[46] H. Wu, K. Yao, Y. Zhu, B. Li, Z. Shi, R. Krishna, *J. Phys. Chem. C* **2012**, *116*, 16609–16618.

[47] W. Schroeder, K. Martin, B. Lorensen, *The Visualization Toolkit: an object oriented approach to 3D graphics*, Kitware, Inc., Clifton Park, New York, USA, 4th ed., **1996**.

[48] D. Dubbeldam, S. Calero, T. Vlugt, R. Krishna, T. Maesen, E. Beerdsen, B. Smit, *Phys. Rev. Lett.* **2004**, *93*, art. no. 088302.

[49] D. Dubbeldam, S. Calero, T. Vlugt, R. Krishna, T. Maesen, B. Smit, *J. Phys. Chem. B* **2004**, *108*, 12301–12313.

[50] S. Calero, D. Dubbeldam, R. Krishna, B. Smit, T. Vlugt, J. Denayer, J. Martens, T. Maesen, *J. Am. Chem. Soc.* **2004**, *126*, 11377–11386.

[51] L. Sarkisov, T. Duren, R. Snurr, *Mol Phys* **2004**, *102*, 211–221.

[52] G. Garberoglio, A. Skoulidas, J. Johnson, *J. Phys. Chem. B.* **2005**, *109*, 13094–13103.

[53] Q. Yang, C. Zhong, *J. Phys. Chem. B.* **2005**, *109*, 11862–11864.

[54] Q. Yang, C. Zhong, *J. Phys. Chem. B.* **2006**, *110*, 17776–17783.

[55] P. Chowdhury, S. Mekala, F. Dreisbach, S. Gumma, *Micropor. Mesopor. Mater.* **2011**, *152*, 246–252.

[56] P. Bárcia, D. Guimarães, P. Mendes, J. Silva, V. Guillerm, H. Chevreau, C. Serre, A. Rodrigues, *Micropor. Mesopor. Mater.* **2011**, *139*, 67–73.

[57] D. Peralta, G. Chaplais, A. Simon-Masseron, K. Barthelet, G. Pirngruber, *Ind. Eng. Chem. Res.* **2012**, *51*, 4692–4702.

[58] J. Lee, D. Olson, L. P. abd T.J. Emge, J. Li, *Adv. Funct. Mater.* **2007**, *17*, 1255–1262.

[59] J. Richardson, Jr., E. Vogt, *Zeolites* **1992**, *12*, 13–19.

[60] J. Smith, J. Pluth, K. Andries, *Zeolites* **1993**, *13*, 166–169.

[61] J. Newsam, M. Treacy, W. T. Koetsier, C. de Gruyter, *Proc. Roy. Soc. A (London)* **1988**, *420*, 375–405.

[62] J. Pluth, J. Smith, *Am. Mineral.* **1990**, *75*, 501–507.

[63] P. Wagner, M. Yoshikawa, M. Lavallo, K. Tsuji, M. Tsapatsis, M. Davis, *Chem. Commun.* **1997**, 2179–2180.

[64] R. Lobo, M. Davis, *J. Am. Chem. Soc.* **1994**, *117*, 3766–3779.

[65] T. Wessels, C. Baerlocher, L. McCusker, E. Creyghton, *J. Am. Chem. Soc.* **1999**, *121*, 6242–6247.

[66] C. Baerlocher, L. McCusker, R. Chiappetta, *Microporous Mater.* **1994**, *2*, 269–280.

[67] J. Hriljac, M. Eddy, A. Cheetham, J. Donohue, G. Ray, *J. Solid State Chem.* **1993**, *106*, 66–72.

[68] D. Olson, *Zeolites* **1995**, *15*, 439–443.

[69] R. Morris, S. Weigel, N. Henson, L. Bull, M. Janicke, B. Chmelka, A. Cheetham, *J. Am. Chem. Soc.* **1994**, *116*, 11849–11855.

[70] K. Fischer, *N. Jb. Miner. Mh.* **1966**, *1*, 1–13.

[71] L. Villaescusa, P. Barrett, M. Camblor, *Angew. Chem. Int. ed.* **1999**, *38*, 1997–2000.

[72] G. Artioli, K. Stahl, *Zeolites* **1993**, *13*, 249–255.

[73] J. Newsam, *J. Phys. Chem.* **1989**, *93*, 7689–7694.

[74] E. Galli, *Rend. Soc. Ital. Mineral. Petrol.* **1975**, *31*, 599–612.

[75] S. Lawton, W. Rohrbaugh, *Science* **1990**, *247*, 1319–1322.

[76] C. Fyfe, H. Gies, G. Kokotailo, C. Pasztor, H. Strobl, D. Cox, *J. Am. Chem. Soc.* **1989**, *111*, 2470–2474.

[77] H. van Koningsveld, H. van Bekkum, J. Jansen, *Acta Cryst. B* **1987**, *43*, 127–132.

[78] J. Schlenker, J. Higgins, E. Valyocsik, *Zeolites* **1990**, *10*, 293–296.

[79] V. Gramlich, *Ph.D. Thesis ETH Zürich Switzerland* **1971**.

[80] C. Fyfe, H. Gies, G. Kokotailo, B. Marler, , D. Cox, *J. Phys. Chem.* **1990**, *94*, 3718–3721.

[81] M. Camblor, A. Corma, M.-J. Diaz-Cabanas, C. Baerlocher, *J. Phys. Chem. B* **1998**, *102*, 44–51.

[82] A. Alberti, G. Cruciani, E. Galli, G. Vezzalini, *Zeolites* **1996**, *17*, 457–461.

[83] P. Wagner, S. Zones, M. Davis, R. Medrud, *Angew. Chem. Int. Ed.* **1999**, *38*, 1269–1272.

[84] L. McCusker, C. Baerlocher, E. Jahn, M. Bulow, *Zeolites* **1991**, *11*, 308–313.

[85] M. Eddaoudi, J. Kim, N. Rosi, D. Vodak, J. Wachter, M. O'Keeffe, O. Yaghi, *Science* **2002**, *295*, 469–472.

[86] N. Rosi, J. Kim, M. Eddaoudi, B. Chen, M. O'Keeffe, O. Yaghi, *J. Am. Chem. Soc.* **2005**, *127*, 1504–1518.

[87] H. Chae, D. Siberio-Pre, J. Kim, M. Eddaoudi, A. Matzger, M.O'Keeffe, O. Yaghi, *Nature* **2004**, *427*, 523–527.

[88] H. Furukawa, N. Ko, Y. Go, N. Aratani, S. Choi, E. Choi, A. Yazaydin, R. Snurr, M. O'Keeffe, J. Kim, O. Yaghi, *Science* **2010**, *329*, 424–428.

[89] I. Eryazici, O. Farha, B. Hauser, A. O. Yazaydın, A. Sarjeant, S. Nguyen, J. Hu, *Cryst. Growth Des.* **2012**, *12*, 1075–1080.

[90] O. Farha, A. Yazaydin, I. Eryazici, C. Malliakas, B. Hauser, M. Kanatzidis, S. Nguyen, R. Snurr, J. Hupp, *Nat. Chem.* **2010**, *2*, 944–948.

[91] K. Barthelet, J. Marrot, D. Riou, G. Ferey, *Ang. Chem. Int. Ed.* **2002**, *41*, 281–284.

[92] C. Serre, F. Millange, C. Thouvenot, M. Nogues, G. Marsolier, D. Louer, G. Ferey, *J. Am. Chem. Soc.* **2002**, *124*, 13519–13526.

[93] C. Serre, C. Mellot-Draznieks, S. Surble, N. Audebrand, Y. Filinchuk, F. Ferey, *Science* **2007**, *315*, 1828–1831.

[94] G. Ferey, C. Serre, C. Mellot-Draznieks, F. Millange, S. Surble, J. Dutour, I. Margiolaki, *Ang. Chem. Int. Ed.* **2004**, *43*, 6296–6301.

[95] G. Ferey, C. Mellot-Draznieks, C. Serre, F. Millange, J. Dutour, S. Surble, I. Margiolaki, *Science* **2005**, *309*, 2040–2042.

[96] V. Guillerm, F. Ragon, M. Dan-Hardi, T. Devic, M. Vishnuvarthan, B. Campo, A. Vimont, G. Clet, Q. Yang, G. Maurin, G. Férey, A. Vittadini, S. Gross, C. Serre, *Angew. Chem. Int. Ed.* **2012**, *51*, 9267–9271.

[97] H. Li, M. Eddaoudi, T. Groy, O. Yaghi, *J. Am. Chem. Soc.* **1998**, *120*, 8571–8572.

[98] D. Dybtsev, H. Chun, K. Kim, *Ang. Chem. Int. Ed.* **2004**, *43*, 5033–5036.

[99] Y. Ling, Z.-X. Chen, F.-P. Zhai, Y.-M. Zhou, L.-H. Weng, D.-Y. Zhao, *Chem. Comm.* **2011**, *47*, 7197–7199.

[100] M. D. H.J. Choi, J. Long, *J. Am. Chem. Soc.* **2008**, *130*, 7848–7850.

[101] D. Zhao, D. Yuan, D. Sun, H. Zhou, *J. Am. Chem. Soc.* **2009**, *131*, 9186–9187.

[102] D. Yuan, D. Zhao, D. Sun, H. Zhou, *Angew. Chem. Int. Ed.* **2010**, *49*, 5357–5361.

[103] J. Cavka, S. Jakobsen, U. Olsbye, N. Guillou, C. Lamberti, S. Bordiga, K. Lillerud, *J. Am. Chem. Soc.* **2008**, *130*, 13850–13851.

[104] A. Schaate, P. Roy, A. Godt, J. Lippke, F. Waltz, M. Wiebcke, P. Behrens, *Chem. Eur. J.* **2011**, *17*, 6643–6651.

[105] A. Yazaydin, R. Snurr, T. Park, K. Koh, J. Liu, M. LeVan, A. Benin, P. Jakubczak, M.Lanuza, D. Galloway, J. Low, R. Willis, *J. Am. Chem. Soc.* **2009**, *131*, 18198–18199.

[106] B. Mu, Y. Huang, K. Walton, *Cryst. Eng. Comm.* **2010**, *12*, 2347–2349.

[107] K. Koh, A. Wong-Foy, A. Matzger, *Ang. Chem. Int. Ed.* **2008**, *120*, 689–692.

[108] A. Cote, A. Benin, N. Ockwig, M. O. A. Matzger, O. Yaghi, *Science* **2005**, *310*, 1166–1170.

[109] H. El-Kaderi, J. Hunt, J. Mendoza-Cortés, A. Côté, R. Taylor, M. O'Keeffe, O. Yaghi, *Science* **2007**, *316*, 268–272.

[110] J. Hunt, C. Doonan, J. LeVangie, A. Côté, O. Yaghi, *J. Am. Chem. Soc.* **2008**, *130*, 11872–11873.

[111] F. Uribe-Romo, J. Hunt, H. Furukawa, C. Klöck, M. O'Keeffe, O. Yaghi, *J. Am. Chem. Soc.* **2009**, *131*, 4570–4571.

[112] K. Park, Z. Ni, A. Cote, J. Choi, R. Huang, F. Uribe-Romo, H. Chae, M. O'Keeffe, O. Yaghi, *P. Natl. Acad. Sci. USA* **2006**, *103*, 10186–10191.

[113] H. Hayashi, A. Côté, H. Furukawa, M. O'Keeffe, O. Yaghi, *Nat. Mat.* **2007**, *6*, 501–506.

[114] R. Banerjee, A. Phan, B. Wang, C. Knobler, H. Furukawa, M. O'Keeffe, O. Yaghi, *Science* **2008**, *319*, 939–943.

[115] W. Morris, B. Leung, H. Furukawa, O. Yaghi, N. He, H. Hayashi, Y. Houndonougbo, M. Asta, B. Laird, O. Yaghi, *J. Am. Chem. Soc.* **2010**, *132*, 11006–11008.

[116] R. Banerjee, H. Furukawa, D. Britt, C. Knobler, M. O'Keeffe, O. Yaghi, *J. Am. Chem. Soc.* **2009**, *131*, 3875–3877.